



HAL
open science

Diffuse Interstellar Bands (DIBs): a new look at an old problem

Meriem El Yajouri

► **To cite this version:**

Meriem El Yajouri. Diffuse Interstellar Bands (DIBs): a new look at an old problem. Astrophysics [astro-ph]. Université Paris sciences et lettres, 2018. English. NNT : 2018PSLEO017 . tel-02122950

HAL Id: tel-02122950

<https://theses.hal.science/tel-02122950>

Submitted on 7 May 2019

HAL is a multi-disciplinary open access archive for the deposit and dissemination of scientific research documents, whether they are published or not. The documents may come from teaching and research institutions in France or abroad, or from public or private research centers.

L'archive ouverte pluridisciplinaire **HAL**, est destinée au dépôt et à la diffusion de documents scientifiques de niveau recherche, publiés ou non, émanant des établissements d'enseignement et de recherche français ou étrangers, des laboratoires publics ou privés.



THÈSE DE DOCTORAT
DE L'UNIVERSITÉ PSL

Préparée à l'Observatoire de Paris

**Diffuse Interstellar absorption Bands (DIBs):
a new look at an old problem**

Soutenue par

Meriem ELYAJOURI

Le 07 Novembre 2018

Ecole doctorale n° 127

**Astronomie et astrophysique
d'Île-de-France**

Spécialité

**ASTRONOMIE ET
ASTROPHYSIQUE**

Composition du jury :

Jacques, LÉBOURLOT Université Paris-Diderot, France	<i>Président</i>
François-Xavier, DESERT IPAG, France	<i>Rapporteur</i>
Paule, SONNENTRUCKER Space Telescope Science Institute, USA	<i>Rapporteuse</i>
Jan, CAMI University of Western Ontario, Canada	<i>Examineur</i>
Nick, COX ACRI-ST, France	<i>Examineur</i>
Christine, JOBLIN IRAP, France	<i>Examinatrice</i>
Alain, OMONT IAP, France	<i>Examineur</i>
Zouhair, BENKHALDOUN Université Cadi Ayyad, Maroc	<i>Membre invité</i>
Rosine, LALLEMENT Observatoire de Paris, France	<i>Directrice de thèse</i>

To my father,

إلى أبي،

'We shall not cease from exploration, and the end of all our exploring will be to arrive where we started and know the place for the first time.'

T. S. Eliot

Acknowledgements

Je tiens à exprimer ma reconnaissance à toutes celles et tous ceux qui m'ont encouragée et qui ont contribué à la réalisation de la présente thèse. Au-delà du grade universitaire, une thèse de doctorat est avant tout une aventure humaine. Et je n'ai pas vu passer les trois dernières années, tellement elles furent riches en émotion, car marquées par des rencontres fascinantes, des données captivantes, des collaborations fructueuses, et surtout beaucoup d'épanouissement.

Tout d'abord je remercie le Domaine d'Intérêt Majeur en Astrophysique et Conditions d'Apparition de la Vie (DIM ACAV) de la Région Île-de-France pour avoir apporté le financement nécessaire à ce projet.

Je tiens à remercier, avec toute mon amitié, ma directrice de thèse Rosine Lallement, à qui je dois ce sujet de recherche. Cette thèse est le fruit d'une collaboration de plus de trois années au sein de son équipe. Une équipe que j'ai intégrée un peu malgré moi car au tout début j'étais décidée à ne faire qu'un stage, mais j'y suis finalement restée plus de trois ans et c'est en grande partie grâce à Rosine. Son encadrement de qualité, son soutien moral et son ouverture d'esprit m'ont donné le courage d'aller jusqu'au bout. Je tiens enfin à la remercier de m'avoir fait assez confiance pour me laisser réaliser un projet qui me tenait à cœur, le SpaceBus. Je lui en suis toujours reconnaissante.

Mes remerciements s'adressent également à Ana Monreal-Ibero qui m'a co-encadrée pendant mon stage du master et durant la première année de cette thèse. Merci d'avoir quotidiennement trouvé du temps entre deux codes Python pour m'accueillir dans la bonne humeur et discuter de l'avancement de mes travaux.

Je tiens à remercier très chaleureusement le jury, qui a porté une grande attention à mon travail et m'a donné de précieux conseils. Je remercie en particulier mes deux rapporteurs, Paule Sonnentrucker d'être venue des États-Unis et François-Xavier Désert de Grenoble et de leur disponibilité bien qu'ils soient très sollicités.

J'adresse mes plus sincères remerciements à Jan Cami et Nick Cox qui m'ont éclairée de leurs conseils avisés et dont les thèmes de recherche ont fortement inspiré cette thèse. Je tiens également à remercier Christine Joblin et Alain Omont qui ont bien voulu être examinateurs. Merci pour votre relecture et pour vos commentaires qui m'ont permis de finaliser mon manuscrit.

J'étais très heureuse que Jacques Lebourlot préside le jury de ma soutenance car il m'a non seulement initiée à la recherche lorsque j'étais son étudiante en master, mais il m'a aussi prodigué, avec sa casquette de directeur de

l'École Doctorale, de nombreux conseils pour bien débiter le troisième cycle universitaire dont cette thèse est l'accomplissement.

Je remercie également Zouhair Benkhaldoun de l'honneur qu'il m'a fait en acceptant d'être membre du jury, sache que j'en suis très fière car si l'astronomie au Maroc tourne avec autant de projets, c'est en grande partie grâce à toi.

Je tiens à remercier toutes les personnes du laboratoire GEPI à commencer par le directeur Piercarlo Bonifacio pour les moyens qu'il a mis à notre disposition. Je remercie également Stephane Thomas et Sabine Kimmel pour leur amabilité et aide. Pour m'avoir accueillie au sein de l'équipe Physique Stellaire et Galactique (PSG), j'ai une pensée particulière à Frederic Arenou, David Katz, Noël Robichon, Monique et François Spite, Catherine Turon, Frédéric Royer, Clément Hottier, Carine Babusiaux, Laura Ruiz Dern et Elisabeth Caffau.

Grazie à ma *co-bureau* Letizia Capitanio, nous avons partagé bien au-delà de notre espace vital au Copernic B, un goût pour le Milieu Interstellaire et les cookies (et un dégoût pour le cidre Framboise). Je te souhaite une bonne continuation pour tes projets, et n'oublie pas : 'surtout la santé !'.

Je tiens maintenant à témoigner ma gratitude aux membres de la collaboration EDIBLES. Je sais la chance que j'ai de travailler au sein de cette collaboration, ce qui, je l'espère, durera longtemps encore. J'ai une pensée particulière (encore une fois) pour Nick Cox, grâce à qui ce projet a vu le jour, il est probablement la personne qui a le plus compté dans ma formation sur les DIBs. Je remercie également Jonathan Smoker, Amin Farhang, Peter Sarre, Farid Salama, Evelyne Roueff, Xavier Bacalla et Harold Linnartz car c'est vraiment un plaisir de collaborer avec des personnes aussi efficaces et sérieuses. Sans oublier Martin Cordiner qui a toujours répondu avec calme et patience aux questions dont je l'accablais. Il ne fait aucun doute que nos échanges autour des DIBs ont marqué mon approche du sujet.

De même, j'adresse mes remerciements aux membres du projet STILISM, en particulier, Quentin Remy et Isabelle Grenier pour les différents échanges et Jean-luc Vergely pour qui les problèmes d'inversion n'ont aucun secret.

Quant au monitorat que j'ai eu l'occasion d'effectuer pendant deux ans à l'Université Paris Diderot, merci aux élèves de l'Université et de l'IUT d'en avoir fait une expérience enrichissante. Je remercie également Isabelle Leborgne, Claude Bazin et Thierry Stoehr pour m'avoir accueillie au sein de leur équipe et Catherine Girard pour le café entre deux cours. De même, je remercie Michel Perreau de m'avoir confié ses TPs de mécanique et Jared Lolli et Thomas Vourc'h pour les différentes améliorations des énoncés.

J'ai toujours attaché une très grande importance à la diffusion des connaissances. Et ces trois dernières années étaient également l'occasion de

découvrir le volet *Outreach* de notre métier. Ma plus belle expérience fut certainement l'organisation du SpaceBus. Il me faut plus particulièrement dire merci à Mehdi Jouahri et Youssef El Aoufir qui ont concrétisé ce rêve. Sachez que ma reconnaissance humaine est sans limite.

A mes amis de l'Observatoire d'Oukaimeden et du club HEPAC, c'est toujours un plaisir de vous rendre visite et de partager une bonne partie de cartes ou une soirée d'observation à Oukaimeden. J'ai une pensée particulière aux camarades thésards à qui je souhaite beaucoup de courage : Taha Shisseh, Hamza Ajeddig, Abdelkarim Boskri, Khalid Berkaoui, Meryem Guennoun, Youssef El Jariri, Jamila Rguig, Amal Loutfi, Youssef Moulane, Dalal El Youssfi et tous les autres !

J'ai eu également la chance d'effectuer une mission de médiation scientifique dans le cadre magnifique du Palais de la découverte. Un grand merci à Sébastien Fontaine, Alain Redding, Thebault Philippe, Monica Rotaru et Nathalie Berthier pour leur dynamisme et leur gentillesse.

A mes amis de l'Uranoscope, en particulier Christian Bourdeille et Dominique Richard et à ceux de *on the moon again*, François Colas, Sylvain Bouley et Brigitte Zanda, merci d'être toujours aussi passionnés.

A mes amis de l'initiative africaine pour les sciences planétaires, David Baratoux, Hasnaa Chennaoui et Maram Kaire, merci pour leur grande implication. Je suis fière de faire partie de cette belle aventure.

Aux chercheurs de l'Observatoire de Paris, Françoise Combes, Alain Dore-soundiram, Vincent Coudé du Foresto, Fabrice Mottez, Daniel Rouen et Didier Pelat, merci pour tout le temps et l'énergie qu'ils consacrent à la diffusion des connaissances et pour leurs conseils toujours pertinents.

Mon parcours n'aurait jamais été ce qu'il est devenu sans mon passage par les Masters 1 et 2 de l'Université Pierre et Marie Curie. J'ai une pensée particulière pour mes enseignants Frédéric Daigne et Marie Christine Angonin qui ont cru en moi et m'ont donné ce goût pour la recherche. Vous avez fait un pari remarquable en soutenant une jeune étudiante tout juste arrivée en France. Merci, sans votre soutien, rien de cela n'existerait. Je remercie également François Levrier, Laurent Verstraete et Stéphane Corbel qui se sont toujours montrés disponibles pour m'aider pendant mon M2. Je souhaite également remercier Jacqueline Plancy, Agnès Leguerer et Géraldine Gaillant pour leur accompagnement et leur encouragement.

Je tiens à présent à remercier une série de personnes qui ont croisé mon chemin et qui ont beaucoup apporté sur le plan moral. A commencer par Jan Cami ! Bien plus qu'un collaborateur, il a toujours été veillant et son aide a vraiment été inestimable. Il est toujours bon de savoir que je peux compter sur son soutien. *Bedankt mentor voor alles wat je me geleerd hebt!*

Je remercie mes amis du master 1 avec une pensée particulière à Gilbert N'Gabo surtout pour les piques-niques et les soirées Opéra. Je te souhaite beaucoup de courage pour ta thèse et je n'oublie pas le voyage au Rwanda.

Aux amazones, Tabatha Sauvaget, Diane Berard, Charlotte Gehan et Isadora Bicalho. Merci pour nos voyages, fous rires et câlins inopinés, que ce soit au Maroc, à Paris ou aux US. J'en garde de supers souvenirs, en particulier, les soirées chez Isa, l'éclipse 2018 et le SpaceBus. Tous ces moments vont me manquer !

Je remercie doublement Isa pour m'avoir épaulée dans les moments difficiles de la thèse, de m'avoir rappelé qu'il fallait manger ou dormir, et d'avoir partagé si souvent son bureau à Denfert et ses biscuits vegan avec moi. *Adoro-te Isa*. Merci d'être devenue une véritable amie.

Sans oublier Guillaume Voisin (pour la chute dans le désert !), Alexandre Le Tiec, Friedrich Anders, Anelise Audibert, Eduardo Balbinot, Benoit Tabone, William Polycarpe, Prasanna Deshapriya, Jean-Baptiste Vielfaure, Miguel Marques, François Joint, Evan Eames et Lisa Bardou pour leur amitié et leur festivité.

A mes amis de la cité universitaire internationale de Paris et tout particulièrement ceux avec qui j'ai cohabité à la maison du Maroc et qui m'ont très souvent encouragée ou accompagnée pendant les nuits blanches à la bibliothèque : Mostafa Mouaddine (surtout pour les fajitas), Mehdi Amraoui (pour les balades nocturnes), Youssef Mourchid (pour les cafés vanille), et la trésorerie team, Zakaria Sebaa, Samih Smidi, Abderafie, Mohamed Ahib, pour leur bonne humeur et leur encouragement.

Merci à la famille Irzi, de me sentir chez eux comme dans une seconde famille. A Soukaina et Fati, merci pour les escapades en voiture, les confidences le long de la Seine et les repas bien caloriques du dimanche et des fêtes.

Merci à la *UIR squad Paris*, Hind El Messaoudi et Mehdi El Hakimi d'avoir été toujours partants pour partager une danse, Aymane Rbai pour les one-man-shows, les concerts de Jazz et les tours en trottinette, Marwane Boutfirass pour *David August*, les mix et les soirées *loup-garou* et Issam Benabdelkader pour les débats passionnants. Je suis heureuse de pouvoir toujours compter sur vous depuis la prépa.

A mes amis d'enfance, Anass Cherkaoui Dekkaki que le hasard de la vie a remis sur mon chemin, Aqil Cheddadi et Chahrazad Bekkaoui. Grâce à vous *le papillon n'oublie pas qu'il a été chenille*.

A Sofia Drissi, que je n'ai sûrement jamais assez remerciée d'avoir été là tout au long de cette aventure, et surtout d'avoir supporté mes insomnies et mon humeur matinale. Merci d'être devenue une véritable confidente. Avec

toute mon affection, j'ai également une pensée pour toute la famille Drissi pour son soutien constant.

A Gatsby le magnifique, merci d'avoir su trouver les mots, en particulier les fameux kika, pour me faire rire et m'apaiser lorsque je doutais. Merci pour l'intrication qui m'a permis de survivre tout au long de ma thèse. Merci pour nos soirées passées à refaire le monde autour d'un verre, au coin d'une rue ou sur un air de Tchaïkovsky. Merci d'avoir cru en moi comme j'aimerais croire en moi-même.

Enfin, je suis infiniment reconnaissante à ma famille, et surtout à mes parents. Merci Papa, merci Maman pour m'avoir soutenue dans mes choix, quels qu'ils soient. A Omar d'avoir cru en cette petite sœur têtue et pour son soutien sans faille, merci d'avoir toujours ajouté une touche d'originalité à mes projets. Sache que je crois beaucoup en toi. A Hakim pour ses défis et surtout pour sa méthode de travail qui a beaucoup influencé la mienne, sans oublier son goût pour le café et la musique. A Imane ma *Nounna*, je la remercie tout particulièrement de son aide pendant la phase terminale de cette thèse, et du coup de main dans l'organisation du workshop et du fameux pot de thèse. J'ai une pensée particulière également à mes grands-parents, Tata Leila, Oumama et surtout au petit dernier, Ismail, qui sans le savoir, m'a donné des moments d'insouciance dans ces derniers mois de rédaction. Vous êtes le moteur de ma progression.

Abstract

The interstellar species responsible for the Diffuse Interstellar Bands (DIBs), the hundreds of irregular absorptions observed since decades in spectra of reddened stars or of galaxies, are still unknown, at the exception of several bands now very convincingly attributed to the buckminsterfullerene cation C_{60}^+ . There is a large consensus recently reached about the nature of the DIB carriers, thought to be large carbonaceous molecules in the gaseous phase of the interstellar medium (ISM). These complex molecules are one of the links in the process cycle linked to the formation of stars (and their planets) by collapse of clouds until the end of the stars life, their explosion and ejection of modified materials into space, matter that will feed subsequent generations of stars. This evolutionary cycle is fundamental and one of the pillars of astrophysics, many outstanding questions are associated with it (evolution of galaxies, dark matter, etc.). Being likely a very large, if not the largest reservoir of organic matter in the Universe, the search for DIB carriers properties and identifications is more than ever of fundamental interest.

The identification of a DIB carrier requires irrefutable coincidences between the observed spectral signatures of a given species in laboratory spectra and their counterparts in astronomical spectra. This proved to be extremely difficult and only the fullerene cation passed this test, as indicated above. One of the difficulties lies in the large and ever-increasing number of mostly uncorrelated DIBs and in the consensus idea that this variety implies the existence of an equally large number of different macromolecules. The laboratory match with astronomical observations can be optimized if the sheer number of possible species to be studied in the laboratory can be limited by constraints on the relevant and realistic spatial conditions, *i.e.*, molecules and ions that should be free, cold (<100 K) and exposed to some sort of energy mostly VUV (vacuum UV) photons. Such preselection can be carried out through in-depth studies of the physical and chemical properties of the DIB carriers. These properties can be based on the analysis of very detailed multi-species data from high spectral resolution observations, statistical studies based on large spectroscopic surveys or specific tomographic studies of selected clouds. The work presented in this thesis corresponds to a combination of these three different observational aspects.

All types of DIB spectral analyses have common data cleaning requirements, in particular the removal of telluric lines, the untangling of stellar-interstellar features and DIB extraction using specific codes and stacking methods, and finally the search for information on dust, known gaseous species and the physical properties associated with each line of sight.

To do this, during this thesis, I learned to deal with these different aspects, to improve or design adapted spectral analysis codes and I was able to contribute to several innovative techniques in related DIB issues.

I have also learned to use extended databases from large programs dedicated to infrared or visible spectroscopy of the stars of the Milky Way.

The work presented in this document is based on spectroscopic surveys and specific observation programs. I made extensive use of the high quality spectra of the SDSS/APOGEE near infrared (NIR) survey, I performed the first analyses of the high resolution-high signal optical spectra of the more recent EDIBLES survey at the VLT, I used the NIR data of a specific program recorded with KMOS at the VLT and, finally, TBL/NARVAL and CFHT/EspaDons optical spectra from the archive or specific programs. The main products of the thesis work are of several types:

- new extended catalogs of NIR DIBs,
- identification of potential new DIBs,
- the first 3D tomography of a DIB in a single dense cloud,
- additional links between ionizing conditions, opacity of dust, molecular content and DIB strength,
- new spectral profiles of about 30 DIBs with many additional details, including the particularly interesting series of low DIBs associated with C_2 molecules and opaque clouds,
- a first empirical relationship between DIB strength, dust extinction and Planck optical depth of emitting dust for off-Plane nearby clouds.

All these results provide additional clues in the search for the formation and destruction of DIB carriers:

- catalogs are ingredients for 3D mapping of a DIB carrier or more generally additional ingredients for 3D mapping of interstellar clouds,
- new DIB candidates and substructures in DIB profiles constrain future identification in the laboratory,
- DIB tomography in individual clouds, hierarchy of DIBs in response to the ionization field and molecules and links with dust absorption and emission may help constraining the processes of formation/destruction/ionization of DIB carriers around and within the molecular clouds.

Contents

Contents	xiii
1 Introduction	1
1.1 Our Galaxy	1
1.2 A Little Bit of History	2
1.2.1 Discovery of dust	2
1.2.2 Discovery of gas	4
1.3 The Interstellar Medium	6
1.4 Recycling the ISM	9
1.5 The Interstellar Matter	10
1.5.1 Interstellar Gas	10
1.5.2 Dust	11
1.6 The Diffuse Interstellar Bands	13
1.6.1 Observational properties	14
1.7 DIB carriers	18
1.7.1 DIB carriers: PAHs?	19
1.7.2 DIB carriers: Fullerenes?	23
1.8 Thesis Overview	24
Part I. Sightlines survey	
<i>"One DIB, many targets"</i>	29
2 A catalog of 1.5273 μm Diffuse Interstellar Bands based on APOGEE Hot Telluric Calibrators	31
2.1 Introduction	32
2.2 The data	33
2.2.1 APOGEE overview	33
2.2.2 The APOGEE telluric standard stars	33
2.2.3 Used information from the APOGEE Archive	34

2.3	Data analysis	35
2.3.1	Profile fitting	36
2.3.2	DIB equivalent width and error estimates	37
2.4	Validation criteria	39
2.4.1	Selection of fitted absorptions	39
2.4.2	Special cases	46
2.5	The catalog	46
2.6	Summary	50
3	A catalog of 1.5273 μm Diffuse Interstellar Bands based on late-type stars	53
3.1	Introduction	53
3.2	Cannon model spectra (new in DR14)	54
3.3	DIB extraction	55
3.3.1	Automated fitting method	55
3.3.2	DIB upper limit estimate in case of no convergence or no DIB detection	57
3.3.3	The catalog	58
3.4	Conclusion	62
	Part II. Potential applications of DIB catalogs	63
4	DIBs as tracers of the nearby ISM	65
4.1	Introduction: DIBs as proxies for column densities of IS matter	65
4.2	Contribution to 3D ISM mapping	68
4.3	First 3D maps based on APOGEE DR14 DIB catalog	87
4.4	Conclusion	88
5	Conditions for DIB formation: a new view on the "skin effect"	91
5.1	Introduction	92
5.2	Description of the public catalogs used in this study	95
5.2.1	SDSS/APOGEE spectra	95
5.2.2	Starhorse extinction and distance database	95
5.2.3	Planck Galactic dust data	95
5.3	DIB and dust extinction	96
5.4	The DIB carrier depletion illustrated with Planck	100
5.5	Conclusion	107
	Part III. Sightlines survey: "Few DIBs, many targets"	111
6	Weak Near-infrared diffuse interstellar bands	113
6.1	Introduction	114
6.2	Data	115

6.2.1	APOGEE TSS data	115
6.2.2	New optical spectra	115
6.3	Catalog of $\lambda\lambda 15617, 15653,$ and 15673 DIBs	116
6.3.1	Fitting method	116
6.3.2	Error estimates	117
6.3.3	DIB characteristics	118
6.4	Search for the weakest bands	121
6.5	Correlative studies	124
6.5.1	NIR-NIR DIB correlations	126
6.5.2	Extraction of optical DIBs from APOGEE TSS follow-up observations	128
6.5.3	NIR-visible comparisons	128
6.5.4	Influence of the environment on the $\lambda 15273$ DIB: detection of an edge effect for the $\lambda 15273$ DIB	130
6.6	Conclusion	131
 Part IV. "One DIB, one cloud"		147
7	Tomography of single cloud	149
7.1	Introduction	150
7.2	Observations and data reduction	151
7.3	Extraction of the interstellar spectrum	152
7.3.1	Synthetic stellar and telluric spectra	152
7.3.2	Fitting method	153
7.4	15273 \AA DIB characterization	154
7.4.1	Simplified inversion	154
7.5	Discussion	158
 Part V. Large survey: "Many DIBs, few carefully selected targets"		161
8	Description of the EDIBLES survey	163
8.1	Overview	163
8.2	Project description, survey sample, and quality assessment (Article B2)	164
9	Towards a new DIB atlas	185
9.1	Line-of-sight structure from extracted IS gaseous lines	185
9.2	Searching for IS features	190
10	Characterization of DIB profiles	197
10.1	C_2 -DIBs profiles	199
10.1.1	Introduction	200

CONTENTS

10.1.2	C ₂ single-cloud sample selection	201
10.1.3	Interstellar C ₂ lines: detection and analysis	203
10.1.4	Extractions of the C ₂ -DIBs	205
10.1.5	Variability of profiles among the eighteen C ₂ -DIBs	211
10.1.6	Prominent sub-structures and average spectral profiles	214
10.1.7	Search for profile variability among the sightlines	216
10.1.8	Correlational studies	219
10.1.9	Summary and conclusion	224
10.2	Profiles of strong DIBs	225
11	Conclusion and perspectives	235
11.1	General conclusions	235
11.2	Novelties	236
11.3	Perspectives	237
A	$\lambda\lambda$15617, 15653, 15673 NIR DIBs toward TSS targets	241
B	Examples of Barnard 68 background star spectra	247
C	EDIBLES data: gas line fitting in the search for cloud structures and mono-cloud sightlines	253
C.1	NaI-UV extractions	253
C.2	NaI D2-D1 line extractions	263
C.3	CaII K-H extractions	274
	Bibliography	285

Chapter 1

Introduction

-Here truly is a hole in the sky-

William Herschel

1.1 Our Galaxy

If one ever gets a chance to walk away from the city, far from the light pollution (or moonlight), one might see the spectacular vision of a huge cosmic city traced over the sky (Fig. 11). This is our Galaxy, the Milky Way, who appears as an extended white trail across the night sky. Unfortunately, being inside the Galaxy, our view is limited to this disk-shaped structure in profile.

The Milky Way is believed to be a barred spiral galaxy, and what we see when we look at this hazy light band of stars is our place from within. We are a part of an enormous star gathering, and the Sun is only one of the 100-400 billion stars that composed spiral arms of the Galaxy.

Once we look at the Milky Way from inside the disk, there appears to be more than stars. The naked eye can distinguish large dark regions – clouds where gas and dust are intimately mixed– which rub shoulders with bright areas, referred to as nebulae which are mainly composed of gas illuminated by nearby stars. These dark spots are produced by dust¹. The clouds pass in front of stars that try to pierce them with light but some clouds manage to completely mask starlight.

¹In astronomy, dust refers to small solid particles, often referred to as "smoke particles". Not to be confused with Philip Pullman's dust, as discussed in His "Dark Materials" trilogy, nor to the household dust.



Figure 11 A view of the Milky Way as seen from a dark site with little light pollution (Oukaimeden Observatory, Morocco). Courtesy: Observatory of Oukaimeden's team.

In fact, the space between the stars is not empty. It contains large quantities of gas and dust called the interstellar medium (ISM). Clouds of all dimensions are pressed in the disk of our galaxy creating some of the most beautiful objects of deep space as illustrated in Fig. 12.

However, the interstellar medium is more than a work of art: it holds the secret of the birth, formation, and death of stars.

1.2 A Little Bit of History

1.2.1 Discovery of dust

In 1784, William Herschel pointed his telescope towards the Scorpius constellation, where he detected an unusual vacant area. This observation led him to publish *"On the Construction of the Heavens"* the following year, a paper where he described this detection as *"a hole in the sky"* (Herschel 1785). Herschel's discovery went unnoticed until the correspondence between his sister Caroline and his son John Herschel in 1833 where she asked him to *"see if there is not something remarkable in the lower part of the Scorpion to be found [...] It was something more than a total absence of stars"* (the entire correspondence can be found in a recent historical review by Wolfgang Steinicke



Figure 12 Hubble's view of the Eagle Nebula. Credit: NASA, ESA, and The Hubble Heritage Team (STScI/AURA).

(Steinicke 2016)). Unfortunately, none of them had understood the hole's cause.

A better understanding was reached in the first quarter of the twentieth century when Edward Emerson Barnard used astrophotography to map out these dark regions and published the first photographic atlas of 182 "*dark markings of the sky*" (Barnard 1919)². Figure 13 shows an example of these regions near Theta Ophiuchi. Barnard regarded many of these dark patches as "*really obscuring bodies nearer to us than the distant stars*". Soon after came the works of Bart J. Bok, who was the first to point a link between Barnard objects and stellar formation through analyzing the inner compact cores, which would later be named after him (Bok 1948).

Barnard clouds and Bok globules are now known as dark clouds (or dense clouds). They appear dark because they do not emit at optical wavelengths and their dust blocks the light of the stars. This extinction property (the dimming of the light from the stars) was introduced by Robert Jules Trumpler (1930), who viewed the interstellar matter as a composition of free atoms, like Ca and Na, as well as "*fine cosmic dust particles of various sizes*" which produce the excess of colors by Rayleigh scattering.

²The Atlas was updated and enlarged in Barnard et al. (1927)

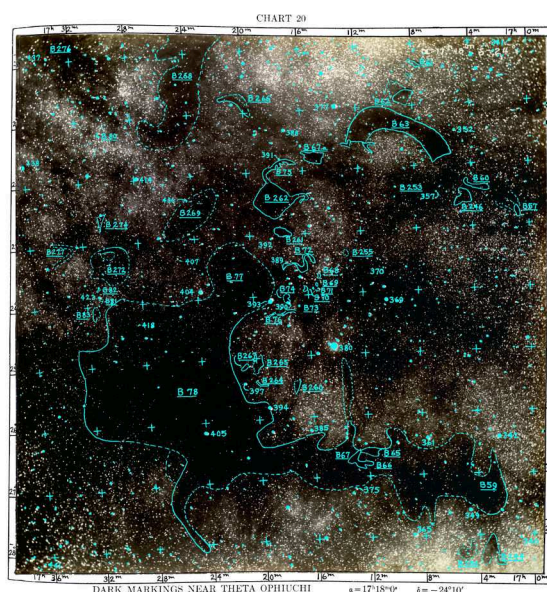


Figure 13 Dark Markings near Theta Ophiuchi. Plate chart number 20 from “*A Photographic Atlas of Selected Regions of the Milky Way*” by (Barnard et al. 1927). The chart shows the region around Theta Ophiuchi star (380). Note the dark S-shaped nebulae B72 (known as the Snake Nebula). Also seen at the north are the curled nebulae B75 and B262. Here, a high concentration of dust and molecular gas absorb practically all visible light emitted from background stars.

1.2.2 Discovery of gas

The first observational evidence of a non-empty environment between the stars comes from spectroscopy. In the winters of 1901/1902 and 1902/1903, Johannes Franz Hartmann observed a series of binary stars, including δ Orionis star from the Orion’s belt. Hartmann (1904) reported, in the spectrum of this latter, the presence of the stationary CaII ‘H’ and ‘K’ absorption lines at 3933 and 3968 Å. One expects a Doppler shift for lines linked to a stellar atmosphere, but those of CaII did not show a sign of wavelength variation. This led Hartmann to conclude that this gas must arise from the intervening medium (the line of sight between the star and Earth) rather than the atmosphere of δ Orionis star. This discovery was the first evidence of the existence of the interstellar matter but was not largely accepted by the scientific community (e.g. Young 1920). We had to wait until Plaskett, Pearce (1933) work to firmly establish the interstellar origin of these features.

Since then, various detections and identifications were reported. The first observations of molecules in the ISM go back to 1941. Taking advantage of the high-resolution optical spectroscopy, diatomic molecules such as CH,

Year	Discovery
1904	Presence of the stationary ionized CaII absorption lines by Hartmann
1919	Heger identified stationary lines of the neutral sodium NaI
1922	First documented discovery of the Diffuse Interstellar Bands (Heger 1922)
1926	First calculations of the physical condition of interstellar matter by Eddington
1933	Discovery of the extraterrestrial radio emission by Jansky
1923	Plaskett, Pearce 's work on narrow CaII lines
1934	Merrill established the interstellar origin of diffuse interstellar bands
1937	Interstellar neutral calcium and potassium by Dunham
1938-40	Reber (1940) confirmed Jansky's discovery of radio waves from the Milky Way
1937-43	First detections of diatomic molecules CH and CN by Swings, Rosenfeld, McKellar, Adams
1941-42	Laboratory spectroscopy confirmed CH ⁺ by Douglas, Herzberg
1945	The prediction by Van de Hulst about the existence of the 21-cm line of HI
1949	Polarization of starlight correlated with reddening was reported first by Hall and then by Hiltner
1951	First emission at 21-cm wavelengths detected by Ewen, Purcell
1963	Discovery of 1.7 GHz interstellar OH emission Weinreb et al.
1968	Ammonia (NH ₃) was the first polyatomic interstellar molecule to be identified by Cheung et al.
1969	H ₂ O molecule was discovered in dense interstellar clouds by Cheung et al.
1970	CO molecule in the Orion Nebula by Wilson et al.

Table 11 Major discoveries and investigations that had a significant impact on the ISM field in the 20th century [1900's-1970's].

CH⁺ and CN were detected in a diffuse cloud. During the twentieth century, our knowledge of the ISM has significantly evolved thanks in particular to laboratory works and to the advent of radio astronomy era (initiated by the discovery of the HI 21-cm line). Moreover, the increasing number and the improvement of observation techniques (CCD) and ground-based telescopes had strongly impacted this field. Table 11 lists some of the highlights of the twentieth century. Starting in the 1970s, space astronomy has opened new wavelength windows to the ISM research field. This has allowed the observation of many unobserved interstellar species (inaccessible from the ground because of telluric lines) through their absorption spectra in the UV range by the satellite Copernicus. This latter has detected many abundant species, including the major discovery of H₂ by [Carruthers \(1970\)](#). Then followed the International Ultraviolet Explorer (IUE), the Hubble Space Telescope (HST) and the Far Ultraviolet Spectroscopic Explorer (FUSE).

This is raising awareness of the importance of the ISM in astrophysics. In fact, the interstellar medium, initially seen as a homogeneous and uniform medium without much interest, became a dynamic and turbulent medium, and the place of birth and death of the stars. The outer galaxies³ also having their interstellar medium, its understanding is of particular importance in the galaxy evolution context. Finally, the study of the ISM is also primordial being systematically a foreground for any extra-solar observation.

³This remark is limited to spiral galaxies. In fact, elliptical ones show a deficit of gas and dust.

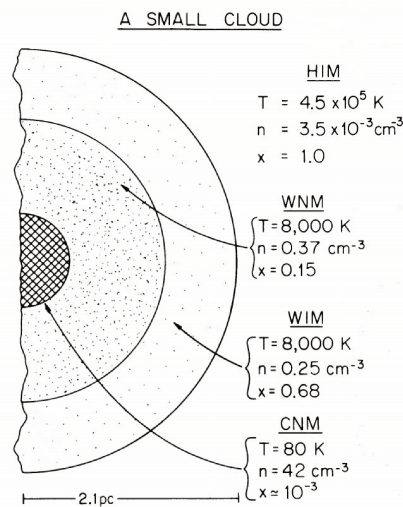


Figure 14 An old schematic description of a small cloud embedded in hot coronal gas by [McKee, Ostriker \(1977\)](#). In the case of immersion, the various phases can be superimposed hierarchically as indicated on this schema. Typical values of Hydrogen density, temperature, and ionization $x=ne/n$ are shown for each phase.

1.3 The Interstellar Medium

The interstellar medium contains the 10% of the “baryonic” material of our Galaxy not included in the stars, in the form of gas (atomic or molecular) and dust, mostly confined to the disk ([Draine 2011](#)). Typically 99% of this mass is in gaseous form, complete with 1% dust. The average density in local ISM is ≈ 1 particle/cm³ ([Whittet 2003](#)) which is extremely low comparing to terrestrial standards although large variations are seen in temperature $T^4 \simeq [10-10^6]$ K and density $n \simeq [10^{-3}-10^6]$ cm⁻³.

The interstellar medium comes in different forms and can be classified in many phases depending on the ionization state of Hydrogen which is the dominant element of the ISM: Ionized atomic hydrogen (H^+ or HII), neutral atomic hydrogen (H^0 or HI), molecular hydrogen (H_2) but also depending on the associated density (diffuse, dense) and temperature (cold, warm, hot). Among the several classifications, the ISM is generally divided into five phases:

- Hot Ionised Medium (HIM) or coronal gas: composed mainly of high ionized hydrogen. This phase is generated by shocked stellar winds and supernovae and occupies about half the volume of gas that fills

⁴In galaxy clusters, the temperature can reach 10^8 K.

the galactic disc and halo. The typical densities are low in the range of 10^{-3} to 10^{-2} cm^{-3} while the kinetic temperature is $\sim 10^6\text{K}$.

- Warm Ionised Medium (WIM) or HII gas: The hydrogen atoms are ionized by the photons (with energy $h\nu > 13.6$ eV) emitted by the surrounding stars. The H^+ ions formed have the ability to recombine with the free electrons. But the process of photoionization is faster than that of recombination, which leads to a medium mostly ionized with a temperature T of $\sim 10^4\text{K}$ and a particle number density varying between 0.2 and 0.5 cm^{-3} .
- Warm Neutral Medium (WNM) or warm HI: In this medium, hydrogen is neutral but has the same temperature as the WIM and a density $n \approx 0.6$ cm^{-3} . Both constitute a large fraction of the volume of the total gas ($\lesssim 50\%$) and generally represent the outer envelopes of a cloud.
- Cold Neutral Medium (CNM): This is the coldest (from 10 to 100 K) and densest (20 to 50 cm^{-3}) phase of the interstellar medium, it is also the largest in mass but remains the lowest in volume. It consists of mainly hydrogen in atomic form and represents the inside of the diffuse clouds shielded from the ionizing radiation. H is neutral due to shielding against photons but still heated by starlight and cosmic rays. Both with WNM can be detected thanks to the line 21 cm from the atomic hydrogen. Note that, within the meaning of this classification, the CNM also includes the molecular phase (see below).

The review by [Ferrière \(2001\)](#) detailed the information on the densities and temperatures.

All CNM, WNM, WIM and HIM phases are found in the diffuse interstellar medium.

In the densest areas of the CNM, we find hydrogen in its molecular form:

- Molecular Medium (Molecular Medium, MM): This phase occupies a very small portion of the interstellar medium but contains 30 - 60% of its mass thanks to its high density $n \approx 10^2 - 10^6$ cm^{-3} .

One has to keep in mind that classifying the ISM into phases has its limitations and remains very schematic. Being heterogeneous and turbulent place, the ISM contains overlapping regions where boundaries are not sharp and hard to separate. For e.g., there are regions dominated by photons known as photodissociation or photodominated region (PDR). It is a sort of a transition between the molecular cloud phase and the WNM or WIM regions surrounding the central star.

- PDR regions: Here, there is non-ionizing radiation for atomic hydrogen ($h\nu < 13.6$ eV), but the dissociation for molecular hydrogen ($h\nu >$

11.2 eV) generates a layer at the interface between the dense medium where the star was born and the HII region it created.

The atomic and molecular cold neutral medium can be divided into four types as introduced in a recent classification by [Snow, McCall \(2006a\)](#). This classification is based on the state of hydrogen and carbon in the gas. Hereafter, this following classification is the one used to distinguish the different environments studied in this thesis:

- **Diffuse atomic clouds** are found throughout our Galaxy, but they are mainly located near the galactic plane. They are generally characterized by low density $n \leq 10^3 \text{ cm}^{-3}$ (or $A_V \leq 2$), cold (10 - 100 K) and are completely exposed to the interstellar radiation field.
- **Diffuse molecular clouds** When the density of the diffuse atomic clouds becomes sufficient ($A_V \geq 0.2 \text{ mag}$ and $n \approx 100 - 500 \text{ cm}^{-3}$) to protect the hydrogen atoms from radiation, H_2 molecules can be formed without being instantly photodissociated. The presence of H_2 triggers complex chemistry as the reactions of the type $\text{X}^+ + \text{H}_2 \longrightarrow \text{XH}^+ + \text{H}$ and then leads to the efficient production of H_3^+ which is involved in many of the chemical reactions producing more complex molecules ([Herbst, Klemperer 1973](#)). In the other hand, the radiation in these clouds remains sufficient to photoionize the atomic carbon C and to photodissociate CO, the carbon is then mostly in C^+ form which initiates the organic chemistry ([van Dishoeck, Black 1986](#)). The kinetic temperature is in the range of [30 - 100] K.
- **Translucent clouds** are transitional objects between the diffuse and dense molecular clouds with a kinetic temperature of ≈ 15 to 50 K. They are defined as clumps of interstellar material with visual extinction between 1 and 5 magnitudes and density varying from 100 to 1000 cm^{-3} . Various translucent clouds have been detected using Spitzer ([Ingalls et al. 2011](#)). Prior to Spitzer, many molecules (H_2 , CH, CN, CO) have been detected in these clouds, for e.g. mm-wave CO absorption ([Liszt, Lucas 2000](#)) and FUSE ([Rachford et al. \(2002\)](#), [Sonnentrucker et al. \(2007a\)](#)).
- **Dark/dense molecular clouds** can give birth to dense cores under the effect of a collapse induced by gravity. In these regions, we find the highest densities of the ISM (10^3 - 10^5 cm^{-3}) and the visual extinction A_V exceeds 5 magnitudes. In these dark cores, the warming of the environment is mainly due to the impact of cosmic rays on grains and gas-grain collisions ([Burke, Hollenbach 1983](#)). The lines of the CO molecule make it possible to trace these dense clouds, because the H_2 molecule is difficult to observe, its electronic transitions in ultraviolet and ro-vibration transitions in the mid-infrared make it not observable from the ground-based telescopes.

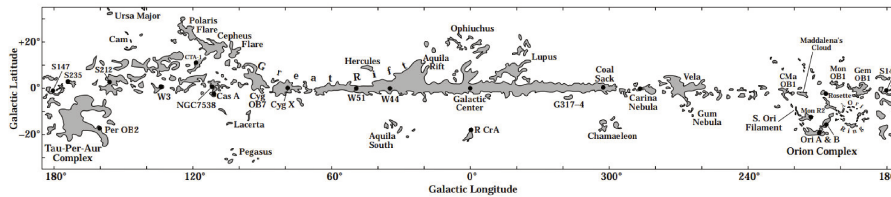


Figure 15 The major molecular cloud complexes as seen in the galactic plan of our Galaxy. From Dame et al. (2001).

1.4 Recycling the ISM

The interstellar medium is constantly evolving and closely linked to the life cycle of stars. In different words, the ISM is the place of birth and death of the stars, endlessly exchanging matter and energy with the latter. Many details of this evolution are still unknown, however we are able to draw its associated major stages.

It all begins when the diffuse clouds merge to produce larger clouds. Although the outer regions of these clouds continuously evaporate in contact with the hot environment where they bathe, some clouds become giant enough to be opaque to light: a large part of this matter is gathered in dense clouds, where the gas becomes molecular, i.e. instead of being composed of isolated atoms these atoms gather in molecules, for example the hydrogen H takes the form of dihydrogen H_2 molecule or the carbon takes the form of carbon monoxide CO.

These molecular clouds merge to become giant clouds and eventually gravitationally collapse on themselves to form stars. The newly formed massive stars trigger the formation of other stars and thanks to their winds and radiation, they dissolve and ionize their environment.

In return, throughout their lives and into their deaths (sometimes explosive), the stars re-inject gas into the interstellar medium or dust for the coldest of them. They enrich this medium with heavy elements that modify the chemical composition of the interstellar medium. Thus, during their evolution, galaxies contain more stars and less interstellar matter, while nucleosynthesis adds more heavy elements to these two components.

Interstellar dust, on the other hand, can be destroyed in whole or in part by radiation. In particular, ice mantles disappear if exposed to ultraviolet light, the rate of this destruction is so high that it must be assumed that they are continuously re-formed in the interstellar medium.

Ionized regions whose source of ionization has been extinguished quickly become neutral again by the recombination. Finally, gradually under the

effect of gravitational condensation, the coldest phases form diffuse clouds which contract and collapse again to evolve towards molecular clouds. This exchange of matter between the stars and the interstellar medium is permanent and occurs not only within of any galaxy but also in the intergalactic medium between galaxies.

1.5 The Interstellar Matter

By mass, the interstellar matter is composed primarily of 70.4% hydrogen (H) and 28.1% helium (He) with trace amounts of 1.5% of heavier elements. The latter are generally metals⁵ such as oxygen (O), carbon (C), nitrogen (N), magnesium (Mg), Silicon (Si), iron (Fe) and sulphur (S). These elements are found in gas phase and in solid dust grains as well.

1.5.1 Interstellar Gas

The interstellar gas absorption lines, in both atomic and molecular form, are very narrow and sharp (in the single-cloud situation), indicating low temperatures and at line shifts indicative of the velocities of interstellar gas clouds⁶.

- **Tracers of atomic gas**

In emission: the neutral atomic gas is commonly traced via the 21 cm hyperfine structure line of hydrogen. In the far infrared, lines of carbon and oxygen atoms and ions are also observed. Transitions lines of heavier species such as argon (Ar), neon (Ne) or sulphur (S) are associated with the most irradiated and ionized regions.

In absorption: Most of the interstellar species have their transitions in the UV range such as Ly α at 1216 Å but the telluric absorption make it difficult to observe from ground-based telescopes. Therefore, the most common absorption tracers are the neutral sodium (NaI) lines, namely the doublet D2 and D1, at 5889.95 and 5895.92 Å, and ionized calcium (CaII or Ca⁺), namely K and H lines, at 3933.66 and 3968.47 Å. NaI is neutral gas tracer more associated with denser cloud, whereas CaII is neutral and partially ionized gas tracer more associated with diffuse clouds. There are also other gaseous tracers such as potassium (KI) at 7665 and 7699 Å) indicative of dense clouds or the "blue" CaI at 4227 Å).

⁵By 'Metals' astronomers mean all elements except hydrogen and helium.

⁶The gas can also be seen in the circumstellar environment. The analysis of the velocity shift helped separate the interstellar gas from possible circumstellar gas which would have the same velocity as the stars it surrounds.

- **Tracers of molecular gas:** The molecular gas is found primarily in dense regions (dark clouds, dense cores and protoplanetary disks) where it is shielded against the dissociating effects of UV photons.

Despite being the most abundant molecule, the presence of H_2 can only be traced by the carbon monoxide (with its isotopologues) via its radio emission line at 2.6 mm. However, since the CO is freezing out on grains at very high densities, other tracers such as HCN or N_2H^+ can be used to probe denser regions such as prestellar cores. To date, over 150 molecules have been uniquely identified in the ISM ⁷.

Finally, as we will see in the next sections, the presence of hydrogenated polycyclic aromatic molecules (PAHs) ubiquitously observed in emission in the infrared range through the infrared emission features (Leger, Puget 1984; Allamandola et al. 1985; Peeters et al. 2002) and the recent discovery of the fullerenes (C_{60} , C_{60}^+ , C_{70}) in regions with intense UV radiation such as planetary nebulae (Cami et al. 2010; García-Hernández et al. 2010), or reflection nebulae (Sellgren et al. 2010; Berné et al. 2013a) but also in the diffuse ISM (Berné et al. 2017) herald the emergence of a new era in the exploration for complex molecules in space.

1.5.2 Dust

Dust grains represent the solid phase of the interstellar medium. They are mainly small solid particles whose dimensions range from nanometer (10^{-9} m) to micron (10^{-6} m) (*smoke* particles). These grains are composed essentially of carbon, oxygen, silicon, iron and generally surrounded by a thin envelope of water ice and ammonia. They are composed of either hydrogenated amorphous carbon or silicates, in other words, soot and sand and sometimes they form aggregates to form larger clumps of grains in dust clouds. Dust does not form in the interstellar medium because it is too tenuous for many molecules to form there. It forms in the vicinity of end-of-life stars when huge amounts of hot matter (atoms, small molecules and clusters) are ejected, either as a stellar wind or via an explosive supernova.

Although their mass represents typically only $\sim 1\%$ of the interstellar matter, dust grains play a critical role in physical and chemical conditions of the ISM:

- Dust is intimately linked to gas and is the main source of environmental heating via the photoelectric effect.

⁷The list can be found at <http://aramis.obspm.fr/mol/index.html> and <http://www.cv.nrao.edu/~awootten/allmols.html>

1. INTRODUCTION

- Dust affects radiation by absorbing and scattering visible and ultraviolet starlight. When heated, the dust grains then re-emit the absorbed energy at shorter wavelengths, in infrared and submillimetre ranges.
- Dust helps star formation by protecting dense cores from UV photons.
- By sticking on the surface of dust grains, various atoms and molecules form ice mantles where chemical reactions are initiated.
- Non-spherical grains can partially align with the interstellar magnetic field, causing a linear polarization of the light (Hall 1949).

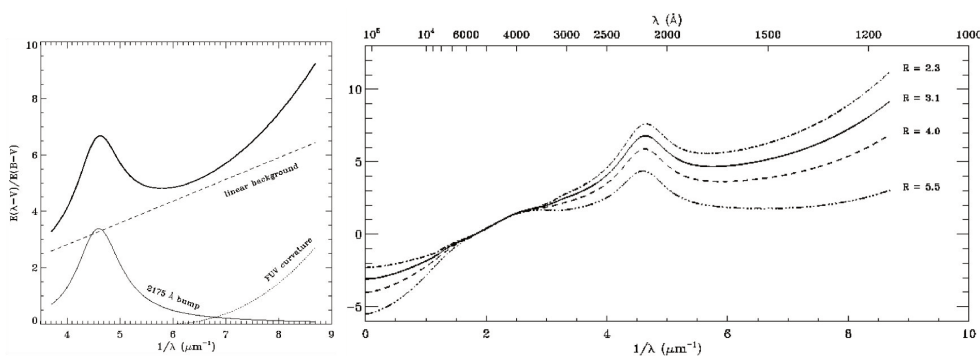


Figure 16 Left: Representative decomposition of the UV extinction curve ($3.3 \mu\text{m}^{-1} < \lambda^{-1} < 8 \mu\text{m}^{-1}$) into three analytical fitting functions from Fitzpatrick, Massa (1990): 1) the linear background component (thin dashed line), 2) the bump component (thin solid curve), and 3) the Far-UV component (thin dotted line). The solid black line is the sum of all these three components and represents the normalized UV extinction curve. Right: Far-IR through UV extinction curves from Cardelli et al. (1989). The extinction curves can be expressed approximately as a 1-parameter family that varies linearly with R^{-1} , where R is the ratio of total to selective extinction at V . R has a mean value in the diffuse ISM of 3.1. Examples of four representative values of $R=\{2.5, 3.1, 4.0, 5.5\}$ are shown. Adapted from <https://ned.ipac.caltech.edu/level5/Fitzpatrick/>

Extinction The dimming of starlight is due to the combination of two distinct physical phenomena: (1) the absorption of photons by dust, and (2) their diffusion on the grains, *i.e.* the change of the incident photons into all directions. The sum of these two phenomena is called interstellar extinction.

The extinction A_λ is the difference of magnitude between the flux $I(\lambda)$ after crossing the dust cloud and the flux $I_0(\lambda)$ at the entrance of the cloud, as

follows:

$$I(\lambda) = I_0(\lambda) e^{-\tau_\lambda} \quad (1.1)$$

$$A_\lambda = -2.5 \log\left(\frac{I(\lambda)}{I_0(\lambda)}\right) = 1.086 \tau_\lambda \quad (1.2)$$

where τ_λ is the optical depth.

For any observation, one must take into account the effect of the interstellar extinction. In the case of a star of absolute magnitude M at the distance d , the apparent magnitude is given by:

$$m(\lambda) = M(\lambda) - 5 + 5 \log(d) + A_\lambda \quad (1.3)$$

The color of the star is also changed in the presence of a cloud. Radiation is more absorbed in blue than in red, A_λ varies like λ^{-1} in the optical range. The standard excess color is the difference between the magnitudes in the large bands B (blue) at 440 nm and V (visible) at 550 nm.

$$E(\lambda - V) = (A_\lambda - A_V) \quad (1.4)$$

The extinction curve is defined by $R_V = A_V / E(B - V)$, the ratio of total to selective extinction at V, or $E(\lambda - V) / E(B - V)$ (Cardelli et al. 1989). Figure 16 shows the interstellar extinction curve from the far-IR through the UV region centered at 2175 Å (UV-bump). On the average extinction curve of the interstellar medium of our Galaxy, $R_V = 3.1$. However, deviations from this value (R ranges between about 2.2 and 5.8) were observed and then refers to a so-called abnormal extinction (e.g. Chini, Wargau 1990). Note that R_V is a powerful tool to measure the dust grain size.

1.6 The Diffuse Interstellar Bands

The spectra of stars viewed through one or several interstellar clouds display a plethora of relatively weak non-stellar absorption features of unknown origin, the so-called Diffuse Interstellar Bands. The first published reference to the DIBs goes to Annie J. Cannon who has misidentified the strongest DIB at 4430 Å as H_γ in her 1890s survey of stellar spectra (Code 1958). Soon followed, the documented discovery of DIBs at 5780 and 5797 Å around the early 20's by Mary lea Heger. Their interstellar origin was established in the 1930s (Merrill 1934, 1936) on the basis of two findings: (1) the stationary bands nature as observed in the velocity variations of spectroscopic binaries (2) their strength increase with distance and with the degree of reddening.

Only the DIBs at 5780, 5797, 6270, and 6283 Å were known before [Herbig \(1975\)](#) identified 39 new ones in the [4400-6850] Å range. Today, more than 400 optical DIBs (400-900 nm) are known (e.g. [Jenniskens, Desert 1994](#); [Hobbs et al. 2009](#)). There are no firm detections in the near-UV ([Bhatt, Cami 2015](#)). The first detection of near-infrared (NIR) DIBs was reported by [Joblin et al. \(1990\)](#) near 11 800 Å and 13 200 Å . Currently, ~ 30 NIR DIBs have been identified ([Foing, Ehrenfreund 1994](#); [Geballe et al. 2011](#); [Cox et al. 2014](#); [Hamano et al. 2015, 2016](#)). NIR DIBs are particularly useful since they allow to make use of highly reddened target stars and explore the densest areas of the ISM. Most measured DIBs have a Galactic origin. Still, they have also been detected in the Magellanic clouds, M 31, and M 33 ([Ehrenfreund et al. 2002](#); [Welty et al. 2006](#); [Cordiner et al. 2008a,b, 2011](#); [van Loon et al. 2013](#)) and in a few line-of-sights toward starburst galaxies or in Type Ia supernovae spectra, for instance ([Heckman, Lehnert 2000](#); [Sollerman et al. 2005](#); [Cox, Patat 2008](#); [Phillips et al. 2013](#)). A DIB radial gradient was established for the first time in a 160 Mpc distant galaxy ([Monreal-Ibero et al. 2015](#)). There is a huge literature devoted to the DIBs and the DIB-related topics. Excellent review papers by [Herbig \(1995\)](#); [Sarre \(2006\)](#), a comprehensive historical review by [McCall, Griffin \(2013\)](#) and the excellent contributions that are published in the proceedings of the DIB-dedicated symposia by [Cox, Cami \(2014\)](#). In the following, we focus on the problem from an observational and spectroscopic angle.

1.6.1 Observational properties

We can make some general comments on the different properties of DIBs based on what we have learned from the astronomical data:

DIBs distribution: Where do we find the DIBs?

- DIBs are seen in the spectra of stars, nearby galaxies such as the Magellanic Clouds (see e.g. [Ehrenfreund et al. 2002](#); [Cox et al. 2007b](#)) and the Andromeda Galaxy (M31) ([Cordiner et al. 2011](#), and references therein), distant galaxies ([Monreal-Ibero et al. 2015](#)), and quasars (towards several sightlines) (e.g. [Lan et al. 2015](#)).
- DIBs are spanning the wavelength range from the near ultraviolet (UV) at $\lambda \gtrsim 4000$ Å to the near infrared (IR) at $\lambda \lesssim 18000$ Å (Fig. 17) which is equivalent to photon energies in the 1-3 eV range. In the UV part, no DIB has been detected (e.g. [Seab, Snow 1985](#); [Snow, Destree 2011](#)).
- Most of DIB observations concern the diffuse (atomic or molecular) ISM. To date, no circumstellar DIB has been found with the possible exception of some detected features toward the planetary nebulae Tc 1 ([Díaz-Luis et al. 2015](#)).

- DIBs are not detected in emission except for the very intriguing case of the Red Rectangle (Sarre 1991; Van Winckel 2014).
- In a general sense, atoms, molecules, and DIBs are spatially grouped based on the study of their radial velocities. Still, minor kinematic disparities exist among all them (e.g. Sonnentrucker et al. 1999).

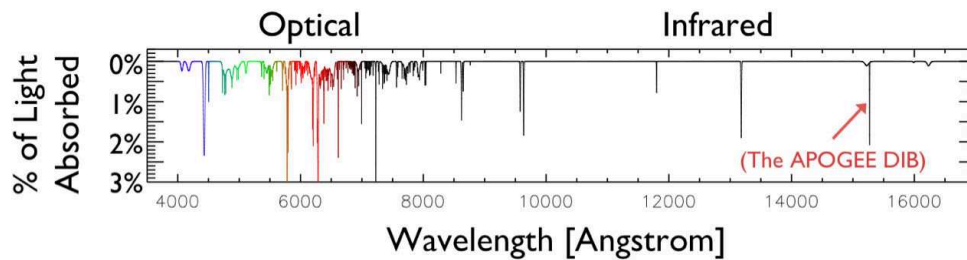


Figure 17 The strongest identified DIBs seen towards an optical-IR spectrum. Adapted from Jenniskens, Desert (1994). Credit: Gail Zasowski.

Appearance, shape and profiles

- DIBs are **broader** than atomic or diatomic interstellar lines⁸ (hence the label *diffuse*) and **show a wide range of widths and intensities** with full widths at half maximum (FWHMs) ranging from ~ 0.4 to ~ 40 Å (for e.g. Hobbs et al. 2009).
- DIBs show a **wide range of intensities** but are not saturated for most of the distant star spectra of the Galaxy.
- Most of DIBs are **asymmetric** with longward or shortward wings (which often makes it difficult to determine the central position in wavelength).
- Some DIBs (often the narrowest ones) show PQR branches indicating the gas-phase molecular nature of the carriers (hence the label *band*). Figure 18 illustrates the case of the DIB at 6614 Å.
- The intrinsically⁹ broad DIBs ($\text{FWHM} \geq 6$ Å) such as the 4430 Å band are very strong, free of any internal structure and are known to be most consistent with a Lorentzian distribution (Snow et al. 2002) or multiple Gaussian modeling (Sonnentrucker et al. 2018).

Correlations

- **Inter-DIB correlations:** DIBs do not correlate well with each other except for the NIR DIBs (Cox et al. 2014) and the well-known 6196 and

⁸Atoms and diatomic molecules have $\text{FWHM} < 0.1\text{\AA}$

⁹Part of the broadening can be due to Doppler splitting

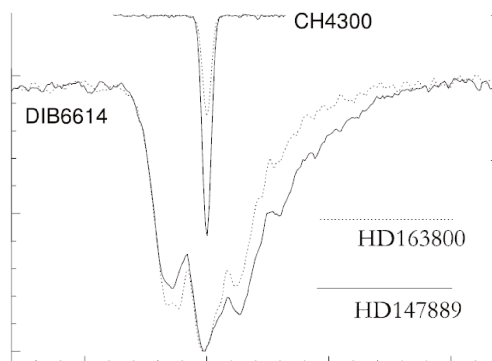


Figure 18 The 6614 DIB profile as seen in the normalized HARPS spectra towards HD 147889 (solid line) and HD 163800 (dashed line). In the top of the figure the interstellar molecular lines CH at 4300 Å are shown for each star. From Galazutdinov et al. (2008).

6614 Å DIBs (Moutou et al. 1999; McCall et al. 2010). As most pairs are not strongly correlated, this indicates that every DIB is due to a specific carrier; however, a certain level of correlation among distinct bands may be an indication that these bands carriers have attributes that exhibit similar responses, although not in an equal manner to interstellar environments (see for e.g. Krelowski, Westerlund 1988; Cami et al. 1997). When existing, DIB-DIB correlations do not always go through zero, this may be indicative of their interrelated properties, e.g. diverse carriers, such as those with distinct ionization potential, generate a variety of DIBs.

- **DIB-extinction:** DIBs are globally correlated with the color excess $E(B-V)$ (also known as the reddening index) although some DIBs tend to be deficient with respect to the extinction towards background stars of dense interstellar clouds (*the skin effect*) (Wampler 1966; Snow, Cohen 1974; Adamson et al. 1994; Lan et al. 2015).
- No correlation is found between DIB strength and the amount of the extinction in the far-UV (FUV) or at least no consensus has been reached (Desert et al. 1995; Xiang et al. 2017, and references therein).
- Failure to confirm the hypothesis that large grains are responsible for the absorption of DIBs through the lack of polarization (Cox et al. 2007a).
- **DIB-gas:** There is a general correlation of DIB strength on the column density of the neutral gas¹⁰, with a global power-law dependence of Herbig (1993a); Friedman et al. (2011). On the contrary, DIBs may be

¹⁰This does not necessarily mean that DIB carriers are neutral

positively or negatively correlated with H₂ (Lan et al. 2015). Some DIBs also correlate with small molecules and radicals.

DIB families

- DIBs are not of common origin. Hence, it is possible to classify DIBs into sets or families. The members of a particular family reveal similar patterns of strength fluctuation among various different lines of sight, while they have weak correlations with the members of other groups, *i.e.* the strength ratios of DIBs belonging to the same family are supposed to be approximately constant and correspond to carriers sharing the same properties. The ratio between the 5780 Å and 5797 Å DIBs is generally used as benchmark to differentiate the families. Based on this behavior, classifications that categorized some DIBs into three groups have been first introduced by Krelowski, Walker (1987); Westerlund, Krelowski (1989).
- Some of DIBs correlate with the column density of C₂ molecules to which they appear to be chemically related. This family is known as C₂-DIBs (Thorburn et al. 2003).
- The DIB spacing has been much studied in a search for a significant pattern but except for a set of weak DIBs regularly spaced near 5778 or 6283 Å DIBs (Jenniskens, Desert 1993), the separation of about 20 cm⁻¹ in pairs of some C₂-DIBs (Thorburn et al. 2003), the detection of a sequence of a weak spaced bands between 6770-6865 Å (Herbig 1988; Krelowski et al. 1997), and within the 5910-5990 Å range (Bondar, Krelowski 2014) and an analysis of vibronic progressions in DIBs (Duley, Kuzmin 2010), no fully convincing spacenumber has been reported thus far (see e.g. Hobbs et al. 2009). Finding regularities is interesting insofar as it could be an indication of a spectroscopic signature such as a signature of the spin-orbit interaction in a linear molecule.

Environmental dependence

- DIBs do not have identical strength ratios towards different lines of sight. It was demonstrated that the mutual correlations and strengths depend on physical conditions, extinctions curves and abundances of the interstellar environment(e.g. Cami et al. 1997; Sonnentrucker et al. 1997; Cox, Spaans 2006). The 5780/5797 ratio has been connected to the environment through the well-known classification into σ -Sco and ζ -Oph type clouds. Sigma-Sco cloud extinction curves are characterized by a pronounced 2175 Å bump and strong FUV rise, whereas ζ -Oph type cloud is showing an extinction curve with weak 2175 Å bump and weak rise of the FUV extinction (Fitzpatrick, Massa 2007). In fact, the 5797 Å DIB is well correlated in ζ -type sightlines while

the 5780 Å DIB becomes stronger towards σ -type clouds. (e.g. [Tielens 2014](#)).

- The formation/destruction of the DIB carriers is at least partially controlled by the UV radiation field ([Ruiterkamp et al. 2005](#); [Cox, Spaans 2006](#)).
- DIBs are controlled by the environmental conditions at parsec scales (e.g. [Vos et al. 2011](#)), and even at very small, hundreds of A.U. scales as shown by (e.g. [Cordiner et al. 2005](#)).

Tracers

- Based on σ and ζ types, The 5780/5797 ratio can be used as a tracer indicating the presence of simple diatomic molecules such as CO, CH, C₂ or an influence of the UV radiation field (see for e.g. [Cami et al. 1997](#); [Friedman et al. 2011](#)). In other words, the 5780 Å DIB may trace atomic gas of diffuse clouds while the 5797 Å DIB will be associated to the dense molecular regions. The 5797/5780 DIB ratio is related to the effective UV radiation field strength; UV exposed environments, σ -type, have ratios < 0.35 , while UV-shielded, ζ -type environments, have ratios ≥ 0.35 ([Vos et al. 2011](#)).
- A major advantage of DIBs over extinction is the measurement of their Doppler shifts, which will make it possible to attribute movement to interstellar complexes and locate those responsible for radio-millimetric emission lines in the frame of the 3D ISM mapping (see [Puspitarini et al. 2015](#)).

1.7 DIB carriers

While [Russell \(1935\)](#) and [Swings \(1937\)](#) proposed large molecules as DIB carriers, [Merrill, Wilson](#) on the other hand proposed dust grain particles to be responsible of DIBs. Since then, there has been a considerable debate about whether species giving rise to the observed DIBs are associated with small solid particles or gas-phase molecules. However, thanks to observational progress a consensus has been reached over the last ten years on their nature: DIB carriers are now thought to be large carbonaceous molecules (≥ 10 –100 atoms) in the gaseous phase but other possibilities (such as non-carbon species) remain open as discussed by [Snow \(2014\)](#).

There are strong arguments working against the solid phase hypothesis. In the case of solid-state, what would cause an absorption like the one observed would be the presence of impurities. But, since DIBs fall at constant wavelengths this would imply the need for exactly the same environment in the solid everywhere along its surface in all clouds and all conditions, which is

highly improbable. As a second strong argument, searches for polarization of the DIB profiles have set stringent upper limits to the polarization efficiency of the carriers. This indicates that a carrier is not attached or part (an impurity) of the dust grains causing the continuum polarization. An additional evidence for the molecular nature of the DIBs carriers is supported by the detection of sub-structures in the line profiles of some DIBs that are extremely similar to PQR branches (rotational contours) of complex gas phase molecules (Sarre et al. 1995; Ehrenfreund, Foing 1996; Królowski, Schmidt 1997; Walker et al. 2001; Cami et al. 2004). Finally, A number of them have a width significantly greater than 1 Å, which excludes small molecules as possible carriers. They could therefore be due to electronic transitions in large molecules.

The most promising carrier candidates are carbon chains, polycyclic aromatic hydrocarbons (PAHs), and fullerenes. A large effort has been devoted over the years for the identification of the DIB carriers. Searches have included PAH cations (Salama et al. 1999; Bréchnignac, Pino 1999), neutral PAHs (Salama et al. 2011; Gredel et al. 2011), carbon chains (Motylewski et al. 2000; Maier et al. 2004), and H₂ (for e.g. Sorokin, Glowina (1999) and have not resulted in the identification of a specific carrier. The only identification came recently for the case of the fullerene cation, C₆₀⁺ (Campbell, Maier 2018, and references therein), providing a link between some DIBs and organic polyatomic molecules and ions.

Jones (2016) proposed a top-down branching model for DIB carrier formation. Figure 19 shows the hierarchical scheme of such tree branching with descending in size and in chemical variety from top to bottom. In such scenario, dehydrogenated, ionized, hetero-cyclic, olefinic and aromatic-rich moieties, that are formed by fragmentation of the large grains or nanoparticles, are believed to carry the DIBs. In what follows we briefly recall the main findings for the most popular candidates: PAHs and fullerenes.

1.7.1 DIB carriers: PAHs?

Infrared emission bands In 1973, Gillett et al. observed for the first time a set of emission bands between 8 and 13 μm in the reflection nebula NGC 7027. The emission bands have been detected in many different astrophysical environments (such as the photodissociation regions, HII regions, and nebulae planetary) especially thanks to the ISO satellite, the *Spitzer Space Telescope* and then AKARI. The strongest signatures can be found at 3.3, 6.2, 7.7, 8.6, 11.3 and 12.7 μm as shown in Fig. 111 (for a recent review, see Tielens 2008). The bands were first called "unidentified infrared bands" or "unidentified infrared features" (Willner et al. 1979) and their origin remained unknown for a decade. But from the moment these bands were combined to the stretching and bending (C-H and C-C) vibration modes characteristic of

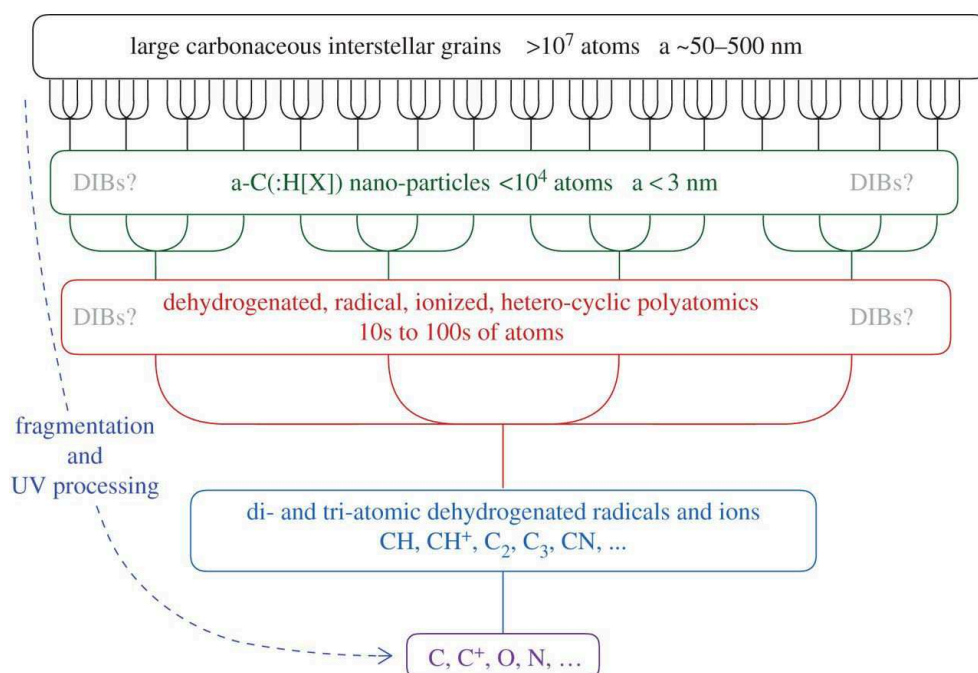


Figure 19 Top-down branching scenario of DIB formation and fragmentation as imagined by Jones (2016). DIB carriers may be formed by fragmentation of large grains, nanoparticles (and smaller) or fragments of dehydrogenated radical and molecular ions. With the destruction of the latter by UV-photoprocessing, non-DIB species and isolated atoms and ions will be formed in the gas. Only the configurations that lead to the most stable fragments that lead to the most stable fragments are shown here. Taken from the tome II of "Dust evolution, a global view" by Jones (2016).

aromatic hydrocarbons (Duley, Williams 1981; Leger, Puget 1984; Allamandola et al. 1985) comes the new name of Aromatic Infrared Bands (AIBs)¹¹. Despite the numerous works, both in molecular physics, Laboratory and astrophysics, no single PAH molecule or related small complex has been firmly identified to date, either by rotational spectroscopy or by observations of the associated infrared emission bands. It should be mentioned that the emission bands only indicate the general class of molecule, and not the specific molecular species (Joblin, Tielens 2011, for a recent review). However, to date, PAHs remain the best candidates to explain infrared bands in emission.

PAHs as DIB carriers Polycyclic aromatic hydrocarbon molecules (PAHs) constitute a family of aromatic hydrocarbons, *i.e.* molecules composed of

¹¹Also called PAH bands

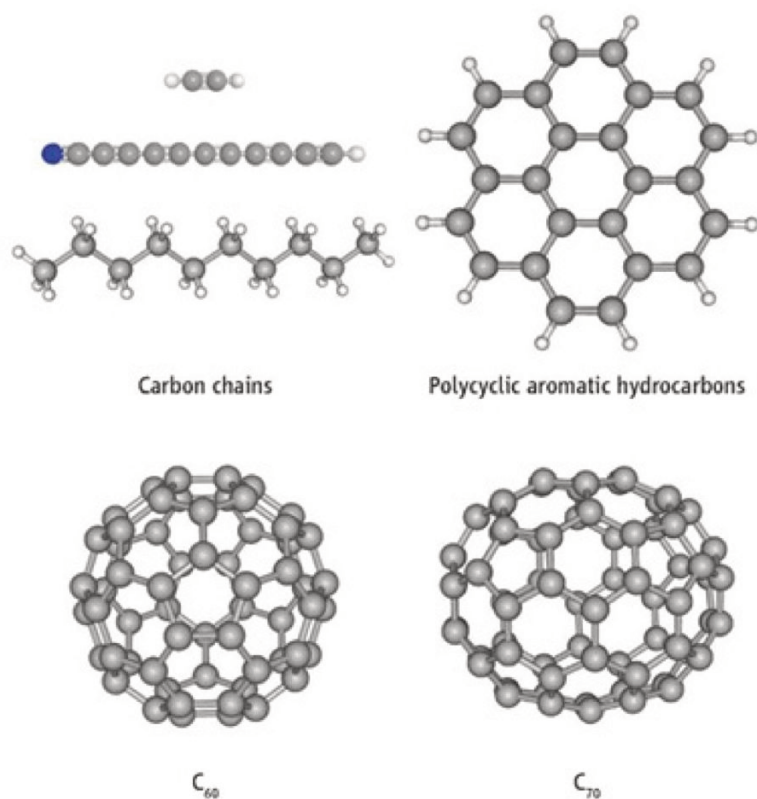


Figure 110 Illustration of some carbon-rich molecules in space. Polyynes (carbon chains) and polycyclic aromatic hydrocarbons (PAHs) and C_{60} are proposed as DIB carriers. Adapted from [Ehrenfreund, Foing \(2010\)](#). Credit: Zan Peeters.

carbon and hydrogen atoms with a structure of organic rings in which the electrons are delocalized. PAHs and their small complexes partially form a key link between small hydrocarbon species and large carbonaceous grain and may encircle the *Very Small Grains* (VSG; [Desert et al. 1986](#)). In the diffuse ISM, [Joblin et al. \(1992\)](#) estimated that $\sim 15\%$ of interstellar carbon is contained in PAHs while [Berné, Tielens \(2012\)](#) estimated less than 3-5% near the stars.

Despite being the best potential carriers for DIBs ([van der Zwet, Allamandola 1985](#); [Leger, D'Hendecourt 1985](#); [Crawford et al. 1985](#); [Salama et al. 1996, 2011](#)), no conclusive identification of DIBs with a known PAH band (neutrals or ions) has been found so far (e.g. [Salama et al. 2011](#); [Steglich et al. 2011](#)). In practice, the PAH-DIB hypothesis is facing many challenges:

- The puzzling absence of PAH signatures in the UV and visible range.
- The overwhelming variety of the PAH species and their closely related

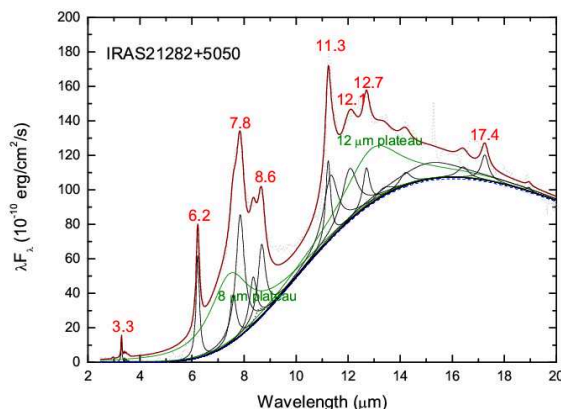


Figure 111 Example of PAH infrared features (labeled in red) in the 2-20 μm emission spectrum of IRAS21282+5050 (a young planetary nebula). The observed data (shown in light dotted curve) have been fitted by a number of discrete features (black) and plateau features (green) above a continuum (blue). From Kwok, Zhang (2013).

derivatives, existing in different sizes and shapes and in ionized and/or dehydrogenated forms.

- Being broader, it is difficult to reliably extract PAH ions bands from astronomical data. There is a need for a depth-analysis to search for the signature of specific PAHs and derive reliable column densities (or upper limits to column densities) specially in the UV range that were being marginally explored. By providing enough constraints on DIBs, this can limit the number of possible candidates to study in the laboratory (see the excellent critical review by Salama, Ehrenfreund 2014). Finally, since the detection of fullerenes (subject of the next section) in 2010 and the very recent first definitive detection of the rotational emission from the cyclic aromatic benzonitrile $c\text{-C}_6\text{H}_5\text{CN}$ by McGuire et al. (2018) in an interstellar cloud ¹² using new data from the National Science Foundation's Green Bank Telescope (GBT), the existence of large carbon-related molecular buildings has become a reality, which also illustrates the carbon-richness and chemical complexity of this environment (see Joblin, Cernicharo 2018).

This gives a new breath to the PAH model and demonstrates the need to make all necessary improvements before excluding PAHs from the DIB carriers candidates.

¹²Cernicharo et al. (2001) have detected Benzene in C-rich protoplanetary nebula CRL618 which represents the first detection of an aromatic compound out of solar system.

1.7.2 DIB carriers: Fullerenes?

Fullerenes In 1985, [Kroto et al.](#) discovered a new form of carbon that could be present in the astrophysical environments¹³. A molecule composed of 60 carbon atoms and arranged into what look like the geodesic domes of the architect R. Buckminster Fuller. Subsequently, these molecules were called buckminstefullerene¹⁴ or buckyballs due to their soccer-ball-shape. However, two questions remained unresolved: does C_{60} and its derivatives exist in the ISM? Can we linked these large molecules to the DIBs?

A positive answer to the first question was given by the detection of the IR emission bands (at 7.0, 8.5, 17.4, and 19.0 μm for C_{60}) in the planetary nebulae Tc 1 (IC 1266) ([Cami et al. 2010](#)). These signatures match the IR active bands of the neutral fullerenes C_{60} and C_{70} detected in the laboratory by Kroto and coworkers. More additional detections were reported in different environments such as the reflection nebulae (NGC7023 [Sellgren et al. 2010](#)) and the proto-planetary nebula IRAS01005+7910 ([Zhang, Kwok 2011](#)). In 2013, [Berné et al.](#) provided a first proof of the presence of the fullerenes in its ionized form by its mid-infrared (MIR) emission in the reflection nebula NGC 7023.

DIB-Fullerenes [Foing, Ehrenfreund \(1994\)](#) found that the laboratory spectrum of the buckminsterfullerene cation C_{60}^+ in argon and neon matrices ([Fulara et al. 1993](#)) would exhibit transitions near the two NIR DIBs at 958 and 963 nm. Additional DIBs at 902, 921, and 926 nm were attributed to C_{60}^+ ([Misawa et al. 2009](#)). The detection of the two strong bands has been confirmed by several teams ([Foing, Ehrenfreund 1997](#); [Galazutdinov et al. 2000](#); [Cox et al. 2014](#); [Hamano et al. 2015, 2016](#); [Walker et al. 2015, 2016, 2017](#); [Lallement et al. 2018b](#)) and some detections of the weaker absorption bands have been reported ([Walker et al. 2015, 2016](#)). However, this identification has long been debated ([Maier 1994](#); [Jenniskens et al. 1997](#)). The main cause of this questioning is that the production of a laboratory spectrum in conditions similar to those of DIB formation (gas-phase with low temperatures) has proven elusive.

Nevertheless, the credibility of the DIB- C_{60}^+ assignment has increased with the laboratory work of the John P. Maier's team. [Campbell et al. \(2015\)](#) had reported a striking match of five DIBs with transitions of the laboratory spectrum of internally cold C_{60}^+ ions. The measurement was achieved with C_{60}^+

¹³Historical note: This discovery earned them the Nobel Prize in Chemistry in 1996. Prior to this work, the existence of C_{60} has been predicted by D.E.H. Jones (under his pseudonym Daedalus) in *New Scientist*, 1966, and with some works in 1970 by E. Osawa, and independently by D.A. Bochvar and Gal'pern

¹⁴The discovery of the fullerene family (C_n) followed that of the buckminsterfullerene, the name was shortened to illustrate the fact that the latter is a type of fullerene

molecules in the gas phase, cooled to 5.8 kelvin. Subsequently, in the face of some rejections (Galazutdinov et al. 2017; Galazutdinov, Krełowski 2017), several laboratory investigations supported this approach by providing additional precisions under appropriate conditions (Campbell et al. 2016a,b; Kuhn et al. 2016; Spieler et al. 2017) and the most recent improvements can be found in Campbell, Maier (2018).

In the frame of astronomical data, it is very challenging to reveal the existence (or lack) of such features from IR ground spectra only as this wavelength range is strongly contaminated by telluric absorption. It requires a careful telluric absorption correction as illustrated by Lallement et al. (2018b). Through dedicated corrections and stacking methods applied to EDIBLES spectra, some substructures in the 9577 Å C_{60}^+ band were detected (see Cami et al. 2018). On the other hand, since the problem can be avoided by using free-telluric data from space-based telescopes, there may be a new avenue in exploring the *newly opened* NIR window with the Space Telescope Imaging Spectrograph (STIS) on board the Hubble Space Telescope (HST) (Cordiner et al. 2017a).

1.8 Thesis Overview

Understanding the evolution of interstellar matter and the physical and chemical processes that govern the early stages of star formation is part of a continuous effort by much of the astrophysical community to answer fundamental questions about the origin of life in the Universe. To do this, it is necessary to acquire a precise knowledge of the composition and life cycle of gas and dust clouds in the interstellar medium. Among the interstellar materials present in space, carbon-based matter under the form of large molecules is of crucial importance since it is part of the chain of processes at work from cloud cooling and collapse to protostars and their protoplanetary systems. Indeed, carbon-based molecules of increasing sizes are detected in comets as missions progress, potentially representing pristine interstellar material. So the study of the formation, processing and destruction of large carbon-bearing species is fundamental.

The composition of interstellar matter and the processes involved are far from being fully understood. In particular, one of the remaining problems in terms of ISM composition is the ubiquitous presence of the many unidentified diffuse interstellar bands detected in our galaxy and other galaxies. These absorption features observed in the spectra of reddened Milky Way stars or in galaxy spectra have puzzled astronomers and spectroscopists for over a century. Since their first discoveries in the 1920s, there has been considerable debate about whether the molecules responsible for the observed DIBs are associated with dust grains or gas-phase molecules. However,

thanks to the progress of observations, a consensus has emerged over the past ten years on their nature: carriers of DIB are now considered as large carbonaceous molecules in the gas phase. No polarization has been detected, and direct evidence of the molecular nature of DIB carriers is supported by the detection of substructures in the linear profiles of some DIBs indicative of rotational contour bands of complex molecules in the gas phase. The most promising candidate carriers are carbon chains, polycyclic aromatic hydrocarbons (PAHs) and fullerenes. PAHs are the most favoured species, being ubiquitously observed in IR emissions. Due to their stability, fullerenes are also good candidates, and C_{60} , C_{60}^+ and C_{70} have also been detected in emission. The only recent identification of the fullerene cation case, C_{60}^+ , provides a link between some DIBs and polyatomic organic molecules and ions.

Further progress in DIB research will undoubtedly come from an active synergy between theoretical work, astronomical observations and laboratory measurements (UV and IR) where the interstellar conditions prevailing in the diffuse ISM can be realistically simulated. This methodology is now at the heart of the ESO Diffuse Interstellar Bands Large Exploration Survey (EDIBLES) in which observing astronomers, laboratory astrophysicists and chemists have joined forces to acquire a new understanding of the physics of DIB carriers.

Until recently, most DIB studies of astronomical spectra had as their main objective the identification of carriers by means of high quality measurements, and therefore focused on a limited number of hot, bright, strongly reddened stars, using increasingly powerful instruments. This thesis corresponds to a shift towards statistical studies: such a trend is made possible and motivated by the increasing number of stellar spectroscopic studies with high multiplex instruments. It is now possible to collect massive amounts of data, both in terms of the number of target stars and of DIBs observed simultaneously. This has paved the way for new types of studies. This thesis presents a large number of DIB extractions from stellar spectroscopic surveys and three of these new analyses:

- Statistical studies on the relationship between DIB's strengths and the physical properties of their hosting clouds.
- Tomographic studies of DIB carriers on small and large spatial scale.
- Extraction of line profiles based on carefully selected sightlines and single-cloud spectra stacking, studies of the profile substructures and spatial variability.
- **Part I, Chapters 2 and 3 - Catalogs based on the SDSS/APOGEE survey**

Chapter 2/3 presents new adjustment methods for stellar spectroscopic surveys that have been developed and fully automated to extract as much information as possible from stellar spectra. I show their application to the near infrared (NIR) spectra of the SDSS/APOGEE H-band survey and the extraction of the 15 273 Å DIB. I started with the early-type stars that were used for the elimination of telluric lines in Data Release 12 (DR12) without being part of the scientific targets, then I continued with the full dataset of science and calibration targets of DR12 belonging to the TYCHO catalog and, finally, with all the science targets consisting mainly of red giants of DR14.

- **Part II, Chapters 4 and 5 - Applications of the DIB catalogs.**

Chapter 4 - 3D ISM mapping

Despite the absence of identifications, optical or NIR DIBs are interstellar cloud tracers and we have tested their use for 3D mapping. We merged the catalogue of DIBs derived from Tycho targets with the extinction data, using a conversion factor based on our DIB-extinction correlation study and taking into account the dispersion around the mean relationship. The merged dataset was inverted to produce a 3D map of the local ISM presented in [Capitanio et al. \(2017\)](#). We also used the latest APOGEE catalog of 15 273 Å DIB for the first 3D inversion based solely on DIBs and compared the 3D map obtained with the one obtained by the extinction for exactly the same targets.

Chapter 5 - Applications under study of the *skin effect*

It has been shown that some of the strong optical DIBs level off with respect to dust reddening (visual extinction) for lines of sight that probe (on average) the denser cores, rather than the diffuse edges, of interstellar clouds. This is called the "skin effect" and the effect is attributed to the influence of the radiation field on the DIB carriers, through charge state variation or formation/destruction processes, or independently to accretion processes. The link with the ionizing field is particularly interesting because it is related to the shielding and thus the clouds depth, and therefore to the properties of the grain. In addition, since near-infrared DIBs can probe more strongly obscured areas, and therefore cores of denser clouds, they are particularly interesting in the context of the skin effect. In this chapter, the skin effect is explored using our APOGEE DIB measurements, in combination with existing, precise estimates of dust extinction for the APOGEE targets. Planck measurements of the optical depth of Galactic dust are also extrapolated from Planck maps for all APOGEE target directions. The ratio between the column of DIB carrier and the extinction (grain column) is found to be strongly negatively correlated with the optical depth of dust in the case of the nearby molecular clouds seen off-Plane and

an empirical relationship between the DIB to dust ratio and the dust optical depth is established.

- **Part III, Chapter 6 - Exploitation of the catalog of the strongest NIR DIB for weak DIB extractions and studies of the response to ionization**

In this chapter I present the results of the massive stacking of APOGEE spectra selected for strength or on the contrary the absence of the strong 15 273 Å DIB. This has made it possible to extract and characterize weak DIBs that were previously detected in only a few lines of sight and to detect new candidates. DIB-DIB ratios were studied, including the first exploration of ratios involving a NIR DIB and a DIB in the visible range. The optical data were obtained from dedicated observations with Sophie at OHP/1.93m and NARVAL at Pic du Midi/TBL. The DIB-DIB ratios contain information on the evolution of the carriers according to physical properties, i.e. radiation field, ISM abundances and particle size distribution. A hierarchy of DIBs ordered by sensitivity to the ionizing field is currently being carried out thanks to the work of several teams (see e.g. [Ensor et al. 2017a](#)) and some of the work done in my thesis has contributed to improving this hierarchy by scaling up the DIB 15 273 Å.

This work has led to the production of catalogues, the characterization of very weak DIBs that were previously barely detected in a few lines of sight, and the detection of new candidates.

- **Part IV: Chapter 7 - Tomography of a DIB carrier in a single dark cloud**

In the frame of a pilot project with VLT/KMOS (ESO 096.C-0931(A), PI: N. Cox), moderate resolution near infrared spectra (H-band) of 85 stars located behind the dark globule Barnard 68 were recorded. In this chapter, I detail how the data were adjusted by the convolved product of a telluric transmission and a stellar model. The telluric spectrum is a TAPAS transmission adjusted according to the air mass and the observation site. The stellar model was built from the SDSS/APOGEE stellar library. Based on a simplified inversion assuming sphericity, and using the edge-to-center distribution of the targets, it was found that the volume density of the 15 273 Å DIB carrier is 2.7 (resp. 7.9) times lower than the average value in the external (resp. central) regions of the cloud ($n(\text{H})$ of $3.5 \times 10^5 \text{ cm}^{-3}$). This is the first DIB tomography in an individual cloud.

- **Part V: Chapters 8, 9, and 10 - The EDIBLES survey**

The VLT/UVES EDIBLES survey is a unique collection of very high signal to noise (reaching 800-1500), high spectral resolution and large

spectral coverage spectra recorded towards more than 100 carefully selected targets. Chapter 8 contains the presentation of the survey. Our contribution corresponds to specific data treatments, including telluric line removal.

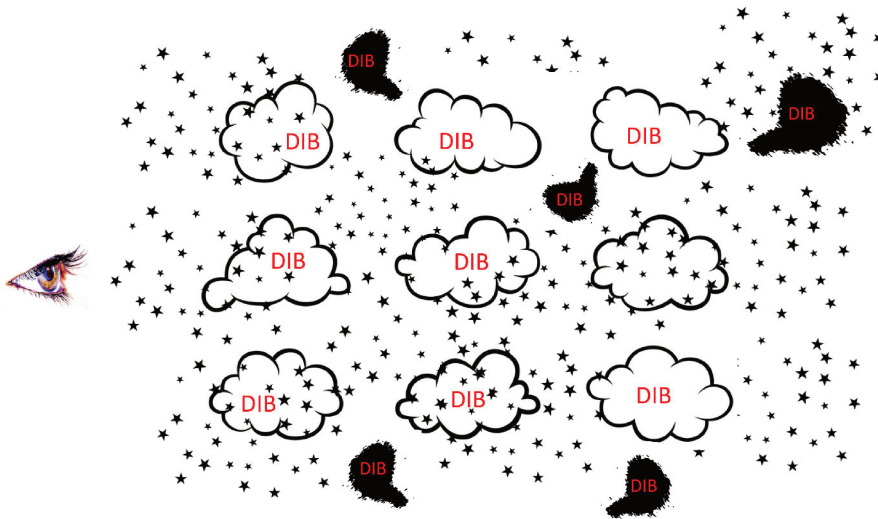
Chapter 9 describes the characterization of the line-of-sight cloud structure of EDIBLES targets. This is a mandatory step, as a number of DIB studies can only be interpreted for lines of sight crossing a single dominant cloud. To this end, several gaseous lines were fitted, in particular using new automated fitting methods. The spectra from the same target recorded at different periods were stacked in a fixed reference frame in order to increase the signal to noise (we choose the stellar frame for facility). Then we selected the seven targets for which only one interstellar cloud is majoritarily producing the absorption (the single-cloud situation). We stacked their spectra in the stellar, telluric and cloud frame respectively and compared the results with the goal of obtaining the best DIB profiles and identifying telluric and stellar potential contaminations.

Chapter 10 describes how EDIBLES data have made it possible to characterize in an unprecedented way the spectral profiles of the main DIBs and the first in-depth study of the low DIBs associated with the C_2 molecule in dense cores. All these DIBs have profiles characterized by substructures, with clear variability from one DIB to another and with some consistent profile changes depending on the line of sight. Such information will be available as a guide for future experimental work carried out under conditions similar to those in the ISM.

- **Part VI: conclusions, perspectives**

Part I

Sightlines survey *"One DIB, many targets"*



Chapter 2

A catalog of 1.5273 μm Diffuse Interstellar Bands based on APOGEE Hot Telluric Calibrators

Based on:

**“A catalog of 1.5273 μm Diffuse Interstellar Bands based on APOGEE
Hot Telluric Calibrators”**

Elyajouri, M.; Monreal-Ibero, A.; Remy, Q.; Lallement, R.

The Astrophysical Journal Supplement Series, Volume 225, Issue 2, article
id. 19, 16 pp. 2016.

Abstract

High resolution stellar spectroscopic surveys provide massive amounts of diffuse interstellar bands (DIBs) measurements. Data can be used to study the distribution of the DIB carriers and those environmental conditions that favor their formation. In parallel, recent studies have also proved that DIBs extracted from stellar spectra constitute new tools for building the 3D structure of the Galactic Interstellar Medium (ISM). The amount of details on the structure depends directly on the quantity of available lines of sight (LOS). Therefore there is a need to construct databases of high-quality DIB measurements as large as possible. We aim at providing the community with a catalog of high-quality measurements of the 1.5273 μm DIB towards a large fraction of the *Apache Point Observatory Galactic Evolution Experiment* (APOGEE) hot stars observed to correct for the telluric absorption and not used for ISM studies so far. This catalog would complement the extensive database recently extracted by [Zasowski et al. \(2015\)](#) from the APOGEE observations and used for 3D ISM mapping. We devised a method to fit the stellar continuum of the hot calibration stars and extracted the DIB from the normalized spectrum. Severe selection criteria based on the

absorption characteristics are applied to the results. In particular limiting constraints on the DIB widths and Doppler shifts are deduced from the HI 21 cm measurements, following a new technique of decomposition of the emission spectra. From $\sim 16\,000$ available *hot telluric* spectra we have extracted ~ 6700 DIB measurements and their associated uncertainties. The statistical properties of the extracted absorptions are examined and our selection criteria are shown to provide a robust dataset. The resulting catalog contains the DIB total equivalent widths, central wavelengths and widths.

2.1 Introduction

In the near-IR, the 1.5273 μm band (hereafter, we will also use 15273 \AA and refer to vacuum wavelengths) falls in the spectral range observed by the *Apache Point Observatory Galactic Evolution Experiment* (APOGEE, [Wilson et al. 2010](#); [Majewski 2012](#)), and this high resolution, high signal, massive survey was used by [Zasowski et al. \(2015\)](#) to trace the 3D structure of the ISM at the large scale based on an unprecedented number of extracted NIR DIBs. Such pioneering work has demonstrated the potential of these methods and consequently that increasing the number of measurements will result in more accurate mapping.

In this chapter we present a work based on a fraction of the spectra of the APOGEE's target from the Data release 12 (DR12) made publicly available. The entire dataset comprises $\sim 160\,000$ stars, most of them cool K and M giants ($T_{\text{eff}} \sim 3500 - 5000$ K). As part of the observing strategy and calibration plan of the survey, $\sim 17\,000$ *hot telluric* stars were also observed (see details in [Sec. 2.2](#)). By definition these are the bluest stars on a given pointing, and thus, most of the times early (i.e. O- to F-type) stars. As such, their almost featureless continua make them ideal targets to extract the information associated to the 1.5273 μm DIB. Our work has been focused on these calibration stars. We have devised a method to fit their stellar continua and we present the resulting catalog of DIB measurements extracted from their spectra. This catalog complements the existing extensive catalog of [Zasowski et al. \(2015\)](#) based on the APOGEE main, cool targets.

The chapter is structured as follows: [Sect. 2.2](#) contains the technical aspects regarding the data used in this work. [Sect. 2.3](#) describes the methods used for continuum fitting and DIB parameter extraction, whereas a detailed description of our criteria to validate a DIB detection and estimate uncertainties is included in [Sect 2.4](#). [Sect. 2.5](#) describes the resulting catalog and its validation. Conclusions are summarized in [Sect. 2.6](#).

2.2 The data

2.2.1 APOGEE overview

The *Apache Point Observatory Galactic Evolution Experiment* (APOGEE) is one of the four Sloan Digital Sky Survey III (SDSS-III, [Eisenstein et al. 2011](#); [Aihara et al. 2011](#)) experiments operated from 2011 to 2014. APOGEE uses a 300-fiber multi-object spectrograph working in the near infrared (*H*-band, 1.51- 1.70 μm) at high spectral resolution ($R \sim 22\,500$, [Wilson et al. 2010](#)). The spectrograph is attached via a fiber optic train to the SDSS 2.5-meter telescope at Apache Point Observatory ([Gunn et al. 2006](#)).

Since the effects of extinction at near-IR wavelengths are reduced, APOGEE has a strong potential to explore dust obscured regions of the Galaxy that are beyond the reach of optical surveys, in particular the inner Galaxy and bulge.

In a given observation, about 230 (out of 300) fibers are allocated for scientific targets selected from the source catalog the *Two Micron All Sky Survey* (2MASS, [Skrutskie et al. 2006](#)).

The $\sim 160\,000$ selected scientific targets are distributed across all Galactic environments. Most of them are red giant stars but there are also special subsamples including stars with measured parameters and abundances from other spectroscopic studies, cluster members, etc. associated to several APOGEE ancillary science programs (see [Zasowski et al. 2013](#), for a detailed description of the different target classes).

In addition to the science targets, a sample of hot stars, also called telluric standards stars (TSSs) or *hot telluric* calibrators are observed (35/300 fibers) to allow for the correction of the telluric absorption lines (see below). Finally, the remaining ~ 35 fibers are allocated for observing blank sky positions to enable sky emission subtraction.

2.2.2 The APOGEE telluric standard stars

The total number of TSSs in the APOGEE survey is nearly $\sim 17\,000$. Ideally, for a good telluric correction one would like to have bright O, B and A stars because of their featureless spectra. Therefore, to maximize the chances of observing stars of these types, the TSSs were selected as the bluest stars on a given plate having a magnitude in the range $5.5 \leq H \leq 11$ and ensuring a uniform distribution over the plate (see [Zasowski et al. 2013](#), for details of TSS selection). Their spectra are used to adjust in an exquisite way the atmospheric transmission and its variability throughout the field, a transmission that is used to remove the telluric lines in all observed targets as illustrated in [Fig. 21](#).

2. A CATALOG OF $1.5273 \mu\text{m}$ DIFFUSE INTERSTELLAR BANDS BASED ON APOGEE HOT TELLURIC CALIBRATORS

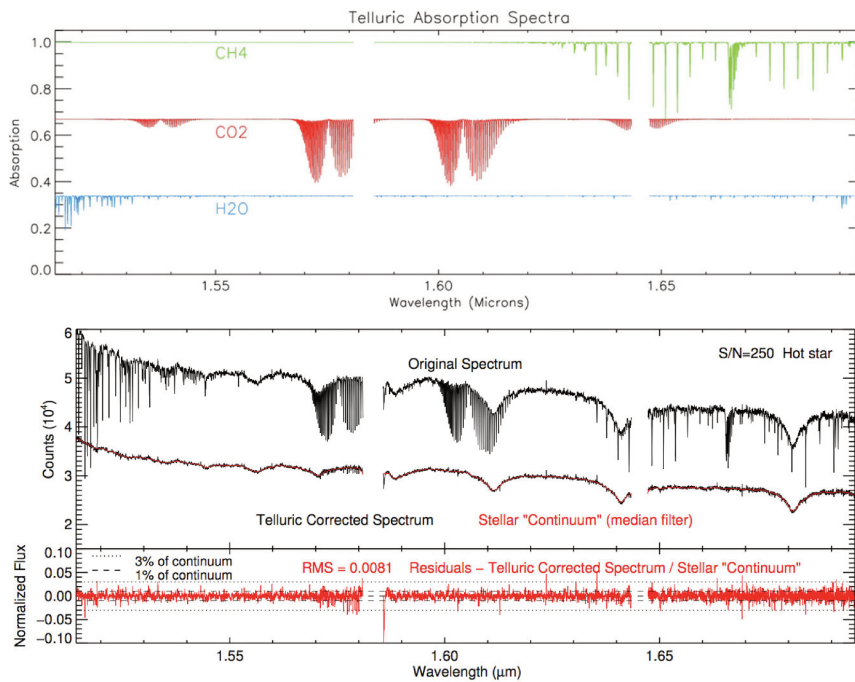


Figure 21 Atmospheric telluric transmission in the APOGEE spectral window. Top: telluric absorption lines of CH_4 (green), CO_2 (red) and H_2O (blue). Bottom: illustration of an APOGEE spectrum of a telluric standard star before and after telluric correction. From [Nidever et al. \(2015\)](#).

It is important to note that the TSSs are corrected for telluric absorption lines in the same way as the science targets. In other words, they benefit from the correction tool they have themselves produced. An interesting point about these stars is that, in addition to their use as tools to decontaminate the telluric absorption, they constitute a highly valuable dataset for ISM studies since their smooth continua are ideal to extract the information associated with DIBs. Here we focus on the strongest $1.5273 \mu\text{m}$ DIB. Work on the weaker absorption bands is presented in Part. III.

The TSS can be identified in the APOGEE data products by means of the APOGEE_TARGET2 bitmask since all these stars are flagged as APOGEE_TELLURIC (bit 9).

2.2.3 Used information from the APOGEE Archive

This work is based on the products from the SDSS data release 12 (DR12, [Alam et al. 2015](#)). This release includes all the data taken between April 2011 and July 2014. The spectra can be downloaded from the Science Archive

Server (SAS) as described on the data access page¹. There are three different types of reduced spectra available (see [Nidever et al. 2015](#); [Holtzman et al. 2015](#)). Here, we use the calibrated, well-sampled, and pseudo continuum-normalized combined 1D spectra. These are available as fits files with four separate extensions: the first one carries the information about the star and the derived stellar parameters, the second one contains the observed spectra, the third one saves the error pixels and the fourth one has a state-of-the-art modeled spectrum S_λ adjusted to the observed one ([García Pérez et al. 2015](#)). The modeled spectra are interpolated from a grid of spectra, itself based on a large sample of model atmospheres ([Mészáros et al. 2012](#)). These modeled spectra are optimized for stars at temperature $3\,800\text{ K} < T < 5\,250\text{ K}$ ([Ahn et al. 2014](#)). The TSSs are *a priori* hotter, and therefore as shown below, small adjustments to the provided modeled spectra were needed.

All the spectra are sampled at same rest wavelength pixel scale, with a constant dispersion in $\log \lambda$, as

$$\log \lambda_i = 4.179 + 6 \times 10^{-6} i \quad (2.1)$$

with 8575 total pixels ($i = 0$ to 8574), giving a rest wavelength range of 15 100.8 to 16 999.8 Å ([Nidever et al. 2015](#)).

We also use the table that summarizes all the parameters derived from the APOGEE spectra (for DR12, allStar-v603.fits), including for each observed individual star its mean barycentric radial velocity, the standard deviation of the mean velocity, the mean ASPCAP parameters and abundances as derived from the combined spectra, and a compilation of ancillary targeting data (see [Nidever et al. 2015](#); [Holtzman et al. 2015](#), for a full description of the data in these files).

2.3 Data analysis

The aim of this work is analyzing the series of $\sim 16\,000$ DR12 TSS spectra that can be downloaded from the APOGEE site to determine the presence (or absence) of the DIB at 15273 Å and measuring its equivalent width in case of positive detection.

Given the volume of data, this needs to be done with as less as possible human intervention.

For that, we took as starting point the methodology presented by [Puspitarini et al. \(2013\)](#) for optical spectra, and adapted it to the peculiarities of APOGEE spectra. At the end, we had a fully automated DIB extraction

¹http://data.sdss3.org/sas/dr12/apogee/spectro/redux/\r5/stars/125_6d/v603/

method able to measure DIB equivalent widths (EWs) without any user interaction during the fit. The code was developed using the IGOR PRO environment². Note that the reduced pseudo-normalized spectra of DR12 are corrected from telluric lines contamination. Thus, no telluric correction is needed.

In the following, we give the details of our fitting technique, we explain how we extracted the EW of the DIB and how we estimated their associated uncertainties.

2.3.1 Profile fitting

We fit each TSS spectrum to a model made out of the product of several components as follows:

$$M_\lambda = [S_\lambda]^\alpha \times DIB[\sigma, \lambda, D] \times (1 + [A] \times \lambda) \quad (2.2)$$

with:

- $[S_\lambda]^\alpha$, *an adjusted stellar spectrum*: S_λ is the initial stellar model provided by the APOGEE project. As we mentioned above, this model is not optimized for the TSSs that are hotter than the main targets. Therefore, even if the velocity of each target star was accurately determined and the global shape of the spectrum was most of the times adequate, the depth of the stellar atmospheric lines was not properly estimated (see Figure 22). We included a scaling factor (α) in order to take this into account and to adjust the model depth to the data.
- $DIB[\sigma, \lambda_c, D]$, *the DIB profile*: It was modeled as a Gaussian function with three free parameters associated to its width (σ), central wavelength (λ_c) and depth (D).
- $(1 + [A] \times \lambda)$, *a local continuum*: this was a simple 1-degree polynomial introduced to model as closely as possible the continuum around the DIB.

We selected a pre-defined spectral range for the fit restricted to the vicinity of the DIB [15 260 – 15 290]Å to determine the above coefficients α , σ , λ_c , D and A . Note that this range was large enough to ensure an adequate sampling of the neighboring Brackett 19-4 stellar line at 1.52647 μm . Errors provided by APOGEE were used to mask

²<http://www.wavemetrics.com>

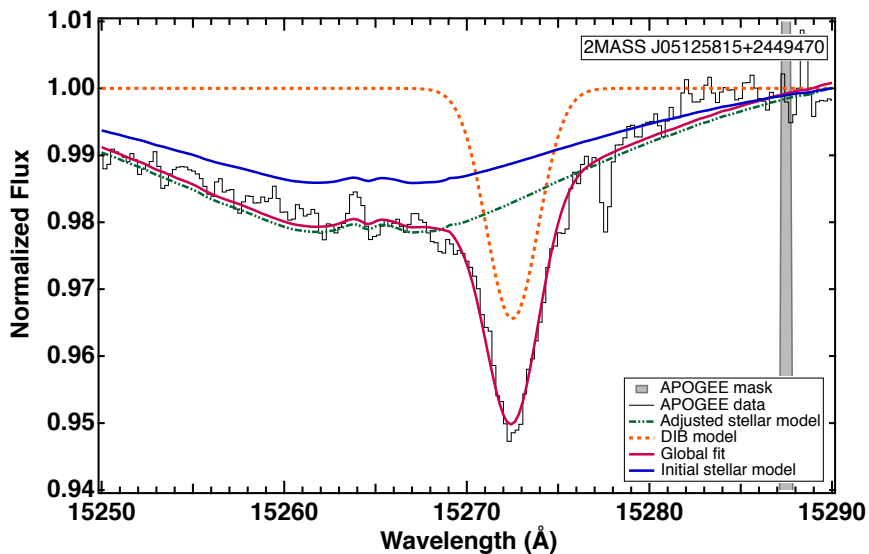


Figure 22 Example illustrating our fitting method. Data as provided by the APOGEE survey are shown in black while the final stellar+DIB modeled spectrum appears in magenta. The initial stellar model provided by APOGEE and the model obtained after application of the scaling factor α are shown in solid blue and dash-dot green lines respectively. The DIB absorption alone is represented with a dashed orange line. A grey band in the red part of the spectrum shows an example of masked region.

those spectral ranges affected by artifacts due to imperfect sky emission correction or other sources of uncertainty. We use the Levenberg-Marquardt algorithm implemented in IGOR PRO to compute the coefficients that minimize the chi-square χ^2 . An example illustrating our fitting procedure is shown in Figure 22.

2.3.2 DIB equivalent width and error estimates

In the following, we explain how we extracted the DIB equivalent width from our fits and how we estimated the uncertainties associated to each of the parameters presented in the catalog.

- *Computation of the DIB equivalent width:* Since none of the previous or present observations reveals any asymmetry of the 15273 Å DIB, and for our sightlines the linear regime prevails, we assume that the actual DIB absorption has a shape that is similar to the mono-Gaussian model. We also neglect the small departures from a Gaussian that result from multiple cloud superimposition that is small compared to other sources of uncertainties. Subsequently, assuming that the continuum $I_0(\lambda)$ is reasonably fitted,

2. A CATALOG OF 1.5273 μm DIFFUSE INTERSTELLAR BANDS BASED ON APOGEE HOT TELLURIC CALIBRATORS

the DIB equivalent width (EW) is the area of the fitted Gaussian and can be simply analytically derived from its parameters as the product of the model DIB's depth D by the coefficient σ :

$$EW = \int_{DIB} \frac{I_0 - I_\lambda}{I_0} d\lambda = \sqrt{2\pi} D \sigma \quad (2.3)$$

where $I(\lambda)$ is the observed spectrum.

- *Computation of standard deviations in residuals:* We calculated the standard deviation of the fit residuals, *data - model*, in a region close to the DIB (region A=[$\lambda_c - 10, \lambda_c + 10$] Å). In addition to this, we performed a second fit using the same function as the one presented in Eq. 2.2 but over the whole spectral range covered by APOGEE. As a matter of fact, we found that the first and third terms of Eq. 2.2 are good enough to represent continuum and Bracket lines in the entire APOGEE spectral region. For this fit the DIB term in the equation has the same restrictions as in the local fit. The DIB is fitted to ensure an optimum placement of the continuum in the DIB region and subsequently everywhere. As a matter of fact, omitting the DIB could bias the continuum in its spectral region and react on the whole fit. The residuals from this additional fit were used to obtain two additional measurements of the standard deviation. The first one was calculated over a *clean* (i.e. free from DIB absorption, strong stellar lines and telluric residuals) spectral range (region B= [15 892-15 959] Å). The second one (region C= [15 200-15 250] Å) corresponds to a region relatively close to the DIB (and also free of DIB) and potentially contaminated by stellar residuals. Hereafter, we will call the standard deviation R for all the three regions, R_A , R_B and R_C . These were used for the selection criteria discussed in Section 2.4. Also, the standard deviation R_A in the narrow spectral range around the DIB is used below to estimate the uncertainty on the DIB equivalent width.

- *Uncertainties on the DIB central wavelength and width:* The IGOR algorithm uses data and fitted model to evaluate the *data-model* standard deviation in the spectral range used for the fit, within the implicit assumption that the fitting function is ideally adapted to the data and the data are characterized by random Gaussian noise. If there are telluric line residuals or any other artefacts that amplify the signal fluctuations, the estimated standard deviation is correspondingly increased and treated as random noise. Based on the standard deviation and the mutual influence of the parameters the algorithm estimates one sigma errors on each parameter. We use these error estimates on both the central wavelength and the width.

- *Uncertainty on the DIB equivalent width:* For this quantity we estimated the error in a very conservative way in order to take into account the depar-

tures from Gaussian noise and the ideal fitting function, as well as potential subsequent misplacements of the continuum level. As a matter of fact in a number of cases telluric absorption or sky emission correction residuals are present and for a number of targets the stellar line shapes are not perfectly fitted. This may result in slight displacements of the fitted continuum that do not impact the line center and impact the width in a negligible way but may impact the depth. For the most conservative estimate of the error we used the standard deviation of region A, coupled to the maximum DIB width deduced for each sightline from HI 21 cm data (see Sect. 2.4). The maximum error was estimated as the equivalent width of a Gaussian with the maximum width of the HI 21 cm line and a depth equal to R_A :

$$err(EW) = \sqrt{2\pi} R_A \sigma_{HI21cm} \quad (2.4)$$

We checked that this conservative error is appropriate to all types of spectra and data quality, including those cases where there are clear residuals linked to stellar or telluric lines. Figure 23 shows the estimated error as a function of the equivalent width for all targets of the catalog. It can be seen from the figure that due to our method based on HI, for the same EW the error is significantly larger in directions where the ISM radial velocity range is very large, mainly here at Galactic longitudes smaller than 70 deg. This confirms that our quoted values are very conservative.

2.4 Validation criteria

2.4.1 Selection of fitted absorptions

We applied a series of tests to the fitted Gaussian absorptions based on the fitted parameters, the signal quality in the DIB region and elsewhere, and finally the LOS direction and the corresponding Galactic gas. The series of tests is schematically represented in Figure 24.

- *First global test*: the first selective test eliminates those absorptions that are deeper than 10% of the continuum (arrow (a) in Figure 24). Those depths are extremely unlikely for Galactic DIBs and especially for the TSSs that are nearby. Indeed, we checked a posteriori that all those cases correspond to spurious detections (stellar lines for the coolest or most metallic objects, unusually strong telluric residuals, etc). We also eliminated simultaneously absorptions centered outside the spectral range [15268-15280] Å. In the red, the corresponding large Doppler shifts of $\geq +137 \text{ km s}^{-1}$ are unrealistic for the nearby ISM. In the blue, the test excludes a tiny fraction of fits with unrealistically high negative Doppler shifts caused by a stellar line (see the histogram in Figure 25).

- *Test on the absorption depth*: as a second test for the selected targets (the arrow (b)), we compared the depth of the fitted absorption line with the

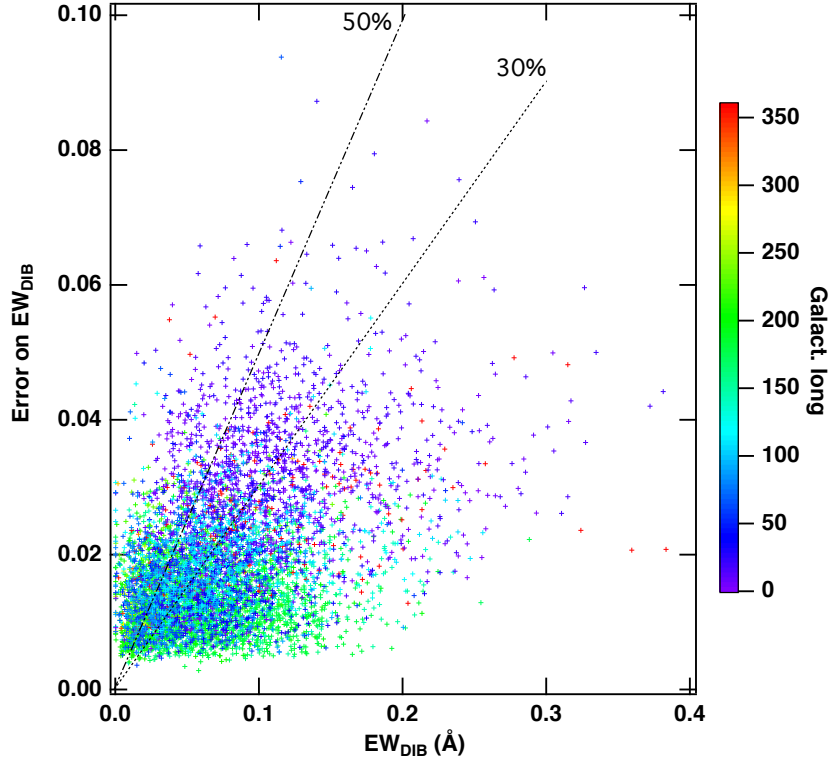


Figure 23 Estimated error on the DIB equivalent width EW for all the targets of the catalog. Above (resp. below) dashed lines relative errors are larger (resp. smaller) than 30 and 50 %. The color scale refers to the Galactic longitude of the target star. Due to our method, relative errors are overestimated for targets at lower longitudes (violet, dark blue signs, see text).

standard deviation on the residuals. This comparison was done in a one- or two-step process. We first compare the absorption depth with the maximum of the three standard deviations R_A , R_B and R_C described in subsection 2.3.2. If it is larger (arrow (d)), then start directly the tests on the width. If the depth is smaller than this maximum, i.e. if the spectrum is globally too noisy to detect the DIB (the arrow (c)) or the DIB is very shallow, we also compared the absorption depth with the local standard deviation R_A only. This second step allows to detect those spectra that are noisy in those spectral ranges far from the DIB but that have a good enough signal to noise in the DIB neighborhood to ensure a detection, i.e. the use of the maximum of the three R_A , R_B and R_C deviations is too restrictive. Absorptions that pass successfully the test (arrow (e)) are then examined for their widths in the same way than the previous ones (arrow(d)) but are flagged differently. The difference in the flags serves to evaluate the quality of the spectrum and

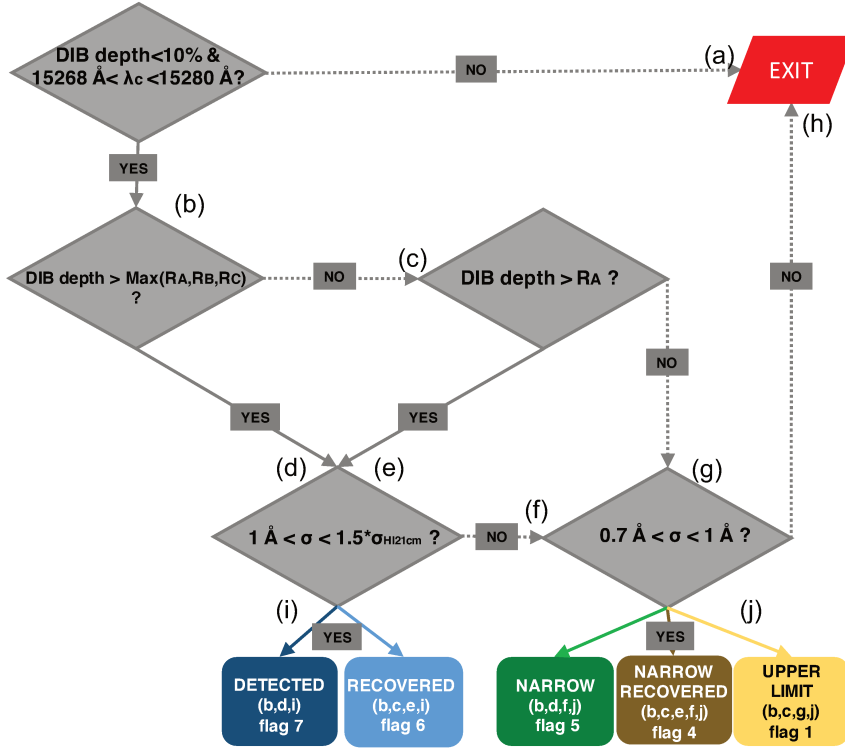


Figure 24 Flowchart compiling our decision criteria to create our catalog. Any spectrum able to reach the bottom part of the flow has a positive DIB detection. The path followed by a given spectrum to be classified has been indicated in the corresponding box with small letters. Flags numbers in each box at bottom are detailed in section 2.5 and included in the catalog.

identify those targets for which models have a shape incompatible with the measurements outside the DIB region. They will be visually inspected one by one. Absorptions who still appear too shallow (arrow (g)) are examined in a different way.

- *Criterion on the width in case of shallow absorptions:* as a third test for those absorptions that appear small with respect to the noise, both locally and in the three spectral regions (i.e. from arrow (g)), we selected the DIBs with a width, σ , within predefined limits. The lower limit of 0.7 \AA is deduced from the results of [Zasowski et al. \(2015\)](#) and in particular from the σ histogram of the whole APOGEE dataset shown in their Figure 6. This histogram shows that a very abrupt decrease occurs at $\simeq 1 \text{ \AA}$, implying that the intrinsic DIB width maybe as small as this value. Taking into account our typical uncertainties on the DIB width, $\text{err}(\sigma) \simeq 0.35$, we finally imposed a lower limit on the width of 0.7 \AA . This criterion has been checked a posteriori to eliminate spurious detections associated to bad pixels or telluric residuals, and simul-

2. A CATALOG OF $1.5273 \mu\text{m}$ DIFFUSE INTERSTELLAR BANDS BASED ON APOGEE HOT TELLURIC CALIBRATORS

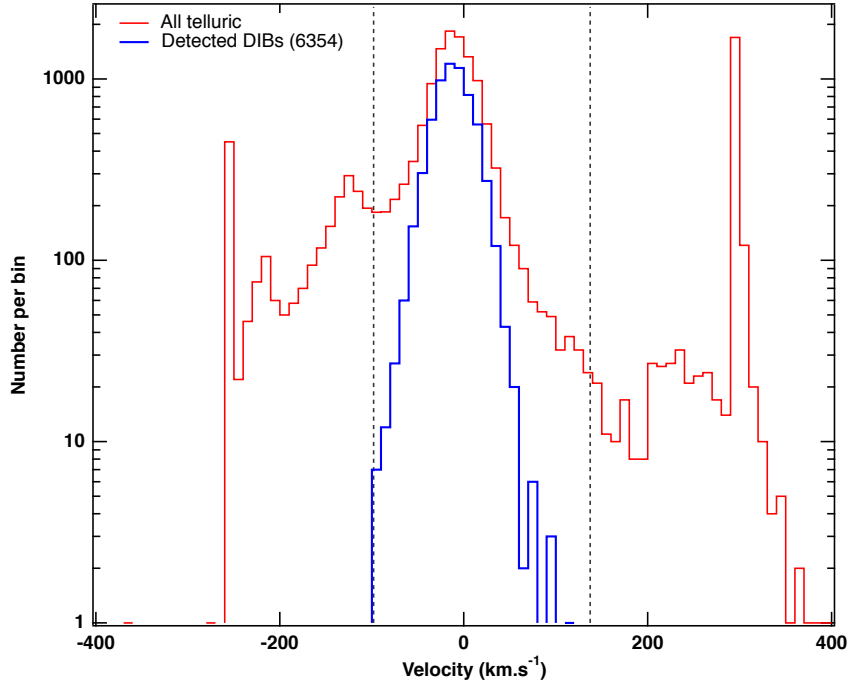


Figure 25 Histogram of the Doppler velocities for all fitted lines (red) and for selected DIBs only (blue). The limiting values used in the first selection step are shown as black vertical lines. Note the exclusion of all unrealistic Doppler velocities falling in the first and last bins and the disappearance of the secondary maximum at $\simeq 130 \text{ km s}^{-1}$ that corresponds to false detections produced by a strong stellar line falling at this wavelength.

taneously to keep actual detections of narrow DIBs. A typical example of such narrow absorptions that pass successfully the test is shown in Figure 26. It can be seen from the figure that it looks convincingly like an actual DIB. The upper limit of 1.0 \AA is chosen for the following reasons: for those absorptions that are very shallow (arrow (g)), this maximum value eliminates flat and elongated features of uncertain origin. Conversely, those very shallow absorptions that are reasonably wide pass the test and are falling in the *upper limit* category (yellow box in Figure 24. For those absorptions that are deeper and correspond to arrow (f), this maximum value will result in definitely rejecting those features that are broader than $1.5 \sigma_{\text{HI}21\text{cm}}$ (see below).

- *Limits on the width σ based on HI 21cm emission spectra:* For all absorptions that exceed the noise level, either globally or locally (arrows (d) and (e)), a subsequent test on the DIB width is performed based on radio 21cm HI spectra. As a matter of fact the velocity range for some fitted absorptions

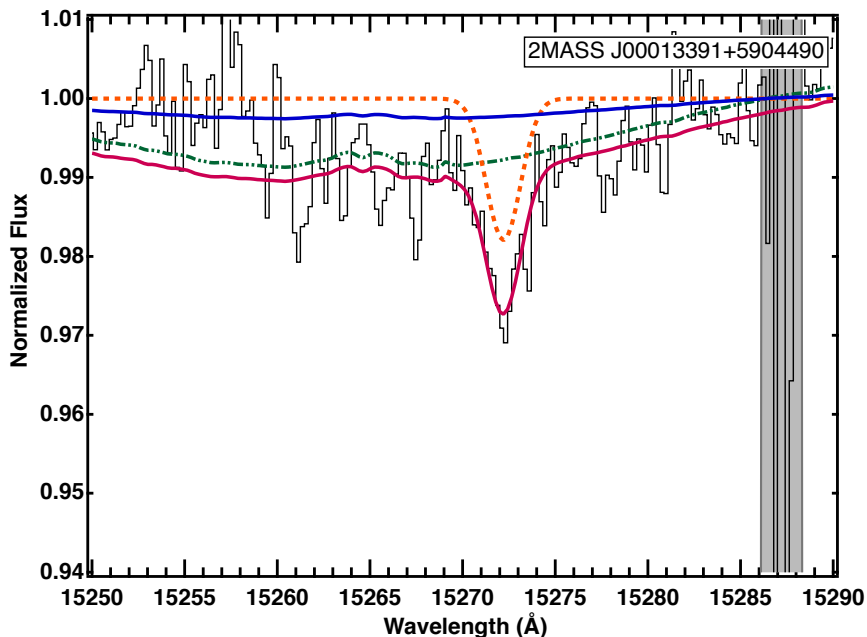


Figure 26 Example of detection of narrow DIB ($0.7 \text{ \AA} < \sigma < 1 \text{ \AA}$): 2MASS J00013391+5904490 with $\sigma = 0.9 \pm 0.1 \text{ \AA}$, $\lambda_c = 15272.2 \pm 0.1 \text{ \AA}$ and $EW = 0.041 \pm 0.021 \text{ \AA}$. Color and symbol code is as in Figure 22.

is clearly not compatible with the velocity distribution in the Galaxy. Such unrealistic absorption widths are caused by an improper modeling of the stellar lines, residuals of telluric lines, or a locally increased level of noise. In order to eliminate these spurious or biased detections from the catalog we added the following constraint on the DIB width based on the radial velocities of the atomic hydrogen gas. Indeed as the HI is the most common and widespread form of gas in the galaxy, its extent in velocity should encompass the velocity extent of the DIB, as verified in previous DIB measurements (see e.g. Puspitarini et al. 2015; Zasowski et al. 2015).

We estimated the maximal radial velocity width of the DIB by constructing a *virtual*, composite DIB based on the HI spectra. To do so we used the results of the HI line decomposition method presented in Planck et al. (2015). We briefly recall the principle of this decomposition.

Fraction of the article written by Quentin Remy and describing his work - The first step is to detect the significant lines in the brightness temperature $T_B(v)$ spectra of the LAB Survey (Kalberla et al. 2005). We measured the dispersion in temperature, T_{rms} , outside the bands with significant emission. In order to limit the number of false detections caused by strong noise fluctuation we clipped the data to zeros except if $T_B(v) > T_{rms}$ in 3 channels (3 km s^{-1}).

2. A CATALOG OF 1.5273 μm DIFFUSE INTERSTELLAR BANDS BASED ON APOGEE HOT TELLURIC CALIBRATORS

Then, using the 5-point-Lagrangian differentiation twice, we computed the curvature d^2T_B/dv^2 in each channel. Lines are detected as negative minima in d^2T_B/dv^2 . False detections triggered by the edges of the clipped regions were eliminated. Then each spectrum is fitted by a sum of pseudo-Voigt functions, one for each detected line. The pseudo-Voigt function is defined as

$$PV = \eta L + (1 - \eta)G \quad (2.5)$$

with $0 < \eta < 1$ the shape factor, L a Lorentzian, and G a Gaussian respectively defined as :

$$L = \frac{h}{1 + \left(\frac{v-v_0}{\sigma}\right)^2} \quad (2.6)$$

and,

$$G = h \exp\left(-\frac{(v-v_0)^2}{\sigma^2}\right) \quad (2.7)$$

where v_0 is the position of the line, σ the width and h the height parameter.

In order to take into account the detection uncertainties, the position of the line v_0 is allowed to vary in a $\pm 4 \text{ km s}^{-1}$ range around the initial position. For each detected line the free parameters η , h , σ , and v_0 are fitted by means of a χ^2 minimization. - *End of fraction from Quentin Remy*

For each LOS the computed HI decomposition is used to construct a *virtual* DIB, the one that would be measured in the spectrum of a star located beyond all the HI clouds, i.e. at the periphery of the Galactic HI disk. To do so, each HI component is associated to a DIB that has a width $\sigma_0 = 1.4 \text{ \AA}$ and a radial velocity equal to the one of the HI line. The chosen width σ_0 corresponds to an upper limit on the intrinsic DIB width that can be derived from the Figure 6 of [Zasowski et al. \(2015\)](#). To convert the HI line into a DIB equivalent width we use the following relationships:

- i) The HI column density is calculated in the optically thin limit:

$$N_{HI} = 1.823 \times 10^{18} \int T_b(v) dv \quad (2.8)$$

where $T_b(v)$ is the 21 cm line brightness temperature at radial velocity v .

- ii) The HI column density is transformed into reddening using the $N_{HI} - E(B - V)$ empirical relation from [Gudennavar et al. \(2012\)](#) and the average $R_v = A_v/E(B - V)$ value of =3.1:

$$A_v = 3.1 \times 1.6 \times 10^{-22} \times N_{HI} \quad (2.9)$$

and finally

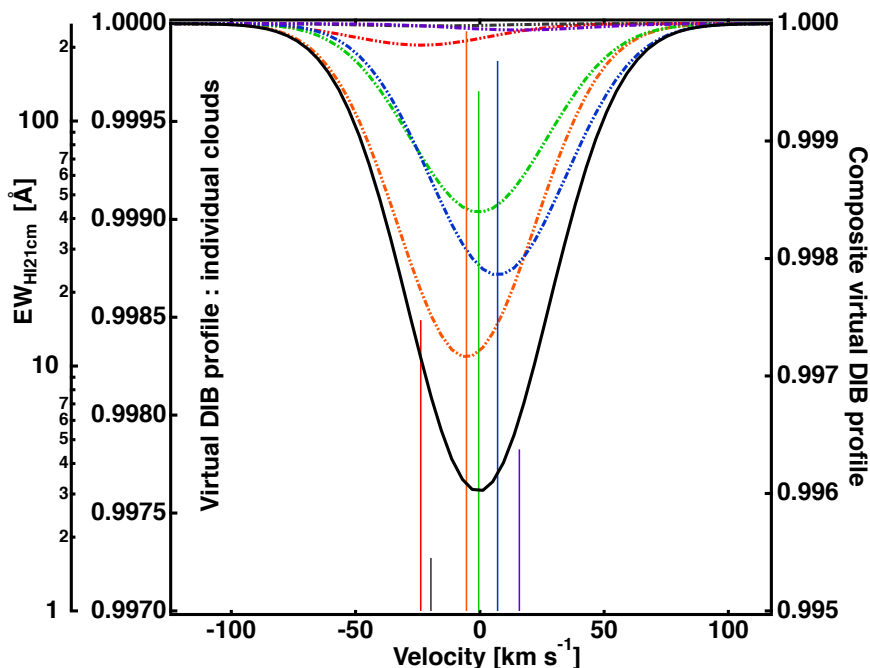


Figure 27 Example illustrating our construction of a *virtual* DIB for a typical LOS with 6 HI clouds. Vertical lines in different colors mark the strength and velocity of the 6 individual HI 21cm components. The corresponding individual Gaussians for the synthetic DIBs are shown using the same colors. The function representing the total *virtual* DIB through the HI disk is plotted in black. Note that for a better visualization, the scales for the total DIB and individual components are different.

- iii) The extinction is converted into a DIB equivalent width using the relation derived by [Zasowski et al. \(2015\)](#):

$$EW_{DIB} = 0.102 \times A_v^{1.01} (\text{\AA}) \quad (2.10)$$

The depth of each individual DIB is computed from the EW and the width. The final *virtual* DIB is the product of those individual DIBs and as such it is broadened to match the velocity distribution of the HI spectrum for the entire path through the Galaxy. Figure 27 illustrates the construction of the *virtual* DIB for a typical LOS with 6 HI clouds. This *virtual* DIB is fitted to a Gaussian and the resulting width σ_{HI21cm} is used to impose a limit on the APOGEE absorption width.

Such a limit is ensuring the compatibility between the measured DIB width and the velocity spread seen in HI. Absorptions that do not pass the test (i) as shown in Figure 24 enter test (f). The broad absorptions will be discarded

Table 21 Summary with statistics of the selected sample

	λ_c (\AA)	σ (\AA)	EW (m\AA)
Mean	15272.42	1.50	78
Std Dev	1.13	0.40	49
Median	15272.43	1.47	69

as discussed above and the narrow lines are reconsidered and classified as shown in Figure 24.

2.4.2 Special cases

We applied target selection criteria and considered separately Be Stars and stars from the field 4529 because they can yield difficulties in fitting. To do so we used the Chojnowski et al. (2015) catalog of Be stars and the information contained in the APOGEE tables. All these spectra have been the subject of one by one visual inspection and only those where the DIB was clearly unambiguously and accurately detected were kept. Figure 28 contains an example of a Be star spectrum and a spectrum from a star in plate 4259.

The different possible outcomes after the selection criteria described in section 4.1 and 4.2 have been flagged from 1 to 7. Figure 28 presents one representative example for each category.

2.5 The catalog

A fraction of the catalog of all detected DIBs is presented in Tab. 22 while a summary of its statistical properties appears in Tab. 21. For the total of 6716 detections or upper limits the catalog lists the 2MASS identification, then the equivalent width, central wavelength and DIB Gaussian width and associated errors. The flag allowing to identify the selection criteria for each target is also added. Finally, we included for completeness the estimated equivalent width for the *virtual DIB* as calculated from the emission in the HI 21 cm line. The various categories (1) Upper limit (2) Stars from plate 4529 (3) Be Stars (4) Narrow recovered DIBs (5) Narrow DIBs (6) Recovered (7) Detected comprise 362, 11, 52, 122, 473, 572 and 5124 TSS targets respectively. Figure 29 shows the location of all TSSs on a sky coordinates plot, distinguishing those that are included in the catalog. It can be seen that at Galactic latitudes smaller than $\simeq 15$ degrees all APOGEE fields contain TSSs with detected DIBs, while at higher latitude some fields have no targets included in this catalog, due to the weakness of the IS column.

The comparison between the velocity distributions of the original sample

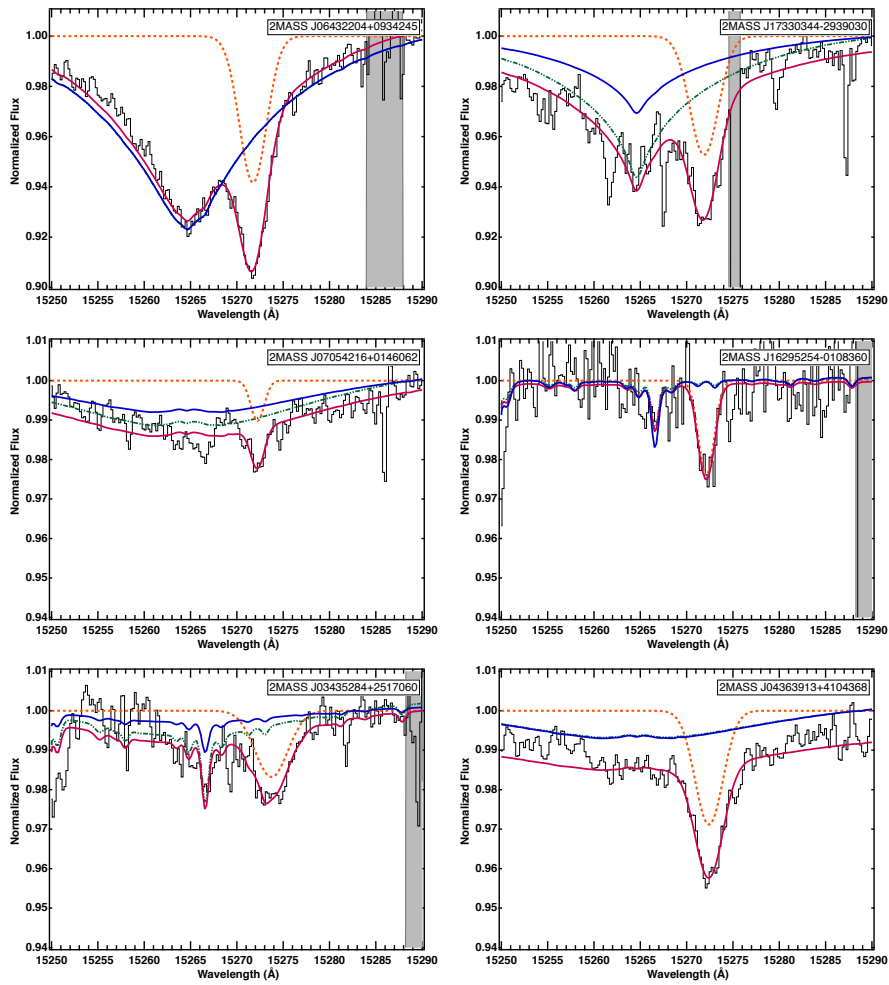


Figure 28 Illustration of the various categories of selected absorptions: (Top left) Detected-flag7; (Top right) Recovered-flag6; (Center left) Narrow-flag5; (Center right) Recovered Narrow DIBs -flag4; (Bottom left) Stars from plate 4529 -flag3; (Bottom right) Be Stars -flag2. Color and symbol code is as in Figure 22.

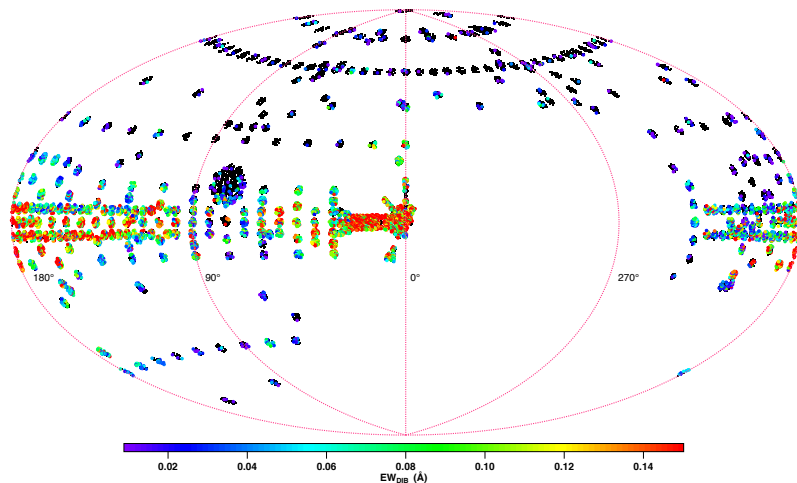


Figure 29 Location of all TSS targets on a sky coordinates plot, distinguishing those that are included in the catalog (colored circles, color representative of the EW) from those not included (black circles).

and the one included in this catalog is presented in Figure 25. Both of them peak at $\sim -20 \text{ km s}^{-1}$. However, while the final distribution resembles to a Gaussian distribution, the original one is quite irregular, with several secondary peaks. In particular those at ~ -260 and -130 km s^{-1} correspond to very strong stellar absorption features that have been successfully eliminated. Note that the final sample presents a relatively small (i.e. $\lesssim 30$) number of detections with high velocities (i.e. $\sim 100 \text{ km s}^{-1}$). After visual inspection of the corresponding spectra, we did not see any evidence for a spurious detection. Therefore we kept those detections in the catalog. They will be the subject of further work. We cannot exclude a similar high velocity tail in the blue due to the threshold imposed to remove spurious identifications due to stellar lines.

Figure 210 displays the distribution of the DIB widths. Only a very small fraction of selected DIBs have sigma above 3 \AA . In the same way, Figure 211 shows that there are very few DIBs (~ 167) with equivalent width $> 200 \text{ m\AA}$. This is not unexpected since TSS are relatively nearby stars, much closer than the APOGEE targets full sample.

Finally, we show in Figure 212 a comparison between the APOGEE measured EWs and the EWs of the *virtual* DIBs described in section 2.4 that are proportional to the total hydrogen column from the LAB Survey (Kalberla et al. 2005), converted into an equivalent width according to equation 2.4. The figure shows that, within the error bars, there is an envelope to all the data points that corresponds roughly to a one-to-one relation. This supports the robustness of our method and the choice of the conversion factor. Data

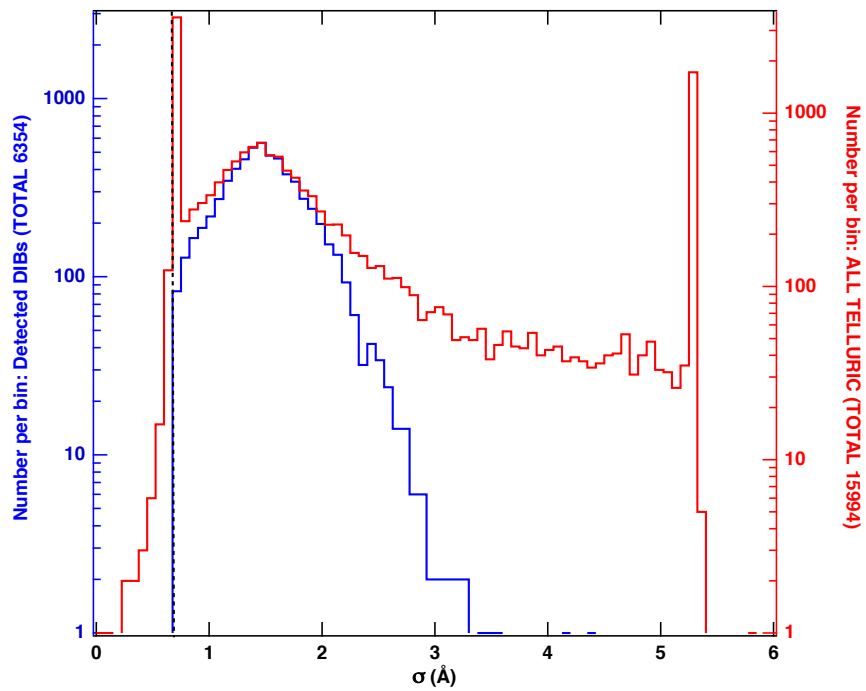


Figure 210 Same as Fig 25 for the DIB width σ . The limiting value 0.7\AA used in the selection step is shown as a black vertical line.

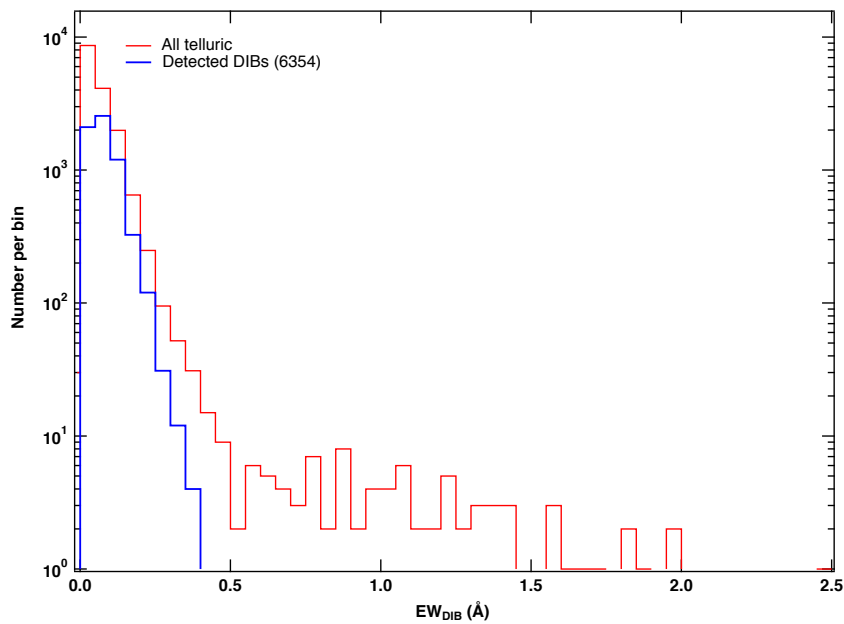


Figure 211 Same as Fig 25 for the DIB equivalent width.

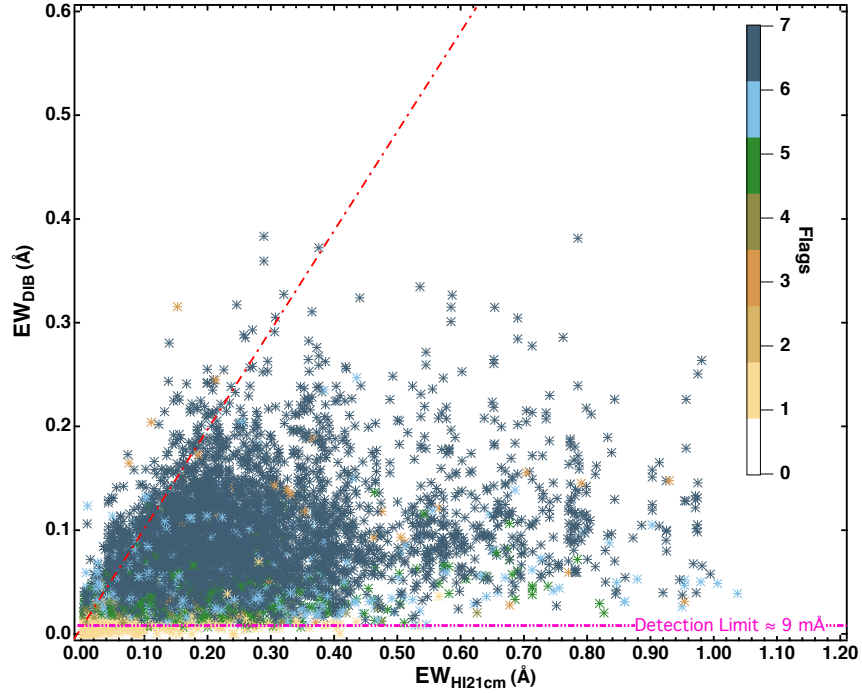


Figure 212 DIB equivalent width as a function of the *virtual* DIB equivalent width that is proportional to the total HI column. The dotted red line is the one-to-one relation (see text). The color code is the same as in Fig 24 with 2 additional colors indicating the special cases of Be stars (orange) and stars from field 4529 (camel) from subsection 2.4.2. A clear detection limit is found at around $9\text{m}\text{\AA}$, indicated by a pink dashed line.

points close to the envelope very likely correspond to target stars located beyond all the HI clouds seen in emission, while points well below the envelope correspond to targets that are in front of at least one cloud.

2.6 Summary

We have analyzed the series of SDSS/APOGEE NIR spectra of the calibration stars used to decontaminate data from telluric absorption lines. Those targets are generally blue stars and the APOGEE *Stellar Parameters and Chemical Abundances Pipeline* (ASPCAP, García Pérez et al. (2015)) stellar models cannot be used straight away. We have used them as a starting point and allowed the model broad stellar features to vary in depth to reproduce the observed continuum. In the region of the $1.5273 \mu\text{m}$ DIB this adjustment has proven to be good enough to allow the extraction of the DIB equivalent width and central radial velocity through Gaussian fitting of the DIB absorp-

Table 22. Sample stars with 15 273 Å DIB detection.

2MASS ID	GLON	GLAT	$\lambda_c \pm err(\lambda)$	$\sigma \pm err(\sigma)$	$EW \pm err(EW)$	Flag	$EW_{H1\ 21cm}$
00001687 + 5903034	116.390	-03.169	15274.0 ± 0.2	1.1 ± 0.2	041 ± 018	7	219
00001877 + 5938132	116.500	-02.595	15272.3 ± 0.1	1.4 ± 0.1	075 ± 019	7	231
00005414 + 5522241	115.740	-06.791	15271.1 ± 0.3	1.9 ± 0.3	058 ± 018	7	109
00010331 + 1549325	105.570	-45.340	15272.0 ± 0.4	0.8 ± 0.5	010 ± 021	1	017
00010512 + 5651581	116.060	-05.332	15271.9 ± 0.4	1.4 ± 0.4	027 ± 014	6	148
00011569 + 6314329	117.320	+00.919	15274.5 ± 0.1	1.5 ± 0.2	097 ± 020	7	313
00013391 + 5904490	116.550	-03.172	15272.2 ± 0.1	0.9 ± 0.1	042 ± 022	5	219
00013919 + 7005554	118.690	+07.639	15272.8 ± 0.2	1.6 ± 0.2	062 ± 011	7	187
00022269 + 6254032	117.380	+00.559	15273.5 ± 0.1	2.0 ± 0.2	128 ± 025	7	279
00023939 + 7109185	118.970	+08.659	15271.7 ± 0.3	1.7 ± 0.3	053 ± 010	7	138
00024298 + 5748303	116.460	-04.450	15272.4 ± 0.2	1.2 ± 0.2	033 ± 016	7	190
00024671 + 1605384	106.240	-45.194	15272.8 ± 0.2	0.7 ± 0.2	016 ± 012	5	017
00024931 + 5709106	116.350	-05.096	15272.7 ± 0.3	1.7 ± 0.3	049 ± 013	6	158
00024931 + 5709106	116.350	-05.096	15272.7 ± 0.2	1.3 ± 0.2	058 ± 017	7	158
00025231 + 5841372	116.650	-03.584	15272.9 ± 0.2	1.8 ± 0.2	069 ± 017	7	223
00025606 + 7014169	118.820	+07.754	15273.2 ± 0.3	1.2 ± 0.3	029 ± 013	7	164
00032397 + 7310282	119.420	+10.631	15268.4 ± 0.5	0.8 ± 0.6	008 ± 016	1	103
00042334 + 5626552	116.430	-05.828	15273.0 ± 0.2	0.8 ± 0.2	024 ± 022	4	141
00044189 + 6939114	118.860	+07.152	15274.4 ± 0.3	0.9 ± 0.3	021 ± 013	4	216
00044627 + 0132128	099.672	-59.211	15271.4 ± 0.6	0.9 ± 0.6	008 ± 009	1	013
00045177 + 5933503	117.060	-02.775	15272.5 ± 0.4	2.2 ± 0.4	066 ± 027	7	230
00045306 + 7048114	119.090	+08.280	15273.6 ± 0.8	1.4 ± 0.8	014 ± 007	6	138
00050083 + 6349330	117.840	+01.414	15271.9 ± 0.1	2.0 ± 0.1	175 ± 030	7	313
00051293 + 5811530	116.860	-04.127	15272.7 ± 0.1	1.2 ± 0.1	060 ± 013	7	223
00051873 + 5758464	116.830	-04.345	15274.0 ± 0.2	1.6 ± 0.2	070 ± 024	7	193
00052394 + 6347207	117.870	+01.370	15271.9 ± 0.1	1.7 ± 0.1	135 ± 019	7	313
00052888 + 5717190	116.730	-05.028	15272.0 ± 0.3	1.2 ± 0.3	026 ± 014	7	158
00052965 + 5722141	116.750	-04.948	15272.3 ± 0.3	1.4 ± 0.3	043 ± 024	7	158
00053673 + 7530446	120.010	+12.901	15272.2 ± 0.2	1.7 ± 0.2	082 ± 023	7	110
00054538 + 6234237	117.700	+00.167	15274.7 ± 0.1	1.4 ± 0.1	133 ± 029	7	293
00060064 + 7001540	119.040	+07.504	15271.3 ± 0.3	1.4 ± 0.3	036 ± 011	7	193
00060945 + 6412287	118.030	+01.768	15272.1 ± 0.1	1.7 ± 0.1	130 ± 023	7	335
00061415 + 0127198	100.290	-59.414	15271.8 ± 0.2	0.8 ± 0.2	023 ± 016	5	014
00063033 + 5719168	116.870	-05.021	15272.8 ± 0.2	0.8 ± 0.2	021 ± 015	5	172
00064418 + 7541165	120.110	+13.062	15271.0 ± 0.4	2.3 ± 0.4	071 ± 026	6	110
00064478 + 0025574	099.822	-60.418	15271.6 ± 0.2	0.7 ± 0.2	024 ± 017	4	019
00064971 + 5737102	116.970	-04.734	15272.7 ± 0.4	2.1 ± 0.5	048 ± 016	7	193
00065832 + 5726544	116.960	-04.906	15272.2 ± 0.4	1.8 ± 0.4	040 ± 017	7	172
00071354 + 5804306	117.100	-04.295	15272.8 ± 0.2	1.2 ± 0.2	041 ± 023	7	193
00072008 + 6241381	117.900	+00.254	15272.9 ± 0.1	1.4 ± 0.1	139 ± 033	7	296
00074256 + 6318026	118.040	+00.845	15271.3 ± 0.1	1.4 ± 0.1	120 ± 022	7	304
00074657 + 5722435	117.050	-04.993	15272.0 ± 0.2	1.4 ± 0.3	043 ± 014	7	172
00074863 + 7040220	119.310	+08.109	15271.7 ± 0.6	0.9 ± 0.6	009 ± 010	4	167
00080292 + 7332356	119.820	+10.934	15271.8 ± 0.2	0.9 ± 0.2	025 ± 022	3	099
00081304 + 6315383	118.090	+00.796	15273.9 ± 0.1	1.3 ± 0.1	085 ± 023	7	304
00085840 - 0015231	100.410	-61.257	15273.3 ± 2.5	0.9 ± 2.7	002 ± 014	1	016
00090905 + 5737124	117.270	-04.786	15271.8 ± 0.2	0.9 ± 0.2	036 ± 015	5	177
00091817 + 7022314	119.380	+07.795	15272.6 ± 0.2	1.2 ± 0.2	038 ± 011	7	167
00092728 + 7447408	120.130	+12.152	15271.4 ± 0.2	0.9 ± 0.2	038 ± 012	5	108
00094423 + 0117063	101.810	-59.865	15272.6 ± 0.4	1.7 ± 0.5	033 ± 014	7	013

Note. — Table 22 is published in its entirety in the electronic edition of the *Astrophysical Journal*. A portion is shown here for guidance regarding its form and content.

2. A CATALOG OF 1.5273 μm DIFFUSE INTERSTELLAR BANDS BASED ON APOGEE HOT TELLURIC CALIBRATORS

tion. Careful and severe examinations of the DIB parameters, the continuum shape and the quality of the adjustment were done. This result in a conservative selection of reliable DIB parameters. In particular all DIB candidates that contradict radial velocity limiting values based on the HI 21 cm spectra have been excluded. A total of 6716 lines of sight are selected and the results are presented in a catalog available from CDS, Strasbourg . The statistical properties of the resulting DIB database show that our selection criteria are fully appropriate.

Since most of the calibration stars are nearby objects (say, within the first kpc), such a DIB catalog can be used to improve 3D maps of the nearby ISM and to complement maps at larger scale as we will see in Chapter 4.

A catalog of 1.5273 μm Diffuse Interstellar Bands based on late-type stars

The latest SDSS/APOGEE data release DR14 (August 2017) has provided an increased number of stellar spectra in the H band and associated stellar models using an innovative algorithm known as *The Cannon*. We took advantage of these novelties to extract as much as possible measurements of the 15 273 Å near-infrared DIB from the red giants stars. We modified our automated fitting methods dedicated for the TSSs and used in Chapter 2 with some adaptations motivated by the change from early- or intermediate-type stars to red giants. A new method has also been developed to quantify the upper limits on DIB strenghts. Careful and thorough examinations of the DIB parameters, the continuum shape and the quality of the adjustment of the model to the data were done. Our analysis has led to the production of a new catalogue containing 124 064 new DIB measurements.

3.1 Introduction

The infrared high resolution ($R \sim 22\,000$) Apache Point Observatory Galactic Evolution Experiment (APOGEE, [Majewski et al. 2017](#)) is one of the programs in the Sloan Digital Sky Survey III (SDSS-III, [Eisenstein et al. 2011](#)). Released APOGEE spectra have a high signal-to-noise (generally above 100) and remarkably well corrected for telluric emission and absorption with residuals generally below 1% as can be seen in figures from [Casey et al. \(2016\)](#). The latest APOGEE Data Release 14 (DR14; [Abolfathi et al. 2018](#)) includes results from APOGEE-1 (September 2011-July 2014) in addition to two years of SDSS-IV APOGEE-2 data (July 2014-July 2016). DR14 APOGEE products contain data from approximately 263 000 stars, all identified by a 2MASS catalogue name. Among the APOGEE stars, there are 231 000 main

scientific targets, mostly red giants intended for various scientific programs and forming part of the Bulge, the Bar, the Disk and the Halo. There are also 27 000 young and hot stars called Telluric Standards Stars (TSSs) which were used to correct telluric absorptions. These hot stars are distributed in all the fields observed by APOGEE (35 stars/field) and were chosen among the bluest in each field. 17 000 of these stars from APOGEE Data Release 12 (DR12; Holtzman et al. 2015) were the subject of a detailed DIB study in Chapter 2. They are particularly interesting because one can easily identify any interstellar signature. However, the new TSS spectra of DR14 are not publicly available.

It is obviously more difficult to extract the DIB from the late-type stars since the interstellar features are blended with deep stellar lines. This explains why most of our reliable DIB-fitting results of Chapter 2 were obtained for hotter stars. However, if the stellar models well reproduce the data, the extraction can be performed without ambiguities due to stellar blends. This is the case of the latest APOGEE data release DR14 which includes the *Cannon* synthetic spectra. In this chapter, instead of using TSSs, our sample is made up of the science targets, mainly red giants stars.

3.2 Cannon model spectra (new in DR14)

Highly detailed model spectra were fitted to the APOGEE data and made publicly available for a large number of targets. These models greatly facilitate the extraction of the diffuse interstellar bands present in the APOGEE spectral intervals. While the DR12 synthetic spectra used the APOGEE Stellar Parameter and Chemical Abundances Pipeline (ASPCAP; García Pérez et al. 2016a) for the derivation of the stellar atmospheric parameters and abundances, in DR14 a new and important change is the introduction of an innovative data-driven machine-learning technique known as “The *Cannon*” (Ness et al. 2015). This algorithm parameterized the spectral fluxes as a function of a set of independently-determined stellar parameters and abundances. For DR14, *Cannon-2* code by Casey et al. (2016) was trained on ASPCAP products for a subset of high S/N giant stars, and the model was applied to all objects within the range of parameters covered by the training set with some modifications listed in Abolfathi et al. (2018).

Here we analyze all available red giant stars (160 000) from the public *Cannon* data products. To do so we used the *CannonStar* file which contain *Cannon* labels, normalized observed spectra and associated uncertainties as well as synthetic spectra for each single star. Such *Cannon* results can be found at path¹/cannon/LOCATION_ID/cannonStar*.fits. The difference between

¹<http://www.sdss.org/sas/dr14/apogee/spectro/redux/r8/stars/l31c/l31c.2>

Cannon and ASPCAP has significant consequences on our DIB extraction, as will be detailed in the next section.

3.3 DIB extraction

3.3.1 Automated fitting method

We used the APOGEE DR 14 normalized spectra and their associated best fit *Cannon* models to extract the 15273 Å DIB through simple Gaussian profile-fitting. The general principles are the same as in the case of the automated code applied to APOGEE DR12 Telluric Standard Stars (TSSs) and are described in Eq. 2.2, Chapter 2. Here we kept the same fitting technique and the same method of classification as in the previous chapter, *i.e.* we fitted the data to the product of an adjusted synthetic spectrum S_λ^α (here *Cannon* instead of ASPCAP), a Gaussian DIB model $DIB[\sigma, \lambda, D]$ and a smooth continuum $(1 + [A] \times \lambda)$ as shown in Eq. 3.1.

$$M_\lambda = [S_\lambda]^\alpha \times DIB[\sigma, \lambda, D] \times (1 + [A] \times \lambda) \quad (3.1)$$

where each DIB is modeled as a Gaussian function with three free parameters associated to its Gaussian RMS width (σ), central wavelength (λ_c) and depth (D) as follows:

$$DIB[\sigma, \lambda, D] = 1 + D \times e^{-\frac{(\lambda - \lambda_c)^2}{2\sigma^2}} \quad (3.2)$$

Prior to the final global fit, the DIB extraction code performs preliminary series of automated tests that allow to measure the residuals between the data and the adjusted stellar model in three spectral regions: the local region around the DIB A = $[\lambda_c - 10 - \lambda_c + 10]$ Å, a region free of DIBs and telluric residuals B = $[15\,911 - 15\,966]$ Å and a narrower region free of DIBs and telluric residuals and closer to the DIB C = $[15\,200 - 15\,239]$ Å. The associated standard deviations R_A , R_B and R_C are used for selection criteria and estimates of the DIB uncertainties. During the fit itself the adjusted Gaussian curve representing the DIB is rejected or selected depending on its depth D , its width σ and spectrum quality criteria derived from the preliminary tests. However, here some fitting constraints have been modified to take into account the differences between the TSSs and the science targets:

- Stellar model adjustment: the *Cannon* stellar models are optimized for red giant stars, and they perfectly reproduce the observed data. It was not the case of the TSSs that are bluer stars for which it was necessary to adjust the stellar models. Here we simplified our constraints on the adjustment of the stellar synthetic spectra. We still allow for a global increase or decrease of all stellar lines, however the prior value for

3. A CATALOG OF 1.5273 μm DIFFUSE INTERSTELLAR BANDS BASED ON LATE-TYPE STARS

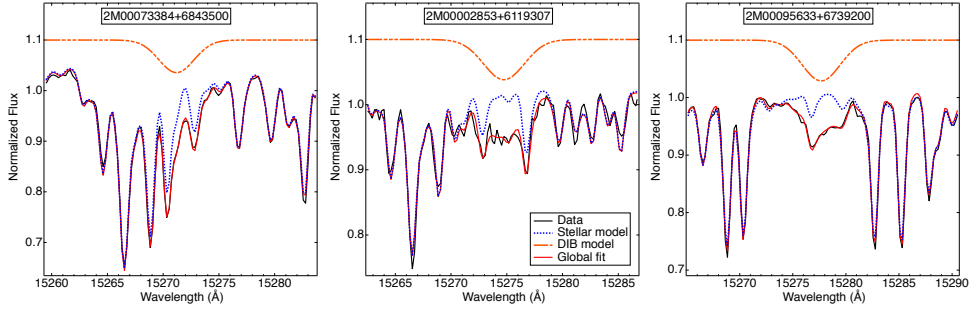


Figure 31 Illustration of DIB extraction towards three red giants stars. In each figure: APOGEE spectra are shown with solid black curves. The initial stellar model provided by APOGEE *Cannon* is shown in solid blue. The DIB absorption alone is represented in orange (with an offset). The solid magenta curves represent the final stellar+DIB modeled spectrum.

the adjustment coefficient α is always unity. The fitted coefficient is always very close to one and the continuum is also always very close to a straight line of value 1.

- DIB depth upper limit: TSSs are nearby stars whereas the APOGEE main targets can be very distant and DIBs can be much stronger. For this reason no upper limit was applied to the DIB depth.
- DIB depth lower limit: the stellar model is so close to the data in all spectral regions that the standard deviation R_A of the data-model residuals in the region close to the DIB (region A) is a good enough estimate of the measurement error on the DIB depth. As a consequence the new acceptance criterion is no longer based on a comparison between the DIB depth and the standard deviations of residuals in regions A, B, and C, but is now solely: Depth $D \geq R_A$.
- DIB radial velocity range: TSSs being nearby stars, the absorbing interstellar matter for those targets is characterized by a narrow radial velocity range. This is no longer the case here for the distant giant stars. As a consequence we widened the allowed interval on radial velocities with respect to the one used for TSSs. Specifically, we now restricted the spectral range for the DIB center to [15 260–15 286] Å.
- DIB width upper limit: we no longer used HI 21cm data to limit the total width of the DIB, instead we used limits based on the FWHM histograms from our study based on TSSs and [Zasowski et al. \(2015\)](#). The latter correspond to a broad range of star distances, broad enough to be valid here.
- DIB width lower limit: we kept the same lower limit of 0.7 Å on the

DIB width, supposed to be close to the intrinsic width as determined by Zasowski et al. (2015) and in Chapter 2 and with some allowance for noise-related uncertainty.

Fig. 31 shows some examples of our fitting method.

3.3.2 DIB upper limit estimate in case of no convergence or no DIB detection

If the adjustment described previously failed by absence of convergence (we call it the *non-convergence* case) or there was convergence but the fitted absorption is found to be smaller than the noise level (we call it the *upper-limit* case, although, as we will see some spectra, at the final stage of analysis, this term is not appropriate), then we re-initiated a second fitting procedure with the goal of extracting equivalent widths or upper limits in a more efficient way with more appropriate initial conditions. The total number of targets falling in the two categories and re-analyzed is 45 393. First, we fitted the combination of a continuum and a depth-variable stellar model to the data (i.e, removing a DIB contribution from the global model), this time masking the DIB area. In case of convergence, this ensures that the fitted continuum and the synthetic spectrum reproduce well the data outside the DIB.

- *Case 1:* If the fit fails again – this is the case when the model is not adapted to the data or if there is a problem of continuum, a new standard deviation on residuals will be calculated based on the difference between the data and the initial model provided by the APOGEE pipeline.
- *Case 2:* If the fit converges then the new residuals (difference between the data and the no-DIB adjusted model) are used for an updated estimate of the standard deviation.

The second step consists in fitting a simple Gaussian to the data-model residuals in the region of the DIB. To do so, we use the same initial guesses and constraints used for the automated fitting method as described in Subsect. 3.3.1.

- If the Gaussian fit does not converge, either because it has not found a solution or because there is a real absence of detectable DIB, then a linear adjustment is performed *i.e.*, on the continuum over the wavelength range chosen for the DIB EW [15 260-15 286] Å. The selected value for the EW is then zero and an upper limit on EW is estimated from the standard deviation of the residuals around the linear fit Std_{dev} and the average value of the width of the 15 273 Å DIB taken as 1.7 Å:

$$EW = 0 \pm 1.7 \times \sqrt{2\pi} \times Std_{dev} \quad (3.3)$$

Some representative examples are shown in Fig. 32.

- If the fit finds a solution, then the coefficients of the fitted Gaussian ($\sigma_{gauss}; D_{gauss}$) will be used either as DIB parameters in case 1 or as initial values for a new automated fit following Eq. 2.2 in case 2. Equivalent widths in both cases will be derived following Eq. 2.3 as $EW = \sqrt{2\pi} D \sigma$ where the widths are $\sigma = \{\sigma_{gauss}; \sigma_{fit}\}$ and the depths are $D = \{D_{gauss}; D_{fit}\}$ respectively. The errors are extracted as follows:

$$Error_{DIB} = 2\sqrt{\pi} \times \sigma \times Error_{depth} + 2\sqrt{\pi} \times \sigma \times Std_{dev} \quad (3.4)$$

These cases are illustrated in Fig. 33. Finally, for better understanding of our algorithm, Fig. 34 shows a graphical representation that maps out our step-by-step process to determine the upper limits. It is interesting to note that this additional treatment is quite productive: for $\sim 2/3$ of cases, the change of initial guesses for the DIB in the fitting procedure allows the Levenberg-Marquardt algorithm to converge to a good solution and a χ^2 significantly smaller than for the first fit. This can be explained by the existence of large Doppler shifts between the star and the absorbing ISM. As a matter of fact, in our first adjustment the initial condition for the DIB center was a null radial velocity of the absorbing medium in the stellar frame. In case of large differences between the star radial velocity and the absorbing ISM radial velocity, the initial position of the DIB center was accordingly distant from the actual DIB center, and in some cases the adjustment could subsequently stop at a secondary χ^2 minimum. This no longer happens in the second adjustment with an initial guess for the DIB center now very close to the best fit at the primary χ^2 minimum. Similarly, peculiar or poorly modeled stellar features could favor a secondary χ^2 minimum during the first adjustment, when they were combined with an initial position of the DIB far from the actual one. Using instead an initial guess much closer to the solution leads to the optimal solution.

3.3.3 The catalog

The extraction procedure allowed to extract EW measurements of the 15 273 \AA DIB for 124 064 different sight-lines. The catalog of equivalent widths and associated uncertainties, radial velocities and widths will be made available at the Strasbourg Data Center (CDS) after merging with the updated catalog of DIBs in the TSS spectra of Data Release 14, when available.

Note that, because the DIB is a weak absorption, despite the high quality of the spectra and stellar models, measurement uncertainties on the EW become on the order of the EW itself for $EW \lesssim 0.02\text{-}0.05 \text{\AA}$. This corresponds to $A_V \lesssim 0.5\text{-}0.8 \text{ mag}$ according to the average relationship (see below). This will result in some limitations in our analyses and correlative studies.

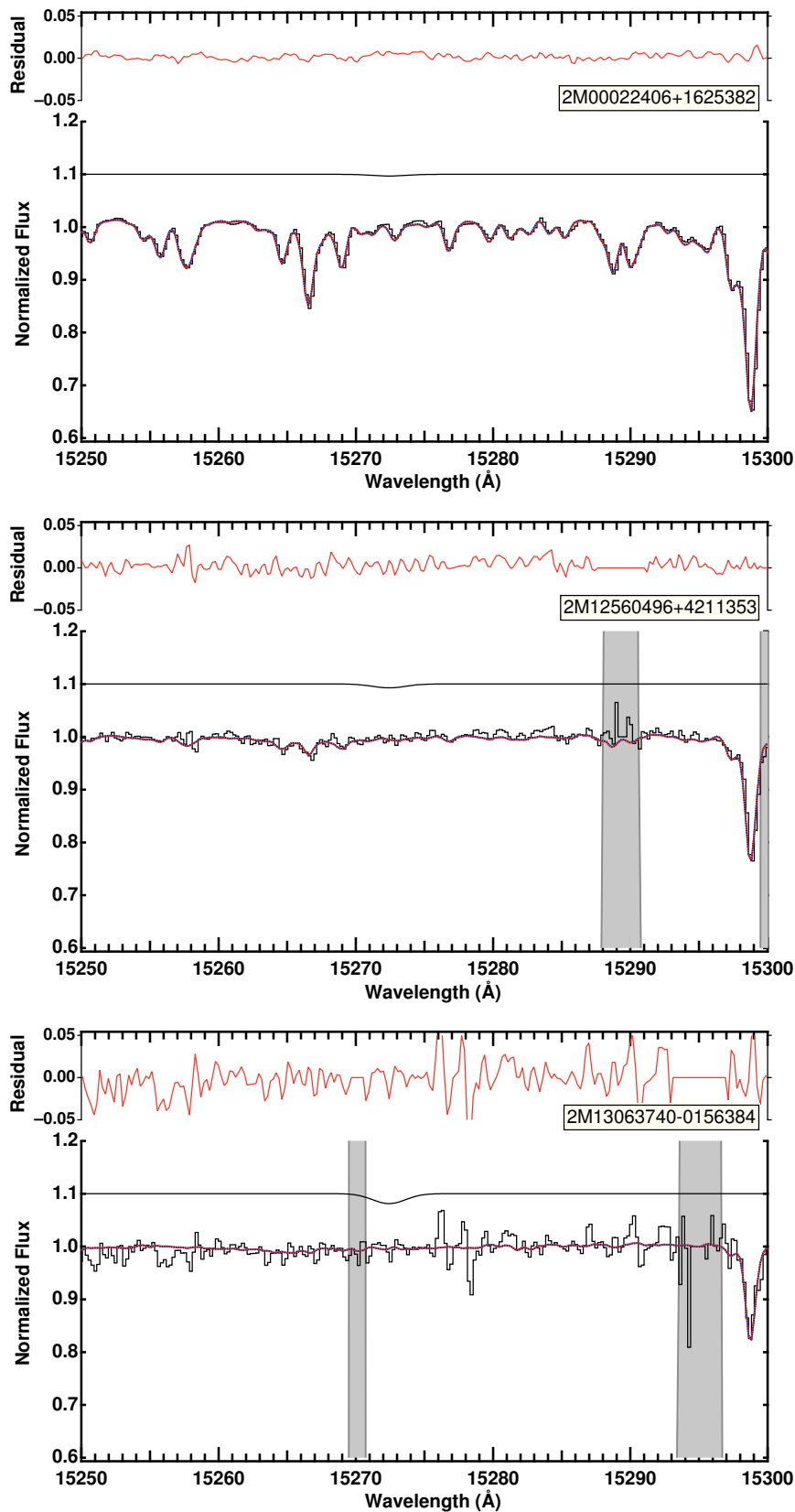


Figure 32 Illustration of DIB upper limit derivation, in the case of non convergence of the initial fitting. A Gaussian DIB profile with the maximum equivalent width compatible with the standard deviation in the data-stellar model residuals is shown at an imposed wavelength of 15272.42 Å in solid black (with an offset).

3. A CATALOG OF $1.5273 \mu\text{m}$ DIFFUSE INTERSTELLAR BANDS BASED ON LATE-TYPE STARS

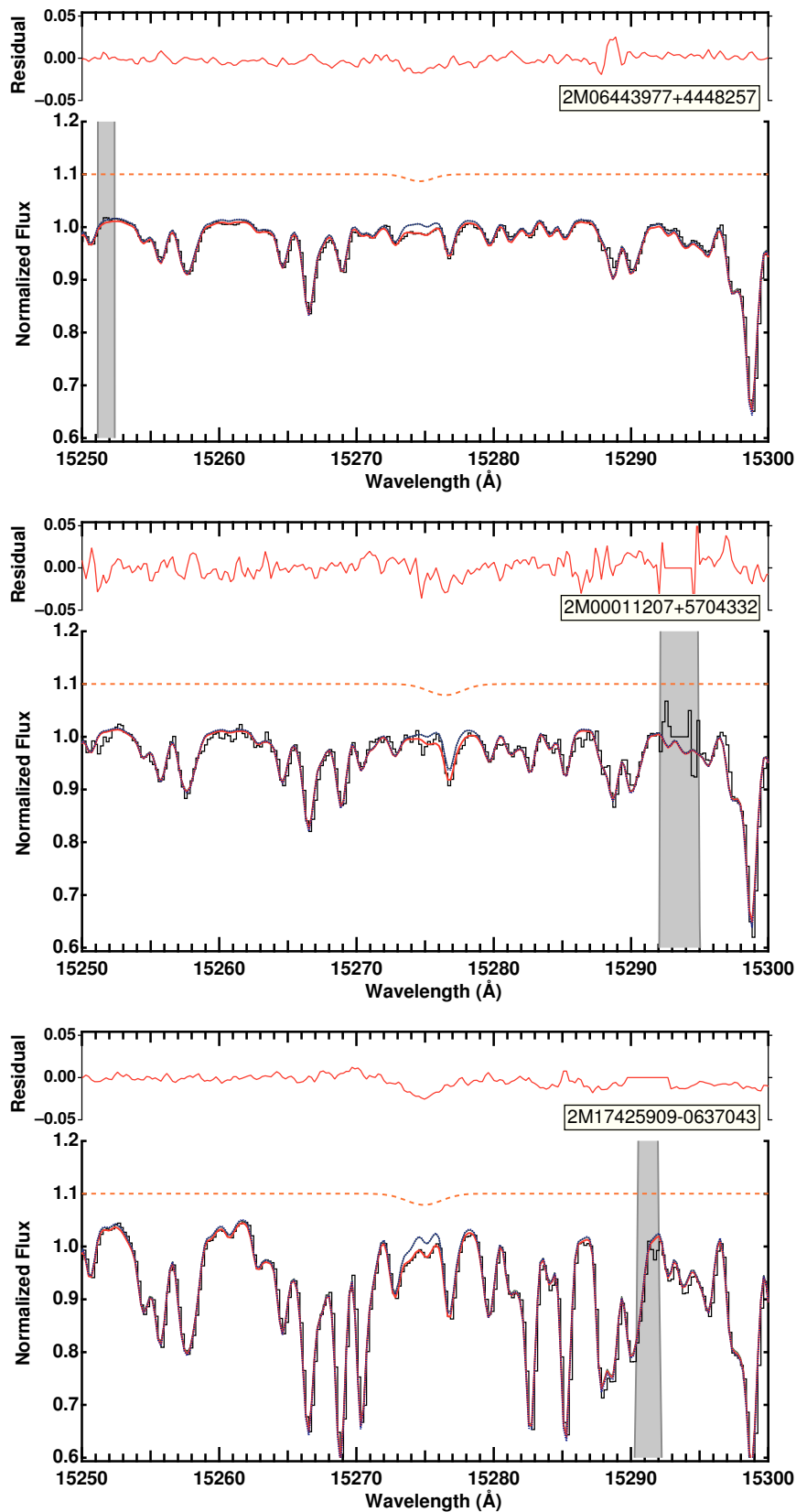


Figure 33 Illustration of DIB extraction in the case of convergence following the derivation of an optimal DIB prior (the initial guess based on the preliminary computation of data-stellar model residuals and its Gaussian fit). The fitted DIB is shown in dashed orange with an offset.

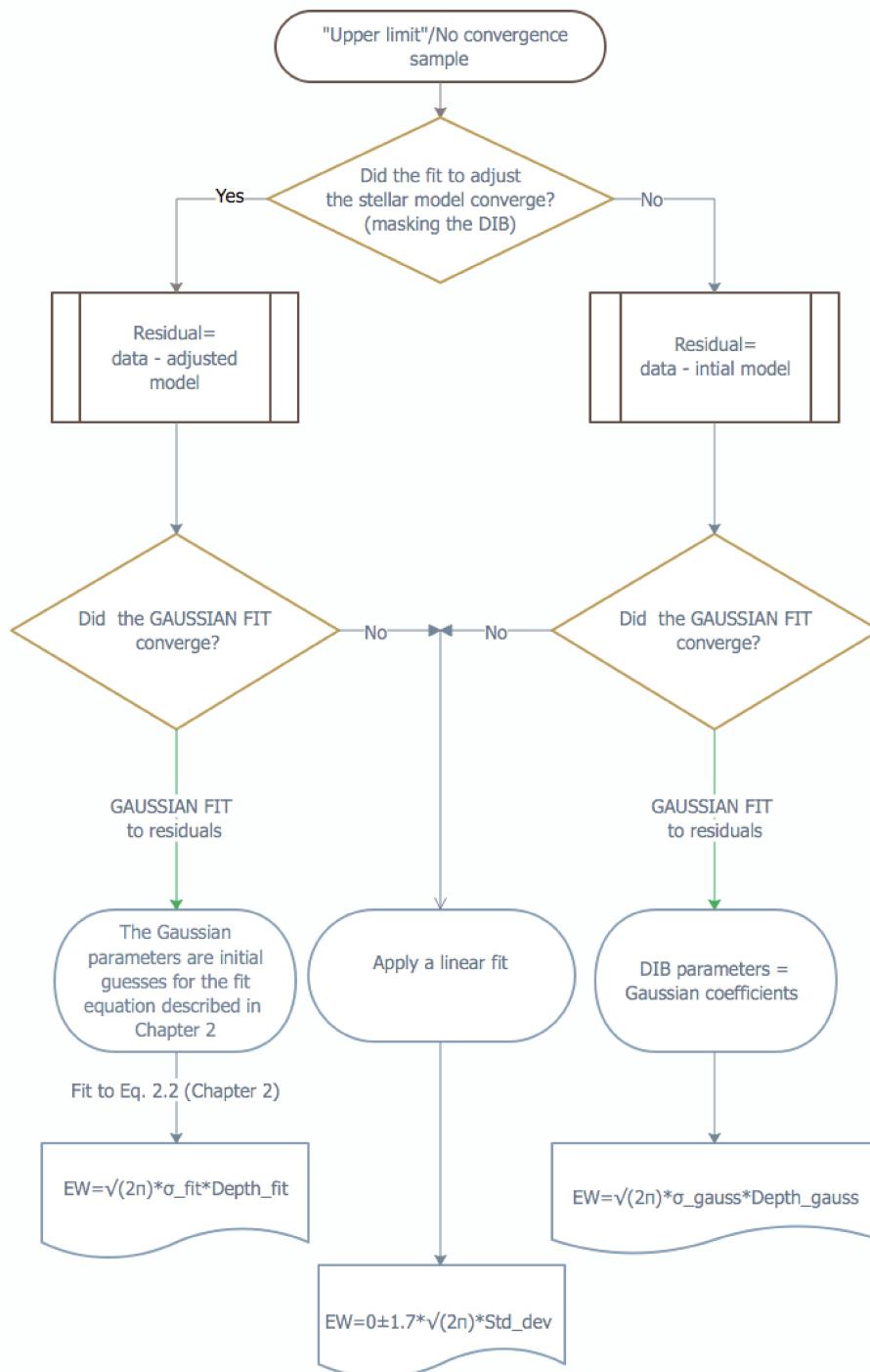


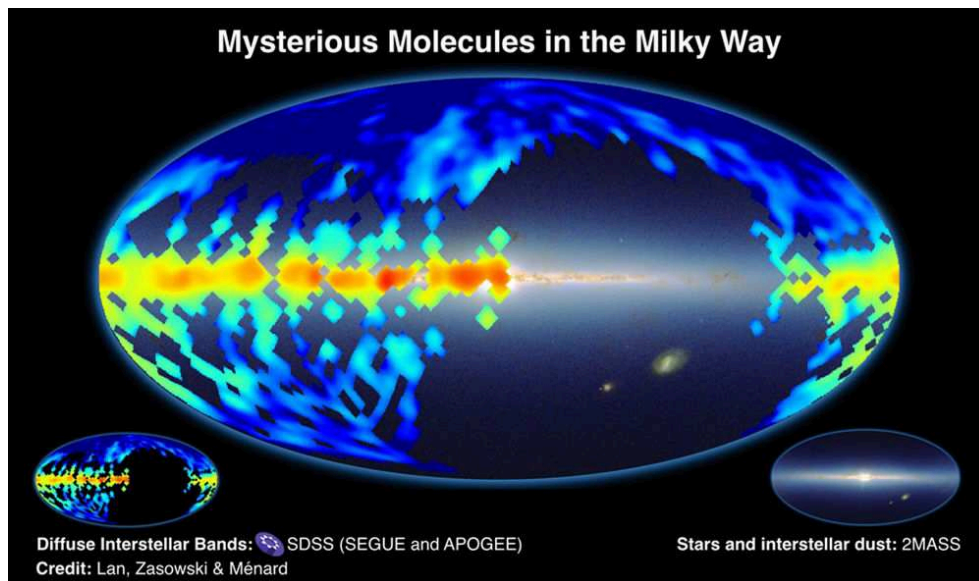
Figure 34 Flowchart compiling our decision criteria to determine the DIB equivalent widths in the upper limit and no convergence cases. Part of the spectra analyzed here are those classified as upper limit in our automated method essentially described by the flowchart in Fig. 24. The width σ_{fit} and the Depth $depth_{fit}$ are the Gaussian parameters derived from the Eq. 2.2. Std_{dev} is the standard deviation derived from the linear fit to residuals over the wavelength region defined to measure the EW of the DIB.

3.4 Conclusion

We have analyzed red giants NIR spectra from the last SDSS/APOGEE survey data release (DR14) with the goal of extracting the 15 273 Å DIB. To do so, we used the code developed in Chapter 2 with some adaptations motivated by the change of target types, namely from early- or intermediate-type stars to red giants. The use of the stellar models computed by means of the data-driven "Cannon" algorithm greatly facilitates the analysis. In the region of the 15 273 Å DIB the adjustment has proven to be good enough to allow the extraction of the DIB equivalent width, width and Doppler velocity through Gaussian fitting of the IS absorption. This resulted in a conservative selection of reliable DIB parameters for a total of 124 064 lines of sight. In the following, we illustrate the potential of these catalogs by means of two examples: DIB as tool for ISM tomography and the study of the conditions of appearance/disappearance of DIBs. These applications will demonstrate the potential interest of such catalogs and the amount of data and analysis one can get from the sightlines surveys.

Part II

Potential applications of DIB catalogs



DIBs as tracers of the nearby ISM

4.1 Introduction: DIBs as proxies for column densities of IS matter

DIBs are clearly correlated with interstellar matter and they have been used to locate spiral arms and build maps of reddening radial profiles (Kos et al. 2014; Puspitarini et al. 2015). The 15 273 Å DIB is correlated with the extinction over at least three orders of magnitude (Zasowski et al. 2015). Thus, it can be used as an independent approach to estimate it or as an initial guess in absence of better information. Note that we will demonstrate in the next chapter the existence of a break of the 15 273 Å DIB proportionality to the extinction at high extinction levels (a saturation related to the so-called “skin effect” already observed for a few DIBs), however this does not prevent the use of DIBs for cloud distance assignments.

We crossmatched the TSS catalog presented in Chapter 2 with the compilation of reddening measurements provided by Lallement et al. (2014) and used to build local 3D maps of the ISM. We have made several tests of DIB-based IS mapping in 3D, starting with very simple constraints on cloud minimum distances up to actual 3D inversion of DIB equivalent widths. Figure 41 shows the comparison between the APOGEE 1.5273 μm DIB equivalent width and the reddening for the 221 stars in common. There is a clear positive correlation showing that the fitted absorptions contain valuable information on the intervening ISM.

The figure also presents the linear fit derived by Zasowski et al. (2015) for the APOGEE cool stars.

Our data points cluster around this relationship in solid agreement with the results obtained for the late-type stars. We note however that the number of *outliers* with very weak DIBs is significantly higher than the number of *outliers* with strong DIBs. A possible explanation of this trend is the influ-

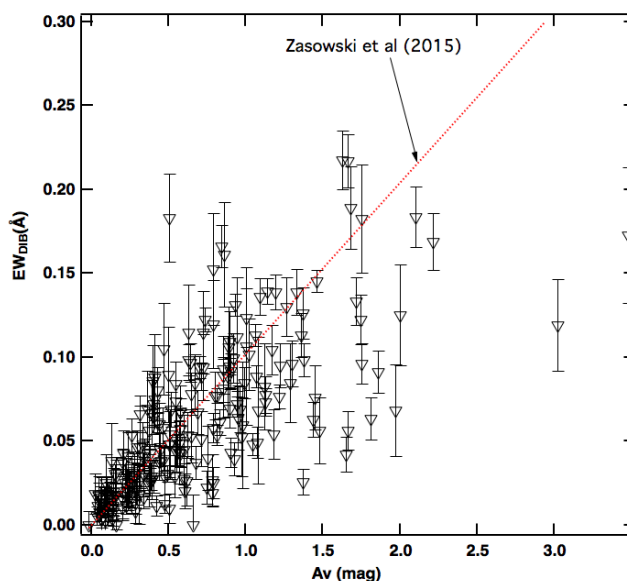


Figure 41 DIB equivalent width as a function of the color excess for the subset of 221 targets described in sect. 2.5. The linear relationship (red curve) is the one fitted to the whole set of APOGEE late-type stars by [Zasowski et al. \(2015\)](#).

ence of the radiation field of the early-type stars that are part of the targets. This effect has been noticed and documented for many years (see e.g. [Vos et al. 2011](#), for a very convincing large study). Indeed, departures from a linear relationship are much weaker when using cooler stars as targets, as shown by [Raimond et al. \(2012\)](#). This effect can be seen as a disappearance of the DIB carrier far outside the cloud under the effect of strong UV fields of unshielded areas, however as we will see later it can also be seen as the disappearance of the DIB carrier deep within the cloud, on the other side of the “skin”. We will come back to this point in the discussion.

Likewise, the catalog can be crossmatched with other DIB data from available optical spectra. Being relatively bright many of them have been the subject of specific investigations, allowing comparisons with other DIBs and atomic or molecular lines. We have found at least 100 targets that have been observed at very high resolution and are available from public archives.

Finally, as mentioned in the Chapter 2, one of our main interests is the ISM 3D tomography. Compared with the extended catalog of [Zasowski et al. \(2015\)](#) that allows mapping the Galactic scales, the TSSs are more appropriate for the nearby ISM. As a proof-of-concept we explored this use in the Taurus-Perseus region. This is illustrated in Figure 42 that shows the dust optical thickness measured by Planck in this area ([Planck Collaboration et al.](#)

4.1. Introduction: DIBs as proxies for column densities of IS matter

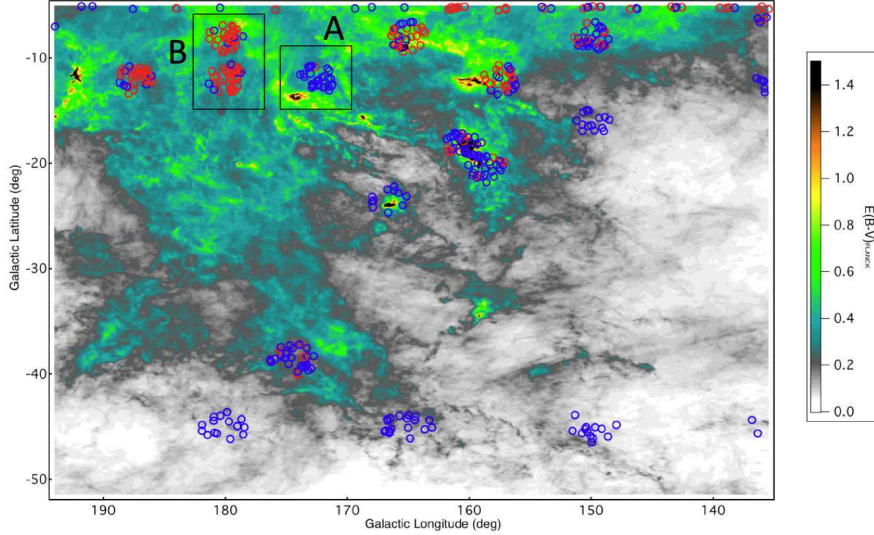


Figure 42 Planck dust optical depth in the Taurus-Perseus region with superimposed APOGEE TSS targets selected for the catalog. Blue (resp. red) markers correspond to a DIB equivalent width lower (resp. higher) than a threshold of $50 \text{ m}\text{\AA}$. In regions devoid of dust (white or pale grey) DIBs are uniformly below the threshold. Towards dense clouds there is a mixed composition that reflects the location of the target (see Figure 43).

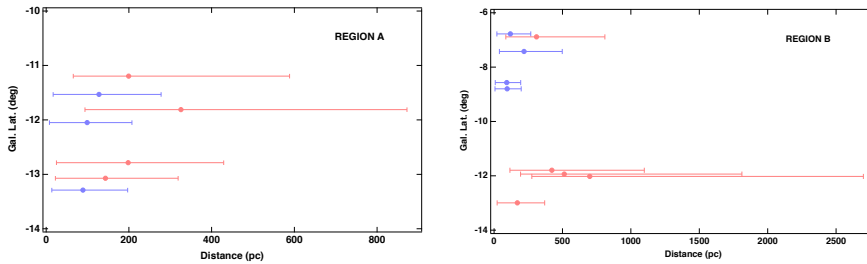


Figure 43 Example of future 3D mapping based on DIBs: DIB strengths and target Hipparcos distances for the two regions A and B from Figure 42. Blue (resp. red) markers correspond to a DIB equivalent width lower (resp. higher) than a threshold of $50 \text{ m}\text{\AA}$. The closest (resp. most distant) targets show consistently negligible (resp. strong) absorption. Accurate and more numerous parallaxes should allow to bracket the distance to the clouds.

2014). Superimposed on the map are the TSS targets color-coded according to the detection (or non-detection) of a DIB with an equivalent width higher than 50 mÅ. The strength of the DIB is always small in regions with negligible or small dust emission while the contrary is seen towards opaque clouds. Note that the “skin effect” we mentioned and that will be studied in Chapter 5 is not apparent here in our ‘YES’ or ‘NO’ DIB simplified criterion.

We selected two regions, marked as A and B in Fig. 42, to explore the use of this catalog to locate the molecular clouds along the line of sight. For that, we used the subset of targets in these areas with Hipparcos parallax (Perryman et al. 1997; van Leeuwen 2007). Figure 43 shows a comparison between the detection (or absence) of a DIB towards a given target and the distance to it. For both cases there is a clear cut-off in distance between this two categories. This allows to bracket the distance to the main absorbing cloud: targets without detection are in front of the clouds while those with detection are well beyond.

For our particular cases the main clouds are at about 150 pc, in agreement with the detailed tomography of Schlafly et al. (2014). Note that we did not update this study of Taurus with TSSs and Gaia DR2 parallaxes yet. The reason is that in order to reach a good precision in cloud distances we need a large number of constraining targets and to add cooler stars. As a consequence, we have planned to preliminary merge with the catalog of DIBs from APOGEE science targets (catalog in progress as explained in Chapter 3).

4.2 Contribution to 3D ISM mapping

Multi-wavelength 2D emission maps of the Galactic interstellar gas and dust are extremely detailed but lack distance information. The production of 3D maps, future tools of wide use, is in progress (e.g., Schlafly et al. 2014; Green et al. 2015). Most are dust maps based on stellar photometric and spectroscopic surveys that provide distance-limited extinction/reddening measurements. As tracers, DIBs (and gas absorption lines) are more powerful than extinction/reddening since they provide valuable information on the line-of-sight cloud structure and the radial velocities of the clouds (kinematics). From the point of view of the Galactic evolution, a better understanding of the interstellar matter cycle requires a deeper knowledge on how the kinematics of the ISM is linked to the properties of the stellar population. Moreover, velocities also allow to link absorption and emission data that possess a spectral information.

As discussed in Part. I we have developed the appropriate spectral analysis tools based on state-of-the-art synthetic spectra to make use of stars of all types (early-type stars and the more numerous late-type stars). Data on

some important nearby cloud complexes are missing from stellar surveys (because they are not the focus) or due to biases towards bright target stars in previous observing programs. Our catalogs from high resolution near-infrared spectra make it possible to probe with accuracy those dense clouds.

[Capitanio et al. 2017](#) illustrated the potential of these catalogs to build detailed 3D maps of the ISM. In this work, we updated and tested several refinements. My contribution was to complement this database with a series of ~ 5000 color excess values estimated from the strength of the $\lambda 15273$ DIB toward stars possessing a Gaia parallax. To do so, the series of 25 409 DR12 spectra with *Tycho* identifier were analyzed using the methodology presented in Part. I as a starting point. All details of my contribution are described in the subsections 2.2.1. to 2.2.3 of [Capitanio et al. \(2017\)](#) presented below. The ultimate goal is extracting the maximum amount of DIBs from available datasets and contributing to the production of Galactic 3D ISM maps as precise as possible, starting with the Local ISM and extending gradually to larger distances following the previous team works ([Lallement et al. 2014](#)). Gaia parallaxes recently published contribute to achieve high spatial resolution and accuracy ([Gaia Collaboration et al. 2016](#)). In addition, the composite data (DIB+extinction) corresponding to $\sim 30,000$ targets using by [Capitanio et al. \(2017\)](#) were merged recently with new extinction measurements from APOGEE-DR14 in [Lallement et al. 2018a](#). The authors mapped the Local Arm using a Bayesian inversion of absorption data with the more accurate and numerous parallaxes provided by Gaia.

Three-dimensional mapping of the local interstellar medium with composite data[★]

L. Capitanio¹, R. Lallement¹, J. L. Vergely², M. Elyajouri¹, and A. Monreal-Ibero¹

¹ GEPI, Observatoire de Paris, PSL Research University, CNRS, Université Paris-Diderot, Sorbonne Paris Cité, Place Jules Janssen, 92195 Meudon, France

e-mail: letizia.capitanio@obspm.fr

² ACRI-ST, Route du Pin Montard, 06904 Sofia-Antipolis, France

Received 21 March 2017/ Accepted 9 June 2017

ABSTRACT

Context. Three-dimensional maps of the Galactic interstellar medium are general astrophysical tools. Reddening maps may be based on the inversion of color excess measurements for individual target stars or on statistical methods using stellar surveys. Three-dimensional maps based on diffuse interstellar bands (DIBs) have also been produced. All methods benefit from the advent of massive surveys and may benefit from *Gaia* data.

Aims. All of the various methods and databases have their own advantages and limitations. Here we present a first attempt to combine different datasets and methods to improve the local maps.

Methods. We first updated our previous local dust maps based on a regularized Bayesian inversion of individual color excess data by replacing HIPPARCOS or photometric distances with *Gaia* Data Release 1 values when available. Secondly, we complemented this database with a series of ≈ 5000 color excess values estimated from the strength of the $\lambda 15273$ DIB toward stars possessing a *Gaia* parallax. The DIB strengths were extracted from SDSS/APOGEE spectra. Third, we computed a low-resolution map based on a grid of Pan-STARRS reddening measurements by means of a new hierarchical technique and used this map as the prior distribution during the inversion of the two other datasets.

Results. The use of *Gaia* parallaxes introduces significant changes in some areas and globally increases the compactness of the structures. Additional DIB-based data make it possible to assign distances to clouds located behind closer opaque structures and do not introduce contradictory information for the close structures. A more realistic prior distribution instead of a plane-parallel homogeneous distribution helps better define the structures. We validated the results through comparisons with other maps and with soft X-ray data.

Conclusions. Our study demonstrates that the combination of various tracers is a potential tool for more accurate maps. An online tool makes it possible to retrieve maps and reddening estimations.

Key words. dust, extinction – ISM: lines and bands – ISM: structure – ISM: supernova remnants – solar neighborhood – local interstellar matter

1. Introduction

Three-dimensional (3D) maps of the nearby and distant Milky Way interstellar medium (ISM) are useful multipurpose tools have been only recently developed at variance with the extremely detailed, multiwavelength 2D emission maps or spectral cubes that have been accumulated over decades. As a matter of fact, a revolution is underway that dramatically changes the situation: photometric, spectrophotometric, and spectroscopic massive stellar surveys have started to provide extinction and absorption data that, coupled with parallax or photometric star distances, bring the third dimension for the ISM, i.e., the distance to the clouds. Thanks to 3D maps of the interstellar matter, structures overlapping on the sky are now converted into distinct clouds distributed at different distances, which will progressively allow emission components to be assigned a well-located production site.

Three-dimensional maps or pseudo-3D maps have already been produced based on various kinds of stellar data; that is mainly photometric extinction but also diffuse interstellar bands

(DIBs) and spectral lines of gaseous species (Marshall et al. 2006; Vergely et al. 2010; van Loon et al. 2013; Welsh et al. 2010; Lallement et al. 2014; Schlafly et al. 2014; Sale & Magorrian 2014; Kos et al. 2014; Schultheis et al. 2014; Zasowski et al. 2015; Green et al. 2015; Schlafly et al. 2015; Rezaei Kh. et al. 2017). Various methods have been used to synthesize the distance-limited data, including full 3D tomographic inversion of individual sightline extinctions (Vergely et al. 2001; Sale & Magorrian 2014), statistical methods based on photometry, and stellar population synthesis or color-color diagrams; see the Monreal-Ibero & Lallement (2015) proceedings for recent developments in this field. In the coming years, maps of increasing quality are expected thanks to continuing or new stellar surveys, on the one hand, and precise *Gaia* parallaxes, on the other hand.

Each mapping technique has its advantages and limitations. Statistical methods require large amounts of targets and are appropriate at large distances, while the synthesis of individual line-of-sight data may work closer to the Sun. Near-infrared (NIR) or infrared (IR) surveys allow one to go deeper in cloud opacities compared to optical data but are more difficult to correct for telluric emissions and absorptions. Maps based on

[★] Our online tool is available at <http://stilism.obspm.fr>

DIBs may slightly suffer from the fact that DIB carriers tend to disappear in dense cores of clouds (Lan et al. 2015), thereby potentially reducing the resolution. Nevertheless, there are numerous DIBs and their combinations may become powerful tools to probe the physical state of the encountered media. Whatever the technique, a major difficulty is associated with the decrease with distance of the achievable spatial resolution in the radial direction, due to increasing uncertainties on target distances. Full 3D inversions that combine the radial and ortho-radial information may partly overcome this difficulty provided they are based on massive datasets, however at the price of strongly increased computing time (see, e.g., Sale & Magorrian 2014).

We present a first attempt to address these limitations by means of a combination of three different datasets as follows: (i) individual color excess measurements from broad- and narrowband photometry of nearby stars (mostly ≤ 500 pc); (ii) NIR DIB equivalent widths (EWs) measured in individual spectra of more distant stars (500–1500 pc); and (iii) color excess measurements at larger distance (up to 3 kpc) based on a statistical analysis of multiband photometric data. Our purpose is to test such an association and its potential for improved 3D mapping of nearby or distant ISM. The first two datasets are merged by means of a conversion from DIB strengths to $E(B - V)$ color excesses. A Bayesian inversion is applied to the resulting composite database. The large distance color excess data are used to build a very low-resolution 3D distribution that is subsequently used as the prior distribution in the Bayesian inversion to replace a plane-parallel homogeneous distribution.

Prior to the combination of these different sources, we analyzed the changes that are induced in the inverted 3D maps based on the first color excess dataset alone when HIPPARCOS or photometric distances are replaced with new *Gaia* Data Release 1 (DR1) parallax distances (the TGAS catalog), when available.

In Sect. 2 we describe the three datasets used in the inversions. In Sect. 3 we briefly recall the Bayesian technique developed in Vergely et al. (2010) and Lallement et al. (2014; hereafter LVV) and the changes introduced in the method. We also describe the hierarchical method developed to build the large-scale prior distribution. Section 4 describes the 3D map evolution introduced successively using *Gaia* distances, the addition of the DIB-based data, and finally the large-scale prior map. Section 5 discusses uncertainties and shows comparisons between the resulting final map and other measurements of cloud distances or cavities. Section 6 discusses the results and perspectives of such composite maps.

2. Data

2.1. Individual color excess data

We started with the reddening dataset of $\approx 22\,500$ sightlines compiled and inverted by LVV. It comprises four different catalogs that were cross-matched and homogenized; for more details about the stellar types and characteristics of the calibration method for each separate dataset, see Vergely et al. (2010), Cramer (1999), Nordström et al. (2004), Dias et al. (2012). Most target stars are nearby ($d \leq 500$ pc), cluster data only correspond to larger distances. The four catalogs are complementary in terms of sky coverage. Of the target distances used for the inversion presented in LVV, 75% were photometric. For one-quarter of these distances the HIPPARCOS distance was preferred. In the four inversions presented here we kept the same error bars on the reddening as those used by LVV. The only difference in the LVV series of targets is the removal of ≈ 400 targets with photometric distances that had no catalog identifications. The

coordinates, brightnesses, estimated distances, and reddening reasonably of these ≈ 400 targets correspond to those of nearby stars. Therefore, these targets were not excluded for the inversion presented in LVV. However, as we discuss in section 4, after the addition of new, more distant APOGEE targets and the subsequent mapping improvement we realized that for these particular targets the color excesses were significantly above other data in the same area. For this reason, we conservatively excluded the targets. Figure 1 shows the distribution of the remaining targets over the sky.

As shown in LVV, the distribution of the targets is highly biased toward low reddening regions in the sky. This had strong consequences on the resulting maps; cavities surrounding the Sun were well defined along with the boundaries of the first encountered dense clouds. On the other hand, clouds located behind foreground dense structures were either not mapped or were very poorly mapped.

2.2. Measurements of DIBs and DIB-based color excess estimates

Except for the recent identification of ionized fullerenes C_{60}^+ , the carriers of the DIBs are still unknown, and it may seem strange to use absorptions due to unknown species for mapping purposes. However the link between DIB strengths and the columns of interstellar matter is strong and successful DIB-based 3D mapping has now been carried out (see Sect. 1). Up to now such mapping used solely DIBs. At variance with these works, here we attempted to merge color excess data and DIB absorption data and perform a unique inversion of a composite dataset. This requires a conversion of DIB equivalent widths into reddening (or the inverse); because none of the DIBs have been shown to be perfectly correlated with the reddening, such a mixing of color excesses computed in so many different ways – for example, with photometric and spectrometric techniques – is potentially hazardous. On the other hand, initial comparisons between DIB equivalent widths and reddening radial profiles in the same sightlines have demonstrated that their similarity (Puspitarini et al. 2015) and global maps also have strong similarities (Kos et al. 2014). Additionally, it is possible to account for the variable $E(B - V)/\text{DIB}$ ratio by increasing error bars on the estimated $E(B - V)$, which we have carried out in this work.

2.2.1. Data

We used the results of the SDSS-III Apache Point Observatory Galactic Evolution Experiment (APOGEE), which is one of the four Sloan Digital Sky Survey III (SDSS-III; Eisenstein et al. 2011; Aihara et al. 2011) experiments. The APOGEE uses a 300-fiber multiobject spectrograph working in the near-infrared (H -band; $1.51\text{--}1.70\ \mu\text{m}$) at high spectral resolution ($R \sim 22\,500$; Wilson et al. 2010). Specifically, we downloaded spectra from the SDSS data release¹ (DR12; Alam et al. 2015), which provides all the data taken between April 2011 and July 2014.

In addition to the $\sim 160\,000$ scientific targets selected from the source catalog of the Two Micron All Sky Survey (2MASS; Skrutskie et al. 2006) and distributed across all Galactic environments, APOGEE contains a sample of $\sim 17\,000$ spectra of hot stars, called telluric standard stars (TSSs). The TSSs form the basis for the correction of the telluric absorption lines across all field types (see Zasowski et al. 2013, for a detailed description of the different target classes). These stars are the bluest

¹ <http://www.sdss.org/dr12/>

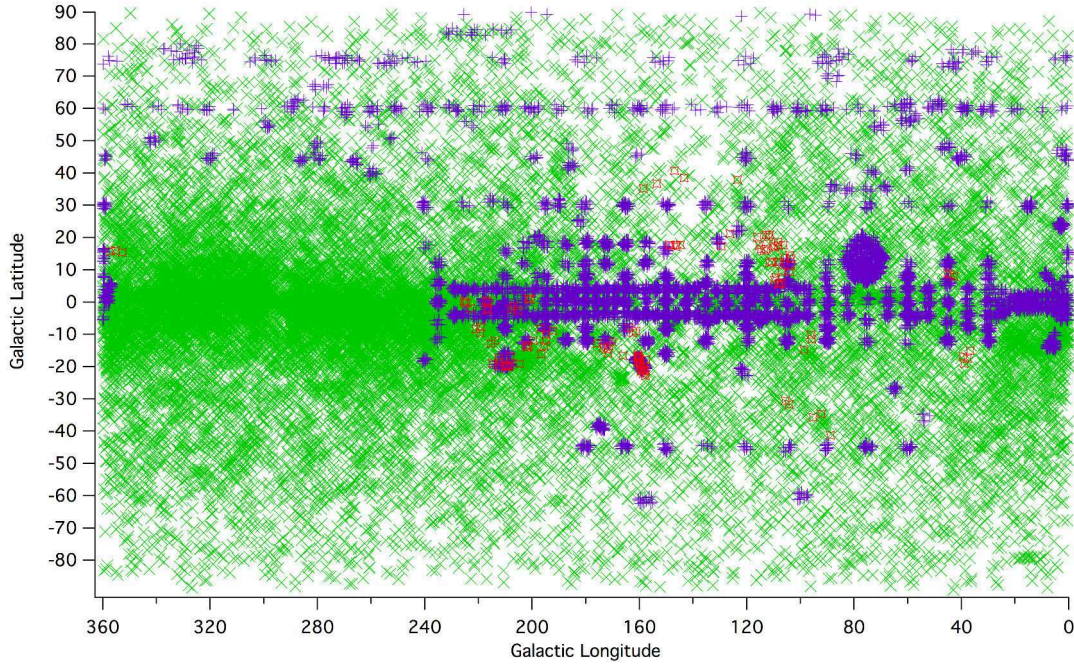


Fig. 1. Location of the targets from the LVV catalog compilation (green crosses) and of the APOGEE target stars retained for the DIB extraction and the inversion (violet signs). Coordinates are Galactic. Also shown are the directions of the molecular clouds of the Schlafly et al. (2014) catalog mentioned in Sect. 5.2 (red signs).

stars on a given APOGEE plate with a magnitude in the range $5.5 \leq H \leq 11$ mag and are therefore hot and bright stars with spectra that are most often featureless.

The APOGEE products contain the decontaminated spectra and synthetic stellar spectra that provide the main stellar line locations and relative depths and widths. Both were used by Elyajouri et al. (2016) to extract a catalog of 115273 DIB measurements from 6700 TSS spectra. Further details on the sample can be found in Elyajouri et al. (2016, and references therein). Weaker DIBs have been further studied based on the same TSS spectra (Elyajouri et al. 2017). Here we focus on the strongest 15 273 Å DIB with the aim of extracting as many accurate measurements as possible from both scientific targets and TSSs possessing a *Gaia* parallax.

We analyzed the series of 25 409 DR12 spectra of targets belonging to the *Tycho* catalog to determine the presence or absence of a detectable DIB at 15 273 Å and measure its equivalent width (resp. an upper limit) in case of positive (resp. negative) detection. We took as a starting point the methodology presented by Elyajouri et al. (2016) for TSSs spectra. We kept the same fully automated fitting technique and method of classification but we adapted the fitting constraints to take into account the inclusion of targets cooler than the TSSs. The code was developed using the IGOR PRO environment ².

2.2.2. Fitting method

We restricted the fit to the spectral range [15 260–15 280] Å in the vicinity of the DIB. This range is wide enough to ensure an adequate sampling of the neighboring Brackett 19-4 stellar line at 15 264.7 Å. We used for the fit the Levenberg-Marquardt algorithm implemented in IGOR PRO².

We fit the data to a combination of an adjusted synthetic spectrum, DIB model, and smooth continuum as shown in

² <http://www.wavemetrics.com>

Eq. (1). Below we provide information specific to each of the equation variables as follows:

$$M_\lambda = [S_\lambda]^\alpha \times DIB[\sigma, \lambda_c, D] \times (1 + [A] \times \lambda), \quad (1)$$

- $[S_\lambda]^\alpha$, an adjusted stellar spectrum, where S_λ is the stellar model provided by APOGEE. We included the scaling factor α to adjust the model stellar line depths to the data.
- $DIB[\sigma, \lambda_c, D]$, the DIB shape was modeled as a Gaussian function allowed to vary in strength, depth, and velocity shift with three free parameters associated with its Gaussian RMS width (σ), central wavelength (λ_c), and depth (D).
- $(1 + [A] \times \lambda)$, a 1-degree polynomial function introduced to reproduce the continuum around the DIB as close possible.

An example illustrating our fitting procedure is shown in Fig. 2.

2.2.3. Selection criteria and error estimates

Residuals, computed as differences between data and model, were used to obtain three measurements of the standard deviations RA, RB, and RC. To do so, we performed the local fit and a second fit over the whole spectral range covered by APOGEE using the same fit function as that presented in Eq. (1).

We selected the standard deviations RA, RB, and RC of the fit residuals, as follows:

- RA from the local fit was calculated in a region $A = [\lambda_c - 10 \text{ Å}; \lambda_c + 10 \text{ Å}]$ close to the DIB.
- RB was calculated over a spectral range $B = [15 890-15 960] \text{ Å}$, which is free of DIB absorption, strong stellar lines, and telluric residuals.
- RC was obtained from region $C = [15 200-15 250] \text{ Å}$ relatively close to the DIB, and is also free of DIB and potentially contaminated by stellar residuals.

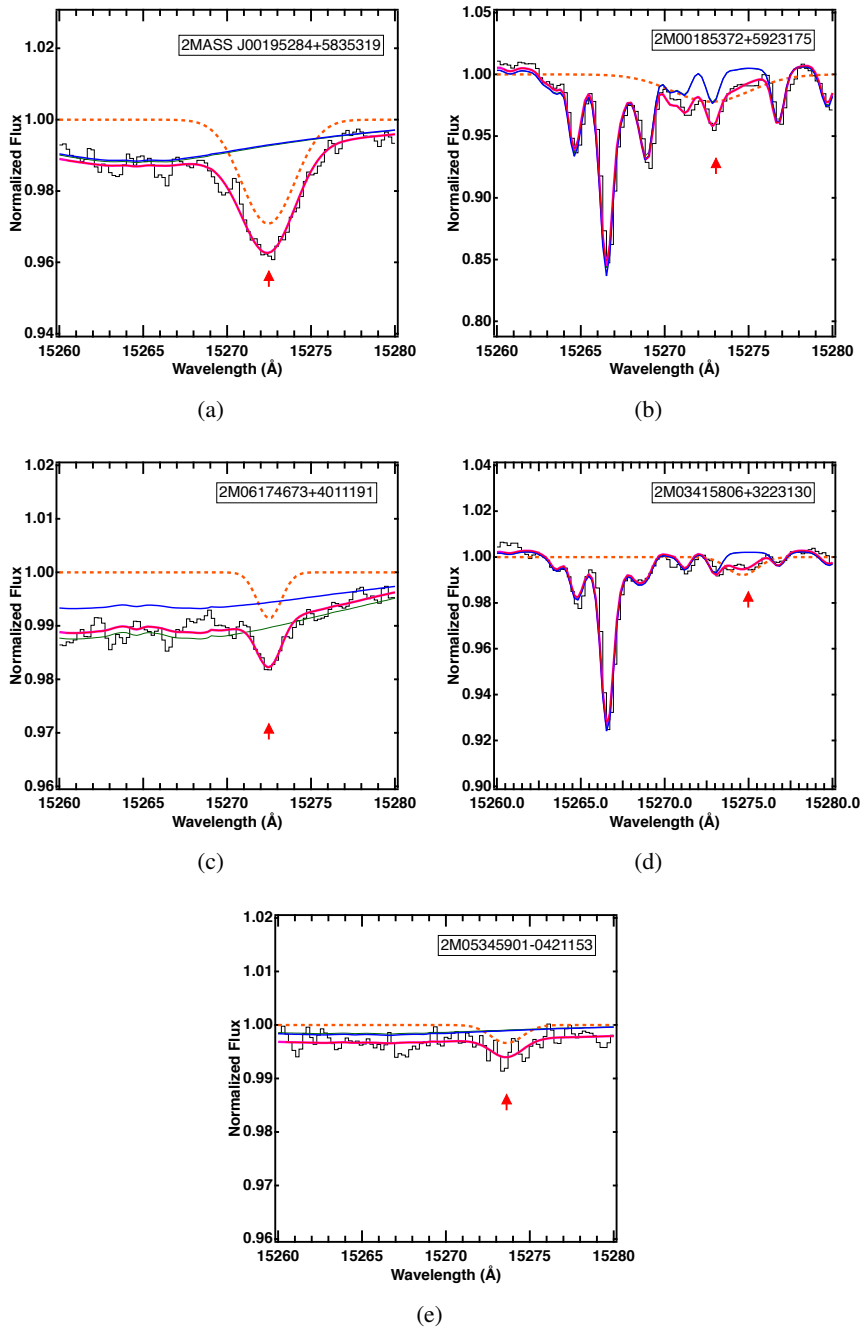


Fig. 2. Illustration of the various categories of DIB extraction: *a)* detected; *b)* recovered; *c)* narrow; *d)* recovered and narrow; *e)* upper limit. APOGEE spectra are shown with solid black curves. The initial stellar model provided by APOGEE and the model obtained after application of the scaling factor are shown in solid blue and green respectively (note that in many cases they are very similar). The DIB absorption alone is represented in orange. The solid magenta curves represent the final stellar+DIB modeled spectrum.

These are used for the selection criteria shown in Table 1 and also used below to estimate the uncertainty on the DIB equivalent width. The uncertainty is conservatively estimated based on the following formula:

$$\delta_{EW} = \sqrt{2\pi} \sigma \max(RA, RB, RC), \quad (2)$$

where σ is the Gaussian rms width that results from the fit. The quantity $\max(RA, RB, RC)$ is the maximum of the three standard deviations.

Table 1 shows the fitting constraints that were used to select our final sample. They are somewhat different from the criteria

of Elyajouri et al. (2016). In particular, we no longer used HI 21 cm data to limit the width of the DIB, but we used limits based on the FWHM histograms built in this previous work. Representative examples illustrating our fitting procedure and the various categories are shown in Fig. 2.

2.2.4. Final data selection for the inversion

Equivalent widths and stellar rest-frame wavelengths are determined from the best-fit parameters in each sightline for the 25 000 attempted spectra of targets belonging to the *Tycho*

Table 1. Fitting constraints of $\lambda 15273$ NIR DIB for the selected APOGEE spectra.

Flags	λ_c Å	Width Å	Depth Å
Detected (4861)	[15 268–15 280]	[1.4–5.5]	$[1.5 \times \max(\text{RA}, \text{RB}, \text{RC}) - 0.1]$
Narrow DIBs (364)	[15 260–15 280]	[1–1.4]	$[1.5 \times \max(\text{RA}, \text{RB}, \text{RC}) - 0.1]$
Recovered DIBs (2515)	[15 268–15 280]	[1.4–5.5]	$[2 \times \text{RA} - 1.5 \times \max(\text{RA}, \text{RB}, \text{RC})]$
Narrow recovered DIBs (420)	[15 268–15 280]	[1–1.4]	$[2 \times \text{RA} - 1.5 \times \max(\text{RA}, \text{RB}, \text{RC})]$
Upper limit (1753)	[15 268–15 280]	≤ 1.4	$\leq 2 \times \text{RA}$

Notes. RA, RB, RC are the standard deviation in three spectral ranges $A = [\lambda_c - 10 \text{ \AA}; \lambda_c + 10 \text{ \AA}]$, $B = [15 890–15 960] \text{ \AA}$ and $C = [15 200–15 250] \text{ \AA}$, respectively.

catalog. We rejected those cases where the fit failed due to low S/N, an inadequate stellar model, or very strong telluric contamination most of the time, and we retained 9913 spectra following the criteria in Table 1. The corresponding targets were cross-matched with the targets of the *Gaia* DR1 catalog (Arenou et al. 2017) to obtain a catalog of 7800 stars with *Gaia* distances. We added to the DIB measurement an additional 50% uncertainty to account for the $E(B - V)/EW$ variability associated with the influence of the physical properties of the encountered media. As a matter of fact, from the most neutral to the most ionized media, this ratio may reach a variability factor of three (see, e.g., Elyajouri et al. 2017). After the additional filtering for our criteria on target distances and distance uncertainties (see Sect. 4.1), only 4886 targets were retained for the present inversion. Other targets will become useful after the next *Gaia* data releases. The number of retained targets is small with respect to the initial number of APOGEE spectra of *Tycho* stars (less than 20%) and targets from the reddening catalog. Despite the limited number of these retained objects, they are precious since they allow us to probe more reddened regions, in particular to reveal a second or third rank of clouds, something often precluded using the bright targets measurements in the optical.

We converted the DIB EW into a color excess using the Zasowski et al. (2015) formula

$$EW = 0.102 A_V^{1.01} \text{ \AA} \quad (3)$$

and the classical average total-to-selective ratio $A_V/E(B - V) = 3.1$ (Savage & Mathis 1979). The relationship established by Zasowski et al. (2015) has been confirmed, by Elyajouri et al. (2016), to be valid locally based on the closer TSSs.

2.3. Subsample of Pan-STARRS color excess measurements

Green et al. (2015) have used Pan-STARRS and 2MASS photometric measurements toward 800 millions targets to build remarkable 3D dust reddening maps with a very high angular resolution (5–15 arcmin) covering distances from ≈ 300 pc to 4–5 kpc. The publicly available maps contain a quality flag that allows to exclude results at small or large distances that are uncertain because of limitations on the number of targets for geometrical or sensitivity reasons. Both surveys were conducted from the Northern Hemisphere. We used those data to build a low-resolution 3D *prior* distribution to be used in our Bayesian inversion in replacement of the previous analytical solution corresponding to a homogeneous plane-parallel opacity.

To do this, we downloaded a grid of Pan-STARRS $E(B - V)$ estimates for lines of sight equally spaced every 0.5 degree in Galactic latitude and longitude and for all distances available from the Pan-STARRS online tool, in this way obtaining

3 071 230 pairs of distance and extinction after exclusion of all data points flagged as uncertain. As result of this process, we do not benefit from the very high angular resolution of the maps, however this information would be lost in our approach. In many directions the first 200 pc are flagged because of the limited number of targets available to define the reddening in the very small solid angle chosen for this Green et al. (2015) study. However this is where the present inversion of individual data may be advantageous. The method applied to these Pan-STARRS results is described in Sect. 3.2.

3. Inversion techniques

3.1. Bayesian inversion of individual sightlines

The Bayesian inversion technique is based on the pioneering work of Tarantola & Valette (1982) and its first developments and applications to the ISM are described in detail in Vergely et al. (2001, 2010), Welsh et al. (2010), Lallement et al. (2014). Briefly, the inversion optimizes an analytical solution for the 3D opacity distribution through the adjustment of all integrated opacities along the target sightlines to the observed color excess data. Because the solution is strongly under-constrained, it is regularized based on the assumption that the 3D solution is smooth. Opacities ψ at two points (x) , (x') in space follow correlation kernels: here $\psi_1(x, x') = \exp(-\frac{\|x-x'\|^2}{2\xi_1^2})$ and $\psi_2(x, x') = \frac{1}{\cosh(-\|x-x'\|/\xi_2)}$, where the first (resp. second) term represents the compact (resp. diffuse) structures. The correlation distances ξ_1 and ξ_2 , which roughly correspond to the minimum size of the computed structures, are evidently limited by the average distance between the target stars. Here we have chosen $\xi_1 = 15$ pc and $\xi_2 = 30$ pc. As we discuss in the next sections, such kernels are valid in internal regions where the target distribution is the densest. The model variance, which controls the departures from the prior distribution, is $\sigma_1 = 0.8$ for the first kernel and $\sigma_2 = 1.0$ for the second (see LVV for its definition). The Tarantola & Valette (1982) formalism allows one to compute the least-squares solution iteratively. For the present maps the convergence is reached in about six iterations. Uncertainties on the reddening and target distance are treated in a combined way (see Vergely et al. 2001). The distribution is computed in a volume of 4 kpc by 4 kpc along the Galactic plane and 600 pc along the perpendicular direction.

Compared to the method used in Lallement et al. (2014), an additional treatment of outliers was introduced. During each iteration except the first two, in case one measured color excess value is found to be incompatible with the kernels and the surrounding data, its error bar is multiplied by 2. This method has proven to solve for data points that have underestimated

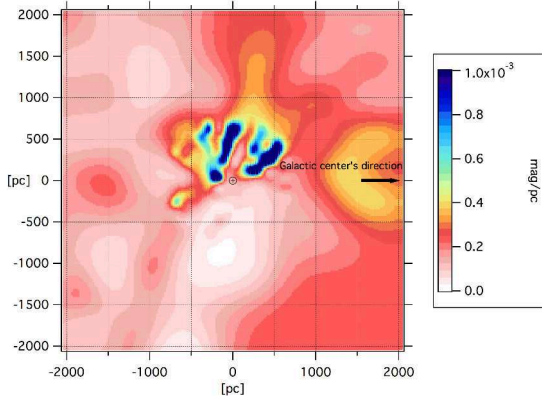


Fig. 3. Galactic plane cut in the very low-resolution 3D opacity distribution to be used as a prior in the inversion. It is based on Pan-STARRS reddening measurements of Green et al. (2015). The Sun is at (0, 0) and the Galactic center to the right. Longitudes increase counter-clockwise. Units are mag pc^{-1} .

errors and eliminates oscillations. The Bayesian approach implemented in Vergely et al. (2001) and subsequent works allows us to include an a priori knowledge of the ISM 3D distribution. This prior distribution can in principle be provided by a model that represents the density variations in the Galactic plane by an analytic law or alternatively by a distribution based on external data. The latter case is fully appropriate to our objective of combining different sources of extinction. As a matter of fact, it is possible to produce density maps by successive refinements following integration of data from different sources in a sequential and non-simultaneous manner. The advantage of such an approach is twofold: first, the amount of data to be integrated at each step is reduced, which makes it possible to reduce computation times and, second, it is easier to see the contribution of each set of data.

In this perspective, a new development was introduced in our inversion code. Now, it is possible to use any 3D prior distribution, i.e., we can replace the homogeneous plane-parallel prior that corresponded to an analytical representation (we used an exponential decrease from the Galactic plane) with any arbitrary precomputed distribution. We used this possibility to test a two-step inversion based on two different datasets as described in Sect. 4.3. The construction of the prior distribution is described in the next section.

3.2. Large-scale prior distribution based on Pan-STARRS

We used the Green et al. (2015) color excess subsample described in 2.3 to develop a low-resolution opacity model extended to large distances, to be used as a prior for the inversion of individual lines of sight as described above. Because this reddening model is based on photometric measurements of hundreds of millions of objects, the Green et al. (2015) model has a very high angular resolution, whereas the radial resolution is limited by uncertainties on photometric distances. In principle our prior distribution is losing all the details contained in the angular variations, first because we start with a coarse angular sampling of 0.5 deg, and also because our full 3D inversion has a spatial resolution limited by the radial distance uncertainties.

Ideal inversions are based on a homogeneous spatial sampling of targets, i.e., a homogeneous volume density of targets and similar uncertainties on their locations at all distances, which allows us to retrieve structures of the same minimal spatial

scale everywhere in space. But for most surveys, including Pan-STARRS, the achievable resolution is dependent on the distance to the Sun, especially owing to distance-dependent uncertainties on the star locations. The sampling of the data in this case does not allow the Nyquist-Shannon criterion to be fulfilled for the same minimal autocorrelation length everywhere; also, some of the energy attributable to high spatial frequencies is likely to be redistributed in low spatial frequencies, especially at large distances or in the radial directions when the sampling is weak. Therefore, we need an approach that allows us to retrieve only the large scales at large distances and all large and small scales at short distances. We implemented a hierarchical approach that allows us to achieve this goal in an iterative way by progressively updating the opacity model. Schematically, we first constructed a low spatial frequency map in a sphere with a large radius (here 5 kpc). In a subsequent step, we estimated spatial frequencies that are higher by a factor of 2, however this time in a smaller sphere (for instance 3 kpc) by removing data at large distances for which the available information does not make it possible to reach these frequencies using the Nyquist-Shannon criterion. The information at large distances is kept under the form of the prior, which is simply the distribution derived from the previous step. This procedure is repeated for increasingly high frequencies until their maxima compatible with the radial sampling (reached at small distances) are obtained. In practice we proceeded as follows:

1. The Pan-STARRS reddening data subsample (see Sect. 2.3) is converted into local opacities ρ_0 through derivation w.r.t. the radial distance R ,

$$\rho_0 = \delta_{E(B-V)} / \delta_R.$$
2. A spatial scale S of restitution of the opacity is fixed, starting with the (large) scale that can possibly be restored on the whole map. The average opacity is computed in a 3D grid of boxes of size $S \times S \times S$. The resulting average opacity is thus dependent on the scale.
3. Based on these average opacities, maps of smoothed opacities are computed by Bayesian interpolation with a smoothing kernel twice as large as S .
4. We then move on to a scale twice smaller. $S/2 \times S/2 \times S/2$ boxes are built and the average opacity is calculated for each box. The dynamics of the average opacity for this set of boxes is stronger. We suppress the boxes that do not fulfill the Nyquist-Shannon criterion for $S/2$.
5. A Bayesian interpolation is carried out again with a smaller smoothing kernel and using the previous map as prior.
6. Again, the scale is divided by two and steps 2) and 3) are performed again for this new scale, etc.

A planar cut along the Galactic plane in the resulting 3D prior is shown in Fig. 3. The Sun is at center and Galactic longitude increases counter-clockwise. As expected, far from the Sun we can only restore the very large scales. On the contrary, one can reach scales on the order of 100 pc within the first few hundreds parsecs. Because Pan-STARRS data are recorded from the Northern Hemisphere, the prior in the fourth (bottom-right) quadrant appears homogeneous at large distances from the Sun. This map can be used as a prior in the inversion of the individual lines of sight for which accurate distances are available, with the goal of improving estimates of opacity fluctuations and refining the distance assignment of the structures (see Sect. 4.3).

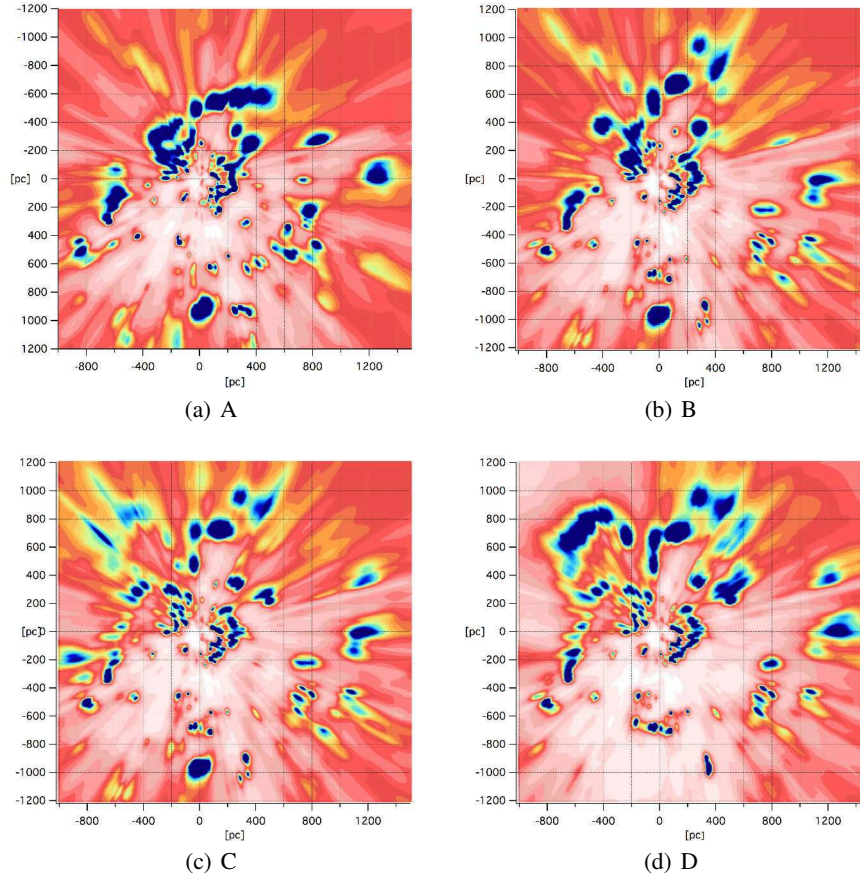


Fig. 4. Galactic plane cut in the 3D opacity distribution resulting from the four successive inversions: *panel a*: A distribution: color excess data alone and HIPPARCOS or photometric distances. *Panel b*: B distribution: same as A except for the replacement of 80% of the initial distances with *Gaia*-DR1 (TGAS) values. For the 20% of stars without *Gaia* distance we kept the previous value. *Panel c*: C distribution: same as B except for the addition of DIB-based color excess estimates for stars with a *Gaia*-DR1 parallax. *Panel d*: D distribution: same as C except for the use of a Pan-STARRS based prior distribution instead of a homogeneous distribution. Color scale, direction of Galactic center, and Sun position are the same as in Fig. 3.

4. Inversion of datasets

4.1. Inverting pre- and post-*Gaia* individual color excess data

In order to test the influence of the new *Gaia* parallax distances we inverted the reddening dataset described in Sect. 2.1 twice with exactly the same method, criteria, and parameters, but with different target distances. The first inversion (A) used the initial HIPPARCOS+photometric distances and errors as in LVV and the second (B) used *Gaia*-TGAS distances and associated errors when available, or unchanged values in the absence of *Gaia* result. *Gaia* DR1 parallaxes are about 20 times more numerous than HIPPARCOS parallaxes and about three to four times more accurate. These characteristics will evolve with the next releases, which will contain many more stars and reduced parallax uncertainties. As in LVV the prior dust opacity is a plane-parallel homogenous distribution decreasing exponentially from the Galactic plane with a scale height of 200 pc. We also similarly retained for the inversion targets closer to the Galactic plane than 1000 pc and less distant than 2601 pc with relative errors on the distance smaller than 33%. The number of targets retained for the first inversion was 22 467 and among these 5106 were assigned their HIPPARCOS distance, and the rest were photometric. In the second inversion 23 444 targets were retained, with about 80% having a *Gaia* parallax. As the *Gaia*-DR1 uncertainties were 3–4 times smaller than HIPPARCOS uncertainties, the number of targets excluded for uncertain distances was

significantly reduced. Importantly, the fraction of photometric distances decreased by a factor of four and *Gaia* distances started to be largely dominant.

The values of the χ^2 per target are computed from the differences between the observed color excesses and the color excesses computed by integration of the model 3D distribution along the target lines of sight. These values are reported in Table 2 for both the prior and final distribution. The value of χ^2 for the prior distribution is significantly higher for the second inversion, reflecting the fact that error bars entering its computation are on average smaller because of the reduced uncertainties on *Gaia*-DR1 distances, especially by comparison with previous uncertainties on the photometric distances. On the contrary, the final χ^2 is lower despite reduced error bars, demonstrating that the found distribution is more compatible with the new distances than with the previous distances.

Panels a and b (top left and right) in Fig. 4 show planar cuts in the two inverted opacity distributions A and B. The plane is parallel to the Galactic plane and contains the Sun. The pre-*Gaia* inverted distribution is not exactly the same as in LVV because of the removal of some targets and the introduction of the new method to treat outliers (see Sect. 3.1). The difference between the two pre- and post-*Gaia* distributions is visible: on average the structures are more compact. Some elongated structures diminished owing to the reduction of distance uncertainties, as in the third and fourth quadrants (bottom left and right); some others

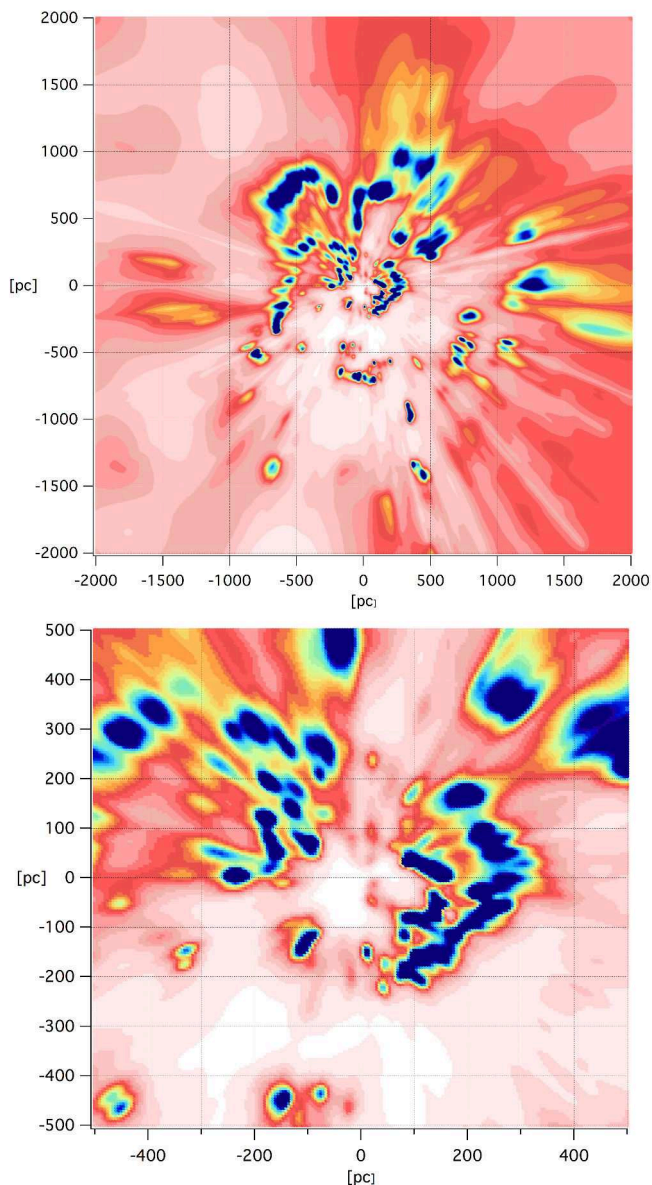


Fig. 5. Planar cut along the Galactic plane in the inverted 3D distribution D shown in Fig. 4, panel d. The color scale is same as in Fig. 3. *Top:* the entire 4000 pc \times 4000 pc computed area. *Bottom:* zoom in a 1000 pc \times 1000 pc area around the Sun.

appeared, which may be due to contradictions between new *Gaia* distances and the remaining photometric distances. The latter regions will have to be carefully studied once all targets benefit from *Gaia* parallaxes. The local bubble keeps its global shape, but looks slightly more complex owing to the higher compactness of structures. At larger distance the most conspicuous difference appears in the first quadrant, in particular in the Cygnus Rift region. At $l \simeq 70^\circ$ the Rift is located significantly farther away in the new inversion, at about 800 pc instead of $\simeq 600$ pc, interestingly now in agreement with the Green et al. (2015) distance assignment. We knew that this was a region of strong oscillations in the first inversion; these oscillations have now disappeared. In the second quadrant there are substantial changes and we start to sketch a ring of clouds, more specifically the very large structure located from 100 to 400 pc is decomposed into two smaller structures.

4.2. Inversion of combined photometric and DIB-based color excess data

The same inversion code was applied to the merged catalog of photometric and DIB-based reddening estimates (inversion C). As can be seen in Table 2, the introduction of the APOGEE targets reduces both the initial and final χ^2 per point. The former decrease means that error bars on the DIB-based estimated $E(B - V)$ s are not underestimated. The latter decrease strongly suggests that the APOGEE targets do not introduce contradictory data and their inclusion produces a reasonable solution. In comparing the new Galactic plane cut in Fig. 4 and the distribution C at the bottom left with the previous inversion with photometric data alone (distribution B, top right), we can clearly see some changes; these changes are particularly apparent in the second quadrant, where some decoupling or fragmentation of large structures into distinct cloud complexes along with new structures at large distances are visible. Since 14% of the APOGEE targets are closer than 20 pc from the Galactic plane, are highly concentrated in this quadrant, and are more distant than the LVV targets, it is not surprising to find most changes there. The fourth quadrant does not change because the APOGEE catalog adds targets observed from the Northern Hemisphere.

Since it is the first time that such measurements of different types are used, which could trigger incoherence in the inversion, it is mandatory to investigate the observed changes in all areas in order to validate this new technique. Four vertical planar cuts in the 3D opacity map are shown in Fig. 9 (Orion region), Fig. 10 (anticenter direction), Fig. 11 (Cepheus region), and Fig. 12 (Perseus region). The Perseus region is discussed in detail in Sect. 4.3. The images show, in the top panel, the B opacity distribution results and, in the middle panel, the C opacity distribution after inclusion of APOGEE data. In principle, the effect of adding coherent data in poorly covered areas should result in the transformation of wide structures into smaller clumps and/or in the appearance of new structures, especially at large distances in locations where there was initially no targets.

The Orion region is well suited for comparisons owing to the existence in similar proportions of targets of the two types beyond 150 pc. There are $\simeq 750$ lines of sight from the photometric catalog and $\simeq 375$ from the APOGEE catalog within the longitude interval $l = (208 : 218^\circ)$. As shown in Fig. 9, the two types of targets are spatially well mixed. If the data were not compatible we would observe radially elongated and/or wide structures in the middle map that were absent in the top. Instead, there are no significant changes, which demonstrates that the two datasets trace the same structures. Indeed, the figure shows that the APOGEE data reinforce the dense structures at 500 and 600 pc, at distances poorly covered by targets with photometric measurements.

Another region suited to a further check is the anticenter region. At variance with the Orion area, the LVV targets are concentrated in the first 100 pc, while APOGEE introduces many more distant targets. Figure 10 shows clearly that this addition allows us to map new clouds beyond 300 pc, in particular to transform a unique wide structure at $\simeq 450$ pc into at least three structures located between 300 and 700 pc, confirming that infrared data such as APOGEE add valuable information in areas where stars are already reddened by close clouds. The structures at small distances already seen in the first map (inversion B) remain in the second map but appear more compact with their relative opacities somewhat changed. Because the sightlines to the distant targets cross the nearby clouds, contributing to their mapping, the increased compactness of the foreground structure

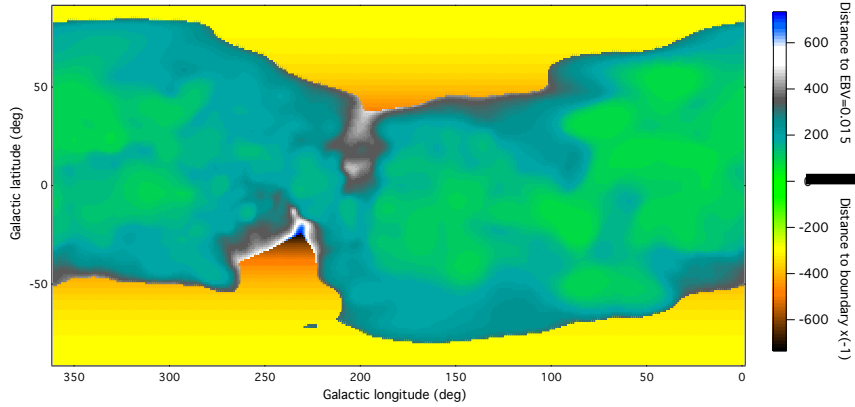


Fig. 6. Local cavity boundaries: the distance at which a color excess of 0.015 mag is reached is plotted as a function of rectangular Galactic coordinates. In very weakly reddened directions for which 0.015 mag is not reached within our computation domain, the distance to the domain boundary is plotted after conversion to negative values. This allows us to distinguish between the two cases well. The figure illustrates well the local warp of gas associated with the Gould belt, i.e., more matter at positive latitudes in the Galactic center hemisphere and at negative latitudes in the anticenter hemisphere. It also reveals very clearly the local bubble openings to the halo at about 210–240° longitude.

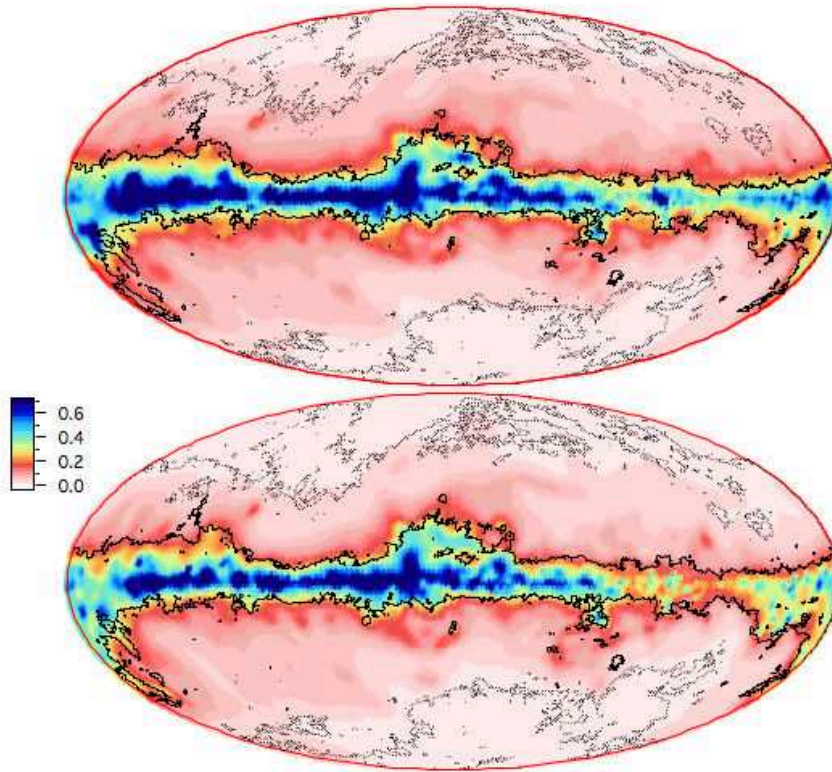


Fig. 7. Full-sky 2D map of opacity distribution integrated from the Sun to the boundaries of our computational domain ($\text{abs}(Z) = 300$ pc, $\text{abs}(X) = 2$ kpc, $\text{abs}(Y) = 2$ kpc). *Top:* LVV results are shown (distribution A). *Bottom:* the final inversion with APOGEE data and the Pan-STARRS based prior distribution are shown (distribution D). Isocontours from Schlegel et al. (1998) for $E(B - V) = 0.025$ and $E(B - V) = 0.32$ are superimposed as dotted and continuous black lines. The map is in Aitoff Galactic coordinates. Longitudes decrease from $+180^\circ$ to -180° from left to right. The color scale refers to $E(B - V)$, linear, in units of mag.

Table 2. Evolution of the prior and final χ^2 per line of sight in the four inversions.

Distribution	Data	Initial χ^2	Final χ^2
A	LVV catalog, HIPPARCOS+phot	5.361	1.100
B	LVV catalog, <i>Gaia</i> -DR1+phot	5.810	1.085
C	LVV catalog + APOGEE, <i>Gaia</i> -DR1+phot	5.080	1.023
D	LVV catalog + APOGEE, <i>Gaia</i> -DR1+phot, Pan-STARRS prior	3.521	1.006

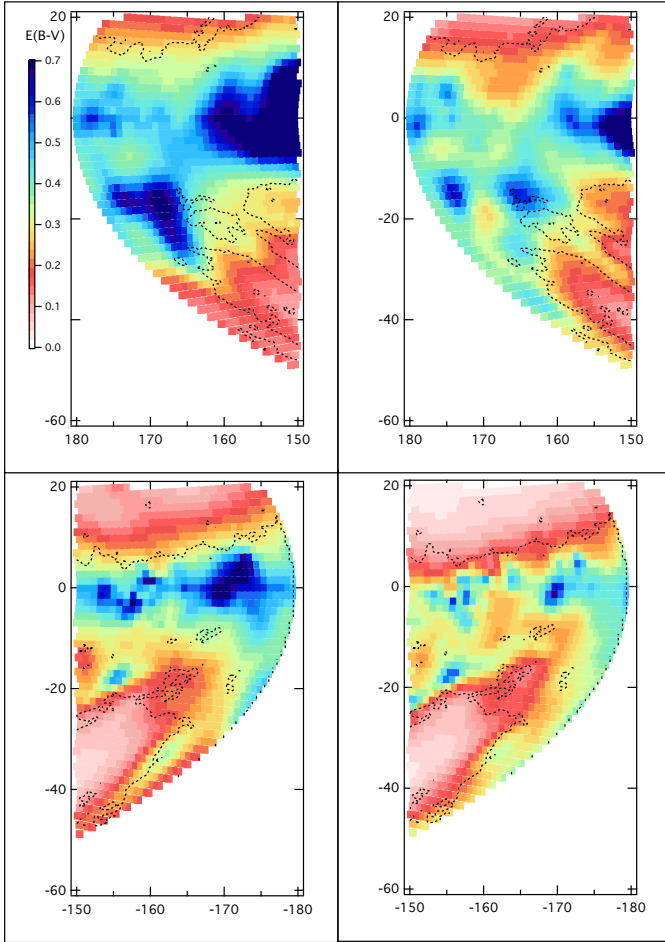


Fig. 8. Same as Fig. 7 for limited regions in the anticenter area. *Left:* LVV data are shown. *Right:* final inversion is shown. Isocontours from Schlegel et al. (1998) for $E(B-V) = 0.025$ are superimposed as dashed black lines.

shows that the new data do not contradict the old data and instead help shape the close clouds.

We finally consider the Cepheus region in the second quadrant (Fig. 11). There are several clouds distributed in the same region of the sky, which is a very good test for the inversions. Here, the number of targets in the longitude interval $l = (105^\circ; 115^\circ)$ increases from 390 to 664. It can be seen that the large structure at distances between 200 and 300 pc and at heights above the Galactic plane between 0 and 150 pc is now more clearly decomposed into three cores and an additional fourth cloud just below the Galactic plane at ≈ 300 pc. This last structure below the Galactic plane had apparently been erroneously associated spatially with a more distant and wide structure at 500 pc. As a result of *Gaia* distances and additional targets, its location has now been better defined. Indeed, the final distribution D (bottom panel of Fig. 11 and Sect. 4.3) confirms this new location. Behind those structures a hole as well as two different more distant clouds are revealed near the Galactic plane. The large structure located at about 400 pc in distribution A, which was derived from only a few targets, is now much better defined and significantly displaced farther away at about 500 pc. This again shows that using infrared data enables the mapping of distributed clouds and holes between them.

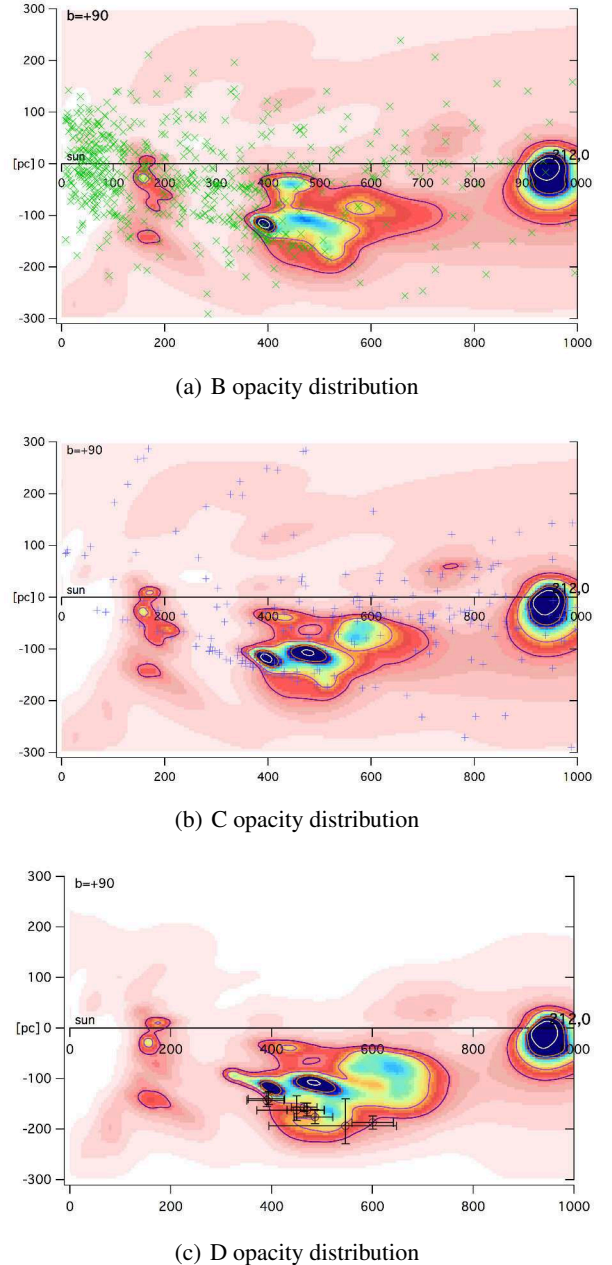
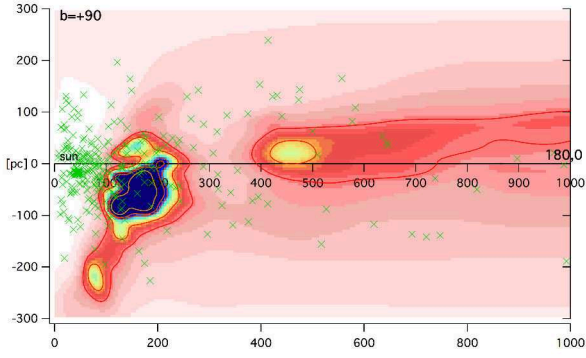


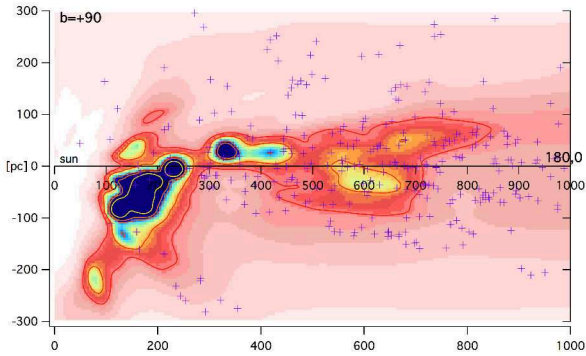
Fig. 9. Comparison between the three B-C-D distributions (see Sect. 4 and Fig. 4) for a vertical plane along $l = 212^\circ$. The X -axis is within the Galactic plane, the Y -axis is toward the North Galactic pole direction. The color scale is the same as in Fig. 3. Iso-contours are superimposed for $\rho_0 = 0.0002, 0.00035, 0.00076, 0.001, \text{ and } 0.002 \text{ mag pc}^{-1}$. The green crosses in *top panel* are the positions of the targets from the LVV catalog in a slice of 10 degrees around the considered vertical plane, violet crosses in *middle panel* are the targets from the APOGEE catalog, and the black circles in *bottom panel* are the molecular clouds positions and associated uncertainties based on the catalog of Schlafly et al. (2014).

4.3. Inversion of merged data using the Pan-STARRS-based prior 3D distribution

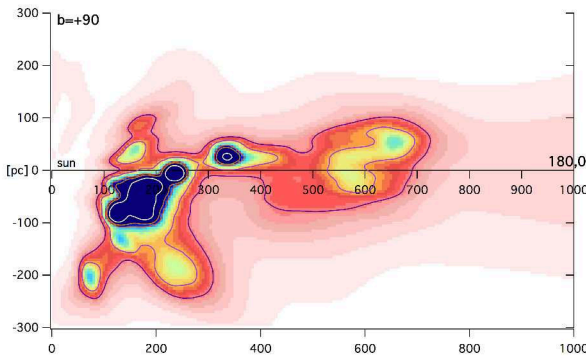
We performed an additional inversion (inversion D) of the set of LVV+ APOGEE targets, this time replacing the plane-parallel homogeneous prior with the large-scale distribution described in Sect. 3.2, based on Green et al. (2015) results. This allowed us to test our new capacity of using an arbitrary 3D prior distribution.



(a) B opacity distribution



(b) C opacity distribution

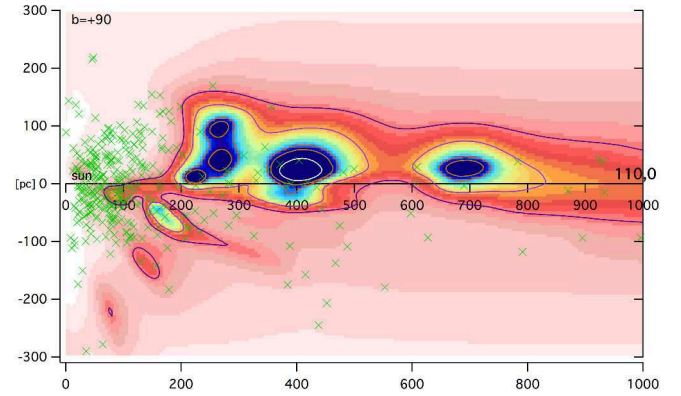


(c) D opacity distribution

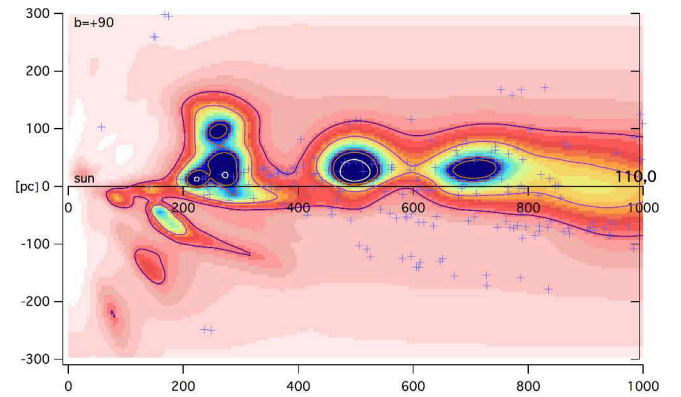
Fig. 10. Same as Fig. 9 for the vertical plane along $l = 180^\circ$ (anticenter region).

In the new prior, the smallest structures allowed are 100 pc wide and the kernel sizes for the largest structures are 800 pc.

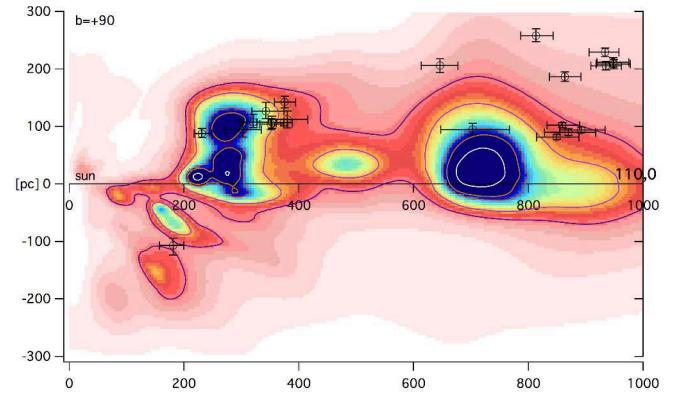
Table 2 shows that using the new prior has the effect of reducing the initial χ^2 per point significantly and decreasing the final χ^2 too. This means that the data for individual sightlines are, not surprisingly, in better agreement with this more realistic prior. A comparison of panels c and d in Fig. 4 shows the differences introduced by using the new prior in the Galactic plane. As expected, the main variations are at large distance, especially beyond 1 kpc, while closer the changes are very small. The same effects are seen out of the Galactic plane, as shown in Fig. 9 (Orion), Fig. 10 (anticenter), Fig. 11 (Cepheus), and Fig. 12 (Perseus), where the bottom panels show the D opacity distribution. There are significant changes far from the Sun and negligible changes closer to the Sun, where the target density is high enough to suppress the influence of the prior. In all cases,



(a) B opacity distribution



(b) C opacity distribution



(c) D opacity distribution

Fig. 11. Same as Fig. 9 for the vertical plane along $l = 110^\circ$ (Cepheus region).

it is interesting to see how the nearby structures connect with the distant very low-resolution Pan-STARRS based distribution. This two-step process allows large-scale and smaller-scale structures to coexist in a map, while avoiding an overinterpretation of the data. Other vertical planes drawn every 30° Galactic longitude are shown in Appendix A. These vertical planes give us a general idea of the nearby ISM distribution out of the Galactic plane.

Figure 5 (upper panel) shows the dust opacity in the Galactic plane for the entire computational area $4000 \text{ pc} \times 4000 \text{ pc}$. As can be seen in the figure, at large distances there are co-existing

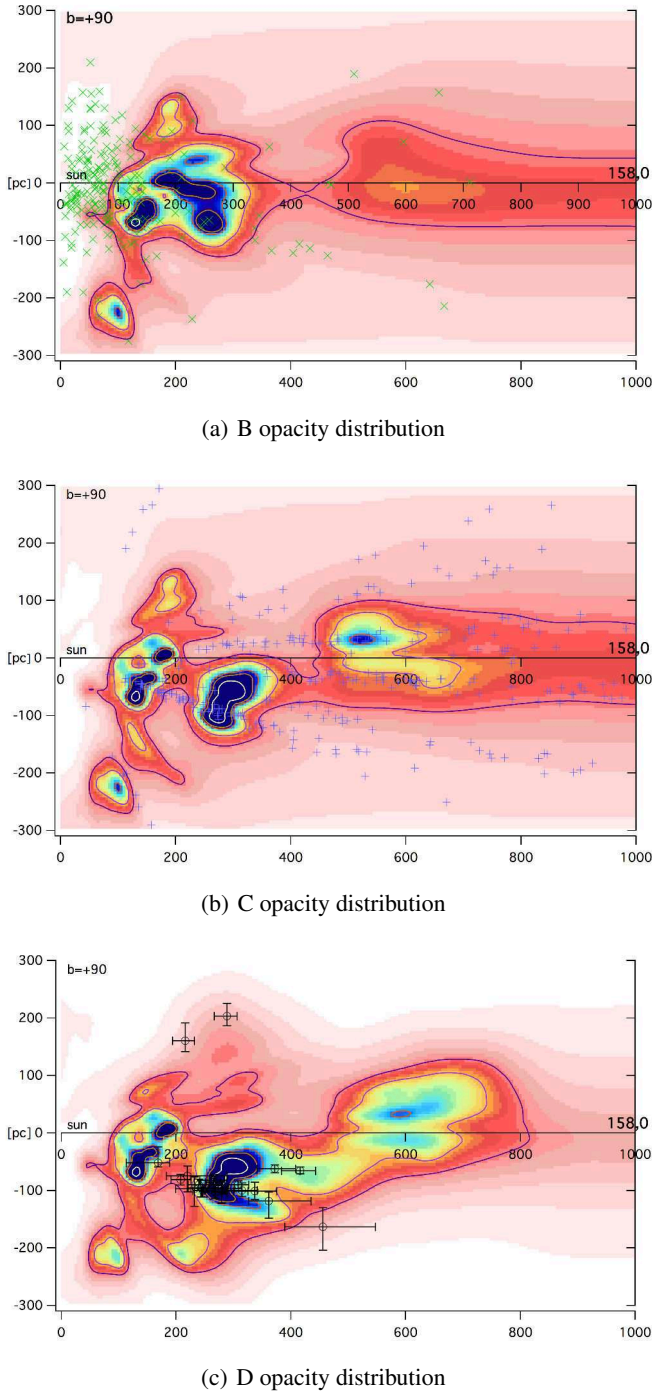


Fig. 12. Same as Fig. 9 for the vertical plane along $l = 158^\circ$ (Perseus region).

compact structures with the minimum size allowed by the kernels and large-scale structures that mainly result from the Pan-STARRS prior. The small structures however should be considered with caution, as is discussed in the next section.

Bottom panel of Fig. 5 shows a zoom in the $1000 \text{ pc} \times 1000 \text{ pc}$ central area. It shows numerous clouds and cavities and that the shape of the so-called local bubble is far from simple. It is well known that the interstellar matter within the first hundreds of parsecs is very complex and characterized by the series of clouds forming the Gould belt, a wide structure tilted w.r.t. the Galactic plane by about 20° (e.g., Perrot & Grenier 2003). The origin of this structure is still a matter of debate

(see, e.g., Lallement 2015 for a recent discussion and suggested origin). Two *chimneys* connect the local bubble to the northern and southern halos forming a hole whose axis is nearly perpendicular to the Gould belt plane; this peculiar structure is illustrated in Fig. 6. The figure shows for all directions the line-of-sight length that corresponds to an integrated color excess $E(B - V) = 0.015 \text{ mag}$. When the distance required to reach this color excess is larger than the distance to the boundary of the computational volume, such as toward high Galactic latitudes, we used this distance multiplied by -1 . The figure shows very clearly the local warp of IS matter as well as the *chimneys* connecting to the halo.

Figure 7 shows 2D color excesses from inversions A (top map) and D (bottom map), which are computed by integrating local opacities from the Sun to the boundaries of our computational domain; the distance to the Galactic plane is smaller than 300 pc and distances along the X and Y axes are smaller than 2000 pc. Iso-contours from Schlegel et al. (1998) for $E(B - V) = 0.025 \text{ mag}$ and $E(B - V) = 0.32 \text{ mag}$ are drawn for comparison. Compared to our previous inversion (A, at top) the structures are more compact for inversion D (at bottom), showing that the data are more consistent and the resolution is improved thanks to *Gaia* distances and additional data. Figure 8 is a zoom in on these 2D maps of A and D integrated color excesses, this time in a limited region of the sky close to the anticenter direction. Compared to our previous inversion, D leads to better agreement with the Schlegel et al. (1998) contours at low reddening, demonstrating that the inclusion of DIB-based data has improved the detection and location of the structures.

5. Uncertainties and comparison with other 3D measurements

5.1. Resolution and errors

Uncertainties on cloud distances and dust columns are strongly dependent on the distance to the Sun due to the combined effect of target space density decrease and target distance uncertainty increase. Additionally, uncertainties vary from one region to the other since databases have strong biases. Theoretically the errors may be calculated for each point in space along with the Bayesian inversion, but this kind of evaluation is very expensive in computation time (Sale & Magorrian 2014). On the other hand less precise error estimates for the distance to the structures and the amount of integrated reddening may be obtained by means of simpler approaches. We present these approaches here.

In the frame of a first simple approach we assumed that the error in distance varies as the achievable resolution, i.e., depends on the target space density. We choose as an estimate of the error at each point the size of the smallest sphere around this point that contains at least 10 targets. Another simpler and computationally faster approach is to calculate again in each point the target density ρ (in pc^{-3}) in a cube of a given size centered on this point and use $(1/\rho)^{1/3}$ as the error estimate. This second technique is less precise because we keep the same volume everywhere in an arbitrary way. The results for the Galactic plane are shown in Fig. 13. The results from both methods are not markedly different and as expected there is a strong increase of the distance uncertainty from the center to the peripheral regions. The error can be compared with a similar estimate by LVV: it can be seen that the addition of the APOGEE targets improves the resolution in a number of regions from the first to third quadrant. The

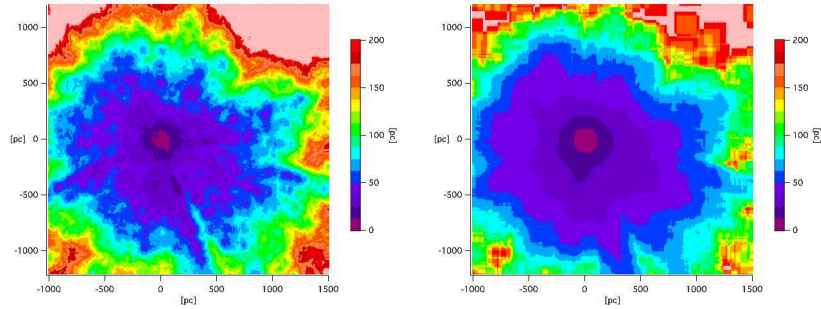


Fig. 13. Error in the distance due to the limited target space density, in the Galactic plane, as estimated from the radii of the smallest spheres that contain at least 10 targets (*left figure*) or from the target density in a cube of side 200 pc (*right*). The pale pink color corresponds to errors larger than 200 pc.

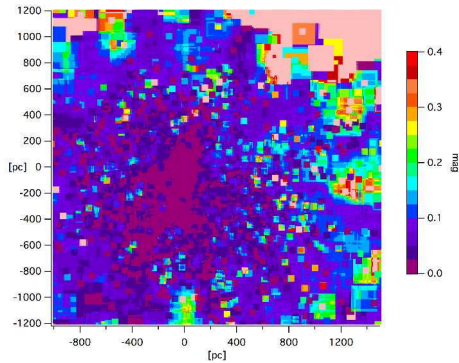


Fig. 14. Estimated error on the integrated color excess for the Galactic plane computed as the mean difference between data and model in a restricted volume (see Sect. 5.1). The pale pink color corresponds to errors larger than 0.4 mag.

errors on cloud localization owing to uncertainties on the target distances are limited by the use of our threshold (see Sect. 4.1).

As already mentioned in LVV, estimating the error on the local dust opacity is meaningless because by principle the clouds have a minimum size and as a consequence the dust is distributed in larger volumes in the model compared to the volumes of the actual, clumpy clouds. This spreading of the opacity in volumes that are wider than the volumes of the actual clouds introduces systematic underestimates of the opacities and integrated reddenings in the cloud cores. As a result, this systematic error is expected to be small for sightlines that do not intercept small, dense cores, but may reach high values in highly reddened regions in case the reddening is generated by one or a few small structures. We come back to this point in Sect. 6. On the other hand, it is possible to give rough estimates of the errors on the reddening (integrated opacity) that are linked to the dataset, independently of the errors due to the assumed cloud minimum size. To do this, for every point in our 3D map we selected all targets contained in a cube of specific size around the considered point, and for those targets we calculated the mean difference between the data and model color excess. Figure 14 shows the results for the Galactic plane with a cube of $50 \times 50 \times 50 \text{ pc}^3$; in case the cube contains less than 10 targets we use a volume of $200 \times 200 \times 200 \text{ pc}^3$. Uncertainties on distances and color excess will be available on our website and displayed interactively.

5.2. Molecular clouds catalogs

Schlafly et al. (2014) produced a catalog of molecular cloud distances based on Pan-STARRS photometric data. Most of the

clouds are out of the Galactic plane, where the number of structures distributed along the sightline is relatively small (see Fig. 1). These authors have mapped the clouds cores with a very high angular resolution, while our inversion produces much wider structures, however it is interesting to use this catalog for a comparison of cloud locations.

In Figs. 9, 12, and the bottom panel of Fig. 11, we superimposed the opacity distribution resulting from our D inversion and the position of the cloud cores identified by Schlafly et al. (2014) with associated error bars on their positions. For the Orion region (galactic longitude = 212° ; Fig. 9), these authors found a sequence of clouds distributed from 400 pc to 600 pc, which are distances similar to the structures appearing after the inversion. In the case of Perseus (galactic longitude = 158° ; Fig. 12), our map also indicates the same distances. In the case of the Cepheus region (galactic longitude = 110° ; Fig. 11) the inversion produces two large, opaque structures above the Galactic plane, the first between 250–300 pc and the second between 700–800 pc. Two groups of high latitude molecular clouds have also been mapped in this region by Schlafly et al. (2014). The closest group is in reasonable agreement with our mapped structures, while the second is at somewhat larger distances. However, in this case our targets are very scarce at high latitude (see upper and middle panels in Fig. 11) and more data are needed to allow a comparison.

5.3. Soft X-ray emitting cavities as signatures of nearby recent supernovae

Following the work of Puspitarini et al. (2014) we searched for cavities in our 3D maps, which can be counterparts of supernova remnants (SNRs) or massive stellar winds. Such cavities are detected through their soft X-ray emission in ROSAT maps. Figure 15 shows four vertical cuts in the 3D distribution along meridian lines crossing the four ROSAT 3/4 keV bright spots labeled 1 to 4 by Puspitarini et al. (2014). The coordinates of those X-ray spots are $(l, b) = (-30^\circ, +14^\circ)$, $(-18^\circ, +18^\circ)$, $(-5^\circ, +9^\circ)$, and $(-8^\circ, -10^\circ)$. In the four cases, we see that at the latitude of the bright spot centers there are cavities surrounded by dense clouds, which is the typical configuration for moderately old SNRs. Moreover, these cavities are not separated from the Sun by opaque clouds, which is a condition for their detection in soft X-rays, since million K gas soft X-rays photons are easily absorbed; more precisely, the cavities must have foreground extinction that is lower than $E(B - V) = 0.1$ to be easily detected. Compared to the previous search using LVV maps, the cavities are now better defined. Interestingly, the two cavities seen in the maps at $(l, b, d) = (-18^\circ, +18^\circ, 125 \text{ pc})$ and $(-30^\circ, +14^\circ,$

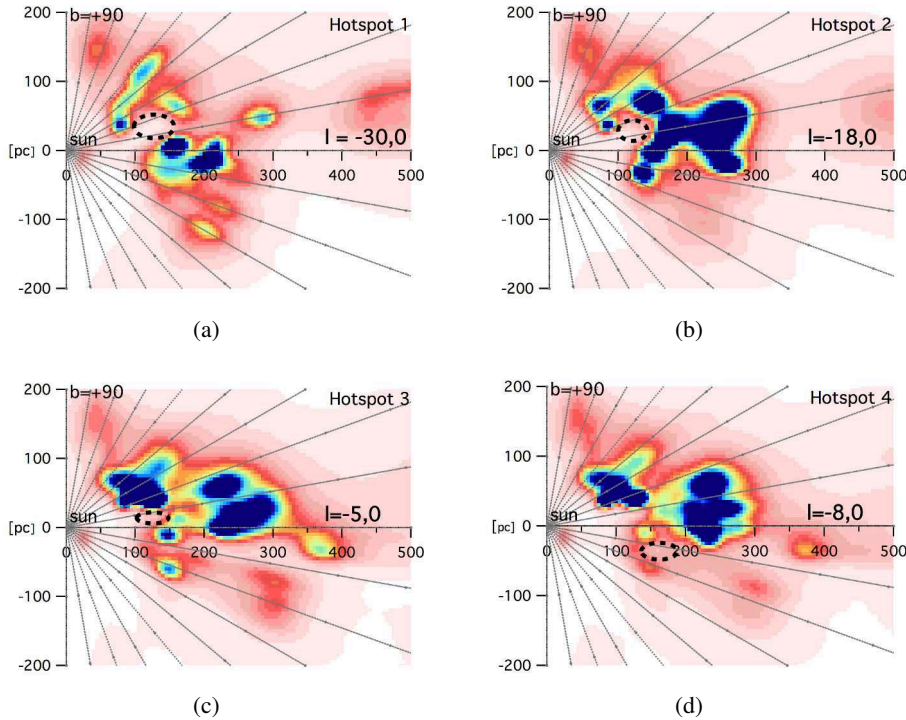


Fig. 15. Four vertical planar cuts in the 3D opacity maps in planes containing the ROSAT 3/4 keV X-ray bright spots labeled 1 to 4 in Puspitarini et al. (2014) and here as *a*) to *d*); the black dashed ellipses show the likely locations of the corresponding SNRs; the latitudinal grid is every 10 deg.

125 pc) are within 3° and 7° , respectively, from the directions of the estimated sites of the two most recent SNRs $(l, b) = (-33^\circ, +11^\circ)$ and $(-17^\circ, +25^\circ)$, in Breitschwerdt et al. (2016), and at similar distances. These authors have used the signature of ^{60}Fe in deep-sea crusts as a sign of recent (about 2.2 million years ago) explosions of supernovae in the solar neighborhood, and, based on proper motions and ages of the young stellar groups, they computed the most probable present locations of the latest explosions. Given the uncertainties associated with their statistical modeling, the small differences between our cavities 1 and 2 and their results is negligible, and these identifications reinforce their model and the ^{60}Fe measurements and interpretations.

6. Conclusions and perspectives

We updated and improved our previous 3D maps of the local interstellar dust, based on the Bayesian inversion of photometry-based color excess measurements, in several ways. Our goal is to analyze the influence of the use of new *Gaia* parallaxes and to test two additional techniques aimed at providing more accurate 3D maps. First, the merging of photometric color excesses with color excesses estimated from diffuse interstellar band absorptions and, second, the use of a non-homogeneous large-scale prior distribution deduced from massive photometric surveys. The first technique increases the number of sightlines available for the inversion and, in turn, the resolution. The second work aims at testing hierarchical techniques to be used for *Gaia* photometric data in the future .

- We replaced ≈ 5100 HIPPARCOS and $\approx 17\,400$ photometric distance measurements with $\approx 18\,700$ new *Gaia*-DR1 available parallactic distances and ≈ 4700 remaining photometric distances. In the resulting maps some elongated structures have been suppressed, which demonstrates that such features were artefacts owing to the lower accuracy of former distances. Significant changes are also seen in specific areas, in particular the Cygnus Rift.

- We extracted by means of a dedicated profile-fitting technique a series of ≈ 5000 equivalent widths of $15\,273\text{ \AA}$ diffuse interstellar bands from SDSS/APOGEE high-resolution spectra of targets possessing a *Gaia* parallax and converted their equivalent widths into $E(B - V)$ color excesses. We allowed for an additional 50% uncertainty to take into account the absence of a strict proportionality between the DIB EW and the color excess $E(B - V)$. We then performed a new inversion using the combination of the previous reddening data and the DIB-based reddening estimates. In general the APOGEE targets are more distant than the previous stars, which results in more extended maps. We do not find any contradiction between previous and new maps in regions where both types of targets are present in similar numbers. Instead, a number of structures that were broad and had low opacities are assigned more complex shapes and denser cores, which suggests that the DIB-based color excess estimates can enter the Bayesian inversion and be used to get better constraints on the cloud locations. This has important consequences because all spectroscopic surveys provide DIB measurements that may help locate the interstellar clouds, especially if all targets have precise parallax measurements.
- We used a subsample of Green et al. (2015) Pan-STARRS reddening estimates to build a low-resolution 3D map by means of a new hierarchical Bayesian interpolation method. This map is used as a prior during the Bayesian inversion of the individual data instead of a homogeneous distribution. We see that such a prior complements well the low distance map by adding spatially averaged large structures farther away. This means that data from statistical methods applied to massive photometric surveys and also future *Gaia* data may be used in conjunction with the databases of individual sightline data.

The resulting 3D maps are significantly improved with respect to the previous maps thanks to the use of *Gaia* parallaxes, the additional DIB database, and the use of a prior. This is demonstrated by the residuals, and especially by the increased compactness of

the structures and the disappearance or decrease of some of the elongated artifacts due to contradictory distances (the *fingers of god*) or lack of targets. Many of these artifacts remain, however, and are expected to disappear when all targets are assigned an accurate distance. In addition, the comparisons with other cloud location assignments and X-ray emitting cavities are encouraging. This shows that future *Gaia* parallax catalogs should considerably help the 3D mapping by allowing the use of a much larger number of targets. Merging photometric and DIB-based color excess estimates does not reveal any contradictory information and instead improves the maps, especially beyond foreground dense clouds. This opens the perspective of using the massive amounts of DIB data that are expected to be provided from high-resolution spectroscopic surveys. Finally, the use of a Pan-STARRS based prior demonstrates the feasibility of hierarchical methods for the inversion based on different datasets or massive amounts of data.

Our distributions are particularly useful at short distances, as they show how cloud complexes and cavities are spatially organized. In this respect, they are also appropriate tools for comparing with multiwavelength emission data, understanding environments of specific objects, computing particle or photon propagation modeled distributions, and searching for unreddened areas in case of stellar photometric model calibrations. In terms of angular resolution, they cannot compete with the distributions based on massive surveys. Especially, owing to the imposed cloud minimum size, opacities, and integrated reddenings toward the cores of the dense clouds can be strongly underestimated. In such nearby, opaque regions a valid approach may be the combination of both types of information, from high angular resolution maps, on the one hand, and from our 3D structure, on the other.

Vertical planar cuts in the 3D distribution are given in Appendix A at longitude intervals of 30° . Our final map is available at <http://stilism.obspm.fr> in its entirety and online tools allow one to obtain reddening curves estimated through integration in the 3D opacity distribution along with rough estimates of the uncertainties on distances of the structures and reddening. We plan to update the maps and improve online tools when additional data are included in the inversion.

Acknowledgements. We deeply thank our referee Katia Ferrière for careful reading of the manuscript and numerous constructive comments. Her corrections and suggestions resulted in significant improvement of the article. L.C. acknowledges doctoral grant funding from the Centre National d'Études Spatiales

(CNES). R.L. and A.M.-I. acknowledge support from the Agence Nationale de la Recherche through the STILISM project (ANR-12-BS05-0016-02) and the CNRS PCMI national program. M.E. acknowledges funding from the Region Ile-de-France through the DIM-ACAV project. This research has made use of the SIMBAD database, operated at CDS, Strasbourg, France.

References

- Aihara, H., Allende Prieto, C., An, D., et al. 2011, *ApJS*, **193**, 29
 Alam, S., Albareti, F. D., Allende Prieto, C., et al. 2015, *ApJS*, **219**, 12
 Arenou, F., Luri, X., Babusiaux, C., et al. 2017, *A&A*, **599**, A50
 Breitschwerdt, D., Feige, J., Schulreich, M. M., et al. 2016, *Nature*, **532**, 73
 Cramer, N. 1999, *New Astron. Rev.*, **43**, 343
 Dias, W. S., Alessi, B. S., Moitinho, A., & Lepine, J. R. D. 2012, VizieR Online Data Catalog, B/ocl
 Eisenstein, D. J., Weinberg, D. H., Agol, E., et al. 2011, *AJ*, **142**, 72
 Elyajouri, M., Lallement, R., Monreal-Ibero, A., Capitanio, L., & Cox, N. L. J. 2017, *A&A*, **600**, A129
 Elyajouri, M., Monreal-Ibero, A., Remy, Q., & Lallement, R. 2016, *ApJS*, **225**, 19
 Green, G. M., Schlafly, E. F., Finkbeiner, D. P., et al. 2015, *ApJ*, **810**, 25
 Kos, J., Zwitter, T., Wyse, R., et al. 2014, *Science*, **345**, 791
 Lallement, R. 2015, *J. Phys. Conf. Ser.*, **577**, 012016
 Lallement, R., Vergely, J.-L., Valette, B., et al. 2014, *A&A*, **561**, A91
 Lan, T.-W., Ménard, B., & Zhu, G. 2015, *MNRAS*, **452**, 3629
 Marshall, D. J., Robin, A. C., Reylé, C., Schultheis, M., & Picaud, S. 2006, *A&A*, **453**, 635
 Monreal-Ibero, A., & Lallement, R. 2015, *Mem. Soc. Astron. It.*, **86**, 515
 Nordström, B., Mayor, M., Andersen, J., et al. 2004, *A&A*, **418**, 989
 Perrot, C. A., & Grenier, I. A. 2003, *A&A*, **404**, 519
 Puspitarini, L., Lallement, R., Vergely, J.-L., & Snowden, S. L. 2014, *A&A*, **566**, A13
 Puspitarini, L., Lallement, R., Babusiaux, C., et al. 2015, *A&A*, **573**, A35
 Rezaei Kh., S., Bailer-Jones, C. A. L., Hanson, R. J., & Fouesneau, M. 2017, *A&A*, **598**, A125
 Sale, S. E., & Magorrian, J. 2014, *MNRAS*, **445**, 256
 Savage, B. D., & Mathis, J. S. 1979, *ARA&A*, **17**, 73
 Schlafly, E. F., Green, G., Finkbeiner, D. P., et al. 2014, *ApJ*, **786**, 29
 Schlafly, E. F., Green, G., Finkbeiner, D. P., et al. 2015, *ApJ*, **799**, 116
 Schlegel, D. J., Finkbeiner, D. P., & Davis, M. 1998, *ApJ*, **500**, 525
 Schultheis, M., Chen, B. Q., Jiang, B. W., et al. 2014, *A&A*, **566**, A120
 Skrutskie, M. F., Cutri, R. M., Stiening, R., et al. 2006, *AJ*, **131**, 1163
 Tarantola, A., & Valette, B. 1982, *Rev. Geophys. Space Phys.*, **20**, 219
 van Loon, J. T., Bailey, M., Tatton, B. L., et al. 2013, *A&A*, **550**, A108
 Vergely, J.-L., Freire Ferrero, R., Siebert, A., & Valette, B. 2001, *A&A*, **366**, 1016
 Vergely, J.-L., Valette, B., Lallement, R., & Raimond, S. 2010, *A&A*, **518**, A31
 Welsh, B. Y., Lallement, R., Vergely, J.-L., & Raimond, S. 2010, *A&A*, **510**, A54
 Wilson, J. C., Hearty, F., Skrutskie, M. F., et al. 2010, in *SPIE Conf. Ser.*, **7735**, 1
 Zasowski, G., Johnson, J. A., Frinchaboy, P. M., et al. 2013, *AJ*, **146**, 81
 Zasowski, G., Ménard, B., Bizyaev, D., et al. 2015, *ApJ*, **798**, 35

Appendix A: Additional figures

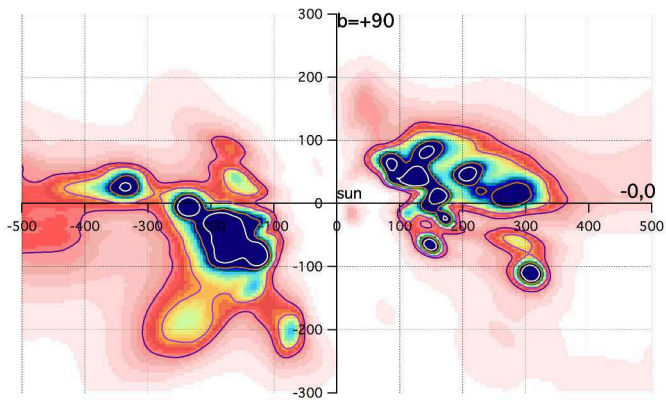


Fig. A.1. Vertical cut in the 3D opacity distribution for D inversion along the meridian plane $l = 0-180^\circ$. Color scale and iso-contours as in Fig. 9.

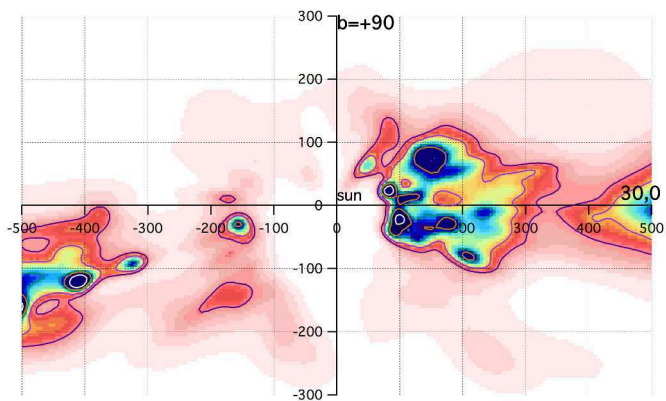


Fig. A.2. Same as Fig. A.1 for the vertical plane along $l = 30-210^\circ$.

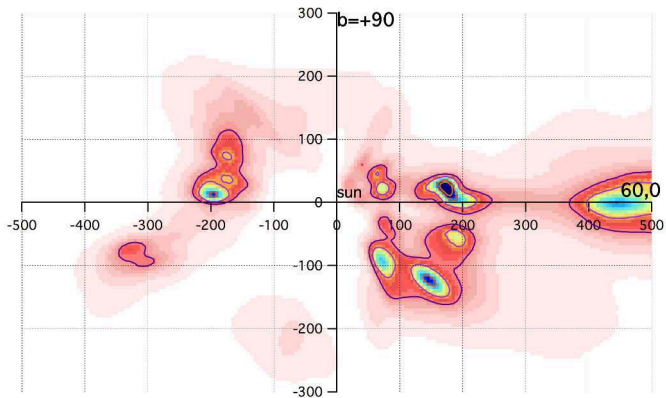


Fig. A.3. Same as Fig. A.1 for the vertical plane $l = 60-240^\circ$.

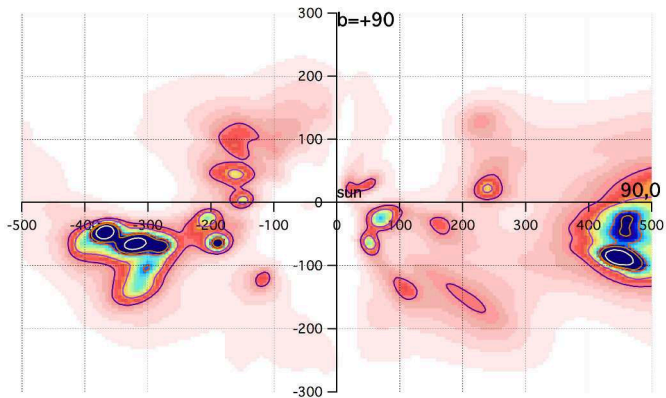


Fig. A.4. Same as Fig. A.1 for the vertical plane $l = 90-270^\circ$ (the rotation plane).

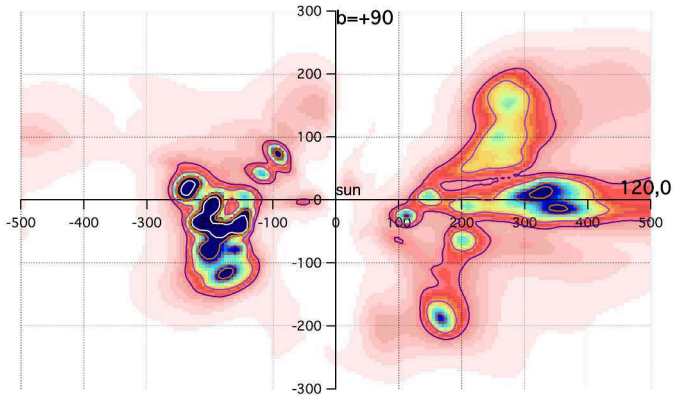


Fig. A.5. Same as Fig. A.1 for the vertical plane $l = 120\text{--}300^\circ$.

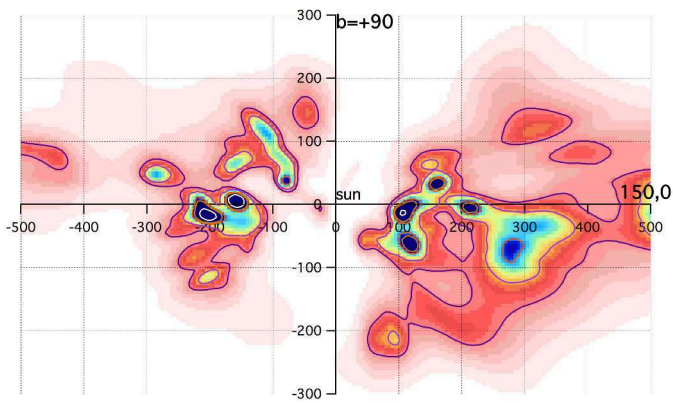


Fig. A.6. Same as Fig. A.1 for the vertical plane $l = 150\text{--}330^\circ$.

4.3 First 3D maps based on APOGEE DR14 DIB catalog

Based on the latest APOGEE DR14 catalog of 124 064 DIB measurements presented in Chapter 3, 3D maps were performed using a full 3D Bayesian tomographic technique. The inversion technique is similar to the one described in Lallement et al. (2018b). Since the inversion code inverts color excesses, the DIB strengths were converted in color excesses using the average $EW-A_V$ relationship (Eq. 5.1) established in Chapter 5.

Similarly to the analysis by Capitanio et al. (2017), we used an analytical prior distribution. For distances we made use of the recently published Data Release 2 (DR12, Arenou et al. 2018) when parallax distances have smaller uncertainties than those associated to the photometric derivation. Photometric distances are those estimated by Queiroz et al. (2018). For the inversion, we restricted our sample to targets with distances shorter than 2600 pc and with a distance from the Plane < 600 pc and we discarded those with relative errors on distance $> 33\%$. By applying these criteria, we obtained a sample of $\sim 40\,000$ stars with color excess estimates and distances. From the resulting catalog, two inversions were made simultaneously and separately. On the one hand, a 3D inversion using color excesses estimated from the DIB strengths and a second one using the color excess of the Starhorse catalog of extinctions¹, inversions are made for exactly the same targets distribution on the sky and the same distances. The main question is how far the distribution of the DIB carriers is similar to the one of the nanometric dust grains (responsible for the extinction).

In practice, the inversion was done in two steps, for the targets in the range of longitudes $0^\circ \leq l \leq 145^\circ$ and then $135^\circ \leq l \leq 360^\circ$. This is justified by the fact that the inversion code is not yet suitable for managing such large datasets. Fig. 45 shows a comparison between the two resulting 3D maps of the galactic plane based on color excess derived from DIBs and extinctions respectively. Note that for this first attempt we do not expect precise and complete maps and this is only an exercise. As a matter of fact the targets are far from being uniformly distributed on the sky as shown in Fig. 44, instead they are concentrated in a limited number of observational fields. Moreover, most stars are located at distances greater than 500 pc. However, we can make some considerations from this preliminary analysis: in both 3D distributions shown in Fig. 45 we can identify the Local Bubble and the GSH238+00+09 cavity, a 500 pc wide empty region in the third quadrant. Both regions are characterized by a very low density of matter. However, the dust-based map shows a stronger depletion than the DIB-based map. This may indicate that the DIB species follow the gas distribution rather

¹This database will be described in Chapter 5

4. DIBs AS TRACERS OF THE NEARBY ISM

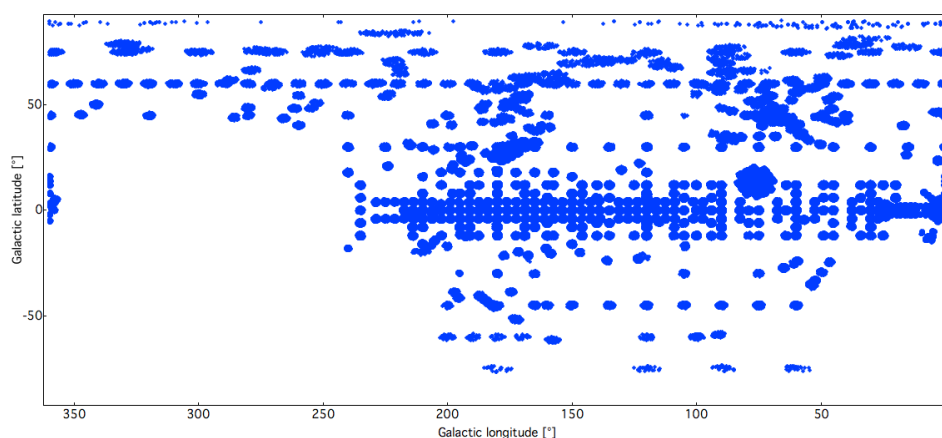


Figure 44 The APOGEE target distribution retained for the inversion in galactic coordinate system.

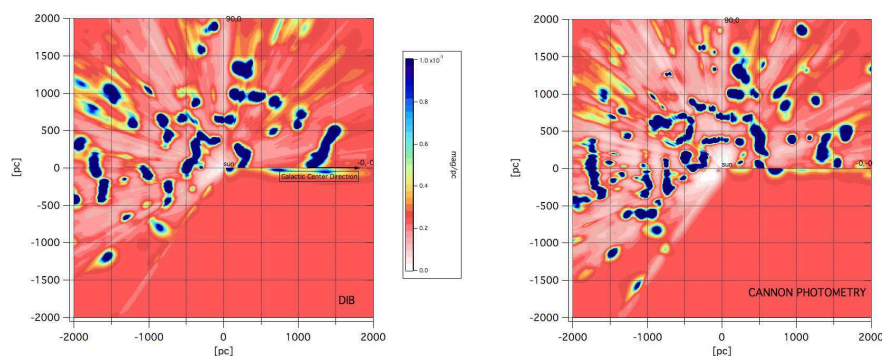


Figure 45 Left) The 3D map of the Galactic plane derived from the DIBs catalog. Right) The same for the 3D map derived from photometric calibration. Color scale is mag pc^{-1} . Courtesy: Letizia Capitanio.

than the dust concentration. A detailed study of the DIB scale height is in progress.

4.4 Conclusion

We have compared our DIB detections in the Taurus-Perseus region with the distribution of dust as traced by Planck, finding a good agreement between the strength/existence of the DIBs and the location of the clouds in the plane of the sky. Likewise, we showed how the use of series of stars with known distances allows to assign distances to the clouds. One more step was the application of inversion methods to the DIBs to recover the 3D structure, as already attempted based on optical absorption lines and extinction (e.g.

Vergely et al. 2010; Lallement et al. 2014; Sale, Magorrian 2014). A strong advantage of NIR DIBs is the potential use of highly reddened target stars and the exploration of dense IS clouds. Moreover, nowadays instrumentation is becoming more and more NIR-IR oriented and large datasets in this spectral range are foreseen. 3D maps of the Galactic ISM are tools of wide use and their quality is expected to increase considerably in future now that the Gaia distances are available. Capitanio et al. (2017) presented such 3D maps from composite data. Finally, DIB-based maps can be compared with dust and gas 3D distributions, providing new diagnostics of the conditions of their formation, ionization and destruction. They can also help interpreting small-structure of ISM clouds and of UV radiation impact on DIBs revealed by high spatial or temporal resolution spectroscopic data (Cordiner et al. 2013; Smith et al. 2013).

Conditions for DIB formation: a new view on the "skin effect"

Based on:

"Updated extraction of the APOGEE 1.5273 μm Near-Infrared Diffuse Interstellar Band: a Planck view on the carrier depletion in dense cores"

Elyajouri, M. & Lallement, R.

In revision, *Astronomy & Astrophysics Journal*.

Abstract

Context. Constraining the spatial distribution of Diffuse Interstellar Band (DIB) carriers and their links with gas and dust are mandatory steps in understanding their role in interstellar chemistry.

Aims. The analysis of the latest SDSS/APOGEE data release DR14, detailed in Chapter 3 of Part I, has led to the production of a new catalog of 124 064 DIBs, allowing us to revisit the correlation between DIB strength and dust reddening.

Methods We compared our DIB measurements with the stellar extinctions A_V from the Starhorse database. We then compared the resulting DIB-extinction ratio with the dust optical depth derived from Planck data, globally and also separately for nearby off-Plane cloud complexes.

Results. Using the new catalog of 124 064 DIB measurements, we were able to revisit the correlation between DIB strength and dust reddening. The new data reveal clearly that the sky-averaged 15 273 Å DIB strength is linearly correlated with A_V over two orders as reported by earlier studies but leveling off with respect to extinction for highly reddened lines-of sight behind dense clouds. The comparison with Planck individual optical depths reveals in a conspicuous way this DIB depletion in the dense cores and shows it applies to all off-Plane dense clouds. Using selected targets located beyond the Orion, Taurus and Cepheus clouds, we derived empirical relationships between the DIB to extinction ratio and the Planck dust optical depth for the three cloud

complexes. Their average is similar to the DIB carrier depletion measured in the dark cloud Barnard 68.

Conclusions. APOGEE measurements confirm the ubiquity of the 15 273 Å DIB carrier decrease with respect to dust grains in dense cloud cores, in a manner that can be empirically related to the dust optical depth reached in the cloud. They also show that the ratio between the DIB equivalent width and the extinction A_V for sightlines with $\tau(353\text{GHz}) \lesssim 2 \times 10^{-5}$ that do not contain dense molecular gas is about four times higher than the constant limit towards which the ratio tends for very long sightlines with many diffuse and dense phases distributed in distance.

Caveat: In this Chapter, the usage of a new stellar modelling method prompted us to correct one of the EW15273 – A_V relation established using this DIB's catalogs (Eqs. 5.1 and 5.2). This EW15273 – A_V relation (Eq. 5.2) is used throughout the manuscript, in prior publications, to derive a variety of physical quantities (Chaps. 4 and 6) or to guide to DIB profile modelling process (Chaps. 2, 3 and 7). The reader must be aware that this correction might have some implications on some of the results of Chaps. 4 and 6. In Chapter 4, the conclusions will be slightly affected since we put a conservative error on the extinction associated with an EW (to account for the variability of this ratio). In Chapter 6, this relation was used to derive the average equivalent width per unit reddening for the three weaker NIR-DIBs listed in Table 62. In this case, it is easy to correct with a simple factor. The other conclusions (e.g. discussions on the skin effect) are not affected and there are no implications on the interpretation of these earlier studies.

5.1 Introduction

In spite of an apparent general correlation between the DIB strengths and the interstellar extinction or reddening, all efforts have failed up to confirm the hypothesis that dust particles are responsible for the absorption of DIBs. One can cite in particular the most stringent limitations on polarization reported by Cox et al. (2007a) who analyzed six strong DIBs (at 5780, 5797, 6196, 6284, 6379 and 6613 Å) and revealed no linear line polarization, a polarization expected for large grain-related carriers. The lack of correlation between DIB strengths and the FUV extinction precludes the small grain-related carriers as well (Desert et al. 1995; Xiang et al. 2017). DIB carriers are then believed to be large molecules in gas phase. The detection of substructures in the profile of some DIBs (as we will see in Chapter 10.1) supports the molecular nature of some DIB carriers.

It remains that the global correlation between most DIBs and optical extinction suggests that dust grains that cause this extinction are associated with/linked to DIB carriers in some way. However, the underlying mechanisms and role of DIB carriers in the multiple physico-chemical reaction chains that occur throughout the ISM life cycle are still unknown and many

open questions remain to be answered: is the DIB carrier density related to the depletion onto the grains? are the grains the carrier formation site?

Fortunately, the new massive stellar spectroscopic surveys can now support statistical studies allowing comparisons between absorption by gaseous species (e.g. CaII, NaI, KI, C₂, CH, CH⁺), DIB carriers and dust that can help clarify their links. Such statistical studies of relationships between DIBs, gas and dust grains as well as ratios between pairs of diffuse bands contain precious information on the molecular content and the evolution of macromolecules and grains in response to the physical properties, the radiation field, the abundances in the ISM, and the grain size distribution. A hierarchy of DIBs ordered by increasing sensitivity to the ionizing field is in progress (e.g. [Enzor et al. 2017a](#)). The link with the ionizing field is particularly interesting as it is related to the depth within the clouds, and thus to the grain properties.

An important observational clue is that some of the strongest optical DIBs have shown to level off with respect to dust reddening for lines-of-sight that probe denser molecular cores, rather than the diffuse edges, of interstellar clouds. Using the Lick Observatory scanning spectrophotometer, [Wampler \(1966\)](#) was the first to notice such an effect for the DIB at 4430 Å in the spectra of background dark cloud stars. It has been also seen by [Snow, Cohen \(1974\)](#) basing it on their study of DIB strengths at 4430, 5780, and 5797 Å in Sco-Oph and Per. They concluded that formation or subsistence of the carrier is inhibited in cloud interiors. Since then, the same effect has been commented in a number of studies ([Strom et al. 1975](#); [Meyer, Ulrich 1984](#); [Wallerstein, Cardelli 1987](#); [Adamson et al. 1991](#); [Herbig 1995](#)). This behaviour has been referred to as the skin effect in the [Herbig \(1995\)](#) review. It is supported by the higher degree of correlation of the DIB strength with HI compared to molecular hydrogen ([Friedman et al. 2011](#)). Moreover, the discovery of unusually low DIBs in the spectra of the star HD52642 by [Snow et al. \(2002\)](#) also confirmed such an interpretation, if, as it is likely, the diffuse outer layers of the dark cloud in front of the star have been stripped away. However, a particular class of DIBs, the so-called C2-DIBs ([Thorburn et al. 2003](#)), seems to be abundant in the dense molecular phase ([Ádámkóvics et al. 2005](#)). For recent reviews including the skin effect see [Snow, McCall \(2006a\)](#) and [Snow \(2014\)](#).

More recently, [Lan et al. \(2015\)](#) reported this behavior for many DIBs towards lines of sight intercepting high latitude molecular clouds using the Sloan Digital Sky Survey (SDSS) star, galaxy and quasar spectra. The authors concluded that the break seen at high E(B–V) values can be quantitatively characterized by the decrease of HI in dense clouds, and higher molecular fraction.

Finally, important additional findings on the skin effect have been brought

by Fan et al. (2017). The authors have performed a large study of eight different, strong optical DIBs and, especially, produced a statistically significant study of the DIB to extinction ratio as a function of various atomic and molecular tracers of the ISM phase. In particular, they found that the relationship between the DIB to extinction ratio and the molecular hydrogen fraction $f(\text{H}_2)$ is characterized by a *lambda-shaped* curve with a peak at $f(\text{H}_2) \simeq 0.3$, definitely showing that the DIB carriers reside predominantly in this range of molecular fraction and tend to decrease in both fully molecular cores and atomic gas. As a result, this study reveals how the physical state of the gas controls the DIB to extinction ratio. Here, the term *skin effect* takes all this sense, since there is indeed a maximum volume density of DIB carriers for a particular molecular fraction, and a decrease above and below this specific fraction value. In what follows, we will only essentially address the depletion in the dense molecular phase, and for this reason we will refer to a depletion effect instead of a *skin effect*.

At least one of the near-infrared (NIR) DIBs, which allow to probe more heavily obscured regions, and thus denser (higher extinction) clouds, also displays a depletion in the dense phase. Using VLT/KMOS moderate resolution ($R = 4000$) near-infrared (H-band) spectra of 85 stars located behind the Barnard 68 dark globule – from the edge to the centre, a tomography of the $15\,273 \text{ \AA}$ near-infrared DIB in an individual dark interstellar cloud has been performed for the first time (see Chapter 7). It has demonstrated the decrease of the $15\,273 \text{ \AA}$ DIB carrier in the denser parts of such dark clouds.

Previous efforts to observe the skin effect either cover small regions around individual clouds, or have insufficient sample sizes to statistically constrain its amplitude. In this work, we expand the studies to a largely unbiased survey covering a significant fraction of the sky as presented in Chapter 3.

Our approach to the problem of the DIB-extinction link involves the use of over one hundred thousand individual lines of sight, focusing exclusively on the strongest DIB in the H-band, at $15\,273 \text{ \AA}$.

We begin the next Sec. 5.2 with a description of the public catalogs used in this study, including a brief discussion of the changes and novelties made in the various surveys. The description of the methods used for DIB extraction and the resulting catalog can be found in Sect. 3.3 of Chapter 3. Only a selective summary will be repeated here. In Sec. 5.3 we revisited the relationship between DIB strength and extinction showing a break at increasing extinction values. A special attention is paid to slight differences in the stellar models of the various pipelines, since correction for this variation is crucial to achieve a good DIB extraction, and we discuss the extinction estimates. Using our results in combination with existing extinction estimates and all-sky dust map, we investigate in Sect. 5.4 both the relationship between their ratio and the dust optical measured by Planck. Our main conclusions are

summarized in Sect. 5.5.

5.2 Description of the public catalogs used in this study

5.2.1 SDSS/APOGEE spectra

The detailed description of the SDSS/APOGEE Data release fourteen (DR14) spectra can be found in Chapter 3. For such targets we possess measurements of DIB strength, Doppler width and mean radial velocity (as described in the Chapter 3), as well as new estimates of the extinction and the distances by other groups. Our goal is to use the maximum number of those targets to search for the existence of a near-IR DIB saturation effect at high extinction, an effect that would be similar to what we have found for the same DIB in the dark cloud Barnard 68 (Chapter 7), and similar to what has been observed for optical DIBs (Lan et al. 2015).

5.2.2 Starhorse extinction and distance database

In order to study the link between the 15 273 Å DIB strength and the color excess (section 5.3), we made use of the stellar extinctions in the visible range A_V calculated with the Bayesian Starhorse method developed by Santiago et al. (2016) and Queiroz et al. (2018). The authors applied the Starhorse code to APOGEE DR 14 data and the associated stellar parameters derived from the Cannon method, therefore there is a consistency in using the results of the StarHorse technique (here version 1) applied to APOGEE DR14 and the Cannon DR14 model spectra.

Starhorse also contains spectrophotometric distances or parallax distances from Gaia TGAS (Gaia Collaboration et al. 2016) when available, as described in Anders et al. (2017). We also made use of these distances for statistical studies (see section 5.4). All catalogs are available to the community via the LineA web page¹.

5.2.3 Planck Galactic dust data

To trace Galactic dust properties in regions with DIB measurements and allow better comparisons with the interstellar dust along the sightlines, we made use of the Planck Legacy archival ² data. The Planck Collaboration used Planck and WMAP data to model the spectral energy distributions of the dust thermal emission and derive an all-sky map of the dust optical depth at 353 GHz, τ_{353} and of the dust temperature, T_D . Here we used the Planck 2015 results described in Planck Collaboration et al. (2016).

¹<http://www.linea.gov.br/020-data-center/acesso-a-dados-3/>

²<https://pla.esac.esa.int/pla/>

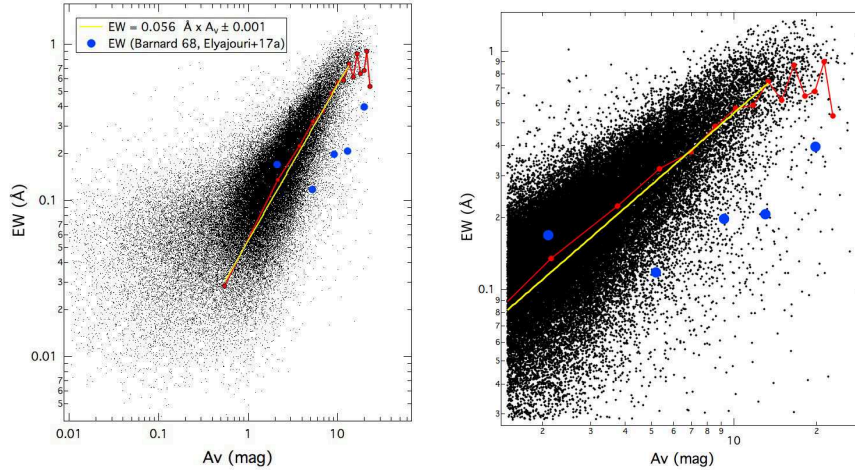


Figure 51 The equivalent width EW of the 15 273 Å DIB as a function of stellar extinction A_V . Black points are the individual sightline measurements. The red circles are the EW medians in each $\Delta A_V = 1.6$ mag, and the yellow line is the fitted EW/ A_V relationship. Superposed are the background stars of Barnard 68 (the larger blue circles).

5.3 DIB and dust extinction

Taking advantage of evolutions and improvements of models and spectra, we have revisited the link between 15 273 Å DIB strength and the extinction.

To do so, we cross-matched our catalog of 15 273 Å DIBs (section 3.3) and the Starhorse *Cannon* database using TOPCAT (Taylor 2005). We removed stars that are flagged with NUMMODELS_BAD, EXTINCTION_BAD and BRIGHT2MASS_WARN in Starhorse catalog. We finally obtained a number of 124 064 stars with DIB detection and photometric extinction and distance.

Figure 51 shows the equivalent width of the DIB as a function of the extinction along the sightline to the target. As expected and firstly discovered by Zasowski et al. (2015) for this DIB, there is a strong correlation between these two quantities that extends over more than two orders of magnitude. We computed the median value of the EW in extinction bins of 1.6 magnitudes, and fitted this median value to a power-law relationship with the extinction bin centers. Using the new catalog we find the following relationship:

$$EW_{\text{DIB}} = 0.056 \times A_V^{0.99 \pm 0.03} \pm 0.001 \text{ (Å)} \quad (5.1)$$

for the range of $A_V = [0.55\text{--}13.35]$ mag. As explained above, our lower threshold is associated with EW error intervals. On the other hand, the upper limit for the linear fit is constrained by the limited number of targets with high

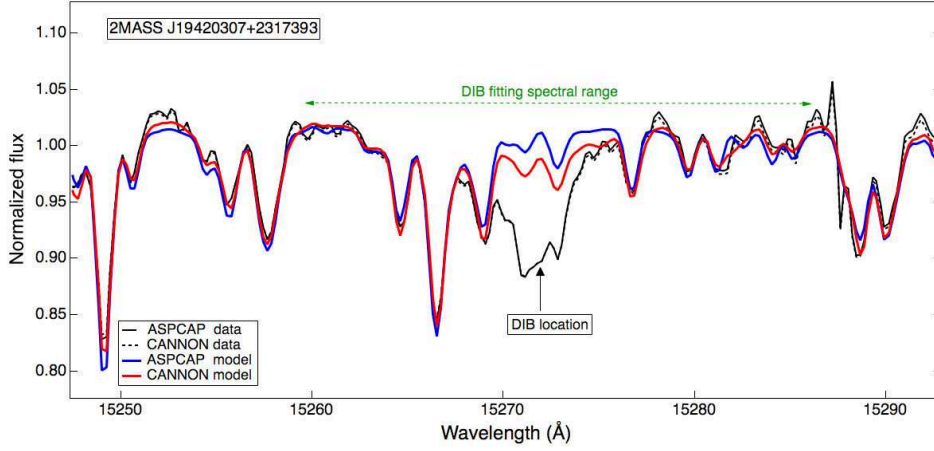


Figure 52 Spectrum of 2MASS J19420307+2317393 from ASPCAP (solid black) and *Cannon* (dashed line) data products. The associated synthetic stellar models are shown in dashed curves. We clearly see the difference between ASPCAP (blue) and *Cannon* (red) models around the 15273 Å DIB location (black arrow). An offset was applied to ASPCAP data and model to facilitate the comparison.

extinctions and chosen to avoid poor statistics. This relationship is significantly different from the previous power-law formula derived by [Zasowski et al. \(2015\)](#) found over three orders of magnitude in both A_V and EW:

$$EW_{\text{DIB}} = 0.102 \times A_V^{1.01} (\text{\AA}) \quad (5.2)$$

We have investigated the reasons for this difference by comparing the EW results for the same individual stars and by visual inspection of the corresponding spectra and models. Fig. 52 shows such an individual comparison. The figure shows that there are changes in the adjusted model spectra in many regions, and that by chance one of the most significant differences happens at the location of the 15273 Å DIB. The Cannon stellar lines are deeper than the corresponding ASPCAP lines, and as a result the fitted DIB has a smaller EW. We further investigated the impact of these differences by cross-matching the catalog of [Zasowski et al. \(2015\)](#) and our catalog for the same target stars. Fig 53 displays the EWs derived by [Zasowski et al. \(2015\)](#) and in this work based on the ASPCAP and Cannon stellar spectra respectively. Both are displayed as a function of the same extinction estimate, here the Cannon value. The slope of the average linear relationship between EW and the extinction is found about 15% smaller in our case compared to the [Zasowski et al. \(2015\)](#) derivations. This may be due to the deeper stellar lines in the Cannon spectral model and the subsequent weaker EWs. This interpretation is strongly reinforced by the observed dependence of the dis-

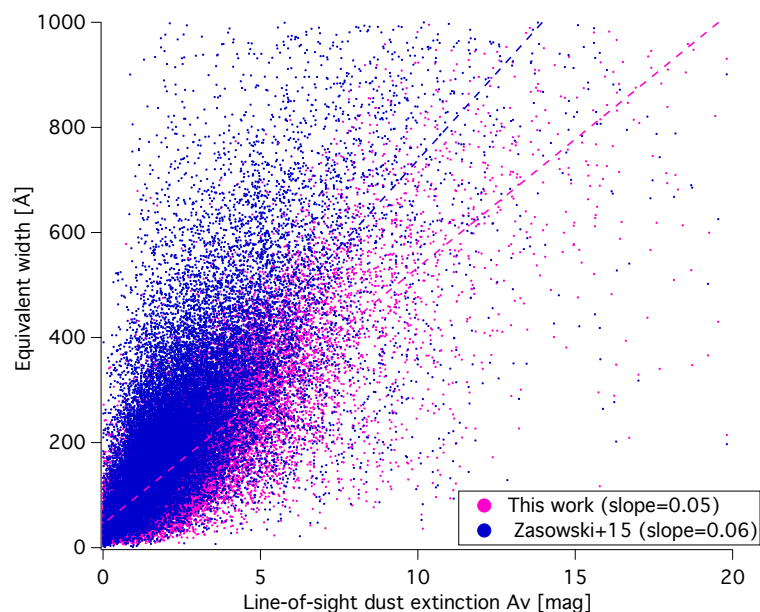


Figure 53 Comparison between the DIB EWs derived in this work and those from the [Zasowski et al. \(2015\)](#) catalog. Both values are plotted as a function of the Cannon extinction value A_V . Linear fits to both datasets (dashed blue and pink lines) are superimposed.

crepancy between the two determinations on the DIB strength, shown in Fig 54. The figure displays the average of the ratio between our determination and the one of [Zasowski et al. \(2015\)](#) in bins of increasing EWs. It is clearly seen that, the stronger the DIB EW, the smaller the difference between the two determinations. We subsequently conclude that a non negligible fraction of the difference between our two relationships can be attributed to the use of different synthetic stellar models. A second reason for the discrepant slopes is the use of different extinction estimates. Fig. 55 displays the RJCE and Cannon values of the extinction A_V for the target stars listed in the table 1 of [Zasowski et al. \(2015\)](#). The average linear relationship between the two estimates is shown in the figure. According to it, RJCE values are on the order of 25% above the Cannon estimates for the set of stars. The two effects, the one due to the use of the Cannon extinction instead of the RJCE estimate on the one hand, and the one due to the slightly different Cannon spectrum on the other hand, both result in a global decrease of the EW to extinction ratio and explain why our DIB to extinction ratio is about 40% below the one found by [Zasowski et al. \(2015\)](#). Fig. 51 also shows that the linear relationship is no longer valid at high A_V values, and that an increasing number of DIBs are significantly lower than predicted by this law. This is the so-called skin effect first detected by [Snow, Cohen \(1974\)](#) and then often found in the

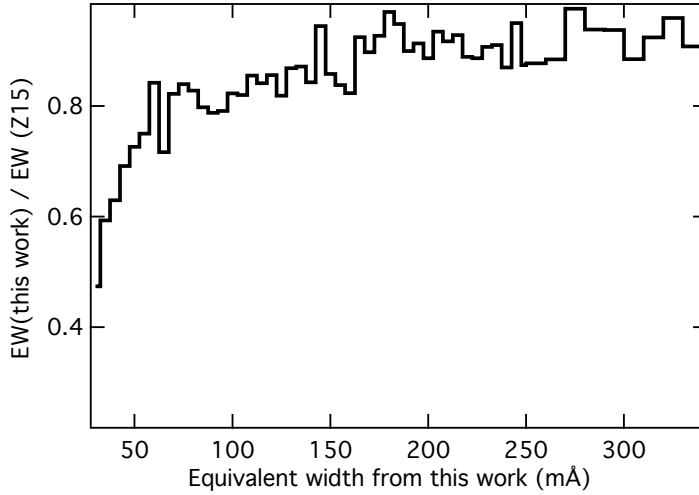


Figure 54 Average ratio between the EW derived in this work using the Cannon models and the EW derived by [Zasowski et al. \(2015\)](#) based on ASPCAP models, here in bins of EWs from our work. The ratio is increasing and reaches an asymptotic value on the order of 0.95 for large EWs above 300mÅ.

spectra of highly reddened stars. This effect is here illustrated in Fig. 51 using averages of DIB EWs in bins of 1.6 mag of A_V extinction. This choice of A_V intervals is a compromise between the need for a minimum number of targets per bin and the maximum discretization over the whole range.

This depletion is better seen when zooming at the break region for high A_V values (right part of Fig. 51). The ratio between the median value of column of DIB carrier and the extinction (column of grains) is clearly decreasing while A_V is increasing. This is clearly due to an increasing number of sightlines with relatively weak DIBs. On the other hand, a large fraction of the sightlines have strong DIBs that remain quasi-proportional to the extinction.

It is interesting to compare the skin effect seen here in a large variety of sightlines with the specific case of a dark cloud, *i.e.* a quasi-perfect monocloud situation in which all the extinction is generated in a unique dense cloud. To do so, we have added to the figure the results obtained in Chapter 7 for the Barnard 68 dark cloud. The corresponding DIB EW data points correspond to some of the largest departures from the values predicted by the linear relation. However, they are still comparable to tens of other similar cases, suggesting that the marked disappearance of DIBs in Barnard 68 is far from an exception.

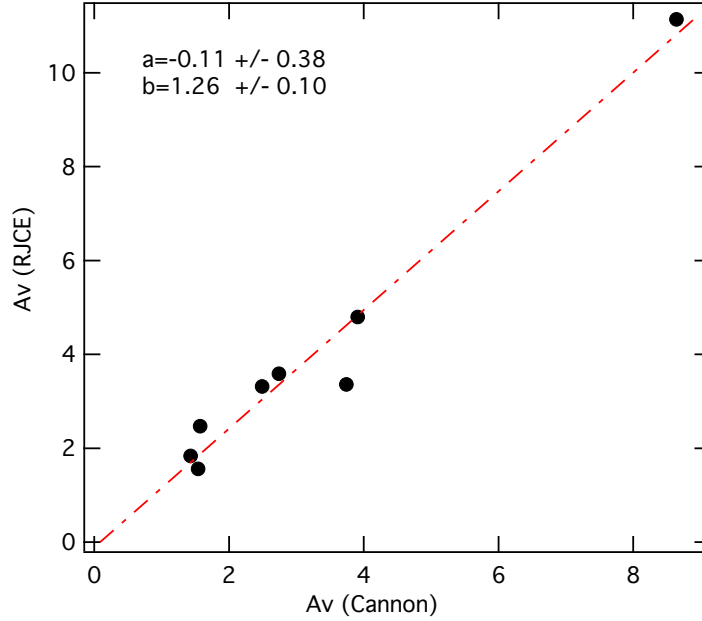


Figure 55 Cannon and RJCE extinction estimates for target stars from Table 1 from [Zasowski et al. \(2015\)](#). The RJCE estimate used by these authors and listed in their table is $\simeq 25\%$ higher than the Cannon estimate used in the present work.

5.4 The DIB carrier depletion illustrated with Planck

A fraction of the APOGEE sightlines is out of the Plane and crosses the nearby clouds of the Gould belt. For those targets that are located behind the main clouds, the observed dust emission is entirely or almost entirely generated by the nearby clouds. For this reason it is interesting to investigate the link between the DIB to extinction ratio and the dust emission. One of the goals is to detect variations among the cloud complexes or conversely some general laws for the skin effect.

Fig. 56 is a map of the Planck optical depth τ_{353} in the region of the nearby Orion clouds (data from [Planck Collaboration et al. \(2016\)](#)). Superimposed on the map are the APOGEE targets, with markers color-coded according to their EW/A_V ratio. To ensure that the stars are located behind the Orion clouds, targets closer than 600 pc were eliminated. In addition, we discarded very low reddening targets and/or very low DIB equivalent widths in order to avoid the corresponding uncertain ratios. The corresponding thresholds are $A_V \geq 0.2$ mag and $EW \geq 0.03$ Å. The DIB carrier disappearance in the dense phase is conspicuously illustrated in this figure: towards all cloud cores ($\tau_{353} \geq 10^{-4}$) the DIB to extinction ratio decreases dramatically. Recip-

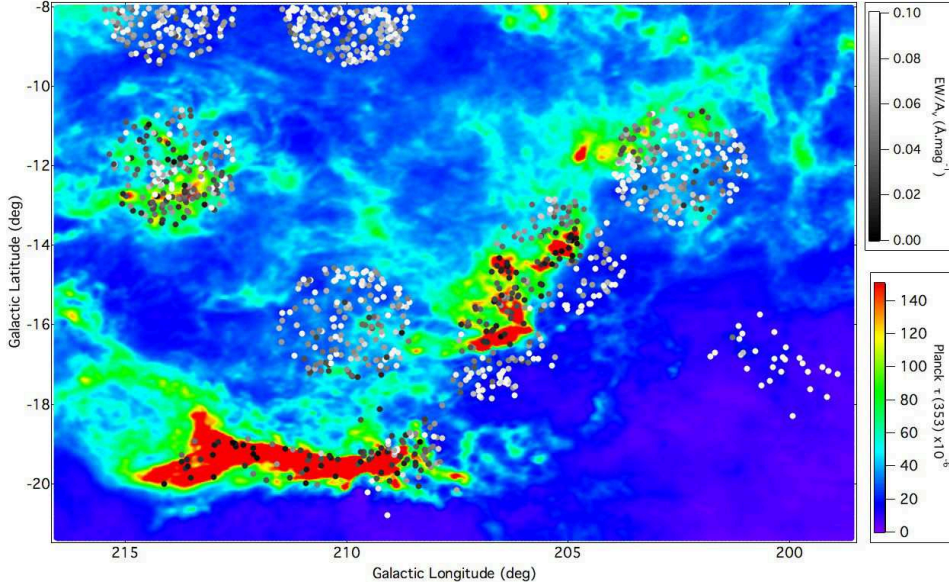


Figure 56 2D map of the Galactic interstellar dust in the Orion region (Planck 353 GHz optical depth, color scale at bottom right). Superimposed are the SDSS/APOGEE target stars contained in the field of view. The Black and white coding of the markers follows the ratio between the 15 273 Å DIB strength and the extinction of the target light in the visible, with white (resp. black) indicative of a high (resp. low) ratio. Towards the cores of the clouds (in red) there is a spectacular decrease of the DIB/extinction ratio. At the cloud periphery, and also outside the clouds that are visible in the Planck image, the ratio is enhanced, reflecting the so-called “skin effect”.

rocallly, in the more diffuse regions the ratio reaches values that are above the average ratio of $\sim 0.06 \text{ \AA mag}^{-1}$. This is the first time such a clear visualization is possible, and it is allowed by the combination of the high-quality APOGEE data and the high quality and spatial resolution of the Planck maps. Similar figures, this time for the Taurus and Cepheus clouds are presented in Fig. 57 and Fig. 58. The same restrictions were applied on A_V and EW , and the lower limits for the target distances were chosen as 1 kpc for Taurus and 1.3 kpc for Cepheus. The same striking association between cloud cores and low DIB-extinction ratios is immediately visible.

A visual inspection of the three figures does not reveal any marked difference between the three cloud associations. In order to quantify better the DIB level off we have represented in Fig. 59 $\log(EW/A_V)$ as a function of $\log(\tau_{353})$ for the three regions and the same selected targets located beyond the clouds. A first attempt to quantify the level off was made by means of a linear fit in the log-log scale for the merged datasets. The resulting best fit

5. CONDITIONS FOR DIB FORMATION: A NEW VIEW ON THE "SKIN EFFECT"

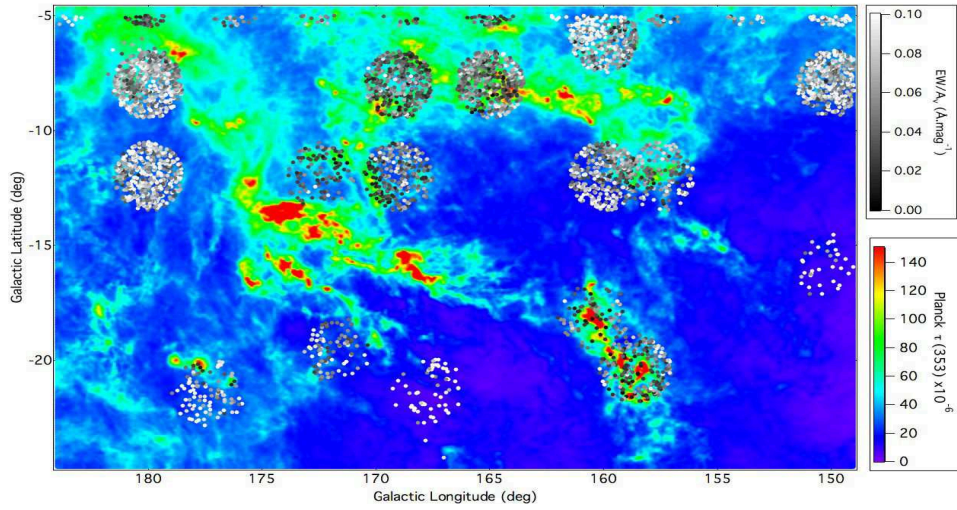


Figure 57 Same as 56 for the Taurus region.

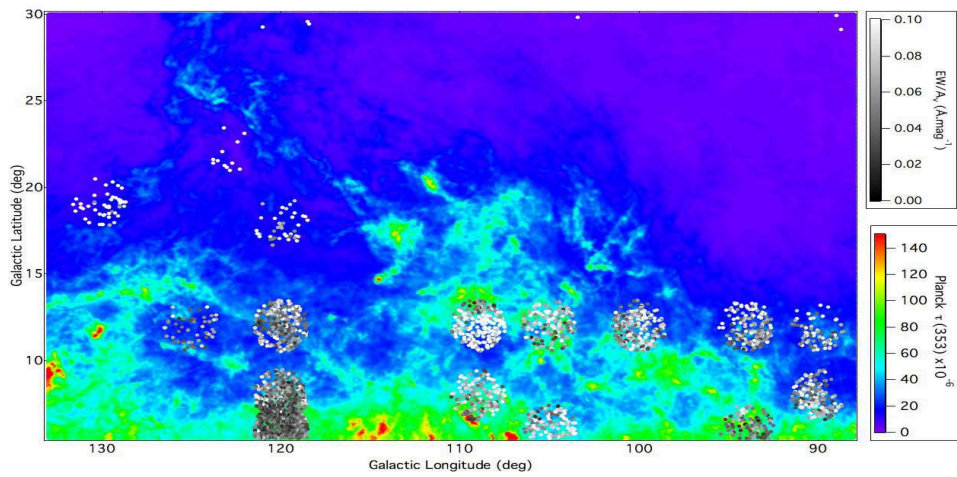


Figure 58 Same as 56 for the Cepheus region.

5.4. The DIB carrier depletion illustrated with Planck

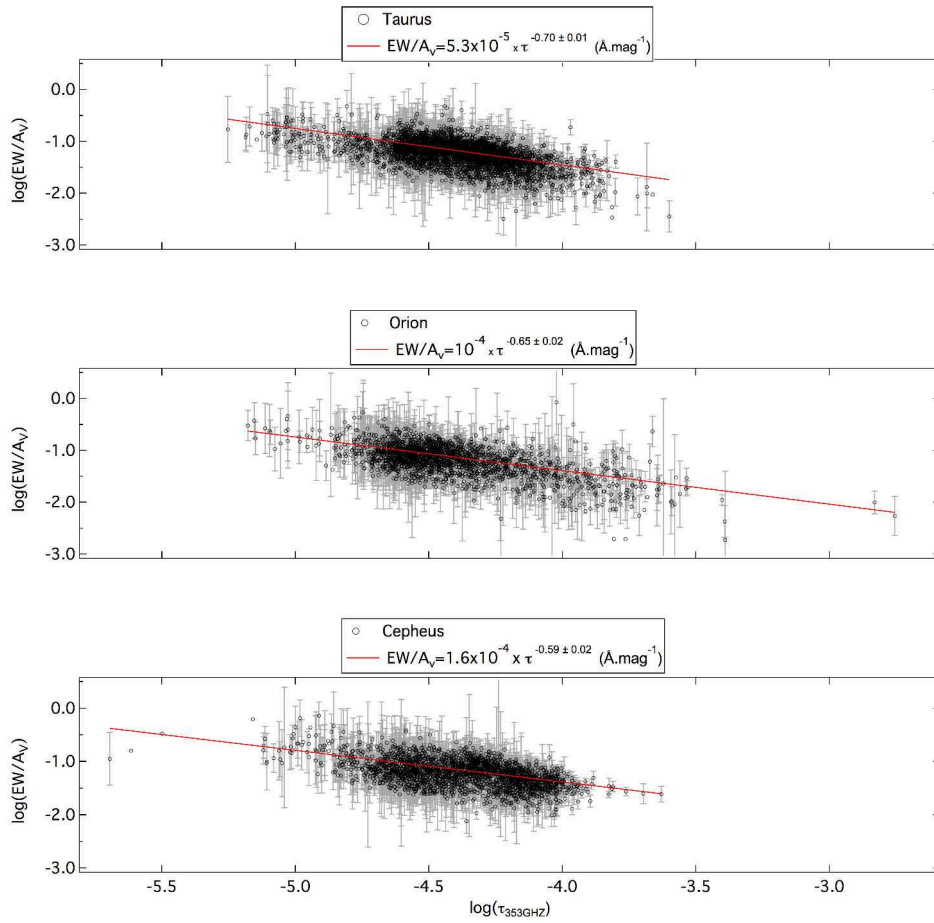


Figure 59 DIB Equivalent width to extinction A_V ratio towards stars behind Taurus (top), Orion (middle) and Cepheus (bottom) cloud complexes, as a function of the dust optical thickness measured by Planck $\tau(353 \text{ GHz})$. Linear fits in the Log-Log scale are shown in red.

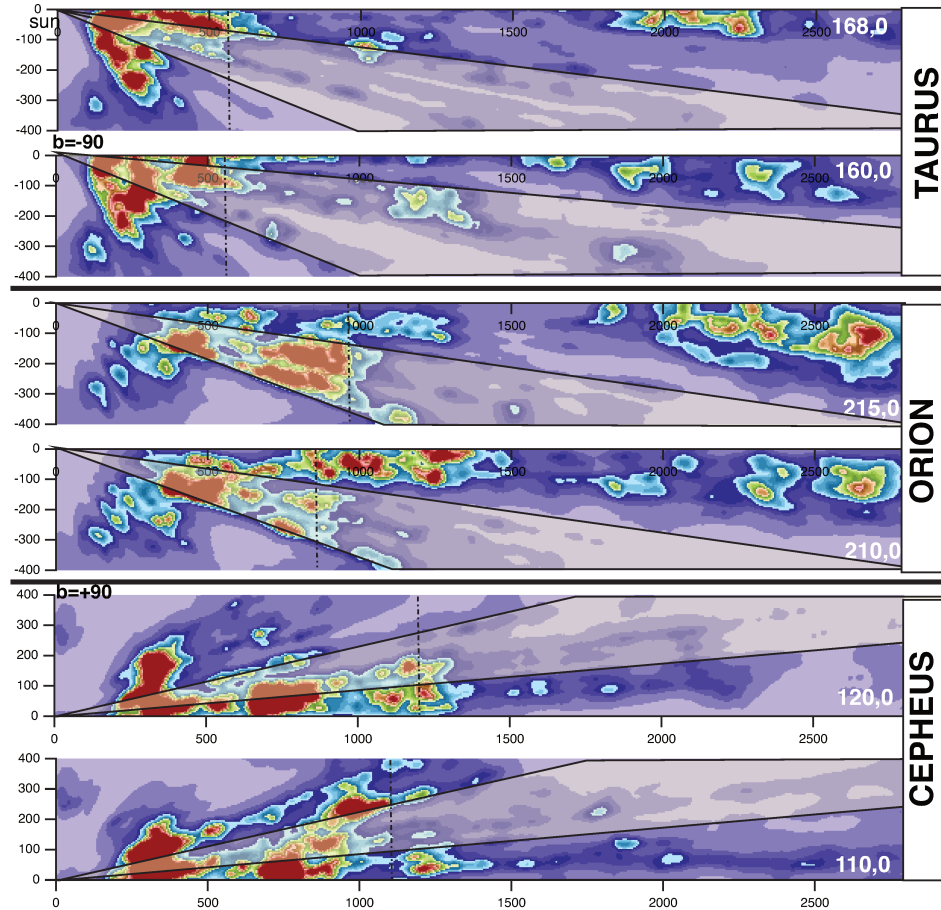


Figure 510 3D distribution of dust in vertical planes containing the Sun and crossing the Taurus, Orion and Cepheus clouds. The North Galactic pole is to the top in each figure. The cloud distribution is based on [Lallement et al. \(2019\)](#). For each cloud group two vertical planes are selected in such a way the number of target sightlines falling very close to at least one of the two planes is maximized. The Galactic longitudes corresponding to each plane are indicate at bottom right of each figure. The dashed black line encloses the densest structures (see text).

relationship between EW/A_V and τ_{353} was found to be:

$$EW/A_V = 7.6 \times 10^{-5} \times \tau_{353}^{-0.66 \pm 0.01} (\text{\AA mag}^{-1}) \quad (5.3)$$

We also performed the same adjustments for the three regions separately, this time taking into account uncertainties on the DIB to EW ratio (the fractional error on the ratio is estimated as the square root of the quadratic sum of fractional errors on the two terms). The adjustments are displayed in Fig 59 and the results were:

$$\textit{Taurus} : EW/A_V = 5.3 \times 10^{-5} \times \tau_{353}^{-0.70 \pm 0.01} (\text{\AA mag}^{-1}) \quad (5.4)$$

$$\textit{Orion} : EW/A_V = 1.0 \times 10^{-4} \times \tau_{353}^{-0.65 \pm 0.02} (\text{\AA mag}^{-1}) \quad (5.5)$$

$$\textit{Cepheus} : EW/A_V = 1.6 \times 10^{-4} \times \tau_{353}^{-0.59 \pm 0.02} (\text{\AA mag}^{-1}) \quad (5.6)$$

$$(5.7)$$

These quantitative results show that the average relationships present some differences from one region to the other, with a slope varying from -0.70 to -0.56 and without overlap of the allowed intervals.

In a search for the origin of such differences, we have made use of three-dimensional maps of the interstellar dust. Such maps are based on extinction measurements for stars at distributed distances and assign locations to the main cloud complexes (Lallement et al. 2019). Fig 510 displays the dust distribution in vertical planes crossing the clouds. For each complex, two vertical cuts are shown, for two longitudes chosen to correspond to large concentrations of target star sightlines. In each vertical plane, the range of Galactic latitudes of the target stars selected in Fig 59 are indicated by shaded sectors. A black line delimits the maximum distance from the Sun to the densest regions in the corresponding sector. The dust differential opacity threshold has been here chosen at 1.5 mag.pc^{-1} . The figures show that most sightlines cross several dense structures, i.e. a sightline does not probe a unique gas phase, instead series of dense and more diffuse regions are distributed along the sightlines. This probably explains the large dispersion of data points in Fig 59, since DIB to extinction ratios for the various phases will be smeared out in different ways depending on the sightlines. However, interestingly, the distance from the Sun to the dense cloud limit increases from Taurus to Orion then to Cepheus (although the increase from Taurus to Orion is much stronger than from Orion to Cepheus), i.e. this distance increases while simultaneously the slope of the DIB to extinction ratio relation with the dust thickness gets shallower. An increase in the limit distances and the number of structures along the sightlines implies that the merging of diffuse and dense regions must be stronger in Orion than in Taurus and even higher in Cepheus compared to Orion. For those reasons, we interpret the change of slope among the three clouds shown in Fig. 59 as an indicator

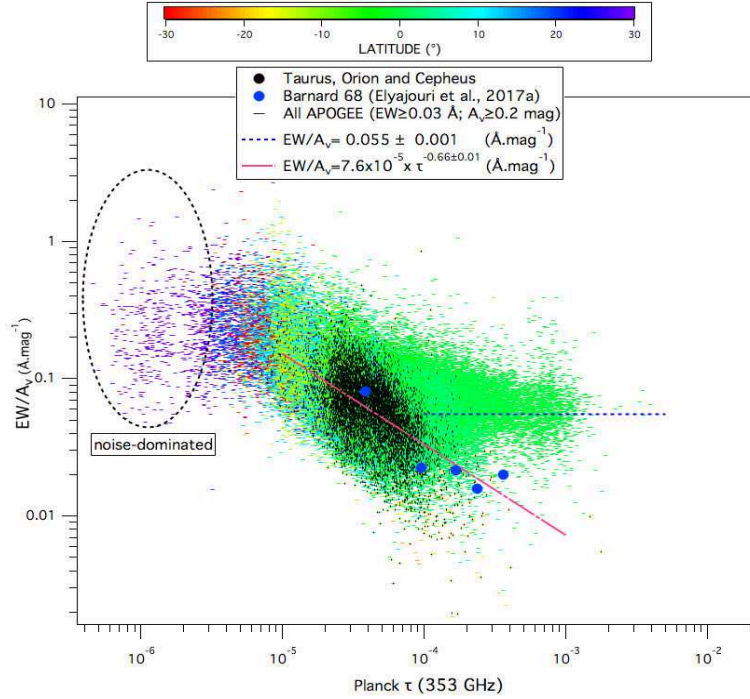


Figure 511 The DIB to extinction ratio EW/A_V as a function of τ_{353} for all APOGEE sightlines with $EW \geq 0.03 \text{ \AA}$ and $A_V \geq 0.2 \text{ mag}$. These limitations ensure a reliable determination of the EW/A_V ratio. Orion, Taurus and Cepheus targets are marked by black signs, while all other targets are color-coded according to the Galactic latitude. Here, one can distinguish three different regimes: high-latitude, low dust sightlines that correspond to nearby diffuse clouds and a high EW/A_V of $\simeq 0.23 \text{ \AA mag}^{-1}$, partially mixed phases in nearby off-Plane cloud complexes following the Taurus-Orion-Cepheus trend (red curve), and distant, high dust optical depth sightlines within the midplane for which the EW/A_V ratio reaches a constant value of $\simeq 0.056 \text{ \AA mag}^{-1}$ (blue dashed curve).

of the strength of phase mixing. In case of Taurus, its smaller number of structures and smaller resulting phase mixing, the level off the DIB is more distinctly linked to the dust column and the slope of the decrease is stronger. This is the opposite for Cepheus. If our interpretation is correct, this implies that the actual DIB to extinction ratio decrease from the diffuse to the dense phase is even stronger than suggested by the slopes in Fig. 59.

Finally, we have attempted to use the Planck data and all APOGEE sightlines to study the DIB level off in all types of configurations. To do so we removed all conditions on the target distances and kept only the lower limits on A_V

and EW imposed to avoid too large uncertainties on the DIB to extinction ratio. The total number of sightlines becomes 75 840. Fig. 511 shows the DIB to extinction ratio as a function of τ_{353} . The Orion, Taurus and Cepheus targets discussed above are marked by black signs, while all other targets are color-coded according to the Galactic latitude. Interestingly, one can distinguish three different regimes: at high latitude, thus for low dust optical depth and mostly nearby clouds, the DIB- A_V ratio apparently stabilizes, i.e. no longer increases with decreasing τ_{353} . It reaches a limit on the order of $\simeq 0.23 \text{ \AA mag}^{-1}$. Such a value is probably representative of very diffuse regions located close to the boundary of the Local Cavity (see, e.g., maps from Capitanio et al. (2017)). The second regime corresponds to the trend observed for the off-Plane Taurus, Orion and Cepheus regions, as already discussed, however this time it also applies to a large number of targets within the Plane. The third regime corresponds to large optical depths and sightlines within the mid-plane (as indicated by the low values of Galactic latitude). Here the ratio is no longer depending on τ_{353} and reaches a limit on the order of $0.05 \text{ \AA mag}^{-1}$, a value very close to the average found from the global linear fit to the data. This value must correspond to a strong mixing of diffuse and dense phases all along the sightlines.

Superimposed in Fig. 511 are the Barnard 68 corresponding data points for the five regions delineated in Chapter 7 that span extinctions A_V between 2 and 20 mag. To convert A_V into τ_{353} we used the average relationship $A_V \simeq 4.5 \cdot 10^4 \tau_{353}$, based on the classical A_V to E(B-V) ratio of 3.1 and the average E(B-V) vs τ_{353} relationship of Remy et al. (2018). It can be seen from the Figure that these data points fall in the middle of the ensemble of data points for Taurus, Orion and Cepheus, i.e., again, the dark globule does not correspond to an exceptional situation in terms of the DIB carrier depletion. This is interesting since Barnard 68 is immersed in a large opaque region with only a few ionizing stars, in strong opposition to Orion.

5.5 Conclusion

We have compared our DIB measurements with their associated visual extinctions extracted from the Starhorse database. We revisited the DIB- A_V relationship first reported by Zasowski et al. (2015) and found the DIB strength average to be linearly correlated with dust extinction over at least two orders of magnitude, however with a smaller equivalent width-to-extinction ratio than the one derived by these authors for the red giants and later by Elyajouri et al. (2016) for the hotter TSS targets: $EW_{\text{DIB}} = 0.056 \times A_V^{0.99 \pm 0.03} (\text{\AA})$. We showed how this variation is explained by the differences between the ASPCAP and Cannon models and by the use of Cannon A_V extinctions instead of A_V extinctions deduced from the RJCE technique.

It has also been found from the global DIB-extinction comparative study that the 15273 Å DIB tends to weaken with respect to extinction in the spectra of stars situated behind dense regions. This break seen at high A_V values is well known as the skin effect (Herbig 1995) and has been observed several times for optical DIBs. In the case of the 15273Å DIB, it was also observed recently in the B68 nearby dark cloud (Elyajouri et al. 2017) with a strength comparable to multiple sightlines from the present study. Very recently, it has been more specifically characterized and quantified for optical DIBs by Fan et al. (2017) who demonstrated the existence of a maximum carrier abundance with respect to dust grains for a molecular H_2 fraction on the order of 0.3.

With the goal of going one step further in the analysis of the DIB carrier depletion in dense cores, we investigated the link between the EW/A_V ratio and the distribution of dust as traced by Planck. In particular, the Taurus, Orion and Cepheus cloud complexes were studied using targets distant enough to be located behind the clouds. The depletion effect is spectacularly illustrated for those cloud complexes, thanks to the high quality of the APOGEE data and of the Planck maps. We have fitted an average relationship between the DIB A_V ratio and the Planck optical depth τ_{353} through a log-log linear formula: $EW/A_V = 7.6 \times 10^{-5} \times \tau_{353}^{-0.66 \pm 0.01} (\text{Å mag}^{-1})$.

We have performed a separate study of the three cloud complexes in a search for potential differences in the DIB depletion effect. For the Taurus clouds (resp. Orion, Cepheus), and taking into account uncertainties on equivalent widths and extinction the coefficients of the log-log linear relationship are: $(5.3 \times 10^{-5}; -0.70 \pm 0.01)$, $(1.0 \times 10^{-4}; -0.65 \pm 0.02)$, $(1.6 \times 10^{-4}; -0.59 \pm 0.02)$ respectively. Using 3D maps of the dust clouds obtained by inversion of stellar individual extinctions (Lallement et al. 2019), we have shown that the decrease of the depletion gradient from Taurus to Cepheus is very likely due to a corresponding increasing number of structures encountered along the paths to the target stars behind the three complexes, and the subsequent increase of phase mixing. Our results provide first empirical average relationships between the 15273Å DIB carrier depletion in molecular clouds as a function of the dust optical depth.

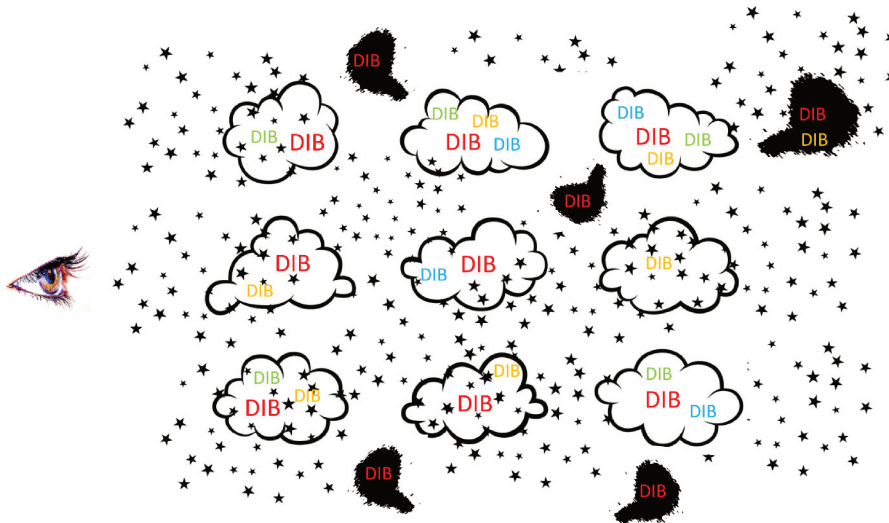
Finally, we have used the entire dataset in an attempt to identify different depletion regimes for the APOGEE sightlines. We found that, not surprisingly, for large dust optical depths exceeding $\sim 10^{-4}$, *i.e.* for low latitude and extended sightlines, the DIB to A_V ratio tends to the mean value of about $0.05\text{-}0.06 \times A_V$ that is characteristic of a strong mixing of diffuse and dense phases distributed along the extended paths. For intermediate τ_{353} values, between $\sim 10^{-5}$ and 10^{-4} we clearly see the same depletion effect that is affecting the nearby off-Plane cloud complexes, now extended to mi-plane targets. Finally, for low values of τ_{353} below 10^{-5} , the DIB to extinction ratio

seems to be constant at $\sim 0.2 \times A_V$, a value significantly above than the strong mixing average. This high value corresponds to the nearby diffuse clouds at the periphery of the local cavity.

The origin of the DIB carrier depletion in dense molecular cores is still unclear. In the context of PAH-like carriers, UV radiation would certainly directly influence the charge state of PAHs (e.g. [Cami et al. 1997](#); [Ruiterkamp et al. 2005](#)) and the resulting disappearance of some DIBs could simply be due to the evolution of the charge state from the outer to inner regions of the clouds. On the other hand, photo-processing and hydrogenation or dehydrogenation may enter in play (e.g. [Vuong, Foing 2000](#)). More recently [Bertaux, Lallement \(2017\)](#) suggested that a general carrier disappearance could additionally be due to coagulation of DIB carriers into aggregates and accretion onto dust grains, as predicted by [Jones \(2016\)](#) in the context of new models of dust. It is well known that grains grow in compact cores, generating the so-called coreshine effect ([Lefèvre et al. 2014](#)) and grain coalescence to form aggregates may also involve macro-molecules associated with DIBs. Future detailed studies of the DIB carrier depletion in regions with differing radiation field, pressure, temperature and grain properties will hopefully help disentangling the different contributions. In this respect, empirical relationships involving dust emission such as those established here may complement observed links with the physical state of the gas such as those of found by [Fan et al. \(2017\)](#) and bring additional clues.

Part III

Sightlines survey: "Few DIBs, many targets"



Chapter 6

Weak Near-infrared diffuse interstellar bands

Published:

"Near-infrared diffuse interstellar bands in APOGEE telluric standard star spectra"

Elyajouri, M., Lallement, R., Monreal-Ibero, A., Capitanio, L., & Cox, N. L. J.
Astronomy & Astrophysics, Volume 600, id.A129, 15 pp.2017a.

Abstract

Information on the existence and properties of diffuse interstellar bands (DIBs) outside the optical domain is still limited. Additional infrared (IR) measurements and IR-optical correlative studies are needed to constrain DIB carriers and locate various absorbers in 3D maps of the interstellar matter. We extended our study of H-band DIBs in *Apache Point Observatory Galactic Evolution Experiment* (APOGEE) Telluric Standard Star (TSS) spectra. We used the strong $\lambda 15273$ band to select the most and least absorbed targets. We used individual spectra of the former subsample to extract weaker DIBs, and we searched the two stacked series for differences that could indicate additional bands. High-resolution NARVAL and SOPHIE optical spectra for a subsample of 55 TSS targets were additionally recorded for NIR/optical correlative studies. From the TSS spectra we extract a catalog of measurements of the poorly studied $\lambda\lambda 15617$, 15653 , and 15673 DIBs in $\simeq 300$ sightlines, we obtain a first accurate determination of their rest wavelength and constrained their intrinsic width and shape. In addition, we studied the relationship between these weak bands and the strong $\lambda 15273$ DIB. We provide a first or second confirmation of several other weak DIBs that have been proposed based on different instruments, and we add new constraints on their widths and locations. We finally propose two new DIB candidates. We compared the strength of the $\lambda 15273$ absorptions with their optical counterparts $\lambda\lambda 5780$, 5797 , 6196 , 6283 , and 6614 .

Using the 5797-5780 ratio as a tracer of shielding against the radiation field, we showed that the $\lambda 15273$ DIB carrier is significantly more abundant in unshielded (σ -type) clouds, and it responds even more strongly than the $\lambda 5780$ band carrier to the local ionizing field.

The optical spectra were collected by our team with the NARVAL spectrograph on the Bernard Lyot telescope (TBL) at Observatoire du Pic du Midi (CNRS/UPS), France, and with the SOPHIE spectrograph on the Observatoire de Haute-Provence (OHP) 1.93m telescope (CNRS/AMU), France.

6.1 Introduction

To date, ~ 30 DIBs have been detected in the near-infrared (NIR; $> 0.9 \mu\text{m}$) (Joblin et al. 1990; Foing, Ehrenfreund 1994; Joblin et al. 1999; Geballe et al. 2011; Cox et al. 2014; Hamano et al. 2015, 2016), and only one band (the $\lambda 15273$ DIB) has been extensively explored, based on the high-quality high spectral resolution and numerous APOGEE spectra (Zasowski et al. 2015). NIR DIBs are particularly useful since they allow us to make use of highly reddened target stars and explore, if present, the densest areas of the ISM. The exact number and relative strengths of the NIR DIBs provide further constraints on their carrier population. The Sloan Digital Sky Survey (SDSS)/APOGEE dataset offers a unique opportunity to extract NIR DIBs and study their properties. In particular, the smooth continua of the bright and early-type stars selected in each field to be used as standards for telluric line corrections (telluric standard stars, TSSs) make them ideal targets for DIB extraction.

Our work has two main aims. On the one hand, we present the results of an analysis of the APOGEE TSS spectra, devoted to the extraction and identification of weak NIR DIBs. The work is a continuation of the extraction of an extensive catalog of measurements of the strong $\lambda 15273$ DIB based on the same TSS data presented in Chapter 2, and makes use of these previous results. On the other hand, we explore the potential of the strongest IR DIB as tracer of the interstellar structure. The chapter is structured as follows: Sect. 6.2 contains a brief description of the datasets. In Sect. 6.3 we describe equivalent width and Doppler shift measurements of the $\lambda\lambda 15617, 15653,$ and 15673 DIBs as well as their properties. Sect. 6.4 describes our exploratory method aiming at confirming (or not) the known weak NIR DIBs and at potentially identifying additional NIR DIBs. Sect. 6.5 presents the optical DIB measurements and the correlations between NIR and optical equivalent widths. Our main conclusions are summarized in Sect. 6.6.

6.2 Data

6.2.1 APOGEE TSS data

This contribution is based on the products from APOGEE, which is one of the SDSS-III experiments (Eisenstein et al. 2011; Aihara et al. 2011). Specifically, we used spectra from the SDSS data release 12¹ (DR12 Alam et al. 2015), which provides all the data taken between April 2011 and July 2014. Each individual spectrum covers from $\sim 15\,100 \text{ \AA}$, to $\sim 16\,700 \text{ \AA}$, at a resolution of $R \sim 22\,500$. The TSSs are used to clean the spectra of the APOGEE targets from telluric absorption lines, including the TSSs themselves. They are the bluest stars on a given APOGEE plate with a magnitude in the range $5.5 \leq H \leq 11 \text{ mag}$, and are therefore hot and bright stars with spectra that are most often (but not always) featureless. These characteristics make them ideal targets to aim at detection of faint DIBs, as we intend here. On the other hand, being hotter than the main APOGEE targets, the TSSs do not have fully adjusted tailored synthetic spectra (García Pérez et al. 2015) (for a TSSs detailed description see Zasowski et al. 2013). The APOGEE products contain the TSS decontaminated spectra and synthetic stellar spectra that provide the main stellar line locations and relative depths and widths. Both have been used in Chapter 2 to extract a catalog of $\lambda 15\,273$ DIB measurements for $\simeq 6\,700$ lines of sight. In continuity of our previous work, we restricted our analysis to the 6700 TSSs for which we detected the $\lambda 15\,273$ DIB. Throughout the analysis we use vacuum wavelengths for the infrared data.

6.2.2 New optical spectra

A subset of ~ 60 target stars from the APOGEE TSS list described in Sect. 6.3 has been observed in the visible with NARVAL, the spectropolarimeter of the Bernard Lyot telescope (2m) at Pic du Midi observatory, used in high-resolution spectroscopic mode ($R \simeq 80,000$). For all data the signal-to-noise ratio (S/N) is between 50 and 100. Two targets were observed twice in order to check the estimated uncertainties. An additional subset of five targets was observed with the SOPHIE spectrograph at the 1.93m telescope of the Haute-Provence Observatory at a resolving power $R \simeq 39,000$. Because the targets have been selected for their good detections of the weak NIR DIBs in the APOGEE spectral range, they were expected to be strongly absorbed and possess a smooth continuum, which has been verified for all of them. The telluric absorption lines were removed in the $\lambda 6283$ DIB spectral intervals using TAPAS model transmittances (Bertaux et al. 2014) and the rope length method described in Raimond et al. (2012).

¹<http://www.sdss.org/dr12/>

6.3 Catalog of $\lambda\lambda 15617, 15653, \text{ and } 15673$ DIBs

Based on earlier results by Cox et al. (2014), it appears that only four DIBs satisfy $EW/FWHM \geq 3$: $\lambda\lambda 15273, 15617, 15653, \text{ and } 15673$ bands in the 15100.08 to 16999.8 Å range. The $\lambda 15273$ DIB is by far the strongest interstellar band in this spectral range and has been extensively studied by Zasowski et al. (2015). In addition, a catalog of $\lambda 15273$ measurements based on the TSSs has been presented in 2. Here we focus on the three other, weaker bands. Based on the few available detections (Geballe et al. 2011; Cox et al. 2014), we expect them to be between two and three times fainter than the band at $\lambda 15273$. The first part of this chapter aims at creating a catalog of equivalent widths and central wavelengths for these three strongest-weak DIBs. Our previous measurements of the strong $\lambda 15273$ DIB serve as a reference for wavelength shifts and enter further correlation studies. In what follows, we describe the creation of the catalog and determine some of its properties.

6.3.1 Fitting method

To maximize the chances of detection of those three fainter DIBs, we use as starting point the 5124 spectra of the catalog in Chapter 2, which were classified as having a well-detected DIB at $\lambda 15273$. After visual inspection, 308 spectra were retained because they display at least one of the three bands. From the extracted DIB EWs and Eq. 3 in Sect. 5, they correspond to an average visual extinction $A_v=1.2$. They are characterized by a very high S/N, with a lowest S/N of 135 and a very high average S/N of 700. This is due to a double selection effect: first, the TSSs are characterized by a higher than average S/N, being the bluest and brightest objects in the field. Second, the visual selection among the TSSs favors the best spectra. As we show below, for such remarkable data DIB extractions are essentially limited by the presence of telluric (and sometimes) stellar line contaminations and not by the noise. We then fit each TSS spectrum to a model made out of the product of several components as follows:

$$M_\lambda = [S_\lambda]^\alpha \times \prod_{i=1}^3 DIB[\sigma, \lambda, D] \times (1 + [A] \times \lambda). \quad (6.1)$$

The variables in this equation are described in detail below.

- $[S_\lambda]^\alpha$, an adjusted stellar spectrum: S_λ is the initial stellar model provided by the APOGEE project. The scaling factor (α) is introduced in order to adjust the model stellar line depths to the data.
- $DIB[\sigma, \lambda_c, D]$, the DIB profile: It was modeled as a Gaussian function with three free parameters associated to its Gaussian RMS width (σ), central wavelength (λ_c) and depth (D) for each DIB. Here we fit the data for the three

DIBs simultaneously ($i=1-3$).

- $(1 + [A] \times \lambda)$, a 1-degree polynomial introduced to model as close as possible the continuum around the three DIBs.

We selected a predefined spectral range for the fit restricted to the vicinity of the three DIBs $[15\,578 - 15\,689]$ Å to determine the above coefficients, the width σ , central wavelength λ_c , and depth D for each one. Table 61 shows the fitting constraints. We fit the three features simultaneously using a unique stellar continuum (a unique scaling factor α), since they are close in wavelength. We note that there is no stellar Brackett line in this spectra region. Errors provided by APOGEE were used to mask the spectral ranges that are affected by artifacts due to imperfect sky emission correction or other sources of uncertainty. Representative examples illustrating our fitting procedure are shown in Fig. 61 and more are presented in appendix A. In each sightline, equivalent widths and stellar rest frame wavelength are determined from the best-fit parameters and are given in Table 65. We rejected those cases from the catalog where the fit failed due to low S/N, an inadequate stellar model, or most of the times very strong telluric contamination. This cleaning rejected more spectra for the broadest $\lambda 15653$ DIB (46 rejections) compared to the narrower bands (13 and 0 rejections for the $\lambda\lambda 15617$ and 15673 bands respectively).

Table 61 Fitting constraints of $\lambda\lambda 15617, 15653,$ and 15673 NIR DIBs.

	spectral range (Å)	σ_{max} (Å)	depth
15617	[15607,15620]	5	≥ 0.0001
15653	[15648,15660]	7	≥ 0.0001
15673	[15668,15680]	4.5	≥ 0.0001

6.3.2 Error estimates

We distinguish two sources of errors, one associated with the noise (δEW_n) at the DIB location, and one associated with the placement of the continuum (δEW_c). In the case of regularly distributed noise, that is, for the equivalent noise level on the sides of the DIB and at the DIB location, these errors can be treated as independent and are added quadratically. Because telluric line residuals and stellar features may be drastically different along the spectrum and from one spectrum to the other, we conservatively added the two errors. Here, we used the following formulation:

$$\delta_{EW} = \delta EW_n + \delta EW_c = 2\sqrt{2}\sigma\delta_{Depth} + 2\sqrt{2}\sigma stdev(data - model). \quad (6.2)$$

δ_{Depth} is the uncertainty on the DIB depth that results from the Gaussian fit. The approximate formula for the first term was derived using a series of

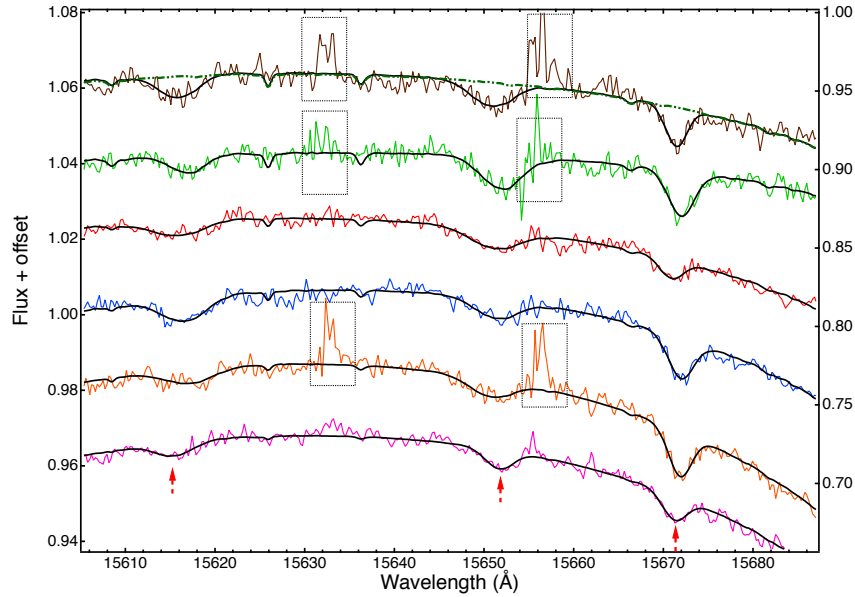


Figure 61 $\lambda\lambda 15617, 15653, 15673$ NIR DIBs toward six TSS targets from the new catalog. Reduced APOGEE spectra are shown with solid color lines: 2MASS J03483498+5048039 (brown), 2MASS J03584538+5222502 (green), 2MASS J00165734+6333108 (red), 2MASS J04360336+3640031 (blue), 2MASS J00274417+6001430 (orange), and 2MASS J00281188+5905318 (pink). Spectra are in the stellar rest frame and vertically offset by $-0.04, -0.02, 0., 0.02, 0.04,$ and 0.06 from bottom to top. The solid black curves represent the fitted model. The dot-dot-dashed green line is an example of an adjusted APOGEE stellar model. The black rectangles indicate the masked regions.

simulations with varying Gaussian noise. The exact mathematical formulation is $\sqrt{\pi}\sqrt{2}\sigma\delta_{Depth}$, that is, $\simeq 1.8\sqrt{2}\sigma\delta_{Depth}$ when the width is fixed during the fit. We conservatively replaced 1.8 by 2 to account for the partially free width. The quantity $\text{stdev}(\text{data-model})$ is the standard deviation in the two regions that define the continuum $[15\,578 - 15\,607]$ Å and $[15\,675 - 15\,683]$ Å. This second term again conservatively assumes that the continuum can be displaced by one standard deviation on both sides of the DIB. The mean values over the whole catalog of these two errors are on the same order. However, their relative values vary strongly from one spectrum to the other. For the spectra shown in Fig. 61 the second term is dominant since the continuum is very well fit, but there are opposite situations.

6.3.3 DIB characteristics

The $\lambda\lambda 15617, 15653,$ and 15673 DIBs have been observed in only a few sight-lines (Geballe et al. 2011; Cox et al. 2014). Here we benefit from the large

amount of measurements to improve their characterization.

Central wavelengths

A very precise determination of the rest wavelength of the strong $\lambda 15273$ DIB has been made by [Zasowski et al. \(2015\)](#) based on the whole APOGEE dataset. Combining this information with our previous measurements of the Doppler shifts of this strong DIB in the TSS spectra allows us to determine the rest wavelengths of the three weak DIBs in a relative way: for each spectrum we computed the difference between the fitted central wavelength of each weak DIB, that is, λ_{15617} , λ_{15653} , or λ_{15673} and the central wavelength of the $\lambda 15273$ DIB, λ_{15273} . While all DIB wavelengths vary from one star to the other due to the IS cloud motions and subsequent Doppler shifts, for a given sightline the Doppler shifts of all DIBs are the same, and as a result, the wavelength intervals between the DIB centroids (e.g., $\Delta\lambda_{15617} = \lambda_{15617} - \lambda_{15273}$) remain approximately constant (we assume that V_r/c is negligible). For each of the three DIBs we computed the average of these wavelengths intervals for all spectra of the catalog and added to the difference the central value $\lambda = 15272.42 \text{ \AA}$ of the strong DIB ([Zasowski et al. 2015](#)). The resulting three central wavelengths and estimated errors are listed in Table 62.

DIB widths and shapes

The large number of measurements for nearby targets allows us to improve estimates of the DIB widths and shapes. Table 62 lists the mean FWHM of all fitted Gaussian absorptions and Fig. 62 displays their distributions. Both show significant differences between the three DIBs, with a width decreasing by a factor 1.5 from the broadest band ($\lambda 15653$) to the narrower ($\lambda 15673$). Owing to the weakness of the DIBs and our selection of the most reddened sightlines, our distribution suffers from biases and it is not possible to derive the intrinsic widths simply from the histograms. However, it is possible to constrain the intrinsic widths to some extent. On one hand, the histograms are asymmetric with a shallower slope toward the high widths, indicating that in addition to broadening due to noise and spectra contamination, there is an additional kinematical broadening. This is particularly visible for the $\lambda\lambda 15617$ and 15653 bands. As a consequence, we can consider the histogram peak as an upper limit on the intrinsic width. On the other hand, the histograms show that there are only very few cases of DIBs narrower than $\simeq 2 \text{ \AA}$, and visual inspection shows that they correspond to large uncertainties. For these reasons we can safely assume that this value corresponds to a lower limit for all our sightlines.

As we discuss in Sect. 6.5 for the TSS targets the velocity spread of the intervening clouds is found to be small by comparison with the optical DIB widths, and this must be also true for the NIR DIBs. Therefore, the 2 \AA cutoff

is very likely the null-broadening low end of the histogram. This results in the reduced intervals for the intrinsic widths: $2 \leq \text{FWHM}(15617) \leq 4.4 \text{ \AA}$, $2 \leq \text{FWHM}(15653) \leq 5.7 \text{ \AA}$, and $2 \leq \text{FWHM}(15673) \leq 3.7 \text{ \AA}$. In the future, more numerous measurements of spectra and velocity structures or high-resolution single-cloud line-of-sight studies will hopefully better constrain the intrinsic widths.

We used the stacked spectra described in Sect. 6.4 to derive the average shape of the $\lambda\lambda 15273$, 15617, and 15673 bands. The $\lambda 15653$ DIB was not considered here because it is quite strongly contaminated by a telluric emission. The average profiles are displayed in Fig. 63 and suggest that the $\lambda\lambda 15617$ and 15673 bands are slightly asymmetric, with a shallower slope of the red wing in a way similar to most optical DIBs. The asymmetry is stronger for the $\lambda 15617$ band. A Gaussian fit to the $\lambda 15273$ band gives $\text{FWHM} = 3.91 \text{ \AA}$, a value slightly lower than the peak value $\text{FWHM} = 4.12 \text{ \AA}$ (or $\sigma = 1.75 \text{ \AA}$) measured by Zaslowski et al. (2015) for high-latitude sight-lines. Our use of bright, often nearby targets may explain that our average width is less affected by cloud velocity dispersion and is closer to the intrinsic width. Gaussian fits to the averaged $\lambda\lambda 15617$ and 15673 profiles provide $\text{FWHM} = 4.2$ and 3.1 \AA , respectively, which corresponds to the maxima in their histograms in Fig 63.

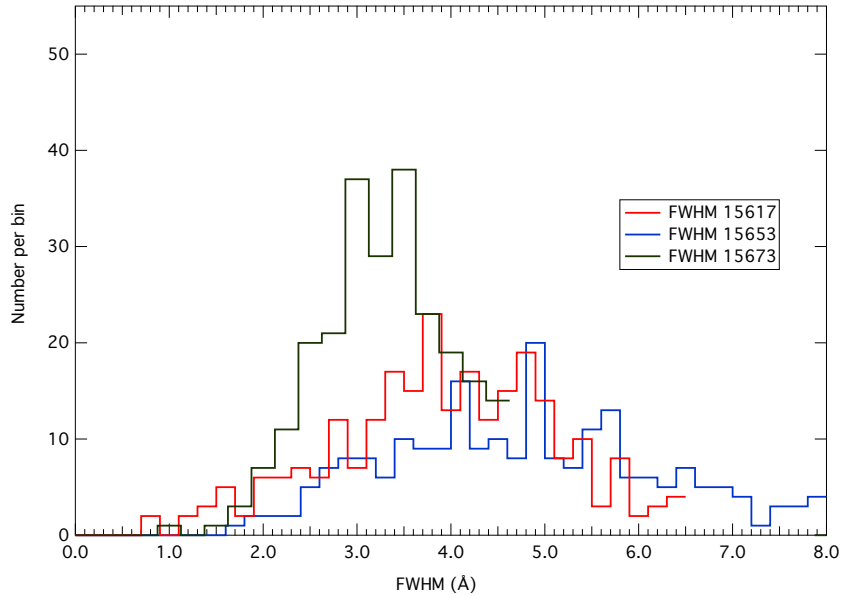


Figure 62 Histograms of the $\lambda\lambda 15617$, 15653, and 15673 DIB widths (FWHM) for the targets of the catalog.

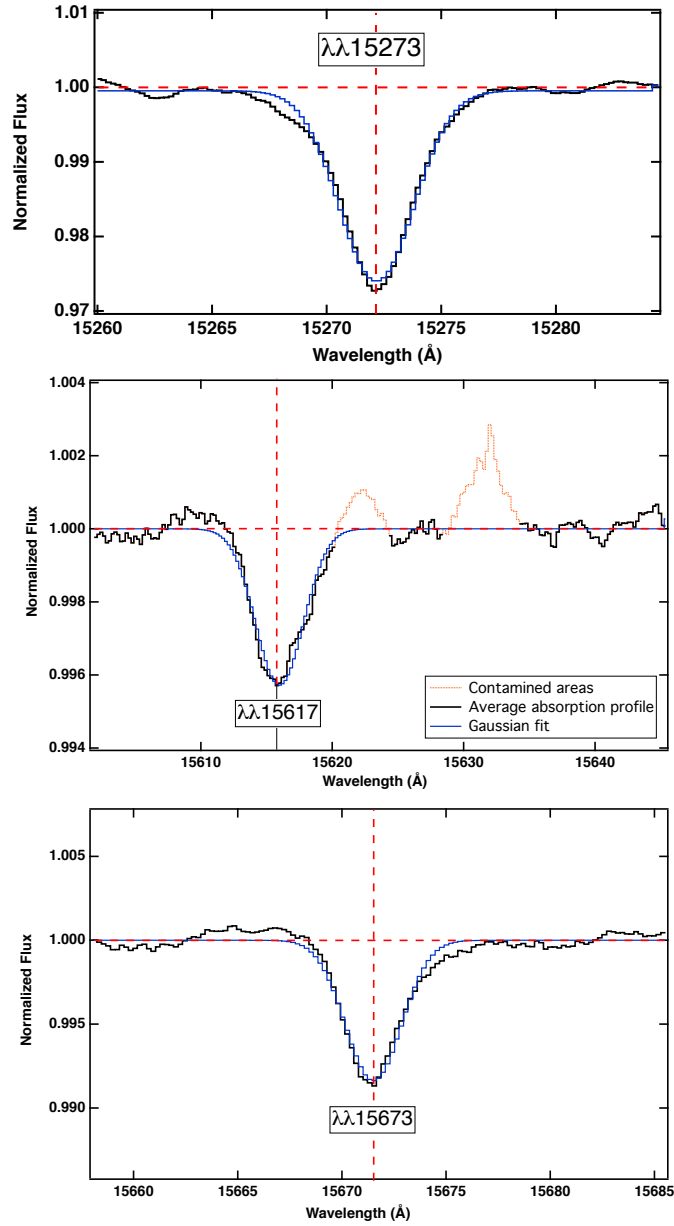


Figure 63 Extracted average normalized profile of the $\lambda\lambda 15273$, 15617 , and 15673 DIBs (see Sect. 6.4 for explanations of the stacked spectra).

6.4 Search for the weakest bands

Table 63 lists all published DIB detections and candidates in the APOGEE wavelength range (except for the strong $\lambda 15273$ DIB), based on the earlier works (Geballe et al. 2011; Cox et al. 2014). For all bands the number of de-

Table 62 Basic properties of $\lambda\lambda 15617, 15653$, and 15673 NIR DIBs.

	λ_c (\AA)	mean FWHM (\AA)	Peak FWHM (\AA)	$EW/E(B-V)$ (*) (m\AA / mag)	No. of successful fits
15617	15616.13 ± 0.07	4.37	4.03	51	295
15653	15651.38 ± 0.07	5.72	4.56	77	262
15673	15671.82 ± 0.03	3.74	3.31	96	308

(*) based on the $\lambda 15273$ DIB

tections is very small and some are quite uncertain. We used the TSS spectra to improve the characterization of these previous detections and tentatively identify new candidates. To do so, we assumed that on average, all DIBs are positively correlated with the strong $\lambda 15273$ band and built two average spectra, one that we call strong-15273, which is made of spectra showing a $\lambda 15273$ band with a high EW, and one that we call weak-15273, which is made of spectra showing a weak EW. The former strong-15273 list starts with our selection of 308 targets of Sect. 6.3 that correspond to highly reddened targets. We selected in this list the spectra for which the standard deviation between the data and the fitted model in the whole 15263-15558 \AA spectral interval is smaller than 1%, and the 16895 \AA stellar line depth is larger than 3%. This second criterion may appear surprising at first sight because it excludes the hottest target stars, but it ensures an excellent modeling of all stellar lines. This appeared to be crucial for the stacking. A total of 164 spectra were retained. For the weak-15273 list we started with the subsample of the full TSS catalog of Chapter 2 that corresponded to the detection of weak DIBs (flag 5). We extracted from this subsample the series of data that meets the same signal quality requirements as for the strong DIBs above. Forty spectra were retained following these criteria. The S/N for the two stacked spectra reaches ~ 2000 -2500 in the clean areas, allowing in principle to detect absorptions as weak as 0.05%. For both subsets the spectra were shifted to a common rest frame (the rest frame of the first target) and were then stacked. The strong-15273 stacked spectrum was used to determine the central wavelengths and average profiles (see the $\lambda\lambda 15273$, 15617, and 15673 DIB profiles in the previous section and Table 62).

The two stacked spectra are displayed in Fig. 64. The figure allows us to compare them in all spectral regions in a search for departures that indicate an absorption feature, based on the assumption that all absorptions are at least partly correlated. The strong-15273 spectrum shows significant departures from the weak-15273 spectrum at the locations of several of the detected DIBs, which confirms their existence: the obvious $\lambda 15273$, the three DIBs $\lambda\lambda 15617$, 15653, and 15673 discussed in the previous section, and the four bands $\lambda\lambda 15990$, 16232, 16573, and 16585. For all of them, except for the $\lambda 15653$ band, which is strongly contaminated by telluric lines and the $\lambda 16232$ band, which appears to be very broad, we have fitted a continuum around each detected or potential DIB in the strong-15273 spectrum and

Table 63 DIB detections in the APOGEE spectral range (except for the strong $\lambda 15273$ DIB) and their widths.

λ_{DIB} (Å)	Geballe11(*) FWHM(Å)	Cox14(**)	This work	This work mean FWHM (Å)
15225	30 ± 10 (4 LOS)	not confirmed	not confirmed	-
15617	10 ± 2 (5 LOS)	3 LOS	295 LOS	4.37
15653	15 ± 4 (6 LOS)	2 LOS	262 LOS	5.72
15673	9 ± 2 (6 LOS)	3 LOS	308 LOS	3.74
15990	9 ± 2 (4 LOS)	not confirmed	confirmed 160 stacked spectra	5.4
16232	24 ± 3 (6 LOS)	1 LOS	confirmed (idem)	17::
16573	(4 LOS)	1 LOS	confirmed (idem)	5.2
16585	(6 LOS)	2 LOS	confirmed (idem)	3.3
16596	(5 LOS)	1 LOS	not confirmed	-
15235	-	-	new candidate?	-
16769	-	-	new candidate	2.8

(*) Geballe et al, 2011, (**) Cox et al, 2014, (::) uncertain, LOS : line of sight

extracted the DIB profile. The continuum-normalized spectra are shown in Figs. 63 and 65. Gaussian fits to the profiles provided the band widths listed in Table 63. For the broad $\lambda 16232$ band we show the difference between the two stacked spectra and the corresponding estimated value of its width. The $\lambda 16232$ width is found to be significantly smaller than earlier results of Geballe et al. (2011).

The comparison between the two stacked spectra does not reveal any marked difference at the location of the tentative $\lambda 15225$ DIB detected by Geballe et al. (2011), in agreement with the absence of detection by Cox et al. (2014). However, we detect a non-negligible depression at 15235 \AA , and we suggest that it is a potential DIB candidate. We do not detect any feature at 16596 \AA , contrary to Geballe et al. (2011) and Cox et al. (2014). We note that this spectral region corresponds to a strong telluric doublet. Finally, we detect a potential candidate at 16769 \AA , as shown in Fig 66. This spectral region corresponds to the left wing of a broad stellar line whose continuum is fit as illustrated in the figure.

The detectability of new weak diffuse bands strongly depends on the spectral interval. It is much lower in intervals contaminated by telluric residuals and at the location of stellar lines. In the cleanest areas, a DIB with $EW/E(B-V) = 11 \text{ m\AA mag}^{-1}$ such as the $\lambda 15990$ DIB can be detected using the stacked spectra, as shown in Fig. 64. However, such a DIB represents here a limit for the method, as can be estimated visually from the figure: DIBs weaker than $EW/E(B-V) \sim 10 \text{ m\AA mag}^{-1}$ and widths on the order of $1\text{-}2 \text{ \AA}$ may remain undetected in the clean areas of the data. Stronger DIBs can also remain undetected in contaminated areas.

6. WEAK NEAR-INFRARED DIFFUSE INTERSTELLAR BANDS

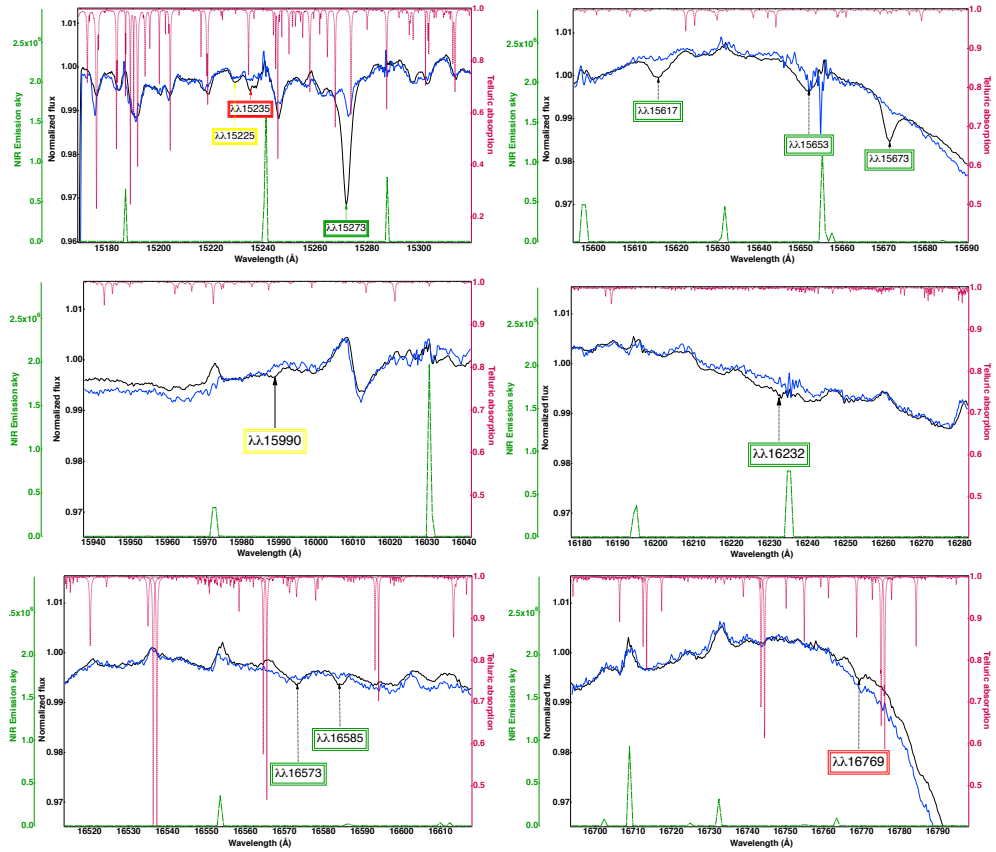


Figure 64 Stacked spectra created from 164 sight lines selected for their strong, well detected $\lambda 15273$ DIB (solid black curve), and for 40 sightlines selected for a combination of high signal, clean spectrum, and weakness of the $\lambda 15273$ DIB (blue solid curve). Before stacking, the spectra have been shifted to a common rest frame. In each figure the pink dashed lines show the telluric models and the green dashed curve displays the NIR emission sky. At the location of an actual DIB we expect the black curve to exhibit a depression by comparison with the blue curve. Telluric absorption and emission spectra allow us to distinguish artifacts that are due to telluric lines and real interstellar absorptions. Weak NIR DIBs detected previously are indicated by colored boxes with the following code: green box: detected by [Geballe et al. \(2011\)](#) and confirmed by [Cox et al. \(2014\)](#); yellow box: detected by [Geballe et al. \(2011\)](#), but not confirmed by [Cox et al. \(2014\)](#); red box: potential new detection.

6.5 Correlative studies

NIR DIB correlative studies are essential in several respects:

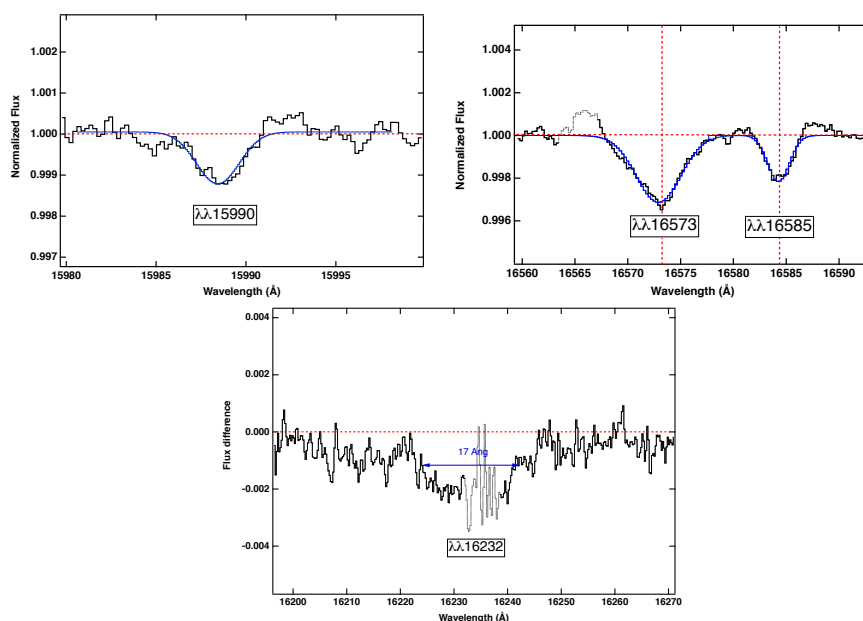


Figure 65 Same as Fig. 63 for the $\lambda\lambda 15990$, 16573, and 16584 DIBs. For the broad $\lambda 16232$ Å band we show the difference between the two stacked spectra and the corresponding estimated value of its width.

- Like all correlations, they contain informations on the carriers and may reveal families of DIBs. Today, NIR DIB-DIB correlation studies are still limited by the small number of NIR DIB measurements for transitions other than the $\lambda 15273$ APOGEE main DIB. Cox et al. (2014) studied the correlations among three NIR DIBs ($\lambda\lambda 11800$, 13180, and 15273) and found correlation coefficients of 0.90 and 0.97. On the other hand, their comparisons with optical DIBs led to a wider range of coefficients, from 0.83 to 0.98. Hamano et al. (2015, 2016) performed an extensive study of NIR DIB correlations for the 20 bands within the $[0.91 - 1.32]$ μm spectral range and found widely distributed correlation coefficients, ranging from 0.45 to 0.99 for NIR-NIR relationships, and ranging from 0.39 to 0.95 for the relationships between four NIR DIBs and eight optical bands.
- DIB - DIB correlations and DIB correlations with the reddening or the gas column are important when the DIBs are to be used for mapping purposes. In principle, any ISM tracer, including DIBs, can be used to assign distances to clouds based on gradients, but the links with other tracers are fundamental for deriving physical quantities.
- Optical DIBs observations cannot be used to trace highly or extremely reddened LOS. In contrast, NIR DIBs may be very useful to have a

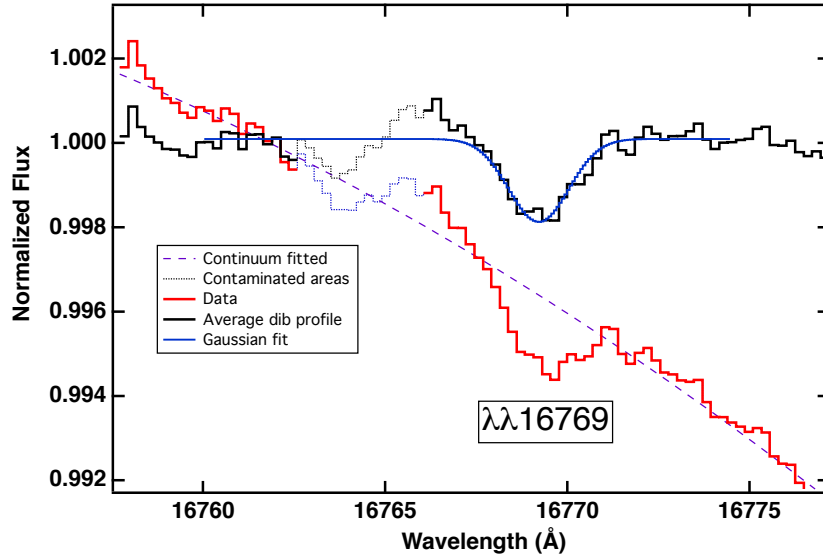


Figure 66 Potential $\lambda\lambda 16769$ DIB candidate. In red is shown the original stacked spectrum. The dashed line is the fitted continuum around the DIB, and the normalized spectrum is shown in black. A spectral interval strongly contaminated by a telluric line and not included in the continuum fitting is shown in pale blue.

proxy of the amount of matter that may be able to penetrate these regions.

Here we have used the APOGEE TSS data and ground-based measurements to study the links between the NIR DIBs we could extract and the links between the APOGEE strong DIB and optical bands in more detail.

6.5.1 NIR-NIR DIB correlations

Figure 67 shows a comparison of the three DIBs $\lambda\lambda 15617$, 15653 , and 15673 with the stronger $\lambda 15273$ band. Despite the large uncertainties, each of the three DIBs is positively correlated with this band. We performed a proportional linear fit using the orthogonal distance regression (ODR) method to take uncertainties on two compared quantities into account. The slopes we found are indicated in the figure. These slopes are used to derive the average equivalent width per unit reddening listed in Table 62, using as a reference the value derived by Zasowski et al. (2015) for the $\lambda 15273$ DIB, namely:

$$EW_{DIB} = 102 \text{ m}\text{\AA} \times A_V^{1.01 \pm 0.01}, \quad (6.3)$$

using the relation between extinction and reddening provided by [Savage, Mathis \(1979\)](#):

$$R = A_V/E(B - V) = 3.1. \quad (6.4)$$

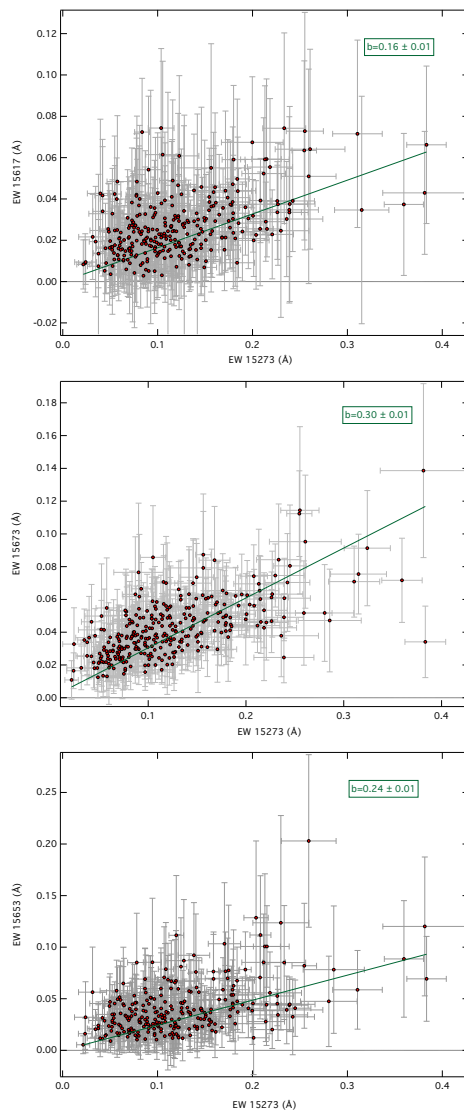


Figure 67 Correlation between the $\lambda\lambda 15617$, 15673 , and 15653 NIR DIBs and the strong $\lambda 15273$ NIR DIB. The slope for the ODR proportional linear fit is shown in each plot.

6.5.2 Extraction of optical DIBs from APOGEE TSS follow-up observations

The equivalent width for the optical DIBs was measured using a modified version of the fitting method described in (Puspitarini et al. 2013). The parameter determination was split into two steps. First, we determined the shift of the DIB by cross-correlation of the observed spectrum with an empirically determined template for the DIB (Puspitarini et al. 2013; Raimond et al. 2012). Then, the shifted spectrum was fit to determine the coefficients associated to the strength of the DIB and small adjustments to the continuum. We note that the DIB at $\lambda 6283$ is in a spectral region with heavy atmospheric absorption. For this specific DIB, we therefore estimated and removed the telluric absorption using TAPAS² (Bertaux et al. 2014). Equivalent widths are listed in Table 64. Reported errors are based on the formal one-sigma statistical errors associated to the fit. Representative examples of fits for each DIB are presented in Fig. 68.

6.5.3 NIR-visible comparisons

We used the subset of APOGEE targets with high-resolution optical spectra to study various relations. In addition to the APOGEE+NARVAL/SOPHIE data, we included the results by Cox et al. (2014). Compared to their results, our targets probe smaller column material, but the number of targets is now strongly increased, namely from 9 to 58 lines of sight. Our goal is to study how the $\lambda 15273$ DIB compares with these optical bands, especially those that are the most or the least sensitive to the line-of-sight type.

We performed ODR linear fits for the five optical DIBs $\lambda\lambda 5780, 5797, 6196, 6283, \text{ and } 6614$. Results presented in Fig. 69 show that the strongest infrared DIB (i.e., the DIB at 15273 \AA) is well related with the strongest optical DIBs, which in turn trace the amount of interstellar matter along a line of sight well (e.g., Merrill 1934; Herbig 1993b). This supports the use of this DIB as a tracer of the extinction, for instance. This is of particular interest to map the extinction along very reddened lines of sight that are impregnable at optical wavelengths. The corresponding Pearson correlation coefficients r and reduced χ^2 s are shown in the Fig. 69. All correlation coefficients are above 0.81, that is, they are similar to the average coefficients for the optical DIBs (Friedman et al. 2011). Interestingly, the best reduced chi-squared of the five DIBs is found for the $\lambda 6283$ band, and the worst correlation is found for the $\lambda 5797$ band, with a variation by a factor of almost 2 between the two bands, which is quite significant. For all DIBs observed by Cox et al. (2014), HD147889 is the most spectacular outlier, followed by HD161056.

²<http://www.pole-ether.fr/tapas/>

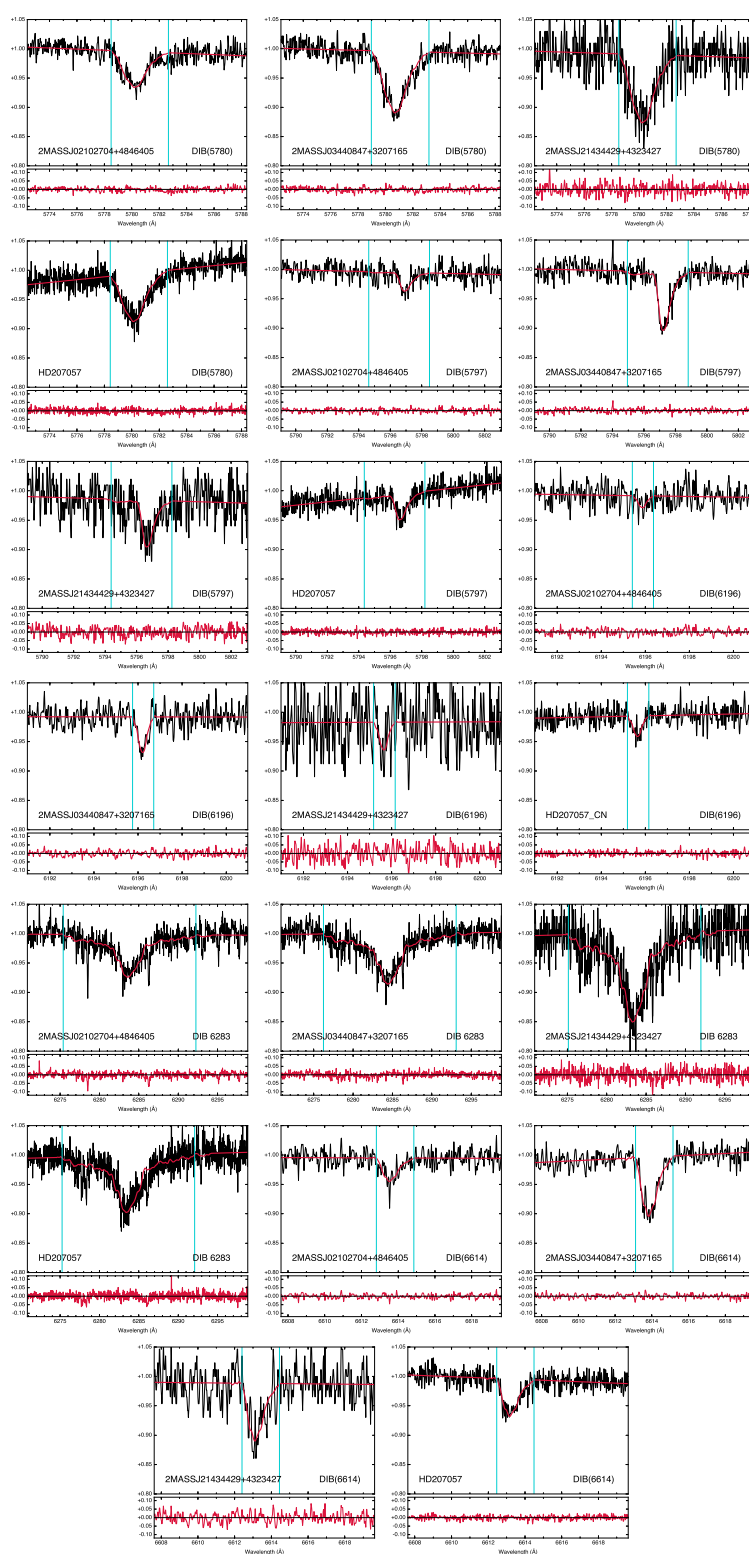


Figure 68 Representative fit examples for the optical DIBs for three stars observed with NARVAL (columns 1-3) and one star observed with SOPHIE (last column). They are ordered from bluer (top) to redder (bottom) band. Each panel contains a main graphic on top, with the observed spectrum in black and the fit in red. Integration limits for estimating the equivalent width are marked in cyan. The auxiliary graphic at the bottom contains the residuals in red.

6.5.4 Influence of the environment on the $\lambda 15\,273$ DIB: detection of an edge effect for the $\lambda 15\,273$ DIB

It is well known that the relative strength of optical DIBs varies with the line of sight (e.g., [Krelowski et al. 1992](#); [Cami et al. 1997](#); [Cox, Spaans 2006](#); [Friedman et al. 2011](#); [Vos et al. 2011](#); [Cordiner et al. 2013](#)), which reflects the reaction of the DIB carriers to the properties of the ISM. On the one hand, the so-called σ -type clouds, named after σ Sco, are associated with low-density clouds and/or locations that are exposed to interstellar UV radiation field. On the other hand, ζ -type clouds, named after ζ Oph, are associated with higher densities areas that are better protected from the UV radiation. Specifically, [Cami et al. \(1997\)](#) found that the $\lambda 5780$ DIB carrier is more abundant in the edge of the clouds (i.e., a σ -type unshielded location), while that of $\lambda 5797$ DIB struggled to survive at these locations and instead reached its maximum in the shielded core of the clouds. Thus the ratio between the strengths of the $\lambda 5797$ and 5780 DIBs is well suited to distinguishing these two types of sight lines, and it has been used as a means to quantify the exposure to the UV radiation (e.g., [Maíz Apellániz et al. 2015](#); [Cordiner et al. 2013](#)): sight lines with low $EW(\lambda 5797)/EW(\lambda 5780)$ values are classified as σ -type, while those with high $EW(\lambda 5797)/EW(\lambda 5780)$ are considered as ζ -type. Different limiting values to separate between these two types of clouds can be found in the literature. As a reference, we use in our discussion a ratio of $EW(\lambda 5797)/EW(\lambda 5780) \simeq 0.32$, as proposed by [Vos et al. \(2011\)](#).

Because only few lines of sight have measurements on both the $\lambda 15\,273$ infrared DIB and the $\lambda 5780$ and $\lambda 5797$ optical DIBs, the reaction of the $\lambda 15\,273$ infrared DIB to the UV radiation field has not been addressed until now, as far as we are aware. Our sample of about 60 lines of sight is large enough to allow us to do so. Since we lack color excess determinations, we cannot use normalized equivalent widths (i.e., $EW/E(B-V)$ ratios), as has been done by [Cami et al. \(1997\)](#), for example. Instead, we make use of a series of optical bands that are known for reacting to the radiation environment in a different manner (from blue to red: $\lambda 5780$, 5797 , 6196 , 6283 , and 6614), and we test the sensitivity of the $\lambda 15\,273$ band to the environment by comparing its strength with the one of each of these bands for all our targets. Individual $5797/5780$ ratios for each target are used as a quantitative measurement of the radiation. In this way, identifying which of the $\lambda 15\,273$ /optical DIB ratios appears independent of the $EW(\lambda 5797)/EW(\lambda 5780)$ ratio allows us to associate the behavior of the infrared DIB with that of this optical DIB, which in turn places constraints on its carrier and assesses its diagnostic potential.

The measured ratios are ordered according to their degree of variability with respect to the $EW(\lambda 5797)/EW(\lambda 5780)$, as presented in [Fig. 610](#). In general, differences between ratios are much larger in the σ -type regime (unshielded) than in the ζ -type regime, where the behavior is smoother even though dif-

ferences still exist. The strongest variation is found for the ratio involving the $\lambda 5797$ DIB, which is weakened in the presence of a strong UV radiation field (Ehrenfreund, Jenniskens 1995; Cami et al. 1997). Conversely, the $\lambda 15273$ infrared DIB follows the $\lambda 5780$ band more closely, and even more so the $\lambda 6283$ band. The comparison with the two other optical DIBs under consideration ($\lambda\lambda 6196$ and 6614) displays an intermediate behavior. Our results therefore point toward a connection between the carriers of $\lambda\lambda 5780$ and 6283 DIBs, and that for the $\lambda 15273$ infrared DIB. For example, we might expect an ionization potential for the carrier of the $\lambda 15273$ infrared DIB smaller than 13.6 eV, as proposed for the $\lambda\lambda 5780$ and 6283 DIBs (Ehrenfreund & Jenniskens 1995).

Our results for the comparisons with the $\lambda 5780$ and $\lambda 5797$ optical DIBs are similar to those obtained by Hamano et al. (2015, 2016) for the 10780, 19792, 11797, 12623, and 13175 Å bands: the NIR DIB is better correlated with the $\lambda 5780$ band. According to these authors, the tight correlations with this band, which is favored in a strong UV field, support the idea that the carriers for the six DIBs are cation molecules. An in-depth discussion of the nature of the $\lambda 15273$ DIB carrier is not possible at this stage, but we would like to highlight here that because both the $\lambda\lambda 5780$ and 6283 DIBs are enhanced in presence of strong radiation fields (Ehrenfreund, Jenniskens 1995; Cami et al. 1997; Vos et al. 2011), our results support the possibility of using the $\lambda 15273$ DIB in a similar way. In other words, this DIB may be a good tool to be used as a proxy of the environmental properties, especially in highly reddened areas.

We emphasize that in the context of 3D ISM mapping the skin effect is a second-order phenomenon. Clouds are assigned a distance by means of positive DIB EW radial gradients, and EW radial gradients are positive at cloud crossings regardless of the amplitude of the skin effect. On the other hand, the enhancement of the $\lambda 15273$ DIB in external layers of clouds exposed to the radiation may prevent an optimal localization of the cloud core, and may instead spread the reconstructed cloud core in a wider volume compared to its actual one. However, given the poor spatial resolution reached by current 3D maps, this is not important. Conversely, future high-resolution and high-quality measurements may take advantage of the skin effect and use the DIB ratios to construct more detailed maps and simultaneously detect the environmental effects.

6.6 Conclusion

In this contribution, we presented an in-depth exploitation of the TSS spectra of the *Apache Point Observatory Galactic Evolution Experiment* (APOGEE), as provided by the SDSS DR12. The work follows the path opened by (Chapter

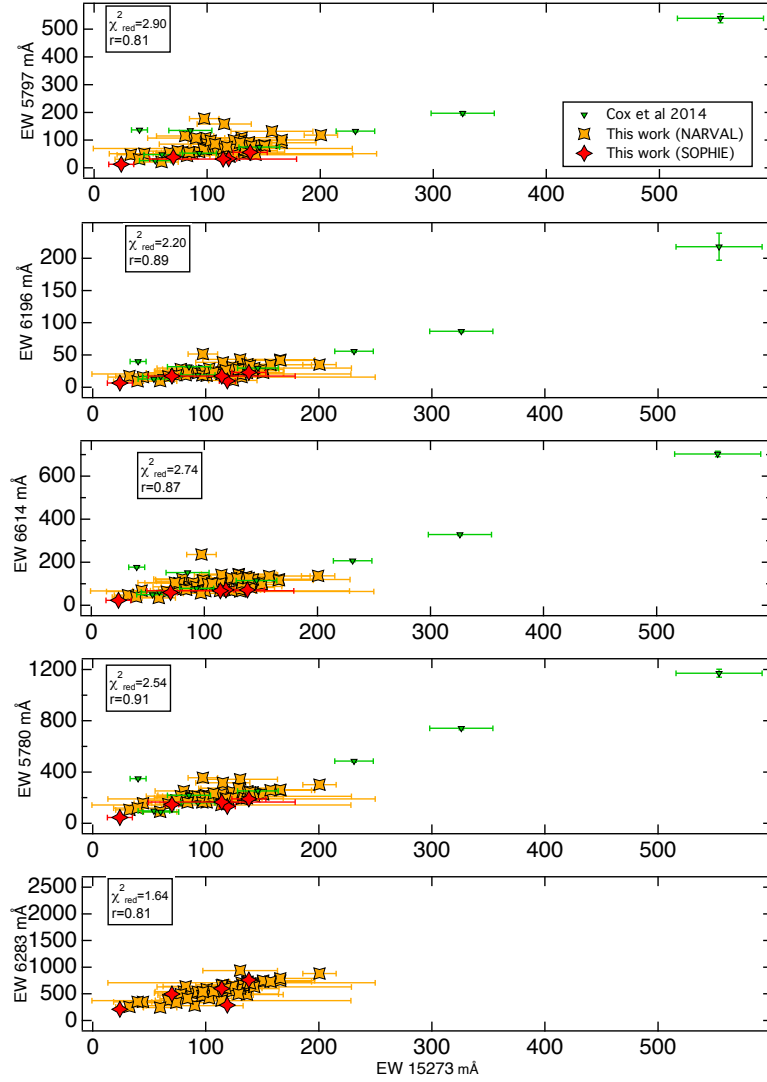


Figure 69 From top to bottom: correlation between the equivalent widths of the strongest NIR λ 15 273 DIB and of the five optical $\lambda\lambda$ 5797, 6196, 6614, 5780, and 6283 DIBs. Compared to the Cox et al. (2014) targets, the OHP-SOPHIE and TBL-NARVAL targets correspond to shorter sight line and weaker absorptions. For the λ 6283 DIB only the latter two datasets are presented. Correlation coefficients r and reduced χ^2 resulting from the linear ODR fit are indicated in each plot.

2; Elyajouri et al. 2016) and makes extensive use of the catalog presented there for the IR DIB at λ 15 273. In addition to the IR data, we make use of high-resolution optical spectra obtained with SOPHIE and NARVAL.

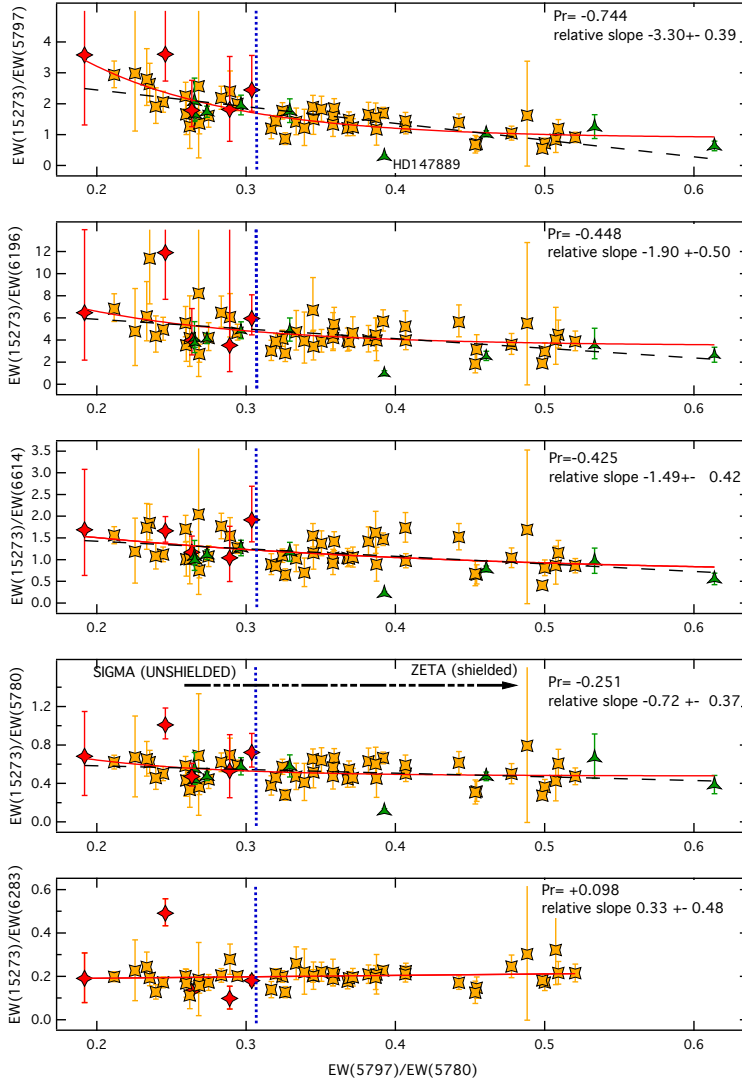


Figure 610 Sensitivity of the $\lambda 15273$ DIB to the radiative environment: ratios of $\lambda 15273$ EWs with five optical DIBs are shown as a function of the radiation-sensitive ratio $EW(5797)/EW(5780)$. The right scale range is chosen from zero to three times the average ratio. An ODR linear fit provides the relative slopes indicated in the figure along with the correlation coefficients. The largest slope is found for $\lambda 5797$ band and the smallest for the $\lambda 6283$ DIB. Here, we show (red line) an exponential fit to the whole dataset and a linear fit (black dashed line).

The main results and conclusions of this work can be summarized as follows.

1. We provide a catalog of measurements of the strength (as traced by

the equivalent width) and central wavelength for $\lambda\lambda 15617$, 15653, and 15673 DIBs with a total number of 295, 262, and 308 detections, respectively. This constitutes the largest compilation of measurements for these DIBs to date.

2. We made use of this large number of detections to characterize in detail the central wavelength, width, and shape of these three DIBs. All of them have a $\text{FWHM} > 2 \text{ \AA}$. The estimated upper limit for the intrinsic widths are 4.4, 5.7, and 3.7 \AA for the $\lambda\lambda 15617$, 15653, and 15673 DIB, respectively. We explored the shape of the DIBs by creating a spectrum of extremely high S/N ratio through stacking. All the three bands seem asymmetric and have a shallower slope in the red wing, similar to what is observed in most optical DIBs. The asymmetry is stronger for the $\lambda 15617$ band. We used the stacked spectrum to derive an average FWHM of 3.9 \AA for the $\lambda 15273$ band. This value is slightly lower than the distribution peak value of 5.1 from [Zasowski et al. \(2015\)](#).
3. We searched for weaker previously reported IR DIBs. To do so, we stacked spectra since the S/N is not good enough to extract measurements for these DIBs in an individual sight line. We confirm the previously reported detection of DIBs at $\lambda\lambda 15990$, 16232, 16573, and 16585. We do not find any absorption feature at $\lambda 16596$, nor at $\lambda 15225$, where DIB candidates have previously been reported ([Geballe et al. 2011](#)). Our in-depth search suggests a possible existence of two additional DIBs at $\lambda\lambda 15235$ and 16769.
4. We provide first average ratios for the four NIR DIBs $\lambda\lambda 15273$, 15617, 15653, and 15673.
5. We used a total of about 60 spectra to explore the relation between the strongest infrared DIB ($\lambda 15273$) and several strong optical DIBs. The IR DIB correlates well with all of them, with Pearson coefficients always higher than 0.8. We fit a linear regression to all the pairs IR DIB - optical DIBs. The best χ^2 is found for the pair involving the DIB at $\lambda 6283$, pointing toward a close relationship between the carriers of these two DIBs.
6. This relationship is confirmed when we explore the behavior of the $\lambda 15273$ DIB with respect to the environment. The IR DIB nicely follows the $\lambda 5780$ band, similarly to the 10780, 19792, 11797, 12623, and 13175 \AA bands ([Hamano et al. 2016](#)), and it even more tightly follows the band at $\lambda 6283$. It therefore probably forms in similar environmental conditions (i.e., in a relatively strong UV radiation field). We propose the $\lambda 15273$ DIB (or a ratio involving this DIB) as an infrared diagnostic of the physical conditions of the ISM. A feature in the near-IR with this capability is particularly relevant since it constitutes a tool able to trace the environmental conditions

in lines of sight that are impenetrable to optical wavelengths. Moreover, we are living in an epoch where astronomy is becoming more and more infrared oriented. For example, the advent of space multi-object spectrographs such as JWST's NIRSPEC will provide massive amounts of NIR "free-telluric" data and highly multiplexed infrared spectrographs for 10 m telescopes like MOONS ([Cirasuolo et al. 2014](#)) will be soon in operation. Likewise, high-resolution spectroscopy with the ELT family will also prioritize the infrared.

Even if our interest is in lines of sight that are transparent enough in the optical, it is therefore desirable to develop equivalent diagnostics at near-IR wavelengths.

Table 64. Extracted equivalent widths for optical DIBs.

2MASS ID	EW ₅₇₈₀ (mÅ)	EW ₅₇₉₇ (mÅ)	EW ₆₁₉₆ (mÅ)	EW ₆₂₈₃ (mÅ)	EW ₆₆₁₄ (mÅ)
TBL					
J02102704+4846405	120.6±3.0	31.3±2.1	9.5±1.9	352.0±8.4	39.1±2.2
J02205086+5519394	165.0±2.6	72.8±1.7	17.9±1.5	589.7±5.9	66.3±2.0
J02255659+5500312	182.2±3.6	43.1±2.5	18.9±2.4	640.6±9.3	76.2±2.8
J03074529+5211022	213.2±3.7	58.4±2.2	22.2±2.2	541.9±8.8	86.3±2.2
J03241477+5030175	106.4±3.2	48.0±2.2	17.5±1.9	257.7±7.9	47.9±2.0
J03302697+4703478	159.6±3.2	51.8±2.1	15.8±1.9	350.2±8.6	68.2±2.3
J03305254+3005529	213.6±4.9	109.0±3.7	22.5±3.4	280.0±10.9	104.3±3.1
J03331168+4604257	151.8±2.8	55.9±1.8	16.9±1.5	379.5±6.0	64.0±1.9
J03403509+4854098	204.0±2.7	53.2±1.8	24.6±1.5	518.1±6.3	86.0±1.9
J03440847+3207165	208.1±3.3	99.3±2.3	28.7±1.9	419.1±7.2	99.1±2.3
J03564617+3925190	249.1±4.1	101.0±2.9	31.1±2.5	551.5±9.1	126.6±2.5
J03580309+3756269	277.6±5.2	98.7±3.2	28.3±2.9	600.5±10.5	142.5±3.1
J04133625+4342167	293.0±4.7	122.7±3.0	35.4±3.1	685.8±9.7	137.3±3.3
J04140539+4348366	223.5±2.7	86.3±1.7	25.1±1.6	478.0±5.9	112.0±1.8
J04315994+3623164	216.4±3.0	68.9±2.0	25.5±2.0	466.5±8.3	116.3±2.2
J04360336+3640031	228.3±3.2	102.9±2.2	32.2±1.8	550.6±7.3	138.8±2.0
J04570053+2155579	276.2±4.2	92.5±2.8	27.4±2.8	496.7±8.4	125.5±3.0
J05000982+2235338	230.2±3.1	56.0±1.9	23.1±1.8	660.3±8.2	102.1±1.9
J05003353+2236565	229.1±3.7	67.2±2.5	28.5±2.2	660.0±12.1	105.1±2.4
J05011186+2336315	236.0±3.6	87.3±2.2	23.1±2.2	545.9±7.1	101.4±2.4
J18140097+0035338	176.4±5.1	107.1±3.5	29.5±3.0	503.9±10.7	121.7±3.3
J19484594+2256137	360.4±4.7	179.3±3.1	51.6±2.4	536.5±8.5	236.6±3.1
J19594179+3054499	92.6±2.6	21.4±1.7	9.7±1.7	243.7±5.7	34.3±1.9
J20012170+2217258	348.1±3.7	108.2±3.3	43.2±2.1	938.1±13.9	145.5±2.1
J20135903+3632379	197.6±2.8	76.1±1.9	26.4±1.5	604.9±6.3	72.5±1.7
J20141795+3709286	164.6±4.2	56.9±2.7	24.5±2.4	414.5±8.3	72.9±3.0
J20145498+3722420	18.9±2.4	5.5±1.7	1.9±1.4	38.6±6.7	10.9±1.8
J20250713+3638161	214.8±4.6	48.1±2.9	29.8±3.4	630.3±10.1	120.3±3.3
J20444908+3157167	256.0±3.1	115.9±2.2	25.5±2.0	544.1±8.7	122.6±2.3
J20451060+5112379	245.9±3.2	79.4±2.0	33.7±1.8	697.3±7.3	127.5±2.0
J20510469+5025102	181.7±4.8	61.3±2.6	18.8±2.5	336.2±10.5	105.4±2.7
J20550326+3928488	145.2±4.0	70.7±2.7	20.6±2.8	375.9±8.8	67.3±2.6
J20564108+3957218	261.9±3.0	133.1±2.2	35.0±1.7	728.5±8.1	136.0±2.0
J20595186+3858384	244.6±5.8	87.4±3.7	32.7±3.9	729.0±11.8	130.5±4.0
J20595186+3858384(2)	253.2±3.3	93.2±2.1	35.7±2.0	712.9±7.5	133.0±2.2
J21100235+4913175	215.0±4.3	57.8±2.7	28.3±2.5	493.3±8.5	102.9±3.1
J21122845+4703145	166.6±2.9	67.6±1.8	18.5±1.6	460.8±6.7	55.8±2.0
J21161964+4901093	305.0±5.4	119.1±3.9	35.3±3.3	883.3±12.0	136.7±3.5
J21183302+6644202	320.7±3.2	160.2±2.0	38.7±1.7	669.6±7.5	141.6±2.0
J21282648+4655259	194.9±2.6	41.3±1.8	17.5±1.4	602.7±8.5	76.7±1.8
J21301511+5626264	266.6±7.6	101.3±5.0	41.6±4.7	792.0±16.1	116.7±5.1
J21301511+5626264(2)	262.4±4.8	91.4±3.6	42.9±3.4	749.7±11.7	121.0±3.1
J21344455+4432322	214.2±2.9	60.1±1.8	20.2±1.5	639.1±7.0	73.8±1.7
J21363278+4303344	196.3±2.7	50.2±1.7	19.3±1.6	696.4±7.4	80.4±1.9
J21373102+5259450	199.1±2.9	57.2±1.9	22.4±1.9	488.3±7.0	88.1±2.5
J21375836+4152509	153.4±3.2	38.3±1.8	11.5±1.4	357.2±6.8	46.1±1.8
J21432261+5850422	211.0±2.6	109.4±1.6	25.5±1.5	457.4±8.1	114.6±2.2
J21434429+4323427	229.8±5.2	81.9±3.5	27.8±3.5	728.2±11.2	106.2±3.4
J21434429+4323427(2)	232.2±7.5	80.0±5.2	22.5±5.0	748.8±16.0	97.3±5.1
J21462326+5212411	35.6±2.3	9.8±1.5	2.3±1.7	93.9±5.7	12.2±1.5
J21502003+3856054	193.1±3.7	51.3±2.6	16.0±2.7	710.4±9.6	64.4±2.7
J21534939+3951119	245.7±4.7	63.7±2.9	25.6±2.6	700.7±10.3	82.9±2.9
J21541026+3952378	242.2±3.1	88.9±2.1	23.3±1.8	720.8±7.2	96.4±2.1
J21551055+5326166	277.8±4.0	76.5±3.0	23.9±2.6	745.8±9.8	108.5±2.6
J22032307+5129046	201.6±4.5	47.7±3.1	10.9±3.2	639.7±10.1	67.1±3.4
OHP					
J19113993+1925541	186.9±3.2	45.1±2.2	15.0±1.2	553.1±9.7	33.2±3.3
J19302526+1741428	63.6±1.7	11.3±1.2	6.6±0.7	203.3±9.0	26.3±1.2
J20025554+4559129	218.5±2.7	49.0±2.9	20.6±1.1	722.6±9.7	77.6±2.6
J21451397+4319554	160.6±2.5	43.3±1.6	16.5±1.1	472.5±7.5	62.3±1.4
J21282648+4655259	124.9±2.7	34.5±2.0	7.0±1.6	251.3±5.8	60.0±1.5

Table 65: Equivalent widths and central wavelengths of the $\lambda\lambda 15617$, 15653, and 15673 DIBs. The wavelengths are in the APOGEE stellar frame and can be converted into heliocentric wavelengths using the stellar radial velocity listed in the last column. This table is published in its entirety in electronic form at the CDS via anonymous ftp to cdsarc.u-strasbg.fr (130.79.128.5) or via <http://cdsweb.u-strasbg.fr/cgi-bin/qcat?J/A+A/>.

2MASS ID	GLON (deg)	GLAT (deg)	EW ₁₅₆₁₇ (mÅ)	EW ₁₅₆₅₃ (mÅ)	EW ₁₅₆₇₃ (mÅ)	λ_{15617}^c (Å)	λ_{15653}^c (Å)	λ_{15673}^c (Å)	Vrad (km.s ⁻¹)
J00052394+6347207	117.87	+1.371	12± 14	56± 31	40±13	15615.7± 0.5	15651.2± 1.0	15670.9± 0.2	-1.37
J00162429+6329460	119.04	+0.890	43± 28	69± 45	47±25	15615.2± 0.6	15651.0± 1.1	15671.2± 0.4	-3.45
J00165734+6333108	119.10	+0.938	27± 23	34± 21	16±11	15615.8± 1.1	15651.2± 0.8	15670.9± 0.6	-2.92
J00194084+6148481	119.19	-0.827	11± 10	41± 21	27±15	15615.9± 0.5	15652.0± 0.8	15671.6± 0.4	-14.22
J00213429+5855479	119.08	-3.718	25± 24	19± 19	30±15	15615.7± 0.9	15649.9± 0.9	15670.9± 0.4	+8.12
J00220340+6211063	119.51	-0.491	24± 67	36± 55	45±14	15616.7± 0.6	15650.3± 0.7	15672.5± 0.3	-25.46
J00231234+6410322	119.86	+1.472	14± 15	33± 18	25±12	15615.8± 0.8	15652.1± 0.8	15672.0± 0.4	-8.62
J00274417+6001430	119.97	-2.707	27± 22	27± 19	38±11	15617.2± 1.1	15650.8± 0.9	15671.9± 0.2	-13.88
J00281188+5905318	119.95	-3.645	16± 18	18± 14	24±13	15615.4± 1.0	15651.6± 0.6	15671.3± 0.4	-4.74
J00283015+6341424	120.39	+0.937	36± 28	14± 18	24±14	15616.7± 0.8	15651.0± 1.1	15671.2± 0.4	-3.18
J00284518+6239253	120.33	-0.100	19± 17	12± 35	62±21	15618.2± 0.6	15655.9± 4.1	15673.4± 0.3	-45.38
J00285254+5527583	119.71	-7.264	9± 14	16± 15	16±10	15617.5± 1.5	15651.7± 1.2	15671.7± 0.6	-25.34
J00300848+6246456	120.50	+0.008	26± 20	33± 24	65±22	15618.6± 0.5	15652.8± 0.7	15673.7± 0.3	-54.10
J00311664+6220376	120.59	-0.436	9± 9	34± 19	34±17	15616.2± 0.4	15652.4± 0.5	15671.9± 0.3	-16.89
J00313144+6010201	120.46	-2.604	19± 22	10± 13	33±15	15615.4± 0.8	15652.2± 0.6	15671.7± 0.3	-11.16
J00313306+6004195	120.45	-2.704	15± 23	29± 26	38±17	15617.0± 1.0	15651.3± 0.8	15671.4± 0.3	-4.13
J00350607+6258585	121.08	+0.170	36± 24	27± 21	46±18	15616.7± 0.8	15652.5± 0.7	15673.4± 0.3	-41.59
J00535925+6000485	123.25	-2.857	29± 39	36± 26	73±20	15618.2± 1.0	15653.9± 0.8	15673.7± 0.2	-62.34
J00544879+6754306	123.25	+5.039	21± 20	56± 43	18±13	15614.6± 0.6	15652.8± 0.9	15670.6± 0.3	+10.96
J01201274+5839597	126.67	-3.996	45± 35	25± 32	30±17	15615.9± 0.4	15651.3± 1.8	15671.1± 0.2	-3.36
J01264564+6309556	126.91	+0.567	37± 29	34± 24	63±26	15615.8± 0.4	15650.7± 0.4	15671.1± 0.2	-3.34
J01300606+6334567	127.22	+1.033	44± 27	92± 51	48±19	15616.5± 0.4	15651.7± 0.9	15672.5± 0.3	-27.22
J01335381+5828560	128.47	-3.932	19± 31	13± 11	31±13	15617.8± 1.5	15649.8± 0.4	15671.0± 0.3	+6.41
J01540050+5801539	131.16	-3.837	12± 16	20± 16	62±21	15615.3± 0.5	15650.2± 0.4	15670.8± 0.2	+1.14
J01581986+5757166	131.73	-3.769	18± 24	39± 35	69±27	15615.8± 0.7	15651.7± 1.9	15672.2± 0.3	-15.37
J02220580+6040337	133.81	-0.266	10± 17	13± 13	27±20	15615.3± 0.6	15651.5± 0.4	15671.3± 0.4	+2.66
J02301257+6156001	134.27	+1.256	74± 46	85± 55	84±34	15615.2± 0.4	15651.4± 0.7	15671.9± 0.2	-12.83
J02364097+5553255	137.36	-4.005	60± 38	30± 24	55±24	15612.0± 0.5	15650.6± 0.4	15671.4± 0.2	-2.16

Table 65: continued.

2MASS ID	GLON (deg)	GLAT (deg)	EW ₁₅₆₁₇ (mÅ)	EW ₁₅₆₅₃ (mÅ)	EW ₁₅₆₇₃ (mÅ)	λ_{15617}^c (Å)	λ_{15653}^c (Å)	λ_{15673}^c (Å)	Vrad (km.s ⁻¹)
J02441271+5639272	138.00	-2.878	35± 18	58± 31	56±16	15616.7± 0.3	15651.3± 0.5	15671.9± 0.1	-11.43
J02570063+6714204	134.65	+7.271	47± 27	45± 25	49±24	15616.2± 0.5	15651.8± 0.6	15672.2± 0.3	-18.21
J03123883+6303146	138.16	+4.436	21± 20	32± 22	26±20	15615.8± 0.5	15650.7± 0.5	15672.3± 0.6	-2.46
J03143063+5410503	142.96	-3.030	61± 45	31± 34	45±18	15616.6± 0.5	15650.9± 1.4	15671.6± 0.2	+2.83
J03163081+5745428	141.33	+0.167	49± 38	47± 27	48±13	15615.2± 0.6	15652.1± 1.0	15671.9± 0.1	-16.36
J03230976+5213502	145.11	-3.985	59± 38	44± 39	60±26	15615.4± 0.5	15650.6± 1.0	15672.1± 0.2	-10.48
J03233011+5208545	145.19	-4.026	59± 35	62± 54	63±18	15616.2± 0.5	15648.6± 1.1	15671.8± 0.2	-2.22
J03250988+5811061	142.06	+1.143	22± 18	59± 39	48±18	15615.8± 0.5	15651.9± 0.8	15671.5± 0.3	-6.43
J03251966+5650252	142.83	+0.035	16± 14	... ± ...	37±17	15616.3± 0.3	15652.9± 0.3	15671.8± 0.3	-10.40
J03254141+4609481	148.84	-8.805	16± 14	30± 20	36±12	15615.6± 0.6	15651.2± 0.9	15671.0± 0.2	+3.46
J03302753+4708196	148.96	-7.537	30± 25	13± 12	33±12	15613.2± 1.0	15650.0± 0.6	15670.6± 0.3	+18.27
J03322659+5203572	146.38	-3.321	6± 9	30± 25	37±17	15614.7± 0.4	15651.9± 0.6	15671.5± 0.2	+1.21
J03403032+4935404	148.87	-4.570	14± 30	16± 18	24±11	15617.4± 1.1	15651.3± 0.7	15671.8± 0.3	-4.79
J03421355+4954547	148.90	-4.147	38± 27	17± 12	61±17	15615.5± 0.8	15651.1± 0.5	15671.9± 0.2	-7.86
J03431661+4958404	148.99	-3.994	18± 18	22± 17	36±12	15616.2± 0.7	15652.5± 0.6	15672.4± 0.3	-14.25
J03441133+5001177	149.08	-3.871	15± 18	21± 23	19±12	15615.5± 0.7	15651.8± 1.1	15671.5± 0.3	+2.57
J03453915+3226242	160.49	-17.443	33± 18	60± 31	37±14	15615.9± 0.7	15652.9± 1.1	15672.5± 0.5	+11.27
J03461161+4759007	150.60	-5.278	13± 66	... ± ...	43±22	15616.9± 0.6	... ± ...	15672.7± 0.4	-13.12
J03483498+5048039	149.15	-2.825	28± 20	37± 23	34±14	15615.8± 0.6	15650.9± 0.6	15671.5± 0.3	-0.32
J03510857+3937512	156.61	-11.213	46± 34	13± 17	55±28	15616.0± 0.6	15650.8± 1.0	15672.6± 0.4	-13.38
J03572191+4701456	152.67	-4.823	45± 38	40± 38	55±40	15615.8± 0.4	15649.8± 0.5	15672.3± 0.3	-13.35
J03582144+5228184	149.26	-0.572	29± 22	22± 20	32±12	15614.2± 0.7	15649.3± 1.0	15670.7± 0.3	+24.78
J03584538+5222502	149.37	-0.602	21± 20	48± 22	44±14	15616.9± 0.7	15651.9± 0.7	15672.0± 0.2	-6.23
J04011751+5310145	149.14	+0.247	14± 18	25± 25	31±13	15615.8± 0.9	15650.5± 2.6	15671.1± 0.3	+8.02
J04022000+5323350	149.12	+0.517	17± 14	50± 29	37±15	15615.6± 0.6	15651.6± 1.3	15672.0± 0.4	-11.13
J04052313+5308558	149.62	+0.636	14± 16	33± 24	23±11	15615.7± 0.9	15650.6± 2.0	15671.3± 0.4	+12.75
J04201999+4541378	156.50	-3.124	24± 36	21± 37	26±20	15615.4± 0.6	15650.5± 1.6	15670.7± 0.5	+14.29
J04213145+5617014	149.16	+4.514	43± 26	37± 19	44±15	15617.9± 0.6	15652.9± 0.9	15673.3± 0.2	-40.27
J04221174+5552136	149.52	+4.289	30± 23	44± 25	40±15	15616.3± 0.6	15652.3± 0.9	15672.0± 0.3	-7.93
J04260563+5530479	150.16	+4.431	39± 20	111± 57	56±22	15617.2± 0.5	15654.5± 0.8	15672.7± 0.3	-21.23
J04292916+3727399	163.63	-7.630	30± 28	25± 24	38±16	15618.0± 0.7	15650.5± 1.4	15671.7± 0.3	+1.50
J04295340+5555169	150.23	+5.100	19± 19	22± 17	33±19	15618.5± 0.8	15652.7± 0.6	15672.2± 0.6	-22.64
J04360336+3640031	165.11	-7.198	38± 20	30± 18	39±11	15616.5± 0.6	15651.3± 0.8	15672.0± 0.3	+2.66
J04362198+4800386	156.72	+0.457	5± 11	33± 23	23±16	15615.6± 0.7	15650.1± 0.5	15670.7± 0.3	+15.70
J04370204+4205520	161.18	-3.426	29± 29	15± 22	39±22	15616.2± 0.6	15651.3± 0.8	15672.2± 0.4	-15.61

Table 65: continued.

2MASS ID	GLON (deg)	GLAT (deg)	EW ₁₅₆₁₇ (mÅ)	EW ₁₅₆₅₃ (mÅ)	EW ₁₅₆₇₃ (mÅ)	λ_{15617}^c (Å)	λ_{15653}^c (Å)	λ_{15673}^c (Å)	Vrad (km.s ⁻¹)
J04375966+5753122	149.52	+7.241	... ± ...	18 ± 12	50 ± 28	... ± ...	15651.2 ± 0.3	15670.8 ± 0.4	+6.65
J04415341+3905530	164.05	-4.726	18 ± 14	10 ± 12	53 ± 22	15615.8 ± 0.4	15650.2 ± 0.7	15671.7 ± 0.4	+15.12
J04420018+5845056	149.21	+8.206	24 ± 26	23 ± 15	48 ± 13	15615.6 ± 0.8	15651.7 ± 0.7	15670.9 ± 0.2	+6.84
J04465646+3945400	164.18	-3.554	15 ± 15	... ± ...	35 ± 15	15615.4 ± 0.6	... ± ...	15671.8 ± 0.3	+4.91
J04470590+3935397	164.33	-3.639	25 ± 18	37 ± 28	36 ± 11	15615.8 ± 0.8	15651.1 ± 2.1	15671.6 ± 0.3	+9.32
J04483353+4019230	163.95	-2.955	19 ± 14	48 ± 37	23 ± 17	15615.1 ± 0.5	15652.0 ± 1.2	15671.2 ± 0.4	+13.24
J04490118+4011539	164.10	-2.968	15 ± 23	22 ± 20	41 ± 17	15618.6 ± 1.6	15650.7 ± 1.2	15672.6 ± 0.4	+0.36
J04491941+3915544	164.86	-3.521	16 ± 20	... ± ...	23 ± 11	15615.8 ± 1.2	... ± ...	15671.4 ± 0.4	+14.07
J04492766+3932129	164.67	-3.327	25 ± 21	17 ± 21	31 ± 13	15615.1 ± 0.7	15649.8 ± 2.3	15671.4 ± 0.4	+15.57
J04493447+3932429	164.67	-3.305	9 ± 9	... ± ...	45 ± 14	15615.8 ± 0.6	... ± ...	15672.2 ± 0.2	-6.10
J04495502+4001234	164.35	-2.948	17 ± 18	... ± ...	48 ± 19	15614.2 ± 1.1	... ± ...	15671.0 ± 0.3	+18.94
J04505777+4011243	164.35	-2.688	42 ± 28	... ± ...	29 ± 11	15617.6 ± 0.7	... ± ...	15670.6 ± 0.3	+23.70
J04592513+4855187	158.49	+3.965	20 ± 27	23 ± 31	70 ± 28	15615.1 ± 0.7	15649.7 ± 0.9	15671.2 ± 0.3	+17.75
J05000982+2235338	179.53	-12.022	12 ± 23	42 ± 28	22 ± 13	15615.6 ± 1.3	15650.8 ± 0.5	15670.8 ± 0.2	+30.92
J05010801+2326203	178.97	-11.340	41 ± 27	11 ± 12	25 ± 13	15615.7 ± 0.7	15652.1 ± 0.7	15671.6 ± 0.4	+15.09
J05021095+2330182	179.07	-11.107	21 ± 23	36 ± 29	43 ± 24	15617.7 ± 0.7	15653.3 ± 1.7	15672.0 ± 0.4	-2.18
J05032736+4004359	165.92	-0.891	5 ± 9	21 ± 16	54 ± 17	15616.3 ± 0.9	15652.1 ± 0.7	15672.9 ± 0.4	-13.69
J05035397+4040598	165.49	-0.455	8 ± 14	14 ± 13	37 ± 16	15615.4 ± 1.0	15650.9 ± 0.7	15672.3 ± 0.5	+6.77
J05041580+3550511	169.38	-3.334	... ± ...	31 ± 31	85 ± 31	... ± ...	15651.2 ± 1.6	15671.5 ± 0.2	+16.98
J05041915+4136083	164.81	+0.166	13 ± 20	23 ± 16	19 ± 10	15616.9 ± 1.5	15650.9 ± 0.7	15671.8 ± 0.5	+7.66
J05042205+2138367	180.90	-11.793	36 ± 27	76 ± 36	60 ± 24	15618.8 ± 0.8	15649.9 ± 0.5	15670.4 ± 0.3	+35.73
J05043026+3539583	169.56	-3.405	16 ± 22	40 ± 23	43 ± 20	15615.9 ± 0.7	15650.5 ± 0.5	15671.3 ± 0.2	+15.77
J05045266+4225516	164.22	+0.751	12 ± 17	17 ± 14	17 ± 15	15614.0 ± 0.8	15650.3 ± 0.5	15670.5 ± 0.6	+30.98
J05051685+4006442	166.11	-0.592	31 ± 27	10 ± 12	37 ± 14	15617.6 ± 0.9	15650.6 ± 0.8	15671.0 ± 0.4	+14.54
J05091936+4206041	164.97	+1.211	48 ± 39	11 ± 15	57 ± 29	15616.0 ± 0.6	15650.5 ± 0.5	15670.7 ± 0.3	-0.74
J05102070+3333407	171.97	-3.700	63 ± 43	82 ± 60	112 ± 26	15616.2 ± 0.4	15650.7 ± 1.2	15671.8 ± 0.1	+1.62
J05125815+2449470	179.43	-8.336	18 ± 12	12 ± 9	43 ± 11	15615.7 ± 0.6	15650.9 ± 1.3	15671.7 ± 0.2	+12.58
J05131788+2450164	179.47	-8.270	22 ± 17	78 ± 45	58 ± 15	15616.7 ± 0.7	15652.9 ± 1.2	15673.1 ± 0.2	-7.84
J05143594+2453505	179.59	-7.995	8 ± 7	... ± ...	45 ± 14	15616.9 ± 0.4	... ± ...	15672.6 ± 0.2	-4.03
J05154849+3737332	169.32	-0.417	17 ± 17	... ± ...	34 ± 19	15614.8 ± 0.7	... ± ...	15672.3 ± 0.2	-6.32
J05154990+2511030	179.51	-7.601	29 ± 17	... ± ...	51 ± 12	15614.8 ± 0.6	... ± ...	15669.9 ± 0.2	+48.57
J05155196+2450235	179.80	-7.792	15 ± 14	57 ± 36	59 ± 11	15615.1 ± 0.9	15652.3 ± 1.2	15671.3 ± 0.2	+20.50
J05160193+2544064	179.08	-7.250	21 ± 16	15 ± 20	50 ± 23	15616.7 ± 0.6	15650.7 ± 3.0	15672.9 ± 0.4	+2.21
J05161625+2355236	180.62	-8.238	15 ± 13	27 ± 16	87 ± 26	15615.5 ± 0.5	15650.2 ± 0.6	15672.1 ± 0.2	+10.50
J05163119+2959412	175.64	-4.716	30 ± 23	31 ± 31	37 ± 28	15614.2 ± 0.3	15647.0 ± 0.4	15669.9 ± 0.3	+40.01

Table 65: continued.

2MASS ID	GLON (deg)	GLAT (deg)	EW ₁₅₆₁₇ (mÅ)	EW ₁₅₆₅₃ (mÅ)	EW ₁₅₆₇₃ (mÅ)	λ_{15617}^c (Å)	λ_{15653}^c (Å)	λ_{15673}^c (Å)	Vrad (km.s ⁻¹)	
J05172665+2536318	179.37	-7.060	7± 14	15± 13	35±14	15616.7± 0.8	15651.1± 0.4	15672.6± 0.3	-2.16	
J05183271+3934291	168.04	+1.146	39± 33	31± 33	47±24	15616.1± 0.7	15650.0± 1.9	15672.5± 0.4	-2.24	
J05192542+3019435	175.72	-4.011	48± 31	... ± ...	54±30	15614.5± 0.6	... ± ...	15672.7± 0.4	+3.93	
J05195542+3922562	168.35	+1.254	19± 22	19± 22	47± 27	21±12	15614.3± 1.0	15648.5± 0.9	15671.9± 0.4	+5.21
J05201627+4427482	164.21	+4.206	13± 12	21± 18	22±12	15616.3± 0.5	15651.3± 1.0	15671.6± 0.3	+2.81	
J05201669+4400087	164.59	+3.945	32± 26	49± 26	32±18	15615.9± 0.9	15651.8± 0.9	15672.4± 0.4	-18.33	
J05205203+3102072	175.32	-3.353	31± 30	59± 52	49±16	15615.9± 0.6	15653.2± 0.7	15671.1± 0.2	+16.14	
J05212271+3600479	171.28	-0.433	14± 17	... ± ...	26±17	15615.7± 0.7	... ± ...	15671.4± 0.4	+7.49	
J05223507+3618015	171.19	-0.069	13± 12	59± 39	29±20	15615.8± 0.5	15649.8± 1.3	15673.1± 0.6	+8.77	
J05225322+2905377	177.17	-4.091	74± 38	53± 41	48±25	15615.8± 0.4	15652.1± 1.1	15672.2± 0.3	+3.59	
J05242835+3011309	176.46	-3.189	17± 16	27± 27	56±22	15615.5± 0.4	15651.6± 2.1	15672.2± 0.3	+4.56	
J05251863+3010006	176.58	-3.053	24± 33	16± 15	70±22	15617.0± 1.2	15650.0± 0.5	15671.6± 0.3	+20.96	
J05275100+2731138	179.09	-4.062	20± 16	37± 29	36±14	15614.9± 0.6	15650.6± 1.5	15670.8± 0.2	+20.44	
J05284397+2716152	179.41	-4.036	24± 22	19± 16	47±16	15615.9± 0.9	15650.7± 0.9	15671.6± 0.3	+14.38	
J05303582+2744298	179.24	-3.432	21± 17	22± 19	40±14	15614.9± 0.5	15649.8± 0.6	15671.0± 0.2	+23.97	
J05324662+2644507	180.34	-3.568	17± 25	81± 47	45±15	15615.1± 1.0	15649.8± 0.9	15671.0± 0.3	+34.95	
J05325168+3305416	175.02	-0.096	21± 17	... ± ...	83±32	15615.9± 0.2	... ± ...	15671.2± 0.2	+3.54	
J05380741+2418520	183.05	-3.859	48± 31	85± 47	43±23	15619.5± 0.6	15650.6± 1.0	15672.8± 0.4	+21.14	
J05422067+2943348	178.95	-0.194	21± 16	76± 38	46±18	15616.1± 0.7	15649.7± 0.9	15671.5± 0.4	+18.68	
J05431996+2757575	180.56	-0.936	22± 14	56± 33	42±20	15615.8± 0.6	15650.3± 1.8	15671.6± 0.5	+17.87	
J05440485+2930048	179.34	+0.009	14± 14	68± 35	24±12	15615.4± 0.7	15651.0± 1.0	15671.4± 0.5	+18.71	
J05441785+3001084	178.93	+0.320	17± 13	46± 19	20±8	15617.2± 0.8	15652.2± 0.7	15672.2± 0.3	+2.19	
J05442116+2743534	180.88	-0.867	12± 14	... ± ...	27±14	15616.6± 1.0	... ± ...	15673.4± 0.7	+4.72	
J05453652+3010038	178.95	+0.640	29± 17	41± 17	30±11	15615.9± 0.6	15651.6± 0.5	15671.8± 0.3	+7.85	
J05464534+2927536	179.68	+0.487	15± 15	75± 56	32±15	15616.0± 0.8	15651.6± 1.6	15672.0± 0.4	+15.22	
J05464904+1212013	194.54	-8.376	23± 29	70± 49	55±24	15618.6± 1.3	15650.4± 1.1	15670.8± 0.3	+39.15	
J05465678+2948516	179.40	+0.703	18± 13	40± 25	25±16	15615.4± 0.6	15651.0± 1.3	15671.4± 0.5	+20.16	
J05470989+2925504	179.75	+0.545	11± 12	33± 17	19±10	15615.5± 0.8	15651.5± 0.7	15671.5± 0.5	+16.40	
J05484133+2819285	180.87	+0.259	35± 23	78± 36	56±18	15616.0± 0.6	15650.3± 0.6	15671.8± 0.2	+12.99	
J05490737+3002444	179.45	+1.227	18± 16	... ± ...	51±16	15615.5± 0.7	... ± ...	15671.6± 0.3	+19.86	
J05492199+2035035	187.59	-3.588	32± 30	29± 20	37±20	15616.8± 0.9	15650.6± 0.9	15671.7± 0.4	+20.84	
J05502984+1323001	193.97	-7.006	10± 15	35± 21	21±17	15616.0± 1.0	15649.4± 0.7	15674.1± 0.9	+25.52	
J05561354+3142415	178.78	+3.385	12± 12	36± 38	34±19	15616.2± 0.6	15649.1± 1.9	15671.6± 0.3	+11.41	
J06001327+1408224	194.49	-4.581	12± 12	... ± ...	36±12	15616.2± 0.6	... ± ...	15671.7± 0.2	+11.59	
J06013301+3126285	179.58	+4.236	22± 25	... ± ...	29±14	15615.6± 1.3	... ± ...	15672.6± 0.4	-2.37	

Table 65: continued.

2MASS ID	GLON (deg)	GLAT (deg)	EW ₁₅₆₁₇ (mÅ)	EW ₁₅₆₅₃ (mÅ)	EW ₁₅₆₇₃ (mÅ)	λ_{15617}^c (Å)	λ_{15653}^c (Å)	λ_{15673}^c (Å)	Vrad (km.s ⁻¹)
J06021392+1452593	194.08	-3.792	23± 24	35± 19	36±16	15613.1± 1.2	15649.6± 0.6	15671.1± 0.5	+30.52
J06172091+0747140	202.10	-3.950	24± 27	... ± ...	46±30	15615.0± 0.4	... ± ...	15670.3± 0.3	+64.24
J06174008-0056459	209.91	-7.942	20± 20	... ± ...	66±16	15615.4± 0.4	... ± ...	15671.8± 0.1	+25.73
J06180772-0022145	209.45	-7.576	20± 15	23± 21	54±11	15614.9± 0.6	15650.7± 1.3	15670.7± 0.2	+42.49
J06190302-0035144	209.75	-7.471	23± 24	... ± ...	66±16	15616.1± 0.9	... ± ...	15672.6± 0.2	+9.16
J06201567+0424355	205.43	-4.892	42± 29	... ± ...	25±11	15617.0± 0.6	... ± ...	15671.0± 0.2	+30.29
J06203139+1615067	195.00	+0.728	17± 18	26± 29	30±14	15617.0± 1.1	15649.8± 2.6	15672.4± 0.5	+4.76
J06205811+1655496	194.45	+1.142	29± 19	... ± ...	37±18	15615.1± 0.7	... ± ...	15671.3± 0.4	+27.91
J06210046+0825395	201.96	-2.850	16± 22	... ± ...	34±21	15616.0± 0.8	... ± ...	15670.8± 0.3	+29.98
J06210794+2209569	189.84	+3.633	28± 38	46± 56	54±19	15617.2± 1.0	15648.2± 1.9	15671.8± 0.3	+15.33
J06214549+3400594	179.30	+9.197	21± 23	17± 14	35±19	15615.4± 0.9	15650.6± 0.7	15671.3± 0.5	+11.94
J06315253+0501591	206.22	-2.039	25± 17	30± 18	47±12	15613.9± 0.6	15649.4± 0.6	15670.0± 0.3	+56.39
J06351414+0114582	209.97	-3.033	25± 22	... ± ...	18±14	15615.6± 0.8	... ± ...	15671.2± 0.4	+31.52
J06372199+0558179	206.02	-0.394	10± 11	64± 35	28±16	15616.4± 0.8	15648.3± 1.8	15672.2± 0.7	+18.59
J06372390+0604442	205.92	-0.337	14± 20	33± 32	29±17	15615.2± 1.4	15648.1± 2.2	15672.8± 0.6	+13.80
J06420526+0012241	211.68	-1.986	7± 20	26± 35	19±14	15614.9± 1.5	15648.1± 2.0	15670.5± 0.3	+48.67
J06421206-0001180	211.90	-2.065	54± 35	... ± ...	29±21	15614.3± 0.5	... ± ...	15670.8± 0.4	+41.86
J06443656+0035213	211.63	-1.250	42± 27	... ± ...	36±17	15615.9± 0.6	... ± ...	15671.0± 0.3	+36.51
J06455605-0126035	213.58	-1.878	20± 17	23± 38	17±8	15614.7± 0.4	15651.5± 4.6	15671.2± 0.1	+40.53
J06460026-0451501	216.65	-3.422	16± 32	34± 28	49±31	15618.2± 1.2	15651.7± 0.7	15672.8± 0.3	+10.99
J06575656+0500002	209.22	+3.721	8± 11	5± 8	10±11	15616.6± 0.8	15650.3± 0.6	15671.2± 0.7	+31.23
J07290723-2003523	234.99	-1.123	30± 21	... ± ...	28±25	15615.6± 0.2	... ± ...	15671.9± 0.3	+36.57
J16295213-1222516	3.53	+23.935	28± 22	18± 20	24±20	15615.8± 0.3	15651.5± 0.9	15671.2± 0.4	+1.36
J16302979-1217509	3.70	+23.864	12± 14	14± 16	17±11	15613.9± 0.9	15651.5± 2.0	15671.0± 0.4	+0.19
J16313011-1248244	3.42	+23.360	7± 14	27± 20	22±14	15615.3± 1.5	15650.1± 1.3	15670.5± 0.5	+5.40
J17181515-2906309	356.58	+4.917	9± 13	67± 32	41±19	15616.7± 0.6	15651.1± 0.8	15670.1± 0.2	+24.70
J17210564-2757272	357.89	+5.057	27± 54	22± 29	54±35	15615.8± 1.1	15651.4± 0.7	15671.2± 0.3	+19.01
J17330783-2946169	357.84	+1.859	... ± ± ...	29±20	... ± ± ...	15672.0± 0.2	-7.60
J17341553-2913063	358.44	+1.953	66± 38	69± 41	34±21	15617.1± 0.3	15652.3± 0.4	15671.7± 0.2	-14.72
J17344915-2456492	2.11	+4.155	32± 29	49± 26	61±28	15614.7± 0.4	15650.1± 0.2	15669.0± 0.2	+34.21
J17345020-2917115	358.45	+1.810	37± 34	88± 56	71±25	15616.0± 0.4	15652.2± 1.1	15672.0± 0.1	-0.57
J17345235-2722089	0.07	+2.839	29± 19	27± 19	65±21	15617.4± 0.3	15653.1± 0.4	15673.4± 0.2	-22.16
J17353172-2718506	0.20	+2.746	72± 57	... ± ...	114±51	15617.0± 0.4	... ± ...	15672.2± 0.2	-12.19
J17363478-2749022	359.90	+2.279	55± 60	39± 29	79±45	15613.4± 0.7	15650.9± 0.2	15672.5± 0.2	-6.43
J17395551-2908460	359.17	+0.948	... ± ± ...	91±35	... ± ± ...	15671.6± 0.2	-0.30

Table 65: continued.

2MASS ID	GLON (deg)	GLAT (deg)	EW ₁₅₆₁₇ (mÅ)	EW ₁₅₆₅₃ (mÅ)	EW ₁₅₆₇₃ (mÅ)	λ_{15617}^c (Å)	λ_{15653}^c (Å)	λ_{15673}^c (Å)	Vrad (km.s ⁻¹)
J17425688–2826194	0.12	+0.760	33± 21	43± 25	49±14	15614.3± 0.4	15650.1± 0.4	15670.6± 0.1	+16.41
J17434172–2437561	3.45	+2.614	... ± ...	55± 39	42±32	... ± ...	15649.5± 0.2	15670.5± 0.2	+14.40
J17435446–2814306	0.40	+0.683	37± 21	53± 27	56±20	15614.8± 0.4	15650.2± 0.8	15669.9± 0.3	+32.63
J17443145–2533198	2.76	+1.972	... ± ...	40± 27	80±37	... ± ...	15649.8± 0.3	15670.1± 0.2	+30.74
J17452350–2802425	0.73	+0.507	9± 22	27± 26	38±19	15616.0± 1.5	15651.1± 1.0	15671.5± 0.4	+4.11
J17453251–2805260	0.71	+0.455	59± 35	100± 70	69±33	15615.6± 0.3	15651.5± 1.2	15671.3± 0.2	+9.47
J17483083–2237243	5.74	+2.712	... ± ...	39± 29	50±28	... ± ...	15650.8± 0.5	15670.5± 0.3	+7.75
J17483083–2237243	5.74	+2.712	... ± ...	45± 46	61±37	... ± ...	15649.4± 0.8	15669.9± 0.3	+27.12
J17494346–2303468	5.51	+2.248	39± 24	32± 36	70±29	15614.1± 0.2	15651.4± 0.6	15670.2± 0.1	+17.01
J17494563–2339013	5.01	+1.939	... ± ...	67± 48	53±40	... ± ...	15651.4± 0.7	15670.7± 0.3	+9.77
J17510378–2930227	0.12	-1.311	30± 23	... ± ...	60±36	15615.0± 0.2	... ± ...	15672.2± 0.3	-5.20
J17515961–3036450	359.28	-2.049	22± 26	128± 74	56±20	15618.0± 0.9	15651.0± 1.1	15672.1± 0.2	-14.85
J17531540–2246568	6.16	+1.691	17± 36	44± 40	23±24	15617.1± 0.8	15651.1± 0.4	15671.7± 0.4	-4.34
J17554830–2125123	7.64	+1.869	24± 31	45± 20	41±24	15616.2± 0.6	15651.9± 0.2	15671.8± 0.3	-4.87
J17575299–2330566	6.06	+0.403	50± 51	203± 83	51±31	15614.9± 0.6	15651.7± 0.6	15670.5± 0.2	+27.12
J17585262–2321007	6.32	+0.288	30± 27	39± 32	37±25	15617.6± 0.3	15652.3± 0.7	15671.6± 0.2	+4.94
J17595744–2329429	6.32	+0.001	64± 48	... ± ...	95±40	15615.7± 0.3	... ± ...	15671.9± 0.2	+7.38
J18000670–2320085	6.47	+0.049	20± 23	25± 29	37±27	15613.5± 0.4	15651.0± 0.9	15671.0± 0.3	+20.75
J18001626–2324407	6.43	-0.020	55± 33	... ± ...	53±22	15615.3± 0.4	... ± ...	15670.2± 0.2	+26.75
J18002789–2949276	0.88	-3.237	2± 5	38± 25	40±16	15619.5± 0.5	15648.4± 0.8	15670.8± 0.3	+15.62
J18021640–1721376	11.92	+2.566	... ± ...	78± 61	47±31	... ± ...	15652.5± 0.7	15671.4± 0.2	+1.83
J18124109–2538325	5.85	-3.572	... ± ...	47± 43	51±29	... ± ...	15651.4± 0.6	15671.4± 0.2	-2.28
J18140101+0011580	28.82	+8.410	5± 14	28± 19	21±15	15616.5± 2.0	15649.5± 0.8	15669.5± 0.8	+13.92
J18140179–1439398	15.65	+1.404	34± 45	... ± ...	24±15	15615.8± 0.9	... ± ...	15671.4± 0.2	-11.09
J18161215–1439207	15.91	+0.945	37± 47	44± 26	60±24	15618.7± 0.8	15651.6± 0.3	15671.6± 0.2	-3.83
J18171609–1527061	15.33	+0.340	34± 55	... ± ...	75±24	15615.0± 0.4	... ± ...	15671.5± 0.2	-1.01
J18175339–1427506	16.27	+0.677	14± 12	11± 21	24±20	15615.9± 0.2	15651.2± 0.7	15671.5± 0.3	-6.20
J18190297–1206360	18.48	+1.542	71± 45	58± 38	70±21	15612.6± 0.4	15648.5± 0.6	15670.8± 0.2	+23.24
J18214300–1740026	13.88	-1.646	23± 27	53± 44	50±29	15615.2± 0.5	15651.0± 0.7	15670.7± 0.2	+12.03
J18215744+0140512	31.06	+7.325	21± 18	16± 20	20±24	15616.0± 0.6	15649.1± 1.2	15670.3± 0.9	+19.00
J18222774–0836442	21.96	+2.446	44± 38	49± 33	51±31	15615.1± 0.4	15651.6± 0.3	15671.0± 0.2	+8.28
J18223170–1718106	14.29	-1.646	16± 25	23± 23	20±18	15614.5± 0.8	15648.9± 0.5	15670.5± 0.4	+18.08
J18231720–0523192	24.91	+3.769	4± 26	53± 30	29±18	15614.4± 3.6	15649.5± 0.4	15670.2± 0.4	+16.04
J18232722–1257110	18.24	+0.197	33± 22	45± 24	46±19	15615.5± 0.5	15650.5± 0.6	15669.7± 0.2	+25.91
J18252154–1120175	19.89	+0.541	42± 29	120± 67	138±53	15613.9± 0.2	15651.1± 0.5	15670.2± 0.1	+33.64

Table 65: continued.

2MASS ID	GLON (deg)	GLAT (deg)	EW ₁₅₆₁₇ (mÅ)	EW ₁₅₆₅₃ (mÅ)	EW ₁₅₆₇₃ (mÅ)	λ_{15617}^c (Å)	λ_{15653}^c (Å)	λ_{15673}^c (Å)	Vrad (km.s ⁻¹)
J18281533-0911334	22.12	+0.910	36± 56	51± 40	27±13	15617.4± 0.8	15651.3± 0.6	15670.1± 0.1	+10.39
J18362077-0642161	25.25	+0.282	36± 31	39± 33	37±20	15613.9± 0.4	15649.5± 0.6	15670.2± 0.3	+23.49
J18373565-0715423	24.90	-0.249	37± 32	34± 27	42±27	15614.9± 0.6	15649.5± 0.6	15670.8± 0.4	+21.77
J18383229-1111196	21.51	-2.256	26± 31	67± 39	34±20	15616.4± 0.5	15650.0± 0.4	15669.4± 0.2	+33.19
J18401462-0242174	29.25	+1.254	17± 21	34± 25	28±12	15614.5± 1.1	15651.3± 2.5	15670.8± 0.3	+7.07
J18403188-0219215	29.62	+1.365	29± 18	77± 63	39±20	15615.0± 0.6	15652.0± 1.9	15670.1± 0.5	+24.60
J18411671-0234002	29.49	+1.088	25± 13	100± 39	46±19	15615.2± 0.4	15651.3± 0.8	15671.2± 0.3	+14.50
J18432830-0220047	29.95	+0.706	38± 19	52± 28	61±15	15614.4± 0.5	15649.3± 2.1	15669.8± 0.2	+32.60
J18433158+0502488	36.53	+4.055	10± 11	31± 27	30±17	15615.2± 0.3	15651.1± 0.4	15671.6± 0.2	+0.57
J18434869+0631442	37.89	+4.661	25± 21	16± 23	28±23	15617.4± 0.6	15652.5± 1.0	15672.4± 0.6	-15.14
J18434968-0157426	30.32	+0.798	27± 18	31± 20	23±11	15614.2± 0.6	15649.2± 0.8	15669.9± 0.4	+21.43
J18441756-0215328	30.11	+0.559	26± 14	... ± ...	40±13	15614.9± 0.6	... ± ...	15670.9± 0.3	+3.05
J18444099-0234170	29.87	+0.329	38± 20	58± 28	44±15	15614.9± 0.5	15650.6± 0.9	15670.7± 0.3	+12.62
J18445041-0332478	29.02	-0.151	7± 44	21± 22	25±17	15614.0± 1.5	15650.6± 0.4	15669.9± 0.8	+14.20
J18451660-0156532	30.50	+0.482	22± 17	26± 21	42±14	15614.7± 0.8	15650.2± 3.0	15670.3± 0.3	+19.92
J18464780-0201134	30.60	+0.111	28± 16	47± 21	40±12	15617.0± 0.8	15653.3± 1.0	15672.5± 0.5	-25.21
J18471949+1345555	44.78	+7.124	20± 17	25± 24	33±24	15617.4± 0.4	15651.3± 0.8	15672.7± 0.6	-14.71
J18474175+1326322	44.53	+6.900	12± 18	49± 31	13±12	15615.9± 0.7	15651.1± 0.6	15671.6± 0.5	-6.94
J18490823-0808488	25.41	-3.197	10± 13	44± 36	28±18	15616.0± 0.4	15649.7± 0.7	15671.0± 0.3	-4.36
J18534172+1412156	45.87	+5.935	40± 35	27± 24	26±12	15614.3± 0.7	15650.9± 0.6	15670.6± 0.2	+4.70
J18544633+1428396	46.24	+5.823	10± 11	20± 22	63±28	15614.6± 0.2	15651.8± 0.5	15672.1± 0.3	-3.39
J18545937-0348492	29.94	-2.527	27± 16	35± 21	35±17	15615.2± 0.5	15649.6± 1.2	15670.5± 0.3	+16.00
J18560093-0334332	30.27	-2.647	22± 18	36± 24	62±25	15616.0± 0.6	15650.9± 0.9	15671.7± 0.3	+0.14
J18574090+0458568	38.08	+0.885	34± 41	87± 59	28±17	15615.3± 0.8	15652.2± 0.7	15671.0± 0.3	+3.43
J18575755-0305423	30.92	-2.860	40± 23	29± 25	31±13	15617.1± 0.7	15651.6± 2.9	15672.2± 0.3	-16.94
J19011320+0510259	38.65	+0.189	32± 21	28± 22	25±21	15614.7± 0.4	15650.5± 0.5	15671.0± 0.5	+7.81
J19013180-0329313	30.97	-3.835	15± 17	23± 22	28±16	15616.6± 0.8	15651.5± 1.1	15671.4± 0.5	-13.92
J19015818-0351352	30.69	-4.099	42± 21	37± 22	41±13	15614.3± 0.4	15650.3± 0.9	15670.3± 0.3	+17.59
J19020621+0301121	36.84	-0.992	33± 36	... ± ...	40±21	15616.3± 0.9	... ± ...	15672.2± 0.4	-11.75
J19024013-0323036	31.19	-4.039	26± 20	19± 18	14±9	15615.8± 0.4	15650.9± 0.7	15671.6± 0.4	-4.83
J19030094-0320315	31.27	-4.097	31± 16	65± 41	34±15	15615.3± 0.6	15651.6± 1.2	15670.5± 0.3	+21.08
J19030644-0330494	31.13	-4.195	16± 21	14± 15	18±13	15615.8± 1.3	15650.2± 1.3	15670.8± 0.5	+0.60
J19050783-0410492	30.76	-4.947	12± 16	46± 26	21±14	15614.5± 0.9	15651.2± 1.1	15670.3± 0.6	+17.94
J19082768+0231104	37.12	-2.633	31± 28	22± 24	24±16	15615.4± 0.7	15649.2± 0.8	15670.4± 0.3	+28.29
J19100158+1053412	44.73	+0.881	39± 19	57± 29	21±11	15615.3± 0.4	15651.8± 0.5	15671.1± 0.2	-6.19

Table 65: continued.

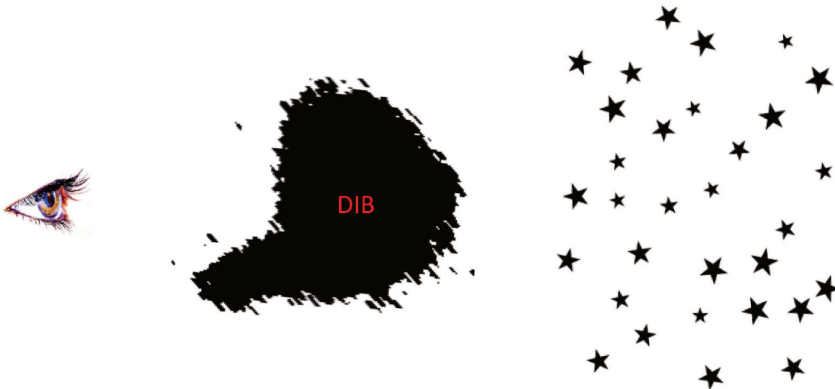
2MASS ID	GLON (deg)	GLAT (deg)	EW ₁₅₆₁₇ (mÅ)	EW ₁₅₆₅₃ (mÅ)	EW ₁₅₆₇₃ (mÅ)	λ_{15617}^c (Å)	λ_{15653}^c (Å)	λ_{15673}^c (Å)	Vrad (km.s ⁻¹)
J19111351-0516357	30.47	-6.797	21± 22	20± 17	31±14	15614.1± 1.0	15649.8± 0.7	15670.1± 0.3	+18.49
J19115599-0607272	29.78	-7.335	18± 15	37± 18	50±17	15615.6± 0.6	15651.4± 0.5	15670.8± 0.3	+5.08
J19142082-0541325	30.44	-7.678	17± 15	51± 30	18±8	15615.0± 0.8	15654.3± 1.1	15670.9± 0.2	-2.45
J19150197-0545077	30.47	-7.857	19± 29	20± 22	26±15	15614.2± 0.9	15651.0± 1.1	15671.1± 0.3	-3.21
J19154916-0518422	30.95	-7.834	34± 18	24± 16	39±14	15614.9± 0.6	15650.4± 0.6	15670.2± 0.2	+16.96
J19171479+0103339	36.83	-5.253	34± 31	31± 24	46±22	15615.0± 0.9	15650.9± 0.7	15671.3± 0.4	-3.31
J19181180-0710285	29.54	-9.196	38± 26	... ± ...	30±14	15615.5± 0.6	... ± ...	15670.6± 0.4	+5.11
J19225969+2557167	59.52	+5.148	15± 20	16± 18	15±11	15617.7± 0.8	15651.3± 0.8	15672.1± 0.3	-24.23
J19241521+1803224	52.67	+1.180	... ± ...	43± 33	38±17	... ± ...	15650.4± 0.5	15671.3± 0.2	-7.90
J19242900+1613000	51.08	+0.261	24± 19	29± 24	47±21	15614.8± 0.2	15649.5± 0.3	15670.8± 0.2	+0.57
J19250859+1644281	51.62	+0.370	24± 41	123±103	74±19	15615.9± 0.4	15648.6± 0.7	15671.7± 0.1	-9.05
J19254369+1614213	51.24	+0.008	19± 20	... ± ...	40±16	15616.1± 0.6	... ± ...	15671.9± 0.2	-16.49
J19260300+0028221	37.33	-7.477	41± 30	... ± ...	52±22	15615.1± 0.7	... ± ...	15671.1± 0.3	-2.51
J19272539+2455174	59.08	+3.780	3± 5	26± 13	58±19	15614.1± 0.4	15650.9± 0.3	15671.0± 0.3	+5.22
J19280210+2554466	60.02	+4.128	41± 26	30± 31	50±20	15615.6± 0.6	15650.7± 2.9	15670.6± 0.3	+10.88
J19285670+2546085	59.99	+3.879	27± 37	45± 27	53±22	15615.3± 0.7	15651.3± 0.6	15671.3± 0.4	-0.94
J19291464+2643005	60.86	+4.270	19± 14	23± 16	36±12	15614.9± 0.6	15651.1± 0.8	15671.1± 0.3	+1.25
J19294113+1811575	53.41	+0.113	67± 31	38± 32	47±27	15616.5± 0.3	15651.3± 0.7	15671.5± 0.3	-8.61
J19302526+1741428	53.06	-0.282	9± 10	32± 34	32±22	15619.7± 0.5	15651.9± 1.4	15671.0± 0.6	-14.05
J19310080+1642015	52.25	-0.884	30± 24	31± 23	50±21	15614.6± 0.5	15650.6± 0.5	15671.2± 0.2	+4.21
J19395931+2300238	58.79	+0.342	18± 32	... ± ...	48±24	15615.6± 0.7	... ± ...	15671.0± 0.4	+7.79
J19421487+2415408	60.13	+0.513	72± 26	32± 24	37±14	15618.6± 0.2	15651.3± 0.9	15671.6± 0.4	-6.11
J19431096+2317454	59.40	-0.152	25± 27	70± 40	74±19	15613.6± 0.4	15649.1± 0.4	15669.9± 0.2	+35.95
J19443791+2432228	60.65	+0.181	28± 23	... ± ...	21±12	15615.6± 0.8	... ± ...	15671.4± 0.5	-4.35
J19454820+2311427	59.62	-0.724	26± 22	... ± ...	47±15	15615.2± 0.8	... ± ...	15671.2± 0.4	+11.91
J19462460+2248027	59.34	-1.043	27± 17	19± 11	30±13	15615.6± 0.7	15650.8± 0.4	15670.6± 0.4	+9.74
J19462630+2351193	60.26	-0.519	10± 20	14± 15	25±15	15615.7± 1.8	15649.3± 1.0	15671.2± 0.8	+1.69
J19462817+2502366	61.29	+0.072	22± 20	... ± ...	36±19	15615.5± 0.6	... ± ...	15671.0± 0.5	-2.33
J19470867+2254587	59.53	-1.131	24± 17	... ± ...	21±9	15615.5± 0.7	... ± ...	15671.5± 0.4	-8.59
J19471035+2316278	59.84	-0.956	31± 19	25± 15	48±21	15616.9± 0.5	15651.4± 0.4	15671.4± 0.4	-5.66
J19480509+2442557	61.19	-0.409	18± 12	... ± ...	37±18	15615.5± 0.6	... ± ...	15671.7± 0.5	-3.73
J19480888+2352357	60.47	-0.846	... ± ...	38± 18	48±19	... ± ...	15650.6± 0.4	15671.0± 0.4	+8.34
J19534599+2236342	60.04	-2.602	24± 23	23± 23	12±12	15615.5± 0.9	15649.2± 1.3	15670.3± 0.7	+14.14
J19581764+2208177	60.18	-3.741	16± 27	42± 28	21±13	15614.2± 1.5	15649.5± 1.3	15670.8± 0.6	+12.84
J20025554+4559129	81.04	+7.941	29± 17	39± 22	37±20	15616.1± 0.5	15650.0± 0.5	15671.0± 0.4	+15.85

Table 65: continued.

2MASS ID	GLON (deg)	GLAT (deg)	EW ₁₅₆₁₇ (mÅ)	EW ₁₅₆₅₃ (mÅ)	EW ₁₅₆₇₃ (mÅ)	λ_{15617}^c (Å)	λ_{15653}^c (Å)	λ_{15673}^c (Å)	Vrad (km.s ⁻¹)
J20125987+2056544	60.99	-7.271	19± 26	20± 19	35±18	15614.4± 1.5	15650.1± 0.9	15671.7± 0.5	-6.97
J20145498+3722420	74.97	+1.425	24± 23	44± 27	62±17	15616.4± 0.6	15651.3± 0.6	15671.7± 0.2	-18.09
J20501250+5139580	90.20	+4.833	18± 14	37± 32	29±17	15617.1± 0.7	15652.8± 2.2	15672.8± 0.6	-27.09
J20513653+5157071	90.56	+4.846	20± 16	25± 17	31±15	15614.3± 0.7	15650.5± 1.6	15670.6± 0.4	+4.40
J21050357+3914203	82.45	-5.225	26± 29	69± 29	63±35	15615.9± 0.6	15650.9± 0.3	15672.0± 0.3	-12.36
J21122845+4703145	89.12	-0.931	5± 20	14± 11	19±12	15603.5± 6.2	15650.8± 0.8	15671.2± 0.7	+7.16
J21161964+4901093	90.99	-0.038	31± 17	45± 23	51±14	15615.2± 0.6	15651.2± 1.6	15671.1± 0.2	-0.82
J21273482+4557570	90.18	-3.542	5± 8	55± 36	29±16	15615.1± 0.7	15652.4± 1.4	15671.5± 0.5	-7.71
J21282592+4647232	90.86	-3.049	25± 20	85± 62	40±24	15614.8± 0.6	15653.0± 1.4	15672.3± 0.5	-1.91
J21282648+4655259	90.96	-2.953	24± 17	111± 57	48±21	15614.5± 0.6	15652.5± 1.0	15671.0± 0.4	+10.95
J21283001+4640249	90.79	-3.141	12± 21	27± 36	30±17	15615.3± 0.7	15648.7± 1.5	15671.1± 0.6	+5.48
J21283396+4611358	90.46	-3.496	15± 17	... ± ...	30±14	15614.9± 0.9	... ± ...	15670.6± 0.5	+7.92
J21304593+5712001	98.28	+4.271	25± 21	17± 19	34±18	15615.1± 0.6	15651.8± 1.0	15671.9± 0.3	-17.27
J21354384+5728035	98.95	+4.013	8± 10	40± 25	31±15	15617.3± 0.5	15651.3± 0.6	15672.3± 0.3	-21.37
J21363278+4303344	89.36	-6.757	15± 18	14± 13	35±11	15615.6± 0.8	15650.7± 0.7	15671.3± 0.3	-0.47
J21380848+5350172	96.78	+1.086	32± 31	30± 25	45±25	15616.5± 0.6	15650.5± 0.5	15672.2± 0.3	-25.51
J21425012+4348456	90.73	-6.954	35± 19	41± 22	33±16	15614.6± 0.5	15650.3± 0.9	15670.7± 0.4	+3.80
J21434429+4323427	90.57	-7.377	20± 17	32± 24	38±15	15615.7± 0.8	15651.2± 1.5	15671.4± 0.3	-9.86
J21444465+4345462	90.96	-7.218	26± 21	60± 33	43±17	15615.5± 0.8	15651.9± 0.9	15670.7± 0.4	+5.10
J21451397+4319554	90.74	-7.602	16± 13	16± 13	28±15	15615.0± 0.4	15650.9± 0.5	15671.7± 0.5	-3.87
J21455910+4337591	91.04	-7.462	3± 9	9± 11	27±15	15615.2± 1.1	15649.9± 0.7	15670.9± 0.5	+6.82
J21481062+5950582	101.74	+4.746	13± 17	31± 20	13±12	15615.3± 0.8	15651.3± 0.7	15670.9± 0.5	-3.62
J21502178+5357414	98.23	+0.012	42± 35	11± 17	36±25	15615.2± 0.7	15651.7± 1.5	15670.3± 0.5	-5.72
J22265453+5338416	102.44	-3.375	24± 23	25± 28	76±42	15618.6± 0.3	15650.7± 0.4	15670.3± 0.3	-34.62
J22313333+5912393	105.87	+1.055	33± 28	41± 30	45±25	15616.9± 0.6	15651.2± 0.9	15672.2± 0.3	-16.35
J22313889+6354117	108.28	+5.083	15± 19	103± 59	58±24	15615.5± 0.7	15651.1± 0.9	15672.4± 0.3	-9.09
J22320081+6311305	107.95	+4.451	22± 21	20± 18	45±22	15615.8± 0.6	15651.6± 0.7	15671.9± 0.4	-10.77
J22323166+5754020	105.31	-0.138	20± 16	43± 45	31±27	15615.9± 0.4	15652.6± 1.2	15672.9± 0.6	-3.74
J22364287+6410480	108.90	+5.043	40± 28	69± 39	52±25	15613.8± 0.4	15650.3± 0.8	15671.7± 0.4	+1.76
J22382828+6431483	109.24	+5.254	37± 30	39± 22	49±16	15615.7± 0.6	15650.9± 0.6	15670.8± 0.2	+5.04
J22410071+6351574	109.16	+4.539	52± 26	85± 46	44±16	15615.8± 0.4	15651.9± 0.8	15670.8± 0.2	-1.40
J22422452+6424041	109.55	+4.936	30± 24	40± 28	63±24	15616.1± 0.6	15651.4± 1.4	15670.9± 0.3	-2.55
J23280614+5825229	112.19	-2.699	27± 20	45± 31	27±18	15615.4± 0.3	15650.8± 0.6	15671.7± 0.3	-1.40
J23540720+5711597	115.20	-4.809	13± 16	24± 22	33±19	15616.0± 0.8	15651.4± 0.9	15671.9± 0.6	-12.98
J23570869+6434065	117.14	+2.309	28± 26	... ± ...	43±19	15616.8± 0.4	... ± ...	15672.6± 0.2	-32.21

Part IV

"One DIB, one cloud"



Tomography of single cloud

Published as Letter to the Editor:

“The 15273 Å diffuse interstellar band in the dark cloud Barnard 68”

Elyajouri, M., Cox, N. L. J., & Lallement, R.

Astronomy & Astrophysics, Volume 605, id.L10, 4 pp. 2017b.

Abstract

High obscuration of background stars behind dark clouds precludes the detection of optical diffuse interstellar bands (DIBs) and hence our knowledge of DIB carriers in these environments. Taking advantage of the reduced obscuration of starlight in the near-infrared (NIR) we used one of the strongest NIR DIBs at 15273 Å to probe the presence and properties of its carrier throughout the nearby interstellar dark cloud Barnard 68. We measured equivalent widths (EW) for different ranges of visual extinction A_V , using VLT/KMOS H-band (1.46–1.85 μm) moderate-resolution ($R \sim 4000$) spectra of 43 stars situated behind the cloud. To do so, we fitted the data with synthetic stellar spectra from the APOGEE project and TAPAS synthetic telluric transmissions appropriate for the observing site and time period. The results show an increase of DIB EW with increasing A_V . However, the rate of increase is much flatter than expected from the EW- A_V quasi-proportionality established for this DIB in the Galactic diffuse interstellar medium. Based on a simplified inversion assuming sphericity, it is found that the volume density of the DIB carrier is 2.7 and 7.9 times lower than this expected average value in the external and central regions of the cloud, which have $n_H \simeq 0.4$ and $3.5 \times 10^5 \text{ cm}^{-3}$, respectively. Further measurements with multiplex NIR spectrographs should allow detailed modeling of such an edge effect of this DIB and other bands and help clarify its actual origin.

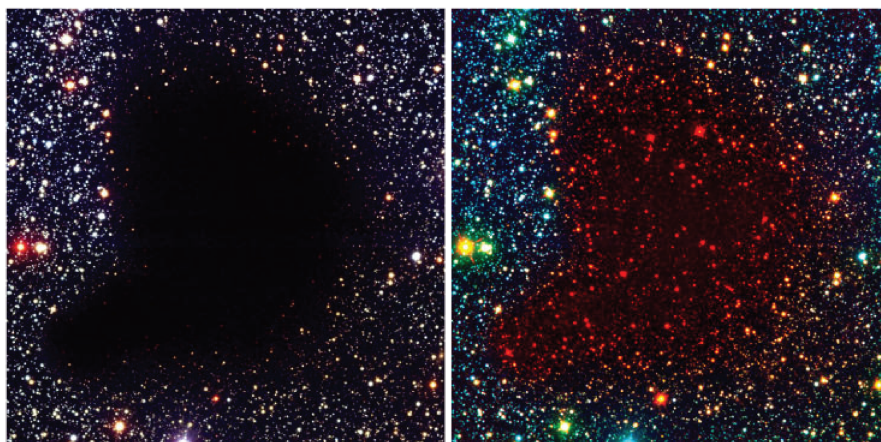


Figure 71 Comparison of two false-color composite images of Barnard 68. On the left, blue, green and near infrared filters are used. The right image is instead a false-color view, where the near infrared is mapped to the green color, the infrared to the red and blue corresponds to the blue light. The latter shows the background stars hidden behind the cloud only visible at the infrared wavelengths. Credit: European Southern Observatory (ESO).

7.1 Introduction

In contrast to the hundreds of optical (400–900 nm) DIBs (Hobbs et al. 2009) only about 20 to 30 near-infrared (NIR; 900–2500 nm) DIBs have been detected in the diffuse ISM (Joblin et al. 1990; Geballe et al. 2011; Cox et al. 2014; Hamano et al. 2016). These NIR DIBs offer a unique additional insight into the overall carrier population. In particular, in the NIR it is easier to probe more highly reddened lines of sight (i.e., $A_V > 10$ mag), either due to a longer column of dust in the line of sight to a distant background source or due to denser environments.

The absence of perfect correlations between different DIBs suggests that most bands arise from different carriers (Cami et al. 1997). Studies of DIBs in the optical reveal there is a clear relation between their presence and neutral and molecular hydrogen abundances as well as with the effective interstellar radiation field strength. The latter particularly affects relative band strength ratios (Vos et al. 2011; Ensor et al. 2017b). Lan et al. (2015) have used massive SDSS datasets and demonstrated that most DIBs level off with respect to the reddening when sightlines cross opaque molecular clouds, and some extreme cases of DIB disappearance have also been found (Snow et al. 2002). This is also consistent with the weakness of NIR DIBs in dense interstellar environments (e.g., Adamson et al. 1994).

Instead of looking at different sightlines that probe different interstellar

clouds, it is also possible to map the evolution of DIB carriers with extinction from the edge (representing diffuse ISM) to the core (representing dense ISM) of a single dark cloud.

Tracing the behaviour of DIBs for A_V up to 10 mag is, at present, only practical when using strong DIBs in the NIR. The 15 273 Å DIB is particularly suited as its presence and properties in the ISM have been studied extensively thanks to the inclusion of this band in the APOGEE NIR survey (Zasowski et al. 2015) and as seen in Part I and also thanks to the strength of this DIB.

Here we present KMOS spectroscopic observations of the 15 273 Å DIB toward 43 background sources probing Barnard 68 (B68). B68 is a nearby (125 pc), relatively isolated, starless Bok globule conveniently situated against a backdrop of Galactic bulge (giant) stars as illustrated in Fig. 71. This globule is often seen as the prototypical case of a Bonner-Ebert sphere and shows a radial averaged extinction law, spanning from a few to several tens of magnitudes in visual extinction, which follows the predicted case very closely (Alves et al. 2001). The radial density and temperature profile of B68 have been reconstructed accurately through NIR extinction and far-infrared and sub-mm emission measurements (e.g., Bergin et al. 2006; Nielbock et al. 2012; Steinacker et al. 2016).

7.2 Observations and data reduction

The KMOS (Sharples et al. 2013) *H*-band spectra of 85 targets toward B68 were obtained in February and March 2016 (Program ID 096.C-0931(A), PI: N. Cox). The targets are located within $\sim 200''$ from the center of the cloud. The 43 targets whose spectra could be used in the analysis (Sect. 7.3) are shown in Fig. 72. The initial target list was based on selecting the 2MASS targets ($J \sim 12 - 16$ mag) at a range of distances from the center of the cloud. The final target selection was governed primarily by finding the most efficient configuration of the KMOS arms for the allocated time. Four instrument setups were defined and executed. Two configurations, in stare mode, were used to obtain spectra of the brightest target ($J = 12-14$ mag) and two for the faintest targets ($J = 14-16$ mag). The sky positions were observed every three science exposures. The parameters, seeing, and airmass are listed in Table 71. For each configuration about 20 arms were assigned to science targets and 3 to 4 arms were used for sky observations. The data were reduced via the KMOS data processing workflow (Davies et al. 2013) within the ESO Reflex environment. Average spectra were extracted from each $2.8'' \times 2.8''$ IFU. In most cases optimal extraction was chosen. In two instances two sources were captured by the IFU and these were extracted separately using average extraction from specified spatial windows.

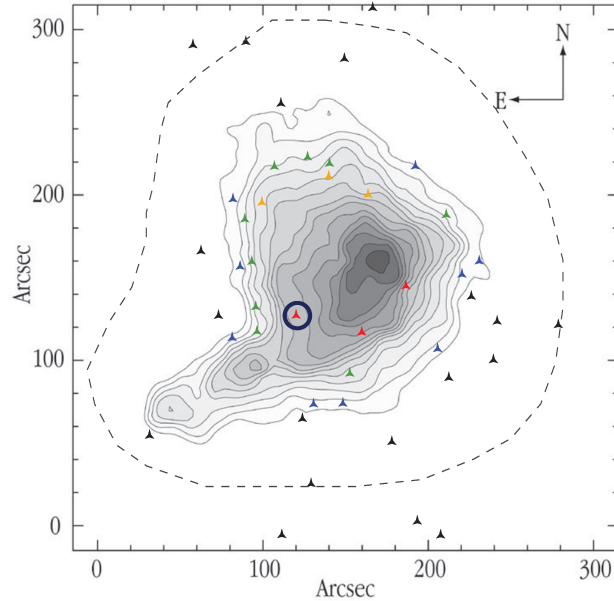


Figure 72 Target positions on the B68 extinction map from [Alves et al. 2001](#). Solid contours correspond to 2 mag steps from $A_V = 4$ to 30 mag. The dashed line represents $A_V = 1.2$ mag. The coordinates at center denote 17h22m39s -23°50'00".

All spectra are in the geocentric frame. The extracted spectra range from 1.425 to 1.867 μm (pixel size of 0.00021582 μm) and the spectral resolving power is $R \sim 4000$ at 1.5273 μm .

Table 71 KMOS observations

Setup	Seeing	Airmass	Date (2016)	Exp. time (s)
Bright #1	0.8''	1.57	02-29	160
Bright #2	1.5''	1.17	02-21	160
Faint #1	1.5''	1.53	03-17	420
Faint #2	2.7''	1.46	02-28	420

7.3 Extraction of the interstellar spectrum

7.3.1 Synthetic stellar and telluric spectra

In order to identify interstellar lines, one needs to fit each spectrum to a (stellar+telluric) model. Unfortunately, 2MASS stars behind B68 have unknown stellar parameters. To carry out a reliable analysis, synthetic models were ex-

tracted from the Apache Point Observatory Galactic Evolution Experiment (APOGEE; [Majewski \(2012\)](#)) Stellar Parameters and Chemical Abundances Pipeline (ASPCAP; [García Pérez et al. 2016b](#)), which provides a synthetic stellar spectrum estimating the main stellar line locations for each giant star. In particular, we used models from the GK grid, which covers 3500–6000 K ([Mészáros et al. 2012](#)). From this set a sample of 1500 ASPCAP models, with $T_{\text{eff}} = 3634 - 6000$ K, has been selected randomly. Since each APOGEE model is given in the corresponding stellar rest frame, the fitting procedure allows for a wavelength shift in order to compensate for the star radial velocity. Telluric transmission models of H₂O adapted to the observing site, date, and zenith angle were retrieved online from the Transmissions of the Atmosphere for ASTromonical data (TAPAS) service ([Bertaux et al. 2014](#)). The stellar and telluric spectra were convolved with a Gaussian instrumental response for R=4000. Fig. 73 shows an example of stellar spectrum and a typical telluric transmission before and after convolution. More fits are presented in appendix B.

7.3.2 Fitting method

Each individual spectrum was fitted by a combination of the convolved synthetic stellar spectrum S_λ and the convolved telluric transmission model T_λ with a 8 Å mask applied at the expected location of the DIB (around 15271 Å). The ill-fit stellar lines regions have also been masked. A linear function (parametrized with A and B) is included to adjust to the continuum level. Our model is described as follows :

$M_\lambda = (S_\lambda(\delta\lambda))^\alpha \times T_\lambda^\beta \times (A \times \lambda + B)$, where α and β are the scaling factors that adjust the stellar and telluric feature depths to the observed flux and $\delta\lambda$ is the free wavelength shift of the model. The mathematically correct formula is the convolved product instead of our product of preliminarily convolved functions. However, we checked that our simplified formula provides very similar fit results, owing to the broad instrumental function, but is much more efficient. As we focus on the strongest NIR DIB 15273, we selected a predefined fraction of the spectral range around the DIB location, i.e., 15216–15424 Å. All parameters A , B , α , β , and $\delta\lambda$ were free to vary. The fit starts with the same initial guess except for the telluric scaling factor, which is chosen according to the date of observation. We performed the adjustment for each of the 1500 ASPCAP models for each target and retained the model with the minimum χ^2 . We require the mean standard deviation to be less than 2.6% outside the DIB, which yields a sample of 43 targets with clean and well-enough fitted spectra. A visual inspection of the residuals ($R_\lambda = \text{observed flux} - \text{total best-fitting model}$) allowed us to confirm the reliability of the procedure and that for selected targets the remaining fluctuations are solely due to the noise. These residuals were used to derive the actual noise level and error bars in individual spectra and stacked spectra

(see below). The S/Ns in individual spectra range from 39 (i.e., our threshold) to $\simeq 125$. Our method is illustrated in Fig. 73. To check the feasibility of the DIB extraction we then performed a simulation using a single spectrum and its fitted model. We added DIB absorptions with various strengths corresponding to the range of extinctions encountered in B68 and following the [Zasowski et al. \(2015\)](#) relation $EW = 102 \text{ m}\text{\AA} \times A_V^{(1.01 \pm 0.01)}$ derived over three orders of magnitude in extinction. Fig. 74 shows that, in case the average law is verified, DIBs can be detected in this individual spectrum provided $A_V \geq 2$.

7.4 15 273 Å DIB characterization

The residuals provide a first estimate of DIB detection or non-detection. However, we found that the DIB depth is often on the order of the noise amplitude. In order to improve the characterization of the DIB, we stacked residuals within groups of stars according to their A_V s in five intervals centered on {2.1; 5.2; 9.2; 13; 19.8} as shown in Fig. 74. The corresponding numbers of targets in each group are {19; 9; 9; 3; 3} and the S/Ns decrease¹ from $\simeq 170$ to $\simeq 75$. Then, we performed two Gaussian fits at the DIB location. We have shown in Chapter 6 that a Gaussian profile is appropriate. The first fit is carried out for a fixed DIB width and location, as if the DIB feature was only due to the dark cloud. In the second, both width and locations were free to vary. Uncertainties on EWs are estimated conservatively from the noise level as in Chapter 2. Fig. 75 shows the measured EW as a function of A_V toward the B68 background star groups. The blue points show EWs with all free fit parameters and the red points correspond to the single cloud case. The results are compatible within error bars, but the fixed width case is found to correspond to a smoother evolution than the free width case, suggesting that this method is more reliable and from now we adopt this solution. The results are compared with expectations from the above galactic average of [Zasowski et al. \(2015\)](#). It can be seen that the measured reddening values at cloud periphery and center would imply 2.7 and 6.8 times higher values.

7.4.1 Simplified inversion

We performed a simplified inversion of DIB carrier columns (here EWs scaled by an unknown fixed number) to retrieve the true radial (3D) structure from the projected (2D) observed structure. We assumed that B68 is spherical and composed of concentric homogeneous spherical shells and

¹Here, the S/N ratio of average spectra increases in each A_V group but the S/Ns are decreasing with increasing A_V as the stars are fainter and the signal becomes weaker from the periphery to the center

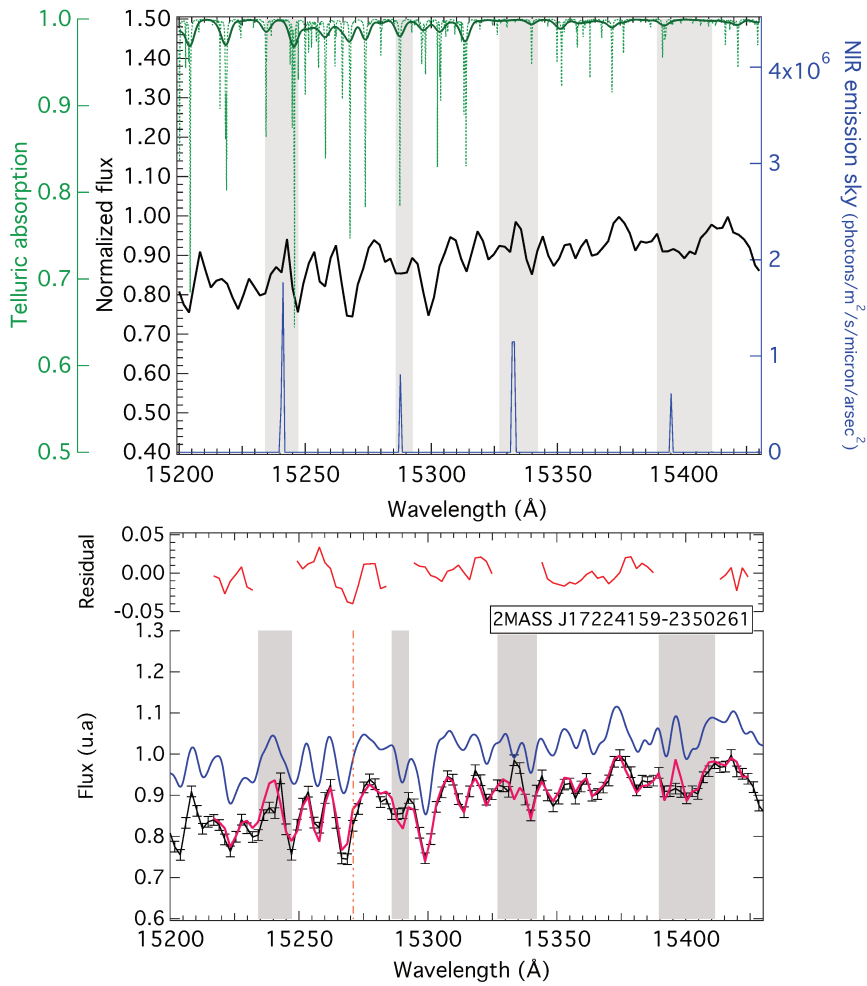


Figure 73 Top: Individual spectrum (black) for the circled target in Fig. 72 and the green data point in Fig. 75. The green lines show the telluric model before and after convolution. Gray rectangles indicate masks at strong sky emission lines (blue). Bottom: Example of fit is shown. The blue curve is the convolved stellar model. The magenta curve is the fitted stellar+telluric model. The dashed orange line shows the DIB position.

the Abel transform can be replaced by an iterative computation starting from the most external layer. The density is assumed to be negligible outside of the most external layer. All parameters depend only on the radial distance r to the center that is proportional to the sightline angular distance from cloud center. The local volume density of the DIB carrier is described by a function $n(\text{DIB})(r)$ (cm^{-3}). The onion peeling algorithm first computes $n(r)$ in the external layer by simply dividing the external column density by

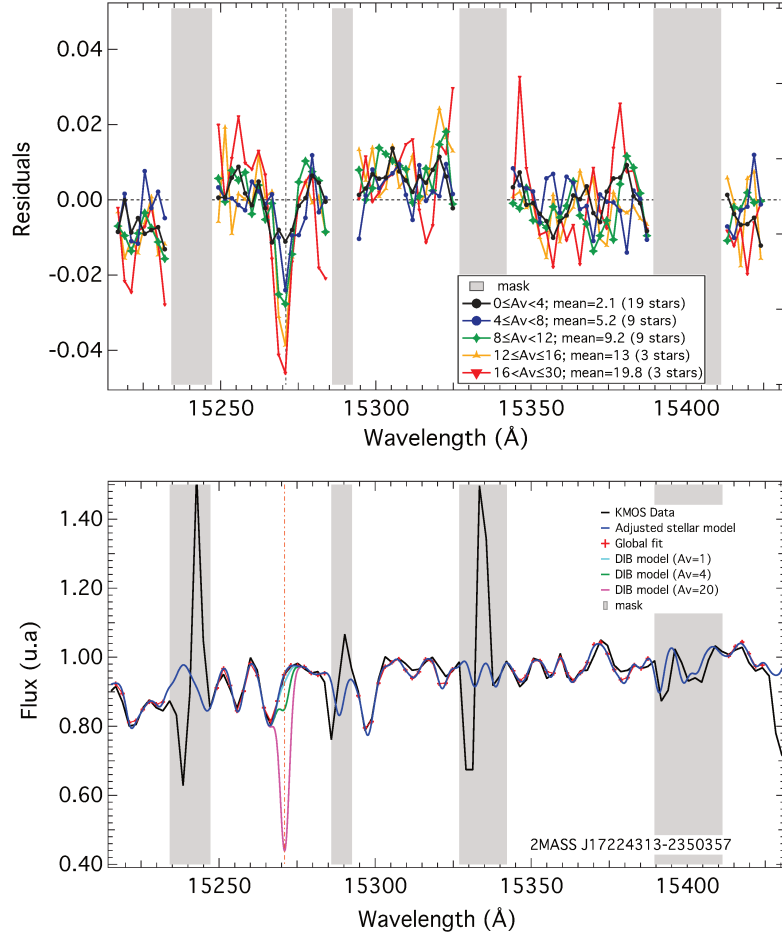


Figure 74 Top: Residuals of model adjustments to the five average spectra (DIB excluded). Colors correspond to those in Fig. 72. Bottom: A target spectrum (in black) and its fitted model outside the DIB region (blue). Simulated Gaussian absorptions representing a DIB with the expected strength for $A_V = 1, 4$ and 20 mag resp. are added.

the path length through the external shell. The next sightline through the adjacent, more internal shell, crosses the first and second shells only and the volume density in the second shell is obtained by dividing the DIB column by the path length through this second shell, after subtraction of the contribution of the path length through the first one, using the previously derived density. This simple computation is iterated until one reaches the cloud central densest sphere. Fig. 75 shows $n(\text{DIB})$ within the five shells (each corresponding to a measured EW). As a check of our procedure we applied the same algorithm to the reddening, i.e., the column of large H nuclei assuming a constant dust to H ratio $N_H = 6.25 \times 10^{25} \text{ E(B-V)}$ and $d=125$

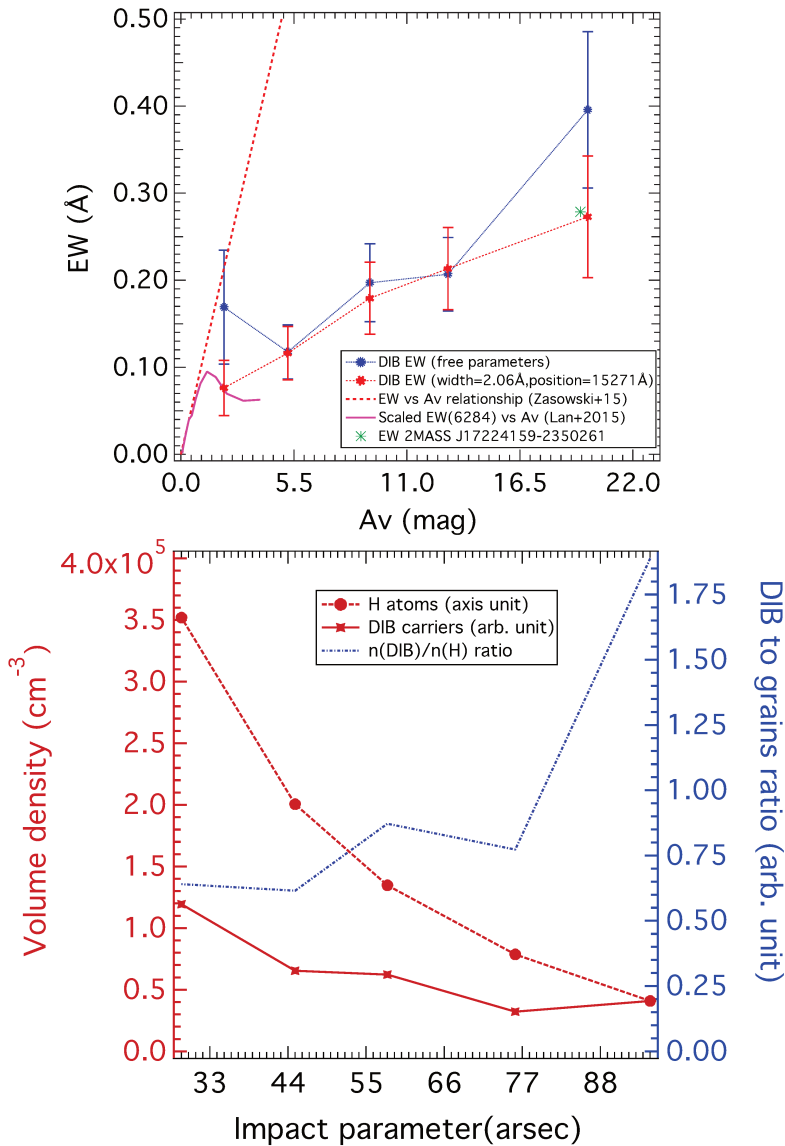


Figure 75 Top: DIB EW vs. A_V for the five average spectra. Blue and red points correspond to the two fitting procedures (see text). The dashed red curve represents the [Zasowski et al. \(2015\)](#) relation. The pink line is the [Lan et al. \(2015\)](#) EW vs. A_V relationship for the 6284 Å DIB, scaled to match the strength of the 15 273 Å DIB at $A_V \leq 1$ (see text). Bottom: Volume density of DIB carrier $n(\text{DIB})$ based on the simplified inversion of EWs (left scale). Also shown is the inverted volume density $n(\text{H})$ based on A_V data. The $n(\text{DIB})$ has been artificially scaled in such a way the two curves cross for the external layer. The ratio between the DIB carrier and H volume densities is also shown (right scale).

pc. The resulting volume densities $n(\text{H})$ range from 0.5 to $3.5 \times 10^5 \text{ cm}^{-3}$ (Fig. 75) and are roughly consistent with the results of [Nielbock et al. \(2012\)](#), showing that despite the limited number of shells the procedure gives reasonable estimates of volume densities. Fig. 75 also shows that the fractional abundance $n(\text{DIB})/n(\text{H})$ decreases by a factor $\simeq 3$ from periphery to center. A simple scaling shows that $n(\text{DIB})/n(\text{H})$ is 2.7 (resp. 7.9) smaller than the average deduced from the [Zasowski et al. \(2015\)](#) law at 0.018 (resp. 0.059) pc from cloud center.

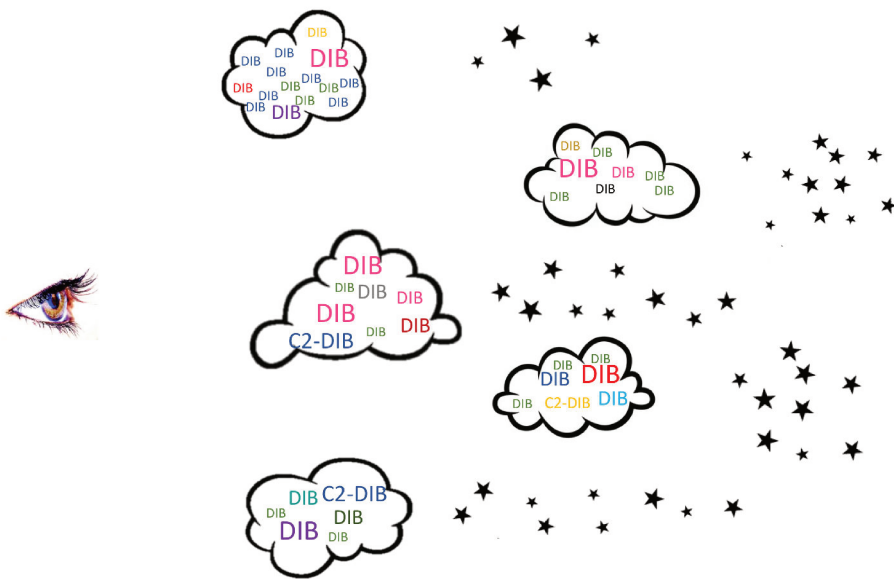
7.5 Discussion

VLT KMOS spectra of stars beyond B68 were used to derive the strengths of the associated 15 273 Å DIB and to infer a first estimate of the volume density distribution of the DIB carrier. Following the general trend established for most optical DIBs (see, e.g., (e.g., [Lan et al. 2015](#)), the DIB EW levels off with respect to the extinction. At $A_V=2.1$ it is already at least 2.7 times below the average level measured along distant sightlines ([Zasowski et al. 2015](#)), and for our most central direction with $A_V \simeq 20$, it is $\simeq 7$ times below this level. In terms of volume densities in the spherical approximation, this corresponds to a 2.7 (resp. 7.9) depletion from periphery ($r=0.018$ pc) to center ($r=0.059$ pc). This 15 273 Å DIB depletion is less severe here than for strong optical DIBs in the remarkable case of the Orion star HD 62542 ([Snow et al. 2002](#)), in particular in the case of the 6284 Å DIB, which is at least 25 times depleted with respect to average shielded ζ -type sightlines ([Ádámkóvics et al. 2005](#)). This may be surprising since both DIBs have similar average responses to the radiation field as seen in the Chapter 6. Fig. 75 compares the dependence on the extinction of the 15 273 Å in B68 and of the 6284 Å DIB in Fig. 9 of [Lan et al. \(2015\)](#). A scaling factor was applied to match the strength of DIB 15 273 Å in the linear region. There is a marked leveling off with respect to the extinction at $A_V \simeq 1$ for both DIBs. Above $A_V=2$ the EW decrease observed for the 6284 Å DIB may be absent for the 15 273 Å DIB, however the overlap in the extinction ranges is too small to reach a firm conclusion. If confirmed, such differences would show that, despite the similarity between the responses to the radiation field, the 15 273 DIB carriers do not behave in the dark cloud B68 as the 6284 DIB carriers in molecular clouds or Orion nebula stripped clouds. The life cycle of the carriers and its drivers are still under study. The UV radiation is recognized to play a primary role and in the context of PAH-like carriers it would certainly directly influence the charge state of PAHs (e.g., (e.g., [Ruiterkamp et al. 2005](#)) and the resulting disappearance of some DIBs. Additional photo-processing and hydrogenation or dehydrogenation likely enter into play (e.g., [Vuong, Foing 2000](#)). [Bertaux, Lallement \(2017\)](#) have suggested that a general carrier disappearance could additionally be due to coagulation into aggregates, as predicted by some evo-

lutionary models of dust (Jones 2016). Our study demonstrates that future measurements using multiplex NIR spectrographs and extended to more DIBs, more targets, and various types of clouds should allow one to probe the volume density distribution of the DIB carriers precisely enough to shed light on the processes that govern their carrier formation and destruction. However, the case of Barnard 68 is still comparable to tens of other similar cases seen in Chapter 5, suggesting that the marked disappearance of DIBs in Barnard 68 is far from an exception.

Part V

Large survey: *"Many DIBs, few carefully selected targets"*



Description of the EDIBLES survey

8.1 Overview

The ESO diffuse interstellar band large exploration survey (EDIBLES) is a Large Programme that is probing the lines-of-sight of ~ 120 bright O and B-type stars over a large spectral range with UVES (Smoker et al. 2009). EDIBLES focuses on the links between the various detectable DIBs and the properties of the diffuse to translucent ISM located in front of the selected targets. The survey is designed to cover different physical and chemical environments.

EDIBLES observations and data reductions are described in detail in Cox et al. (2017) listed below and illustrated in Fig. 9 of this article. The S/N values for most sightlines are 400–1000 in the red part, 300–400 in the UV and ≥ 300 in the near-IR. Two additional data treatments are necessary to realize the goals aimed for in this study.

First, we have corrected all individual exposures recorded with the 564-nm setting (including both the Red Upper and Red Lower detectors) for their telluric lines. The method follows the first of the two procedures described in Cox et al. (2017). It is appropriate for moderately weak lines and uses TAPAS synthetic spectra adapted to the observing site and season (Bertaux et al. 2014). In addition to the telluric correction of the entire spectra, we have used the same method to remove the weak telluric lines that contaminate the spectral region comprising the C₂ Phillips system. During the correction process, we noticed an additional system of narrow telluric lines in the 5780–5815 Å region that are lacking in the present TAPAS model. These very weak lines have been added very recently to the HITRAN database and correspond to the $b^1\Sigma_g^+$ ($v=3$)- $X^3\Sigma_g^-$ ($v=0$) band of O₂ (Gordon et al. 2017). Pending their introduction into TAPAS, we have used a weakly reddened star and extracted the system of lines in this spectral area. We have used this empirical transmittance in the same way as the TAPAS one. At the time

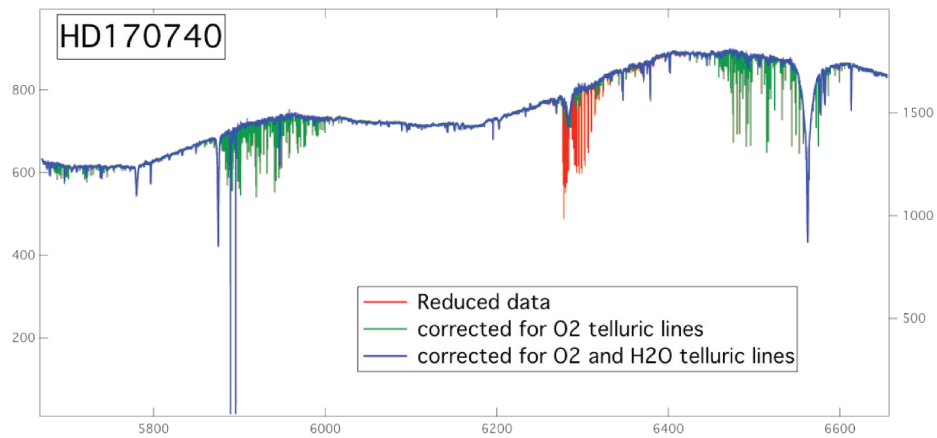


Figure 81 Example of O₂ and water telluric lines correction applied to the spectrum of HD 170740.

of writing this document, TAPAS has now updated its codes to include these systems.

Second, we have stacked the individual multiple exposures of the same target, using the original spectra or the telluric-corrected spectra if necessary. The spectra were Doppler-corrected and interpolated to produce a single spectrum in the heliocentric frame. The spectra obtained with the different spectral configurations have been concatenated. For overlapping spectral intervals we have not averaged the data; instead we have chosen the data obtained with the grating configuration providing the best S/N, i.e., the 437 nm setting was selected in the 346 nm/437 nm overlap region, and the 560 nm-RedL was selected in the 564 nm-RedL/564 nm-RedU overlap region.

8.2 Project description, survey sample, and quality assessment (Article B2)

The ESO Diffuse Interstellar Bands Large Exploration Survey (EDIBLES)

I. Project description, survey sample, and quality assessment

Nick L. J. Cox^{1,2}, Jan Cami^{3,4}, Amin Farhang⁵, Jonathan Smoker⁶, Ana Monreal-Ibero^{7,8,9}, Rosine Lallement⁷, Peter J. Sarre¹⁰, Charlotte C. M. Marshall¹⁰, Keith T. Smith^{11,12}, Christopher J. Evans¹³, Pierre Royer¹⁴, Harold Linnartz¹⁵, Martin A. Cordiner^{16,17}, Christine Joblin^{1,2}, Jacco Th. van Loon¹⁸, Bernard H. Foing¹⁹, Neil H. Bhatt³, Emeric Bron²⁰, Meriem Elyajouri⁷, Alex de Koter^{21,14}, Pascale Ehrenfreund²², Atefeh Javadi⁵, Lex Kaper²¹, Habib G. Khosroshadi⁵, Mike Laverick¹⁴, Franck Le Petit²³, Giacomo Mulas²⁴, Evelyne Roueff²³, Farid Salama²⁵, and Marco Spaans²⁶

(Affiliations can be found after the references)

Received 31 March 2017 / Accepted 21 July 2017

ABSTRACT

The carriers of the diffuse interstellar bands (DIBs) are largely unidentified molecules ubiquitously present in the interstellar medium (ISM). After decades of study, two strong and possibly three weak near-infrared DIBs have recently been attributed to the C_{60}^+ fullerene based on observational and laboratory measurements. There is great promise for the identification of the over 400 other known DIBs, as this result could provide chemical hints towards other possible carriers. In an effort to systematically study the properties of the DIB carriers, we have initiated a new large-scale observational survey: the ESO Diffuse Interstellar Bands Large Exploration Survey (EDIBLES). The main objective is to build on and extend existing DIB surveys to make a major step forward in characterising the physical and chemical conditions for a statistically significant sample of interstellar lines-of-sight, with the goal to reverse-engineer key molecular properties of the DIB carriers. EDIBLES is a filler Large Programme using the Ultraviolet and Visual Echelle Spectrograph at the Very Large Telescope at Paranal, Chile. It is designed to provide an observationally unbiased view of the presence and behaviour of the DIBs towards early-spectral-type stars whose lines-of-sight probe the diffuse-to-translucent ISM. Such a complete dataset will provide a deep census of the atomic and molecular content, physical conditions, chemical abundances and elemental depletion levels for each sightline. Achieving these goals requires a homogeneous set of high-quality data in terms of resolution ($R \sim 70\,000\text{--}100\,000$), sensitivity (S/N up to 1000 per resolution element), and spectral coverage (305–1042 nm), as well as a large sample size (100+ sightlines). In this first paper the goals, objectives and methodology of the EDIBLES programme are described and an initial assessment of the data is provided.

Key words. ISM: lines and bands – ISM: clouds – ISM: molecules – dust, extinction – stars: early-type – local interstellar matter

1. Introduction

The unknown identity of the carriers of all but two diffuse interstellar bands (DIBs) constitutes the longest standing spectroscopic enigma of modern astronomy (Sarre 2006). Two features at 5797 and 5780 Å, which are now known to be interstellar in origin, were first noted by Heger (1922) and studied in relation to interstellar gas and dust by Merrill & Wilson (1938). At present, over 400 of these interstellar absorption features are known (for a handful of sightlines), superimposed on an otherwise nearly smooth interstellar extinction curve (Herbig 1995; Galazutdinov et al. 2000; Hobbs et al. 2008). Only recently has the attribution of a pair of near-infrared DIBs (Foing & Ehrenfreund 1994) to C_{60}^+ been confirmed with laboratory gas phase experiments (Campbell et al. 2015; Kuhn et al. 2016) along with the tentative astronomical detection of three more predicted bands (Walker et al. 2015, 2016), though this needs further verification and investigation (Galazutdinov et al. 2017; Cordiner et al. 2017). This is an exciting result because C_{60} (Cami et al. 2010; Sellgren et al. 2010), and C_{60}^+ (Berné et al. 2013) have also recently been

detected in space through their mid-infrared emission spectra. This identification may be a chemical clue towards identifying further DIB carriers; so far only C_3 (Haffner & Meyer 1995; Maier et al. 2001; Schmidt et al. 2014) and C_{60}^+ have been identified as pure polyatomic carbon species in the diffuse ISM and this leaves a large gap to be filled in our current understanding of the carbon chemical network in diffuse clouds. It is possible that the detection of C_{60}^+ hints at a long predicted important role of polycyclic aromatic hydrocarbons (PAHs) in the ISM (Van der Zwet & Allamandola 1985; Léger & d’Hendecourt 1985; Salama et al. 1996). Recent laboratory (Zhen et al. 2014) and modelling (Berné et al. 2015) works support the proposal by Berné & Tielens (2012) that fullerenes may form upon photo-dissociation of large PAH precursors.

Observational surveys (e.g. Herbig 1993; Friedman et al. 2011; Kos & Zwitter 2013) have shown that the strength of the strongest ~ 20 of the DIBs correlates roughly linearly with the amount of dust and gas, measured by the reddening $E(B - V)$ or the column density of atomic hydrogen $N(H I)$, respectively. This indicates a thorough mixing of the DIB carriers with

interstellar matter (Cox 2011). However, a large real scatter is observed in these relations with gas and dust, and the relative strengths of several bands are known to have an environmental dependence (Cox & Spaans 2006); some bands vary as a function of radiation strength between different lines-of-sight (Krelowski & Walker 1987; Cami et al. 1997; Vos et al. 2011; Friedman et al. 2011). The scatter is also partly due to multiple cloud structures along sightlines. The relationship between several DIBs and, for example, C₂ and CN, has been investigated (Thorburn et al. 2003; Weselak et al. 2008), but generally the link with di-atomic species is not well understood. This relation between DIBs and reddening has not been investigated for the remaining >380 bands. Whether or not there is a direct physical connection between DIB carriers and dust grains, e.g. in terms of depletion onto grains or as carrier formation sites, remains to be seen – so far no polarisation signal has been detected for the twenty strongest DIBs (Cox et al. 2011).

Studies of selected bands in a dozen sightlines have revealed a complex substructure in the narrowest bands (Sarre et al. 1995; Ehrenfreund & Foing 1996; Galazutdinov et al. 2008) which show small variations with local temperature (Cami et al. 2004; Kaźmierczak et al. 2010a), typical for a molecular carrier. Substructure has also been identified in weak DIBs, but line-of-sight variations are less well studied (Galazutdinov et al. 2005). On the other hand, broader DIBs do not contain substructure (Snow 2002; Galazutdinov et al. 2008), which may be due to lifetime broadening of the absorption band (Linnartz et al. 2010). Considerations of the available elemental abundances and plausible oscillator strengths lead to the conclusion that abundant large organic molecules are suitable candidates (Léger & d’Hendecourt 1985; Huang & Oka 2015). The combination of observational studies, theoretical models, and laboratory astrophysics indicates that candidate carriers should primarily be sought among a large number of possible carbon-based organic molecules (see Sarre 2006, for a review; and Cami & Cox 2014, for an overview of recent progress).

Ongoing and future large spectroscopic surveys offer the possibility to study (mostly the strongest) DIBs in large areas of the sky. For example, Lan et al. (2015) and Baron et al. (2015) constructed DIB strength maps from SDSS spectra, Kos et al. (2014) produced pseudo-3D maps for the 8621 Å DIB using the RAVE survey, Zasowski et al. (2015) and Elyajouri et al. (2016) used the APOGEE near-infrared survey to study the distribution of the 15 267 Å near-infrared DIB. The spatial distribution and properties of DIBs can also be studied in smaller fields-of-view (van Loon et al. 2009; Raimond et al. 2012; Puspitarini et al. 2015) or closer regions, such as the Local Bubble (Farhang et al. 2015; Bailey et al. 2016).

In the last decade it has also been firmly established that many band carriers are universal; DIBs have been detected and surveyed in the Magellanic Clouds (Cox et al. 2006, 2007; Welty et al. 2006; van Loon et al. 2013; Bailey et al. 2015), in M 31 and M 33 (Cordiner et al. 2008, 2011), and in individual sightlines in more distant galaxies (Junkkarinen et al. 2004; Sollerman et al. 2005; Lawton et al. 2008; Cox & Patat 2008, 2014; Monreal-Ibero et al. 2015). DIB carriers therefore constitute an important reservoir of (organic) material throughout the Universe.

Identifying the DIB carriers and understanding their properties must come from high-quality data in the nearby Galactic interstellar medium (ISM). Identification of the carrier species will directly impact our understanding of interstellar chemistry, and can help reconstruct 3D line-of-sight properties if

related to specific environments. It is clear that the ultimate confirmation must come from a direct comparison between astronomical, theoretical, and laboratory spectra over a broad wavelength range. A commonly applied and straightforward approach is to acquire laboratory spectra of possible candidate carriers taken under astrophysical relevant conditions until an unambiguous match with the astronomical data is found. With the notable exception of the above mentioned work on C₆₀⁺ previous studies have thus far failed, such as attempts to link PAH cations (Bréchnignac & Pino 1999; Salama et al. 2011, 1999; Romanini et al. 1999), neutral PAHs (Salama et al. 2011; Gredel et al. 2011), carbon chains (Motylewski et al. 2000; Maier et al. 2004), or H₂ (Sorokin & Glowina 1999; Ubachs 2014) to the DIBs. The search for a laboratory match can be optimised if the most likely candidates can be pre-selected out of the vast collection of possible species, and if the relevant conditions can be accurately constrained. Hence it is necessary to unravel the physical and chemical properties of the DIB carriers through analysis and modelling of observations. This includes deriving environmental conditions that affect their strength/profile shapes, as well as understanding the molecular physics and spectroscopy of candidate carriers.

This paper presents the observational overview of the ESO Diffuse Interstellar Bands Large Exploration Survey (EDIBLES) and how we intend to use the obtained spectra in our long-term goal of reverse-engineering the molecular characteristics of DIB carriers. In Sect. 2 we describe the scientific goals and immediate objectives of EDIBLES. Section 3 describes the methodology and survey design. The survey target selection is discussed in Sect. 4 and the data processing steps are described in Sect. 5. Section 6 discusses several confounding factors such as telluric and stellar spectral lines. In Sect. 7 we present a preview of the EDIBLES data and illustrate their scope and quality. A brief summary is given in Sect. 8.

2. Scientific goals and immediate objectives

The primary science goal of EDIBLES is to reverse-engineer molecular characteristics of DIB carriers, through studying the behaviour of DIBs in relation to the physical and chemical parameters of their environment. This approach differs from earlier work in which attempts to identify DIBs were based mainly on direct comparisons of astronomical and laboratory or theoretical spectra. A large systematic high-fidelity survey of the diffuse-to-translucent ISM is necessary to realise this approach.

The aim is to assemble a sample of interstellar spectra with sufficiently high spectral resolution and signal-to-noise ratio to allow detailed analysis of numerous DIBs and known atomic and molecular absorption lines in the same lines-of-sight. At the same time, our sample is designed to sample a wide range of interstellar conditions, in terms of reddening, molecular content and radiation field, within a practical observing time.

With EDIBLES we plan to compile the global properties of a large ensemble of both weak and strong DIBs, and variations therein, as a function of depletion (patterns) and local physical conditions. The new dataset should allow us to: (a) determine the relation between weak and strong DIBs by identifying correlations and sequences; (b) identify (sets of) DIBs that correlate with different physical conditions in the ISM, and assess whether the DIBs can be used to determine those conditions as a remote diagnostic tool; (c) study the physico-chemical parameters that influence the DIB properties, by using state-of-the-art chemical modelling, combined with extensive auxiliary line-of-sight data (e.g. on dust); and (d) constrain the chemical composition of the

DIB carriers by studying their relation to interstellar elemental abundances (depletion levels) and dust grain properties and composition derived from, for example, the UV-visual extinction (including the conspicuous 2175 Å UV bump) and optical polarisation curves.

A number of studies have attempted to investigate links between the physical and chemical conditions of the ISM and the properties of the DIBs. However, most studies focus only on a few strong bands in a moderate-to-large number (≈ 100) of sightlines (Friedman et al. 2011; Vos et al. 2011; Zasowski et al. 2015), or on many DIBs in just a few sightlines (Cami et al. 1997; Tuairisg et al. 2000; Hobbs et al. 2008, 2009). Hence, more recent progress in the field has been limited to the study of only a handful of the strongest DIBs due to high demands on the signal-to noise ratio (S/N), spectral resolution, the removal of stellar and telluric lines, and the lack of large, uniform data sets. EDIBLES is designed to fill this gap, making just such a large, uniform data set available and thus enabling a large and systematic study of the physical and chemical parameters that are expected to directly influence the formation efficiency and spectroscopic response of DIB carriers.

3. Methodology and survey design

EDIBLES provides the community with optical (~ 305 – 1042 nm) spectra at high spectral resolution ($R \sim 70\,000$ in the blue arm and $100\,000$ in the red arm) and high signal-to-noise (S/N; median value ~ 500 – 1000), for a statistically significant sample of interstellar sightlines. Many of the > 100 sightlines included in the survey already have auxiliary available ultraviolet, infrared and/or polarisation data on the dust and gas components.

Studies of DIBs typically report data such as equivalent width, central depth, profile shape and substructure identification. These cannot easily be compared between surveys due to differences in the instrumentation, data quality and analysis procedures – e.g. continuum normalisation and measurement of spectroscopic lines. Archival material comprises a heterogeneous sample of spectra with varying S/N, resolving power, and spectral coverage. To achieve the goals and objectives described above requires a large and homogeneous survey of UV/visible spectroscopic tracers across a broad spectral range, covering a broad variety of interstellar environments. From this self-consistent set of observations we can extract:

1. Accurate column density measurements (or upper limits) for the most important atomic and molecular species, across a wide spectral range. These can be used to assess the velocity structure of the line-of-sight (in particular to determine radial velocity differences between species; e.g. Bondar et al. 2007), derive depletion levels of metals, infer and compute physical conditions (within the limitations imposed by the current knowledge on interstellar processes), using diffuse cloud PDR models (Le Petit et al. 2006) or turbulent energy dissipation models (cf. Flower & Pineau des Forêts 2015; Godard et al. 2014; Bron 2014).

For the photo-chemistry and derivation of particle density, radiation fields, turbulent energy dissipation, the key transitions are those of CN $\lambda\lambda 3874, 7906$, CH $\lambda\lambda 3879, 4300$, and CH⁺ $\lambda\lambda 3958, 4232$ Å, together with H₂ (from archival UV spectroscopy). For example, rotational temperatures can be derived from bands of C₂ ($\lambda 8756$) and C₃ ($\lambda 4053$), and cosmic ray ionisation rates can be derived from OH⁺ abundances ($\lambda\lambda 3300$ – 3600 Å). CH measurements can be

used to estimate the H₂ column density (Danks et al. 1984; Weselak et al. 2004).

2. Accurate measurements of DIB profiles (asymmetries, wings, substructure) and variations therein. Substructure can be related to molecular properties/sizes of carrier species (Kerr et al. 1996; Ehrenfreund & Foing 1996; Huang & Oka 2015) with variations due to changes in the rotational temperature (Cami et al. 2004; Kaźmierczak et al. 2010b) or the presence of hot bands (Marshall et al. 2015).
3. Updated measurements of peak positions of weak (per unit reddening) diffuse bands along single cloud sightlines.
4. Measurements and cross-correlation of over 50 weak and strong bands along the most reddened sightlines ($E(B - V) > 0.4$ mag). Correlations between strong and weak bands might reveal additional information on groups (or families) of DIBs, but it should be noted that a strong correlation between DIBs is not a necessarily a guarantee that they have a common carrier (McCall et al. 2010; Krelowski et al. 2016).
5. Stacking analyses to search for molecules and/or DIBs which are too weak to be seen in individual spectra.
6. Firm detection limits or abundance constraints on specific molecular carriers for which laboratory spectra are obtained.
7. Variations in interstellar species due to the small-scale structure of the diffuse ISM (Cordiner et al. 2013; Smith et al. 2013).

To achieve our objectives efficiently we use the Ultraviolet Visual Echelle Spectrograph (UVES; Dekker et al. 2000; Smoker et al. 2009) mounted on the 8-m second Unit Telescope (UT2) of the ESO (European Southern Observatory) Very Large Telescope at the Paranal Observatory. The relative brightness of nearby early-type stars allows the observation strategy to take advantage of poor observing conditions and twilight hours that would otherwise be under-utilised. The programme is running as a Large “Filler” Programme (ESO ID 194.C-0833, PI. N. L. J. Cox), which has been allocated 280 h of observing time. About 8500 science exposures with a total exposure time of 229 h (with blue and red arm exposures taken simultaneously) have been collected between September 2014 and May 2017. The program is expected to be completed by late 2017.

UVES has two arms, red and blue, which can be used simultaneously by inserting a dichroic mirror (Dekker et al. 2000). To obtain coverage of the entire spectral range accessible with UVES, we use two instrumental settings per target: setting #1: 346+564 and setting #2: 437+860, where the pairs of numbers refer to the central wavelengths in nanometres of the two arms. Together this provides near-continuous wavelength coverage from ~ 305 to 1042 nm. The blue and red arm slit widths are $0.4''$ and $0.3''$, respectively, yielding nominal resolving powers $R = \lambda/\Delta\lambda$ of $\sim 71\,000$ and $\sim 107\,000$. Table 1 presents a summary of the instrumental setups. The EDIBLES data presented here were collected over a period of two years, and it is therefore important to realize that the UVES resolution is not fully stable with time¹, but the values listed in Table 1 were typically realised in the actual spectra.

The “filler”-type observation strategy means that observations are often executed in non-optimal (and unpredictable) conditions e.g. in terms of seeing, cloud coverage, sky emission/air glow, lunar phase, and water vapour content. This needs to be taken into account in the implementation of the observations. Despite these limitations, S/N ratios of 200–300 per exposure

¹ http://www.eso.org/observing/dfo/quality/UVES/reports/HEALTH/trend_report_ECH_RESOLUTION_DHC_HC.html

Table 1. UVES instrument setups used.

Setting (nm)	Arm	Slit width (")	Resolving power	Spectral range (nm)
346	blue	0.4	71 000	304.2–387.2
564	red-L	0.3	107 000	461.6–560.8
	red-U			566.9–665.3
437	blue	0.4	71 000	375.2–498.8
860	red-L	0.3	107 000	670.4–853.9
	red-U			866.0–1042.0

Notes. The two spectrograph arms are used to collect data for a pair of wavelength regions simultaneously. A second setup allows the gaps to be covered with another pair of settings. For each setting we give the slit width, nominal resolving power, and nominal wavelengths covered. Red-L and Red-U refer to the spectra recorded with the Red Lower EEV CCD and the Red Upper MIT CCD (cf. Sect. 5).

can be reached in short exposure times for the bright ($2 < V < 6$ mag) targets, and up to 20 exposures (to avoid saturation of individual frames) are obtained for each to build up higher S/N. Observations are divided into observing blocks (OBs) for a specific instrument setting and target. OB execution times range from ~ 20 min for the bright ($V < 6$ mag) stars up to ~ 45 min for the fainter ($6 < V < 9$) stars.

Additional flat-field calibration exposures were taken during the day-time (when possible, subject to operational constraints) to reduce residual fringing that would persist with the standard UVES calibration plan and to increase the overall S/N ratio. Details of the flat-field corrections are given in Sect. 5.

4. Target survey sample selection and characteristics

We constructed a statistically representative survey sample that probes a wide range of interstellar environment parameters including reddening $E(B - V)$, visual extinction A_V , total-to-selective extinction ratio R_V , and molecular hydrogen fraction f_{H_2} . This is essential to (a) trace depletion patterns from diffuse \rightarrow translucent clouds, (b) study the effect of shock- and photo-processing, (c) probe the behaviour of DIBs with respect to grain properties, and (d) identify unusual DIB environments.

During target selection the following factors were taken into account:

- Given that f_{H_2} depends non-linearly on A_V , due to the transition from atomic to molecular hydrogen driven by H_2 self-shielding, we require numerous sightlines probing $A_V \sim 1\text{--}3$ mag and below, in small increments ΔA_V .
- The dust grain properties and attenuation of UV photons (important for photo-chemistry) are constrained by the extinction curve, i.e. the A_V and R_V parametrisation (Valencic et al. 2004; Fitzpatrick & Massa 2007) or from fitting with a well-defined dust-PAH extinction model (Mulas et al. 2013).
- Preference is given to sightlines with auxiliary atomic/molecular data, such as HI and H_2 measurements (Jenkins 2009; Gudennavar et al. 2012), optical polarisation data (Whittet et al. 1992; Weitenbeck 2008), or Mg/Fe abundances (Voshchinnikov et al. 2012).

Where two targets with similar interstellar conditions are available, we preferentially selected targets which are brighter and/or of earlier spectral type.

The target list is given in Table A.1 (their Galactic distribution is shown in Fig. 1). Columns (1) to (3) provide basic information on the target id (HD number) and coordinates (RA/Dec). Columns (4) and (5) list the spectral type and corresponding literature reference. The interstellar line-of-sight dust extinction properties, $E(B - V)$, R_V , A_V , are given in Cols. (6) to (9). Columns (10) and (11) list the atomic and molecular hydrogen abundances with the molecular fraction f_{H_2} listed in Col. (12).

The total number of selected targets amounts to 114 (of which 96 have been observed at least once as of May 2017) and comprises mostly bright O and B stars ($V \approx 2\text{--}7$ mag with a small fraction $7 < V < 9$ mag). The sample probes a wide range of interstellar dust extinction properties ($E(B - V) \sim 0\text{--}2$ mag; $R_V \sim 2\text{--}6$; $A_V \sim 0.1\text{--}4.5$ mag) and molecular content ($f_{\text{H}_2} \sim 0.0\text{--}0.8$). The histograms in Fig. 2 illustrate the range of parameters included in the survey sample. In Fig. 3 we show comparisons between visual extinction, A_V , and the measured neutral hydrogen column density $N(\text{HI})$, molecular hydrogen column density $N(\text{H}_2)$, and total hydrogen column density $N(\text{H}_{\text{tot}}) (=N(\text{HI})+2N(\text{H}_2))$. As noted above H_2 can be estimated using the CH transitions (Danks et al. 1984; Weselak et al. 2004).

5. Data processing

Acquiring high-S/N spectra with UVES is challenging in the context of EDIBLES for a number of reasons. For example, small errors in the wavelength calibration at the edges of individual adjacent orders can cause the appearance of ripples in the continuum in high-S/N exposures. Moreover, the unpredictable seeing and other observing conditions inherent in a filler programme mean that individual exposure times cannot be optimised for the actual sky conditions.

The overall quality of all 8500 science and ~ 1600 flat exposures was checked visually. This visual inspection led us to discard about 150 exposures that appeared corrupted. This could, for example, be due to sudden changes in weather conditions or premature termination of exposures. In addition, we carefully inspected for the presence of incorrect thorium-argon lamp, format-check, and flat field exposures that could result in faulty order tracing or wavelength calibration solutions (see also below).

Within a sequence of observations (20–40 min including overheads) the change in barycentric velocity correction is small ($< 0.1 \text{ km s}^{-1}$ per hour) so the spectra can be averaged without compromising the velocity precision. However, exposures taken on different nights were not averaged. This is to preserve multi-epoch information – specifically for spectroscopic binaries and the search for time-variable interstellar absorption – and to avoid addition of misaligned interstellar features due to variations in the barycentric velocity of the frame of the observer.

The data reduction was performed by two semi-independent teams, one using version 5.7.0 of the UVES pipeline (Ballester et al. 2000), esorex (version 3.12; ESO CPL Development Team 2015) integrated in a Python pipeline (hereafter Reduction “A”), and the other using the 4.4.8 version of the UVES pipeline (Reduction “B”).

Each set of around 20 science frames was processed with the same set of calibration frames. For the format check, order definition and wavelength calibrations these were the nearest in time, with the master bias and master flats using frames taken typically over several days or weeks. In general, both data reductions used similar parameters for the different pipeline recipes, but with a

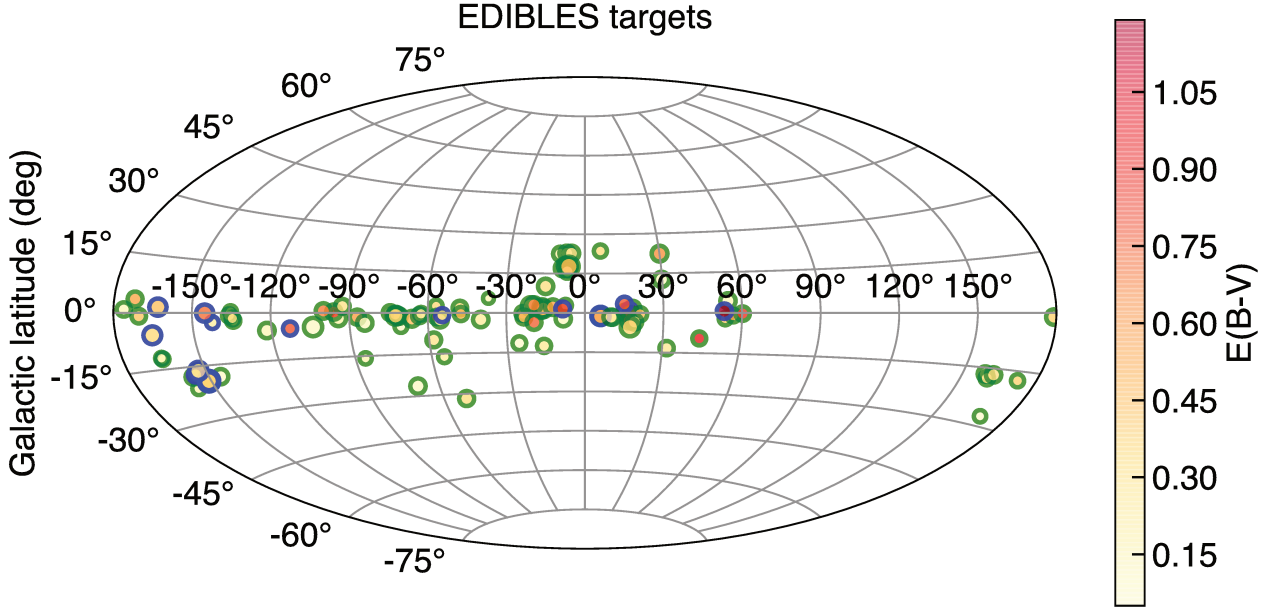


Fig. 1. Galactic distribution of EDIBLES targets. The symbol size reflects the value of R_V , while the interior colour represents the line-of-sight reddening, $E(B - V)$. Symbols with green edges represent the observed targets, while blue edges correspond to the targets to be observed by the end of the programme.

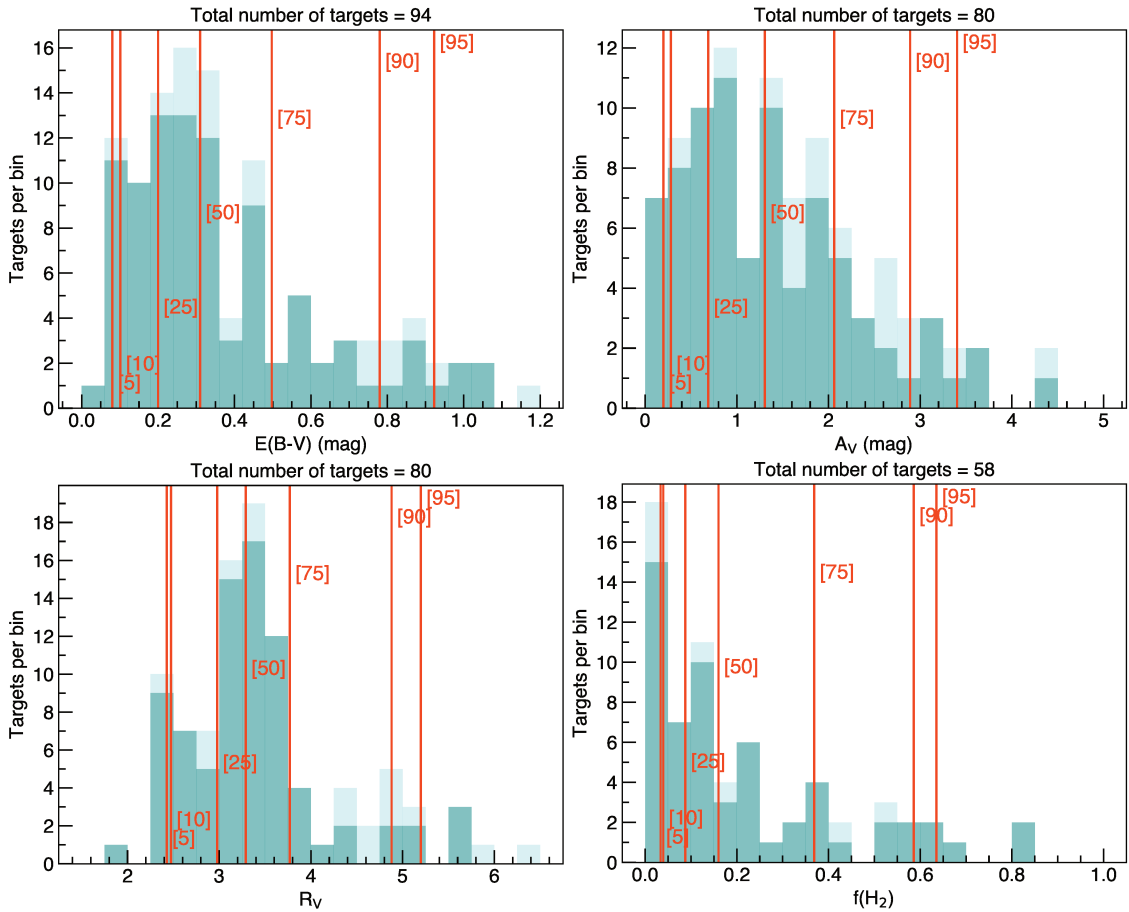


Fig. 2. Number of selected targets as function of reddening $E(B - V)$, extinction A_V , the ratio of total-to-selective extinction $R_V (=A_V/E(B - V))$, and the fraction of molecular hydrogen f_{H_2} for the target sample. The number of observed targets with reported values for each quantity are given at the top of each panel. The dark blue and light blue distributions correspond to the samples of observed and observed + foreseen targets. The vertical red lines indicate the value of the 5, 10, 25, 50, 75, 90, and 95 percentiles of each sample. The labels are located such that they trace the cumulative target distribution.

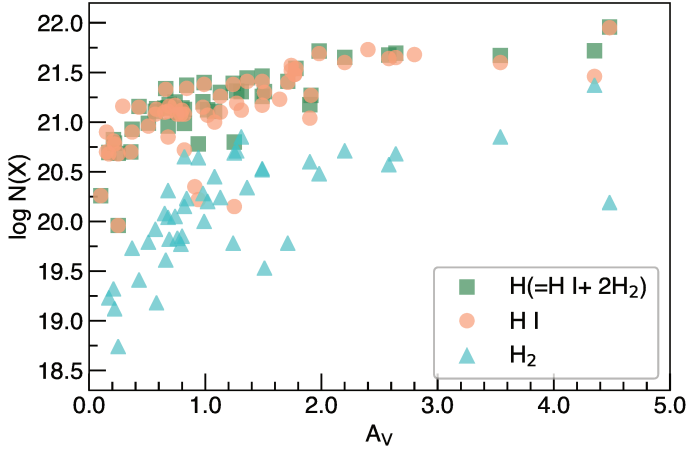


Fig. 3. Relation between visual extinction, A_V , and neutral hydrogen column density $N(\text{H I})$, molecular hydrogen column density $N(\text{H}_2)$, and total hydrogen column density $N(\text{H}_{\text{tot}})$, computed as $N(\text{H I}) + 2N(\text{H}_2)$. Note that some EDIBLES lines-of-sight are not included since no direct H I or H_2 measurements are available.

few differences. Reduction “A” adopts optimal merging, applies the blaze correction and uses about 100–130 flats for each arm, while reduction “B” uses optimal merging and takes the nearest 140 flat field frames.

In the following we provide a detailed description of the different data processing steps and discuss their impact on the quality of the reduced spectra. The differences between reductions “A” and “B” are discussed in relation to the blaze correction and order merging step.

Bias. To subtract the CCD bias level in science frames, we created a master bias frame by median-stacking a set of 50 (reduction “A”) or 25 (reduction “B”) bias exposures, using the `uves_cal_mbias` recipe. To handle the bad columns in the REDL CCD, by default the recipe interpolates across bad pixels but does not apply this interpolation in science frames. This inconsistency creates boxy emission-like artifacts in the reduced spectra. To avoid this from occurring, high-quality bias frames are carefully pre-selected and the data are processed without interpolating over bad pixels.

Order definition. In order to find the physical position of echelle orders in the X and Y directions of spectral frames for a given instrument setting, `esorex` uses a physical model based on the instrument configuration, ambient pressure, the humidity, slit width, central wavelength, camera temperature and CCD rotation angle. The physical model then predicts the X and Y pixel position corresponding to the nominal orders and stores the calculations into the guess line and order tables. These tables are then normally used as the initial values for identifying the specific positions of the orders.

To accurately detect the order positions, `esorex` defines a search box on the detected lines in the arc lamp frames and tries to match the predicted position of the physical model lines. The following procedure robustly detects the order positions:

1. measure the raw X and Y pixel positions of the thorium-argon lines on an arc frame exposure by defining a $60 \times 60 \text{ pix}^2$ square search box;
2. compute the difference of predicted and detected order positions;

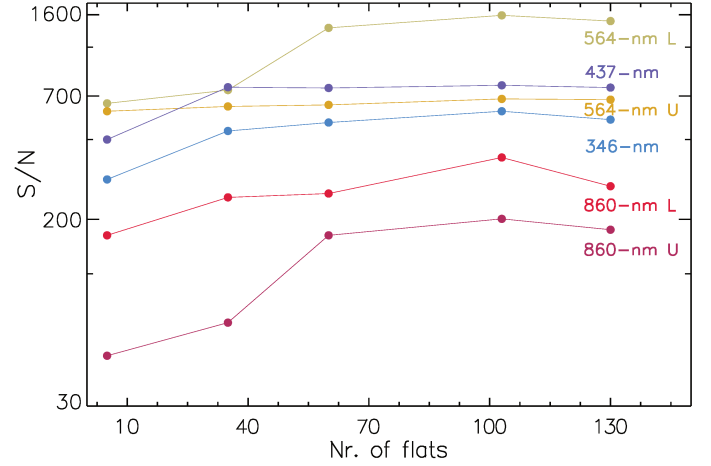


Fig. 4. Comparison of the S/N of HD 23180 with changing number of flat frames. The S/N ratios plotted for each instrument setting are average values of S/N measured in five different continuum regions in the respective setting.

3. decrease the size of the search box to $40 \times 40 \text{ pix}^2$, iterate the X and Y shifts to search for residuals less than ± 1 pixel and to reduce the root-mean-square (rms) values;
4. fit a 2D Gaussian function to XY pixel positions within a “fit box” centred at the predicted line positions;
5. for reduction “B” additional iterations of the `format check` are done using different values of the CCD rotation offset, selecting the one with the maximum number of lines found;
6. and, finally, perform a 2D second-order polynomial fit in XY to the fitted line positions.

The highlighted values in the above steps are our tuned parameters in the `uves_cal_predict` recipe.

Flat fielding. The flat-fielding is applied, to the 2D frame, before the order extraction (see below). This is known as the pixel flat-fielding method. The standard UVES pipeline uses only five flat field frames, which limits the maximum S/N. To demonstrate the necessity for accurate flat-fielding to reach the required S/N ratio, we reduced 11 science frames of HD 23180 using a different number of flat field frames to build the master flat frame. As shown in Fig. 4, increasing the number of flat fields helps to increase the final S/N. More than 100 flat field frames do not cause the S/N to increase further, indicating that flat fielding is no longer the limiting factor on the S/N. In the case of the 860-nm setting the S/N drops between 100 and 130 applied flats due to the presence of several bad-quality flat frame exposures. For the final reduction these were rejected and we selected as many as possible, usually about 100, good quality flat frames. By using the additional flat fields, we were able to improve the final S/N by factors of two to five, depending on the wavelength.

Note that the intensity (photon counts) of normal flats are very low in the UV ($< 320 \text{ nm}$). Therefore, to improve the quality of the first-orders of the 346-nm arm spectra, a final master flat is constructed by combining a set of normal flats with flats obtained by exposing with a deuterium calibration lamp. The merging was done at orders 145 and 146 around 321 nm with the master deuterium-lamp flat being used bluewards of this and the normal flat redwards. This is to avoid as much as possible spurious absorption-line features in the final science spectrum

Table 2. Wavelength calibration uncertainties for the thorium-argon frames corresponding each of the observed UVES settings for HD 23180.

Arm	Uncertainty (\AA)	Uncertainty (m s^{-1})
346-nm	6.4×10^{-4}	52
437-nm	7.8×10^{-4}	54
564-nm L	4.5×10^{-4}	26
564-nm U	7.0×10^{-4}	34
860-nm L	8.3×10^{-4}	33
860-nm U	1.1×10^{-3}	36

caused by emission features in the deuterium lamp redwards of 321 nm.

Order extraction. Various possible extraction methods were tested and we find that the *average* extraction method with performing a flat fielding before the extraction (see above) leads to a higher S/N with respect to other methods (such as optimal extraction), which is generally the case for high S/N spectroscopy. This method also reduces the fringing seen in the red wavelengths ≥ 700 nm, although does not entirely remove it. Figure 5 shows that displays parts of an extracted science spectrum near the gap between the upper and lower CCDs. The fringing is much worse in the lower thinned EEV chip than in the upper MIT thick chip (Smoker et al. 2009).

Cosmic ray rejection and hot pixels. To remove the cosmic rays and possible hot pixels we applied a sigma-clipping method to each extracted spectrum. The default sigma-clipping threshold value in *esorex* is $\kappa = 10$, but to identify all induced hot pixels we set this $\kappa = 6$ to be sure that all cosmic/hot pixels are removed and no real data are clipped.

Wavelength calibration. UVES wavelength calibration errors are typically in the range of $0.1\text{--}0.5 \text{ km s}^{-1}$ (Whitmore et al. 2010). To achieve an accurate wavelength calibration, the dispersion relation is obtained by extracting the thorium-argon arc lamp frames using the same weights as those used for the science objects. Therefore, first we reduced the science frames with an optimal extraction method to generate a pixel weight map. Then by applying this weight map to the wavelength calibration, an accurate wavelength calibration with a statistical error less than $5 \times 10^{-4} \text{ \AA}$ typically in all central wavelengths (for more details see Table 2) and a systematic uncertainty less than $1.7 \times 10^{-4} \text{ \AA}$ is achieved. To optimize the number of lines used in the wavelength calibration solution we tested a tolerance value ≈ 0.07 pixels to reject the line identification with wavelength residuals worse than the tolerance. For the final iterations of the fit of the wavelength calibration solutions we set the sigma-clipping to $\kappa = 3$. Further improvements to the wavelength calibration are being studied for the public release of the data. For example, there is a temperature and density dependent shift (which can be as much as 1 pixel and different for the different wavelength regions) in the position of the thorium-argon lines (UVES User Manual). This can be potentially corrected by taking into account the difference between the observation and calibration temperatures and pressures. Also, we foresee improvements to the final wavelength calibration in the 860 nm Red-U arm, where

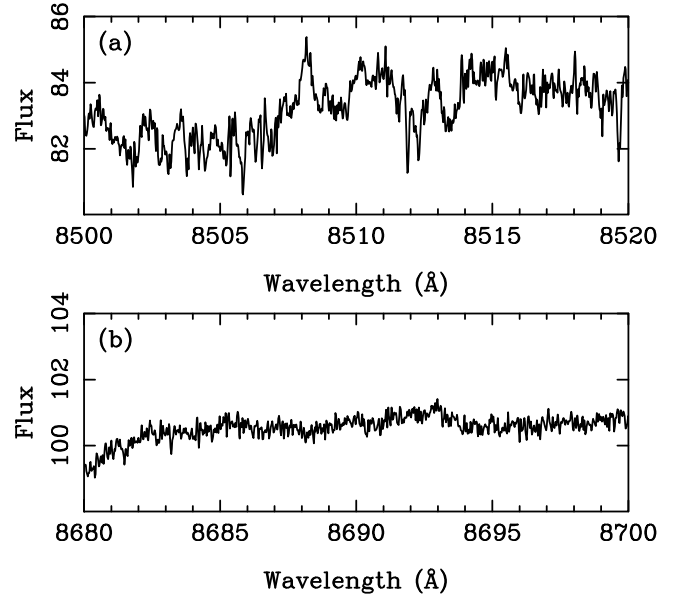


Fig. 5. *a)* Part of the extracted spectrum of HD 23180 taken using the Red Lower EEV CCD (Red-L). *b)* Ditto but for Red Upper MIT CCD (Red-U). The latter is a thick chip so fringing is much reduced compared with the EEV detector. The vertical scale is the same in both cases.

there are few thorium-argon lines, by cross-referencing with a model telluric transmission spectrum.

Blaze function and order merging. Previous analyses of data obtained with UVES demonstrate that the shape and position of the blaze function is the primary source of problems in the order overlap regions. The continuum changes vary smoothly over subsequent orders, which may be related to the fact that the blaze profiles produced by UVES are not the same as the theoretical predictions. Accordingly, the blaze function at the overlapping regions is not sufficiently well characterised, therefore by averaging the overlap regions some artificial features appear and cause the signal level to fall off at the end of the orders. Irregular variations in the continua at the edges of orders are likely due to a mismatch between the paths of the light from the star and the flat-field lamp (Nissen 2008) and result in discontinuities where orders have been merged.

For reduction “B”, no blaze correction was performed. Optimal merging provided the best results in the overlapping regions for both reductions “A” and “B”. Figure 6 shows a comparison of reductions “A” and “B” for HD 23180 in a spectral region with two overlapping orders. Reduction “B” reveals a mismatch of the order-overlapping regions, resulting in a jump in the spectra at 5855 \AA not present in the reduction “A” spectrum.

Quality control. The S/N of the spectra as a function of wavelength was estimated by fitting a first order polynomial to regions of the spectra in bins of 1 \AA and measuring the residual in each 0.02 \AA wavelength bin. Table 3 lists the median S/N (per 2-pixel “resolution-element”) for each setting, together with the respective continuum wavelength regions. In Fig. 7 we compare for HD 184915 the spectra obtained with the dedicated EDIBLES processing presented here and the default archive data products

Table 3. Median S/N per “resolution-element” (0.04 Å spectral bin) for each UVES setting/arm configuration for all available EDIBLES spectra.

Setting	Arm	λ -range (nm)	Median S/N (0.04 Å bin)	Sample size
346	blue	339.3–339.4	780 ^a	204
437	blue	398.8–398.9	1070 ^a	187
564	red-L	511.0–511.1	1090 ^b	205
	red-U	613.1–613.2	1020 ^b	205
860	red-L	675.35–6754.55	670 ^b	184
	red-U	869.9–870.0	880 ^b	183

Notes. ^(a) Reduction “A”. ^(b) Reduction “B”.

(ADP) provided by ESO². The increase in S/N (labelled in the figure) is almost a factor two for both the Red-L and Red-U spectra (cf. Table 1). For each target the different settings/arms generally have different S/N ratios. This is primarily due to (1) the choice of targets which are often brighter in *V* band compared to *B* band (i.e. reddening), and (2) the lower efficiency of UVES in the very blue and very red parts of the accessible wavelength range. In terms of S/N reduction “A” performs slightly better than reduction “B” for the 346-nm setting, both perform similar for the 437-nm and 860-nm settings, while reduction “B” performs better for the 564-nm setting. The main difference between the two reductions is in terms of the order-merging jumps. In addition, there are small, though noticeable differences in the “noise” between both reductions. The reduction scheme “A” is adopted as the primary scheme for results shown in this work. Both reductions are therefore retained for reference and as a control for spurious features.

As an example, the final continuum normalised EDIBLES UVES spectrum of HD 170740 (from reduction “A”) is shown in full in Fig. 8, where each panel corresponds to one of the instrument settings (Table 1). A closer view of this spectrum is shown in Appendix B. All processed EDIBLES spectra will be released as new “Phase 3” data to the ESO archive later in the project.

6. Telluric and stellar features

6.1. Earth transmission spectrum

A large number of weak and strong telluric oxygen and water absorption bands arise from molecules present in the Earth atmosphere covering nearly the full DIB range. In addition, for the near-UV spectral domain (300–350 nm) a correction for atmospheric ozone needs to be applied.

These telluric lines can be removed or modelled by using bright, early-type star spectra recorded in the same conditions as the targets, or by using synthetic atmospheric transmittance spectra. The former method requires observing (unreddened) standard stars at roughly similar airmass, shortly before or after the primary science target observations. This procedure is not possible within the filler observation strategy, and as the EDIBLES targets are themselves bright this would double

² These spectra are generated by ESO’s Quality Control Group for all UVES point-source observations. The pipeline processing is done automatically through a dedicated workflow (with no fine-tuning of pipeline parameters specific to the needs of our programme). The 1d-extracted spectra are ingested into the ESO archive as so-called “Phase 3” data products.

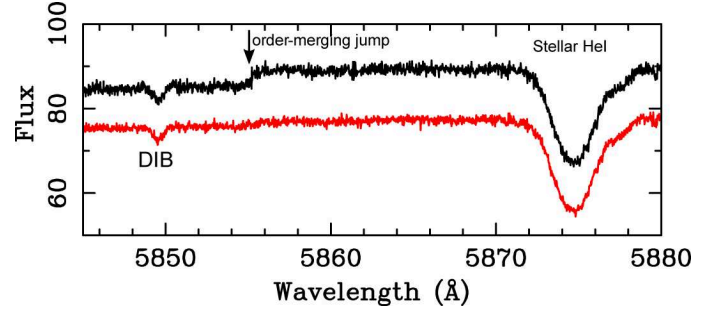


Fig. 6. Close-up view of a region including two overlapping orders in the 564-nm setting for HD 23180 for both reduction “A” (bottom red trace) and reduction “B” (top black trace). The small jump in the continuum at approximately 5855 Å seen in reduction B (top black trace) is due to imperfect merging of two echelle orders. The apparent difference in S/N is due to alternative choices of wavelength sampling.

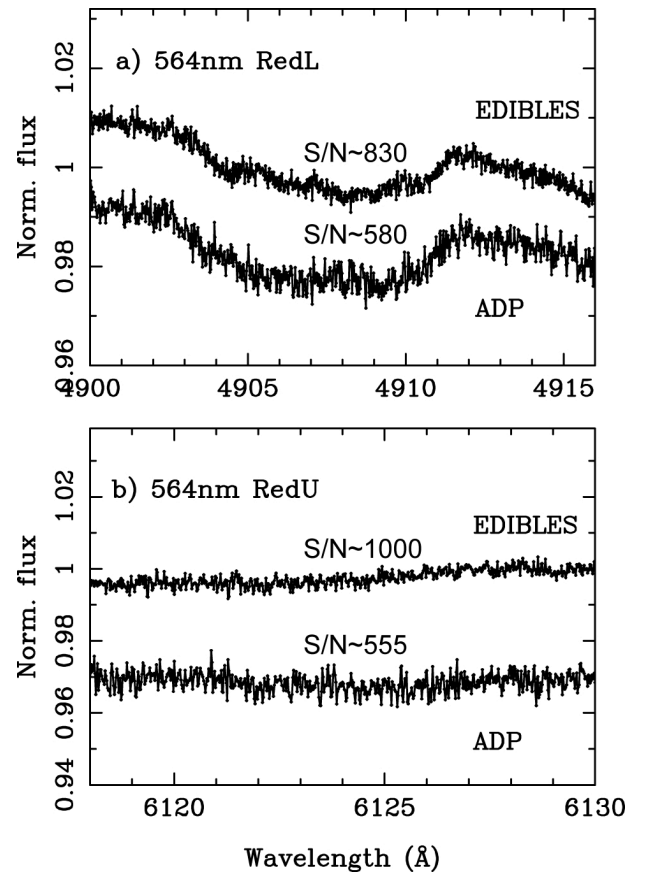


Fig. 7. Comparison between the ADP and EDIBLES processing of HD 184915 spectra (0.02 Å binsize). The S/N measurements, taken at 4912–4913 Å and 6129–6130 Å for the Red-L and Red-U spectra, are given in the *top* and *bottom* panels. Resampling to 0.04 Å binsize (i.e. corresponding to the spectral resolution) further increases the S/N by factor $\sqrt{2}$.

the required observing time. The latter method has the advantage of saving observing time, avoiding features associated with the standard star and benefits from the increase in quality and availability of the molecular databases. The first tests of atmospheric spectra correction were performed based on the following approach.

First, the telluric transmittance is optimally adapted to each target. Paranal observing conditions are downloaded from the

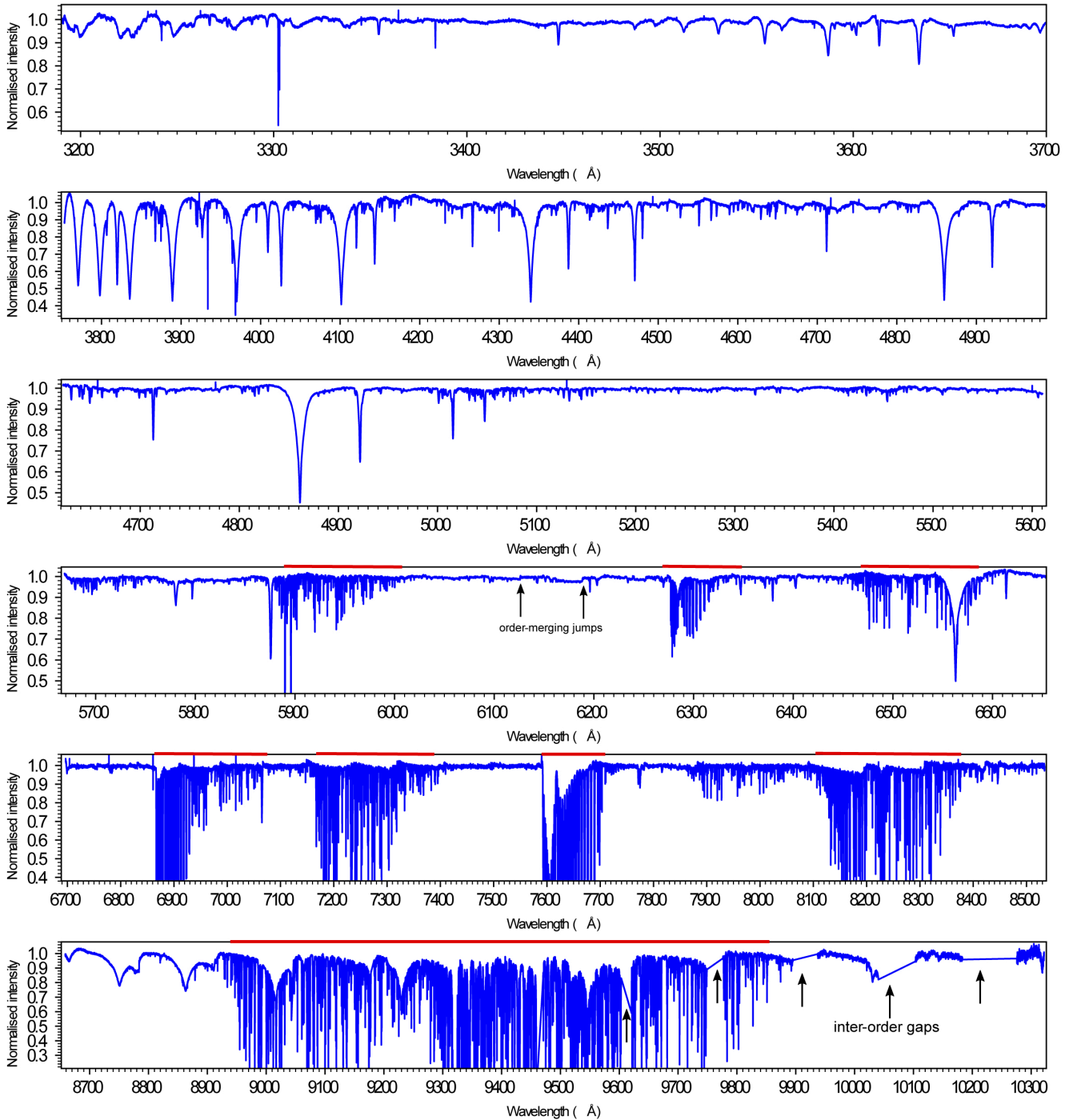


Fig. 8. EDIBLES UVES spectra of HD 170740 (B2 V) for each setting *from top to bottom*: 346B, 437B, 564L, 564U, 860L, 860U. This overview figure is a demonstration of the data quality. The main gaps in wavelength coverage are between 5610–5670 Å and 8530–8680 Å which correspond to the physical separation of the Red-L and Red-U detectors in both the 564 and 860-nm settings. Note also the inter-order gaps, several are indicated with arrows, in the 860-nm Red-U spectrum above ~ 9600 Å as well as several conspicuous regions containing bands of closely-spaced telluric absorption lines (indicated with red horizontal bars) mostly in the Red-L and Red-U 860-nm spectra (*bottom two panels*). Two order-merging jumps are indicated in the *fourth panel*. A more detailed version of this figure is shown in Fig. B.1 where specific interstellar species are labeled and a synthetic DIB spectrum is shown for comparison.

TAPAS facility³ (Bertaux et al. 2014). The TAPAS transmittance spectra are based on the latest HITRAN molecular database (Rothman et al. 2013), radiative transfer computations (Line-By-Line Radiative Transfer Model; Clough & Iacono 1995), and are computed for atmospheric temperature, pressure and

composition interpolated by the ETHER data centre⁴ based on a combination meteorological field observations and other information.

Then, in regions of moderate absorption (i.e. less than 70% at line centers before instrumental broadening), a simple method

³ <http://ether.ipsl.jussieu.fr/tapas/>

⁴ www.pole-ether.fr

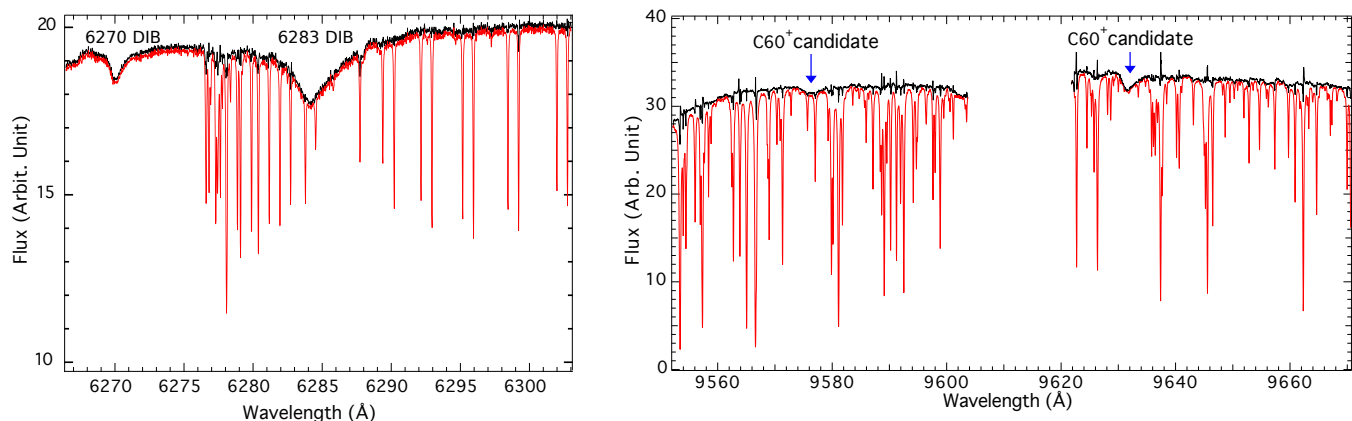


Fig. 9. *Left:* example of telluric line correction in the weak line regime by means of the *rope-length* method applied to the spectrum of HD 170740. Telluric lines of O_2 are corrected first, then H_2O lines. *Right:* example of telluric line correction in the strong line regime by means of a two-step method and a composite instrumental profile adjustment (see text). Residuals remain at the location of the deepest lines, especially when the model does not predict their shape and exact Doppler shift very accurately. The positions of the 9577 and 9632 Å DIBs attributed to C_{60}^+ are indicated.

called *rope-length* minimization is used (Raimond et al. 2012). Briefly, the algorithm searches for the minimal length of the spectrum that is obtained after division of the data by the transmittance model. To do so the column of the absorbing species, the Doppler shift and the width of the instrumental function by which the transmittance model is convolved are all tuned. The method uses the fact that when the telluric lines are not well reproduced, strong maxima and minima remain after the data-model division and the spectrum length increases. On the contrary, if the modelled lines follow very well the observed ones, the corrected spectrum is smooth. An example of correction is shown in Fig. 9 for the 6284 Å DIB. Here the *rope-length* method has been first applied to the O_2 lines, then in a subsequent step the O_2 -corrected spectrum is corrected for the weak H_2O lines that are also present in this spectral region.

For regions of stronger telluric lines, division by deep lines induces overshoot and the exact shape of the telluric profiles and of the instrumental function becomes crucial. The simple *rope-length* method alone is no longer appropriate. We have tested an iterative method that is a combination of the *rope-length* method and a classical fitting. In a first step we excluded all spectral intervals around the centres of the deep lines and performed a *segmented rope-length* optimization, i.e. the algorithm searches for the model parameters that minimize the sum of the lengths of the individual spectral segments. We then divided the data by the corresponding adjusted model and performed a running average of the divided spectrum to obtain an approximate stellar continuum. We then fitted the data to the convolved product of this continuum and a telluric transmittance. The instrumental function is now modelled as the sum of a Gaussian and a Lorentzian, which allows weak extended wings to be taken into account. The instrumental profile is the same for all lines within the corrected interval. The parameters defining these two components as well as the column of the absorbing species are free to vary during the adjustment. The data were then divided by this updated model. This process can be iterated and stopped when there is no longer any decrease of the “*rope-length*”. An example of such a two-step correction is shown in Fig. 9 for the spectral region of the C_{60}^+ 9577 and 9632 Å DIBs. There are still some residuals, but these are limited mostly to the deepest, (partially) saturated telluric lines. This occurs particularly when these lines are slightly Doppler shifted or broadened due to atmospheric pressure in a way that is not fully predicted by the model. For a description

of such effects see Bertaux et al. (2014). Nevertheless, the DIBs at 9577 and 9632 Å, assigned to be due to C_{60}^+ as mentioned in the introduction, stand out clearly in the telluric corrected spectrum. The three weaker DIBs between 9350 and 9450 Å reported by Walker et al. (2015), though not yet confirmed independently (Galazutdinov et al. 2017; Cordiner et al. 2017) present significant challenges for detection due to the presence of strong, saturated telluric water lines in this spectral range. We intend to investigate the C_{60}^+ bands in more detail later in the EDIBLES project, but this will depend upon the accuracy and success of the telluric line modelling for each line-of-sight (as there are numerous saturated atmospheric water absorption lines in this wavelength region) as well as the stellar atmosphere modelling required to account for, for example, contribution of Mg II (as discussed in Galazutdinov et al. 2017).

6.2. Stellar spectra

In addition to the goals discussed above, the EDIBLES observations provide high-quality spectra of the target stars themselves. These span the full spectral range of early-type stars, from early O-type dwarfs through to late B-type supergiants (plus a couple of later/cooler stars). Published spectral classifications of the sample are summarised in Tables A.1 and A.2.

All of the O-type EDIBLES targets have been observed as part of the Galactic O-Star Spectroscopic Survey (GOSSS), a comprehensive survey of bright Galactic O stars at a resolving power of $R \sim 2500$ (Sota et al. 2011, 2014). The detailed O-star classifications quoted in Tables A.1 and A.2 are the GOSSS types – a thorough description of the classification criteria was given by Sota et al. (2011), including an overview of the various classification qualifiers used to convey additional information on the spectra (their Table 3).

In contrast, most of the B-type stars in the EDIBLES sample have not been subject to such morphological rigour with high-quality digital spectroscopy. Work is underway within the GOSSS to better define spectral standards and the classification framework for early B-type stars (Villaseñor et al., in prep.), with a few stars overlapping with the EDIBLES sample. Nonetheless, the high-quality, high-resolution spectra from EDIBLES will be useful to refine the classification framework for B-type stars, particularly compared to similar efforts in the Magellanic Clouds (e.g. Evans et al. 2015).

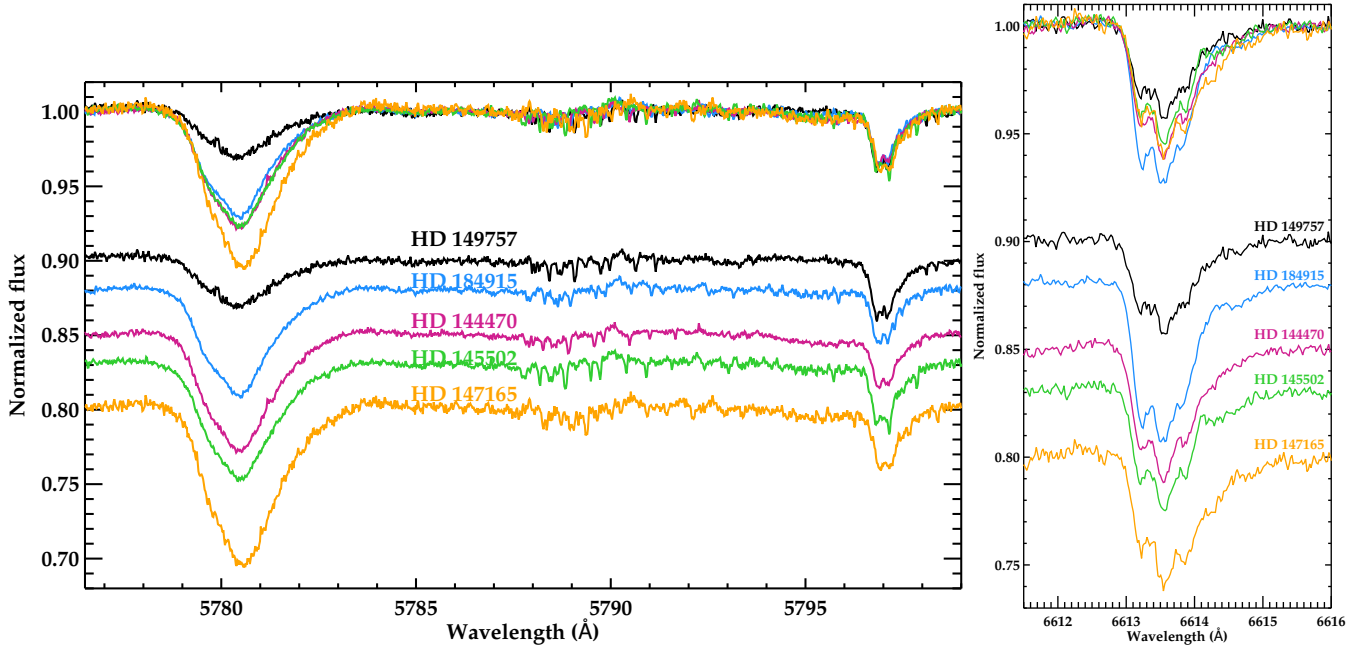


Fig. 10. An illustration of the quality of the spectra for the 5780 and 5797 Å (*left*) and 6614 Å (*right*) DIBs. For each target all observed spectra were co-added in the heliocentric reference frame. The five targets shown have comparable $E(B - V)$ values (Tables A.1 and A.2), and thus have similar 5797 Å DIB strengths. The well established, strongly variable 5780/5797 ratio can be seen in the spectra, with the intensity of 5780 absorption inversely related to the molecular gas fraction, f_{H_2} (Tables A.1 and A.2). The five spectra are shown superimposed on each other at the top of the panels. Note that because of generally poor observing conditions there are numerous weak and narrow atmospheric water features present (particularly noticeable around 5788–5792 Å) that could influence the 5797 Å profile. In the future these features will be removed using the method described in Sect. 6.

In the short-term we will inspect the EDIBLES data in the context of classification, to update/refine spectral types as required – whether arising from the added information of the high-resolution UVES data (cf. lower-resolution spectroscopy from the GOSSS, for example), or simply from intrinsic spectral variability, which is seen in many early-type stars. This will ensure the best parameters are adopted in estimating stellar colours, thence the line-of-sight extinctions. We will also look for evidence of spectroscopic binaries in targets with multiple observations (and/or relevant archival data, see, e.g., Sect. 7.4). Our longer-term objective is a quantitative analysis of the stellar spectra to determine their physical parameters (effective temperature, gravities, rotational velocities, mass-loss rates etc.), employing tools developed specifically for the analysis of early-type spectra (e.g. Mokiem et al. 2005; Simón-Díaz et al. 2011). Ultimately this will help removal of stellar features from the EDIBLES spectra to aid analysis of the interstellar features.

7. Quality assessment: the interstellar spectrum

In this section we highlight the interstellar lines and bands observed for a few selected lines-of-sight.

7.1. EDIBLES

As noted above, the full spectrum of HD 170740 is shown as an example in Figs. 8 and B.1. For initial guidance in identifying the DIBs in this line-of-sight the average ISM DIB spectrum (Jenniskens & Désert 1994), scaled to $E(B - V) = 0.5$ mag, is shown in the latter figure. This reference spectrum includes broad DIBs not included in e.g. Hobbs et al. (2009) but which appear to be present in the observed spectrum.

In Fig. 10 we compare the three strong DIBs at 5780, 5797 Å (Heger 1922; Merrill & Wilson 1938) and 6614 Å for single-cloud lines-of-sight towards five EDIBLES targets, HD 149757, HD 184915, HD 144470, HD 145502, and HD 147165. The line of sight reddening, $E(B - V)$, for these sightlines differs by less than 0.17 mag (cf. Table A.1). The spectra are averages of individual exposures co-added in the heliocentric rest frame and subsequently continuum normalised (but not otherwise scaled other than to offset them in the figure).

As expected, for sightlines with such small variations in reddening, the 5797 Å DIB profiles have similar central depths (insensitive to f_{H_2} ; Cami et al. 1997). The large variations in the strength of the 5780 Å DIB are thought to be related to variations in the local interstellar conditions. The sightline with the weakest 5780 Å DIB is more neutral as indicated by the large molecular fraction, whereas the sightline with the strongest 5780 Å DIB has the highest atomic column density. However, while the 6614 Å DIB of the former is also the weakest, the latter does not exhibit the strongest 6614 Å DIB, thus indicating that additional parameters must play a role in determining the DIB carrier column density.

7.2. EDIBLES versus CES

High-resolution ($R = 220\,000$) spectra of the 6614 Å band have been recorded using the Coude Échelle Spectrograph (CES) fed by the fibre link with the Cassegrain focus of the 3.6 m telescope at La Silla Observatory (Galazutdinov et al. 2002). A signal-to-noise of ~ 600 – 1000 was achieved. Comparison of the EDIBLES and CES data is shown in Fig. 11 for HD 184915, HD 144470 and HD 145502 and the main features are in good agreement. Of the three principal absorption components, the

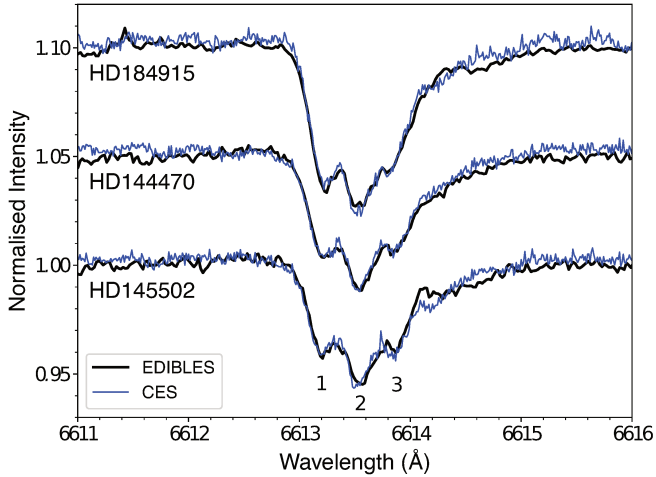


Fig. 11. Comparison of the 6614 Å DIB for HD 184915, HD 144470, and HD 145502 obtained with EDIBLES (black solid line; this work, $R \sim 110\,000$) and the CES (blue solid line; Galazutdinov et al. 2002; $R \sim 220\,000$). The sub-structure components 1, 2, and 3 are labelled in the bottom trace (see text).

shortest wavelength feature (component 1) is relatively strong for HD 184915 in both studies, whereas components 1 and 3 have comparable intensities for the lines-of-sight towards HD 144470 and HD 145502. No significant additional structure is evident in the higher resolution CES spectra.

7.3. EDIBLES versus AAT

To assess the quality of our spectra with respect to previous studies, we compared our EDIBLES spectrum of HD147888 (obtained in a single exposure on 2016-08-08) with a spectrum obtained using the Anglo-Australian Telescope (AAT) in June 2004 by Cordiner et al. (2013). The AAT spectra were obtained using the UCLES instrument at a resolving power of 58 000 and have $S/N \sim 900$. Cordiner et al. (2013) reduced their data using a custom procedure, taking special care to optimally correct for CCD non-linearity, scattered light subtraction and flat fielding, as well as wavelength calibration. A comparison between the EDIBLES and AAT spectra is shown in Fig. 12 for the 6614 Å DIB, which makes for a good general test case due to the presence of narrow and broad features within its profile. Apart from differences in the wavelengths of the telluric features, and a slight difference in the overall spectral slope (presumably due to uncorrected differences between the UVES and UCLES blaze functions), the spectra are almost identical within the noise. Slight differences in the depths and widths of the substructure peaks are attributable to the higher resolution of the UVES spectrum. The overall excellent match demonstrates the quality of our EDIBLES reduction procedure. For reference we show also the ADP spectrum, which uses only 5 flat-field frames; the large increase in S/N when using our custom flat-field processing is apparent.

7.4. EDIBLES versus UVES POP

To further illustrate the quality of the data we compared spectra of two targets, HD 148937 (Fig. 13) and HD 169454 (Fig. 14), which were both observed as part of the EDIBLES survey and the UVES Paranal Observatory Project (POP; Bagnulo et al. 2003). The UVES POP programme gathered a library of high-resolution, high S/N spectra of (field) stars across the

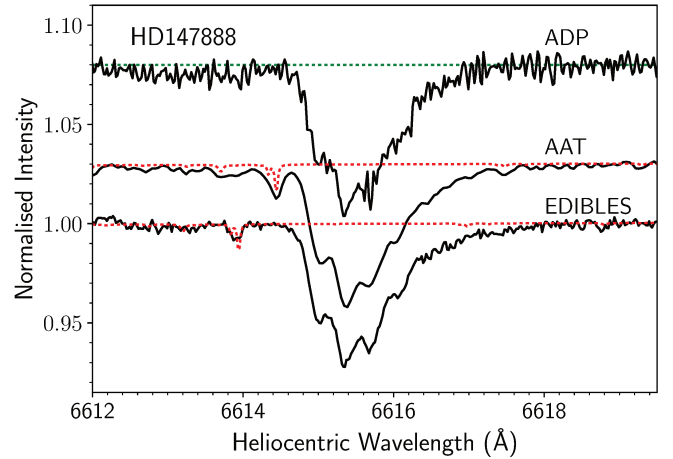


Fig. 12. Comparison of the 6614 Å DIB for HD 147888 (ρ Oph D) obtained with EDIBLES (this work, $R \sim 110\,000$) and the AAT (Cordiner et al. 2013, $R \sim 58\,000$). The top spectrum labeled “ADP” is the spectrum obtained with the standard ESO archive pipeline processing (i.e. using the default number of 5 flat-field frames). The red dotted line represents the telluric absorption spectrum, shifted to match the heliocentric rest frame of each target; highlighting the presence of a small telluric absorption feature at 6614/6614.5 Å.

Hertzsprung-Russell diagram. The spectra in the figures have been scaled in intensity to facilitate comparison, but not continuum normalised.

Figure 13 shows the NH and OH⁺ lines in the sightline towards HD 169454. The top panels in Fig. 14 compare the sodium doublets at ~ 3303 Å (see also Hunter et al. 2006) and ~ 5895 Å for the sightline towards HD 148937. The bottom panel compares several weak and strong DIBs in the HD 148937 line-of-sight. In each panel the EDIBLES and UVES POP spectra are shown in black and red, respectively. The average ISM synthetic DIB spectrum (adapted from Jenniskens & Désert 1994) is shown in green and a generic Paranal model telluric spectrum⁵ is shown in orange. The agreement between stellar and interstellar features in the EDIBLES and UVES POP is excellent, where the EDIBLES data generally reach a higher S/N .

The two right-hand panels of Fig. 14 reveal apparent variations between the EDIBLES data compared to the UVES POP spectrum. The strong absorption in the POP data at ~ 6384 Å coincides with the order ends/overlap, and appears to be an artefact of the order merging. In contrast, the significant change in the He I 5876 absorption seems robust. In the context of HD 148937 being a peculiar magnetic star, this variation is quite remarkable. This aspect will be discussed elsewhere.

These comparisons with existing data for selected sightlines show the excellent data quality of the spectra acquired within EDIBLES, illustrating its potential for detailed studies of physical conditions and DIB properties in the diffuse ISM.

8. Summary

In this first of a series of papers we have presented the design and scope of the ESO Diffuse Interstellar Bands Large Exploration Survey (EDIBLES). We presented the scientific goals and the immediate objectives of EDIBLES, along with the survey sample and its characteristics.

At the time of writing (May 2017), spectra had been acquired for 96 targets from 114 in the overall programme. These spectra

⁵ Generated from the ESO SkyCalc Sky Model Calculator.

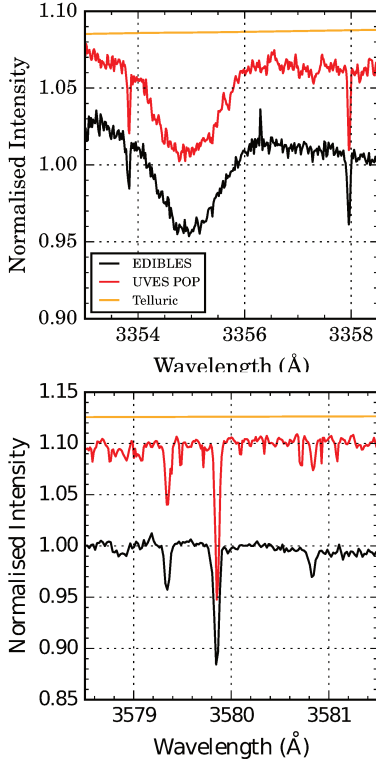


Fig. 13. Comparison of EDIBLES (black) and UVES POP (red) spectra of HD 169454 for interstellar lines of NH ($\lambda\lambda 3353.92$, 3358.05 Å; *top*) and CN(1 – 0) ($\lambda\lambda 3579.45$, 3579.96 , and 3580.9 Å; Meyer et al. 1989; *bottom*); the telluric spectrum is shown in orange. HD 169454 is a blue supergiant (B1 Ia) – the broad stellar line in the spectrum is He I $\lambda 3355$ Å.

cover the wavelength range from 305 to 1042 nm at a spectral resolving power of $\sim 70\,000$ – $110\,000$. We have presented the data-processing steps employed to reduce the survey data so far.

The median S/N ratio (per 0.04 Å spectral bin) varies from ~ 600 – 700 hundred in the blue (<400 nm) and near-infrared (>800 nm) ranges, to ≥ 1000 in the green-red (500 – 700 nm). To illustrate the quality and scope of the new spectra we have compared (1) EDIBLES and AAT spectra of the 6613 Å DIB towards HD 147888, (2) EDIBLES and CES spectra of the 6613 Å DIB for the sightlines towards HD 184915, HD 144470 and HD 145502, and (3) EDIBLES and UVES POP spectra of HD 148937 and HD 169454.

Upcoming papers in this series will present in detail the array of scientific results that are being explored with the EDIBLES data set. Once the program is completed the advanced data products (merged and normalised spectra) will be released to the community through the ESO Science Archive and the CDS/ViZieR service.

Acknowledgements. This work is based on observations collected at the European Organisation for Astronomical Research in the Southern Hemisphere under ESO programmes 194.C-0833 and 266.D-5655. The EDIBLES project was initiated at the IAU Symposium 297 “The Diffuse Interstellar Bands” (Cami & Cox 2014); the support of the International Astronomical Union for this meeting is gratefully acknowledged. N.L.J.C. thanks the Paranal Observatory staff and the ESO User Support Department for their assistance with successfully executing the observations. The authors thank both the Royal Astronomical Society and the Lorentz Center for hosting workshops, and Jacek Krelowski for making available the CES (ESO) data. We thank the referee for constructive comments that helped improve the paper. The research leading to these results has received

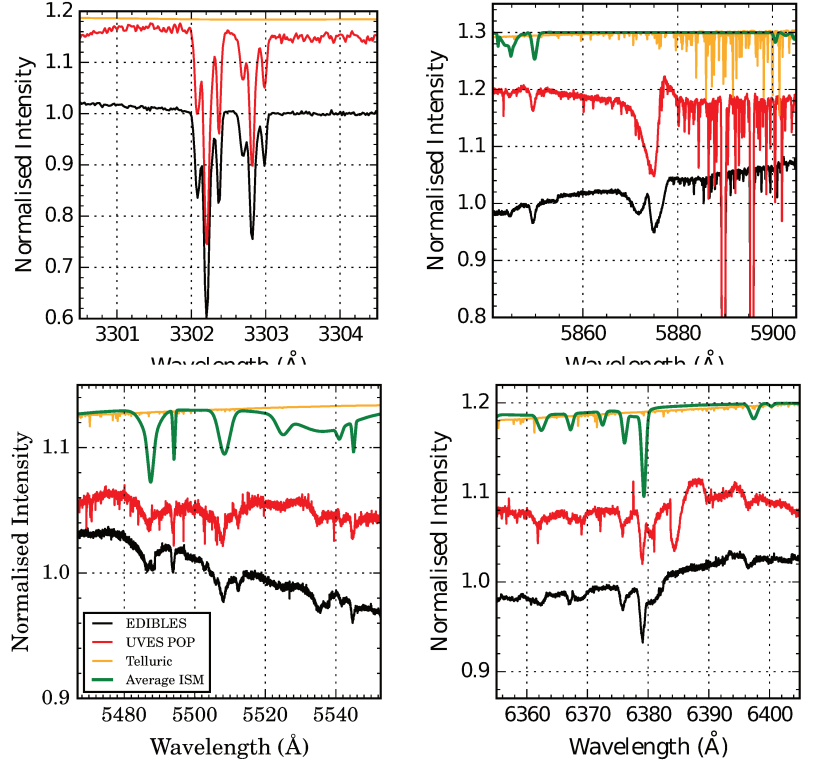


Fig. 14. Comparison of EDIBLES (black) and UVES POP (red) spectra of HD 148937 (O6 f?p) for the interstellar Na lines (UV, *top left*; D, *top right*) and DIBs at $\lambda\lambda 5480$ – 5545 Å (*lower left*) and $\lambda\lambda 6360$ – 6379 Å (*lower right*). The telluric spectrum is shown in orange, and the average ISM DIB spectrum is related in green. The apparent feature at 6384 Å in the UVES POP data (*bottom right panel*) is related to the order merging, but the significant change in the He I 5876 line (*top right panel*) appears astrophysical in nature.

funding from the European Research Council under the European Union’s Seventh Framework Programme (FP/2007-2013) ERC-2013-SyG, Grant Agreement No. 610256 NANOCOSMOS. F.S. acknowledges the support of NASA through the APRA SMD Program. A.M.I. acknowledges support from Agence Nationale de la Recherche through the STILISM project (ANR-12-BS05-0016-02) and from the Spanish PNAYA through project AYA2015-68217-P.

References

- Abt, H. A., & Morgan, W. W. 1969, *AJ*, **74**, 813
 Bagnulo, S., Jehin, E., Ledoux, C., et al. 2003, *The Messenger*, **114**, 10
 Bailey, M., van Loon, J. T., Sarre, P. J., & Beckman, J. E. 2015, *MNRAS*, **454**, 4013
 Bailey, M., van Loon, J. T., Farhang, A., et al. 2016, *A&A*, **585**, A12
 Ballester, P., Modigliani, A., Boitquin, O., et al. 2000, *The Messenger*, **101**, 31
 Baron, D., Poznanski, D., Watson, D., et al. 2015, *MNRAS*, **451**, 332
 Berné, O., & Tielens, A. G. G. M. 2012, *Proc. Nat. Acad. Sci.*, **109**, 401
 Berné, O., Mulas, G., & Joblin, C. 2013, *A&A*, **550**, L4
 Berné, O., Montillaud, J., & Joblin, C. 2015, *A&A*, **577**, A133
 Bertaux, J. L., Lallement, R., Ferron, S., Boonne, C., & Bodichon, R. 2014, *A&A*, **564**, A46
 Bondar, A., Kozak, M., Gnaciński, P., et al. 2007, *MNRAS*, **378**, 893
 Bréchnignac, P., & Pino, T. 1999, *A&A*, **343**, L49
 Bron, E. 2014, Ph.D. Thesis, Université Paris Diderot, Paris, France
 Cami, J., & Cox, N. L. J. 2014, *The Diffuse Interstellar Bands*, IAU Symp., 297
 Cami, J., Sonnentrucker, P., Ehrenfreund, P., & Foing, B. H. 1997, *A&A*, **326**, 822
 Cami, J., Salama, F., Jiménez-Vicente, J., Galazutdinov, G. A., & Krelowski, J. 2004, *ApJ*, **611**, L113
 Cami, J., Bernard-Salas, J., Peeters, E., & Malek, S. E. 2010, *Science*, **329**, 1180
 Campbell, E. K., Holz, M., Gerlich, D., & Maier, J. P. 2015, *Nature*, **523**, 322
 Clough, S. A., & Iacono, M. J. 1995, *J. Geophys. Res.*, **100**, 16
 Cordiner, M. A., Smith, K. T., Cox, N. L. J., et al. 2008, *A&A*, **492**, L5

- Cordiner, M. A., Cox, N. L. J., Evans, C. J., et al. 2011, *ApJ*, 726, 39
- Cordiner, M. A., Fossey, S. J., Smith, A. M., & Sarre, P. J. 2013, *ApJ*, 764, L10
- Cordiner, M. A., Cox, N. L. J., Lallement, R., et al. 2017, *ApJ*, 843, L2
- Cowley, A., Cowley, C., Jaschek, M., & Jaschek, C. 1969, *AJ*, 74, 375
- Cox, N. L. J. 2011, in *EAS Pub. Ser. 46*, eds. C. Joblin, & A. G. G. M. Tielens, 349
- Cox, N. L. J., & Patat, F. 2008, *A&A*, 485, L9
- Cox, N. L. J., & Patat, F. 2014, *A&A*, 565, A61
- Cox, N. L. J., & Spaans, M. 2006, *A&A*, 451, 973
- Cox, N. L. J., Cordiner, M. A., Cami, J., et al. 2006, *A&A*, 447, 991
- Cox, N. L. J., Cordiner, M. A., Ehrenfreund, P., et al. 2007, *A&A*, 470, 941
- Cox, N. L. J., Foing, B. H., Cami, J., & Sarre, P. J. 2011, *A&A*, 532, A46
- Danks, A. C., Federman, S. R., & Lambert, D. L. 1984, *A&A*, 130, 62
- Dekker, H., D'Odorico, S., Kaufer, A., Delabre, B., & Kotzlowski, H. 2000, in *Optical and IR Telescope Instrumentation and Detectors*, eds. M. Iye, & A. F. Moorwood, *Proc. SPIE*, 4008, 534
- Ehrenfreund, P., & Foing, B. H. 1996, *A&A*, 307, L25
- Elyajouri, M., Monreal-Ibero, A., Remy, Q., & Lallement, R. 2016, *ApJS*, 225, 19
- ESO CPL Development Team 2015, *EsoRex: ESO Recipe Execution Tool, Astrophysics Source Code Library* [[record ascl:1504.0003](https://arxiv.org/abs/1504.0003)]
- Evans, C. J., Smartt, S. J., Lee, J.-K., et al. 2005, *A&A*, 437, 467
- Evans, C. J., Kennedy, M. B., Dufton, P. L., et al. 2015, *A&A*, 574, A13
- Farhang, A., Khosroshahi, H. G., Javadi, A., et al. 2015, *ApJ*, 800, 64
- Feast, M. W., Thackeray, A. D., & Wesselink, A. J. 1957, *MmRAS*, 68, 1
- Fitzgerald, M. P. 1970, *A&A*, 4, 234
- Fitzpatrick, E. L., & Massa, D. 2007, *ApJ*, 663, 320
- Flower, D. R., & Pineau des Forêts, G. 2015, *A&A*, 578, A63
- Foing, B. H., & Ehrenfreund, P. 1994, *Nature*, 369, 296
- Friedman, S. D., York, D. G., McCall, B. J., et al. 2011, *ApJ*, 727, 33
- Galazutdinov, G. A., Musaev, F. A., Krelowski, J., & Walker, G. A. H. 2000, *PASP*, 112, 648
- Galazutdinov, G., Moutou, C., Musaev, F., & Krelowski, J. 2002, *A&A*, 384, 215
- Galazutdinov, G. A., Han, I., & Krelowski, J. 2005, *ApJ*, 629, 299
- Galazutdinov, G. A., LoCurto, G., & Krelowski, J. 2008, *ApJ*, 682, 1076
- Galazutdinov, G. A., Shimansky, V. V., Bondar, A., Valyavin, G., & Krelowski, J. 2017, *MNRAS*, 465, 3956
- Garrison, R. F., & Gray, R. O. 1994, *AJ*, 107, 1556
- Garrison, R. F., Hiltner, W. A., & Schild, R. E. 1977, *ApJS*, 35, 111
- Godard, B., Falgarone, E., & Pineau des Forêts, G. 2014, *A&A*, 570, A27
- Gray, R. O., Napier, M. G., & Winkler, L. I. 2001, *AJ*, 121, 2148
- Gredel, R., Carpentier, Y., Rouillé, G., et al. 2011, *A&A*, 530, A26
- Gudennavar, S. B., Bubbly, S. G., Preethi, K., & Murthy, J. 2012, *ApJS*, 199, 8
- Guetter, H. H. 1968, *PASP*, 80, 197
- Haffner, L. M., & Meyer, D. M. 1995, *ApJ*, 453, 450
- Heger, M. L. 1922, *Lick Observatory Bulletin*, 10, 141
- Hendry, E. M. 1982, *PASP*, 94, 169
- Herbig, G. H. 1993, *ApJ*, 407, 142
- Herbig, G. H. 1995, *ARA&A*, 33, 19
- Hiltner, W. A. 1956, *ApJS*, 2, 389
- Hiltner, W. A., Garrison, R. F., & Schild, R. E. 1969, *ApJ*, 157, 313
- Hobbs, L. M., York, D. G., Snow, T. P., et al. 2008, *ApJ*, 680, 1256
- Hobbs, L. M., York, D. G., Thorburn, J. A., et al. 2009, *ApJ*, 705, 32
- Holberg, J. B., Oswalt, T. D., Sion, E. M., Barstow, M. A., & Burleigh, M. R. 2013, *MNRAS*, 435, 2077
- Houk, N. 1978, *Michigan catalogue of two-dimensional spectral types for the HD stars*
- Huang, J., & Oka, T. 2015, *Molecular Physics*, 113, 2159
- Humphreys, R. M. 1973, *A&AS*, 9, 85
- Hunter, I., Smoker, J. V., Keenan, F. P., et al. 2006, *MNRAS*, 367, 1478
- Jenkins, E. B. 2009, *ApJ*, 700, 1299
- Jenniskens, P., & Désert, F.-X. 1994, *A&AS*, 106, 39
- Junkkarinen, V. T., Cohen, R. D., Beaver, E. A., et al. 2004, *ApJ*, 614, 658
- Kaźmierczak, M., Schmidt, M. R., Bondar, A., & Krelowski, J. 2010a, *MNRAS*, 402, 2548
- Kaźmierczak, M., Schmidt, M. R., Galazutdinov, G. A., et al. 2010b, *MNRAS*, 408, 1590
- Kerr, T. H., Hibbins, R. E., Miles, J. R., et al. 1996, *MNRAS*, 283, 1105
- Kos, J., & Zwitter, T. 2013, *ApJ*, 774, 72
- Kos, J., Zwitter, T., Wyse, R., et al. 2014, *Science*, 345, 791
- Krelowski, J., & Walker, G. A. H. 1987, *ApJ*, 312, 860
- Krelowski, J., Galazutdinov, G. A., Bondar, A., & Beletsky, Y. 2016, *MNRAS*, 460, 2706
- Kuhn, M., Renzler, M., Postler, J., et al. 2016, *Nature Communications*, 7, 13550
- Lan, T.-W., Ménard, B., & Zhu, G. 2015, *MNRAS*, 452, 3629
- Lawton, B., Churchill, C. W., York, B. A., et al. 2008, *AJ*, 136, 994
- Le Petit, F., Nehmé, C., Le Bourlot, J., & Roueff, E. 2006, *ApJS*, 164, 506
- Léger, A., & d'Hendecourt, L. 1985, *A&A*, 146, 81
- Lesh, J. R. 1968, *ApJS*, 17, 371
- Levato, H. 1975, *A&AS*, 19, 91
- Levato, H., & Abt, H. A. 1976, *PASP*, 88, 712
- Levenhagen, R. S., & Leister, N. V. 2006, *MNRAS*, 371, 252
- Linnartz, H., Wehres, N., van Winckel, H., et al. 2010, *A&A*, 511, L3
- Maier, J. P., Lakin, N. M., Walker, G. A. H., & Bohlender, D. A. 2001, *ApJ*, 553, 267
- Maier, J. P., Walker, G. A. H., & Bohlender, D. A. 2004, *ApJ*, 602, 286
- Mamajek, E. E., Meyer, M. R., & Liebert, J. 2002, *AJ*, 124, 1670
- Marshall, C. C. M., Krelowski, J., & Sarre, P. J. 2015, *MNRAS*, 453, 3912
- Massey, P., Johnson, K. E., & Degioia-Eastwood, K. 1995, *ApJ*, 454, 151
- McCall, B. J., Drosback, M. M., Thorburn, J. A., et al. 2010, *ApJ*, 708, 1628
- Merrill, P. W., & Wilson, O. C. 1938, *ApJ*, 87, 9
- Meyer, D. M., Roth, K. C., & Hawkins, I. 1989, *ApJ*, 343, L1
- Mokiem, M. R., de Koter, A., Puls, J., et al. 2005, *A&A*, 441, 711
- Monreal-Ibero, A., Weibacher, P. M., Wendt, M., et al. 2015, *A&A*, 576, L3
- Morgan, W. W., & Keenan, P. C. 1973, *ARA&A*, 11, 29
- Morgan, W. W., & Roman, N. G. 1950, *ApJ*, 112, 362
- Morgan, W. W., Code, A. D., & Whitford, A. E. 1955, *ApJS*, 2, 41
- Motylewski, T., Linnartz, H., Vaizert, O., et al. 2000, *ApJ*, 531, 312
- Mulas, G., Zonca, A., Casu, S., & Cecchi-Pestellini, C. 2013, *ApJS*, 207, 7
- Nissen, P. E. 2008, in *2007 ESO Instrument Calibration Workshop*, eds. A. Kaufer, & F. Kerber, 365
- Osawa, K. 1959, *ApJ*, 130, 159
- Parsons, S. B., & Ake, T. B. 1998, *ApJS*, 119, 83
- Puspitarini, L., Lallement, R., Babusiaux, C., et al. 2015, *A&A*, 573, A35
- Raimond, S., Lallement, R., Vergely, J. L., Babusiaux, C., & Eyer, L. 2012, *A&A*, 544, A136
- Renson, P., & Manfroid, J. 2009, *A&A*, 498, 961
- Romanini, D., Biennier, L., Salama, F., et al. 1999, *Chem. Phys. Lett.*, 303, 165
- Rothman, L. S., Gordon, I. E., Babikov, Y., et al. 2013, *J. Quant. Spectr. Rad. Transf.*, 130, 4
- Salama, F., Bakes, E. L. O., Allamandola, L. J., & Tielens, A. G. G. M. 1996, *ApJ*, 458, 621
- Salama, F., Galazutdinov, G. A., Krelowski, J., Allamandola, L. J., & Musaev, F. A. 1999, *ApJ*, 526, 265
- Salama, F., Galazutdinov, G. A., Krelowski, J., et al. 2011, *ApJ*, 728, 154
- Sarre, P. J. 2006, *J. Mol. Spectr.*, 238, 1
- Sarre, P. J., Miles, J. R., Kerr, T. H., et al. 1995, *MNRAS*, 277, L41
- Schild, R. E., & Chaffee, F. 1971, *ApJ*, 169, 529
- Schmidt, M. R., Krelowski, J., Galazutdinov, G. A., et al. 2014, *MNRAS*, 441, 1134
- Sellgren, K., Werner, M. W., Ingalls, J. G., et al. 2010, *ApJ*, 722, L54
- Sharpless, S. 1952, *ApJ*, 116, 251
- Simón-Díaz, S., Castro, N., Herrero, A., et al. 2011, *J. Phys. Conf. Ser.*, 328, 012021
- Smith, K. T., Fossey, S. J., Cordiner, M. A., et al. 2013, *MNRAS*, 429, 939
- Smoker, J., Haddad, N., Iwert, O., et al. 2009, *The Messenger*, 138, 8
- Snow, T. P. 2002, *ApJ*, 567, 407
- Sollerman, J., Cox, N., Mattila, S., et al. 2005, *A&A*, 429, 559
- Sorokin, P., & Glowina, J. H. 1999, in *H2 in Space, meeting held in Paris, France, September 28th–October 1st, 1999*, eds. F. Combes, & G. Pineau des Forêts (Cambridge University Press), *Astrophysics Series*
- Sota, A., Maíz Apellániz, J., Walborn, N. R., et al. 2011, *ApJS*, 193, 24
- Sota, A., Maíz Apellániz, J., Morrell, N. I., et al. 2014, *ApJS*, 211, 10
- Stebbins, J., & Kron, G. E. 1956, *ApJ*, 123, 440
- Steele, I. A., Negueruela, I., & Clark, J. S. 1999, *A&AS*, 137, 147
- Thorburn, J. A., Hobbs, L. M., McCall, B. J., et al. 2003, *ApJ*, 584, 339
- Tuairisg, S. Ó., Cami, J., Foing, B. H., Sonnentrucker, P., & Ehrenfreund, P. 2000, *A&AS*, 142, 225
- Ubachs, W. 2014, in *IAU Symp. 297*, eds. J. Cami, & N. L. J. Cox, 375
- Valencic, L. A., Clayton, G. C., & Gordon, K. D. 2004, *ApJ*, 616, 912
- Van der Zwet, G. P., & Allamandola, L. J. 1985, *A&A*, 146, 76
- van Loon, J. T., Smith, K. T., McDonald, I., et al. 2009, *MNRAS*, 399, 195
- van Loon, J. T., Bailey, M., Tatton, B. L., et al. 2013, *A&A*, 550, A108
- Vos, D. A. I., Cox, N. L. J., Kaper, L., Spaans, M., & Ehrenfreund, P. 2011, *A&A*, 533, A129
- Voshchinnikov, N. V., Henning, T., Prokopenko, M. S., & Das, H. K. 2012, *A&A*, 541, A52
- Walborn, N. R. 1971, *ApJS*, 23, 257
- Walborn, N. R. 1976, *ApJ*, 205, 419
- Walker, G. A. H., Bohlender, D. A., Maier, J. P., & Campbell, E. K. 2015, *ApJ*, 812, L8
- Walker, G. A. H., Campbell, E. K., Maier, J. P., Bohlender, D., & Malo, L. 2016, *ApJ*, 831, 130
- Wegner, W. 2003, *Astron. Nachr.*, 324, 219
- Weitenbeck, A. J. 2008, *Acta Astron.*, 58, 433

- Welty, D. E., Federman, S. R., Gredel, R., Thorburn, J. A., & Lambert, D. L. 2006, *ApJS*, 165, 138
- Weselak, T., Galazutdinov, G. A., Musaev, F. A., & Krelowski, J. 2004, *A&A*, 414, 949
- Weselak, T., Galazutdinov, G. A., Musaev, F. A., & Krelowski, J. 2008, *A&A*, 484, 381
- Whitmore, J. B., Murphy, M. T., & Griest, K. 2010, *ApJ*, 723, 89
- Whittet, D. C. B., Martin, P. G., Hough, J. H., et al. 1992, *ApJ*, 386, 562
- Zasowski, G., Ménard, B., Bizyaev, D., et al. 2015, *ApJ*, 798, 35
- Zhen, J., Castellanos, P., Paardekooper, D. M., Linnartz, H., & Tielens, A. G. G. M. 2014, *ApJ*, 797, L30
- ¹⁰ School of Chemistry, The University of Nottingham, University Park, Nottingham NG7 2RD, UK
- ¹¹ Royal Astronomical Society, Burlington House, Piccadilly, London W1J 0BQ, UK
- ¹² AAAS Science International, Clarendon House, Clarendon Road, Cambridge CB2 8FH, UK
- ¹³ UK Astronomy Technology Centre, Royal Observatory, Blackford Hill, Edinburgh, EH9 3HJ, UK
- ¹⁴ Instituut voor Sterrenkunde, KU Leuven, Celestijnenlaan 200D, BUS 2401, 3001 Leuven, Belgium
- ¹⁵ Sackler Laboratory for Astrophysics, Leiden Observatory, Leiden University, PO Box 9513, 2300 RA Leiden, The Netherlands
- ¹⁶ Astrochemistry Laboratory, NASA Goddard Space Flight Center, Code 691, 8800 Greenbelt Road, Greenbelt, MD 20771, USA
- ¹⁷ Department of Physics, The Catholic University of America, Washington, DC 20064, USA
- ¹⁸ Lennard-Jones Laboratories, Keele University, ST5 5BG, UK
- ¹⁹ ESTEC, ESA, Keplerlaan 1, 2201 AZ Noordwijk, The Netherlands
- ²⁰ ICCM, 28049 Madrid, Spain
- ²¹ Anton Pannekoek Institute for Astronomy, University of Amsterdam, 1090 GE Amsterdam, The Netherlands
- ²² George Washington University, Washington DC, USA
- ²³ LERMA, Observatoire de Paris, PSL Research University, CNRS, Sorbonne Universités, UPMC Université Paris 06, 92190 Meudon, France
- ²⁴ INAF–Osservatorio Astronomico di Cagliari, via della Scienza 5, 09047 Selargius, Italy
- ²⁵ NASA Ames Research Center, Space Science & Astrobiology Division, Moffett Field, California, USA
- ²⁶ Kapteyn Institute, University of Groningen, 9712 Groningen, The Netherlands
-
- ¹ Université de Toulouse, UPS-OMP, IRAP, 31028 Toulouse, France
- ² CNRS, IRAP, 9 Av. colonel Roche, BP 44346, 31028 Toulouse, France
- ³ Department of Physics and Astronomy, The University of Western Ontario, London, ON N6A 3K7, Canada
- ⁴ SETI Institute, 189 Bernardo Avenue, Suite 100, Mountain View, CA 94043, USA
- ⁵ School of Astronomy, Institute for Research in Fundamental Sciences, 19395-5531 Tehran, Iran
- ⁶ European Southern Observatory, Alonso de Cordova 3107, Vitacura, Santiago, Chile
- ⁷ GEPI, Observatoire de Paris, PSL Research University, CNRS, Université Paris-Diderot, Sorbonne Paris Cité, Place Jules Janssen, 92195 Meudon, France
- ⁸ Instituto de Astrofísica de Canarias (IAC), 38205 La Laguna, Tenerife, Spain
- ⁹ Universidad de La Laguna, Dpto. Astrofísica, 38206 La Laguna, Tenerife, Spain

Appendix A: Survey sample

Table A.1 lists spectral classifications and line-of-sight parameters for the observed EDIBLES targets to date; Table A.2 lists the additional observations that will supplement the data discussed here in due course. The R_V and A_V extinction values are taken (in order of preference) from Valencic et al. (2004), Fitzpatrick & Massa (2007), or Wegner (2003). H1 and H₂ column densities are from Jenkins (2009). The interstellar reddening, $E(B - V)$, was computed from $(B - V)_J$ colours (taking the average from Tycho-2 and Simbad $B - V$ colours; Mamajek et al. 2002) and the published spectral classifications, adopting intrinsic colours from Fitzgerald (1970).

References for the spectral classifications in Col. 4 of both tables are: M50 (Morgan & Roman 1950); S52 (Sharpless 1952);

M55 (Morgan et al. 1955); H56 (Hiltner 1956); S56 (Stebbins & Kron 1956, classification originally from W. W. Morgan; F57 (Feast et al. 1957); O59 (Osawa 1959); G68 (Guetter 1968); L68 (Lesh 1968); A69 (Abt & Morgan 1969); C69 (Cowley et al. 1969); H69 (Hiltner et al. 1969); S71 (Schild & Chaffee 1971); W71 (Walborn 1971); H73 (Humphreys 1973); M73 (Morgan & Keenan 1973); L75 (Levato 1975); L76 (Levato & Abt 1976); W76 (Walborn 1976); G77 (Garrison et al. 1977); H78 (Houk 1978); H82 (Hendry 1982); G94 (Garrison & Gray 1994); M95 (Massey et al. 1995); P98 (Parsons & Ake 1998); S99 (Steele et al. 1999); G01 (Gray et al. 2001); E05 (Evans et al. 2005); L06 (Levenhagen & Leister 2006); R09 (Renson & Manfroid 2009); S11 (Sota et al. 2011); H13 (Holberg et al. 2013); S14 (Sota et al. 2014).

Table A.1. Targets observed for EDIBLES.

Identifier	RA J2000	Dec J2000	Spectral type	Ref.	$E(B - V)$ mag	R_V	A_V mag	Ref.	$\log N(\text{H I})$ cm^{-2}	$\log N(\text{H}_2)$ cm^{-2}	f_{H_2}
HD 22951	03:42:22.7	+33:57:54.1	B0.5 V	M55	0.23	–	–		21.04	20.46	0.35
HD 23016	03:42:19.0	+19:42:00.9	B8 Ve	S99	0.05	2.30	0.12	W03	–	–	–
HD 23180	03:44:19.1	+32:17:17.7	B1 III	G77	0.28	3.11	0.93	V04	20.88	20.60	0.51
HD 24398	03:54:07.9	+31:53:01.1	B1 Ib	L68	0.29	2.63	0.89	W03	20.8	20.67	0.60
HD 27778	04:23:59.8	+24:18:03.6	B3 V	O59	0.36	2.59	0.91	V04	20.35	20.72	0.82
HD 34748	05:19:35.3	–01:24:42.8	B1.5 Vn	L68	0.13	2.61	0.29	W03	21.16	–	–
HD 36486	05:32:00.4	–00:17:56.7	O9.5 II Nwk	S11	0.16	–	–		20.19	14.68	0.00
HD 36695	05:33:31.5	–01:09:21.9	B1 V	L68	0.08	2.45	0.15	W03	20.7	–	–
HD 36822	05:34:49.2	+09:29:22.5	B0 III	L75	0.14	2.64	0.21	W03	20.81	19.32	0.06
HD 36861	05:35:08.3	+09:56:03.0	O8 III ((f))	S11	0.13	2.46	0.22	W03	20.78	19.12	0.04
HD 37022	05:35:16.5	–05:23:23.2	O7 Vp	S11	0.31	5.73	1.78	V04	21.54	17.55	0.00
HD 37041	05:35:22.9	–05:24:57.8	O9.5 IVp	S11	0.21	5.67	1.13	V04	–	–	–
HD 37061	05:35:31.4	–05:16:02.6	B0.5 V	S71	0.52	4.29	2.40	V04	–	–	–
HD 37367	05:39:18.3	+29:12:54.8	B2 IV-V	L68	0.37	3.55	1.49	V04	21.17	20.53	0.31
HD 37903	05:41:38.4	–02:15:32.5	B1.5 V	S52	0.34	3.74	1.31	V04	21.12	20.85	0.60
HD 38771	05:47:45.4	–09:40:10.6	B0.5 Ia	W71	0.07	–	–		20.52	15.68	0.00
HD 40111	05:57:59.7	+25:57:14.1	B1 Ib	L68	0.11	3.05	0.37	W03	20.9	19.73	0.12
HD 41117	06:03:55.2	+20:08:18.4	B2 Ia	W71	0.41	3.12	1.25	V04	20.15	20.69	0.87
HD 43384	06:16:58.7	+23:44:27.3	B3 Iab	L68	0.54	3.29	1.91	W03	21.27	–	–
HD 53975	07:06:36.0	–12:23:38.0	O7.5 Vz	S11	0.20	3.25	0.62	W03	21.13	19.18	0.02
HD 54439	07:08:23.2	–11:51:08.6	B2 IIIIn	M55	0.27	2.73	0.79	V04	–	–	–
HD 54662	07:09:20.3	–10:20:47.8	O7 Vz var? (SB2)	S14	0.32	3.12	0.81	W03	21.38	20.00	0.08
HD 55879	07:14:28.3	–10:18:58.5	O9.7 III	S11	0.13	2.47	0.15	W03	20.9	–	–
HD 57061	07:18:42.5	–24:57:15.8	O9 II (SB2+SBE)	S14	0.12	3.57	0.36	W03	20.7	15.48	0.00
HD 66194	07:58:50.6	–60:49:28.1	B2 Vne	A69	0.15	2.25	0.41	W03	–	–	–
HD 66811	08:03:35.1	–40:00:11.3	O4 I(n)fp	S14	0.08	5.01	0.25	W03	19.96	14.45	0.01
HD 73882	08:39:09.5	–40:25:09.3	O8.5 IV (SB1+SBE)	S14	0.68	3.56	2.46	V04	21.11	21.08	0.65
HD 75309	08:47:28.0	–46:27:04.0	B2 Ib/II	H78	0.16	3.53	1.02	V04	21.07	20.20	0.21
HD 75860	08:50:53.2	–43:45:05.4	BC2 Iab	W76	0.87	3.44	3.10	W03	–	–	–
HD 79186	09:11:04.4	–44:52:04.4	B5 Ia	H69	0.28	3.21	1.28	V04	21.18	20.72	0.41
HD 80558	09:18:42.4	–51:33:38.3	B6 Ia	H69	0.57	3.35	2.01	W03	–	–	–
HD 81188	09:22:06.8	–55:00:38.4	B2 IV	L75	0.10	–	–		19.95	17.70	0.01
HD 91824	10:34:46.6	–58:09:22.0	O7 V((f))z (SB1)	S14	0.25	3.35	0.80	V04	21.12	19.85	0.10
HD 93030	10:42:57.4	–64:23:40.0	B0.2 Vp	W76	0.08	2.43	0.10	W03	20.26	15.02	0.00
HD 93205	10:44:33.7	–59:44:15.5	O3.5 V((f)) + O8 V	S14	0.34	3.25	1.24	V04	21.38	19.78	0.05
HD 93222	10:44:36.2	–60:05:29.0	O7 V((f))z	S14	0.34	4.76	1.71	V04	21.4	19.78	0.05

Table A.1. continued.

Identifier	RA J2000	Dec J2000	Spectral type	Ref.	$E(B - V)$ mag	R_V	A_V mag	Ref.	$\log N(\text{H I})$ cm^{-2}	$\log N(\text{H}_2)$ cm^{-2}	f_{H_2}
HD 93843	10:48:37.8	-60:13:25.5	O5 III(fc) SB1?	S14	0.27	3.89	0.66	V04	21.33	19.61	0.04
HD 94493	10:53:15.1	-60:48:53.2	B0.5 Ib:	H73	0.23	3.57	0.82	V04	21.08	20.15	0.19
HD 99953	11:29:15.1	-63:33:14.2	B2 Ia	M55	0.45	3.69	1.77	V04	-	-	-
HD 103779	11:56:58.0	-63:14:56.7	B0.5 Iab	G77	0.24	3.29	0.69	V04	21.16	19.82	0.08
HD 104705	12:03:23.9	-62:41:45.8	B0.5 III	M55	0.23	2.81	0.65	V04	21.1	20.08	0.16
HD 109399	12:35:16.5	-72:43:00.8	B0.5 Ib	H73	0.26	3.26	0.68	W03	21.11	20.04	0.15
HD 111934	12:53:37.6	-60:21:25.4	B1.5 Ib	E05	0.34	2.45	1.25	V04	-	-	-
HD 112272	12:56:33.7	-64:21:39.2	B0.5 Ia	M55	0.85	3.09	3.09	V04	-	-	-
HD 113904	13:08:07.2	-65:18:21.7	O9 III	S14	0.20	3.63	0.76	W03	21.08	19.83	0.10
HD 116852	13:30:23.5	-78:51:20.5	O8.5 II-III((f))	S14	0.20	2.42	0.51	V04	20.96	19.79	0.12
HD 122879	14:06:25.2	-59:42:57.3	B0 Ia	W76	0.34	3.15	1.13	V04	21.26	20.24	0.16
HD 124314	14:15:01.6	-61:42:24.4	O6 IV(n)((f))	S14	0.49	2.97	1.49	W03	21.41	20.52	0.21
HD 133518	15:06:56.0	-52:01:47.2	B2 Vp	G77	0.13	1.79	0.27	W03	-	-	-
HD 135591	15:18:49.1	-60:18:51.5	O8 IV((f))	S14	0.20	3.57	0.79	W03	21.08	19.77	0.09
HD 143275	16:00:20.0	-22:37:18.1	B0.3 IV	M73	0.19	3.09	0.43	W03	21.15	19.41	0.04
HD 144470	16:06:48.4	-20:40:09.1	B1 V	W71	0.21	3.37	0.74	V04	21.17	20.05	0.13
HD 145502	16:11:59.7	-19:27:38.5	B2 V (SB2)	L75	0.27	-	-		21.07	19.89	0.12
HD 147084	16:20:38.2	-24:10:09.8	A5 II	G01	0.78	-	-		-	-	-
HD 147165	16:21:11.3	-25:35:34.1	B1 III	W71	0.37	3.86	1.47	V04	21.17	20.05	0.13
HD 147683	16 24 43.7	-34 53 37.5	B3: Vn (SB2)	G77	0.29	-	-		21.20	20.68	0.38
HD 147888	16:25:24.3	-23:27:36.8	B3 V:	F57	0.44	3.89	1.98	V04	21.69	20.48	0.11
HD 147889	16:25:24.3	-24:21:07.1	B2 V	H56	1.03	3.95	4.35	V04	-	-	-
HD 147933	16:25:35.1	-23:26:48.7	B2 IV	H69	0.43	5.74	2.58	V04	21.64	20.57	0.15
HD 147934	16:25:35.0	-23:26:46.0	B2 V	H69	0.43	-	-		-	-	-
HD 148605	16:30:12.5	-25:06:54.8	B2 V	M73	0.07	3.18	0.25	W03	20.68	18.74	0.02
HD 148937	16:33:52.4	-48:06:40.5	O6 f?p	S14	0.65	3.28	2.20	W03	21.60	20.71	0.21
HD 149038	16:34:05.0	-44:02:43.1	O9.7 Iab	S14	0.31	4.92	1.08	V04	21.00	20.45	0.36
HD 149404	16:36:22.6	-42:51:31.9	O8.5 Iab(fp) (SB2)	S14	0.67	3.53	2.19	V04	-	-	-
HD 149757	16:37:09.5	-10:34:01.5	O9.2 IVnn	S14	0.32	2.55	0.82	V04	20.72	20.65	0.63
HD 150136	16:41:20.4	-48:45:46.8	O3.5-4 III(f*) + O6 IV	S14	0.43	3.27	1.64	W03	-	-	-
HD 151804	16:51:33.7	-41:13:49.9	O8 Iaf (SB2)	S14	0.34	4.33	1.30	V04	21.08	20.26	0.23
HD 152248	16:54:10.1	-41:49:30.1	O7 Iabf + O7 Ib(f)	S14	0.47	3.68	1.51	V04	-	20.92	-
HD 152408	16:54:58.5	-41:09:03.1	O8: Iafpe	S14	0.44	4.17	1.75	V04	21.27	20.38	0.21
HD 152424	16:55:03.3	-42:05:27.0	OC9.2 Ia (SB1)	S14	0.66	3.23	2.07	W03	-	-	-
HD 153919	17:03:56.8	-37:50:38.9	O6 Iafcp (SB1E)	S14	0.59	3.58	1.97	V04	-	-	-
HD 154043	17:05:18.9	-47:04:08.5	B2 Iab	H78	0.80	3.30	2.57	W03	-	-	-

Table A.1. continued.

Identifier	RA J2000	Dec J2000	Spectral type	Ref.	$E(B - V)$ mag	R_V	A_V mag	Ref.	$\log N(\text{HI})$ cm^{-2}	$\log N(\text{H}_2)$ cm^{-2}	f_{H_2}
HD 155806	17:15:19.3	-33:32:54.3	O7.5 V((f)z(e)	S14	0.27	2.48	0.57	W03	21.08	19.92	0.12
HD 157246	17:25:23.7	-56:22:39.8	B1 Ib	H69	0.06	2.82	0.17	W03	20.68	19.23	0.07
HD 157978	17:26:19.0	+07:35:44.3	G0/K0 II: + A1	P98	0.64	3.72	2.42	W03	-	-	-
HD 158926	17:33:36.5	-37:06:13.8	B2 IV + DA.79	H13	0.10	-	-		19.23	12.70	0.00
HD 161056	17:43:47.0	-07:04:46.6	B1.5 V	L68	0.58	-	-		21.23	-	-
HD 164073	18:02:00.6	-48:48:37.7	B3III/IV	H78	0.22	2.96	0.62	V04	-	-	-
HD 164353	18:00:39.0	+02:55:53.6	B5 Ib	M50	0.10	-	-		21.00	20.26	0.27
HD 166937	18:13:45.8	-21:03:31.8	B8 Iab(e)	G94	0.22	-	-		-	-	-
HD 167264	18:15:12.9	-20:43:41.8	O9.7 Iab	S14	0.24	3.26	0.98	V04	21.15	20.28	0.21
HD 167838	18:17:37.7	-15:25:50.6	B5 Ia	M55	0.55	3.39	2.13	V04	-	-	-
HD 167971	18:18:05.9	-12:14:33.3	O8 Iaf(n) + O4/5	S11	1.01	3.44	3.54	V04	21.6	20.85	0.26
HD 169454	18:25:15.2	-13:58:42.3	B1 Ia	W76	1.03	3.37	3.64	V04	-	-	-
HD 170740	18:31:25.7	-10:47:45.0	B2 V	S56	0.45	3.01	1.51	V04	21.03	20.86	0.58
HD 170938	18:32:37.8	-15:42:05.9	B1 Ia	M55	0.97	3.34	3.47	W03	-	-	-
HD 171957	18:38:04.5	-14:00:16.9	B9 IV	C69	0.27	-	-		-	-	-
HD 172694	18:42:16.6	-16:25:41.0	B1: Vne	G68	0.34	5.04	1.86	W03	-	-	-
HD 180554	19:16:13.0	+21:23:25.4	B4 IV	L68	-	-	-		-	-	-
HD 184915	19:36:53.5	-07:01:38.9	B0.5 IIIIn	L68	0.24	3.07	0.68	W03	20.85	20.31	0.37
HD 185418	19:38:27.5	+17:15:26.1	B0.5 V	M55	0.42	2.54	1.27	V04	21.19	20.71	0.40
HD 185859	19:40:28.3	+20:28:37.5	B0.5 Ia	L68	0.56	2.74	1.64	V04	21.23	-	-
HD 186745	19:45:24.3	+23:56:34.4	B8 Ia	M55	0.88	3.10	2.98	W03	-	-	-
HD 186841	19:45:54.0	+24:05:47.0	B0.5 I	M95	0.95	2.89	3.01	W03	-	-	-
HD 203532	21:33:54.6	-82:40:59.1	B3 IV	H69	0.30	3.37	0.94	V04	20.22	20.64	0.84
HD 303308	10:45:05.9	-59:40:06.4	O4.5 V((fc)) (SB1?)	S14	0.43	3.02	1.36	V04	21.41	20.34	0.15

Table A.2. Observations planned to complete the EDIBLES sample.

Identifier	RA J2000	Dec J2000	Spectral type	Ref.	$E(B - V)$ mag	R_V	A_V mag	Ref.	$\log N(\text{H I})$ cm^{-2}	$\log N(\text{H}_2)$ cm^{-2}	f_{H_2}
HD 36982	05:35:09.8	-05:27:53.3	B1.5 Vp	S52	0.31	4.84	1.74	V04	21.57	–	–
HD 37020	05:35:15.8	-05:23:14.3	B0.5 V	L76	0.28	6.33	1.77	V04	21.48	–	–
HD 37021	05:35:16.1	-05:23:07.3	B0 V	G68	0.30	5.84	2.80	V04	21.68	–	–
HD 37023	05:35:17.2	-05:23:15.6	B1.5 Vp	L06	0.37	4.82	1.74	V04	–	–	–
HD 37128	05:36:12.8	-01:12:06.9	B0 Ia	M50	0.09	–	–		20.45	16.57	0.04
HD 38087	05:43:00.6	-02:18:45.4	B5 V	S71	0.28	4.93	1.48	V04	20.91	20.64	0.52
HD 39680	05:54:44.7	+13:51:16.9	O6 V:[n]pe var	S11	0.33	4.73	1.51	W03	21.3	19.53	0.03
HD 45314	06:27:15.8	+14:53:21.1	O9: npe	S11	0.13	4.42	1.90	V04	21.04	20.60	0.42
HD 49787	06:49:55.5	-05:30:47.5	B1 V:pe	M55	0.20	2.39	0.43	W03	–	–	–
HD 50820	06:54:42.0	-01:45:23.4	B3 IVe + K2 II	H82	0.72	4.39	3.38	W03	–	–	–
HD 61827	07:39:49.3	-32:34:42.2	B3 Iab	G77	0.78	2.98	2.68	W03	–	–	–
HD 114886	13:14:44.4	-63:34:51.8	O9 III + O9.5 III	S14	0.28	2.90	0.84	W03	21.34	20.23	0.13
HD 156201	17:17:45.5	-35:13:27.0	B0.5 Ia	G77	0.91	3.23	2.78	W03	–	–	–
HD 164740	18:03:40.0	-24:22:43.0	O7: V + sec.	S14	0.90	5.03	4.48	V04	21.95	20.19	0.03
HD 164906	18:04:25.8	-24:23:08.3	B0 Ve	L06	0.44	4.57	2.06	V04	–	–	–
HD 165319	18:05:58.8	-14:11:53.0	O9.7 Ib	S11	0.78	3.25	2.70	W03	–	–	–
HD 168076	18:18:36.4	-13:48:02.0	O4 III(f)	S11	0.76	3.47	2.64	V04	21.65	20.68	0.18
HD 183143	19:27:26.6	+18:17:45.2	B7 Ia	M55	1.19	–	–		–	–	–

Towards a new DIB atlas

9.1 Line-of-sight structure from extracted IS gaseous lines

For most DIB analyses, it is mandatory to have a knowledge of the line-of-sight structure in order to take into account the cloud multiplicity. This is the case for any study of the saturation or skin-effect. This is the reason why we performed the profile-fitting of the neutral sodium and the ionized calcium lines in order to infer the number, velocity shifts and column-densities of the intervening clouds. Such information will allow to know whether the dominant reddening is produced by one main cloud or multiple ones and attribute a weight to the target in our search for the saturation effect (high weight for mono-cloud sightlines, low weight for multi-cloud sightlines). In addition and independently, the spectral information for all targets will allow to locate the absorbing clouds and test the relationship between the reddening and DIB vertical scale heights.

In order to select single-cloud sightlines, we have fitted the NaI 3302.368 and 3202.987 Å UV doublet (hereafter, NaIB) and the NaI 5889.95/5895.92 Å D₂-D₁ doublet (hereafter, NaI). We have also fitted the ionized calcium CaII, namely K and H lines, at 3933.66 and 3968.47 Å. Due to the intrinsic weakness of the transitions for the NaI UV doublet, there is no or very little saturation and it is easy to determine the number of intervening interstellar clouds with gas columns large enough to produce detectable DIBs. In the case of the 5889.95/5895.92 Å doublet there is a strong saturation and line broadening for many clouds, precluding a clear component separation. Instead, these transitions have been used to check the structure deduced from the UV doublet. We modeled the absorption lines of the doublets as convolved products of Voigt profiles in combination with a polynomial continuum, and we determined the radial velocities of the major components (see, e.g. [Puspitarini, Lallement 2012](#)).

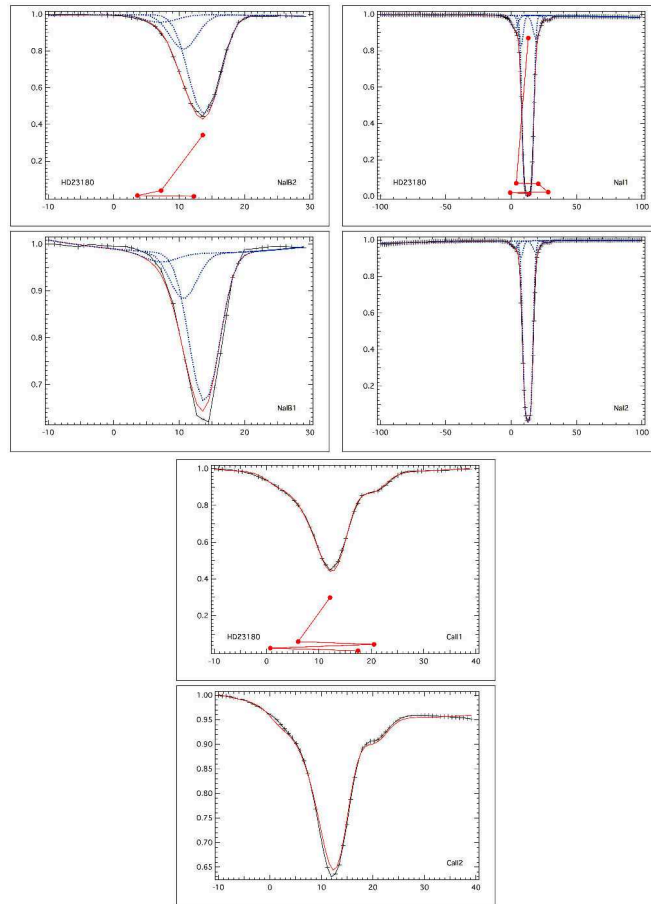


Figure 91 Illustration of global analysis of the NaI 3302.368 and 3202.987 Å UV doublet (NaIB; left), the NaI 5889.95/5895.92 Å D₂-D₁ doublet (NaI; middle) and the K and H Ca II lines at 3933.66 and 3968.47 Å (Ca II; right) for HD23180. Left axis is flux in arbitrary unit and the bottom axis is heliocentric velocity (km s⁻¹). Data are shown with marked black lines. The red line shows the global fit. The blue dashed line shows the voigt profile for each component (not shown for Ca II). The different red dots show the successive initial guesses for the location of each additional cloud.

Here the shape of the continuum and the number of clouds are determined in a new and totally automated way. To do so, the noise standard deviation is initially measured in regions adjacent to the sodium lines. Model adjustments are then made iteratively for an increasing number of clouds until the residuals in the sodium/calcium area become equivalent to the standard deviation. The prior radial velocity of each additional cloud is derived from the location of the minimum in the residuals from the previous step of adjustment. A representative example is show in Fig. 91. Note that in some cases such like the one from the Figure, the data may not be well fitted at the bottom of the lines, due to the existence of close blends, but even if the depth of the interstellar lines is not properly estimated, the velocity of each cloud component is accurately determined and the global shape of the modeled spectrum is most of the times adequate. This determination will be sufficient for DIB studies.

Table 91 Interstellar lines extraction summary

	$\lambda_1-\lambda_2$ (Å)	Successful fits
NaI (D ₂ -D ₁)	5889.95-5895.92	88
NaIB (UV doublet)	3302.37-3202.98	78
CaII (H&K)	3933.66-3968.47	83

However, sometimes the minimization procedure does not reach the absolute minimum values. This is the case of some multi-cloud sightlines with very saturated NaI-D₂-D₁ lines. Failure to converge can be fixed by a manual/classical fit where we choose ourselves the minimas as illustrated in Fig. 92. This method has been applied to a dozen spectra that can be found in Figs. 18 and 19, appendix C.

Table 91 lists the wavelengths of the interstellar lines and the number of successful automated fits. All spectra and fit results are presented in appendix C and were inspected visually to confirm the presence or absence of multiple velocity components. The flow chart in Fig. 93 outlines the types of decisions made after the visual inspection of all EDIBLES targets.

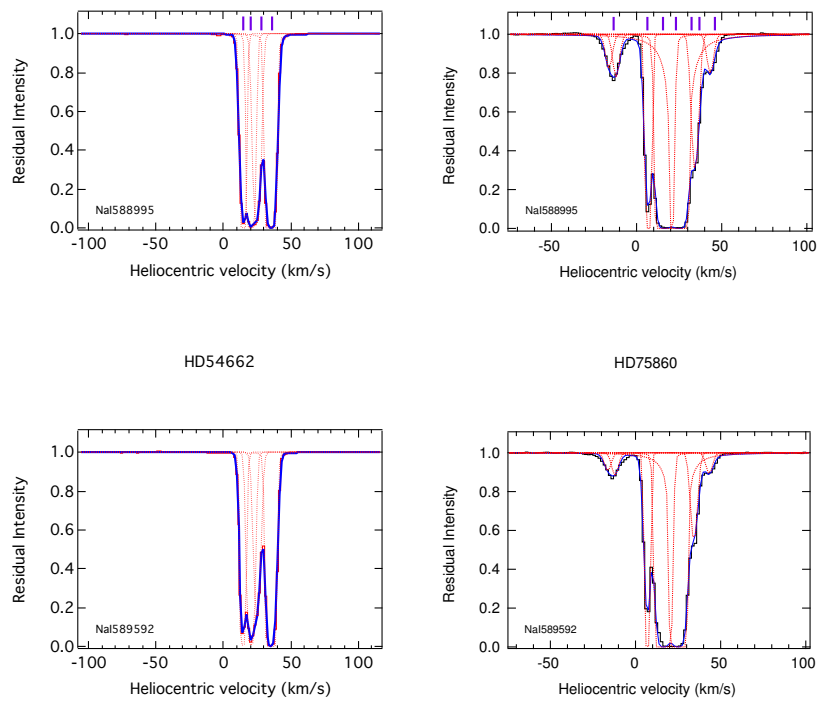


Figure 92 Examples of classical profile fitting results of the NaI-D2-D1 normalized spectra: HD54662 (left) and HD75860 (right). Data are shown in marked red lines. The blue curve displays the fit. The thick red lines show the individual interstellar lines model before convolution.

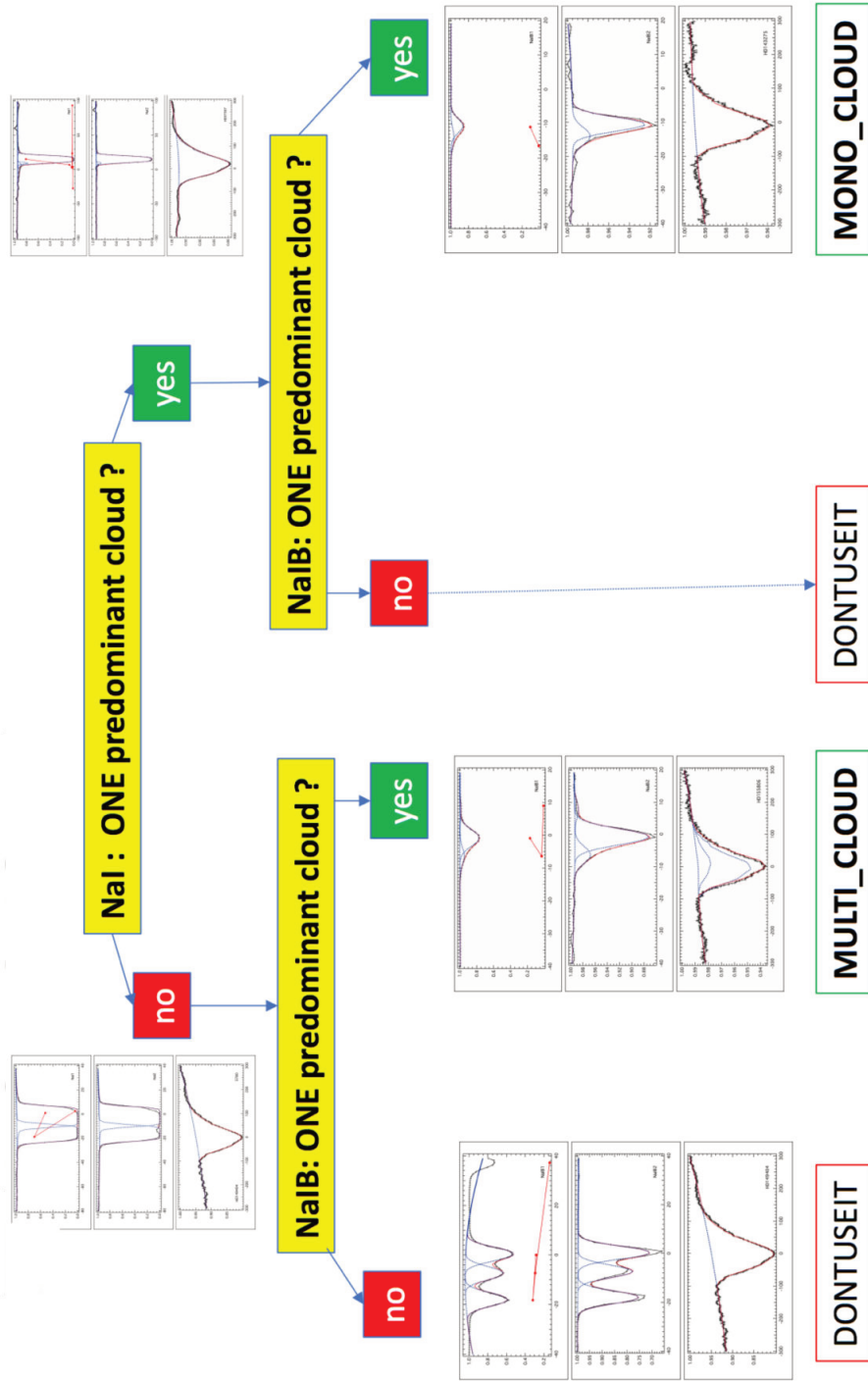


Figure 93 Visual Inspection and selection of EDIBLES mono and multi clouds sightlines.

9.2 Searching for IS features

There are several methods to extract the interstellar information from stellar spectra. The historical one consists in the use of binary stars. Due to the stationary nature of the interstellar lines, the comparison of spectroscopic binaries at different orbital phases allows to distinguish stellar absorptions from those of interstellar origin. Such a technique was used by [Hobbs et al. \(2008\)](#) to establish their DIB survey toward the double-lined spectroscopic binary HD 204827. The census of the DIBs by [Herbig \(1975\)](#), [Jenniskens, Desert \(1994\)](#), [Tuairisg et al. \(2000\)](#) and [Hobbs et al. \(2009\)](#) used another approach based on the comparison among pairs of reddened and unreddened standards matching the same spectral type. Most recently, [Sonnentrucker et al. \(2018\)](#) published a modern homogeneous census of the broadest DIBs using a compilation of reddened and unreddened stars of different spectral types.

[Bhatt, Cami 2015](#) were the first to perform a sensitive survey of interstellar lines in the near-UV by using a “superspectrum” in all kinds of reference frames (geocentric, telluric, stellar and interstellar). This useful tool was also presented in Chapter 6 for the near-infrared range. We make use of this method by looking at DIBs in a co-added spectrum of twenty single cloud targets. In this work in progress, an atlas based on a “superspectrum” (and also considering spectra of individual targets) will allow to confirm/reject some weak DIB candidates, to discover new ones, to give insight into line profiles and to update the previous surveys. A good example that highlights the feasibility of such technique in the framework of EDIBLES is the HD 170740 spectrum shown in Fig. 94 where DIB locations and widths from [Hobbs et al. \(2009\)](#) are overplotted. It is possible to see almost all of optical DIBs, allowing such features to be easily detected in a carefully constructed “superspectrum”.

This technique was applied separately for the mono-cloud and multi-cloud samples. We will undoubtedly use the mono-cloud situation for the production of the atlas (in particular to characterize the profiles), but we deliberately kept the superspectrum of the multi-cloud targets. Since those are more reddened, they can confirm the existence of a potential interstellar feature that was too weak to be discerned in the mono-cloud “superspectrum” or in single observation. In the mono-cloud stacking case, the normalized spectra were shifted to their respective interstellar frame using the radial velocities already determined in Chapter 9.1. In the multi-clouds case it is difficult to assign to the sightline an interstellar radial velocity that would correspond to the dominant component, instead we performed a cross-correlation of each spectrum with the deepest line of the NaI doublet of a reference star (selected among the sample). Each star spectrum was then shifted by the amount deduced from the cross-correlation. These

9.2. Searching for IS features

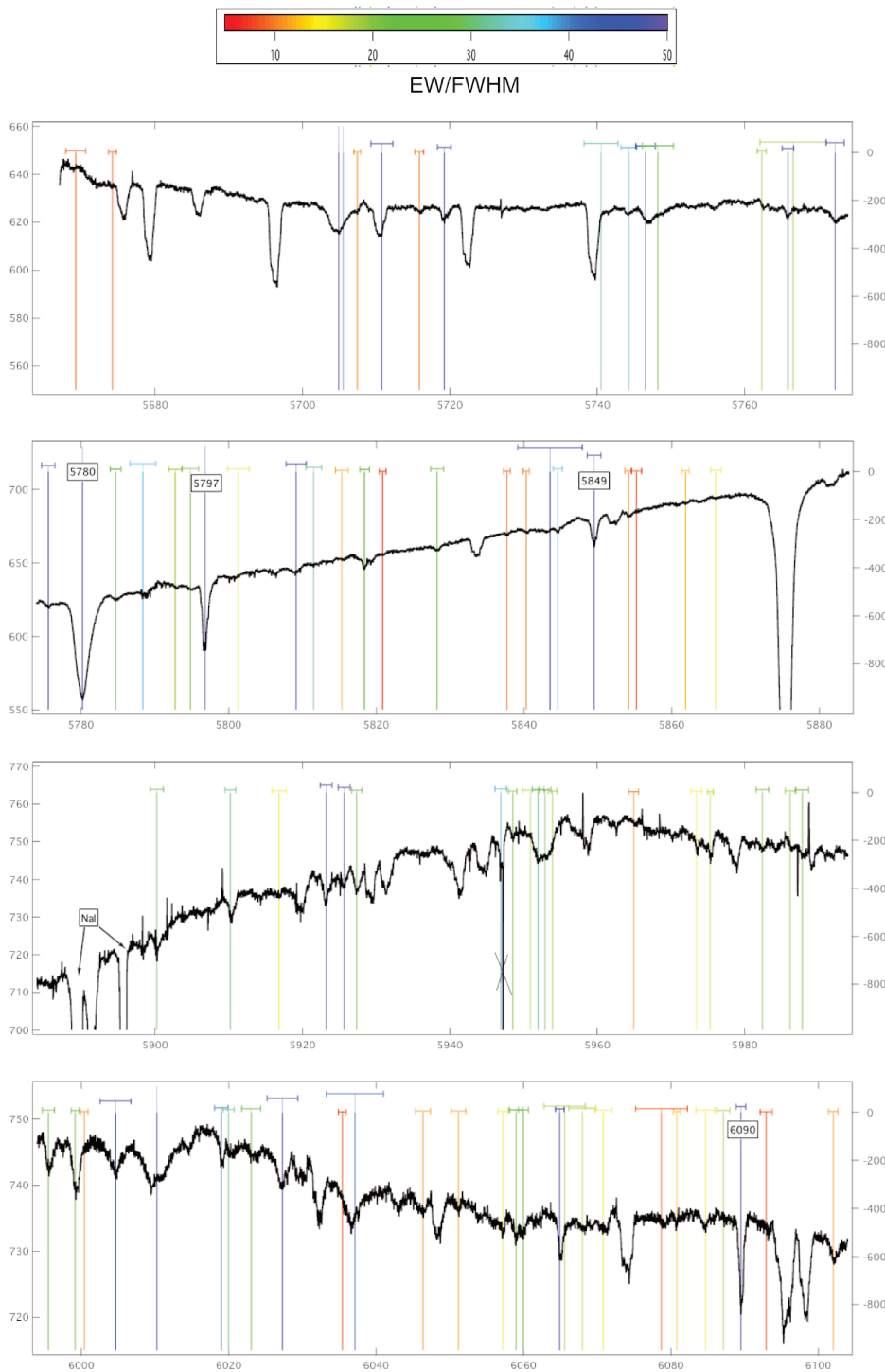


Figure 94 EDIBLES HD170740 spectrum: Comparison with the Hobbs (2009) DIB atlas (star HD183143). The horizontal lines show the DIB width ($2 \times \text{FWHM}$). The vertical lines display the position of DIBs. Color coding indicates EW/FWHM ratio.

9. TOWARDS A NEW DIB ATLAS

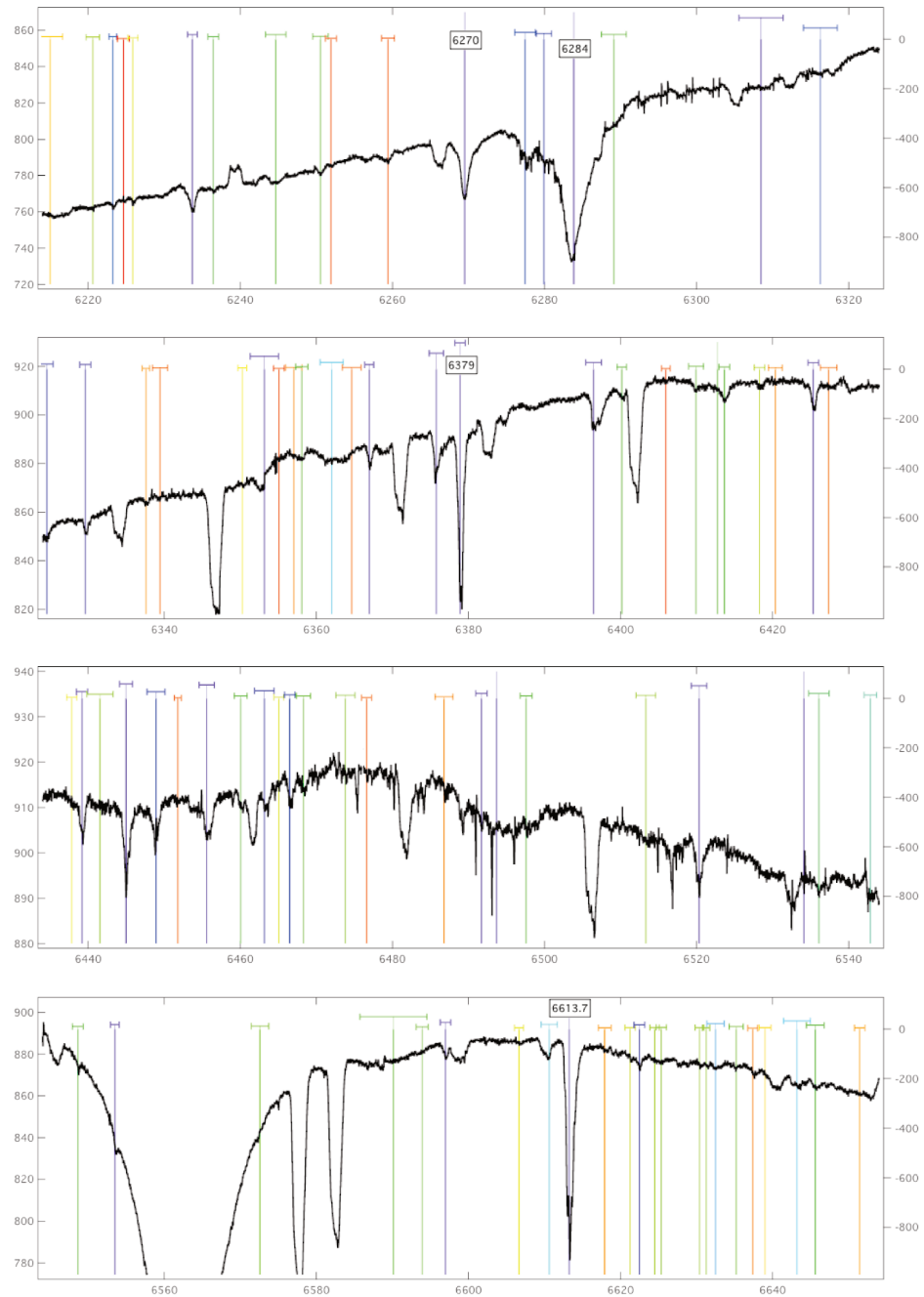


Figure 94 Continued.

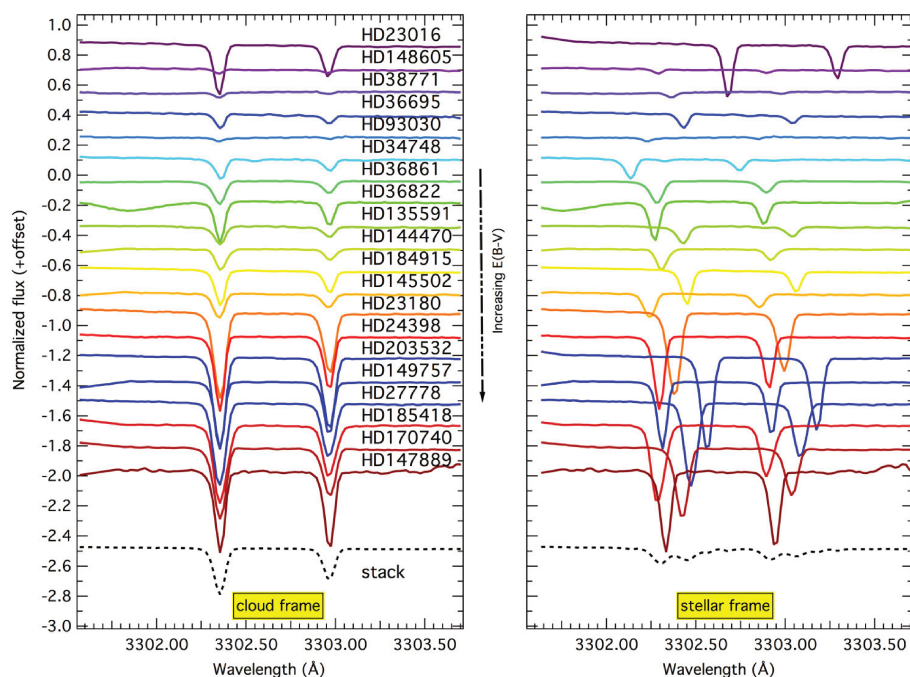


Figure 95 Spectra for all mono-cloud sightlines in the interstellar frame (left) and in stellar frame (right). The corresponding superspectra are shown in dashed black at the bottom.

spectra were visualized and then co-added (no weighting). The same processes were performed in the stellar frame. The stellar radial velocities are either collected from the literature or by cross-correlating with the He II or H_{α} (6605 Å) stellar lines. Stacking in the stellar frame and in the frame of the main cloud should allow to disentangle interstellar and stellar features as shown for in Figs. 95 and 96.

Figure 95 displays a sample of 20 mono-cloud spectra around the interstellar NaI-UV doublet in the interstellar and stellar frame. The corresponding stacked spectra are also shown. While the stacked spectrum in the cloud frame reveals a very well defined interstellar NaI-UV doublet, the same features are broadened in the stellar frame. A similar effect is seen in the multi-cloud situation in Fig. 96.

In practice, the atlas will be done after inspection of the velocity structure and selection of a dozen of mono-cloud targets characterized by one single very strong component dominating the others. Then comes the time of careful inspection for hundreds of DIBs. As an illustration, we show in Fig. 97 the profile of the 5849 Å DIB when co-adding the mono-cloud (top) and multi-cloud (bottom) spectra in the interstellar (black) and stellar (red)

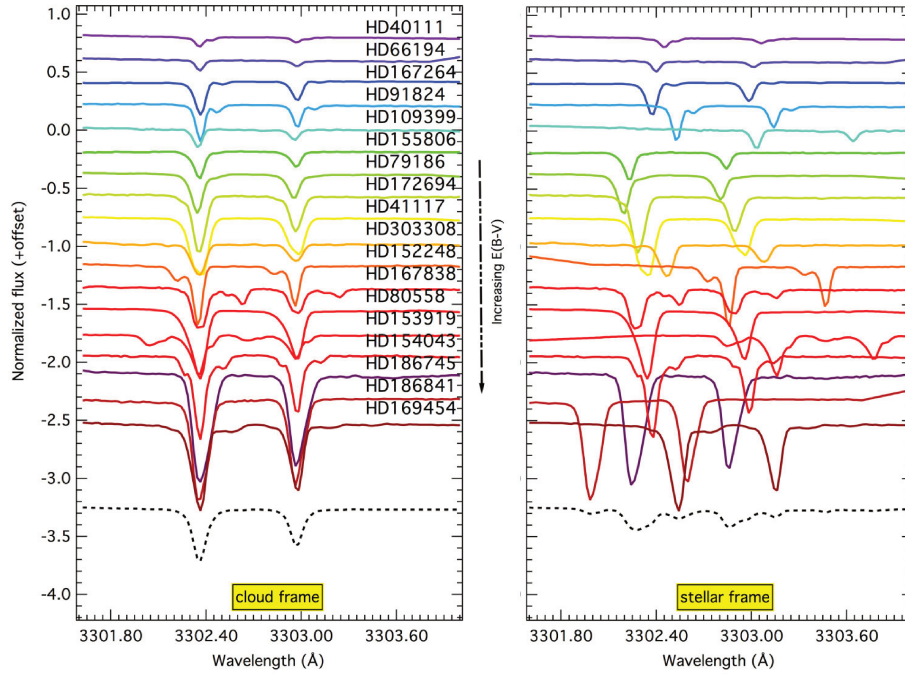


Figure 96 Same as Fig. 95 but for the EDIBLES multi-cloud l.o.s. These targets clearly show multiple components.

frame. The mono-cloud superspectrum may be easily used to detect DIB sub-structures in the cloud rest frame, the DIB profile is sharp showing sub-peaks. Such peaks are less apparent in the case of multi-cloud profile which is smoother and then not suitable for intrinsic profile characterization. However, the fact that the absorption remains deeper than in the mono-cloud case confirms its interstellar nature.

Indeed, the co-addition in the stellar frame obviously spread out the DIB and makes it weaker. Similarly, the superspectra of the Ca II and the 5890/5896 Å NaI lines in Fig. 98 are displayed. It is noteworthy that the study presented in this section is an exploratory work and constitutes a basis for the establishment of a large census of DIBs which will be presented and detailed in a future project.

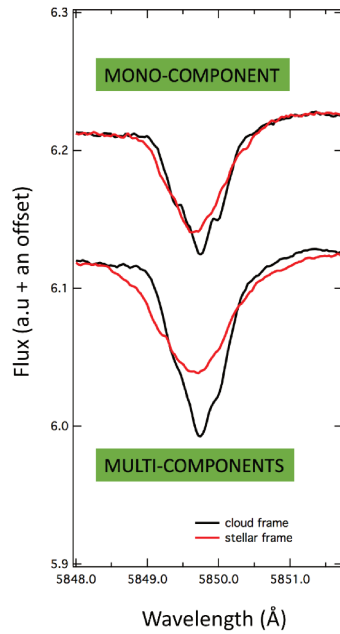


Figure 97 Superspectra around the 5849 Å DIB constructed in the interstellar frame (black) for the mono-cloud (top) and multi-cloud (bottom) situation. Overplotted in red are the superspectra shifted and stacked in the stellar frame. The y-axis is given in arbitrary units.

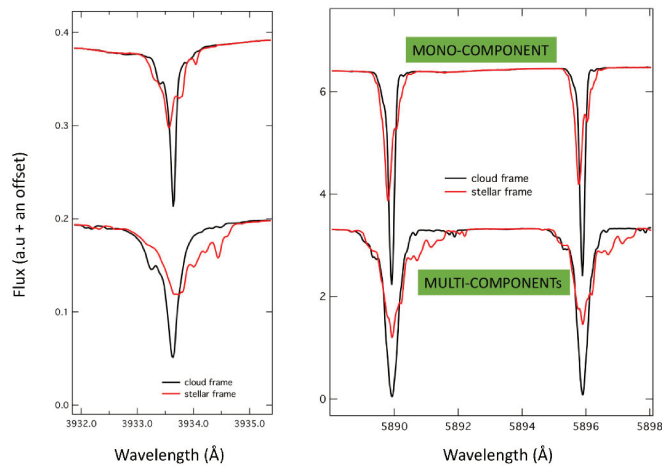


Figure 98 Same as Fig. 97 for the CaII line at 3933.6 Å (left) and the 5890/5896 Å NaI doublet.

Characterization of DIB profiles

Many of the DIB carriers are thought to be large carbonaceous molecules in the gaseous phase, but except for the very likely identification of C_{60}^+ (Campbell et al. 2015; Cordiner et al. 2017b; Spieler et al. 2017; Walker et al. 2017; Lallement et al. 2018b), none of these bands has been definitely assigned to any given species.

Identifying the DIB carriers and measuring their response to physical conditions and chemical compositions of interstellar clouds is of high importance. This would add to our knowledge of the molecular inventory of these clouds in which molecules were detected with increasing numbers of atoms (up to 18) during the last decade, with a large gap however for the pure-carbon molecules between C_2 and C_3 (Schmidt et al. 2014) on one hand and the fullerenes C_{60} and C_{70} on the other hand, leaving considerable room for other species. It also would be key to understanding the life cycle of cosmic dust and carbonaceous compounds from dying star ejected envelopes to the birth places of new stars and planetary systems.

Sub-structures in DIB profiles are indicative of the molecular structure of carriers and guide the data towards better comparisons with laboratory spectra. However, such measurements require high-performance spectrographs and to date their use has been restricted to relatively strong DIBs and a limited number of sightlines. In fact, disentangling the spectral components requires high spectral resolution, and, furthermore, is restricted to target stars for with only a small Doppler broadening along the line-of-sight — the so-called single-cloud situation, to avoid blends and sub-structures arising from nearly overlapping bands in different clouds. Moreover, the analysis of DIB profiles towards a carefully selected sample of spectra from different spectral types and corrected from telluric lines allows us to conclude with confidence that the observed substructures are neither telluric nor stellar in origin. The EDIBLES survey provides a sufficient number of such mono-clouds spectra with high resolution and high S/N ratio and thus facilitates

the study of both strong and weak DIBs.

Such a high quality gives also the possibility to increase our understanding about the origin of the variation of DIB profiles (the slight difference in width from star to star). Since this can be explained by the variation of the rotational/vibrational temperature of the carrier species, modelling these resolved profiles will provide the link between the observed spectral variations and the changes in temperature and thus will allow to derive molecular constants that characterize the carriers (constraints on the size and geometry of the possible carrier species).

10.1 C₂-DIBs profiles

Based on:

“The EDIBLES survey III. C₂-DIBs and their profiles”

M. Elyajouri, R. Lallement, N. L. J. Cox, J. Cami, M. A. Cordiner, J.V. Smoker, A. Fahrang, P. J. Sarre, H. Linnartz
Astronomy & Astrophysics, Volume 616, id.A143, 19 pp.

Abstract

An unambiguous identification of the carriers of the diffuse interstellar bands (DIBs) would provide important clues to the life cycle of interstellar matter. The so-called C₂-DIBs are a class of weak bands that fall in the blue part of the optical spectrum and are associated with high column densities of the C₂ molecule. DIB profile structures constrain potential molecular carriers, but their measurement requires high signal-to-noise, high-resolution spectra and the use of sightlines without Doppler splitting, as typical for a single-cloud situation. Spectra from the ESO Diffuse Interstellar Bands Large Exploration Survey (EDIBLES) conducted at the Very Large Telescope (ESO/Paranal) were explored to identify single-cloud and high C₂ column sightlines, extract the corresponding C₂-DIBs and study their strengths and profiles, and to investigate in detail any sub-structures. The target selection was made based on profile-fitting of the 3303 and 5895 Å NaI doublets and the detection of C₂ lines. The C₂ (2-0) (8750–8849 Å) Phillips system was fitted using a physical model of the host cloud. C₂ column densities, temperatures as well as gas densities were derived for each sightline. Eighteen known C₂-DIBs and eight strong non-C₂ DIBs were extracted towards eight targets, comprising seven single-cloud and one multi-cloud line-of-sights. Correlational studies revealed a tight association of the former group with the C₂ columns, whereas the non-C₂ DIBs are primarily correlated with reddening. We report three new weak diffuse band candidates at 4737.5, 5547.4 and 5769.8 Å. We show for the first time that at least 14 C₂-DIBs exhibit spectral sub-structures which are consistent with unresolved rotational branches of molecular carriers. The variability of their peak separations among the bands for a given sightline implies that their carriers are different molecules with quite different sizes. We also illustrate how profiles of the same DIB vary among targets and as a function of physical parameters, and provide tables defining the sub-structures to be compared with future models and experimental results.

Contributions: For this work, the entire analysis has been made in the frame of this thesis, at the exception of the C₂ line system fitting, i.e. the second paragraph of Sect.10.1.3 and the corresponding table 102 performed by Martin Cordiner.

10.1.1 Introduction

A sub-class of DIBs, the so-called C₂-DIBs, is particularly interesting because they are detected in interstellar clouds that are characterized by high columns of the C₂ molecule (Thorburn et al. 2003; Galazutdinov et al. 2006; Kaźmierczak et al. 2014), i.e., environments more closely chemically related to the cool, dense molecular clouds where stars form, as opposed to the more diffuse, warmer clouds that pervade the Galaxy. Profiles of several C₂-DIBs and some other weak DIBs have been examined also by Galazutdinov et al. (2002) and Słyk et al. (2006). Asymmetries were found, but in the case of the weak C₂-DIBs these were only seen for the 4963, 5418, 5512, 5541 and 5546 Å bands. Distinct sub-structures were found towards HD 147889 for the 4734, 5175, 5418, 5512, 5546 and 6729 Å DIBs by Galazutdinov et al. (2008).

In the case of the C₂-DIBs, the study of their profiles is particularly difficult. The weakness of the absorption requires a very high signal-to-noise ratio (S/N), a careful correction of telluric lines and disentangling from weak stellar features. In addition, because they are narrow (~ 0.5 Å), the single-cloud condition¹ is even more stringent. Very high resolution spectra commonly reveal that an apparent single absorption can actually be decomposed into absorptions in several closely related clouds, reflecting the quasi-fractal nature of the dense interstellar matter (Welty, Hobbs 2001). However, the clumps are generally fragments of the same complex, and often share a common environment and consequently possess very similar physical properties. Sightlines with high C₂ columns are crossing a cloud core with a density $\gtrsim 100$ cm⁻³ (higher than the typical diffuse interstellar medium (ISM)). It is a relatively rare situation, and therefore, the probability of crossing two independent cloud cores with identical radial velocities and with interstellar columns on the same order is low, i.e., C₂ sightlines with a single absorption offer a good probability of being dominated by a single structure. Detecting and studying the C₂-DIBs is one of the goals of the ESO/VLT EDIBLES survey. EDIBLES is devoted to a deep analysis of the DIB properties and is particularly suited for the study of weak DIBs and their sub-structures, thanks to the high resolution of the UVES spectrograph, and, especially, thanks to the high S/N reaching 800 for a large fraction of the targets (Cox et al. 2017). In addition, the large spectral coverage allows the simultaneous study of many gaseous absorption lines across the entire blue to the near-infrared range, like OH⁺ that can be used as tracer for the cosmic ray ionization rate (Bacalla et al. 2018).

Here we present an analysis of individual C₂-DIBs in EDIBLES spectra

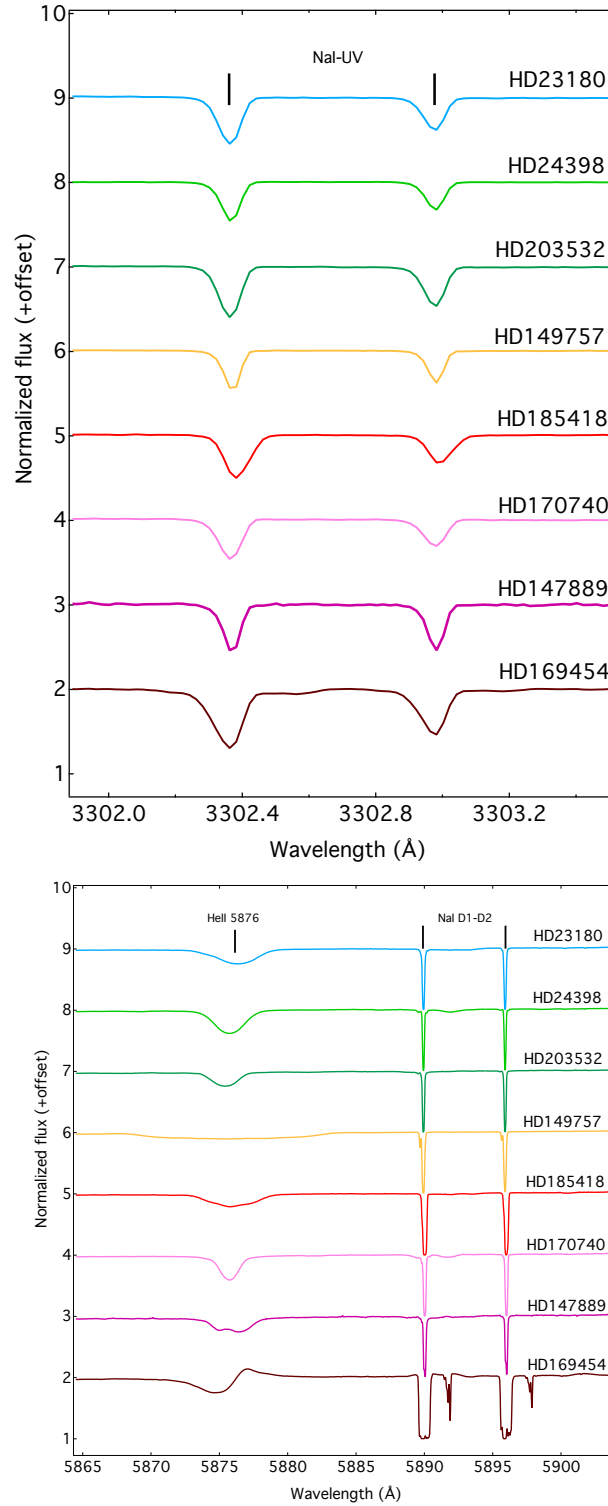
¹Note that the term single-cloud does not necessarily imply the existence of a unique homogeneous cloud but rather, a very narrow velocity dispersion of matter along the line-of-sight (much less than the instrumental resolution)

recorded along seven single-cloud and one multi-cloud lines-of-sight. We additionally show the results of a technique allowing to better reveal spectral sub-structures, namely the stacking of spectra of different target stars after they have been Doppler shifted to the cloud reference frame. Stacking spectra to enhance the S/N of band profiles has proved to be efficient to reveal DIBs (see, e.g. [Lan et al. 2015](#)), however, this is the first use of stacking in a search for profile sub-structures. In doing so, we have examined other absorption bands that may correspond to so far unreported C₂-DIBs.

The observations, the telluric removal and the single-cloud selection have already been described in the previous chapters of this Part V. In Sect. 10.1.2 we describe the selection of the C₂ sightlines and in Sect. 10.1.3 the analysis of the C₂ lines. Sect. 10.1.4 presents the selected spectra in the intervening cloud frame, in the spectral regions of the C₂-DIBs classified by [Thorburn et al. \(2003\)](#). We also show the spectral regions containing our potentially new C₂-DIBs. In Sect. 10.1.5 we list the wavenumber intervals between the observed absorption sub-peaks, when measurable, and study their variability among the bands. In Sect. 10.1.6 we present our optimal profiles obtained by co-addition of the spectra of three targets that have relatively deep DIBs and very similar kinetic temperatures and show how these vary as a function of the kinetic temperature derived from the C₂ analysis. We compare the profiles of each C₂-DIB towards several targets characterized by different C₂ excitation temperatures in Sect. 10.1.7. Finally, several correlational studies are presented in Sect. 10.1.8. They reveal a distinction between C₂ and non-C₂ DIBs. We discuss the various results in Sect. 10.1.9.

10.1.2 C₂ single-cloud sample selection

Highly reddened lines-of-sight typically intersect more than one interstellar cloud ([Welty, Hobbs 2001](#)). Consequently, the resulting DIBs then represent some ill-defined average of the DIB properties along line-of-sight conditions, which complicates the interpretation. In the case of sub-structure studies, the existence of clouds at various radial velocities has the effect of smoothing and suppressing the structures. Therefore, we restrict our study of the C₂-DIBs to single-cloud sightlines, characterized by small Doppler broadening in atomic lines. In order to select single-cloud sightlines, we have fitted the NaI 3302.368/3202.987 Å UV doublet and the NaI 5889.95/5895.92 Å D₂-D₁ doublet. Chapter 9.1 describes in details this selection. Fig. 101 shows the lack of Doppler splitting in the interstellar NaI lines for the single-cloud selected lines-of-sight which also have detectable C₂ transitions and are subsequently kept in the present study. The selected EDIBLES target stars that satisfy all conditions are: HD 24398, HD 203532, HD 149757, HD 185418, HD 170740 and HD 147889. Note that, in the case of HD 23180, [Welty, Hobbs \(2001\)](#) have found two distinct NaI lines at $R \sim 600\,000$, at variance with



202 Figure 101 NaI doublet at 3302.368/3202.987 Å (left), and NaI D1-D2 and the stellar HeII (right) line are shown for the seven selected single-cloud line-of-sight (one main cloud component) and the multi-cloud target HD 169454. The NaI spectra have been shifted to their air rest wavelengths. The same velocity shift has been applied to the NaI D1-D2 lines. The applied color coding is used in all other figures as well.

Table 101 Single-cloud lines-of-sight properties.

Identifier	Star		ISM					
	Spectral type	$v \sin(i)$ (km s ⁻¹)	E(B-V) ^a (mag)	R_V	Ref R_V ^b	$f(\text{H}_2)$ ^c	NaI-UV velocity (km s ⁻¹)	5797/5780 ^d
HD 23180	B1 III	100	0.28	3.11	V04	0.51	13.8±0.3	0.73 (ζ)
HD 24398	B1 Ib	43	0.29	2.63	W03	0.60	14.2±0.2	0.53 (ζ)
HD 203532	B3 IV	-	0.30	3.37	V04	0.84	15.2±0.2	0.48 (ζ)
HD 149757	O9.2 IVnn	303	0.32	2.55	V04	0.63	-14.2±0.5	0.43 (ζ)
HD 185418	B0.5 III _n	-	0.42	2.54	V04	0.40	-10.7±0.5	0.30 (σ)
HD 170740	B2 V	25	0.45	3.01	V04	0.58	-9.9±1.5	0.26 (σ)
HD 147889	B2 V	100	1.03	3.95	V04	0.62	-6.7±1.0	0.41 (ζ)
HD 169454 ^e	B1 Ia	49	1.03	3.37	V04	-	-9.9±1.5	0.34 (σ)

^a E(B-V) is based on photometry and intrinsic colors.

^b From [Valencic et al. \(2004\)](#) (V04) and [Wegner \(2003\)](#) (W03).

^c From [Jenkins \(2009\)](#).

^d The 5797/5780 DIB ratio is related to the effective UV radiation field strength; UV exposed environments, σ -type, have ratios < 0.35, while UV-shielded, ζ -type environments, have ratios \geq 0.35 (c.f. [Vos et al. 2011](#)).

^e HD 169454 is not a single-cloud line-of-sight but it is used for comparison (c.f. Sect. 10.1.7).

HD 24398 and HD 149757 that show only one component at the same resolution. However, we keep HD 23180 in the analysis since the Doppler splitting is very low and we assume that the two velocity components belong to two clumps of the same cloud.

Table 101 lists their spectral type, radial velocity and rotation velocity as well as the line-of-sight reddening E(B-V), the total-to-selective extinction ratio R_V , the molecular H₂ fraction $f(\text{H}_2)$, and the heliocentric radial velocity of the dominant absorbing cloud. Note that we also added to Fig. 101, to Table 101 and to our study the target star HD 169454. As shown in Fig. 101, this line-of-sight does not represent a single-cloud situation, instead there are two main clouds with radial velocities differing by $\simeq 5$ km s⁻¹, and many more other smaller clouds. We have kept this target for comparison, and also because it is characterized by high reddening E(B-V), strong C₂ lines and deep diffuse bands.

10.1.3 Interstellar C₂ lines: detection and analysis

As stated above, the second requirement for our target sample is that they additionally possess detectable C₂ lines. All combined spectra have been visually inspected for the presence of the C₂ (1-0), (2-0) and (3-0) Phillips bands. This requirement greatly reduces the number of appropriate sight-lines. Fig. 102 shows the (2-0) C₂ Phillips lines for the resulting sample. The (2-0) band has been chosen for further analysis due to its high oscillator strength, lack of contamination and apparent absence of CCD fringing residuals that adversely affect analysis of the (1-0) band.

Column densities for C₂ were derived using a custom fitting procedure written in Python. The (2-0) spectra in the range 8750–8785 Å were normal-

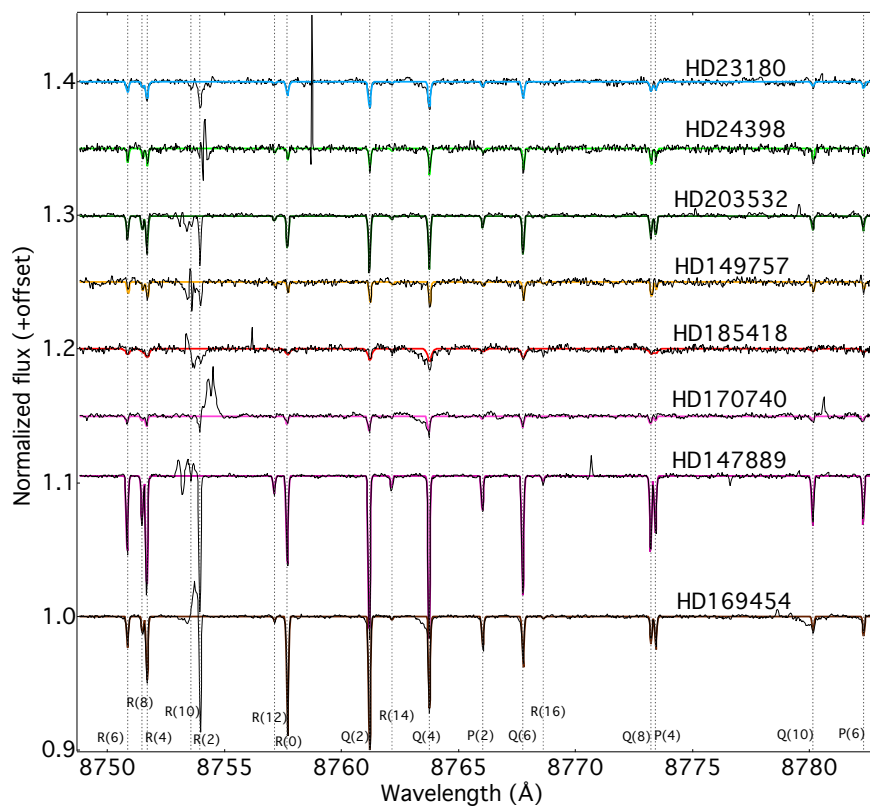


Figure 102 Observed Phillips (2-0) C_2 bands and their best-fitting model profiles. The R_{10} and R_2 lines at 8753.949 and 8753.578 Å have not been included in the fit because of the presence of a CCD artifact near these wavelengths that could not be corrected by flat-fielding. In some cases, $Q(4)$ line is blended with a suspected DIB (or stellar line).

ized to remove the stellar continuum, and the C_2 spectrum was fitted using a model consisting of Gaussian absorption profiles characterized by a single Doppler shift (v) and broadening parameter (b), convolved with the 2.8 km s^{-1} UVES point spread function. The model opacity spectrum was generated as a function of column density (N), kinetic temperature (T_{kin}) and $H + H_2$ number density (n) using the excitation model of [van Dishoeck, Black \(1982\)](#). Tabulated level populations were obtained from McCall's C_2 Calculator (<http://dib.uiuc.edu/c2/>; see also [Snow, McCall 2006b](#)) on a finely-sampled T, n grid. Transition wavelengths and oscillator strengths were taken from [Sonnentrucker et al. \(2007b\)](#). The set of variable model parameters (v, b, N, T, n), defined in Table 102, was optimized using Levenberg-Marquardt χ^2 minimization until the best fit to the observed spectrum was obtained. The resulting parameter values for each sightline are given in

Table 102 Gas kinetic temperature T_{kin} , volume density n , column density N , Doppler b parameter, radial velocity v derived from Phillips (2-0) C₂ system for the selected sightlines, and C₂ column density normalized to extinction $N(\text{C}_2)/E(\text{B-V})$.

Identifier	This work						Kazmierczak et al. ^a	
	T_{kin} (K)	n (cm ⁻³)	$\log N(\text{C}_2)$ (cm ⁻²)	b (km s ⁻¹)	v (km s ⁻¹)	$N(\text{C}_2)/E(\text{B-V})$	T_{02} (K)	ref
HD 23180	44.7 ^{+5.9} _{-3.6}	346.5 ^{+68.3} _{-46.7}	13.31 ± 0.02	1.95 ± 0.10	13.61 ± 0.06	7.3 × 10 ¹³	20±7	K09
HD 24398	56.7 ^{+10.9} _{-8.4}	211.5 ^{+51.9} _{-30.2}	13.30 ± 0.02	0.93 ± 0.13	13.97 ± 0.06	6.9 × 10 ¹³	-	
HD 203532	40.7 ^{+1.2} _{-1.3}	282.1 ^{+10.1} _{-10.2}	13.58 ± 0.01	1.06 ± 0.04	15.40 ± 0.01	1.3 × 10 ¹⁴	-	
HD 149757	52.2 ^{+10.9} _{-7.9}	199.2 ^{+40.6} _{-21.1}	13.26 ± 0.02	0.90 ± 0.15	-14.34 ± 0.06	5.6 × 10 ¹³	42±42	K10b
HD 185418	66.8 ^{+6.2} _{-8.2}	-	13.1 ± 0.1	3.55 ± 0.30	-10.73 ± 0.20	3.3 × 10 ¹³	-	
HD 170740	45.4 ^{+7.5} _{-5.8}	248.5 ^{+42.9} _{-31.1}	13.15 ± 0.02	1.83 ± 0.11	-8.80 ± 0.07	3.1 × 10 ¹³	14±5	K10b
HD 147889	44.1 ^{+0.4} _{-0.5}	260.7 ^{+3.2} _{-3.9}	14.09 ± 0.01	0.98 ± 0.01	-7.49 ± 0.01	1.2 × 10 ¹⁴	49±7	K10a
HD 169454	18.8 ^{+0.2} _{-0.2}	356.1 ^{+3.3} _{-2.4}	13.85 ± 0.01	0.90 ± 0.01	-8.92 ± 0.01	7.1 × 10 ¹³	23±2	K10a

^a Sources are K09: Kazmierczak et al. (2009), K10a: Kazmierczak et al. (2010a) and K10b: Kazmierczak et al. (2010b).

Table 102, and the best-fitting spectral models are shown in Fig. 102. A complete description of all the EDIBLES C₂ spectra and their properties will be presented in a separate study (Cordiner et al., in prep.). Parameter uncertainties ($\pm 1\sigma$) were generated using Monte Carlo noise resampling with 200 replications.

10.1.4 Extractions of the C₂-DIBs

Extraction of individual C₂-DIBs We have analyzed the spectral regions that correspond to the series of 18 DIBs classified as C₂-DIBs by Thorburn et al. (2003), using the DIB wavelength centers listed in this work. For each sightline and each DIB, we have fitted a third order polynomial continuum around the DIB, normalized the spectrum based on this continuum, then determined the DIB equivalent width (EW) as the area between the spectrum and the normalized continuum. Figs. 103, 104, 105, 106, and 107 show the normalized spectra around each C₂-DIB for the seven single-cloud targets and HD 169454. These figures also show our choice of the spectral areas on both sides of the band used for continuum-fitting as well as for the spectral interval used for the EW measurements. As stated in the introduction, it is essential here to identify weak and narrow overlapping stellar lines. In lieu of observing additional, lightly reddened stars of similar spectral types to be used as spectral standards, we used the eight targets together and the fact that stellar line widths must correlate with the rotations (at variance with DIBs). To do so we have used the full spectrum to estimate the rotational broadening for each target. We also used the rotation velocities $v\sin(i)$ listed in Table 101 when available from the CDS-Simbad

website. For example, visual inspection of the stellar HeII 5876 Å line in Fig. 101 shows that HD 149757, HD 185418 are fast rotators while HD 23180, HD 24398, HD 203532, HD 170740 have narrower photospheric lines; in these latter cases, we checked even more carefully for the presence of narrow stellar lines in the DIB spectral regions that could mimic DIBs or DIB sub-structures (see the cases of 4727, 4963, 5541, 5546, 5762, 6729; Table 3 from [Slyk et al. 2006](#)). In the case of the 4734, 5170, 5175, and 6729 Å DIBs, we found that the continuum is contaminated by stellar lines that fall just outside the DIB and, as shown in Figs. 103, 104, 105, 106 and 107 these lines have been excluded from the fitted spectral interval during the continuum-fitting. In the case of the 4727 Å DIB, it has a double structure suggestive of a blend with a stellar feature on its red side. However, the width of this structure appears to be independent of the stellar rotation. Rather, its shape is perfectly correlated with the main absorption. Therefore, we concluded that this absorption is part of the DIB or an additional, blended DIB, and we measured the total equivalent width of both structures, as shown in Fig. 103. The situation for the 5003 Å DIB is quite different. There we find a blend with an additional absorption, however, this absorption is absent in three other sightlines. We conclude that this feature must be of stellar origin and we keep only the three clean bands.

We used the residuals of continuum fitting to estimate the standard deviation in each DIB spectral interval and for each target. This standard deviation was used in a Monte-Carlo noise resampling with 100 replications and we estimated in this way the uncertainty on each DIB EW. All EWs and their uncertainties are listed in Table 103. In exactly the same way, we measured the EWs and associated uncertainties for eight strong non-C₂ DIBs, and the results are also listed in Table 103. Their EWs are used in Sect. 10.1.8.

Inspection of Figs. 103-107 reveals clearly that sub-structures do exist for at least 14 DIBs. The shapes look very similar to those of the strong bands in previous work which have been studied in depth and found to be compatible with rotational contours of large molecules. There are strong differences from one band to another, with two or three individual branches, depending on the band, accompanied in some cases by a broad red wing. Fig. 108 summarizes the observed variety of DIB profiles.

Potential additional weak C₂-DIBs In the course of this study we noticed three weak absorption features resembling DIBs falling at the same wavelength when spectra are shifted to the cloud frame, i.e. being very likely of interstellar origin. Fig. 109 displays the spectra of the targets that show clearly these features. The relative strengths are roughly similar to those found for the other C₂-DIBs, which reinforces their identification as new DIBs. These potentially new bands are centered at 4737.5, 5547.4 and 5769.8 Å, respectively. Their weakness prevents identification of sub-

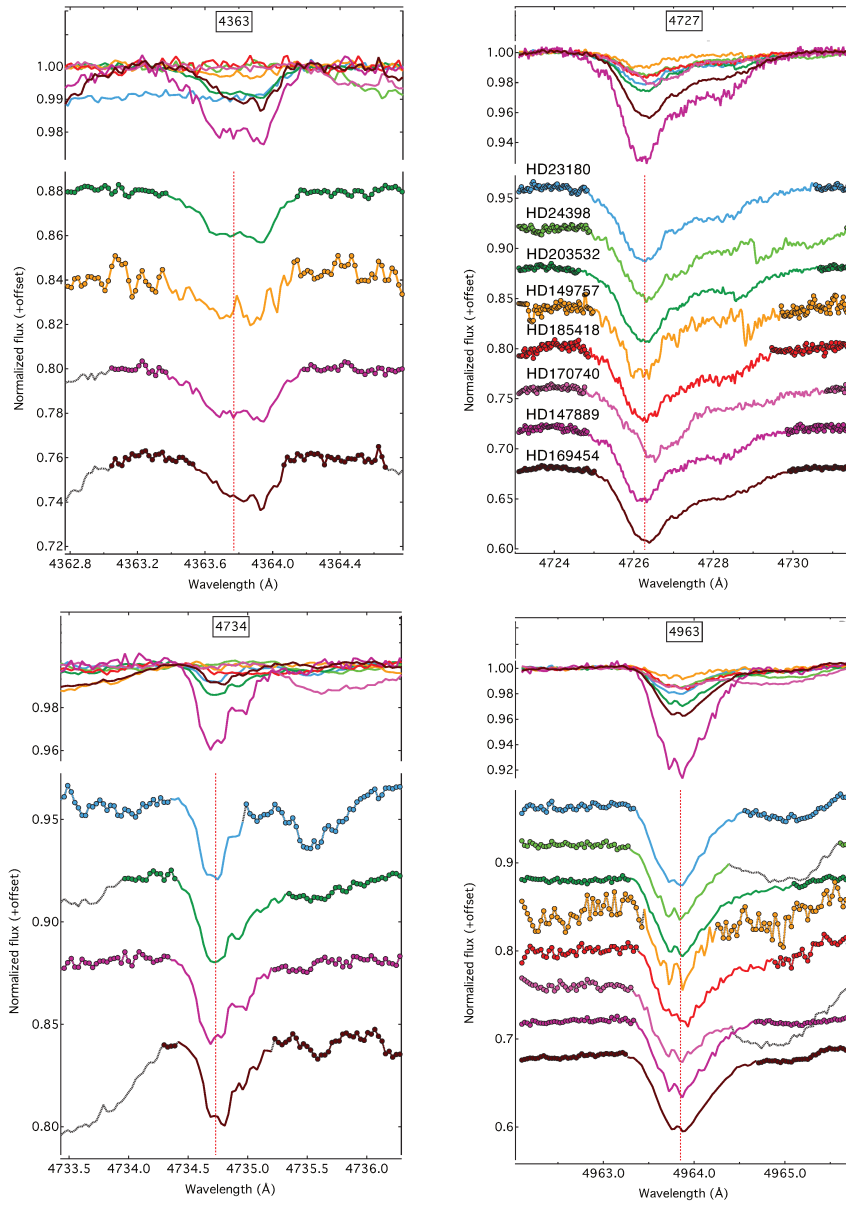


Figure 103 The 4363, 4727, 4734, and 4963 C₂-DIBs recorded along seven single-cloud and one multi-cloud line-of-sight. Top in all four panels: overlaid C₂-DIB profiles at the same vertical scale for all stars. Bottom in all four panels: same C₂-DIB vertically displaced and depth-equalized profiles. The red dashed line shows the DIB location. See for color coding Fig. 101.

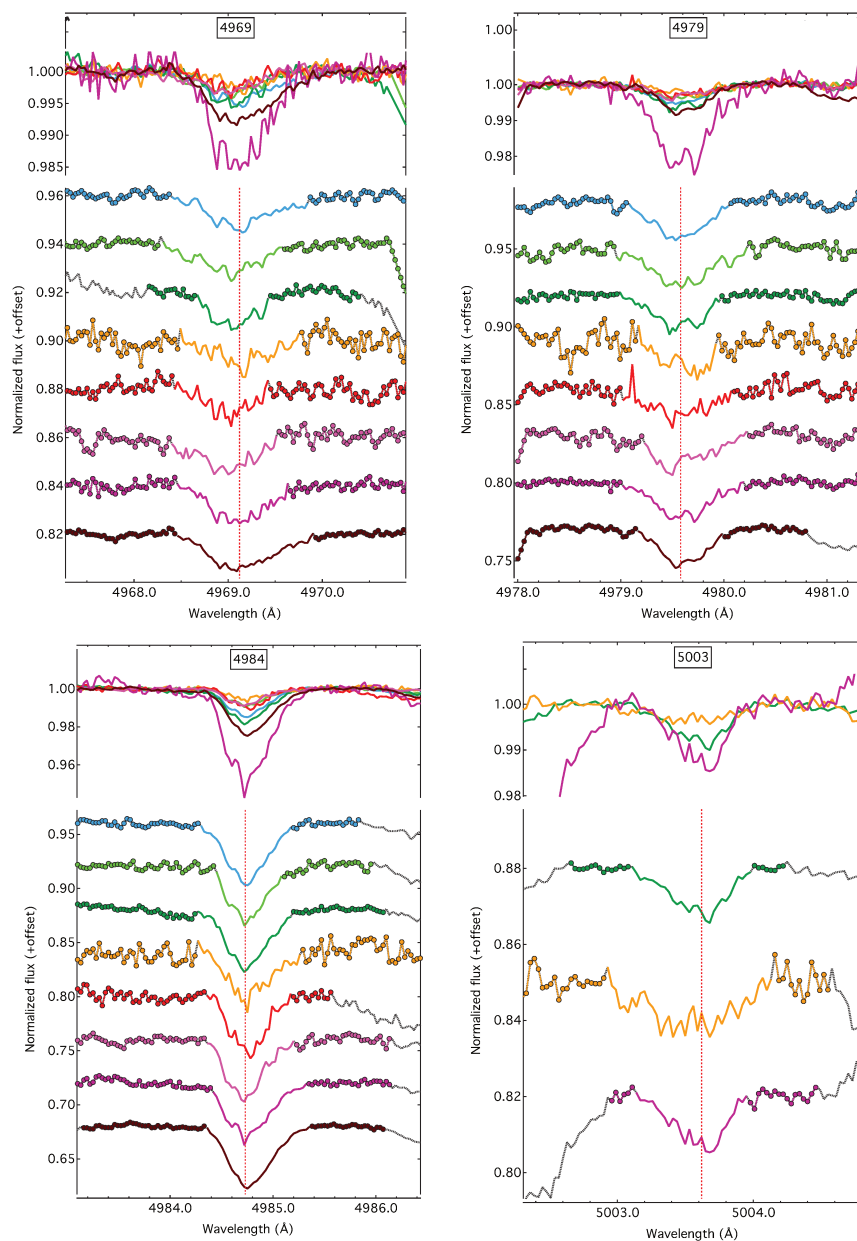


Figure 104 The 4969, 4979, 4984, and 5003 C₂-DIBs recorded along seven single-cloud and one multi-cloud line-of-sight. Top in all four panels: overlaid C₂-DIB profiles at the same vertical scale for all stars. Bottom in all four panels: same C₂-DIB vertically displaced and depth-equalized profiles. The red dashed line shows the DIB location. See for color coding Fig. 101. 5003 Å band is blended with stellar lines.

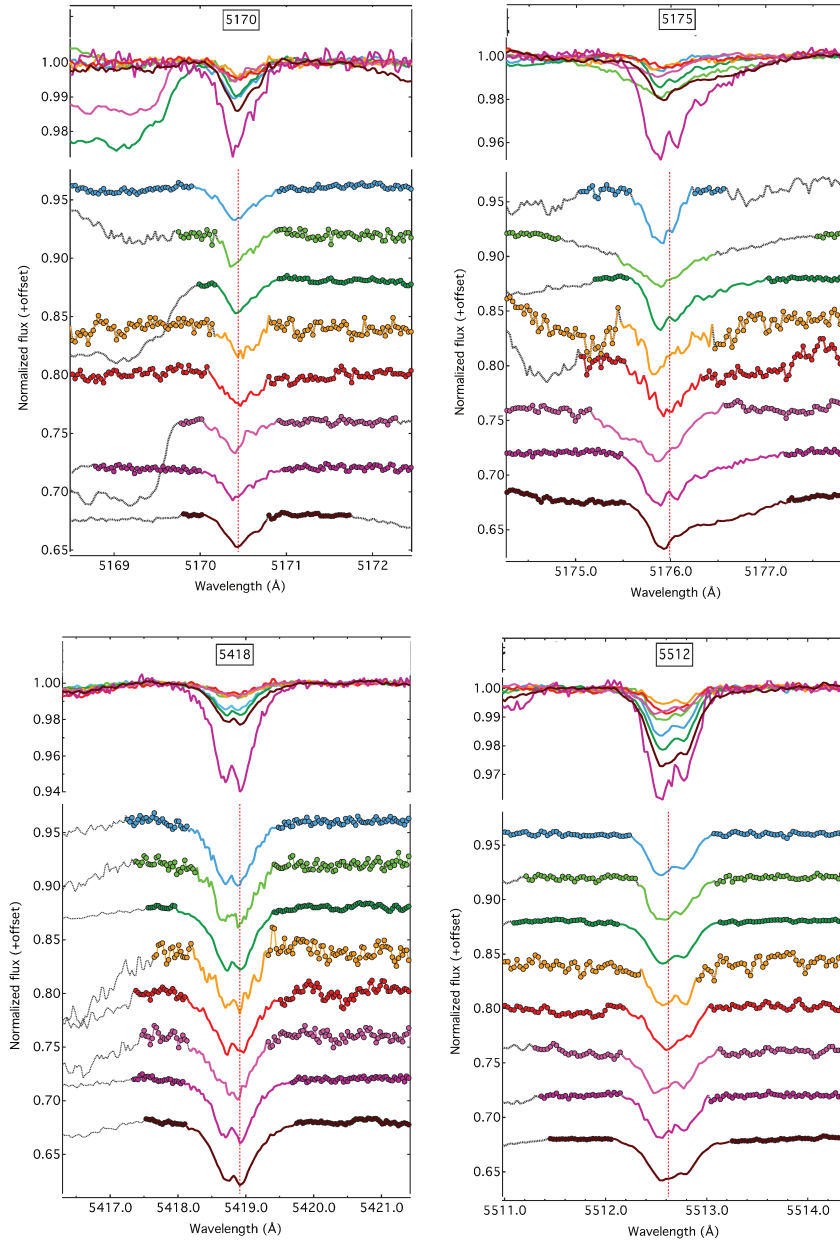


Figure 105 The 5170, 5175, 5418, and 5512 C₂-DIBs recorded along seven single-cloud and one multi-cloud line-of-sight. Top in all four panels: overlaid C₂-DIB profiles at the same vertical scale for all stars. Bottom in all four panels: same C₂-DIB vertically displaced and depth-equalized profiles. The red dashed line shows the DIB location. See for color coding Fig. 101.

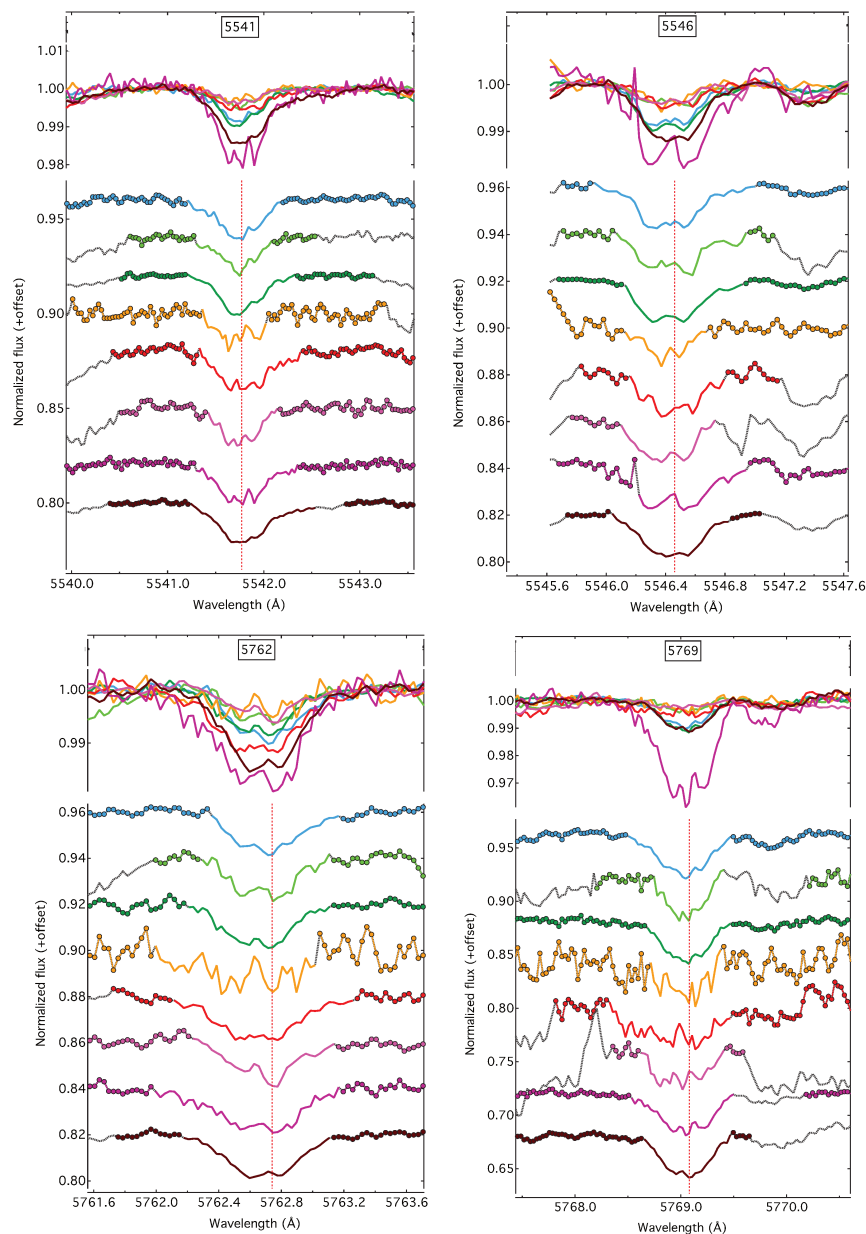


Figure 106 The 5541, 5546, 5762, and 5769 C₂-DIBs recorded along seven single-cloud and one multi-cloud line-of-sight. Top in all four panels: overlaid C₂-DIB profiles at the same vertical scale for all stars. Bottom in all four panels: same C₂-DIB vertically displaced and depth-equalized profiles. The red dashed line shows the DIB location. See for color coding Fig. 101.

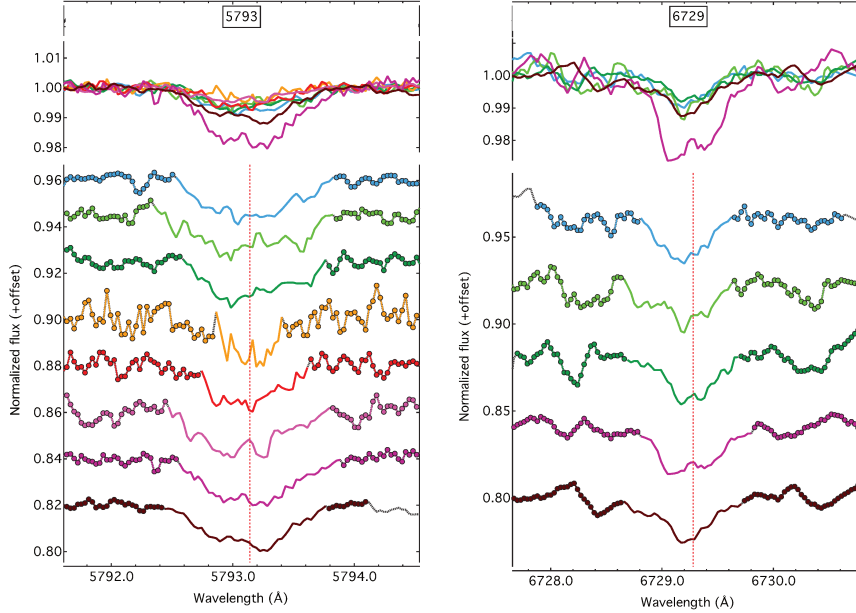


Figure 107 The 5793 and 6729 C₂-DIBs recorded along seven single-cloud and one multi-cloud line-of-sight. Top in all four panels: overlaid C₂-DIB profiles at the same vertical scale for all stars. Bottom in all four panels: same C₂-DIB vertically displaced and depth-equalized profiles. The red dashed line shows the DIB location. See for color coding Fig. 101.

structures in their profiles. Two of them are found to lie 1 Å to longer wavelength of a strong C₂-DIB. Further measurements will help in confirming these new bands. We excluded them from the correlational studies that are discussed in Sect. 10.1.8 due to large uncertainties in their EWs. For this reason, it is not possible to ascertain their C₂-DIB nature with confidence.

10.1.5 Variability of profiles among the eighteen C₂-DIBs

The main result of this study is the appearance of sub-structures with two or three sub-peaks in at least 14 C₂-DIBs, the remaining four being too weak or too contaminated (at 5003, 5762, 5793 and 6729 Å) to draw a definite conclusion. The two and three sub-peak profile structures are consistent with partially resolved rotational PQR-type branch structures and as such hint for a molecular nature of the involved carriers. It is recognised that it is not proven that the substructures are due to rotational branches and that the shortest wavelength component is an R feature, but for ease of discussion we have chosen this interpretation and to label the components as P (located at the longest wavelengths), Q and R (shortest wavelengths). When treating

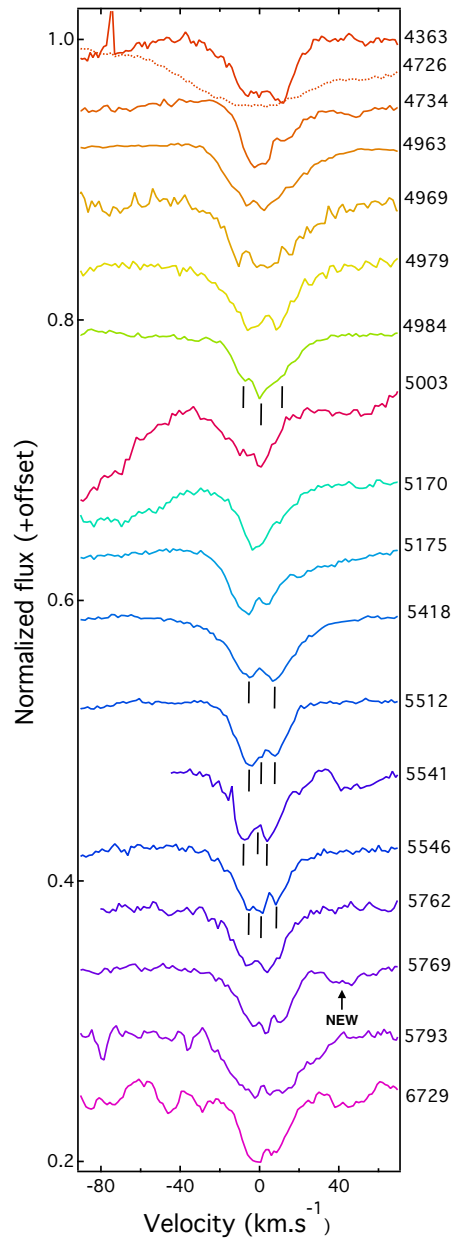


Figure 108 Extracted average C₂-DIB profiles (i.e., from stacking profiles of HD 23180, HD 203532, and HD 147889) normalized to the same depth of 4963 Å DIB. Tick marks refer to the location of sub-peaks of Table 104.

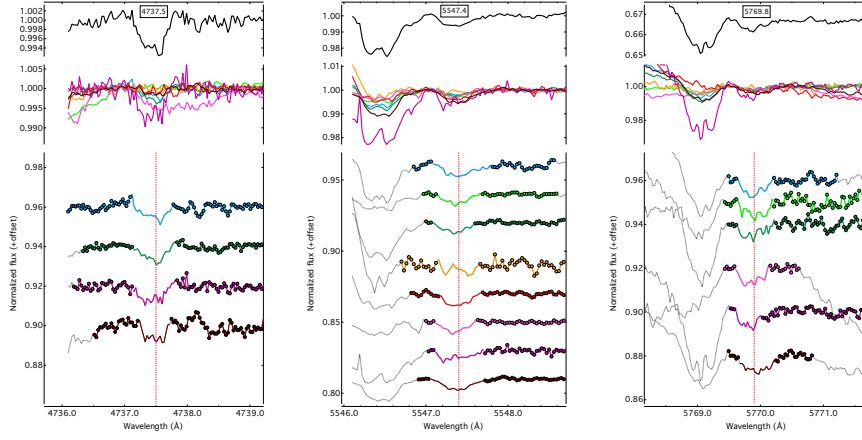


Figure 109 Potential new detection of weak C₂-DIBs at 4737.5, 5547.4 and 5769.8 Å (they appear toward sightlines where the other C₂-DIBs are well-detected). The red dashed line shows the DIB location. Top graphs (black) in all three panels: extracted average normalized profile of C₂-DIBs created from stacking three single-cloud targets: HD 23180, HD 203532 and HD 147889, shown below. Middle in all three panels: overlaid C₂-DIB profiles at the same vertical scale for all stars. Bottom in all three panels: same C₂-DIB vertically displaced and depth-equalized profiles. The red dashed line shows the DIB location. The wavelengths are in the interstellar rest frame. See for color coding Fig. 101.

the profiles as molecular rotational contours, we assume that the upper state rotational constants are smaller than in the ground state. Selection rules can then result in different types of transitions resulting in either a two-peak profile similar to the 5797 or 6196 Å DIB profiles that then represent unresolved P and R branches or a three-peak profile that additionally displays a central Q branch. With these conventions, we have determined the peak positions of the sub-peaks (in wavenumber space; ν_P , ν_Q and ν_R) and we have extracted the wavenumber intervals ($\Delta_{\nu_{PQ}} = \nu_Q - \nu_P$, $\Delta_{\nu_{QR}} = \nu_R - \nu_Q$ and $\Delta_{\nu_{PR}} = \nu_R - \nu_P$) between them in all relevant cases. This was done based on visual selection of regions possessing a well-defined minimum or secondary minimum, and subsequent fitting of the bottom region of each sub-structure with a second order polynomial to extract the minimum location. The C₂-DIB sub-structure peak separations $\Delta_{\nu_{PQ}}$, $\Delta_{\nu_{QR}}$ and $\Delta_{\nu_{PR}}$ are listed in Table 104. These values are given in cm⁻¹, as this unit offer a wavelength independent value that allows a direct comparison between the different C₂-DIBs. We did not attempt to fit the profiles with the product of individual components, as the choice of the number of components is quite subjective, especially in the case of the presence of red wings or for the weakest bands. According to the results of Table 104 and as can be seen for all DIBs in Fig. 108, the peak

10. CHARACTERIZATION OF DIB PROFILES

Table 103 DIB equivalent widths.

DIB (Å)	23180	24398	203532	149757	185418 (mÅ)	170740	147889	169454
C ₂ -DIBs								
4363	- ^a	<0.3	4.3±0.2	1.3±0.4	< 0.4	< 0.2	11.1±0.4	4.4± 0.2
4727 ^a	46.7±0.9	38.3±0.7	55.3±1.1	17.0±1.0	35.8±1.0	45.3±1.0	155.4±2.9	95.0±1.1
4734	2.3±0.8	<0.5	6.5±0.7	<0.6	<4	<0.5	15.2±0.9	3.2±0.4
4963	12.0±0.8	9.6±0.3	21.2±0.4	3.8±0.6	11.6±0.7	11.2±0.3	51.9±0.9	24.8±1.0
4969	3.8±0.3	2.5±0.2	2.8±0.2	1.4±0.5	1.5±0.3	2.2±0.3	9.7±0.8	6.4±0.3
4979	3.0±0.3	2.5±0.3	3.6±0.3	1.3±0.4	1.9±0.3	2.0±0.3	14.1±0.9	3.9±0.3
4984	6.6±0.3	3.6±0.3	8.2±0.4	2.4±0.5	4.0±0.3	3.6±0.2	24.4±1.1	11.2±0.3
5003	- ^a	- ^a	4.1±0.2	2.6±0.5	- ^a	- ^a	5.6±0.5	- ^a
5170	4.5±0.4	1.6±0.2	3.2±0.5	1.3±0.5	1.9±0.3	1.9±0.3	11.1±0.8	5.3±0.2
5175	2.3±0.2	13.5±0.4	7.9±0.3	2.8±0.8	2.3±0.5	6.2±0.5	31.7±1.0	16.1±0.8
5418	10.3±0.4	5.1±0.3	12.3±0.3	3.7±0.4	5.4±0.4	5.1±0.3	40.8±0.9	16.4±0.3
5512	7.5±0.3	5.0±0.2	10.6±0.3	2.2±0.4	3.8±0.4	4.5±0.3	18.2±0.5	14.6±0.3
5541	4.5±0.3	2.1±0.2	4.7±0.2	1.4±0.3	3.3±0.3	1.7±0.2	10.9±0.8	9.3±0.3
5546	4.0±0.4	2.0±0.3	4.7±0.3	1.5±0.4	1.9±0.3	1.7±0.1	8.2±0.8	5.7±0.3
5762	4.6±0.3	2.7±0.2	4.1±0.3	2.8±0.5	7.2±0.5	2.3±0.3	11.6±1.0	8.1±0.3
5769	4.8±0.4	1.5±0.3	5.2±0.3	<2	<4.5	1.2±0.2	20.6±0.8	5.4±0.3
5793 ^b	6.3±0.7	5.3±0.6	5.3±0.4	1.7±0.4	3.9±0.5	3.3±0.4	15.8±1.0	8.7±0.3
6729	4.2±0.6	5.1±1.5	3.5±0.7	<5	<4	<4	15.5±1.5	6.6±1
New C ₂ -DIB candidates								
4737.5	0.8±0.3	<0.4	1.2±0.2	<0.5	<0.5	blend ^a	3.0±0.7	0.5±0.2
5547.4	0.7±0.2	0.9±0.2	0.8±0.1	<0.7	1.3±0.2	0.9±0.1	2.5±0.6	2.0±0.3
5769.8	1.0±0.2	0.7±0.2	0.7±0.2	<1.3	<1.5	0.7±0.1	1.9±0.7	1.8±0.2
Selected strong DIBs								
5850	31.1±0.6	20.4±0.7	28.0±0.3	10.9±0.6	27.6±0.6	21.0±0.4	64.6±1.0	61.0±0.7
5797	58.6±1.0	51.4±0.6	53.1±1.1	28.3±0.9	80.3±1.2	61.2±0.9	143.5±2.5	158.4±2.3
5780	80.0±0.9	97.2±0.8	108.6±0.9	65.6±1.3	266.1±1.8	237.0±1.6	346.9±2.9	463.9±2.2
6196	12.6±0.6	13.6±0.7	12.7±0.6	8.5±0.7	33.7±2.1	23.7±0.9	34.8±1.6	52.4±0.6
6234	5.9±0.7	5.9±0.5	4.7±0.3	2.2±1.0	9.1±0.7	11.6±0.4	14.4±1.4	15.1±1.2
6376	7.8±0.6	7.7±0.6	7.7±0.7	5.0±0.7	17.3±1.2	10.4±0.9	34.1±2.4	20.0±1.5
6379	37.6±0.6	57.4±0.7	43.2±0.4	15.2±0.7	71.5±0.7	55.6±0.7	82.4±1.8	93.3±1.4
6614	45.3±0.7	60.2±0.6	57.7±0.6	41.4±1.0	166.3±0.9	120.0±0.6	160.6±2.1	182.6±1.1

^a blended with stellar lines

^b possible telluric residuals

relative amplitudes and peak sub-structure separations are quite different among the DIBs. The separation between the P and R branch scales roughly with $B \times T$, where B is the rotational constant and T the carrier's rotational temperature (but see Huang, Oka 2015). Therefore for the same cloud and within the assumption of the same physical conditions, this observed variability implies that the sizes of the carriers for the different C₂-DIBs are most likely quite different.

10.1.6 Prominent sub-structures and average spectral profiles

The generally low signal strengths do not allow clear identifications of sub-structures for all combinations of DIBs and targets. A classical method used to increase the S/N and enhance weak features is the co-addition of profiles. Some caution is needed here since different sightlines may correspond to

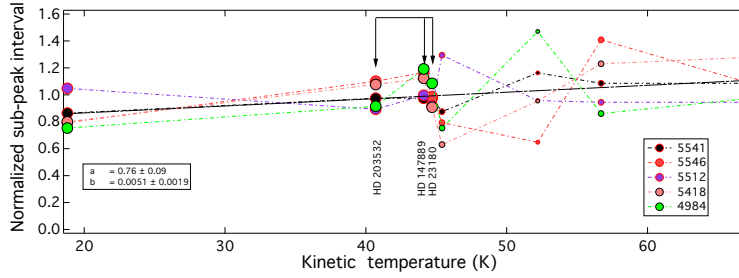


Figure 1010 Normalized spectral intervals between the sub-peaks in the profiles of several C₂-DIBs as a function of the C₂-based kinetic temperature (see text) of each target. Uncertainties on the intervals can be deduced visually from the drawn profiles in Figs. 103, 104, 105, 106, and 107, and are on the order of the data point dispersion. The dashed line is a linear fit to the average over the five different DIBs. The size of the marker indicates the reliability of the sub-peak interval determination, again visually determined from the quoted figures. The three targets used for the co-addition of the DIB profiles are marked by arrows.

different shapes of the same DIB, in this case co-adding sub-structures is not physical. This could be the case if the carrier internal population distributions were markedly different from one sightline to another in response to different excitations. Indeed, such peak-to-peak variations have been observed and used to place constraints on the rotational excitation temperatures of the 6614 and 6196 Å DIB carriers (Cami et al. 2004; Kaźmierczak et al. 2009). In order to test the co-addition feasibility, we have used the sub-peak intervals of Table 104 to estimate upper limits on the profile variability. We discarded all cases for which peak determinations were too uncertain, which resulted in the selection of only five bands. For each type of interval, we normalized it by simply dividing by the mean value of the sub-peak intervals over all eight targets. Fig. 1010 displays the resulting normalized intervals between the sub-peaks, here as a function of the kinetic temperature T_{kin} for the corresponding target, derived from the C₂ analysis. Fig. 1010 shows that the variations from one sightline to the other for the same band are significantly smaller than the dispersion among the normalized intervals of the various DIBs for the same target, although a weak increase with temperature is discernible. It is difficult to draw firm conclusions from this, given the uncertainties in our sub-peak wavelengths. Three stars, namely HD 23180, HD 203532 and HD 147889 have the deepest absorption bands and are characterized by a good S/N, thus have relatively clear sub-structures. Fig. 1010 confirms that for these three targets (marked by arrows) the sub-peak interval variability is the smallest. For this reason, we performed a co-addition of the profiles over these three targets only. Before

the co-addition, the normalized DIB profiles were shifted to a common interstellar rest frame and elevated at a power in such a way that their depths are the same for the three targets. The average profiles are displayed in Fig. 108. Although they can not be considered as pure intrinsic profiles (as stated above, rotational contours may change from one target to the other), these average profiles are free from telluric or stellar contamination and we believe they are our most accurate representation of each DIB structure. Such information complements well that contained in the series of individual measurements. On the other hand, it is often difficult to preclude profile variation and for this reason we discuss the DIBs towards each of the three selected stars separately in the next section.

10.1.7 Search for profile variability among the sightlines

With the goal of going one step further in the validation of the average profiles, we investigated the potential variations of DIB profiles for the three selected single-cloud targets. In particular, measurements of the C_2 molecule rotational temperatures T_{02} defined as the average excitation temperature of the two (resp. three and four) lowest rotational levels of the ground electronic state have been performed by [Kaźmierczak et al. \(2009\)](#) and [Kaźmierczak et al. \(2010a\)](#) for two of these single-cloud sightlines. The temperatures are different: $T_{02} = 20$ K for HD 23180 and 49 K for HD 147889.

Figs. 1011, 1012 and 1013 show the 18 C_2 -DIB profiles for the three EDIBLES targets after normalization to reach the same maximum depth. We also show the normalized profiles for the multi-cloud target HD 169454. It is interesting to disentangle the effects of Doppler broadening due to cloud multiplicity and broadening due to increase of the excitation temperature. Coincidentally, $T_{02} = 23$ K for HD 169454, is very similar to the value measured for HD 23180. Moreover, profiles of the 6196 Å DIB have been investigated for this star as well as for HD 147889 and HD 23180 by [Kaźmierczak et al. \(2009\)](#). In order to better visualize differences, we show the profiles that correspond to HD 147889 superimposed on the three others because for this sightline the sub-structures are the most prominent. After careful inspection of all comparison figures, we identified three categories of DIBs.

The first category corresponds to the existence of sub-structures for the four targets, and no detected variation in the total width of the band nor in the locations of the sub-peaks. Falling in this category are DIBs 4727, 4734, 4963, 4984, 5418, 5512 and 5541 Å (Fig. 1011) confirming an earlier result by [Galazutdinov et al. \(2008\)](#) for the 4963, 5418 and 5512 Å DIBs. Therefore, for those bands the stacking is justified as a means to enhance the profile structures. It is worth noting that for 4984, 5512 and 5541 Å DIBs the sub-structures are smoother in the case of lower temperatures.

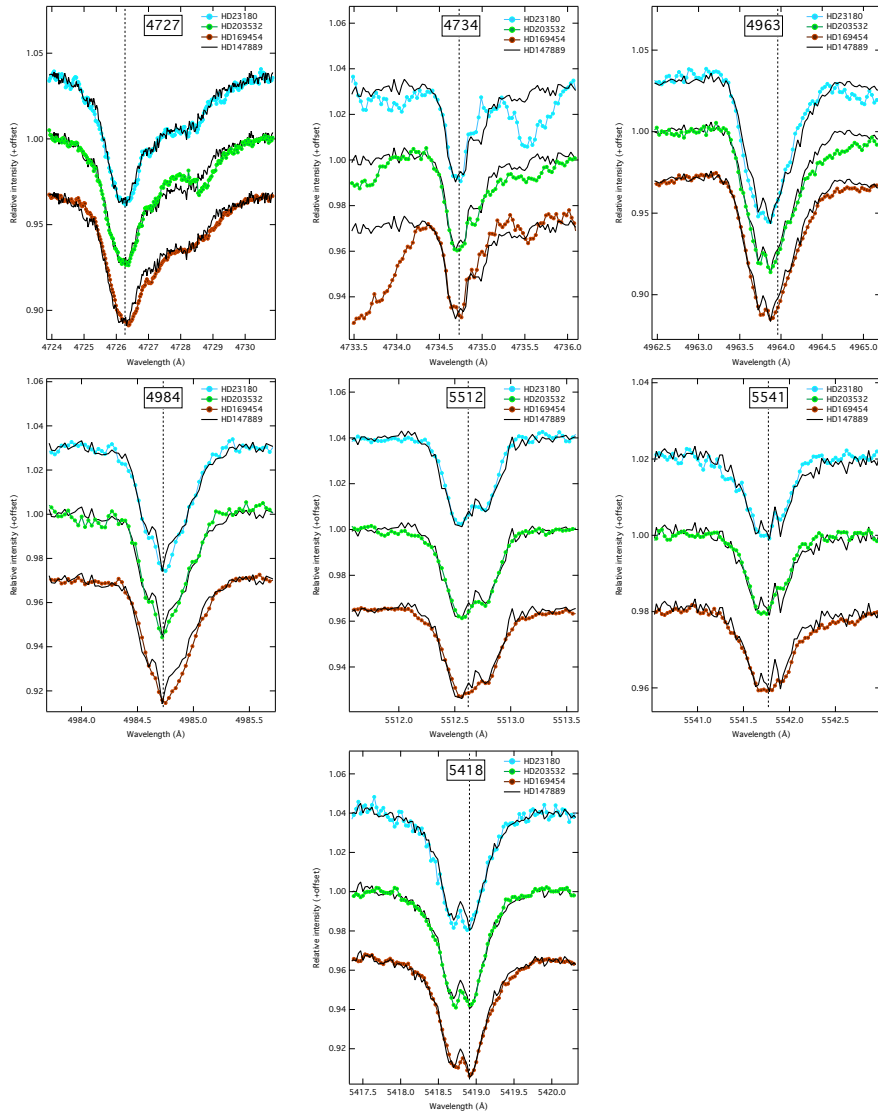


Figure 1011 Comparison between C₂ DIB profiles normalized to their central depths toward HD 23180 (blue), HD 203532 (green), HD 147889 (black) and HD 169454 (brown). The first three targets are those chosen for profile co-additions, for which results are shown in previous figures. The C₂ excitation temperatures are 20, 23 and 49K for HD 23180, HD 169454 and HD 147889 respectively (see Table 102).

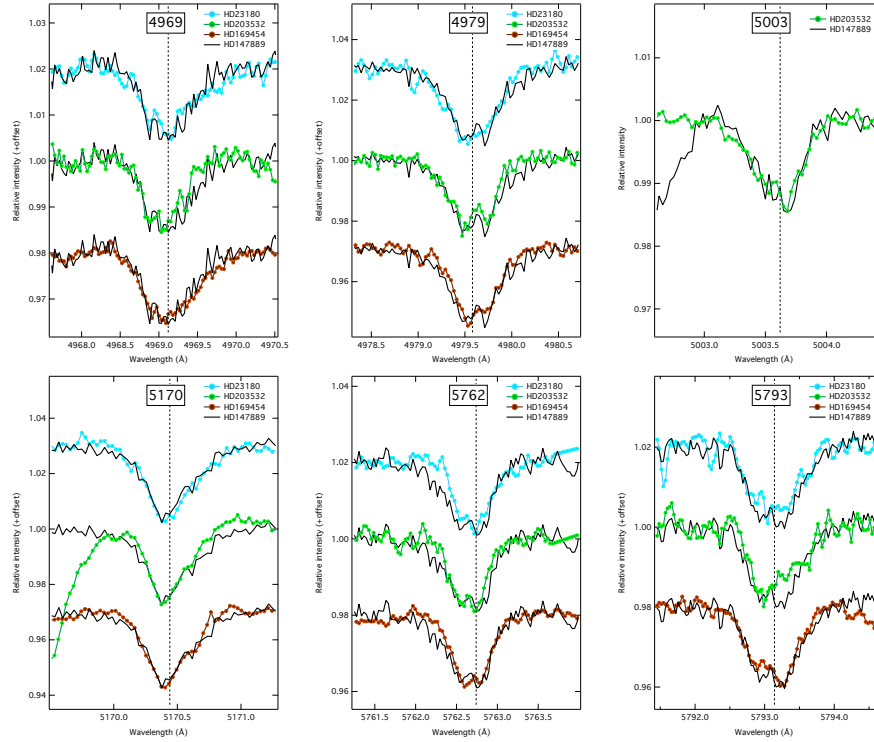


Figure 1012 Same as Fig. 1011 but for 4969, 4979, 5003, 5170, 5762, and 5793 Å.

The second category corresponds to the weakest bands for which individual profiles do not clearly reveal sub-structures well above the noise and no apparent variations of the total width. In those cases, the co-addition is justified since it simply improves the S/N. This is the case for the 4969, 4979, 5003, 5170 DIBs (Fig. 1012). In the case of the 5762 and 5793 Å DIBs the co-addition does not bring any improvement. We believe this may be due to the effect of telluric residuals (see the remark on the HITRAN database in Sect. 8.1 of Chapter 8) that become very important for targets with the weakest absorbing column. Note that these are the two weakest of all C₂-bands. Further measurements and improved telluric corrections are needed to confirm their sub-peaks.

The third DIB category corresponds to the detection of profile variations among the four targets, and this may potentially reveal a response to the excitation temperature. Indeed, the full DIB width appears smaller for HD 23180 ($T_{02} = 20$ K) and, to a lesser extent, for HD 203532 (unmeasured T_{02}) compared to HD 147889 ($T_{02} = 49$ K). Interestingly, these DIBs are also narrower for the multi-cloud star HD 169454 ($T_{02} = 23$ K) than for HD 147889, an effect opposite to the expected broadening due to cloud multiplicity. Moreover,

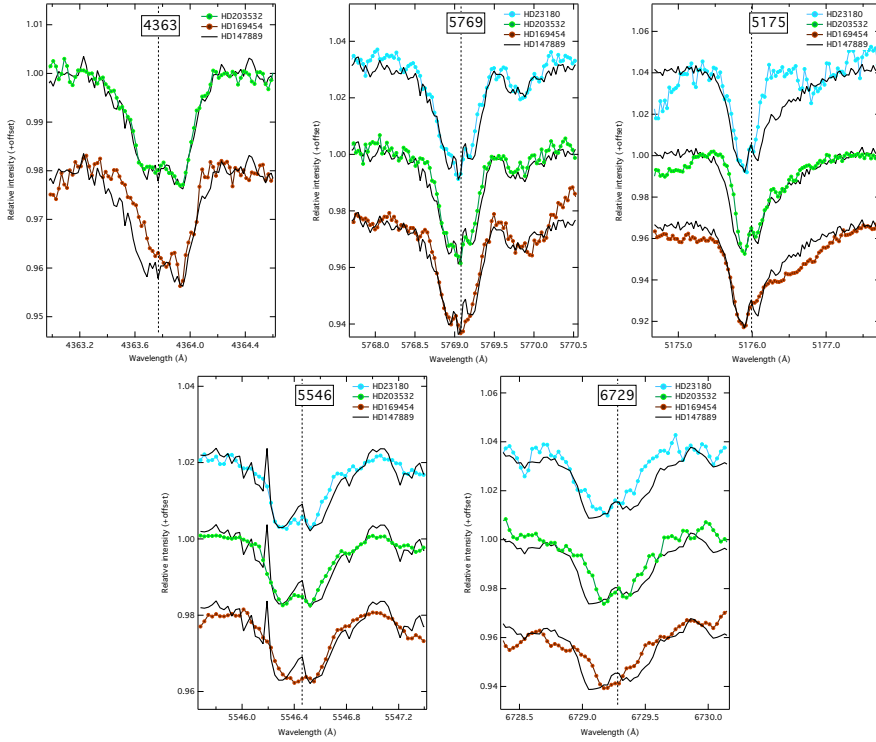


Figure 1013 Same as Fig. 1011 but for 4363, 5769, 5175, 5546 and 6729 Å.

the amplitudes of the sub-peaks appear smaller for HD 23180, HD 203532 and HD 169454 compared to HD 147889. Falling in this category are the 4363, 5541, and 5769 Å DIBs. Identical, but less clearly measured effects can also be seen for DIBs 5175, 5546, and 6729 Å. If these simultaneous variations in width and peak amplitudes are actually linked to the variation of the rotational excitation, then for these DIBs the average profile does not correspond to any intrinsic profile. However, we have kept these average profiles in Fig. 108. Interestingly, the DIBs from this third category are all very tightly correlated with the C₂ column, as discussed in the next section.

10.1.8 Correlational studies

Correlations with the C₂ column Our combined measurements of C₂ columns and weak DIB equivalent widths towards single-cloud targets constitute an ideal dataset for the study of any link between the C₂ molecule and each DIB carrier. Fig. 1014 displays the equivalent widths of the recorded C₂-DIBs as a function of the C₂ column density $N(\text{C}_2)$. We have superimposed on each figure the corresponding previous measurements from Galazutdinov et al. (2006). We did not include the 5003 Å band which was not studied by Galazutdinov et al. (2006) and for which we have only three valid data

points due to heavy stellar contamination. It can be seen that all our data points fall within the set of points from these authors, revealing good agreement with all these measurements. On the other hand, it can be seen that the correlation with $N(C_2)$ is significantly tighter in the case of our targets. We interpret this as a consequence of our accurate determination of $N(C_2)$, the excellent signal-to-noise of EDIBLES spectra, our careful selection of mono-cloud sightlines and correction for telluric and stellar features. Note that we have also included the multi-cloud sightline HD 169454 in these figures. The corresponding data point always falls within the Galazutdinov et al. (2006) set of points. However, for many DIBs it is the most discrepant point if one considers our results only. This is a strong indication that the C_2 -DIBs are very well correlated with the C_2 molecule, and that a large fraction of the dispersion around the linear relationship is due to cloud multiplicity.

Respective influence of C_2 column and reddening The existence of a good correlation with $N(C_2)$ is not a sufficient condition for qualification as C_2 -DIB and this has been discussed in detail by Galazutdinov et al. (2006) and Kaźmierczak et al. (2014). One way to establish this qualification is to compare the dependencies of the measured EWs on both the C_2 column and another parameter representing the quantity of interstellar matter, e.g. the reddening or the gas column. A C_2 -DIB is one that is more tightly correlated with $N(C_2)$ than with these other parameters. Inspired by the study ofENSOR et al. (2017a), we have used our new EDIBLES dataset of C_2 and non- C_2 DIBs to perform a simplified parametric analysis restricted to the reddening and $N(C_2)$.

For each DIB we performed a linear regression between the DIB EWs and both $E(B-V)$ and the column $N(C_2)$:

$$EW = a \times N(C_2) + b \times E(B - V), \quad (10.1)$$

We took into account uncertainties on EWs but assumed $E(B-V)$ and $N(C_2)$ are known with accuracy. We then computed $A = a/\sigma(a)$ and $B = b/\sigma(b)$, $\sigma(a)$ and $\sigma(b)$ being the standard deviations found from the adjustment for the partial derivatives a and b . Since $E(B-V)$ and $N(C_2)$ are assumed to be accurately defined, the dimensionless quantities A and B represent the tightness of the links between the DIB and each of the two variables $E(B-V)$ and $N(C_2)$. We then normalized the vector A, B in the system of reference $N(C_2)$ and $E(B-V)$ by dividing A and B by $\sqrt{A^2 + B^2}$. Fig. 15 is a representation of the corresponding "vectors". The orientation of each vector points to the parameter that governs the DIB strength (for vectors oriented vertically or horizontally) or, in intermediate cases, represents their respective influence. Note that we performed the regression with and without inclusion of HD 169454 (the multi-cloud target) and of the highly reddened HD 147889 to test their influence. We find that the regression results do not change

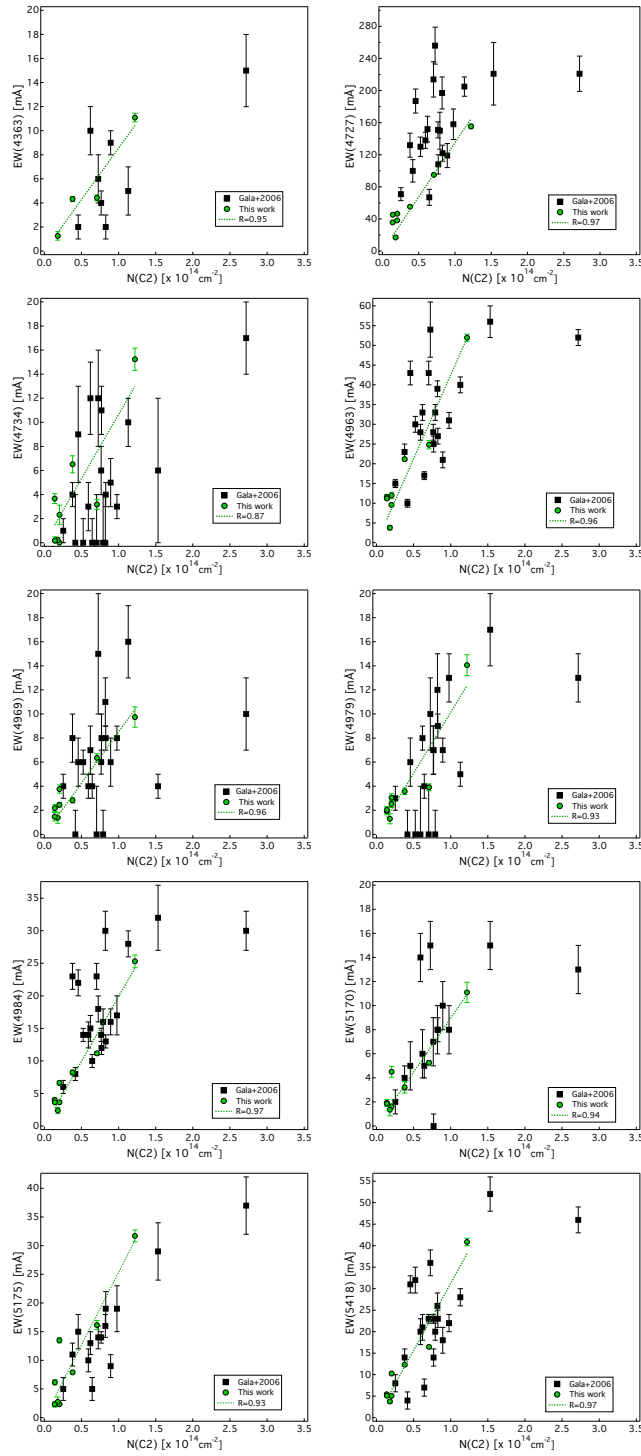


Figure 1014 Correlations between the DIB equivalent widths and the C₂ column (green filled circles). Superimposed as black squares are the results of Galazutdinov et al. (2006). R is the Pearson coefficient for our data only. The multi-cloud target HD 169454 value corresponds to $N(C_2) = 0.71 \times 10^{14} \text{ cm}^{-2}$

10. CHARACTERIZATION OF DIB PROFILES

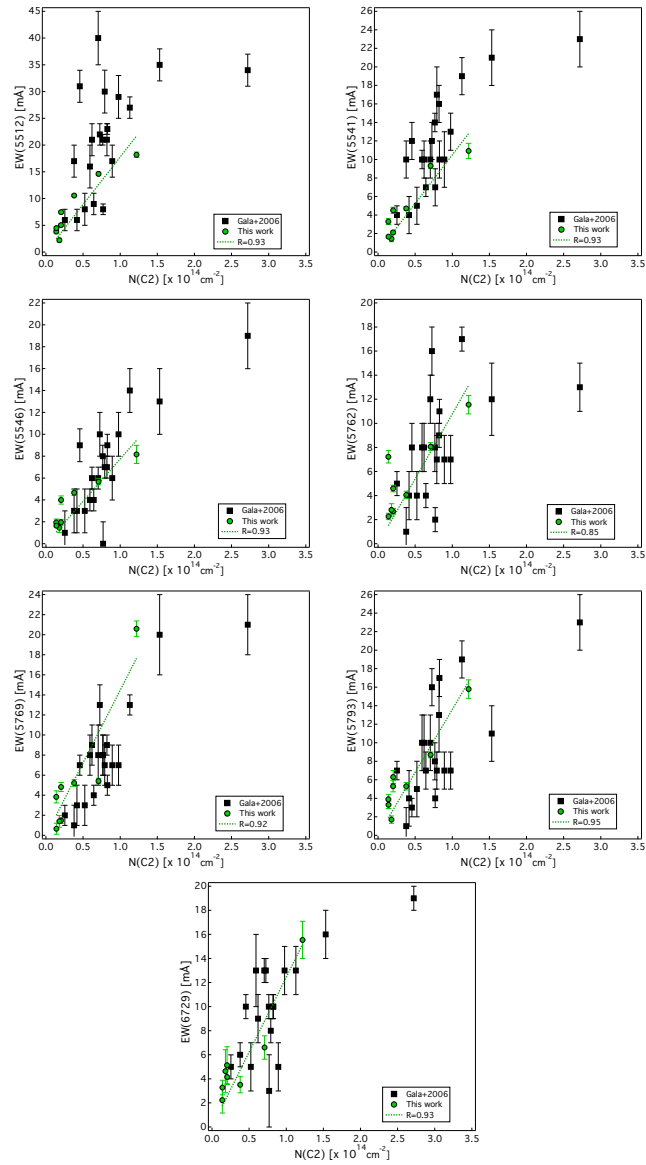


Figure 14 Continued.

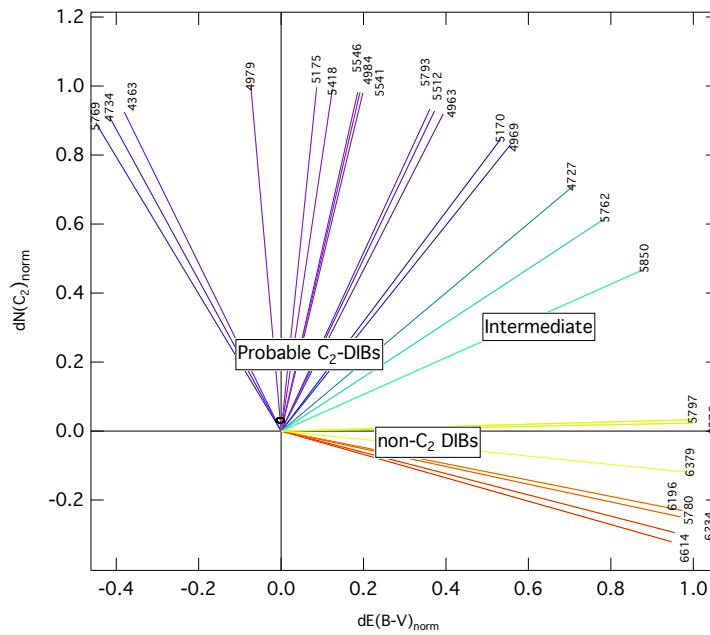


Figure 15 Decomposition of the C₂ and reddening influence.

significantly except for the weak 6729 Å band that has clearly the most contaminated spectrum (see Fig. 107). We removed this DIB from the regression and show the results that were obtained using all targets.

Fig. 15 reveals a gap between two series of DIBs. The first series corresponds to strong positive correlation with $N(C_2)$ and weak or even negative correlation with $E(B-V)$. The list of bands from this series is in total agreement with the 17 C₂-DIBs reported by Thorburn et al. (2003) in their Table 4.a as their main C₂-DIBs. In terms of relative correlation with C₂, the rankings of all six C₂-DIBs which are common to the two studies indeed agree to within the stated uncertainties. Moreover, our most tightly correlated 4734 and 5769 Å bands are also those noticed by these authors as their main C₂-DIBs. Remarkably, the $E(B-V)$ correlation coefficient for those two bands is found to be negative. The second series corresponds to the strong DIBs that follow the reddening $E(B-V)$ rather than C₂. At the margin of the C₂-DIBs group is the particular 5850 Å DIB. Interestingly, it has been classified as non-C₂ DIB (Kazmierczak et al. 2010b) and as C₂-DIB (Kazmierczak et al. 2014) in subsequent analyses. This band is definitely peculiar and deserves further study. Finally, we note that 4727 and 5762 Å DIBs seem to be similarly correlated to $E(B-V)$ and $N(C_2)$.

Table 104 C₂ DIB sub-structure peak separations (cm⁻¹).

HD	4984			5418 ^a		5512			5541			5546		
	$\Delta_{v_{PQ}}$	$\Delta_{v_{QR}}$	$\Delta_{v_{PR}}$	$\Delta_{v_{PR}}$	$\Delta_{v_{PQ}}$	$\Delta_{v_{QR}}$	$\Delta_{v_{PR}}$	$\Delta_{v_{PQ}}$	$\Delta_{v_{QR}}$	$\Delta_{v_{PR}}$	$\Delta_{v_{PQ}}$	$\Delta_{v_{QR}}$	$\Delta_{v_{PR}}$	
23180	0.60	0.60	1.20	0.58	-	-	0.71	0.49	0.39	0.88	0.32	0.29	0.61	
24398	0.60	0.36	0.96	0.79	-	-	0.73	0.49	0.49	0.98	0.29	0.58	0.87	
203532	0.42	0.60	1.02	0.79	-	-	0.68	0.29	0.58	0.88	0.36	0.32	0.68	
149757	0.83	0.81	1.64	0.62	-	-	0.74	0.39	0.65	1.04	-	-	0.39	
185418	0.73	0.35	1.08	0.83	0.46	0.27	0.73	0.38	0.59	0.97	0.39	0.29	0.68	
170740	0.45	0.39	0.84	0.41	0.49	0.49	0.98	0.29	0.49	0.78	-	-	0.49	
147889	0.48	0.85	1.33	0.73	0.35	0.42	0.77	0.48	0.39	0.87	-	-	0.72	
169454	0.48	0.36	0.84	0.52	0.31	0.49	0.80	0.49	0.29	0.78	-	-	0.49	

^a The 5418 DIB shows a two sub-peak profile structure.

10.1.9 Summary and conclusion

We have used the high-quality spectra of the EDIBLES survey to select those sightlines that are characterized by both a high C₂ column and a single Doppler component of interstellar absorption (the single-cloud criterion). To achieve the selection, EDIBLES spectra were corrected for atmospheric lines, exposures of the same target were combined and the spectral intervals co-added to form a unique spectrum. The C₂ selection was based on the detection of the C₂ (2-0) (8750–8849 Å) Phillips system and the single-cloud selection was based on profile-fitting of the NaI UV and optical doublets. Seven targets were selected and studied together with one multi-cloud sightline.

The C₂ Phillips bands were fitted to extract the C₂ column, radial velocity and kinetic temperature as well as the gas volume density for each sightline. The absorption bands of the 18 (Thorburn et al. 2003) C₂-DIBs were extracted. Their equivalent widths as well as the EWs of eight strong DIBs were measured and are provided with their measurement uncertainties. Three additional C₂-DIB candidates were detected. The C₂-DIB EWs were compared with the reddening and the C₂ column by means of a linear regression on both quantities. Two categories of DIBs were derived, with a significant gap between the two. The first category corresponds to those classified as C₂-DIBs by Thorburn et al. (2003) and the second to the strong DIBs more tightly correlated with the reddening. A particular case is the 5850 Å band which seems to belong to a different family. In the case of the C₂-DIBs, their EWs are found to be very tightly correlated with C₂ column densities. We interpret this as a consequence of accurate N(C₂), high signal-to-noise, a careful selection of mono-cloud sightlines and correction for telluric and stellar features.

Individual profiles are presented for all targets and DIBs. We also co-added the DIB profiles of three different sightlines to enhance the sub-structures. The main result of this study is the presence of sub-structures with two or

three sub-peaks in at least 14 DIBs, the remaining two being too weak to draw a definite conclusion. The two and three sub-peak profile structures are consistent with unresolved rotational branch structures of a molecular carrier. The two sub-peak profiles are very similar to those of the strong 6196 or 5797 Å DIBs, while the three sub-peak profiles are very similar to the one of the strong 6614 Å DIB. The profiles of the 18 C₂ DIBs were studied as a function of the transition and as a function of the sightline:

- Profile variability among the C₂-DIBs for the same sightline:

The differences in peak relative amplitudes and peak sub-structure separations found among the 18 C₂ bands suggest that they correspond to different molecular carriers or electronic transition symmetries, and factors governing the level populations.

- Profile variability among the targets for the same C₂-DIB:

Three C₂-DIB categories were derived. Several C₂-DIBs appear to keep identical profiles among targets characterized by different C₂ rotational temperatures, however, for others, there is a potential detection of a response to the temperature, namely a global broadening of the absorption band and slightly larger separations between the internal sub-structures at higher temperature. Such effects are similar to those detected for the 6614 Å band by [Cami et al. \(2004\)](#) and for the 6196 Å band by [Kaźmierczak et al. \(2009\)](#), and are likely associated with shifting Boltzmann maxima of rotational branches of the molecular carrier. Finally, for a fraction of the DIBs, the variability (or absence of variability) could not be assessed due to their weakness.

10.2 Profiles of strong DIBs

Most of the strong and narrow optical DIBs have been found to have asymmetric profiles, and in the case of the strongest ones such as DIBs 5797 and 6614 Å ([Sarre et al. 1995](#); [Ehrenfreund, Foing 1996](#); [Galazutdinov et al. 2002](#)), 5850, 6234 and 6270 Å (e.g. [Krełowski, Schmidt 1997](#); [Galazutdinov et al. 2002](#)), 6376, 6379 and 6196 Å ([Walker et al. 2001](#)), sub-structures have been clearly identified which may be consistent with unresolved rotational branch structures associated with electronic transitions of gas-phase molecules.

Figures [16,17,18,19,20,21,22](#) and [23](#) represent our first attempt to find the best observed profiles of the 5780, 5797, 5850 and 6196, 6234, 6376, 6379 and 6614 DIBs. The method for the extraction of these strong DIBs has already been described in the previous section in exactly the same way we used for the intriguing subset of weaker DIBs, the so-called C₂-DIBs.

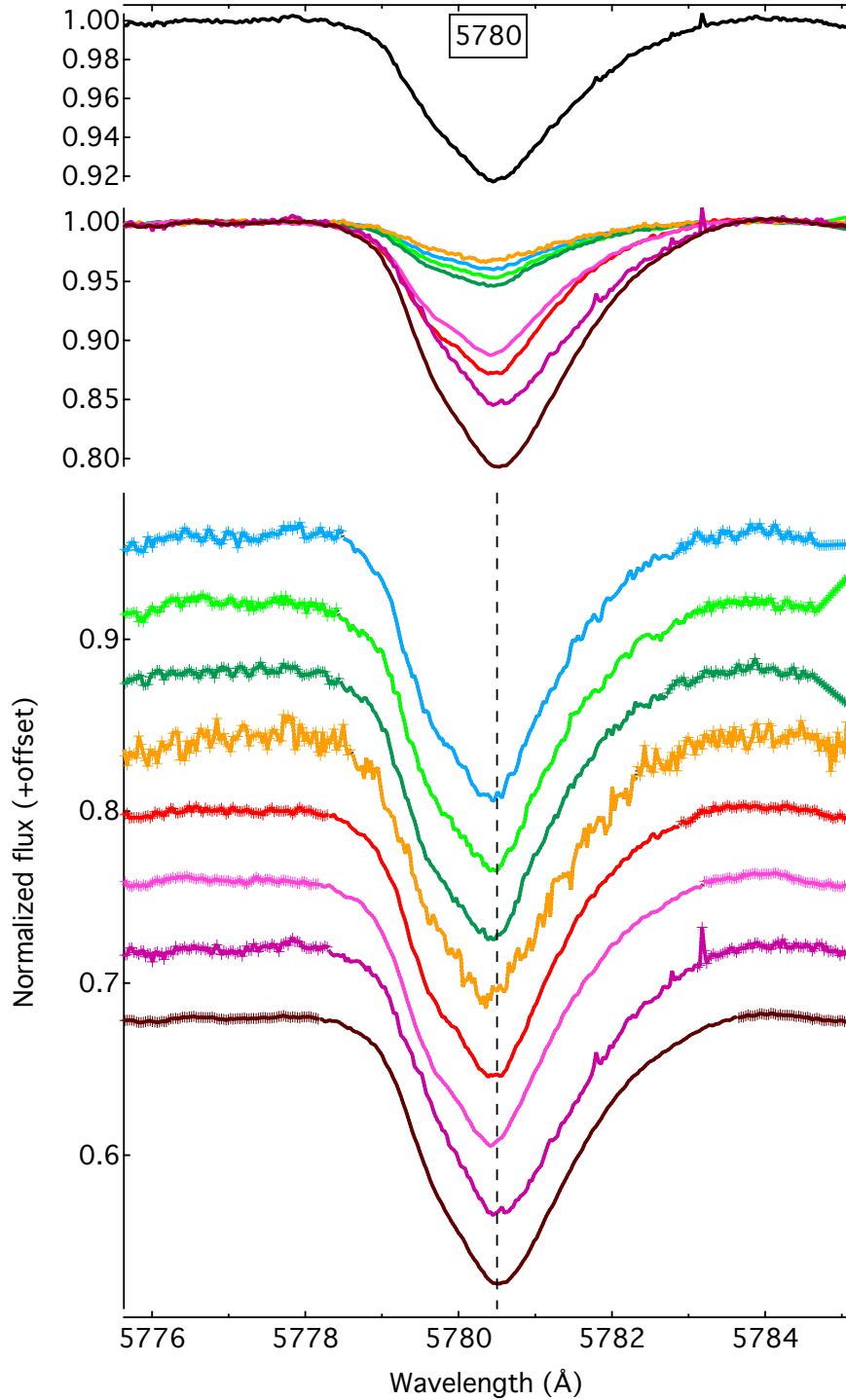


Figure 16 The 5780 DIB recorded along seven single-cloud and one multi-cloud line-of-sight. Top in all panels: normalized average profile. Middle in all panels: overlaid DIB profiles at the same vertical scale for all stars. Bottom in all panels: same DIB vertically displaced and depth-equalized profiles. The black dashed line shows the DIB location.

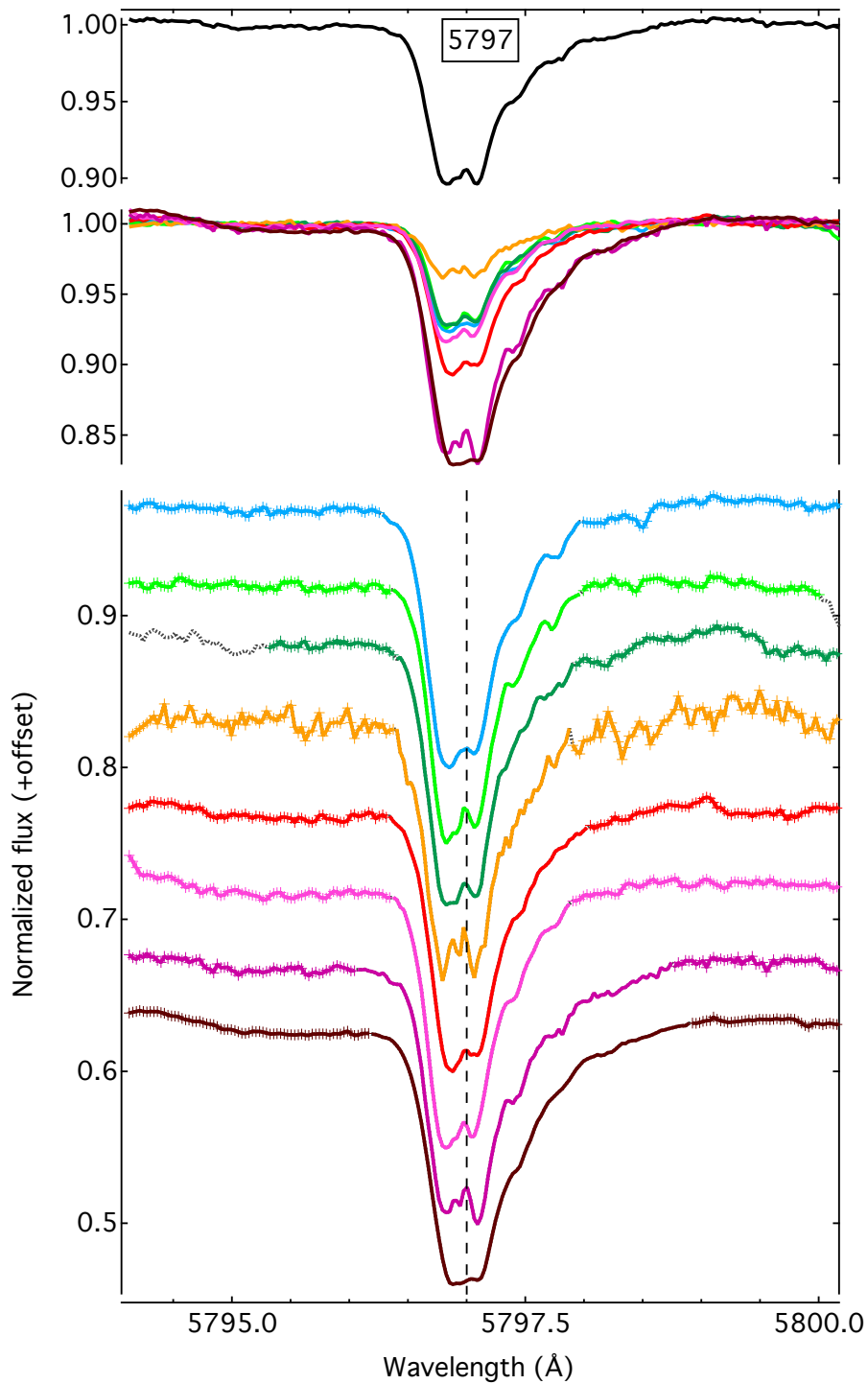


Figure 17 The 5797 DIB recorded along seven single-cloud and one multi-cloud line-of-sight. Top in all panels: normalized average profile. Middle in all panels: overlaid DIB profiles at the same vertical scale for all stars. Bottom in all panels: same DIB vertically displaced and depth-equalized profiles. The black dashed line shows the DIB location.

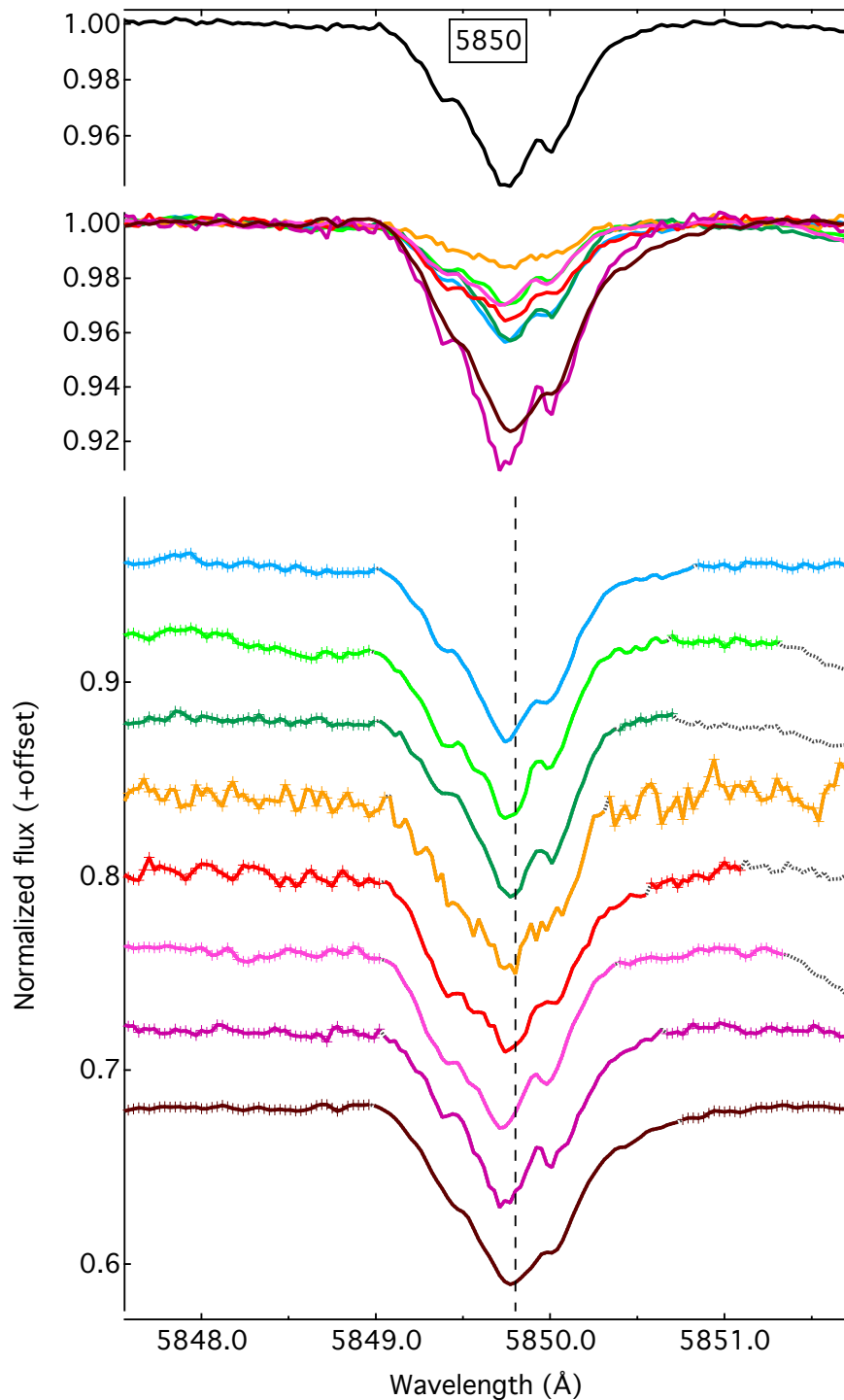


Figure 18 The 5850 DIB recorded along seven single-cloud and one multi-cloud line-of-sight. Top in all panels: normalized average profile. Middle in all panels: overlaid DIB profiles at the same vertical scale for all stars. Bottom in all panels: same DIB vertically displaced and depth-equalized profiles. The black dashed line shows the DIB location.

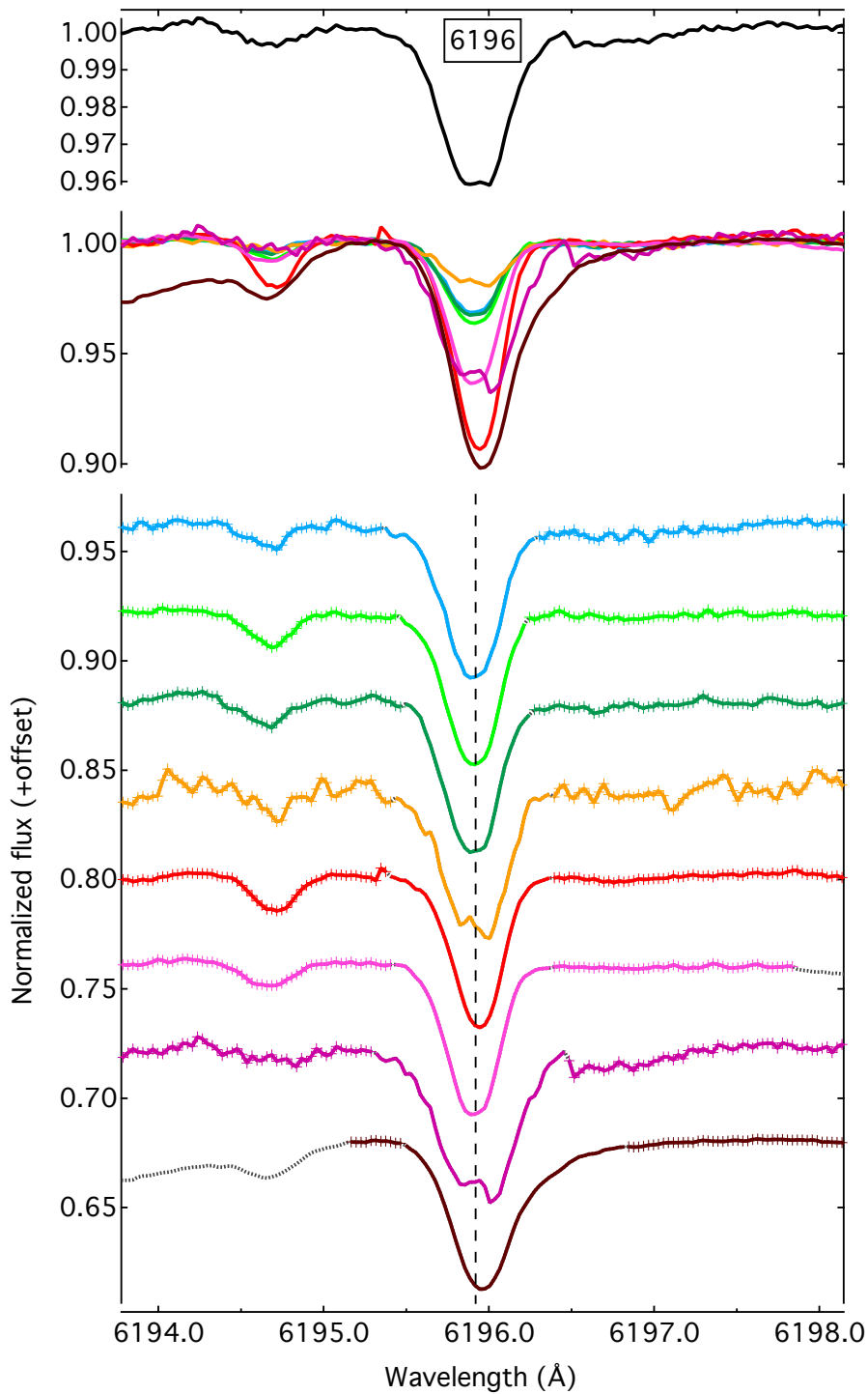


Figure 19 The 6196 DIB recorded along seven single-cloud and one multi-cloud line-of-sight. Top in all panels: normalized average profile. Middle in all panels: overlaid DIB profiles at the same vertical scale for all stars. Bottom in all panels: same DIB vertically displaced and depth-equalized profiles. The black dashed line shows the DIB location.

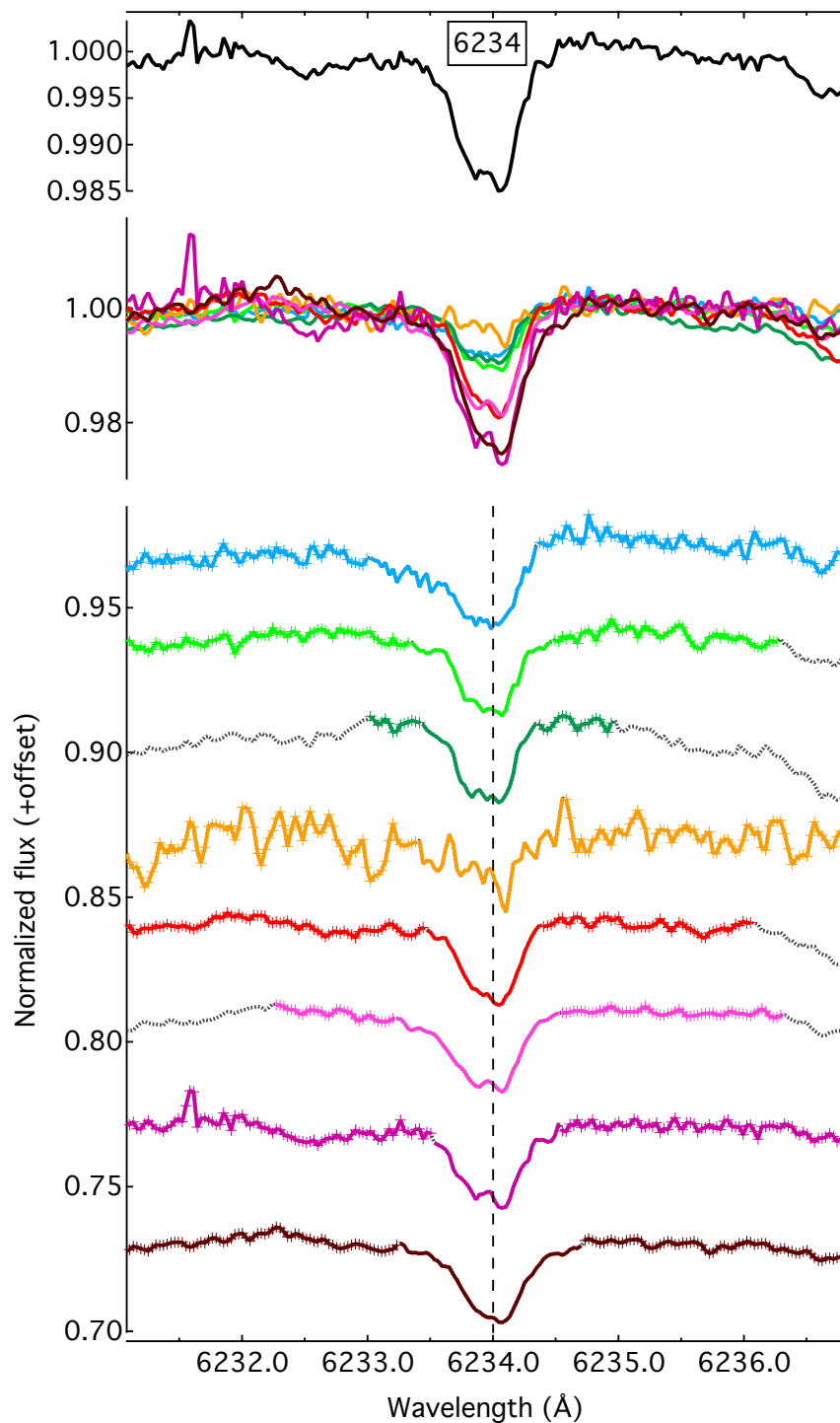


Figure 20 The 6234 DIB recorded along seven single-cloud and one multi-cloud line-of-sight. Top in all panels: normalized average profile. Middle in all panels: overlaid DIB profiles at the same vertical scale for all stars. Bottom in all panels: same DIB vertically displaced and depth-equalized profiles. The black dashed line shows the DIB location.

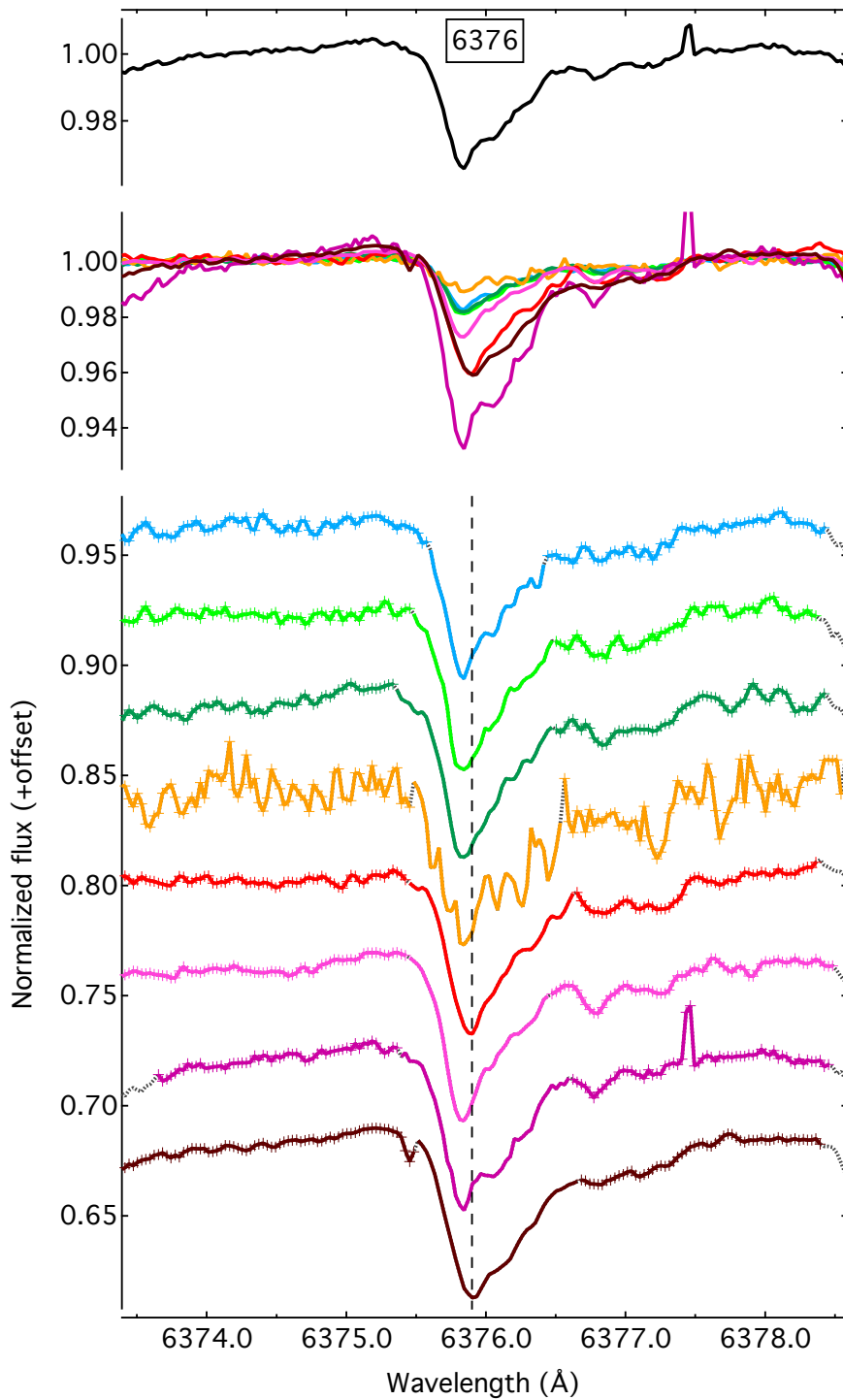


Figure 21 The 6376 DIB recorded along seven single-cloud and one multi-cloud line-of-sight. Top in all panels: normalized average profile. Middle in all panels: overlaid DIB profiles at the same vertical scale for all stars. Bottom in all panels: same DIB vertically displaced and depth-equalized profiles. The black dashed line shows the DIB location.

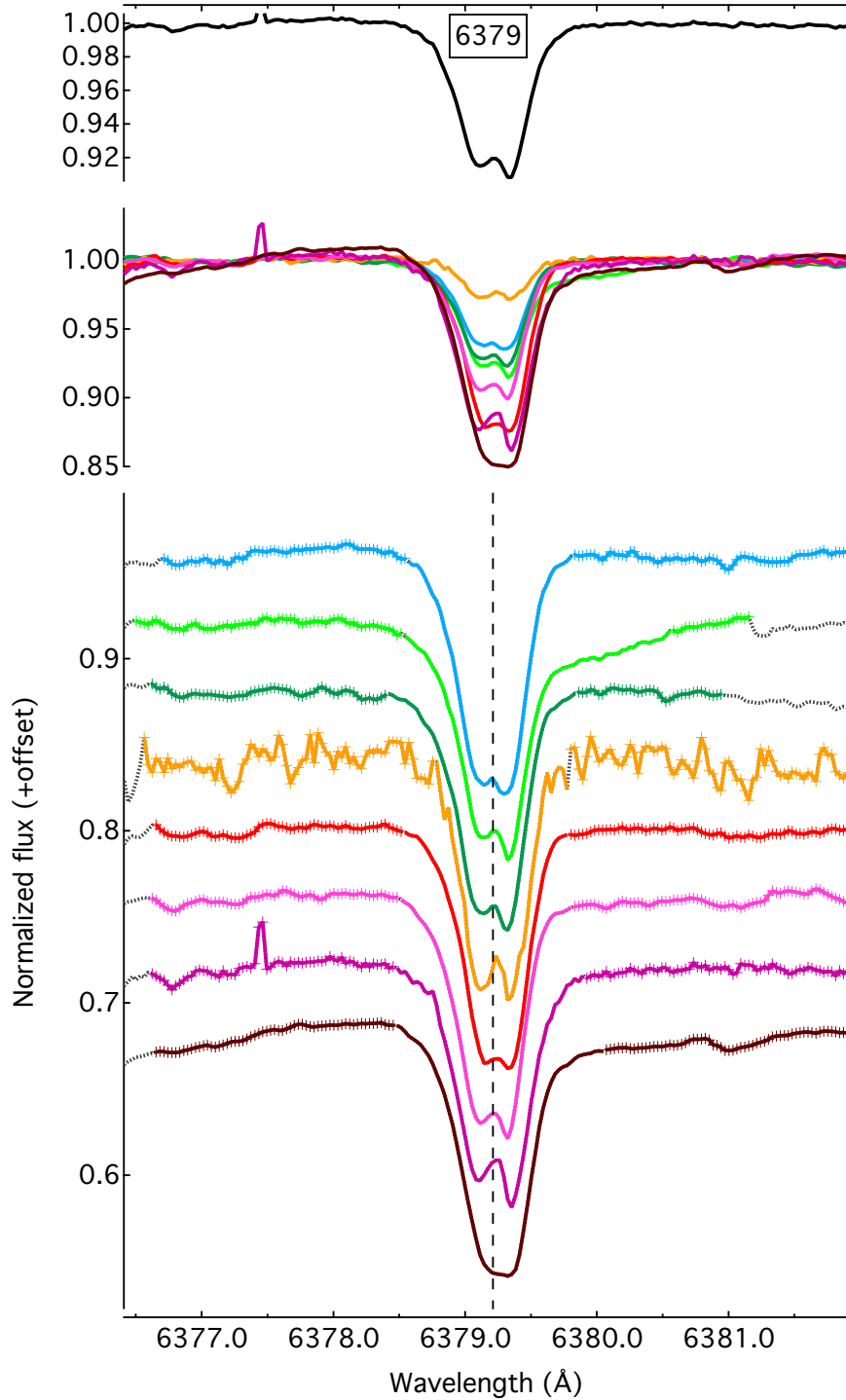


Figure 22 The 6379 DIB recorded along seven single-cloud and one multi-cloud line-of-sight. Top in all panels: normalized average profile. Middle in all panels: overlaid DIB profiles at the same vertical scale for all stars. Bottom in all panels: same DIB vertically displaced and depth-equalized profiles. The black dashed line shows the DIB location.

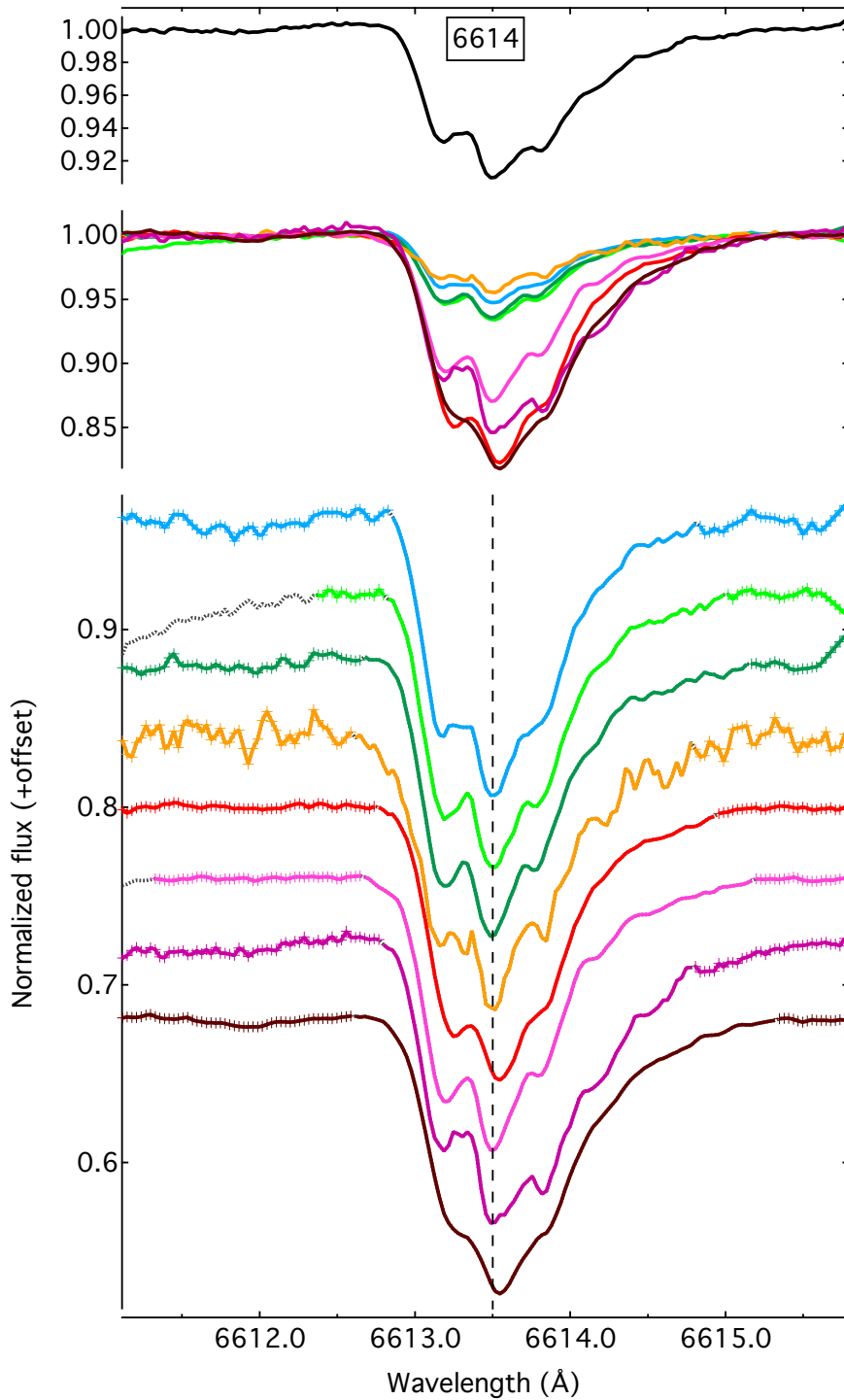


Figure 23 The 6614 DIB recorded along seven single-cloud and one multi-cloud line-of-sight. Top in all panels: normalized average profile. Middle in all panels: overlaid DIB profiles at the same vertical scale for all stars. Bottom in all panels: same DIB vertically displaced and depth-equalized profiles. The black dashed line shows the DIB location.

Conclusion and perspectives

11.1 General conclusions

Four years ago, [N. L. J. Cox, J. Cami \(2014\)](#) published a road map following the excellent contributions of the International Astronomical Union symposium (IAU 297) devoted to DIBs. They pointed out the importance of spectral and sightline surveys by introducing for the first time the two concepts of "*all DIBs, few targets*" and "*few DIBs, many targets*". This thesis is along these lines insofar as it takes advantage of both approaches (and beyond). Each kind brings a new statistical or tomographic spectroscopic view at three very different scales in program size, namely (i) the APOGEE massive survey by using a single NIR DIB and then few additional weak NIR DIBs, (ii) the High S/N and large spectral coverage EDIBLES survey, (iii) and a program of a multiplex instrument (KMOS) in a restricted sky region.

In this thesis work I improved or developed several techniques adapted to observational spectroscopy from the near UV to the infrared, in particular by means of massive surveys, with the goal of extracting as most as possible and as reliable as possible measurements of DIBs. The developments helped to surmount the following difficulties:

- the identification and separation of stellar, interstellar and telluric signatures,
- the handling of massive datasets, and the need to use automated analyses.

In practice, I made use of the following recent advances:

- Considerable improvement in stellar models allowing the use of cold stars.
- Considerable improvement in telluric models allowing the detection (or rejection) of new features.

- New multi wavelength tools for target selections.

The combination of the new techniques, tools and models has made possible to take advantage of the large amount of available data from massive stellar spectroscopic surveys (APOGEE), from the excellent, high S/N ratio data from dedicated DIB surveys (EDIBLES) or from specific exploratory programs (KMOS/B68).

11.2 Novelties

1. Thanks to sightlines surveys, massive data were exploited. Subsequently, catalogs were produced and numerous statistical studies were carried out in order to compare the DIBs strengths with the environmental conditions and the properties of their hosting clouds (APOGEE catalogs and the *skin effect* illustrated by Planck).
2. The second novel aspect is the tomographic one. The Barnard 68 study is the first tomography of a DIB carrier in a single cloud. On the large scale, the construction of 3D ISM maps based on composite data, namely reddening and DIBs (Capitanio et al. 2017) and the 3D tomography based on APOGEE DIBs are the first of this type. Such tomographic studies constitute prototypes of future three-dimensional studies of DIB carriers with JWST's NIRSpec or with future ground surveys or dedicated programs (SPIROU, WEAVE, 4MOST, MOONS...).
3. Prior to EDIBLES measurements, only a few DIBs had been observed with high enough signal and resolution to disentangle their spectral substructures. In the case of EDIBLES, not only the signal S/N is unprecedentedly high, but a careful selection of appropriate targets has also been done to extract reliable profiles, the *single-cloud* selection, *i.e.* sightlines characterized by a small Doppler broadening and where only one (or one dominating) interstellar cloud determines the DIB spectrum. Combined with the new APOGEE profiles and also the new DIB candidates from both surveys, this represents a new source of potential identifications.
4. New potential identifications require confirmation and additional inspection of data in a search for weaker or simply overlooked features. The second novel aspect of this thesis resides in the combined stellar, interstellar and telluric technique improvements and the use of a *super-spectrum* technique, *i.e.* the comparison of selected spectra co-added in the stellar and interstellar frames. This is mandatory to place constraints on the additional features and the confirmation (or refutation) of observed features. The main goal is the building of the most comprehensive and reliable atlas of DIBs.

11.3 Perspectives

Progress in DIB-focused research will undoubtedly come from an active synergy between theoretical work, astronomical observations and laboratory measurements from the UV to the IR spectral domains. In the laboratory, the interstellar conditions reigning in the diffuse ISM can realistically be simulated and DIBs carrier analogues can be generated from the vast collection of possible candidates¹.

The laboratory match with astronomical observations can be optimized if the sheer number of possible species to be studied in the laboratory can be constrained under relevant and realistic space conditions. The preselection can be done through in-depth studies of the physical and chemical properties of the DIB carriers based on a robust data analysis of high spectral resolution observations.

In this respect, the advent of massive surveys opens a new era and new possibilities for future detections and/or exclusions of certain DIB carriers and confirmation/rejection of PAHs/Fullerenes hypothesis.

In the future, the main goal will be to provide quantitative information and data analysis for interpreting observations from ground- (SPIROU/CFHT, EDIBLES/ESO-VLT, NASA IRTF and NOAO Kitt Peak Telescopes), airborne- (SOFIA), and space-based observatories – Hubble Space Telescope (HST) Imaging Spectrograph (STIS) or James Webb Space Telescope (JWST) Near Infrared Spectrometer (NIRSpec) – in order to derive robust constraints and to reduce the list of proposed molecules studied in the lab. On the other hand, the near-UV part of the EDIBLES data is the object of ongoing studies that should bring new constraints on the existence of DIBs in this domain, and subsequent constraints on the carriers. The NIR window with HST will also bring some constraints of the IR C₆₀ bands. Note that the resolution of STIS at 0.9 – 1.0 μm is $\sim 10\,000$ and a S/N ~ 700 can be achieved with special techniques.

These studies would be possible to extend to the mid-infrared (MIR)² thanks to the advent of SOFIA Third Generation instrument, the High-Resolution Mid-Infrared Spectrometer (HIRMES) that will cover the [25 – 122] μm spectral range with resolving powers ranging from 600 to 100 000 and the Echelon-Cross-Echelle Spectrograph (EXES) that operates in the 4.5 – 28.3

¹In the laboratory, one could not get close to the required density, but with the supersonic jet expansions, collision-free gas flows which is a good analogue for low densities can be created.

²For this spectral range, there may be new DIBs but most certainly not in the classical sense, *i.e.* as the ones currently known are generally accepted to be due to electronic transitions then it would need a rather special molecule to have two electronic states so close in energy. Moreover, as the absorption coefficient scales with frequency this means absorption will be weaker than for UV/vis.

μm wavelength region, at high ($R \sim 50\,000 - 100\,000$), medium ($R \sim 5\,000 - 20\,000$) and low ($R \sim 1\,000 - 3\,000$) spectral resolution.

Indeed, the advent of multi-object spectrographs such as JWST's NIRSpec and SPIROU ($R=70\,000$) will provide massive amounts of data and new detections that will serve the basis for a wide range of analysis about NIR DIBs. The multi-object mode allows for simultaneously observing more than 100 sources over a field of view larger than 3 arcmin square, and NIRSpec will be the first spectrograph in space that has this capability. In addition, through the DIBs there is a direct connection between the DIBs and prominent features in the C_{60} bands that will be studied by JWST. In this context, more correlations with IR bands are expected with the new laboratory investigation of the NIR and MIR spectral signatures of PAHs and derivatives.

DIB-based maps and their comparison with radiation and 3D dust and gas distributions open new windows to better understand the conditions of formation and disappearance of DIB carriers. Future surveys (from ground and space), resulting databases, and environmental and tomographic studies will bring more and more stringent constraints on the DIB formation and destruction/ionization/accretion sites. Particularly promising is the GAIA mission that considerably helps the tomography by providing distances with unprecedented accuracy, a huge database of extinctions and a huge number of 8620 Å DIBs. Refining our understanding of DIB carriers is also crucial to understand the interstellar lifecycle and at what stage they are involved in the chain and process of star formation. An approach to tackle these open questions, consists of studying the tomography of dense clouds with JWST's NIRSpec as already done with the dense cloud Barnard 68. All these investigations will open the possibility to shed light of whether, how, when, and where the DIB carriers are formed in interstellar clouds. The ultimate goal of the future research is to compare new high-quality observational data obtained through innovative signal analysis approaches with the unique set of laboratory data available to provide solid constraints on the nature of the DIB carriers and, possibly, the identification of DIBs with specific molecular carriers. A result that will have profound implications for our understanding of the Molecular Universe.

In light of the many results that were obtained as part of the thesis, there are many implications that this work might have in shaping a vision for future laboratory astrophysics investigations. The results obtained as part of the thesis have many potential implications for future laboratory investigations or observational programs.

- **Spectroscopy:**

The most important input is accurate data on wavelengths and line profiles (bandwidths) - this is what we can compare the laboratory data with. With 400 DIBs in a domain of ~ 600 nm, chances of a coincidence

are rather high, but a coincidence does not need to be a match. Here, extra-observational data can be really helpful in identifying bands unambiguously. See e.g. figs 3-9 in [Schmidt et al. \(2014\)](#).

In the case that the data allow to resolve rotational profiles (separate P/R branch or wings that give information on the Delta B's involved), astronomical observations could give a clue for the size of the molecule. See for e.g. the paper by [Huang, Oka \(2015\)](#) where the authors assigned a double peak DIB structure to a 2P-X2P transition assuming a chain length of 6-8 atoms. The C2-DIBs study is another example, where the identification of sub-structures may add more info on the structure of the underlying carrier. This then can be tested in the laboratory, by selecting precursors that may result in species absorbing in the observed wavelength domain with almost the right spectroscopic properties.

- **Environmental conditions:**

By exploring environmental conditions by means of observations of other (non-DIB) species in parallel to the DIBs themselves, one may determine those parameters that favor DIB formation or disappearance: radiation fields (ions vs non-ions), existence of shockwaves, presence of molecules that may hint for a chemical network. Not only optical but also IR, sub-mm and radio astronomical data can be helpful to further paint the picture. Ideally, one may obtain correlations between such intensities of a specific DIB and quantities of a particular molecule (similarly to the still unexplained C2-DIBs case).

- **Alternative clues?**

Band-band correlations and relative intensity levels among bands suspected to be due to the same carrier: Refined observations with surveys could better assess correlations or absence of correlations between bands and their relative levels. These are crucial inputs for potential identifications of absorbing species (any absence of a band predicted with high intensity contradicts an identification based on a band with smaller intensity).

Band-dust grain relationships: Improved correlative studies between DIBs and grain properties (based on reddening curves or polarization) could give clues for DIB carrier accretion onto grains and coagulation.

Appendix A

**$\lambda\lambda$ 15617, 15653, 15673 NIR DIBs
toward TSS targets**

A. $\lambda\lambda 15617, 15653, 15673$ NIR DIBs TOWARD TSS TARGETS

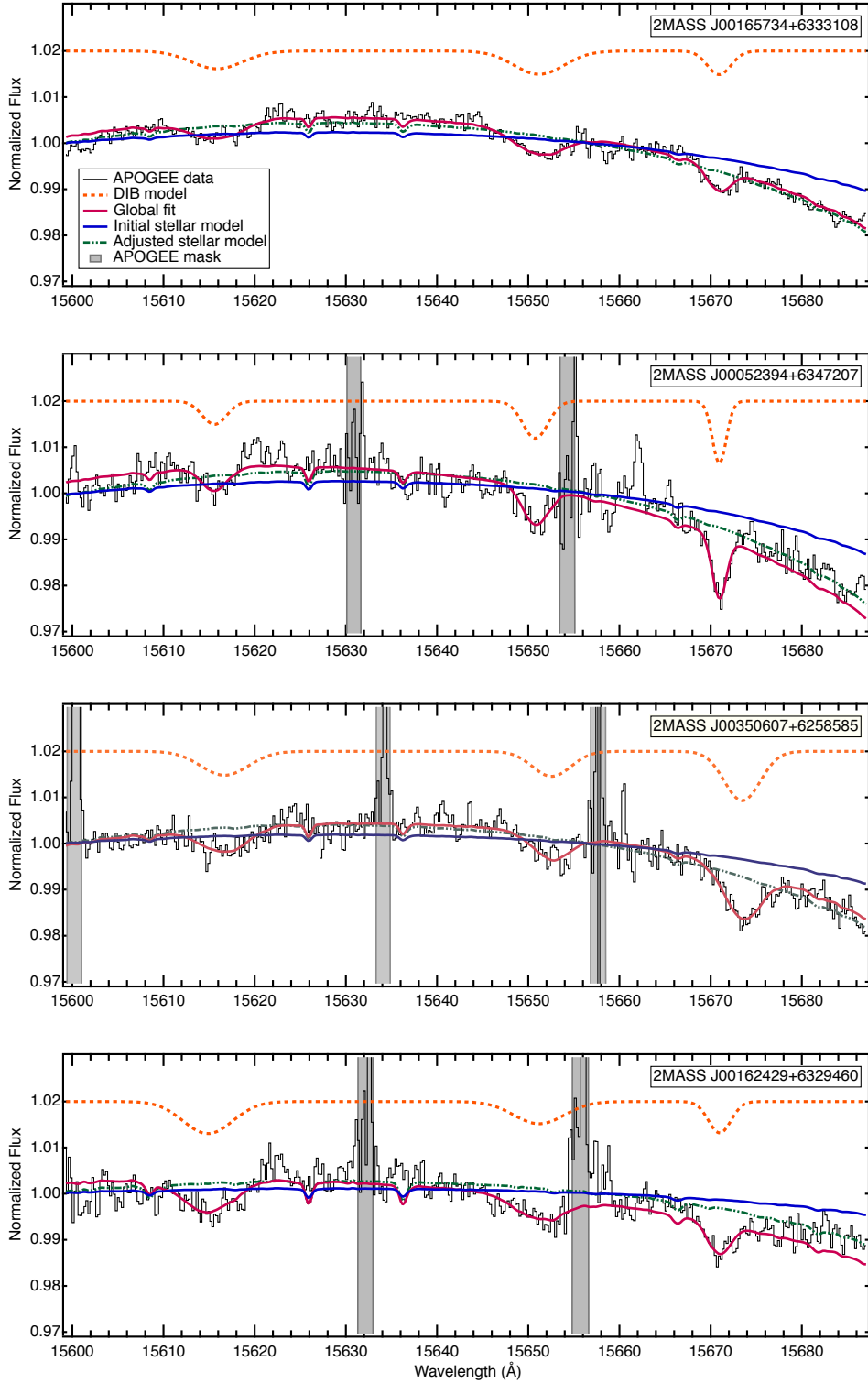


Figure 1 $\lambda\lambda 15617, 15653, 15673$ NIR DIBs toward APOGEE TSS targets. APOGEE spectra are shown with solid black lines. The initial synthetic models are shown in blue. The dot-dot-dashed green lines display the adjusted APOGEE stellar model. The solid magenta curves represent the fitted model. The gray rectangles indicate the masked regions.

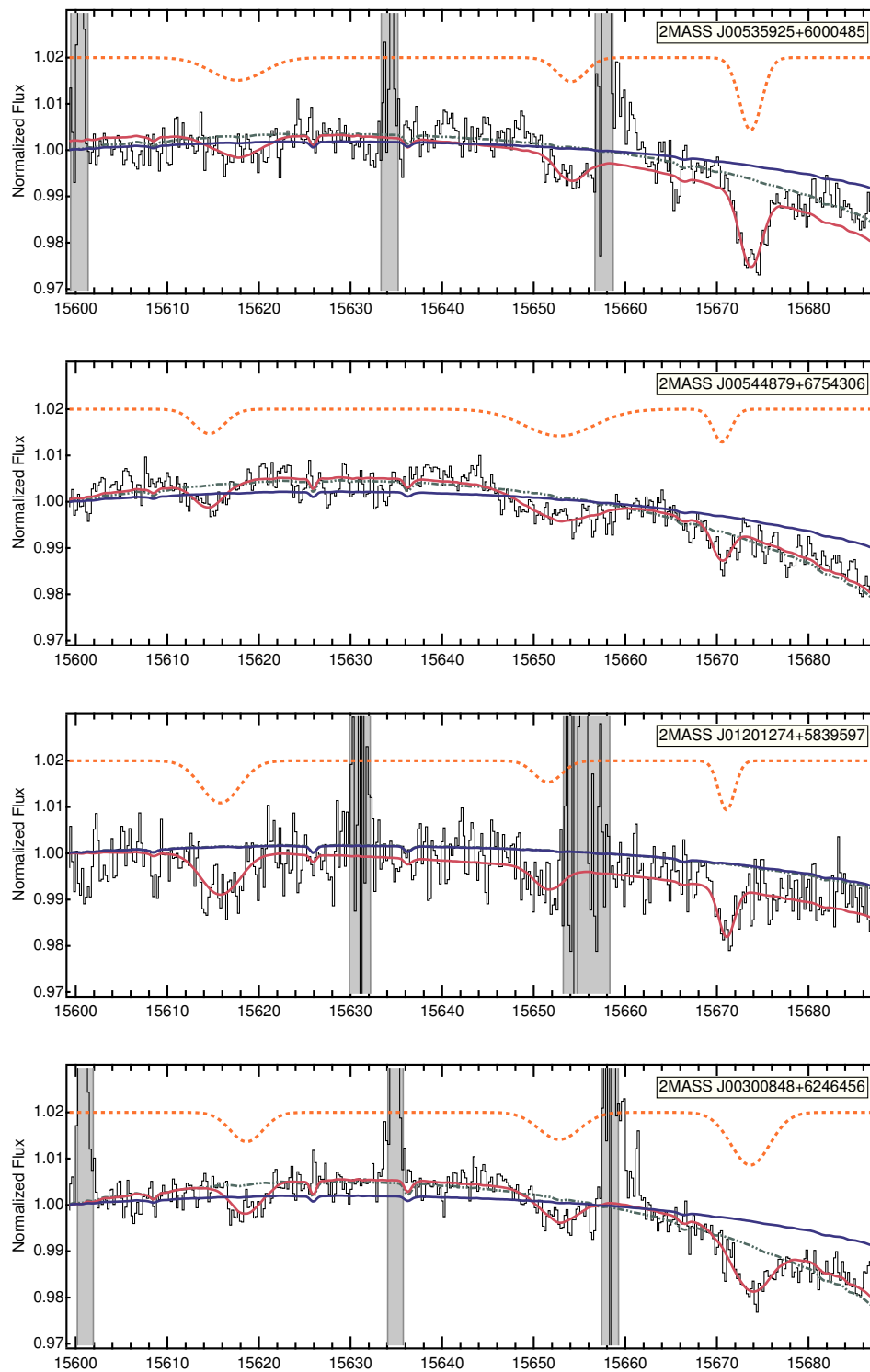


Figure 2 Same as Fig. 1.

A. $\lambda\lambda 15617, 15653, 15673$ NIR DIBs TOWARD TSS TARGETS

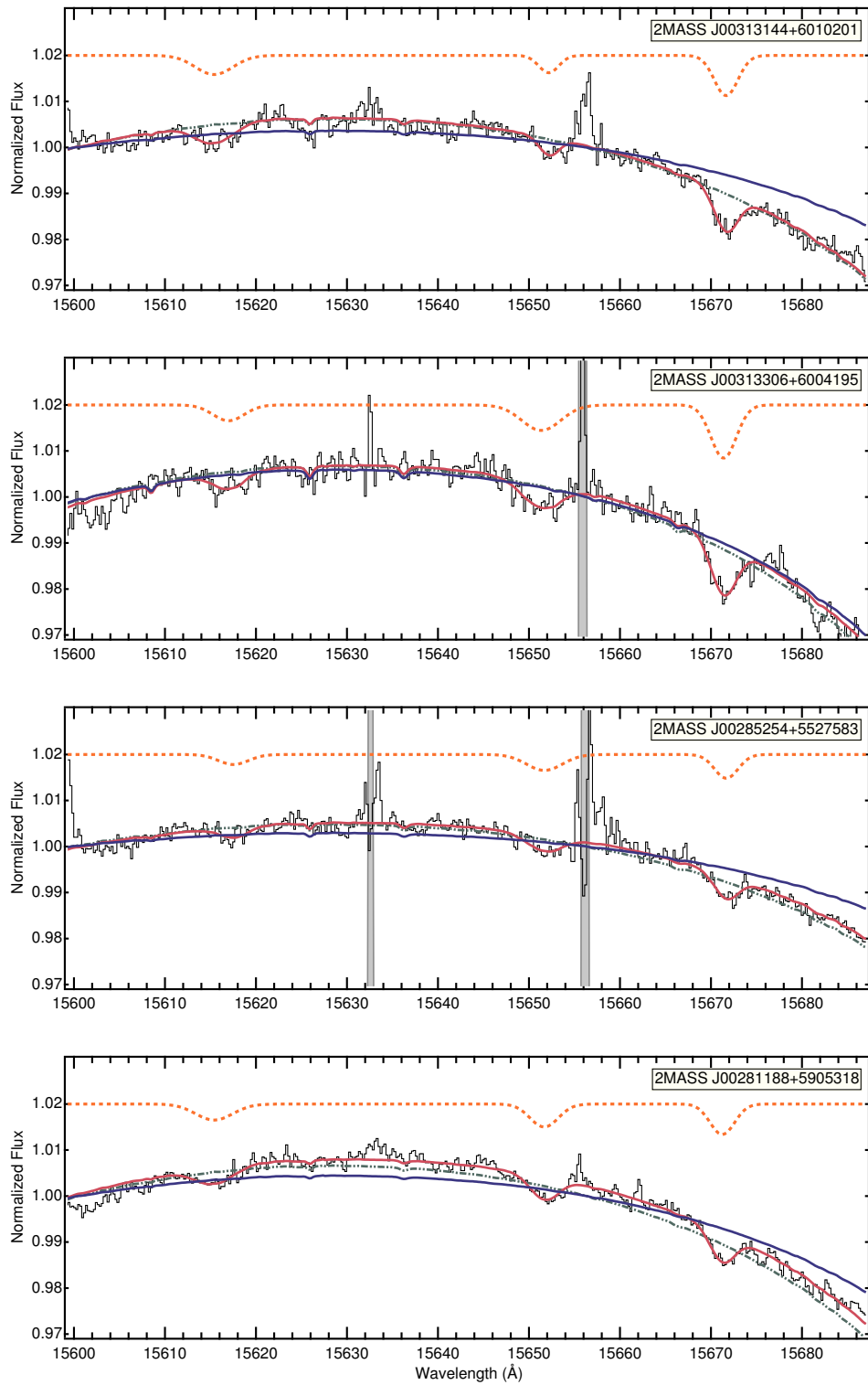


Figure 3 Same as Fig. 1.

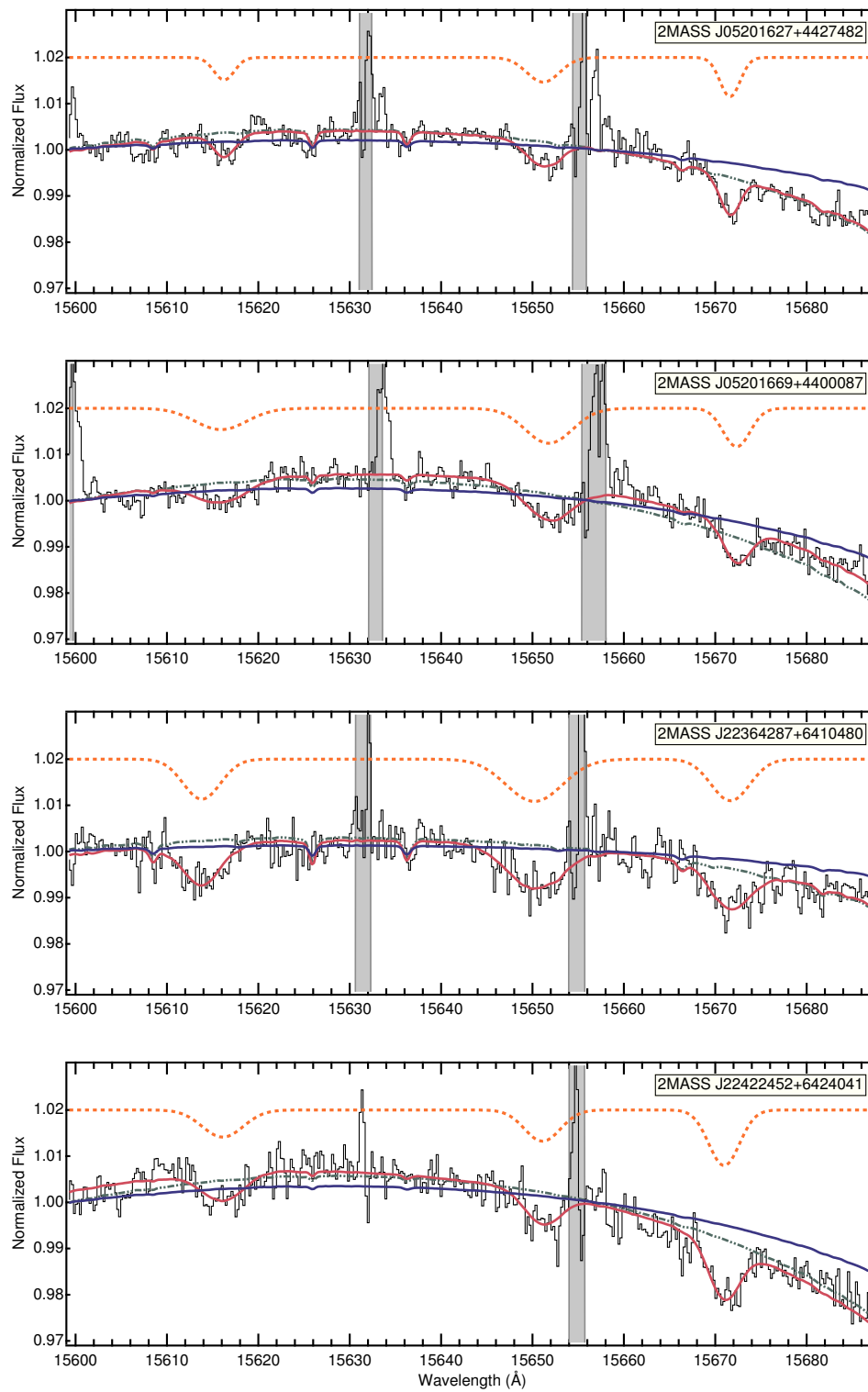


Figure 4 Same as Fig. 1.

A. $\lambda\lambda 15617, 15653, 15673$ NIR DIBs TOWARD TSS TARGETS

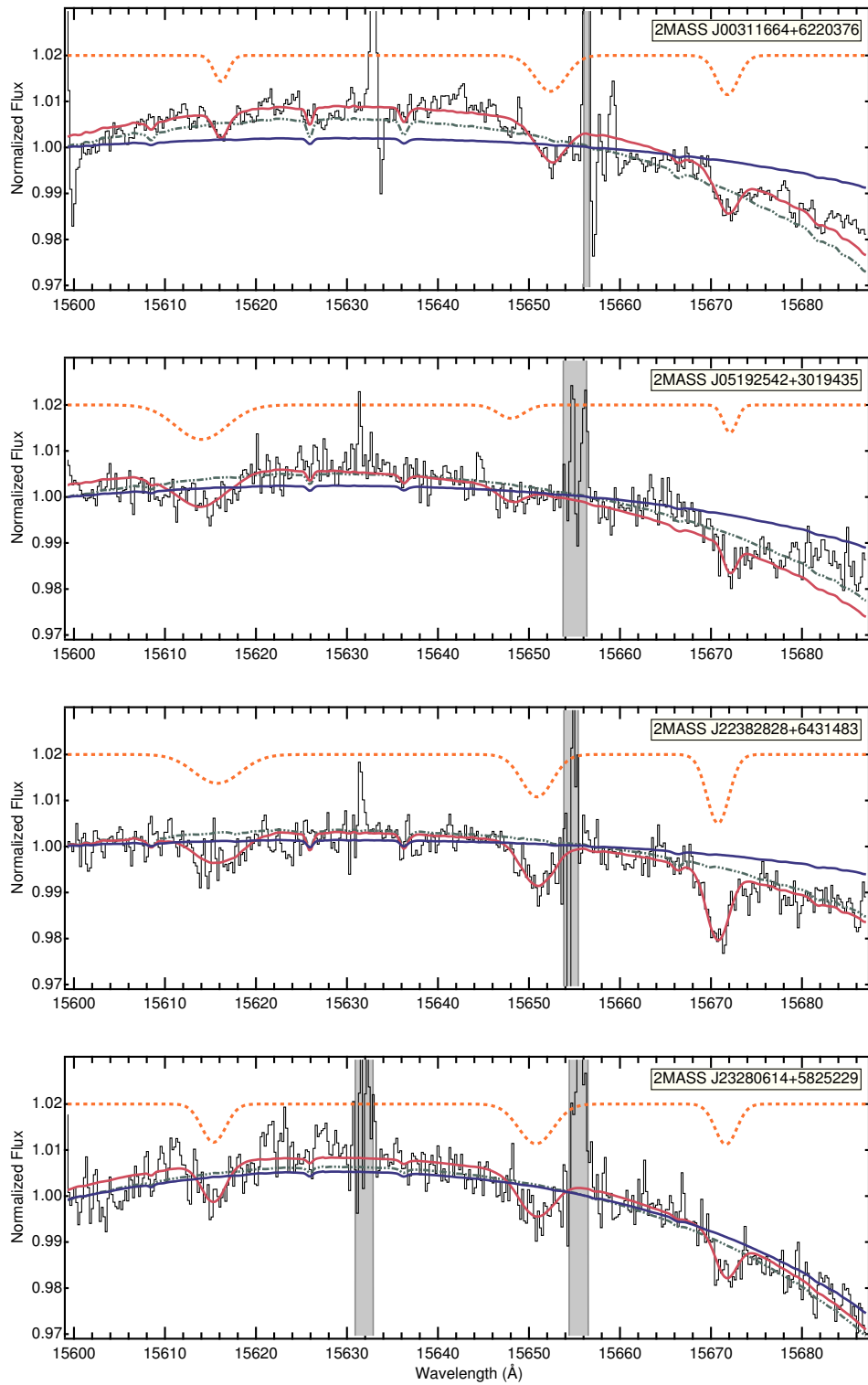


Figure 5 Same as Fig. 1.

Appendix B

**Examples of Barnard 68 background
star spectra**

B. EXAMPLES OF BARNARD 68 BACKGROUND STAR SPECTRA

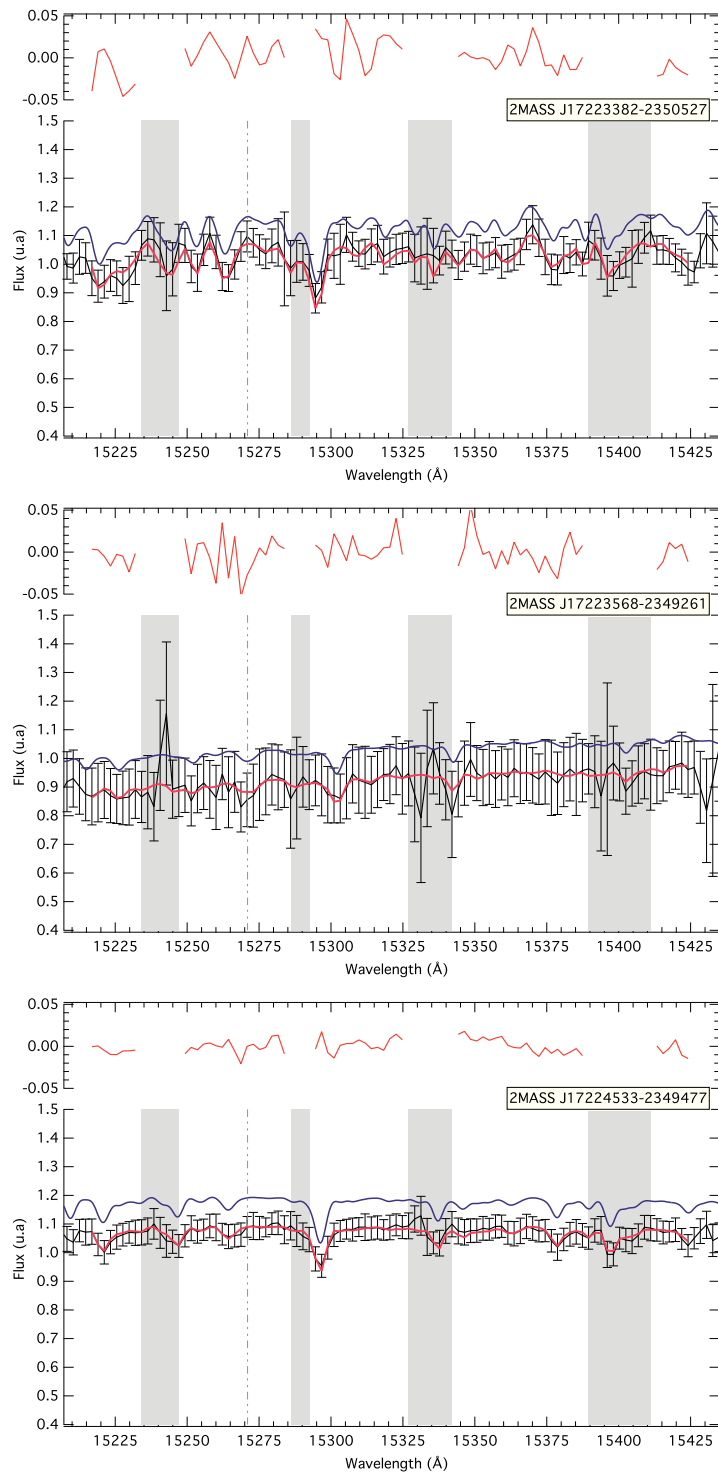


Figure 1 Examples of fit. In each figure: The blue curve is the convolved stellar model. The magenta curve is the fitted stellar+telluric model. The dashed orange line shows the DIB position. Residuals are shown in red.

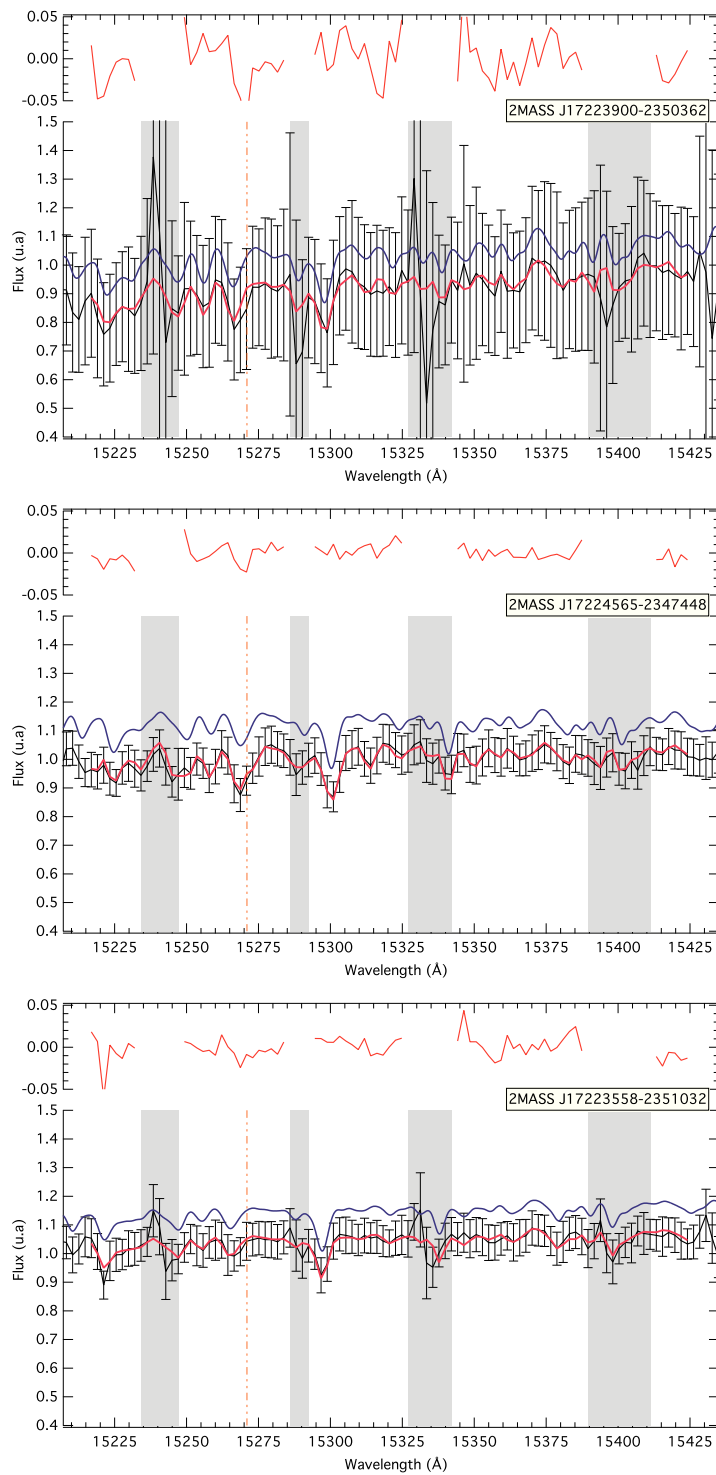


Figure 2 Same as Fig. 1.

B. EXAMPLES OF BARNARD 68 BACKGROUND STAR SPECTRA

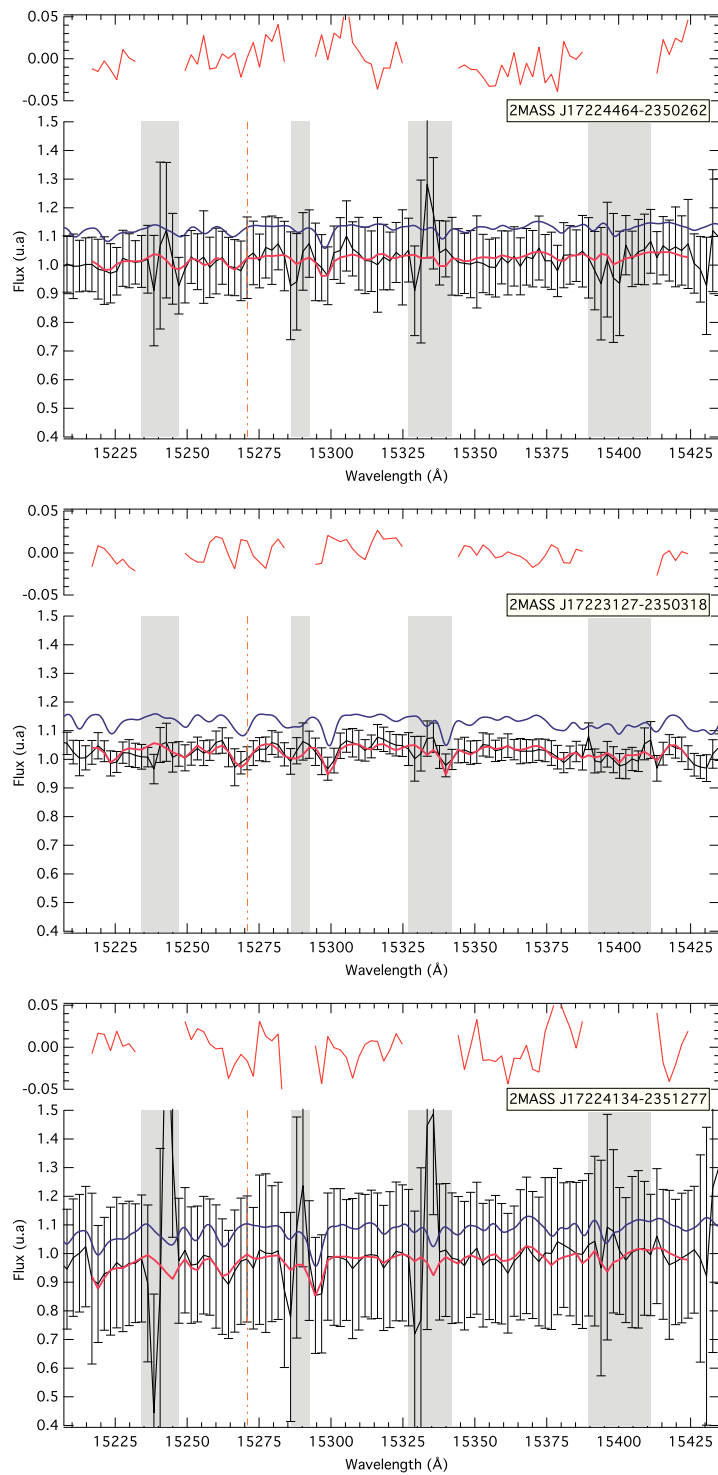


Figure 3 Same as Fig. 1.

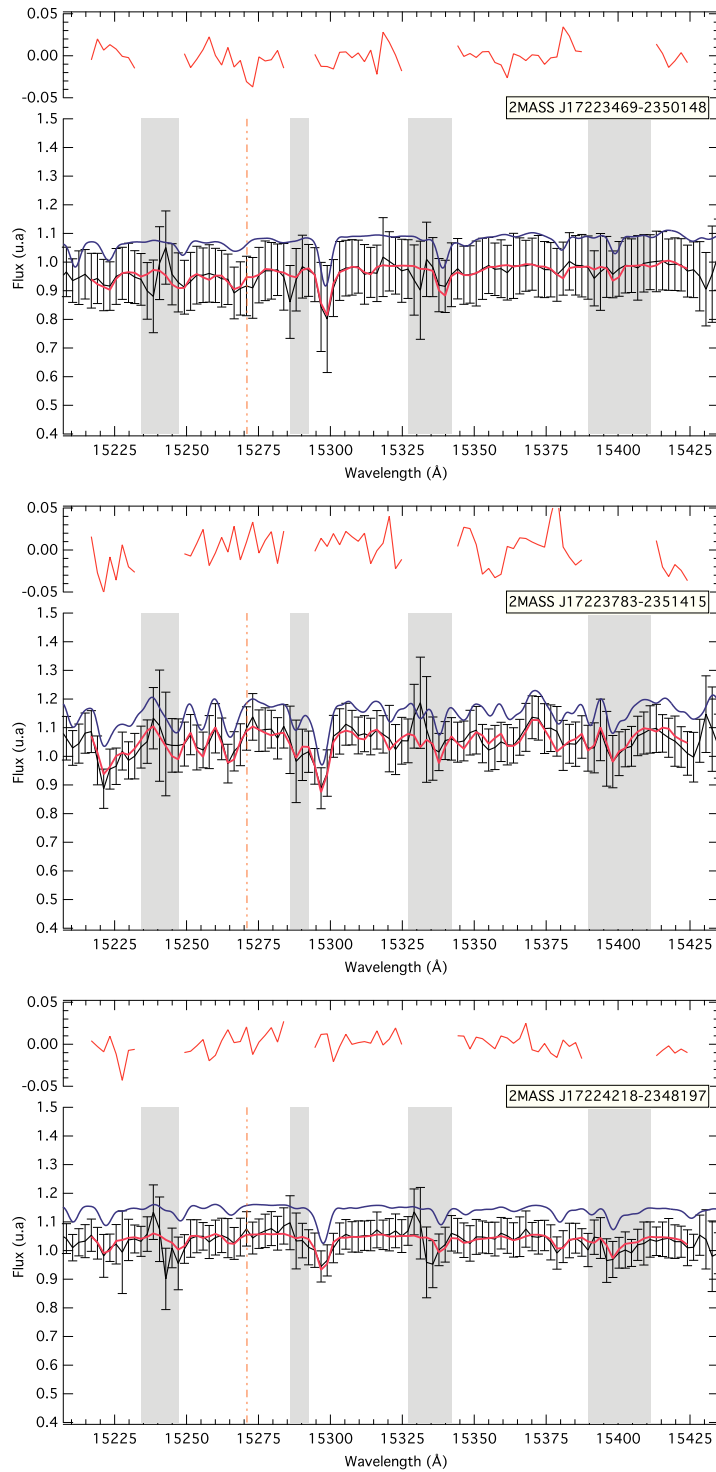


Figure 4 Same as Fig. 1.

B. EXAMPLES OF BARNARD 68 BACKGROUND STAR SPECTRA

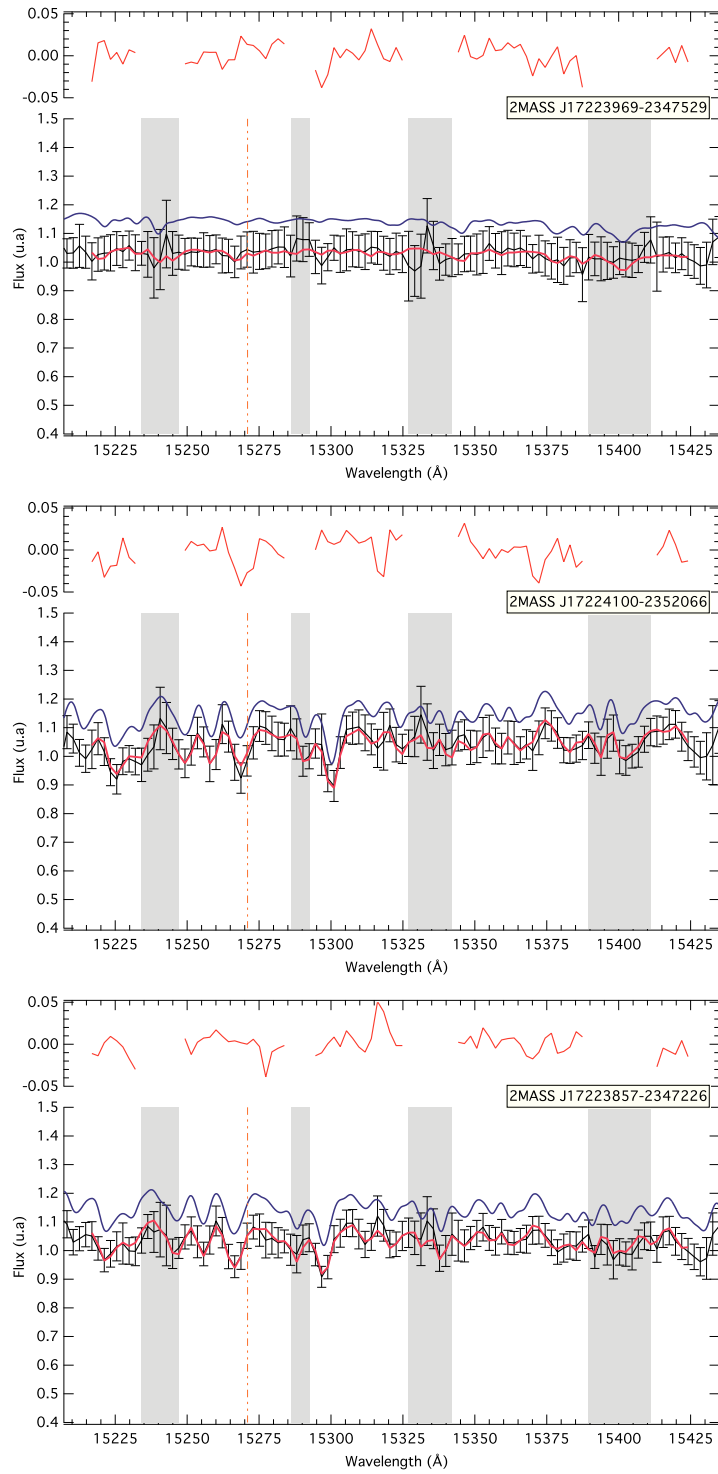


Figure 5 Same as Fig. 1.

Appendix C

EDIBLES data: gas line fitting in the search for cloud structures and mono-cloud sightlines

C.1 NaI-UV extractions

C. EDIBLES DATA: GAS LINE FITTING IN THE SEARCH FOR CLOUD STRUCTURES AND MONO-CLOUD SIGHTLINES

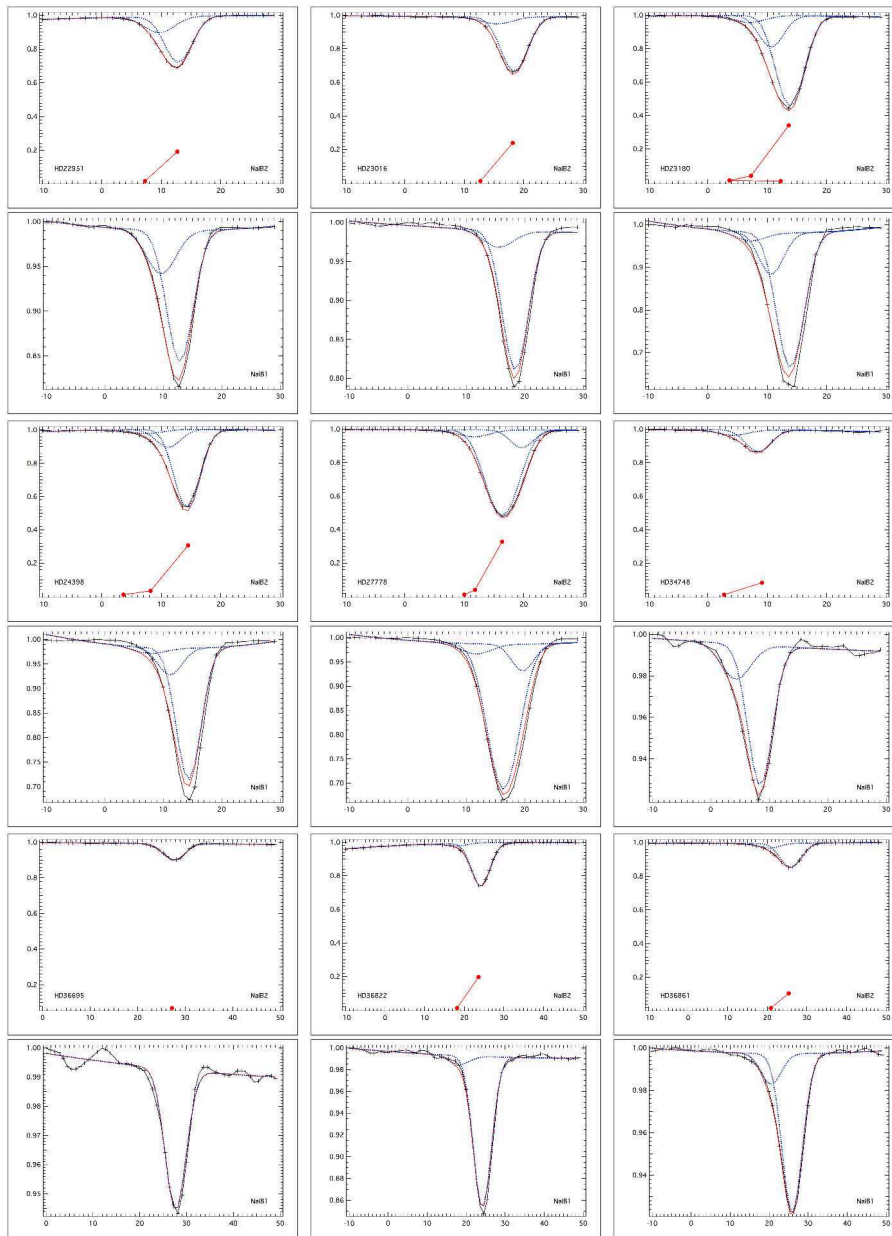


Figure 1 Illustrations of the multi-cloud automated fitting of the NaI–UV interstellar lines. Marked black lines show the observed data. The red lines display the fit. The profiles of each component is shown in blue dashed lines.

C.1. NaI-UV extractions

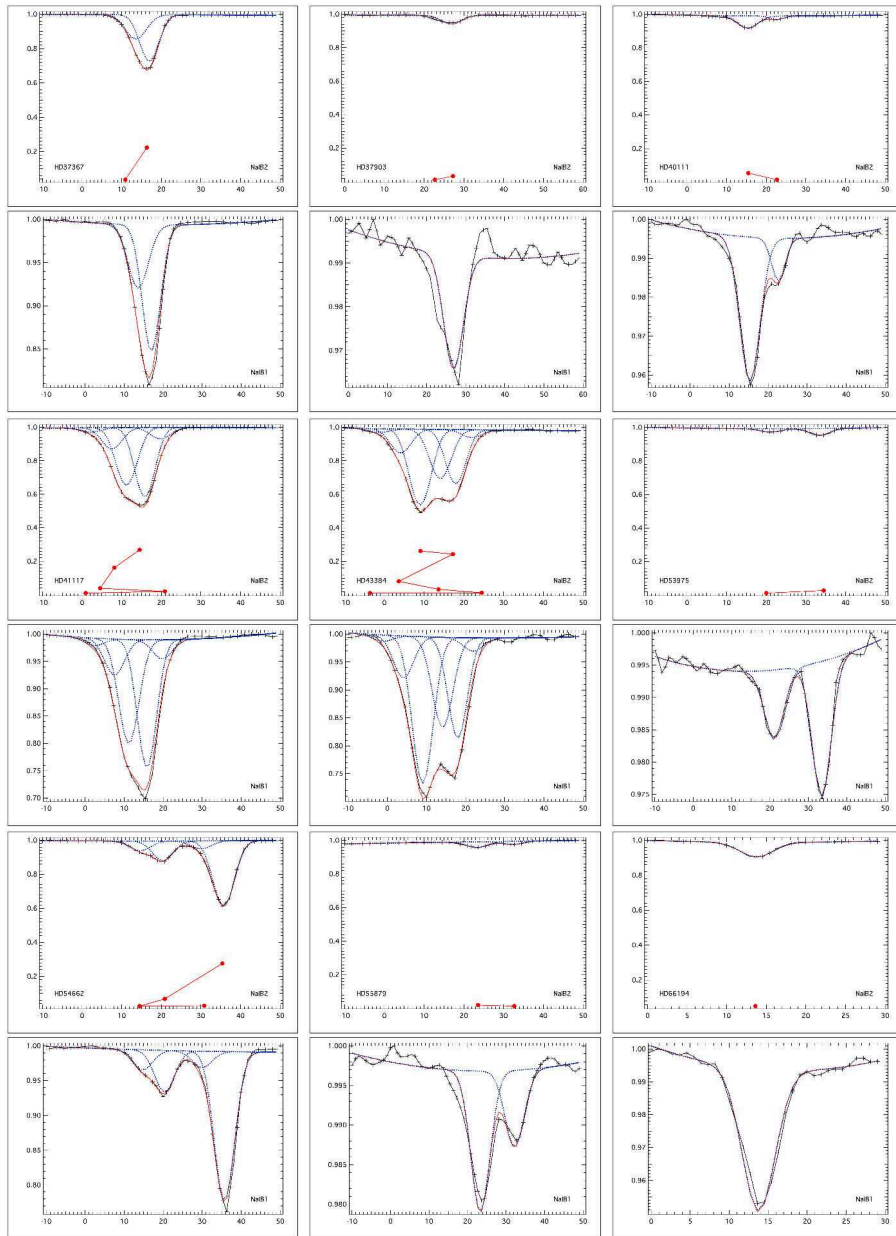


Figure 2 Continued.

C. EDIBLES DATA: GAS LINE FITTING IN THE SEARCH FOR CLOUD STRUCTURES AND MONO-CLOUD SIGHTLINES

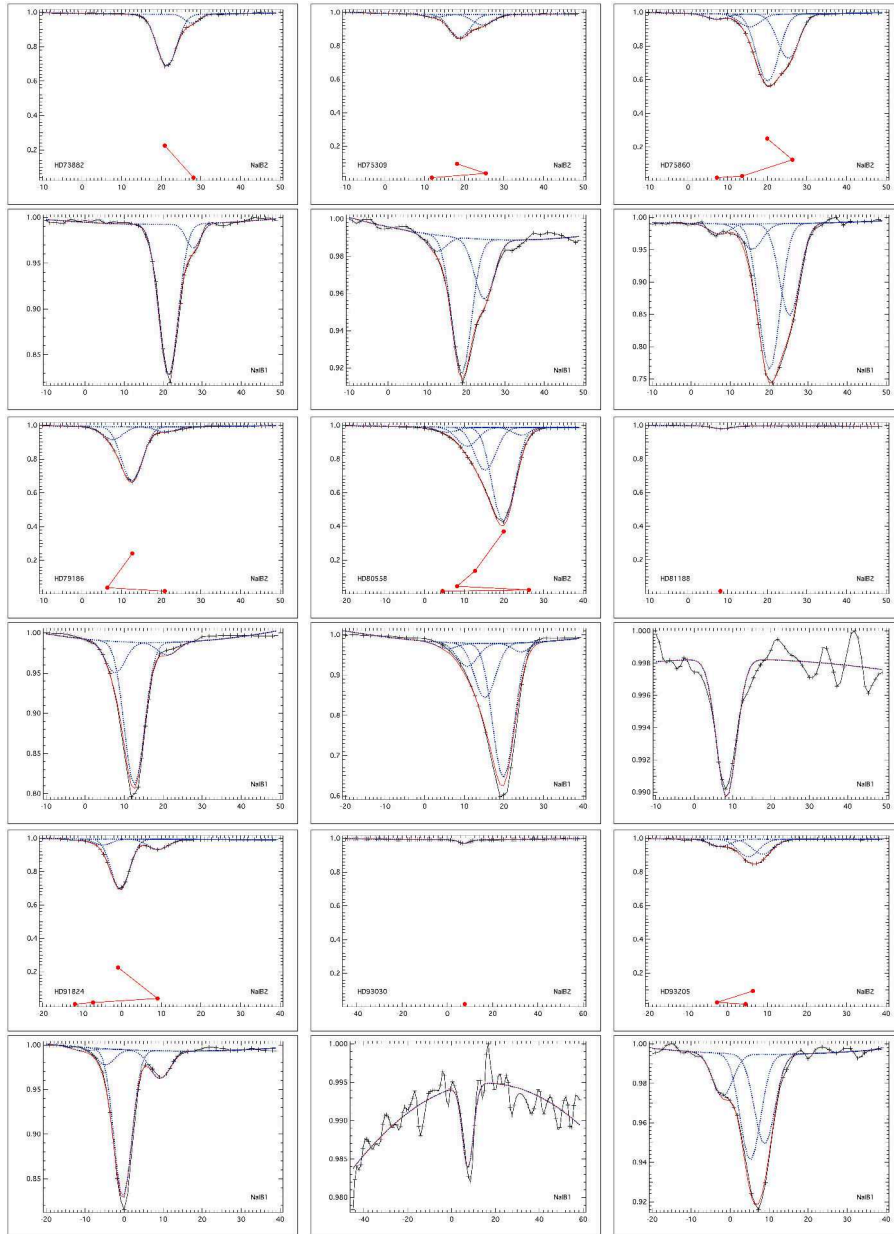


Figure 3 Continued.

C.1. NaI-UV extractions

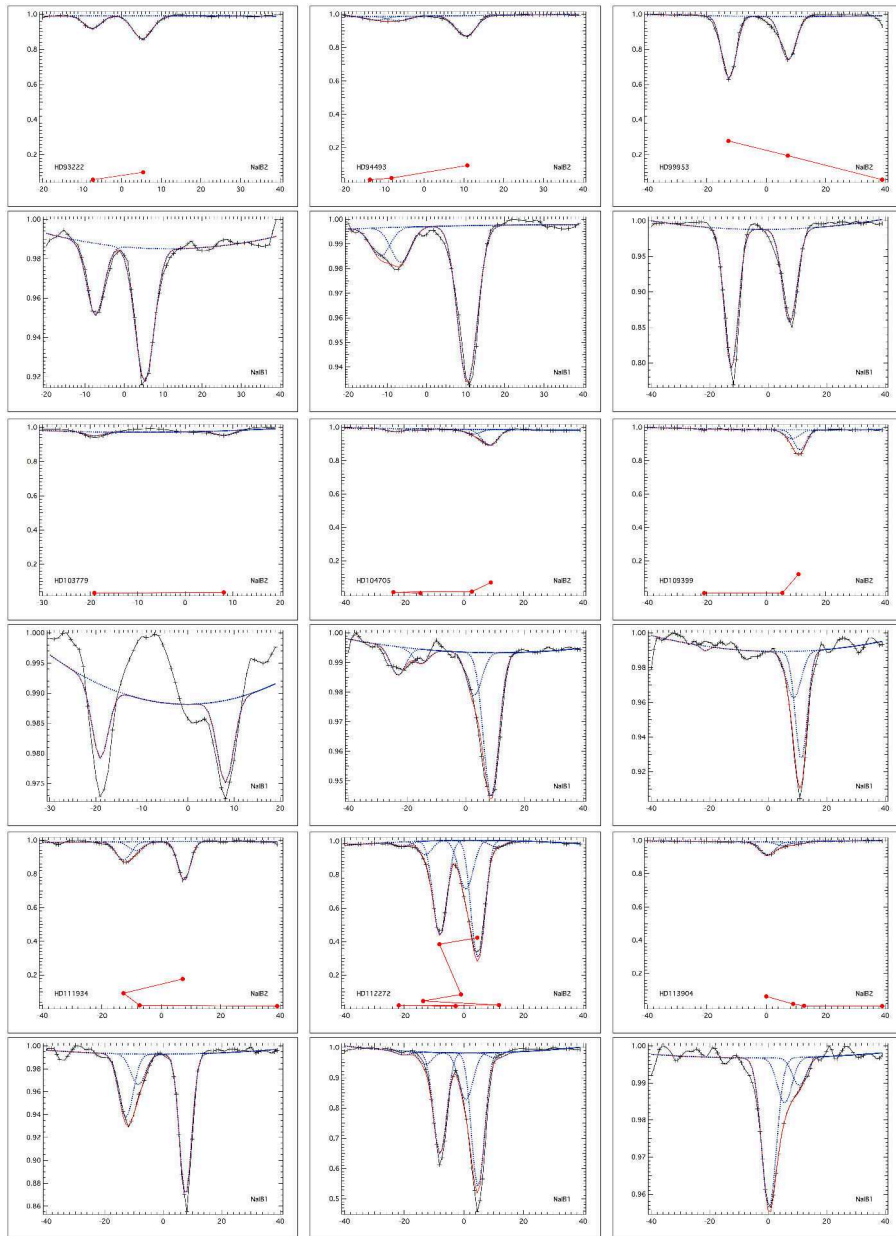


Figure 4 Continued.

C. EDIBLES DATA: GAS LINE FITTING IN THE SEARCH FOR CLOUD STRUCTURES AND MONO-CLOUD SIGHTLINES

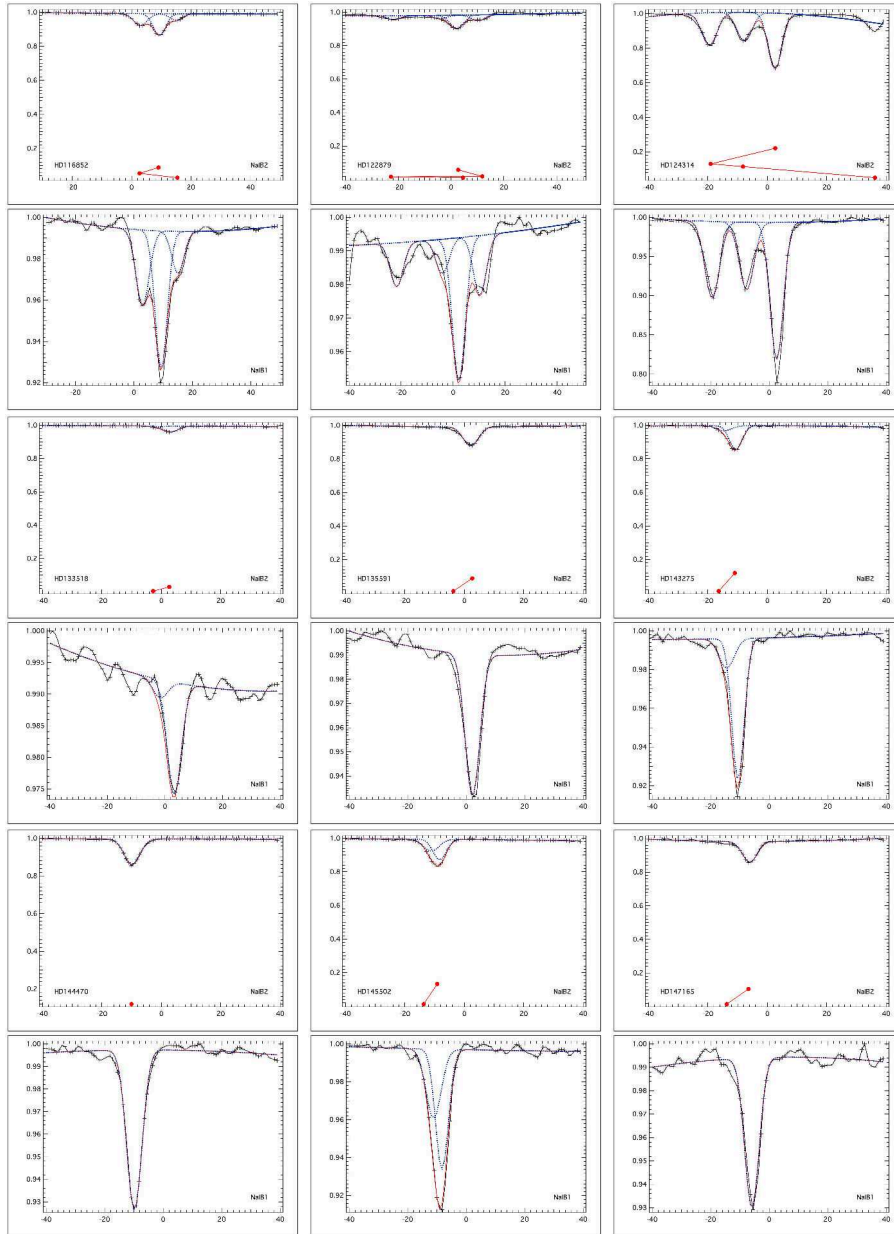


Figure 5 Continued.

C.1. NaI-UV extractions

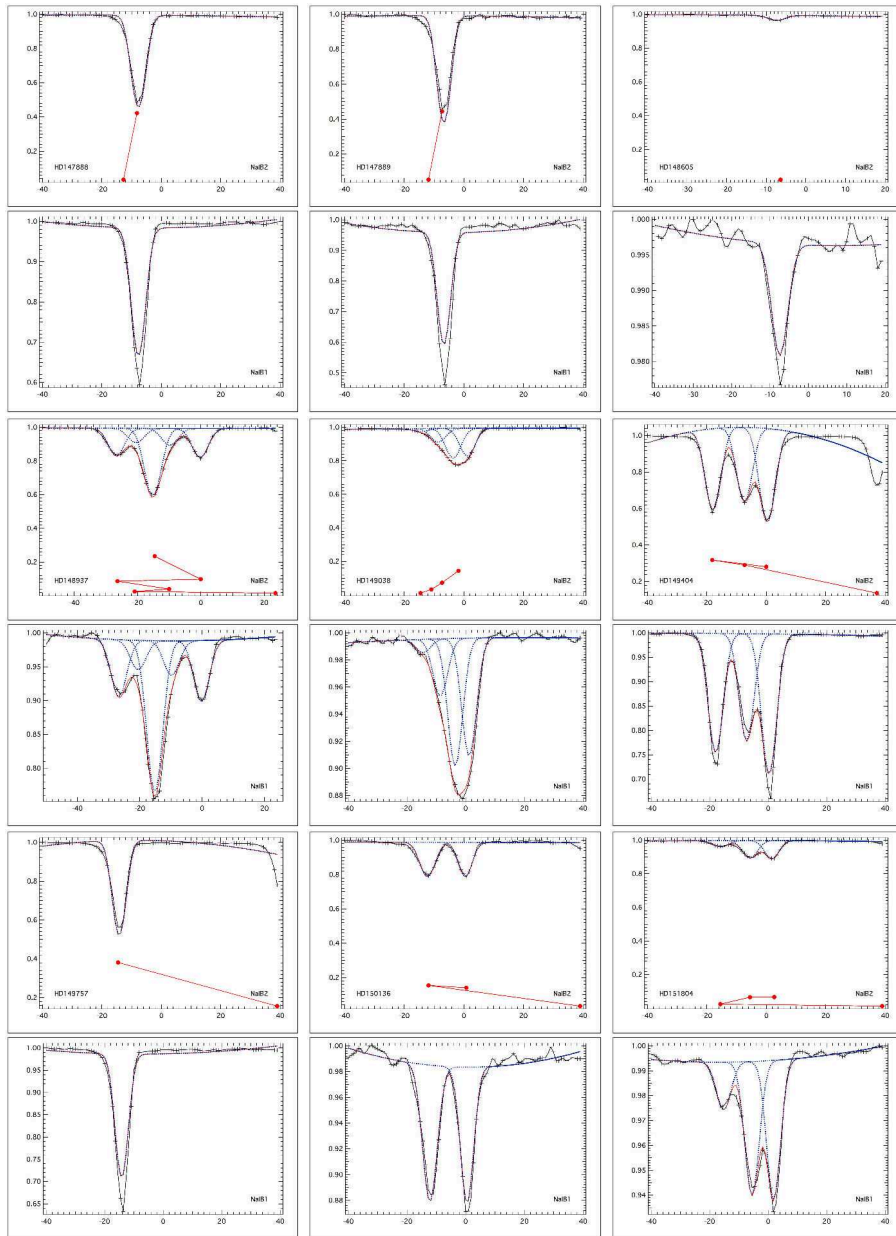


Figure 6 Continued

C. EDIBLES DATA: GAS LINE FITTING IN THE SEARCH FOR CLOUD STRUCTURES AND MONO-CLOUD SIGHTLINES

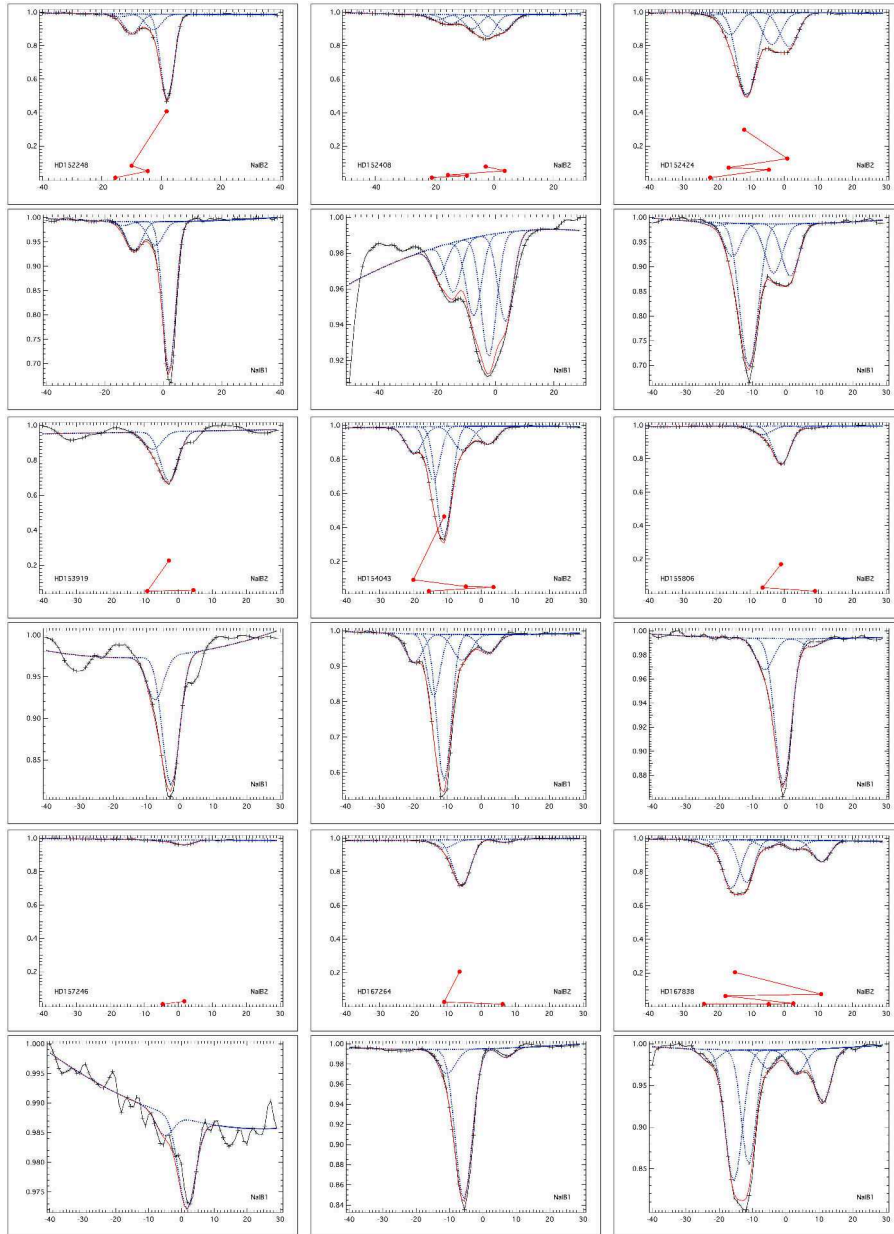


Figure 7 Continued.

C.1. NaI-UV extractions

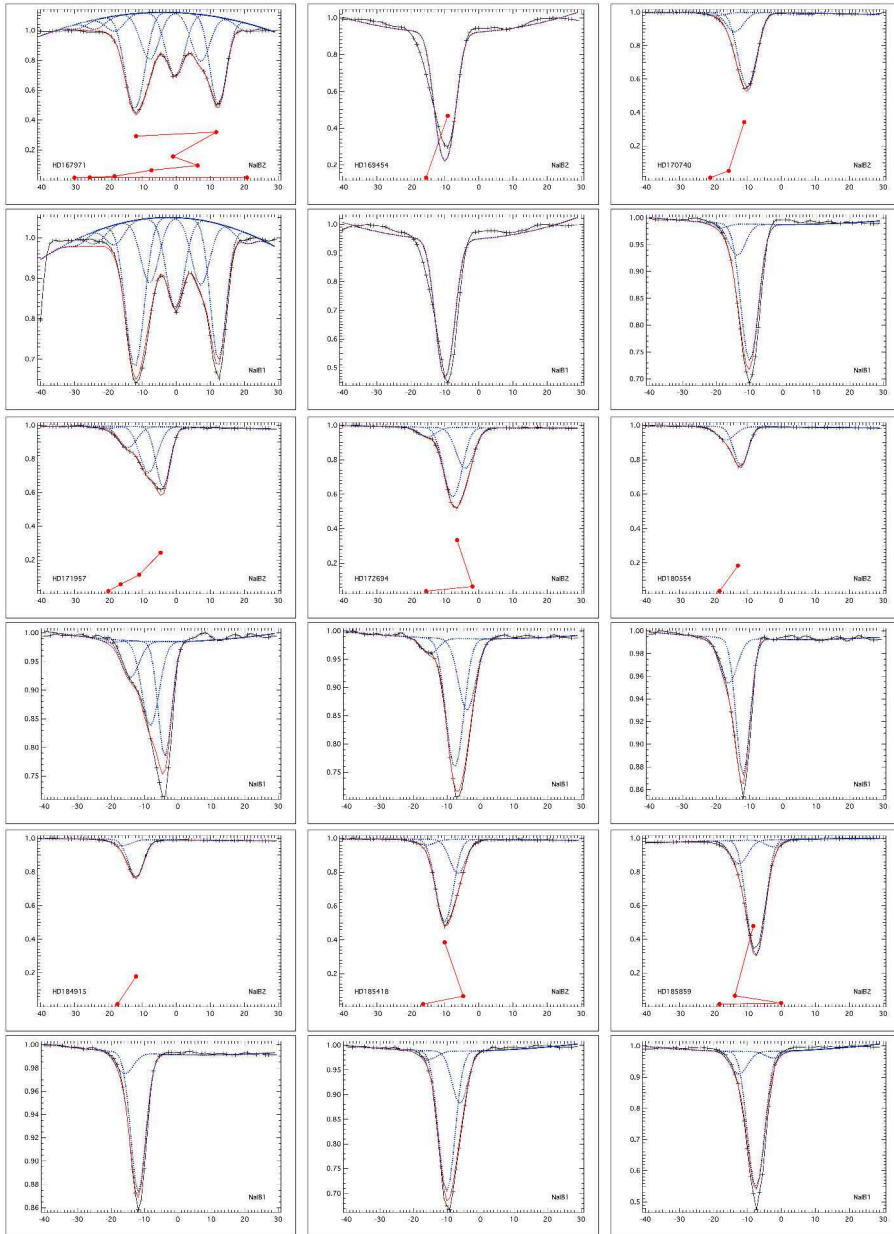


Figure 8 Continued.

C. EDIBLES DATA: GAS LINE FITTING IN THE SEARCH FOR CLOUD STRUCTURES AND MONO-CLOUD SIGHTLINES

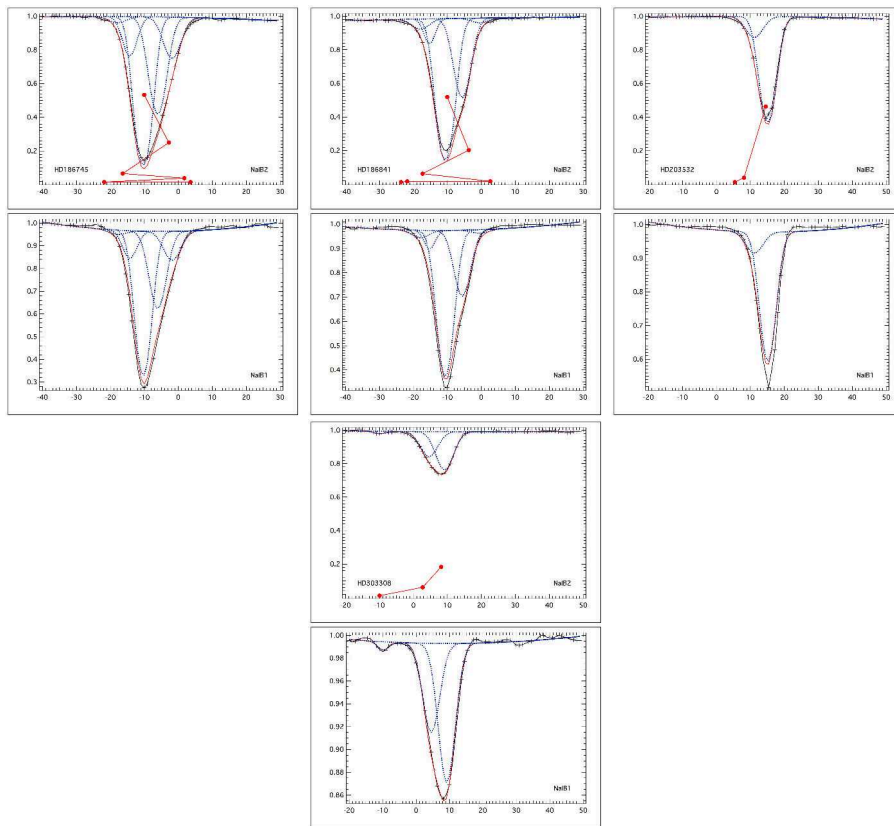


Figure 9 Continued.

C.2 NaI D2-D1 line extractions

C. EDIBLES DATA: GAS LINE FITTING IN THE SEARCH FOR CLOUD STRUCTURES AND MONO-CLOUD SIGHTLINES

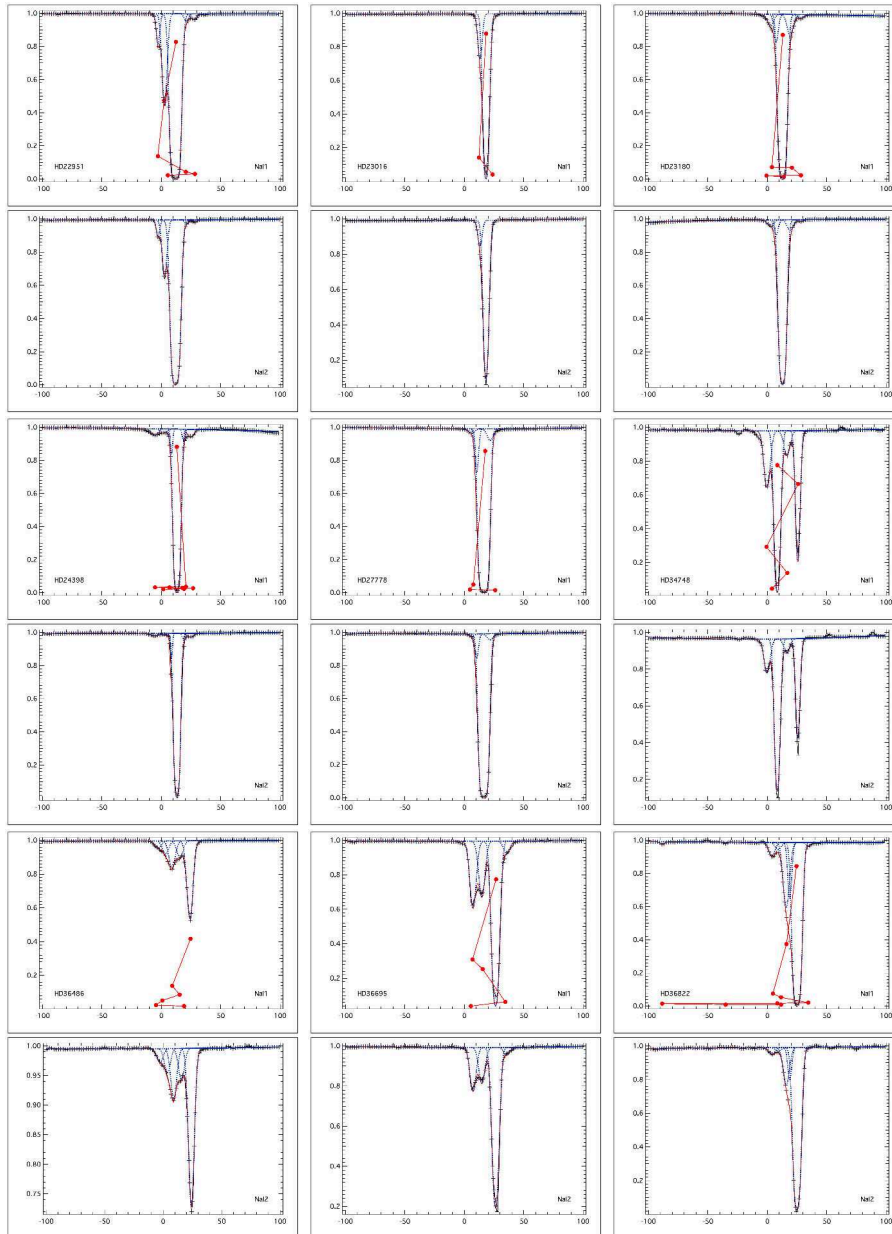


Figure 10 Illustrations of the multi-cloud automated fitting of the NaI D2-D1 interstellar lines. Marked black lines show the observed data. The red lines display the fit. The profiles of each component is shown in blue dashed lines. The stars shown here are: HD22951, HD23016, HD23180, HD24398, HD27778, HD34748, HD36486, HD36695, and HD36822.

C.2. NaI D2-D1 line extractions

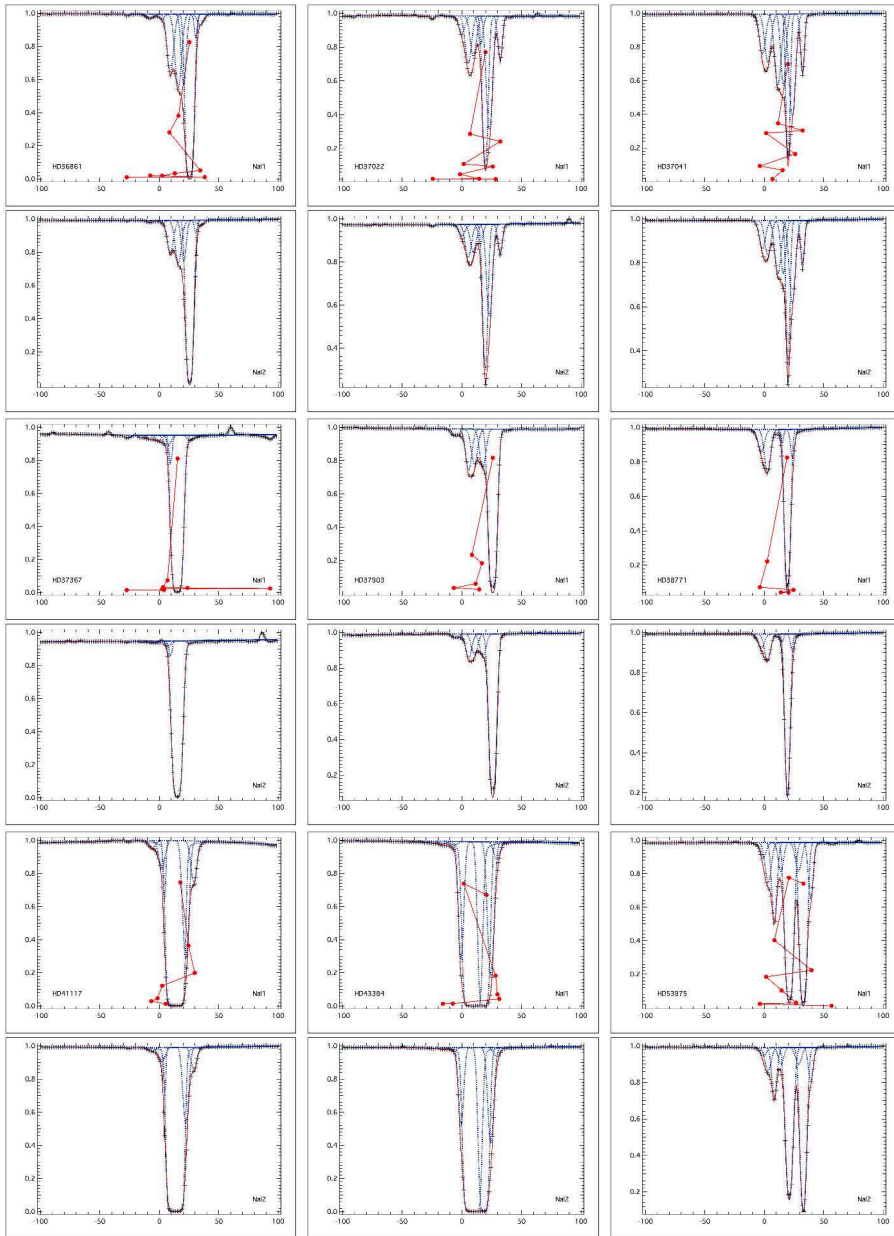


Figure 11 Same as Fig. 10 but for HD36861, HD37022, HD37041, HD37367, HD37903, HD38771, HD41117, HD43384, and HD53975.

C. EDIBLES DATA: GAS LINE FITTING IN THE SEARCH FOR CLOUD STRUCTURES AND MONO-CLOUD SIGHTLINES

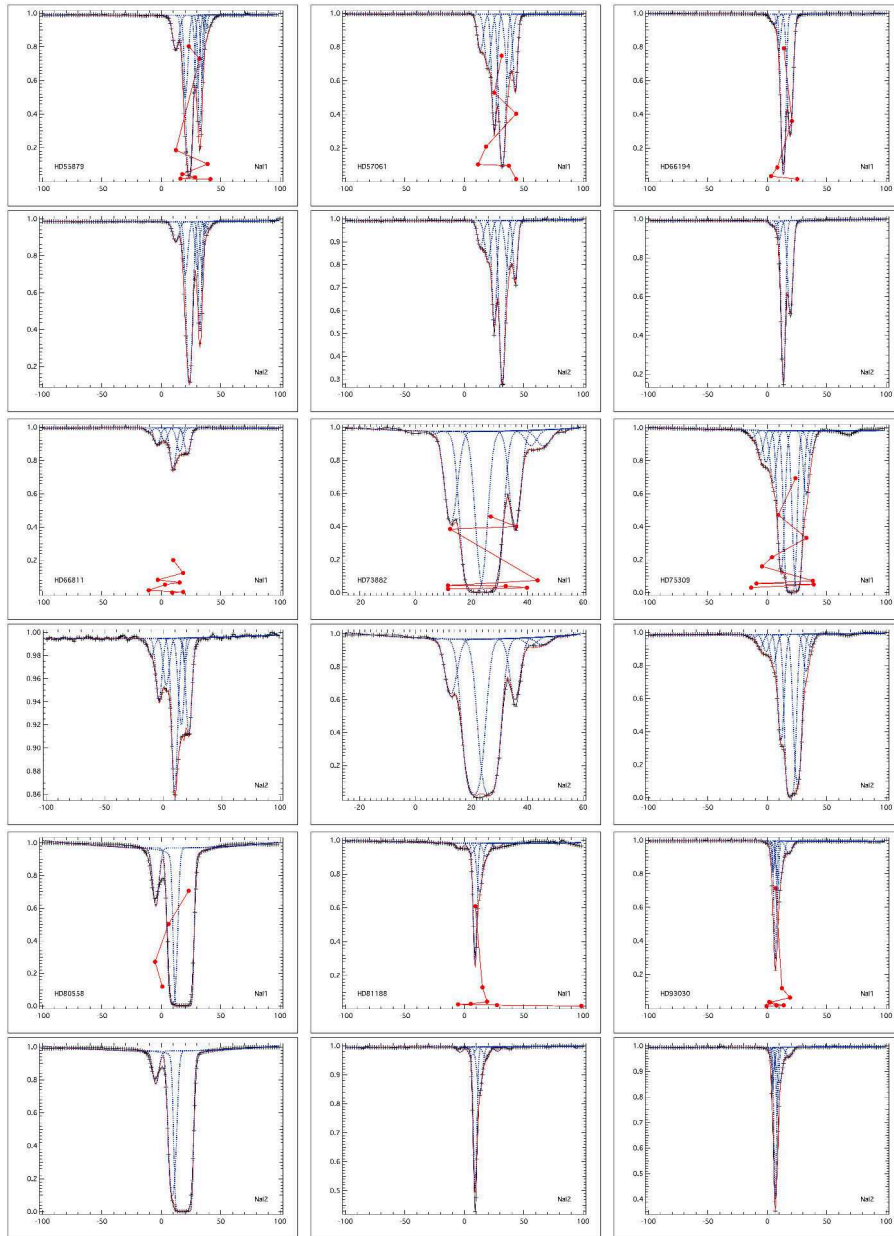


Figure 12 Same as Fig. 10 but for HD55879, HD57061, HD66194, HD66811, HD73882, HD75309, HD80558, HD81188, and HD93030.

C.2. NaI D2-D1 line extractions

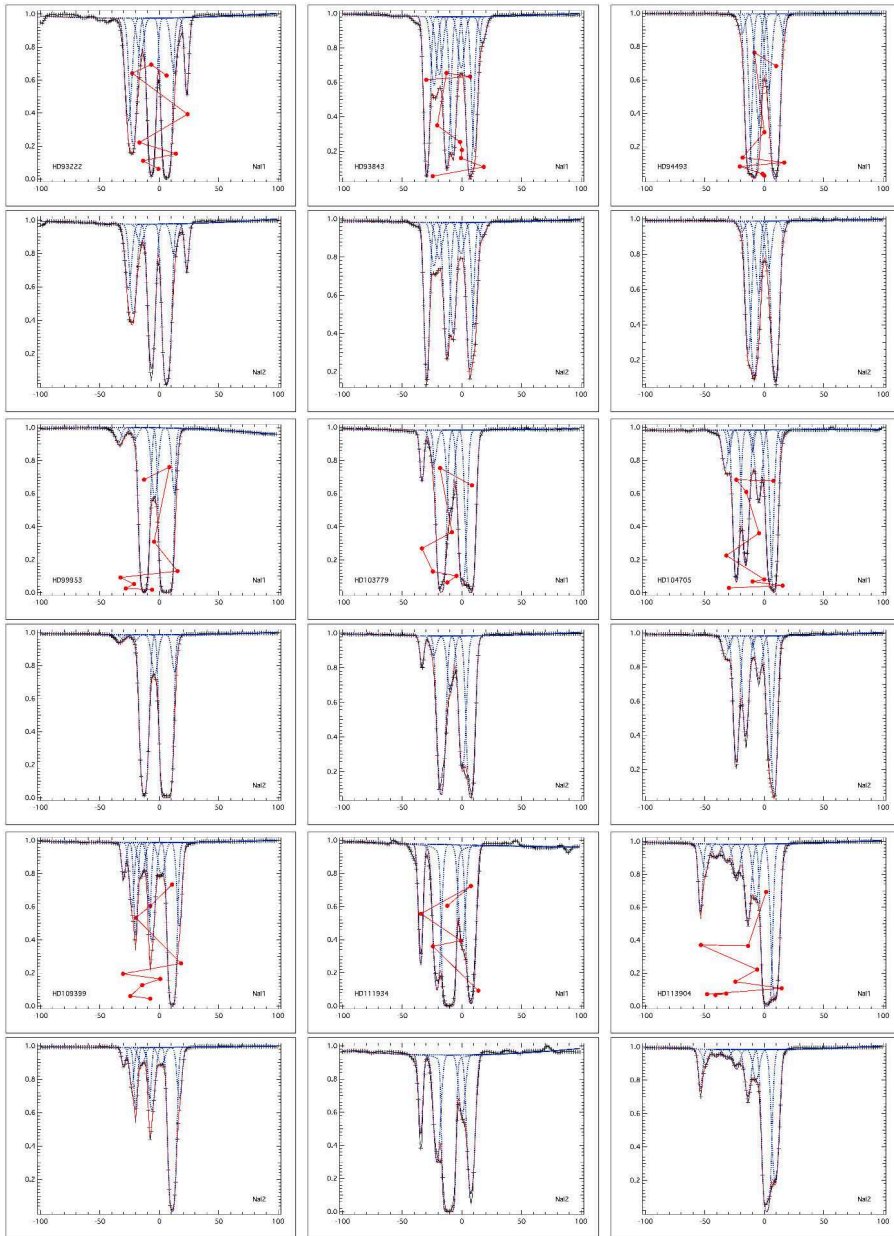


Figure 13 Same as Fig. 10 but for HD93222, HD93843, HD99953, HD103779, HD104705, HD109399, HD111934, and HD113904.

C. EDIBLES DATA: GAS LINE FITTING IN THE SEARCH FOR CLOUD STRUCTURES AND MONO-CLOUD SIGHTLINES

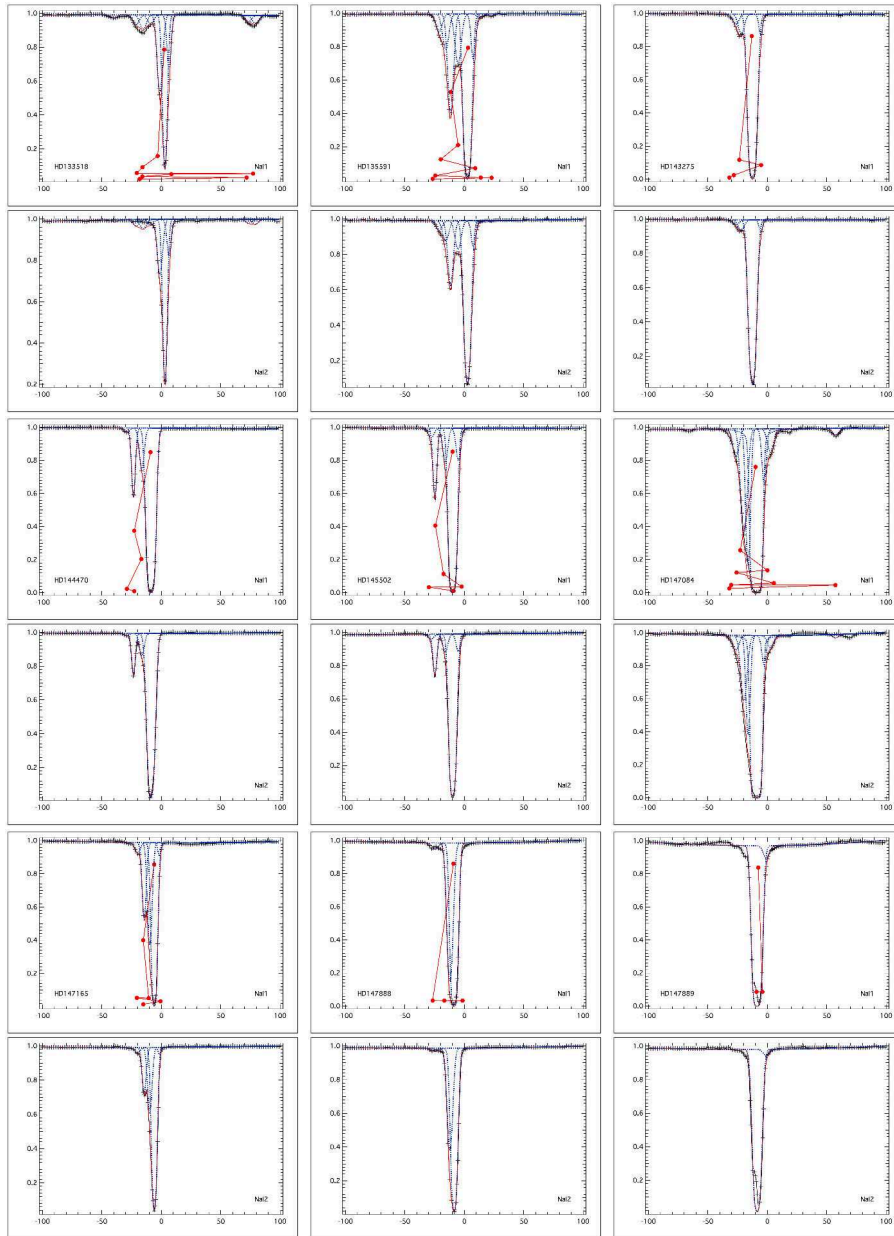


Figure 14 Same as Fig. 10 but for HD133518, HD135591, HD143275, HD144470, HD145502, HD147084, HD147165, HD147888, and HD147889.

C.2. NaI D2-D1 line extractions

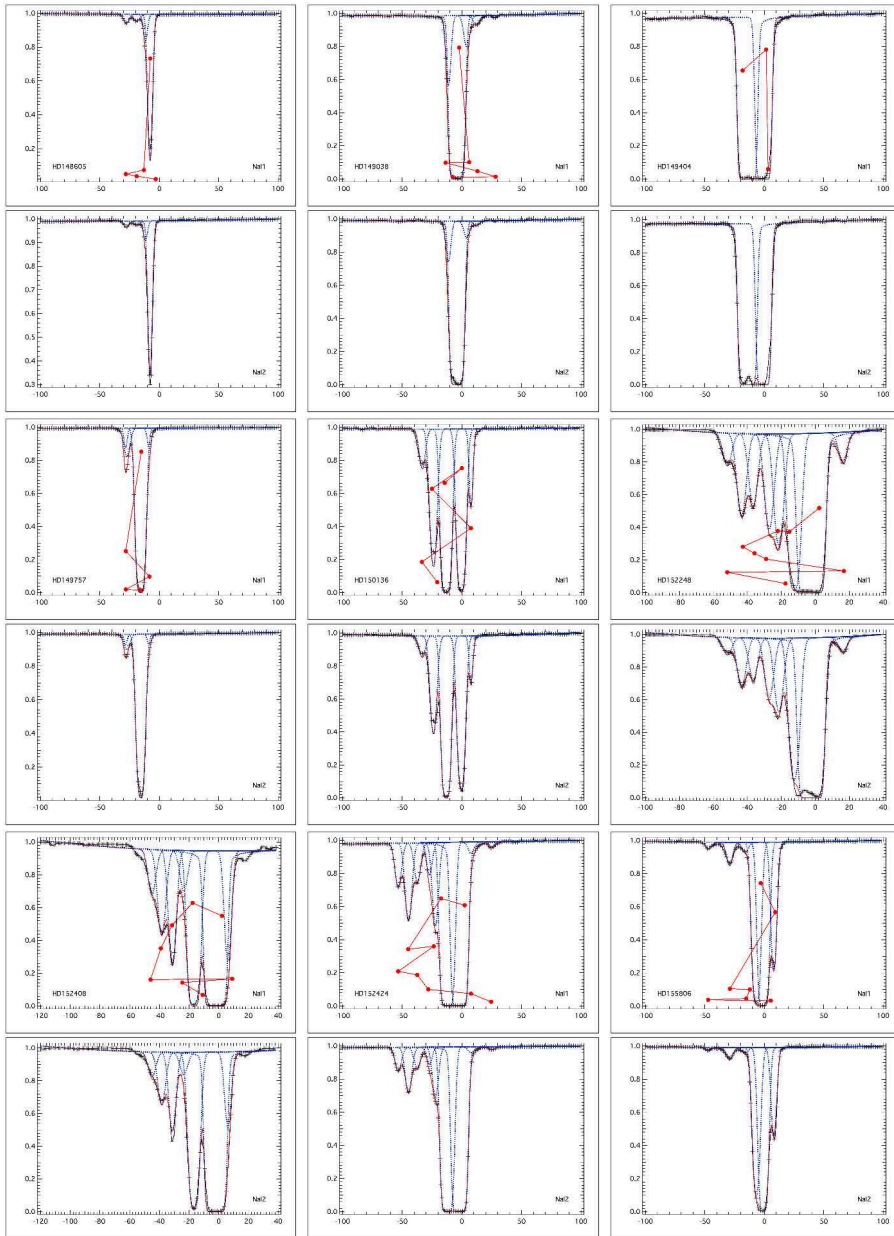


Figure 15 Same as Fig. 10 but for HD148605, HD149038, HD149404, HD149757, HD150136, HD152248, HD152408, HD152424, and HD155806.

C. EDIBLES DATA: GAS LINE FITTING IN THE SEARCH FOR CLOUD STRUCTURES AND MONO-CLOUD SIGHTLINES

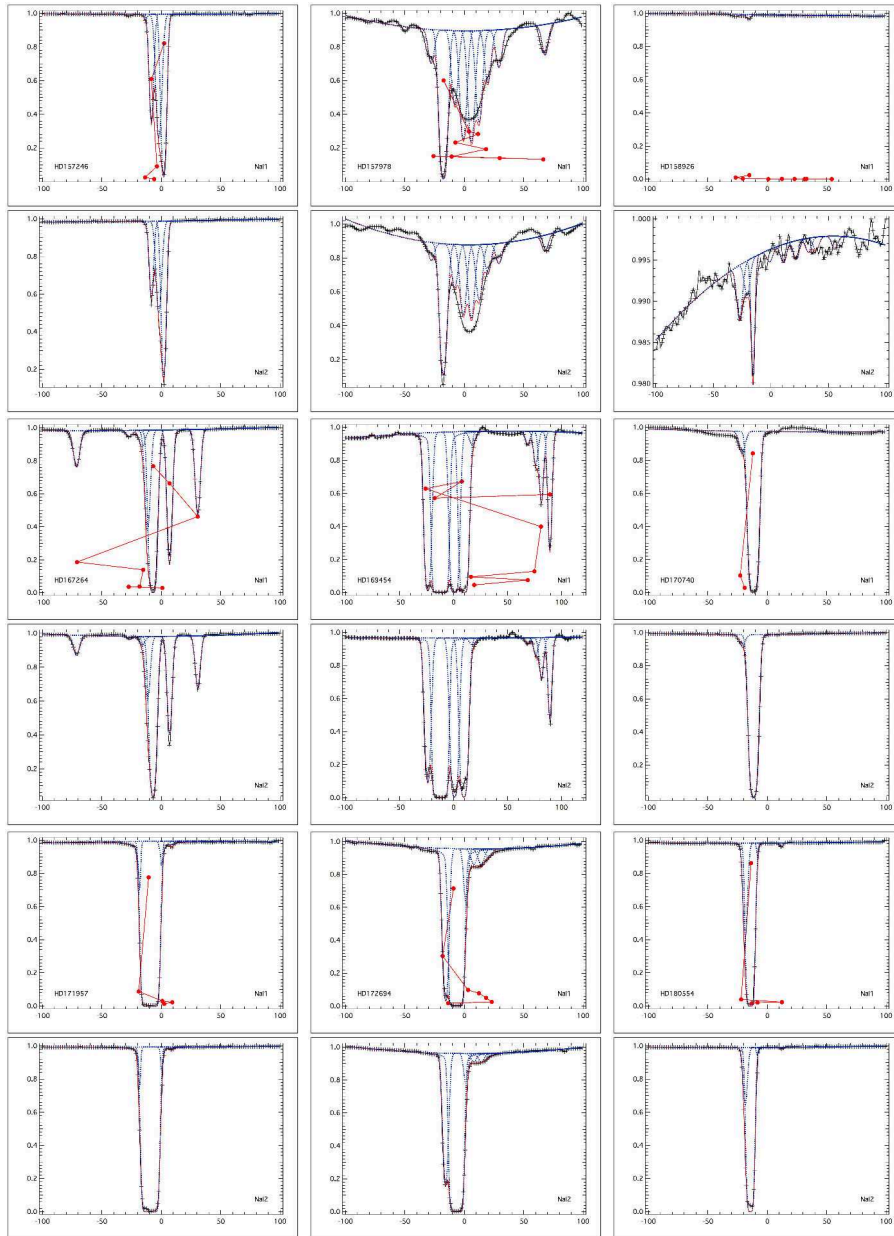


Figure 16 Same as Fig. 10 but for HD157246, HD157978, HD158926, HD167264, HD169454, HD170740, HD171957, HD172694, and HD180554.

C.2. NaI D2-D1 line extractions

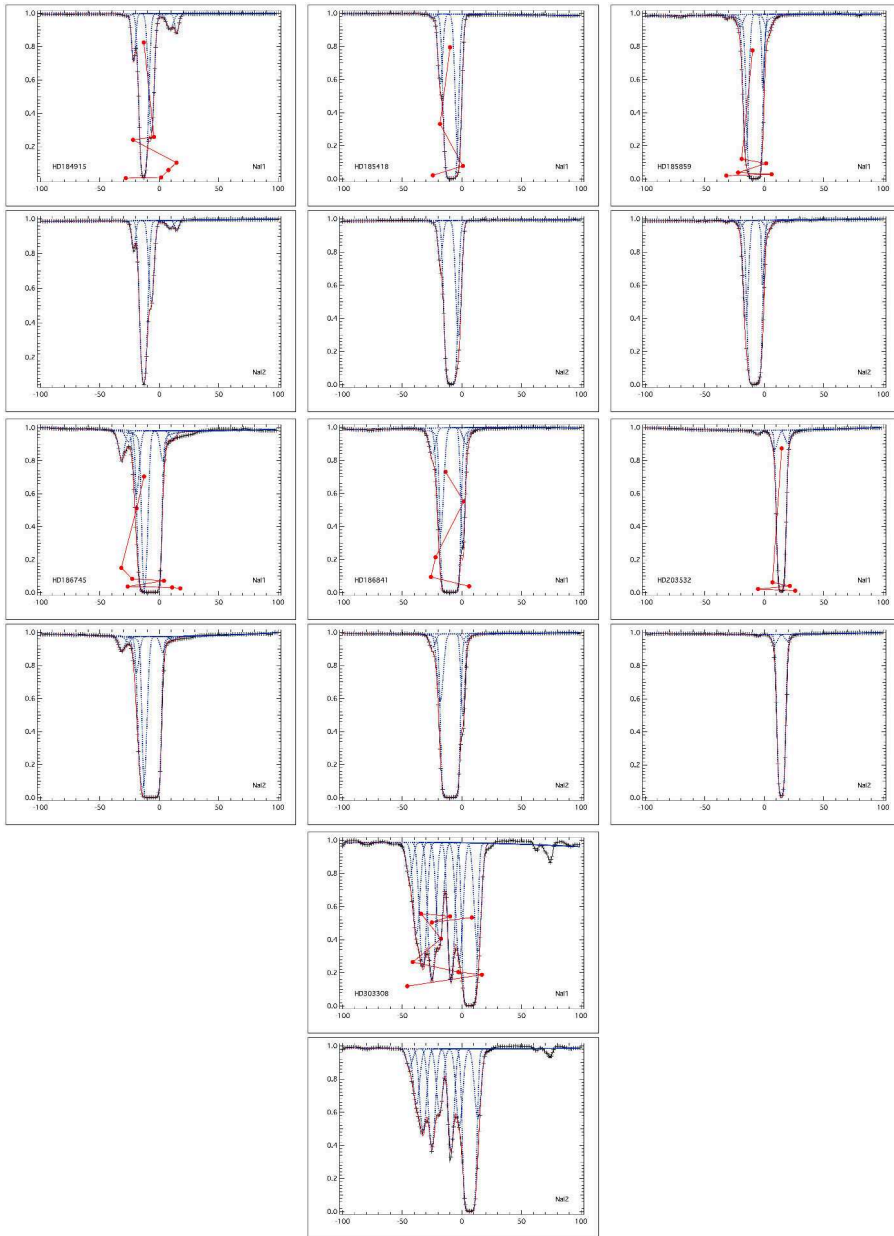


Figure 17 Same as Fig. 10 but for HD184915, HD185418, HD185859, HD186745, HD186841, HD203532, and HD303308.

C. EDIBLES DATA: GAS LINE FITTING IN THE SEARCH FOR CLOUD STRUCTURES AND MONO-CLOUD SIGHTLINES

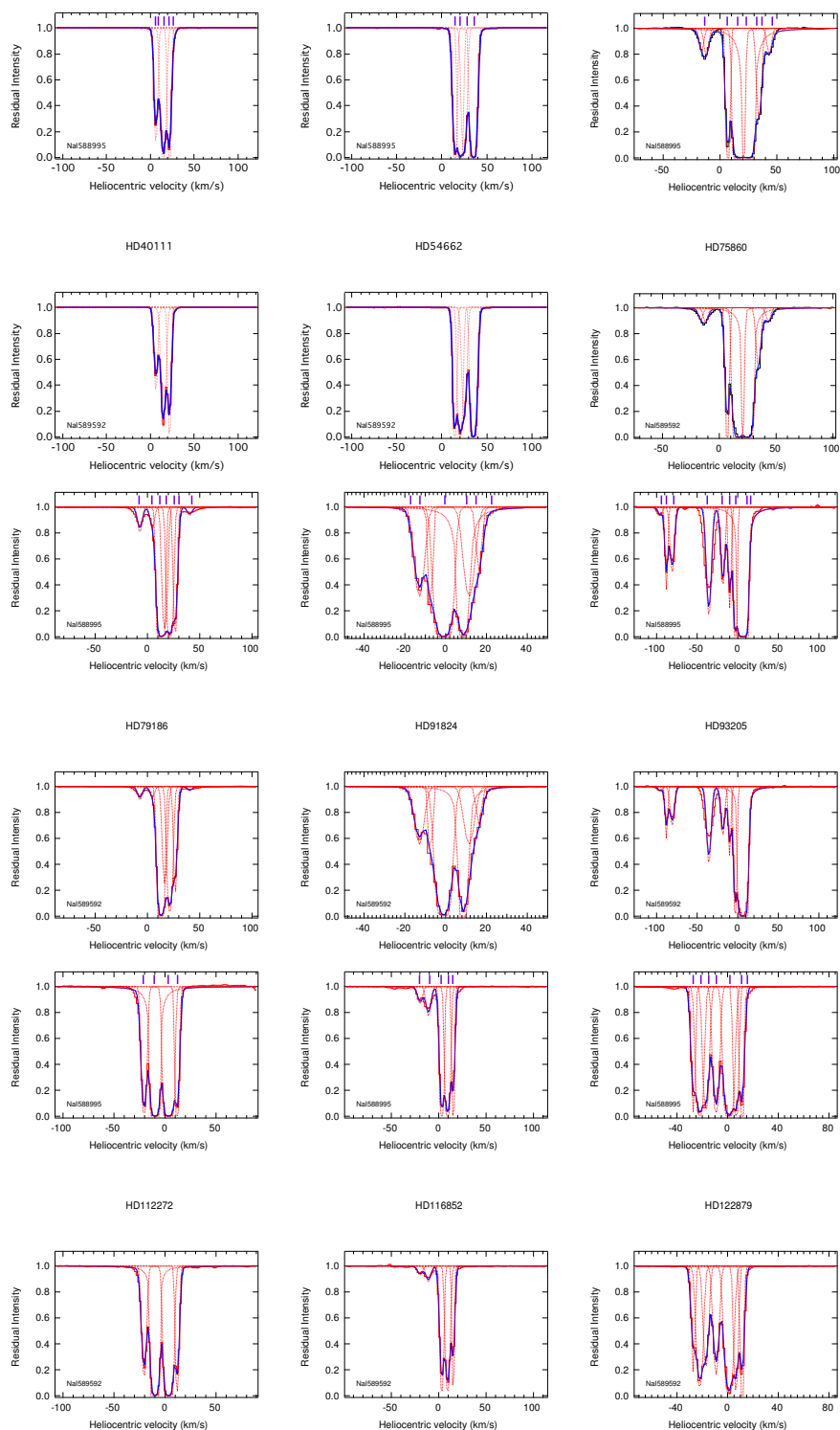


Figure 18 Examples of classical profile fitting results of the NaI D2-D1 normalized spectra. Data are shown in marked red lines. The blue curve displays the fit. The thick red lines show the individual interstellar lines model before convolution. The stars shown here are: HD40111, HD54662, HD75860, HD79186, HD91824, HD93205, HD112272, HD116852, HD122879.

C.2. NaI D2-D1 line extractions

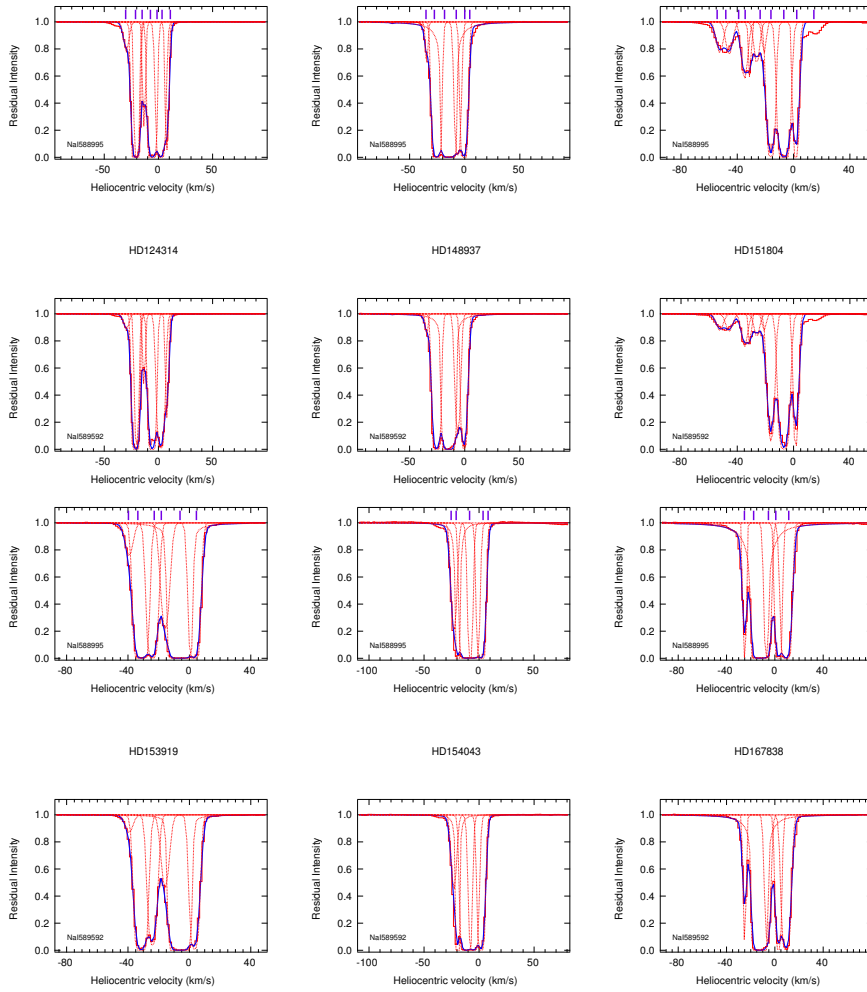


Figure 19 Same as Fig. 18 but for HD124314, HD148937, HD151804, HD153919, HD154043, and HD167838.

C.3 Call K-H extractions

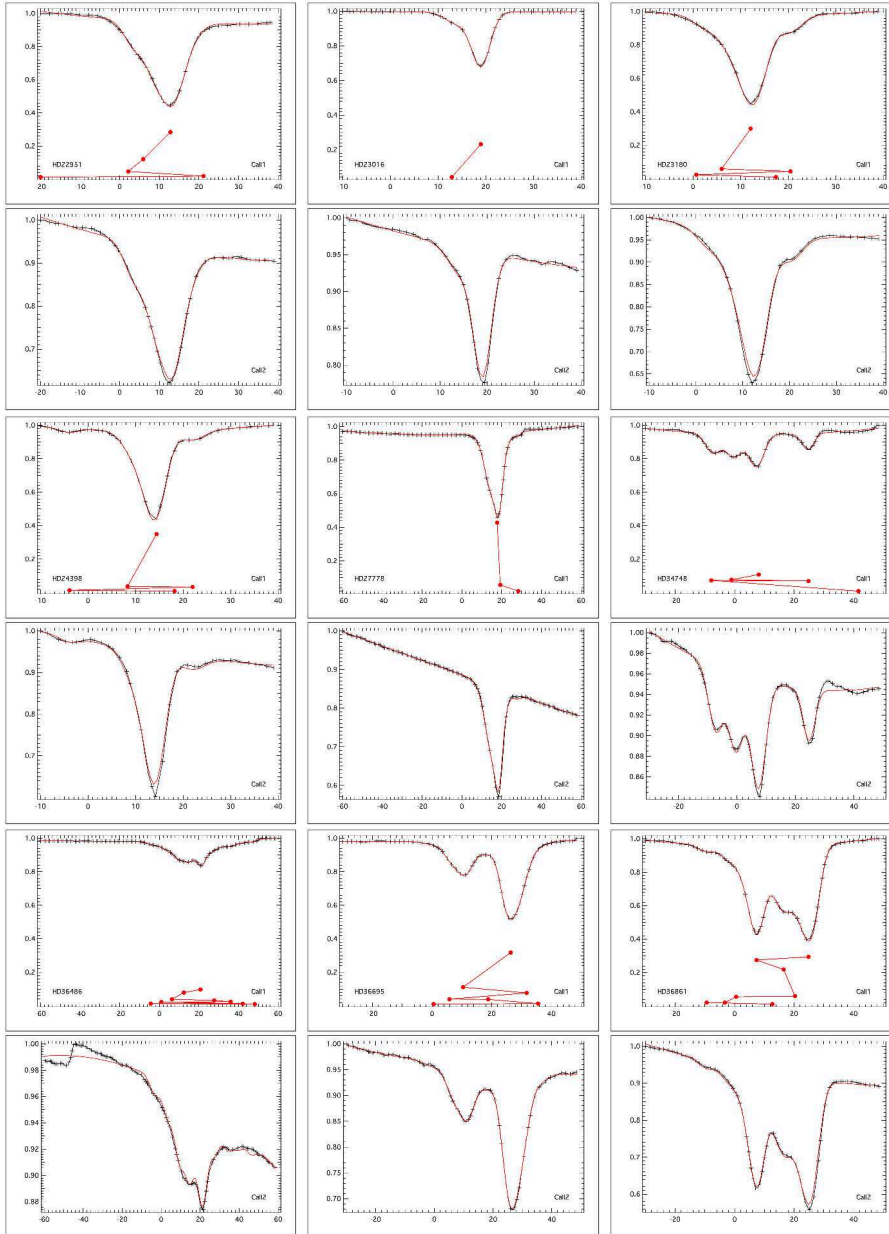


Figure 20 Illustrations of the multi-cloud automated fitting of the CaII K-H interstellar lines. Marked black lines show the observed data. The red lines display the fit.

C. EDIBLES DATA: GAS LINE FITTING IN THE SEARCH FOR CLOUD STRUCTURES AND MONO-CLOUD SIGHTLINES

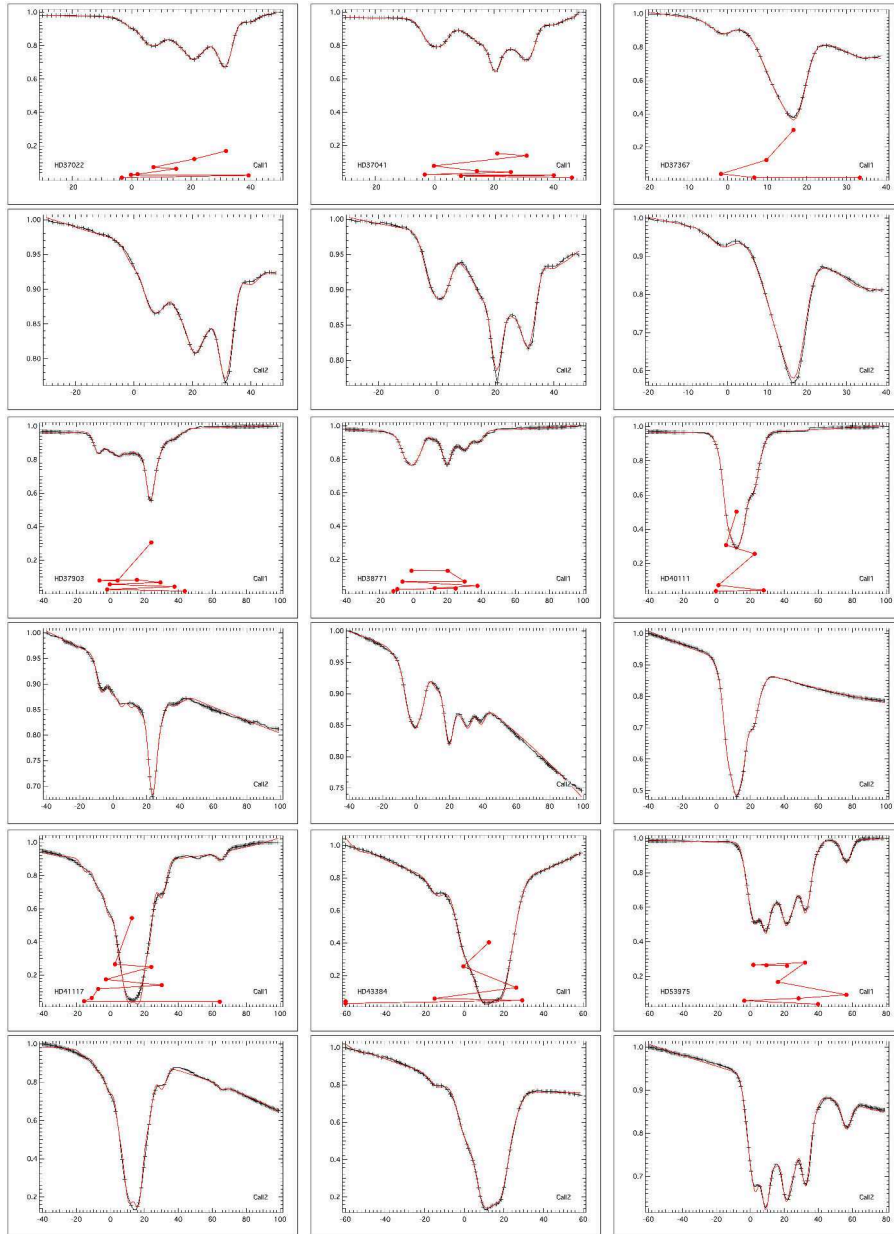


Figure 21 Continued.

C.3. CaII K-H extractions

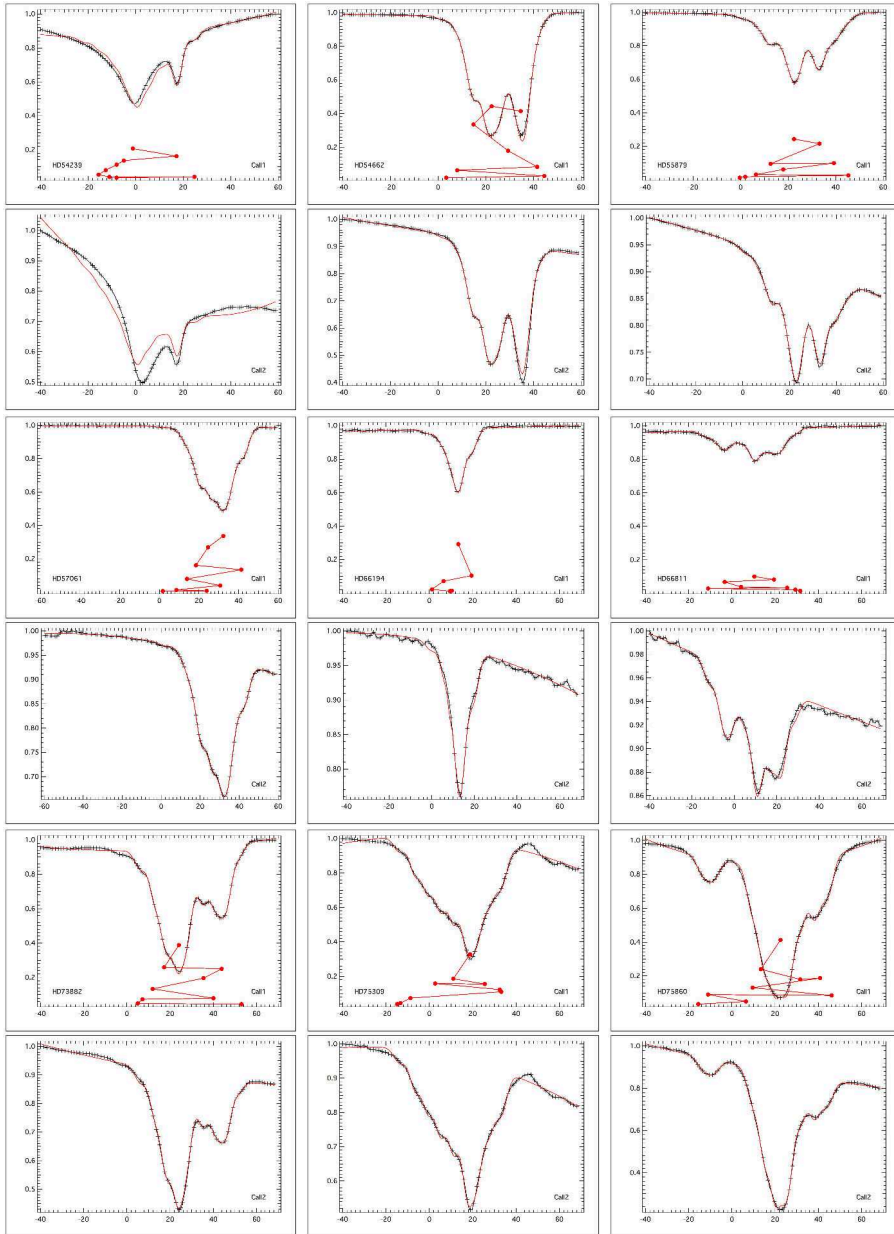


Figure 22 Continued.

C. EDIBLES DATA: GAS LINE FITTING IN THE SEARCH FOR CLOUD STRUCTURES AND MONO-CLOUD SIGHTLINES

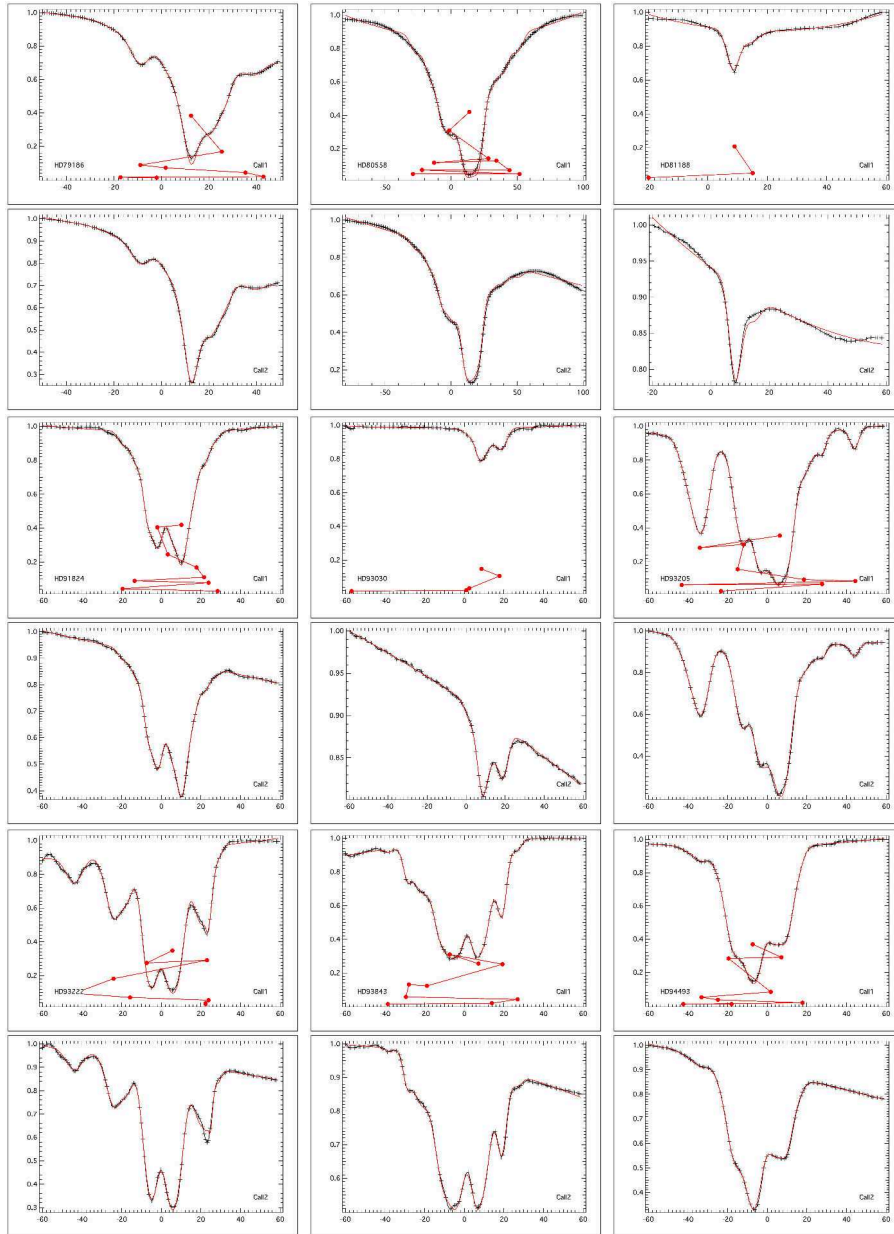


Figure 23 Continued.

C.3. CaII K-H extractions

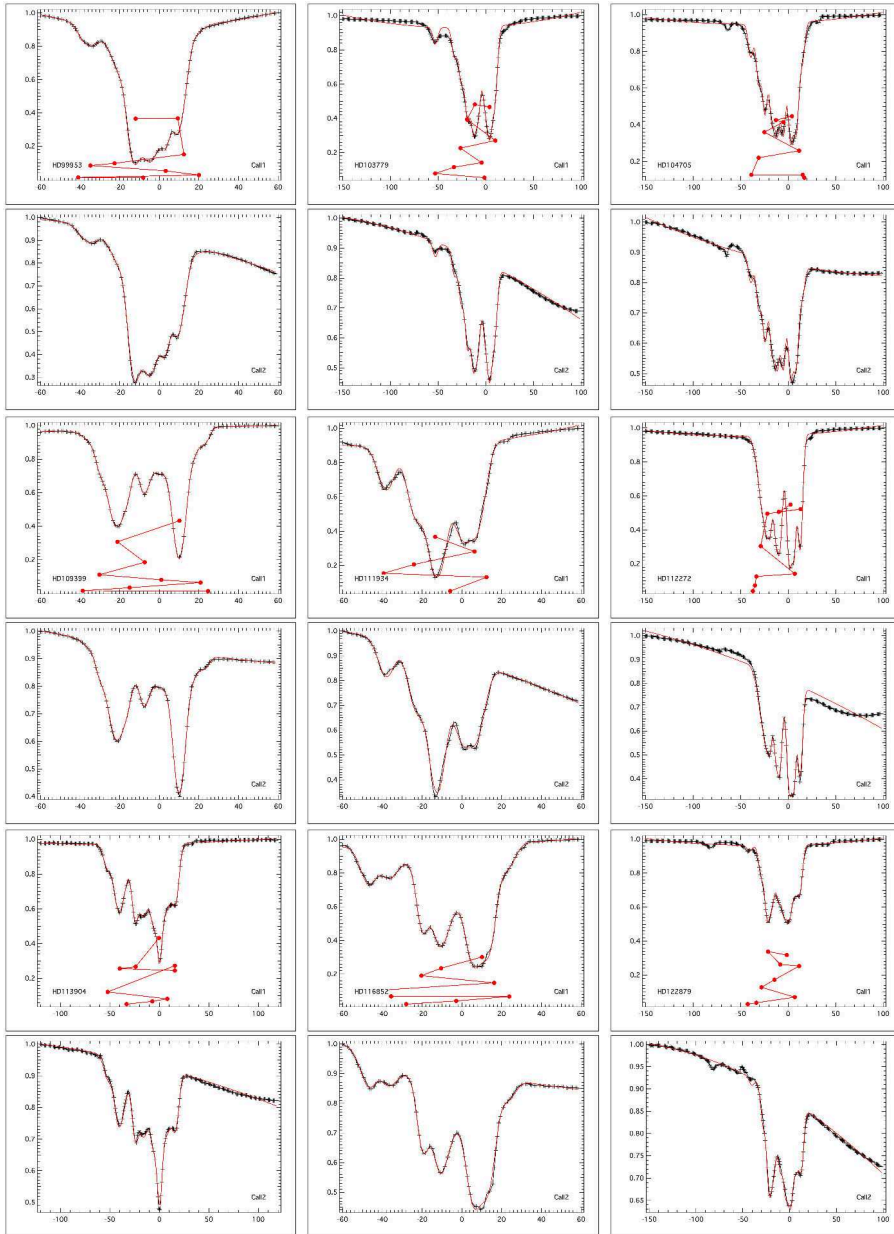


Figure 24 Continued.

C. EDIBLES DATA: GAS LINE FITTING IN THE SEARCH FOR CLOUD STRUCTURES AND MONO-CLOUD SIGHTLINES

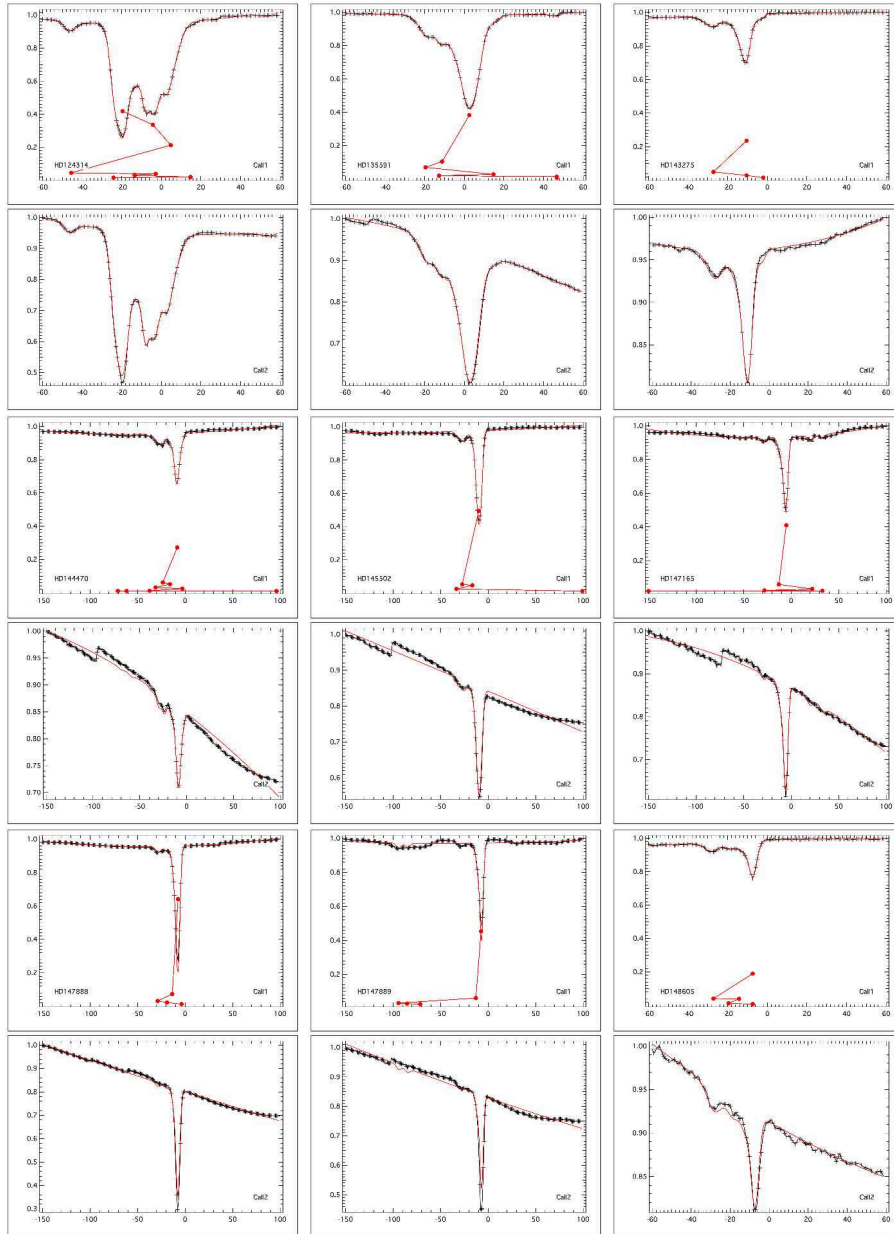


Figure 25 Continued.

C.3. CaII K-H extractions

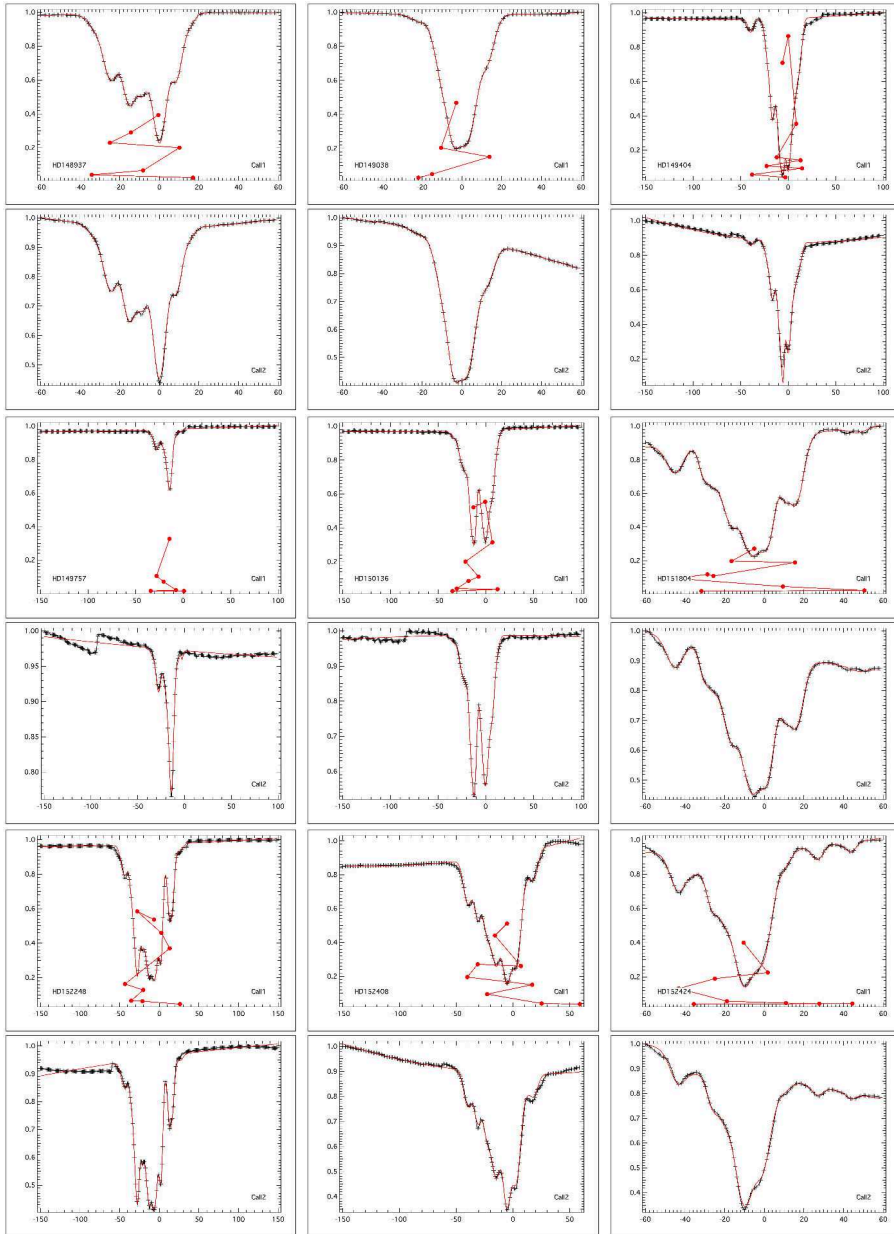


Figure 26 Continued.

C. EDIBLES DATA: GAS LINE FITTING IN THE SEARCH FOR CLOUD STRUCTURES AND MONO-CLOUD SIGHTLINES

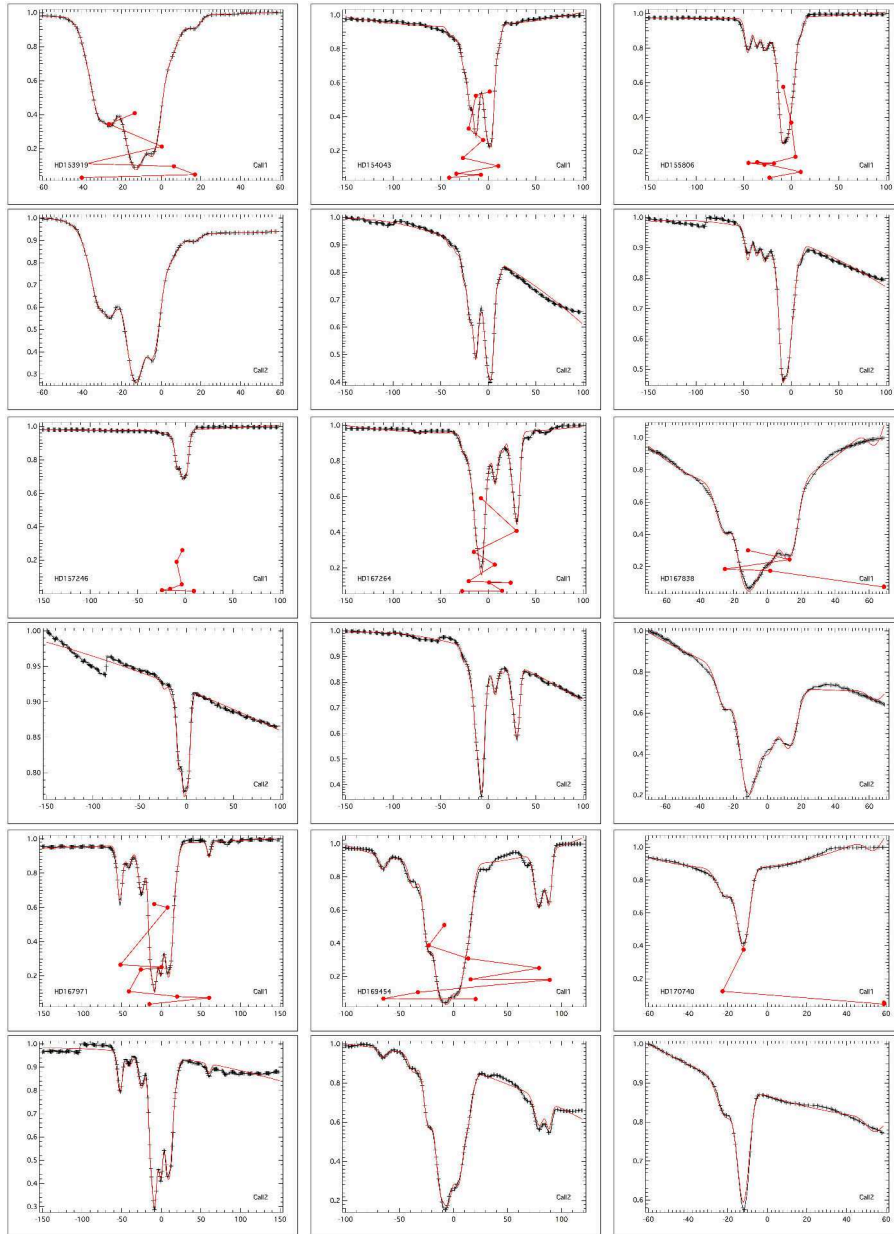


Figure 27 Continued.

C.3. CaII K-H extractions

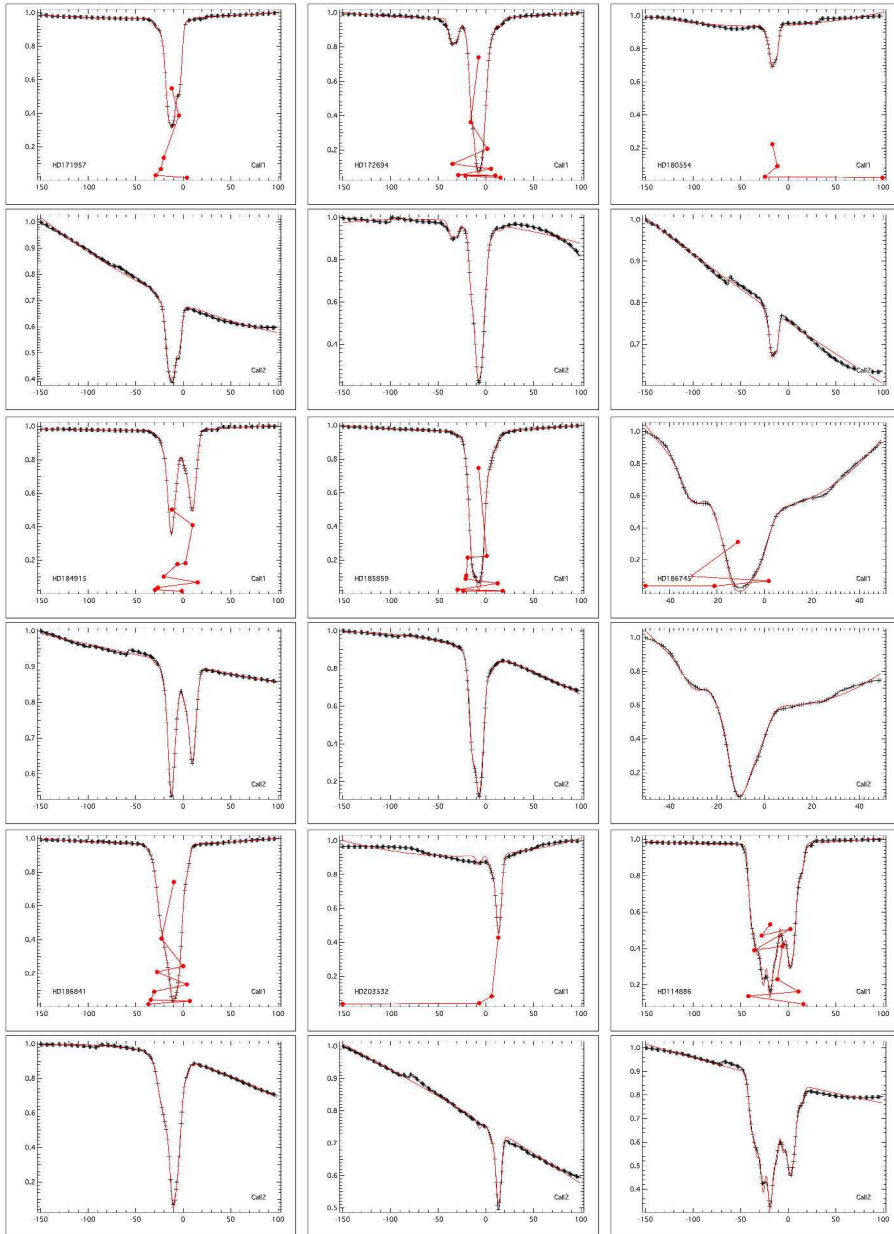


Figure 28 Continued.

Bibliography

- Abolfathi B., Aguado D. S., Aguilar G., Allende Prieto C., Almeida A., Tasnim Ananna T., Anders F., Anderson S. F., Andrews B. H., Anguiano B., al. et.* The Fourteenth Data Release of the Sloan Digital Sky Survey: First Spectroscopic Data from the Extended Baryon Oscillation Spectroscopic Survey and from the Second Phase of the Apache Point Observatory Galactic Evolution Experiment // *ApJS*. IV 2018. 235. 42.
- Ádámkóvics M., Blake G. A., McCall B. J.* Diffuse Interstellar Bands Toward HD 62542 // *ApJ*. VI 2005. 625. 857–863.
- Adams W. S.* Some Results with the COUDÉ Spectrograph of the Mount Wilson Observatory. // *ApJ*. I 1941. 93. 11.
- Adamson A. J., Kerr T. H., Whittet D. C. B., Duley W. W.* A Search for the 13175-A Infrared Diffuse Band in Dense Environments // *MNRAS*. VI 1994. 268. 705.
- Adamson A. J., Whittet D. C. B., Duley W. W.* Diffuse interstellar bands in the Taurus dark clouds // *MNRAS*. IX 1991. 252. 234–245.
- Ahn C. P., Alexandroff R., Allende Prieto C., Anders F., Anderson S. F., Anderton T., Andrews B. H., Aubourg É., Bailey S., Bastien F. A., al. et.* The Tenth Data Release of the Sloan Digital Sky Survey: First Spectroscopic Data from the SDSS-III Apache Point Observatory Galactic Evolution Experiment // *ApJS*. IV 2014. 211. 17.
- Aihara H., Allende Prieto C., An D., Anderson S. F., Aubourg É., Balbinot E., Beers T. C., Berlind A. A., Bickerton S. J., Bizyaev D., Blanton M. R., Bochanski J. J., Bolton A. S., Bovy J., Brandt W. N., Brinkmann J., Brown P. J., Brownstein J. R., Busca N. G., Campbell H., Carr M. A., Chen Y., Chiappini C., Comparat J., Connolly N., Cortes M., Croft R. A. C., Cuesta A. J., da Costa L. N., Davenport J. R. A., Dawson K., Dhital S., Ealet A., Ebelke G. L., Edmondson E. M., Eisenstein D. J., Escoffier S., Esposito M., Evans M. L., Fan X., Femenía Castellá B.,*

- Font-Ribera A., Frinchaboy P. M., Ge J., Gillespie B. A., Gilmore G., González Hernández J. I., Gott J. R., Gould A., Grebel E. K., Gunn J. E., Hamilton J.-C., Harding P., Harris D. W., Hawley S. L., Hearty F. R., Ho S., Hogg D. W., Holtzman J. A., Honscheid K., Inada N., Ivans I. I., Jiang L., Johnson J. A., Jordan C., Jordan W. P., Kazin E. A., Kirkby D., Klaene M. A., Knapp G. R., Kneib J.-P., Kochanek C. S., Koesterke L., Kollmeier J. A., Kron R. G., Lampeitl H., Lang D., Le Goff J.-M., Lee Y. S., Lin Y.-T., Long D. C., Loomis C. P., Lucatello S., Lundgren B., Lupton R. H., Ma Z., MacDonald N., Mahadevan S., Maia M. A. G., Makler M., Malanushenko E., Malanushenko V., Mandelbaum R., Maraston C., Margala D., Masters K. L., McBride C. K., McGehee P. M., McGreer I. D., Ménard B., Miralda-Escudé J., Morrison H. L., Mullally F., Muna D., Munn J. A., Murayama H., Myers A. D., Naugle T., Neto A. F., Nguyen D. C., Nichol R. C., O'Connell R. W., Ogando R. L. C., Olmstead M. D., Oravetz D. J., Padmanabhan N., Palanque-Delabrouille N., Pan K., Pandey P., Pâris I., Percival W. J., Petitjean P., Pfaffenberger R., Pforr J., Phleps S., Pichon C., Pieri M. M., Prada F., Price-Whelan A. M., Raddick M. J., Ramos B. H. F., Reylé C., Rich J., Richards G. T., Rix H.-W., Robin A. C., Rocha-Pinto H. J., Rockosi C. M., Roe N. A., Rollinde E., Ross A. J., Ross N. P., Rossetto B. M., Sánchez A. G., Sayres C., Schlegel D. J., Schlesinger K. J., Schmidt S. J., Schneider D. P., Sheldon E., Shu Y., Simmerer J., Simmons A. E., Sivarani T., Snedden S. A., Sobeck J. S., Steinmetz M., Strauss M. A., Szalay A. S., Tanaka M., Thakar A. R., Thomas D., Tinker J. L., Tofflemire B. M., Tojeiro R., Tremonti C. A., Vandenberg J., Vargas Magaña M., Verde L., Vogt N. P., Wake D. A., Wang J., Weaver B. A., Weinberg D. H., White M., White S. D. M., Yanny B., Yasuda N., Yèche C., Zehavi I. The Eighth Data Release of the Sloan Digital Sky Survey: First Data from SDSS-III // *ApJS*. IV 2011. 193. 29.
- Alam S., Albareti F. D., Allende Prieto C., Anders F., Anderson S. F., Anderton T., Andrews B. H., Armengaud E., Aubourg É., Bailey S., *al. et.* The Eleventh and Twelfth Data Releases of the Sloan Digital Sky Survey: Final Data from SDSS-III // *ApJS*. VII 2015. 219. 12.
- Allamandola L. J., Tielens A. G. G. M., Barker J. R. Polycyclic aromatic hydrocarbons and the unidentified infrared emission bands - Auto exhaust along the Milky Way // *ApJ*. III 1985. 290. L25–L28.
- Alves J. F., Lada C. J., Lada E. A. Internal structure of a cold dark molecular cloud inferred from the extinction of background starlight // *Nature*. I 2001. 409. 159–161.
- Anders F., Queiroz A. B., Chiappini C., Santiago B. X., Fernández-Trincado J. G., Meza A., *the SDSS-IV/APOGEE Collaboration*. The DR14 APOGEE-TGAS catalogue: Precise chemo-kinematics in the extended solar vicinity // *ArXiv e-prints*. VIII 2017.

- Arenou F., Luri X., Babusiaux C., Fabricius C., Helmi A., Muraveva T., Robin A. C., Spoto F., Vallenari A., Antoja T., Cantat-Gaudin T., Jordi C., Leclerc N., Reylé C., Romero-Gómez M., Shih I.-C., Soria S., Barache C., Bossini D., Bragaglia A., Breddels M. A., Fabrizio M., Lambert S., Marrese P. M., Massari D., Moitinho A., Robichon N., Ruiz-Dern L., Sordo R., Veljanoski J., Eyer L., Jasniewicz G., Pancino E., Soubiran C., Spagna A., Tanga P., Turon C., Zurbach C.* Gaia Data Release 2. Catalogue validation // *A&A*. VIII 2018. 616. A17.
- Bacalla X. L., Linnartz H., Cox N. L. J., Cami J., Roueff E., Smoker J. V., Farhang A., Bouwman J., Zhao D.* The EDIBLES survey IV. Cosmic ray ionization rates in diffuse clouds from near-ultraviolet observations of interstellar OH⁺ // *A&A*. 2018.
- Barnard E. E.* On the dark markings of the sky, with a catalogue of 182 such objects. // *ApJ*. I 1919. 49.
- Barnard E. E., Frost E. B., Calvert M. R.* A Photographic Atlas of Selected Regions of the Milky Way. 1927.
- Bergin E. A., Maret S., van der Tak F. F. S., Alves J., Carmody S. M., Lada C. J.* The Thermal Structure of Gas in Prestellar Cores: A Case Study of Barnard 68 // *ApJ*. VII 2006. 645. 369–380.
- Berné O., Cox N. L. J., Mulas G., Joblin C.* Detection of buckminsterfullerene emission in the diffuse interstellar medium // *A&A*. VIII 2017. 605. L1.
- Berné O., Mulas G., Joblin C.* Interstellar C₆₀⁺ // *A&A*. II 2013a. 550. L4.
- Berné O., Mulas G., Joblin C.* Interstellar C₆₀⁺ // *A&A*. II 2013b. 550. L4.
- Berné O., Tielens A. G. G. M.* Formation of buckminsterfullerene (C₆₀) in interstellar space // *Proceedings of the National Academy of Science*. I 2012. 109. 401–406.
- Bertaux J.-L., Lallement R.* Diffuse interstellar bands carriers and cometary organic material² // *MNRAS*. VII 2017. 469. S646–S660.
- Bertaux J. L., Lallement R., Ferron S., Boonne C., Bodichon R.* TAPAS, a web-based service of atmospheric transmission computation for astronomy // *A&A*. IV 2014. 564. A46.
- Bhatt N. H., Cami J.* A Sensitive Spectral Survey of Interstellar Features in the Near-UV [3050-3700 Å] // *ApJS*. II 2015. 216. 22.
- Bok B. J.* Dimensions and Masses of Dark Nebulae // *Harvard Observatory Monographs*. 1948. 7. 53.
- Bondar A., Krętowski J.* A Possible New Sequence of DIBs // *The Diffuse Interstellar Bands*. 297. II 2014. 135–137. (IAU Symposium).

- Bréchignac P., Pino T.* Electronic spectra of cold gas phase PAH cations: Towards the identification of the Diffuse Interstellar Bands carriers // *A&A.* III 1999. 343. L49–L52.
- Burke J. R., Hollenbach D. J.* The gas-grain interaction in the interstellar medium - Thermal accommodation and trapping // *ApJ.* II 1983. 265. 223–234.
- Cami J., Bernard-Salas J., Peeters E., Malek S. E.* Detection of C_{60} and C_{70} in a Young Planetary Nebula // *Science.* IX 2010. 329. 1180.
- Cami J., Cox N. L., Farhang A., Smoker J., Elyajouri M., Lallement R., Bacalla X., Bhatt N. H., Bron E., Cordiner M. A., de Koter A., Ehrenfreund P., Evans C., Foing B. H., Javadi A., Joblin C., Kaper L., Khosroshahi H. G., Laverick M., Le Petit F., Linnartz H., Marshall C. C., Monreal-Ibero A., Mulas G., Roueff E., Royer P., Salama F., Sarre P. J., Smith K. T., Spaans M., van Loon J. T., Wade G.* The ESO Diffuse Interstellar Band Large Exploration Survey (EDIBLES) // *The Messenger.* III 2018. 171. 31–36.
- Cami J., Salama F., Jiménez-Vicente J., Galazutdinov G. A., Krelowski J.* The Rotational Excitation Temperature of the $\lambda 6614$ Diffuse Interstellar Band Carrier // *ApJ.* VIII 2004. 611. L113–L116.
- Cami J., Sonnentrucker P., Ehrenfreund P., Foing B. H.* Diffuse Interstellar Bands in single clouds: new families and constraints on the carriers. // *A&A.* X 1997. 326. 822–830.
- Campbell E. K., Holz M., Gerlich D., Maier J. P.* Laboratory confirmation of C_{60}^+ as the carrier of two diffuse interstellar bands // *Nature.* VII 2015. 523. 322–323.
- Campbell E. K., Holz M., Maier J. P., Gerlich D., Walker G. A. H., Bohlender D.* Gas Phase Absorption Spectroscopy of C_{60} and C_{70} in a Cryogenic Ion Trap: Comparison with Astronomical Measurements // *ApJ.* V 2016a. 822. 17.
- Campbell E. K., Holz M., Maier J. P., Gerlich D., Walker G. A. H., Bohlender D.* Gas Phase Absorption Spectroscopy of C_{60} and C_{70} in a Cryogenic Ion Trap: Comparison with Astronomical Measurements // *ApJ.* V 2016b. 822. 17.
- Campbell E. K., Maier J. P.* Isomeric and Isotopic Effects on the Electronic Spectrum of $\{C\}_{60}^+-He$: Consequences for Astronomical Observations of $\{C\}_{60}^+$ // *ApJ.* V 2018. 858. 36.
- Capitanio L., Lallement R., Vergely J. L., Elyajouri M., Monreal-Ibero A.* Three-dimensional mapping of the local interstellar medium with composite data // *A&A.* X 2017. 606. A65.

- Cardelli J. A., Clayton G. C., Mathis J. S.* The relationship between infrared, optical, and ultraviolet extinction // *ApJ*. X 1989. 345. 245–256.
- Carruthers G. R.* Rocket Observation of Interstellar Molecular Hydrogen // *ApJ*. VIII 1970. 161. L81.
- Casey A. R., Hogg D. W., Ness M., Rix H.-W., Ho A. Q., Gilmore G.* The Cannon 2: A data-driven model of stellar spectra for detailed chemical abundance analyses // *ArXiv e-prints*. III 2016.
- Cernicharo J., Heras A. M., Tielens A. G. G. M., Pardo J. R., Herpin F., Guélin M., Waters L. B. F. M.* Infrared Space Observatory's Discovery of C₄H₂, C₆H₂, and Benzene in CRL 618 // *ApJ*. I 2001. 546. L123–L126.
- Cheung A. C., Rank D. M., Townes C. H., Thornton D. D., Welch W. J.* Detection of NH₃ Molecules in the Interstellar Medium by Their Microwave Emission // *Physical Review Letters*. XII 1968. 21. 1701–1705.
- Cheung A. C., Rank D. M., Townes C. H., Thornton D. D., Welch W. J.* Detection of Water in Interstellar Regions by its Microwave Radiation // *Nature*. II 1969. 221. 626–628.
- Chini R., Wargau W. F.* Abnormal extinction and pre-main sequence stars in M 16 (NGC 6611) // *A&A*. I 1990. 227. 213–219.
- Chojnowski S. D., Whelan D. G., Wisniewski J. P., Majewski S. R., Hall M., Shetrone M., Beaton R., Burton A., Damke G., Eikenberry S., Hasselquist S., Holtzman J. A., Mészáros S., Nidever D., Schneider D. P., 10 J., Zasowski G., Bizyaev D., Brewington H., Brinkmann J., Ebelke G., Frinchaboy P. M., Kinemuchi K., Malanushenko E., Malanushenko V., Marchante M., Oravetz D., Pan K., Simmons A.* High-Resolution H-Band Spectroscopy of Be Stars With SDSS-III/Apogee: I. New Be Stars, Line Identifications, and Line Profiles // *AJ*. I 2015. 149. 7.
- Cirasuolo M., Afonso J., Carollo M., Flores H., Maiolino R., Oliva E., Paltani S., Vanzi L., Evans C., Abreu M., Atkinson D., Babusiaux C., Beard S., Bauer F., Bellazzini M., Bender R., Best P., Bezawada N., Bonifacio P., Bragaglia A., Bryson I., Busher D., Cabral A., Caputi K., Centrone M., Chemla F., Cimatti A., Cioni M.-R., Clementini G., Coelho J., Crnojevic D., Daddi E., Dunlop J., Eales S., Feltzing S., Ferguson A., Fisher M., Fontana A., Fynbo J., Garilli B., Gilmore G., Glauser A., Guinouard I., Hammer F., Hastings P., Hess A., Ivison R., Jagourel P., Jarvis M., Kaper L., Kauffman G., Kitching A. T., Lawrence A., Lee D., Lemasle B., Licausi G., Lilly S., Lorenzetti D., Lunnay D., Maiolino R., Mannucci F., McLure R., Minniti D., Montgomery D., Muschelok B., Nandra K., Navarro R., Norberg P., Oliver S., Origlia L., Padilla N., Peacock J., Pedichini F., Peng J., Pentericci L., Pragt J., Puech M., Randich S., Rees P., Renzini A., Ryde N., Rodrigues M., Roseboom I., Royer F., Saglia R., Sanchez A., Schiavon*

- R., Schnetler H., Sobral D., Speziali R., Sun D., Stuik R., Taylor A., Taylor W., Todd S., Tolstoy E., Torres M., Tosi M., Vanzella E., Venema L., Vitali E., Wegner M., Wells M., Wild V., Wright G., Zamorani G., Zoccali M. MOONS: the Multi-Object Optical and Near-infrared Spectrograph for the VLT // *Ground-based and Airborne Instrumentation for Astronomy V*. 9147. VII 2014. 91470N. (Proc. SPIE).
- Code A. D. A Pre-Discovery Observation of the Diffuse Interstellar Band λ 4430 // *PASP*. VIII 1958. 70. 407–409.
- Cordiner M. A., Cox N. L. J., Evans C. J., Trundle C., Smith K. T., Sarre P. J., Gordon K. D. A Survey of Diffuse Interstellar Bands in the Andromeda Galaxy: Optical Spectroscopy of M31 OB Stars // *ApJ*. I 2011. 726. 39.
- Cordiner M. A., Cox N. L. J., Lallement R., Najarro F., Cami J., Gull T. R., Foing B. H., Linnartz H., Lindler D. J., Proffitt C. R., Sarre P. J., Charnley S. B. Searching for Interstellar $\{\{\rm{C}}\}\}_{60}^{+}$ Using a New Method for High Signal-to-noise HST/STIS Spectroscopy // *ApJ*. VII 2017a. 843. L2.
- Cordiner M. A., Cox N. L. J., Lallement R., Najarro F., Cami J., Gull T. R., Foing B. H., Linnartz H., Lindler D. J., Proffitt C. R., Sarre P. J., Charnley S. B. Searching for Interstellar $\{\{\rm{C}}\}\}_{60}^{+}$ Using a New Method for High Signal-to-noise HST/STIS Spectroscopy // *ApJ*. VII 2017b. 843. L2.
- Cordiner M. A., Cox N. L. J., Trundle C., Evans C. J., Hunter I., Przybilla N., Bresolin F., Salama F. Detection of diffuse interstellar bands in M 31 // *A&A*. III 2008a. 480. L13–L16.
- Cordiner M. A., Fossey S. J., Sarre P. J. Discovery of small-scale-structure in the large molecule/dust distribution in the diffuse ISM // *IAU Symposium*. 235. 2005. 45. (IAU Symposium).
- Cordiner M. A., Fossey S. J., Smith A. M., Sarre P. J. Small-scale Structure of the Interstellar Medium toward ρ Oph Stars: Diffuse Band Observations // *ApJ*. II 2013. 764. L10.
- Cordiner M. A., Smith K. T., Cox N. L. J., Evans C. J., Hunter I., Przybilla N., Bresolin F., Sarre P. J. Diffuse interstellar bands in M 33 // *A&A*. XII 2008b. 492. L5–L8.
- Cox N. L. J., Boudin N., Foing B. H., Schnerr R. S., Kaper L., Neiner C., Henrichs H., Donati J.-F., Ehrenfreund P. Linear and circular polarisation of diffuse interstellar bands // *A&A*. IV 2007a. 465. 899–906.
- Cox N. L. J., Cami J. A Road Map for the Identification of the Diffuse Interstellar Band Carriers // *The Diffuse Interstellar Bands*. 297. II 2014. 412–415. (IAU Symposium).

- Cox N. L. J., Cami J., Farhang A., Smoker J., Monreal-Ibero A., Lallement R., Sarre P. J., Marshall C. C. M., Smith K. T., Evans C. J., Royer P., Linnartz H., Cordiner M. A., Joblin C., van Loon J. T., Foing B. H., Bhatt N. H., Bron E., Elyajouri M., de Koter A., Ehrenfreund P., Javadi A., Kaper L., Khosroshadi H. G., Laverick M., Le Petit F., Mulas G., Roueff E., Salama F., Spaans M. The ESO Diffuse Interstellar Bands Large Exploration Survey (EDIBLES) . I. Project description, survey sample, and quality assessment // *A&A*. X 2017. 606. A76.
- Cox N. L. J., Cami J., Kaper L., Ehrenfreund P., Foing B. H., Ochsendorf B. B., van Hooff S. H. M., Salama F. VLT/X-Shooter survey of near-infrared diffuse interstellar bands // *A&A*. IX 2014. 569. A117.
- Cox N. L. J., Cordiner M. A., Ehrenfreund P., Kaper L., Sarre P. J., Foing B. H., Spaans M., Cami J., Sofia U. J., Clayton G. C., Gordon K. D., Salama F. Interstellar gas, dust and diffuse bands in the SMC // *A&A*. VIII 2007b. 470. 941–955.
- Cox N. L. J., Patat F. Interstellar atoms, molecules and diffuse bands toward SN2006X in M 100 // *A&A*. VII 2008. 485. L9–L12.
- Cox N. L. J., Spaans M. The effects of metallicity, radiation field and dust extinction on the charge state of PAHs in diffuse clouds: implications for the DIB carrier // *A&A*. VI 2006. 451. 973–980.
- Crawford M. K., Tielens A. G. G. M., Allamandola L. J. Ionized polycyclic aromatic hydrocarbons and the diffuse interstellar bands // *ApJ*. VI 1985. 293. L45–L48.
- Dame T. M., Hartmann D., Thaddeus P. The Milky Way in Molecular Clouds: A New Complete CO Survey // *ApJ*. II 2001. 547. 792–813.
- Davies R. I., Agudo Berbel A., Wiezorrek E., Cirasuolo M., Förster Schreiber N. M., Jung Y., Muschelok B., Ott T., Ramsay S., Schlichter J., Sharples R., Wegner M. The Software Package for Astronomical Reductions with KMOS: SPARK // *A&A*. X 2013. 558. A56.
- Desert F. X., Boulanger F., Leger A., Puget J. L., Sellgren K. Nature of very small grains - PAH molecules or silicates? // *A&A*. IV 1986. 159. 328–330.
- Desert F.-X., Jenniskens P., Dennefeld M. Diffuse interstellar bands and UV extinction curves. The missing link. // *A&A*. XI 1995. 303. 223.
- Díaz-Luis J. J., García-Hernández D. A., Kameswara Rao N., Manchado A., Cataldo F. A search for diffuse bands in fullerene planetary nebulae: evidence of diffuse circumstellar bands // *A&A*. I 2015. 573. A97.
- Douglas A. E., Herzberg G. Note on CH⁺ in Interstellar Space and in the Laboratory. // *ApJ*. IX 1941. 94. 381.

- Draine B. T.* Physics of the Interstellar and Intergalactic Medium. 2011.
- Duley W. W., Kuzmin S.* Vibronic Progressions in Several Diffuse Interstellar Bands // *ApJ*. IV 2010. 712. L165–L168.
- Duley W. W., Williams D. A.* The infrared spectrum of interstellar dust - Surface functional groups on carbon // *MNRAS*. VII 1981. 196. 269–274.
- Dunham T.* Interstellar Neutral Potassium and Neutral Calcium // *Publications of the Astronomical Society of the Pacific*. 1937. 49, 287. 26.
- Eddington A. S.* Bakerian Lecture. Diffuse Matter in Interstellar Space // *Proceedings of the Royal Society of London Series A*. VII 1926. 111. 424–456.
- Ehrenfreund P., Cami J., Jiménez-Vicente J., Foing B. H., Kaper L., van der Meer A., Cox N., D'Hendecourt L., Maier J. P., Salama F., Sarre P. J., Snow T. P., Sonnentrucker P.* Detection of Diffuse Interstellar Bands in the Magellanic Clouds // *ApJl*. IX 2002. 576. L117–L120.
- Ehrenfreund P., Foing B. H.* Resolved profiles of diffuse interstellar bands: evidence for rotational contours of gas phase molecules. // *A&A*. III 1996. 307. L25–L28.
- Ehrenfreund P., Jenniskens P.* The Environment Dependence of Diffuse Interstellar Bands // *The Diffuse Interstellar Bands*. 202. 1995. 105. (Astrophysics and Space Science Library).
- Ehrenfreund Pascale, Foing Bernard H.* Fullerenes and Cosmic Carbon // *Science*. 2010. 329, 5996. 1159–1160.
- Eisenstein D. J., Weinberg D. H., Agol E., Aihara H., Allende Prieto C., Anderson S. F., Arns J. A., Aubourg É., Bailey S., Balbinot E., al. et.* SDSS-III: Massive Spectroscopic Surveys of the Distant Universe, the Milky Way, and Extra-Solar Planetary Systems // *AJ*. IX 2011. 142. 72.
- Elyajouri M., Cox N. L. J., Lallement R.* The 15 273 Å diffuse interstellar band in the dark cloud Barnard 68 // *A&A*. IX 2017. 605. L10.
- Elyajouri M., Monreal-Ibero A., Remy Q., Lallement R.* A Catalog of 1.5273 um Diffuse Interstellar Bands Based on APOGEE Hot Telluric Calibrators // *ApJS*. VIII 2016. 225. 19.
- Ensor T., Cami J., Bhatt N. H., Soddu A.* A Principal Component Analysis of the Diffuse Interstellar Bands // *ApJ*. II 2017a. 836. 162.
- Ensor T., Cami J., Bhatt N. H., Soddu A.* A Principal Component Analysis of the Diffuse Interstellar Bands // *ApJ*. II 2017b. 836. 162.

- Ewen H. I., Purcell E. M.* Observation of a Line in the Galactic Radio Spectrum: Radiation from Galactic Hydrogen at 1,420 Mc./sec. // *Nature*. IX 1951. 168. 356.
- Fan H., Welty D. E., York D. G., Sonnentrucker P., Dahlstrom J. A., Baskes N., Friedman S. D., Hobbs L. M., Jiang Z., Rachford B., Snow T. P., Sherman R., Zhao G.* The Behavior of Selected Diffuse Interstellar Bands with Molecular Fraction in Diffuse Atomic and Molecular Clouds // *ApJ*. XII 2017. 850. 194.
- Ferrière K. M.* The interstellar environment of our galaxy // *Reviews of Modern Physics*. X 2001. 73. 1031–1066.
- Fitzpatrick E. L., Massa D.* An analysis of the shapes of ultraviolet extinction curves. III - an atlas of ultraviolet extinction curves // *ApJS*. I 1990. 72. 163–189.
- Fitzpatrick E. L., Massa D.* An Analysis of the Shapes of Interstellar Extinction Curves. V. The IR-through-UV Curve Morphology // *ApJ*. VII 2007. 663. 320–341.
- Foing B. H., Ehrenfreund P.* Detection of two interstellar absorption bands coincident with spectral features of C_{60}^+ // *Nature*. V 1994. 369. 296–298.
- Foing B. H., Ehrenfreund P.* New evidences for interstellar $C_{60}^+ \hat{+} \hat{+}$. // *A&A*. I 1997. 317. L59–L62.
- Friedman S. D., York D. G., McCall B. J., Dahlstrom J., Sonnentrucker P., Welty D. E., Drosback M. M., Hobbs L. M., Rachford B. L., Snow T. P.* Studies of Diffuse Interstellar Bands V. Pairwise Correlations of Eight Strong DIBs and Neutral Hydrogen, Molecular Hydrogen, and Color Excess // *ApJ*. I 2011. 727. 33.
- Fulara J., Lessen D., Freivogel P., Maier J. P.* Laboratory evidence for highly unsaturated hydrocarbons as carriers of some of the diffuse interstellar bands // *Nature*. XII 1993. 366. 439–441.
- Gaia Collaboration, Brown A. G. A., Vallenari A., Prusti T., de Bruijne J. H. J., Mignard F., Drimmel R., Babusiaux C., Bailer-Jones C. A. L., Bastian U., et.* Gaia Data Release 1. Summary of the astrometric, photometric, and survey properties // *A&A*. XI 2016. 595. A2.
- Galazutdinov G., Stachowska W., Musaeov F., Moutou C., Lo Curto G., Krelowski J.* Fine structure of profiles of weak diffuse interstellar bands // *A&A*. XII 2002. 396. 987–991.

- Galazutdinov G. A., Gnaciński P., Han I., Lee B.-C., Kim K.-M., Krelowski J.* On the diffuse bands related to the C₂ interstellar molecule // *A&A*. II 2006. 447. 589–595.
- Galazutdinov G. A., Krelowski J.* Looking for the Weak Members of the C_{60}^+ Family in the Interstellar Medium // *Acta Astron.* VI 2017. 67. 159–169.
- Galazutdinov G. A., LoCurto G., Krelowski J.* High-Resolution Profiles of Diffuse Interstellar Bands // *ApJ*. VIII 2008. 682. 1076–1086.
- Galazutdinov G. A., Musaev F. A., Krelowski J., Walker G. A. H.* Narrow Diffuse Interstellar Bands: A Survey with Precise Wavelengths // *PASP*. V 2000. 112. 648–690.
- Galazutdinov G. A., Shimansky V. V., Bondar A., Valyavin G., Krelowski J.* C₆₀⁺ - looking for the bucky-ball in interstellar space // *MNRAS*. III 2017. 465. 3956–3964.
- García-Hernández D. A., Manchado A., García-Lario P., Stanghellini L., Villaver E., Shaw R. A., Szczerba R., Perea-Calderón J. V.* Formation of Fullerenes in H-containing Planetary Nebulae // *ApJ*. XI 2010. 724. L39–L43.
- García Pérez A. E., Allende Prieto C., Holtzman J. A., Shetrone M., Mészáros S., Bizyaev D., Carrera R., Cunha K., García-Hernández D. A., Johnson J. A., Majewski S. R., Nidever D. L., Schiavon R. P., Shane N., Smith V. V., Sobek J., Troup N., Zamora O., Bovy J., Eisenstein D. J., Feuillet D., Frinchaboy P. M., Hayden M. R., Hearty F. R., Nguyen D. C., O’Connell R. W., Pinsonneault M. H., Weinberg D. H., Wilson J. C., Zasowski G.* ASPCAP: The Apogee Stellar Parameter and Chemical Abundances Pipeline // *ArXiv e-prints*. X 2015.
- García Pérez A. E., Allende Prieto C., Holtzman J. A., Shetrone M., Mészáros S., Bizyaev D., Carrera R., Cunha K., García-Hernández D. A., Johnson J. A., Majewski S. R., Nidever D. L., Schiavon R. P., Shane N., Smith V. V., Sobek J., Troup N., Zamora O., Weinberg D. H., Bovy J., Eisenstein D. J., Feuillet D., Frinchaboy P. M., Hayden M. R., Hearty F. R., Nguyen D. C., O’Connell R. W., Pinsonneault M. H., Wilson J. C., Zasowski G.* ASPCAP: The APOGEE Stellar Parameter and Chemical Abundances Pipeline // *AJ*. VI 2016a. 151. 144.
- García Pérez A. E., Allende Prieto C., Holtzman J. A., Shetrone M., Mészáros S., Bizyaev D., Carrera R., Cunha K., García-Hernández D. A., Johnson J. A., Majewski S. R., Nidever D. L., Schiavon R. P., Shane N., Smith V. V., Sobek J., Troup N., Zamora O., Weinberg D. H., Bovy J., Eisenstein D. J., Feuillet D., Frinchaboy P. M., Hayden M. R., Hearty F. R., Nguyen D. C., O’Connell R. W., Pinsonneault M. H., Wilson J. C., Zasowski G.* ASPCAP: The APOGEE Stellar Parameter and Chemical Abundances Pipeline // *AJ*. VI 2016b. 151. 144.

- Geballe T. R., Najarro F., Figer D. F., Schlegelmilch B. W., de La Fuente D. Infrared diffuse interstellar bands in the Galactic Centre region // *Nature*. XI 2011. 479. 200–202.
- Gillett F. C., Forrest W. J., Merrill K. M. 8 - 13-micron spectra of NGC 7027, BD +30 3639, and NGC 6572. // *ApJ*. VII 1973. 183. 87–93.
- Gordon I. E., Rothman L. S., Hill C., Kochanov R. V., Tan Y., Bernath P. F., Birk M., Boudon V., Campargue A., Chance K. V., Drouin B. J., Flaud J.-M., Gamache R. R., Hodges J. T., Jacquemart D., Perevalov V. I., Perrin A., Shine K. P., Smith M.-A. H., Tennyson J., Toon G. C., Tran H., Tyuterev V. G., Barbe A., Császár A. G., Devi V. M., Furtenbacher T., Harrison J. J., Hartmann J.-M., Jolly A., Johnson T. J., Karman T., Kleiner I., Kyuberis A. A., Loos J., Lyulin O. M., Massie S. T., Mikhailenko S. N., Moazzen-Ahmadi N., Müller H. S. P., Naumenko O. V., Nikitin A. V., Polyansky O. L., Rey M., Rotger M., Sharpe S. W., Sung K., Starikova E., Tashkun S. A., Auwera J. V., Wagner G., Wilzewski J., Wcisło P., Yu S., Zak E. J. The HITRAN2016 molecular spectroscopic database // *J. Quant. Spec. Radiat. Transf.*. XII 2017. 203. 3–69.
- Gredel R., Carpentier Y., Rouillé G., Steglich M., Huisken F., Henning T. Abundances of PAHs in the ISM: confronting observations with experimental results // *A&A*. VI 2011. 530. A26.
- Green G. M., Schlafly E. F., Finkbeiner D. P., Rix H.-W., Martin N., Burgett W., Draper P. W., Flewelling H., Hodapp K., Kaiser N., Kudritzki R. P., Magnier E., Metcalfe N., Price P., Tonry J., Wainscoat R. A Three-dimensional Map of Milky Way Dust // *ApJ*. IX 2015. 810. 25.
- Gudennavar S. B., Bubbly S. G., Preethi K., Murthy J. A Compilation of Interstellar Column Densities // *ApJS*. III 2012. 199. 8.
- Gunn J. E., Siegmund W. A., Mannery E. J., Owen R. E., Hull C. L., Leger R. F., Carey L. N., Knapp G. R., York D. G., Boroski W. N., Kent S. M., Lupton R. H., Rockosi C. M., Evans M. L., Waddell P., Anderson J. E., Annis J., Barentine J. C., Bartoszek L. M., Bastian S., Bracker S. B., Brewington H. J., Briegel C. I., Brinkmann J., Brown Y. J., Carr M. A., Czarapata P. C., Drennan C. C., Dombeck T., Federwitz G. R., Gillespie B. A., Gonzales C., Hansen S. U., Harvanek M., Hayes J., Jordan W., Kinney E., Klaene M., Kleinman S. J., Kron R. G., Kresinski J., Lee G., Limmongkol S., Lindenmeyer C. W., Long D. C., Loomis C. L., McGehee P. M., Mantsch P. M., Neilsen E. H. Jr., Neswold R. M., Newman P. R., Nitta A., Peoples J. Jr., Pier J. R., Prieto P. S., Protopopou A., Rivetta C., Schneider D. P., Snedden S., Wang S.-i. The 2.5 m Telescope of the Sloan Digital Sky Survey // *AJ*. IV 2006. 131. 2332–2359.
- Hall J. S. Observations of the Polarized Light from Stars // *Science*. II 1949. 109. 166–167.

- Hamano S., Kobayashi N., Kondo S., Ikeda Y., Nakanishi K., Yasui C., Mizumoto M., Matsunaga N., Fukue K., Mito H., Yamamoto R., Izumi N., Nakaoka T., Kawanishi T., Kitano A., Otsubo S., Kinoshita M., Kobayashi H., Kawakita H.* Near-infrared Diffuse Interstellar Bands in 0.91-1.32 μm // *ApJ*. II 2015. 800. 137.
- Hamano S., Kobayashi N., Kondo S., Sameshima H., Nakanishi K., Ikeda Y., Yasui C., Mizumoto M., Matsunaga N., Fukue K., Yamamoto R., Izumi N., Mito H., Nakaoka T., Kawanishi T., Kitano A., Otsubo S., Kinoshita M., Kawakita H.* Near Infrared Diffuse Interstellar Bands Toward the Cygnus OB2 Association // *ApJ*. IV 2016. 821. 42.
- Hartmann J.* Investigations on the spectrum and orbit of delta Orionis. // *ApJ*. V 1904. 19.
- Heckman T. M., Lehnert M. D.* The Detection of the Diffuse Interstellar Bands in Dusty Starburst Galaxies // *ApJ*. VII 2000. 537. 690–696.
- Heger M. L.* Stationary Sodium Lines in Spectroscopic Binaries // *PASP*. XII 1919. 31. 304–305.
- Heger M. L.* Further study of the sodium lines in class B stars // *Lick Observatory Bulletin*. 1922. 10. 141–145.
- Herbig G. H.* The diffuse interstellar bands. IV - The region 4400-6850 A // *ApJ*. II 1975. 196. 129–160.
- Herbig G. H.* The diffuse interstellar bands. VI - New features near 6800 A // *ApJ*. VIII 1988. 331. 999–1003.
- Herbig G. H.* The diffuse interstellar bands. IX - Constraints on the identification // *ApJ*. IV 1993a. 407. 142–156.
- Herbig G. H.* The diffuse interstellar bands. IX - Constraints on the identification // *ApJ*. IV 1993b. 407. 142–156.
- Herbig G. H.* The Diffuse Interstellar Bands // *ARA&A*. 1995. 33. 19–74.
- Herbst E., Klemperer W.* The Formation and Depletion of Molecules in Dense Interstellar Clouds // *ApJ*. X 1973. 185. 505–534.
- Herschel W.* On the Construction of the Heavens. // *Philosophical Transactions of the Royal Society of London Series I*. 1785. 75. 213–266.
- Hiltner W. A.* Polarization of Radiation from Distant Stars by the Interstellar Medium // *Nature*. II 1949. 163. 283.

- Hobbs L. M., York D. G., Snow T. P., Oka T., Thorburn J. A., Bishof M., Friedman S. D., McCall B. J., Rachford B., Sonnentrucker P., Welty D. E. A Catalog of Diffuse Interstellar Bands in the Spectrum of HD 204827 // *ApJ*. VI 2008. 680. 1256–1270.
- Hobbs L. M., York D. G., Thorburn J. A., Snow T. P., Bishof M., Friedman S. D., McCall B. J., Oka T., Rachford B., Sonnentrucker P., Welty D. E. Studies of the Diffuse Interstellar Bands. III. HD 183143 // *ApJ*. XI 2009. 705. 32–45.
- Holtzman J. A., Shetrone M., Johnson J. A., Allende Prieto C., Anders F., Andrews B., Beers T. C., Bizyaev D., Blanton M. R., Bovy J., Carrera R., Chojnowski S. D., Cunha K., Eisenstein D. J., Feuillet D., Frinchaboy P. M., Galbraith-Frew J., García Pérez A. E., García-Hernández D. A., Hasselquist S., Hayden M. R., Hearty F. R., Ivans I., Majewski S. R., Martell S., Meszaros S., Muna D., Nidever D., Nguyen D. C., OConnell R. W., Pan K., Pinsonneault M., Robin A. C., Schiavon R. P., Shane N., Sobeck J., Smith V. V., Troup N., Weinberg D. H., Wilson J. C., Wood-Vasey W. M., Zamora O., Zasowski G. Abundances, Stellar Parameters, and Spectra from the SDSS-III/APOGEE Survey // *AJ*. XI 2015. 150. 148.
- Huang J., Oka T. Constraining the size of the carrier of the $\lambda 5797.1$ diffuse interstellar band // *Molecular Physics*. VIII 2015. 113. 2159–2168.
- Ingalls J. G., Bania T. M., Boulanger F., Draine B. T., Falgarone E., Hily-Blant P. Spitzer Infrared Spectrograph Detection of Molecular Hydrogen Rotational Emission towards Translucent Clouds // *ApJ*. XII 2011. 743. 174.
- Jansky K. G. Radio Waves from Outside the Solar System // *Nature*. VII 1933. 132. 66.
- Jenkins E. B. A Unified Representation of Gas-Phase Element Depletions in the Interstellar Medium // *ApJ*. VIII 2009. 700. 1299–1348.
- Jenniskens P., Desert F. X. Complex Structure in Two Diffuse Interstellar Bands // *A&A*. VII 1993. 274. 465.
- Jenniskens P., Desert F.-X. A survey of diffuse interstellar bands (3800–8680 Å) // *A&As*. VII 1994. 106.
- Jenniskens P., Mulas G., Porceddu I., Benvenuti P. Diffuse interstellar bands near 9600Å: not due to C60plus yet. // *A&A*. XI 1997. 327. 337–341.
- Joblin C., Cernicharo J. Detecting the building blocks of aromatics // *Science*. I 2018. 359. 156–157.
- Joblin C., D’Hendecourt L., Leger A., Maillard J. P. Detection of diffuse interstellar bands in the infrared // *Nature*. VIII 1990. 346. 729–731.

- Joblin C., Leger A., Martin P.* Contribution of polycyclic aromatic hydrocarbon molecules to the interstellar extinction curve // *ApJ*. VII 1992. 393. L79–L82.
- Joblin C., Maillard J. P., de Peslouan P., Vauglin I., Pech C., Boissel P.* Probing the connection between PAHs and hydrogen (H, H₂) in the interstellar medium and in the laboratory // *H₂ in Space*. 1999. 16.
- Joblin C., Tielens A. G. G. M.* PAHs and the Universe: A Symposium to Celebrate the 25th Anniversary of the PAH Hypothesis. 46. VI 2011. (EAS Publications Series).
- Jones A. P.* Dust evolution, a global view: II. Top-down branching, nanoparticle fragmentation and the mystery of the diffuse interstellar band carriers // *Royal Society Open Science*. XII 2016. 3. 160223.
- Kalberla P. M. W., Burton W. B., Hartmann D., Arnal E. M., Bajaja E., Morras R., Pöppel W. G. L.* The Leiden/Argentine/Bonn (LAB) Survey of Galactic HI. Final data release of the combined LDS and IAR surveys with improved stray-radiation corrections // *A&A*. IX 2005. 440. 775–782.
- Kaźmierczak M., Gnaciński P., Schmidt M. R., Galazutdinov G., Bondar A., Krelowski J.* Excitation temperature of C₂ and broadening of the 6196 Å diffuse interstellar band // *A&A*. V 2009. 498. 785–791.
- Kaźmierczak M., Schmidt M., Weselak T., Galazutdinov G., Krelowski J.* C₂ and Diffuse Interstellar Bands // *The Diffuse Interstellar Bands*. 297. II 2014. 121–124. (IAU Symposium).
- Kaźmierczak M., Schmidt M. R., Bondar A., Krelowski J.* Abundances and rotational temperatures of the C₂ interstellar molecule towards six reddened early-type stars // *MNRAS*. III 2010a. 402. 2548–2558.
- Kaźmierczak M., Schmidt M. R., Galazutdinov G. A., Musaev F. A., Betelesky Y., Krelowski J.* Centrosymmetric molecules as possible carriers of diffuse interstellar bands // *MNRAS*. XI 2010b. 408. 1590–1597.
- Kos J., Zwitter T., Wyse R., Bienaymé O., Binney J., Bland-Hawthorn J., Freeman K., Gibson B. K., Gilmore G., Grebel E. K., Helmi A., Kordopatis G., Munari U., Navarro J., Parker Q., Reid W. A., Seabroke G., Sharma S., Siebert A., Siviero A., Steinmetz M., Watson F. G., Williams M. E. K.* Pseudo-three-dimensional maps of the diffuse interstellar band at 862 nm // *Science*. VIII 2014. 345. 791–795.
- Krelowski J., Schmidt M.* Intrinsic Profiles of Strong Diffuse Interstellar Bands // *ApJ*. III 1997. 477. 209–217.

- Krelowski J., Schmidt M., Snow T. P.* Groupings of Strong and Weak Diffuse Interstellar Bands Formed by Common Carriers // *PASP*. X 1997. 109. 1135–1144.
- Krelowski J., Snow T. P., Seab C. G., Papaj J.* Spatial correlation between CH, CN and the diffuse interstellar band carriers // *MNRAS*. X 1992. 258. 693–696.
- Krelowski J., Walker G. A. H.* Three families of diffuse interstellar bands? // *ApJ*. I 1987. 312. 860–867.
- Krelowski J., Westerlund B. E.* High-resolution profiles of diffuse interstellar bands as functions of the structure of the interstellar medium // *A&A*. I 1988. 190. 339–341.
- Kroto H. W., Heath J. R., O'Brien S. C., Curl R. F., Smalley R. E.* C(60): Buckminsterfullerene // *Nature*. XI 1985. 318. 162.
- Kuhn M., Renzler M., Postler J., Ralser S., Spieler S., Simpson M., Linnartz H., Tielens A. G. G. M., Cami J., Mauracher A., Wang Y., Alcamí M., Martín F., Beyer M. K., Wester R., Lindinger A., Scheier P.* Atomically resolved phase transition of fullerene cations solvated in helium droplets // *Nature Communications*. XI 2016. 7. 13550.
- Kwok Sun, Zhang Yong.* Unidentified Infrared Emission Bands: PAHs or MAONs? // *The Astrophysical Journal*. 2013. 771, 1. 5.
- Lallement R., Babusiaux C., Vergely J. L., Katz D., Arenou F., Valette B., Hottier C., Capitanio L.* Gaia-2MASS 3D maps of Galactic interstellar dust within 3 kpc // *arXiv e-prints*. II 2019.
- Lallement R., Capitanio L., Ruiz-Dern L., Danielski C., Babusiaux C., Vergely L., Elyajouri M., Arenou F., Leclerc N.* Three-dimensional maps of interstellar dust in the Local Arm: using Gaia, 2MASS, and APOGEE-DR14 // *A&A*. IX 2018a. 616. A132.
- Lallement R., Cox N. L. J., Cami J., Smoker J., Fahrang A., Elyajouri M., Cordiner M. A., Linnartz H., Smith K. T., Ehrenfreund P., Foing B. H.* The EDIBLES survey II. The detectability of C₆₀⁺ bands // *A&A*. VI 2018b. 614. A28.
- Lallement R., Vergely J.-L., Valette B., Puspitarini L., Eyer L., Casagrande L.* 3D maps of the local ISM from inversion of individual color excess measurements // *A&A*. I 2014. 561. A91.
- Lan T.-W., Ménard B., Zhu G.* Exploring the diffuse interstellar bands with the Sloan Digital Sky Survey // *MNRAS*. X 2015. 452. 3629–3649.

- Lefèvre C., Pagani L., Juvela M., Paladini R., Lallement R., Marshall D. J., Andersen M., Bacmann A., McGehee P. M., Montier L., Noriega-Crespo A., Pelkonen V.-M., Ristorcelli I., Steinacker J. Dust properties inside molecular clouds from coreshine modeling and observations // *A&A*. XII 2014. 572. A20.
- Leger A., D'Hendecourt L. Are polycyclic aromatic hydrocarbons the carriers of the diffuse interstellar bands in the visible? // *A&A*. V 1985. 146. 81–85.
- Leger A., Puget J. L. Identification of the 'unidentified' IR emission features of interstellar dust? // *A&A*. VIII 1984. 137. L5–L8.
- Liszt H., Lucas R. The structure and stability of interstellar molecular absorption line profiles at radio frequencies // *A&A*. III 2000. 355. 333–346.
- Maier J. P. Interstellar detection of C_{60}^+ // *Nature*. VIII 1994. 370. 423–424.
- Maier J. P., Walker G. A. H., Bohlender D. A. On the Possible Role of Carbon Chains as Carriers of Diffuse Interstellar Bands // *ApJ*. II 2004. 602. 286–290.
- Maíz Apellániz J., Barbá R. H., Sota A., Simón-Díaz S. The little-studied cluster Berkeley 90. II. The foreground ISM // *A&A*. XI 2015. 583. A132.
- Majewski S. R. APOGEE – SDSS-III's Other Milky Way Experiment // American Astronomical Society Meeting Abstracts #219. 219. I 2012. 205.06. (American Astronomical Society Meeting Abstracts).
- Majewski S. R., Schiavon R. P., Frinchaboy P. M., Allende Prieto C., Barkhouser R., Bizyaev D., Blank B., Brunner S., Burton A., Carrera R., Chojnowski S. D., Cunha K., Epstein C., Fitzgerald G., García Pérez A. E., Harty F. R., Henderson C., Holtzman J. A., Johnson J. A., Lam C. R., Lawler J. E., Maseman P., Mészáros S., Nelson M., Nguyen D. C., Nidever D. L., Pinsonneault M., Shetrone M., Smee S., Smith V. V., Stolberg T., Skrutskie M. F., Walker E., Wilson J. C., Zasowski G., Anders F., Basu S., Beland S., Blanton M. R., Bovy J., Brownstein J. R., Carlberg J., Chaplin W., Chiappini C., Eisenstein D. J., Elsworth Y., Feuillet D., Fleming S. W., Galbraith-Frew J., García R. A., García-Hernández D. A., Gillespie B. A., Girardi L., Gunn J. E., Hasselquist S., Hayden M. R., Hekker S., Ivans I., Kinemuchi K., Klaene M., Mahadevan S., Mathur S., Mosser B., Muna D., Munn J. A., Nichol R. C., O'Connell R. W., Parejko J. K., Robin A. C., Rocha-Pinto H., Schultheis M., Serenelli A. M., Shane N., Silva Aguirre V., Sobek J. S., Thompson B., Troup N. W., Weinberg D. H., Zamora O. The Apache Point Observatory Galactic Evolution Experiment (APOGEE) // *AJ*. IX 2017. 154. 94.
- McCall B. J., Drosback M. M., Thorburn J. A., York D. G., Friedman S. D., Hobbs L. M., Rachford B. L., Snow T. P., Sonnentrucker P., Welty D. E. Studies of

- the Diffuse Interstellar Bands. IV. The Nearly Perfect Correlation Between $\lambda\lambda 6196.0$ and 6613.6 // *ApJ*. I 2010. 708. 1628–1638.
- McCall B. J., Griffin R. E.* On the discovery of the diffuse interstellar bands // *Proceedings of the royal society A*. 469. IX 2013. 20120604. (Proceedings of the royal society A).
- McGuire B. A., Burkhardt A. M., Kalenskii S., Shingledecker C. N., Remijan A. J., Herbst E., McCarthy M. C.* Detection of the aromatic molecule benzonitrile ($c\text{-C}_6\text{H}_5\text{CN}$) in the interstellar medium // *Science*. I 2018. 359. 202–205.
- McKee C. F., Ostriker J. P.* A theory of the interstellar medium - Three components regulated by supernova explosions in an inhomogeneous substrate // *ApJ*. XI 1977. 218. 148–169.
- McKellar A.* Wave Lengths of the CH Band Lines // *PASP*. X 1940. 52. 312.
- Merrill P. W.* Unidentified Interstellar Lines // *PASP*. VIII 1934. 46. 206–207.
- Merrill P. W.* Stationary Lines in the Spectrum of the Binary Star Boss 6142 // *ApJ*. III 1936. 83. 126.
- Merrill P. W., Wilson O. C.* Unidentified Interstellar Lines in the Yellow and Red // *ApJ*. I 1938. 87. 9.
- Mészáros S., Allende Prieto C., Edvardsson B., Castelli F., García Pérez A. E., Gustafsson B., Majewski S. R., Plez B., Schiavon R., Shetrone M., de Vicente A.* New ATLAS9 and MARCS Model Atmosphere Grids for the Apache Point Observatory Galactic Evolution Experiment (APOGEE) // *AJ*. X 2012. 144. 120.
- Meyer D. M., Ulrich R. K.* Observations of diffuse interstellar bands toward T Tauri stars // *ApJ*. VIII 1984. 283. 98–105.
- Misawa T., Gandhi P., Hida A., Tamagawa T., Yamaguchi T.* Identification of New Near-Infrared Diffuse Interstellar Bands in the Orion Nebula // *ApJ*. VIII 2009. 700. 1988–1993.
- Monreal-Ibero A., Weilbacher P. M., Wendt M., Selman F., Lallement R., Brinchmann J., Kamann S., Sandin C.* Towards DIB mapping in galaxies beyond 100 Mpc. A radial profile of the $\lambda 5780.5$ diffuse interstellar band in AM 1353-272 B // *A&A*. IV 2015. 576. L3.
- Motylewski T., Linnartz H., Vaizert O., Maier J. P., Galazutdinov G. A., Musaev F. A., Krelowski J., Walker G. A. H., Bohlender D. A.* Gas-Phase Electronic Spectra of Carbon-Chain Radicals Compared with Diffuse Interstellar Band Observations // *ApJ*. III 2000. 531. 312–320.

- Moutou C., Krelowski J., D'Hendecourt L., Jamroszczak J. On correlations between diffuse interstellar bands // *A&A*. XI 1999. 351. 680–688.
- Ness M., Hogg D. W., Rix H.-W., Ho A. Y. Q., Zasowski G. The Cannon: A data-driven approach to Stellar Label Determination // *ApJ*. VII 2015. 808. 16.
- Nidever D. L., Holtzman J. A., Allende Prieto C., Beland S., Bender C., Bizyaev D., Burton A., Desphande R., Fleming S. W., García Pérez A. E., Hearty F. R., Majewski S. R., Mészáros S., Muna D., Nguyen D., Schiavon R. P., Shetrone M., Skrutskie M. E., Sobeck J. S., Wilson J. C. The Data Reduction Pipeline for the Apache Point Observatory Galactic Evolution Experiment // *AJ*. XII 2015. 150. 173.
- Nielbock M., Launhardt R., Steinacker J., Stutz A. M., Balog Z., Beuther H., Bouwman J., Henning T., Hily-Blant P., Kainulainen J., Krause O., Linz H., Lippok N., Ragan S., Risacher C., Schmiedeke A. The Earliest Phases of Star formation (EPoS) observed with Herschel: the dust temperature and density distributions of B68 // *A&A*. XI 2012. 547. A11.
- Peeters E., Hony S., Van Kerckhoven C., Tielens A. G. G. M., Allamandola L. J., Hudgins D. M., Bauschlicher C. W. The rich 6 to 9 μm spectrum of interstellar PAHs // *A&A*. VIII 2002. 390. 1089–1113.
- Perryman M. A. C., Lindegren L., Kovalevsky J., Hoeg E., Bastian U., Bernacca P. L., Crézé M., Donati F., Grenon M., Grewing M., van Leeuwen F., van der Marel H., Mignard F., Murray C. A., Le Poole R. S., Schrijver H., Turon C., Arenou F., Froeschlé M., Petersen C. S. The HIPPARCOS Catalogue // *A&A*. VII 1997. 323.
- Phillips M. M., Simon J. D., Morrell N., Burns C. R., Cox N. L. J., Foley R. J., Karakas A. I., Patat F., Sternberg A., Williams R. E., Gal-Yam A., Hsiao E. Y., Leonard D. C., Persson S. E., Stritzinger M., Thompson I. B., Campillay A., Contreras C., Folatelli G., Freedman W. L., Hamuy M., Roth M., Shields G. A., Suntzeff N. B., Chomiuk L., Ivans I. I., Madore B. F., Penprase B. E., Perley D., Pignata G., Preston G., Soderberg A. M. On the Source of the Dust Extinction in Type Ia Supernovae and the Discovery of Anomalously Strong Na I Absorption // *ApJ*. XII 2013. 779. 38.
- Planck , Fermi Collaborations , Ade P. A. R., Aghanim N., Aniano G., Arnaud M., Ashdown M., Aumont J., Baccigalupi C., Banday A. J., Barreiro R. B., Bartolo N., Battaner E., Benabed K., Benoit-Lévy A., Bernard J.-P., Bersanelli M., Bielewicz P., Bonaldi A., Bonavera L., Bond J. R., Borrill J., Bouchet F. R., Boulanger F., Burigana C., Butler R. C., Calabrese E., Cardoso J.-F., Casandjian J. M., Catalano A., Chamballu A., Chiang H. C., Christensen P. R., Colombo L. P. L., Combet C., Couchot F., Crill B. P., Curto A., Cuttaia F., Danese L., Davies R. D., Davis R. J.,

- de Bernardis P., de Rosa A., de Zotti G., Delabrouille J., Désert F.-X., Dickinson C., Diego J. M., Digel S. W., Dole H., Donzelli S., Doré O., Douspis M., Ducout A., Dupac X., Efstathiou G., Elsner F., Enßlin T. A., Eriksen H. K., Falgarone E., Finelli F., Forni O., Frailis M., Fraisse A. A., Franceschi E., Frejsel A., Fukui Y., Galeotta S., Galli S., Ganga K., Ghosh T., Giard M., Gjerløw E., González-Nuevo J., Górski K. M., Gregorio A., Grenier I. A., Gruppuso A., Hansen F. K., Hanson D., Harrison D. L., Henrot-Versillé S., Hernández-Monteagudo C., Herranz D., Hildebrandt S. R., Hivon E., Hobson M., Holmes W. A., Hovest W., Huppenberger K. M., Hurier G., Jaffe A. H., Jaffe T. R., Jones W. C., Juvela M., Keihänen E., Keskitalo R., Kisner T. S., Kneissl R., Knoche J., Kunz M., Kurki-Suonio H., Lagache G., Lamarre J.-M., Lasenby A., Lattanzi M., Lawrence C. R., Leonardi R., Levrier F., Liguori M., Lilje P. B., Linden-Vørnle M., López-Caniego M., Lubin P. M., Macías-Pérez J. F., Maffei B., Maino D., Mandolesi N., Maris M., Marshall D. J., Martin P. G., Martínez-González E., Masi S., Matarrese S., Mazzotta P., Melchiorri A., Mendes L., Mennella A., Migliaccio M., Miville-Deschênes M.-A., Moneti A., Montier L., Morgante G., Mortlock D., Munshi D., Murphy J. A., Naselsky P., Natoli P., Nørgaard-Nielsen H. U., Novikov D., Novikov I., Oxborrow C. A., Pagano L., Pajot F., Paladini R., Paoletti D., Pasian F., Perdereau O., Perotto L., Perrotta F., Pettorino V., Piacentini F., Piat M., Plaszczynski S., Pointecouteau E., Polenta G., Popa L., Pratt G. W., Prunet S., Puget J.-L., Rachen J. P., Reach W. T., Rebolo R., Reinecke M., Remazeilles M., Renault C., Ristorcelli I., Rocha G., Roudier G., Rusholme B., Sandri M., Santos D., Scott D., Spencer L. D., Stolyarov V., Strong A. W., Sudiwala R., Sunyaev R., Sutton D., Suur-Uski A.-S., Sygnet J.-F., Tauber J. A., Terenzi L., Tibaldo L., Toffolatti L., Tomasi M., Tristram M., Tucci M., Umata G., Valenziano L., Valiviita J., Van Tent B., Vielva P., Villa F., Wade L. A., Wandelt B. D., Wehus I. K., Yvon D., Zacchei A., Zonca A. Planck intermediate results. XXVIII. Interstellar gas and dust in the Chamaeleon clouds as seen by Fermi LAT and Planck // *A&A*. X 2015. 582. A31.
- Planck Collaboration*, Abergel A., Ade P. A. R., Aghanim N., Alves M. I. R., Aniano G., Armitage-Caplan C., Arnaud M., Ashdown M., Atrio-Barandela F., *al. et.* Planck 2013 results. XI. All-sky model of thermal dust emission // *A&A*. XI 2014. 571. A11.
- Planck Collaboration*, Adam R., Ade P. A. R., Aghanim N., Alves M. I. R., Arnaud M., Ashdown M., Aumont J., Baccigalupi C., Banday A. J., *al. et.* Planck 2015 results. X. Diffuse component separation: Foreground maps // *A&A*. IX 2016. 594. A10.
- Plaskett J. S., Pearce J. A. Determination of the K-term, the solar motion, and the galactic rotation from the radial velocities of 849 O to B7 stars // *Publications of the American Astronomical Society*. 7. 1933. 225–226. (Publications of the American Astronomical Society).

- Puspitarini L., Lallement R.* Distance to northern high-latitude HI shells // *A&A*. IX 2012. 545. A21.
- Puspitarini L., Lallement R., Babusiaux C., Chen H.-C., Bonifacio P., Sbordone L., Caffau E., Duffau S., Hill V., Monreal-Ibero A., Royer F., Arenou F., Peralta R., Drew J. E., Bonito R., Lopez-Santiago J., Alfaro E. J., Bensby T., Bragaglia A., Flaccomio E., Lanzafame A. C., Pancino E., Recio-Blanco A., Smiljanic R., Costado M. T., Lardo C., de Laverny P., Zwitter T.* The Gaia-ESO Survey: Extracting diffuse interstellar bands from cool star spectra. DIB-based interstellar medium line-of-sight structures at the kpc scale // *A&A*. I 2015. 573. A35.
- Puspitarini L., Lallement R., Chen H.-C.* Automated measurements of diffuse interstellar bands in early-type star spectra. Correlations with the color excess // *A&A*. VII 2013. 555. A25.
- Queiroz A. B. A., Anders F., Santiago B. X., Chiappini C., Steinmetz M., Dal Ponte M., Stassun K. G., da Costa L. N., Maia M. A. G., Crestani J., Beers T. C., Fernández-Trincado J. G., García-Hernández D. A., Roman-Lopes A., Zamora O.* StarHorse: a Bayesian tool for determining stellar masses, ages, distances, and extinctions for field stars // *MNRAS*. V 2018. 476. 2556–2583.
- Rachford B. L., Snow T. P., Tumlinson J., Shull J. M., Blair W. P., Ferlet R., Friedman S. D., Gry C., Jenkins E. B., Morton D. C., Savage B. D., Sonnentrucker P., Vidal-Madjar A., Welty D. E., York D. G.* A Far Ultraviolet Spectroscopic Explorer Survey of Interstellar Molecular Hydrogen in Translucent Clouds // *ApJ*. IX 2002. 577. 221–244.
- Raimond S., Lallement R., Vergely J. L., Babusiaux C., Eyer L.* A southern hemisphere survey of the 5780 and 6284 Å diffuse interstellar bands: correlation with the extinction // *A&A*. VIII 2012. 544. A136.
- Reber G.* Cosmic Static // *Proceedings of the IRE*. II 1940. 28. 68–70.
- Remy Q., Grenier I. A., Marshall D. J., Casandjian J. M.* Cosmic-rays, gas, and dust in nearby anti-centre clouds. III. Dust extinction, emission, and grain properties // *A&A*. VIII 2018. 616. A71.
- Ruiterkamp R., Cox N. L. J., Spaans M., Kaper L., Foing B. H., Salama F., Ehrenfreund P.* PAH charge state distribution and DIB carriers: Implications from the line of sight toward ζ ASTROBJ HD 147889/ ζ ASTROBJ // *A&A*. III 2005. 432. 515–529.
- Russell H. N.* The analysis of spectra and its application in astronomy (George Darwin Lecture, 1935) // *MNRAS*. VI 1935. 95. 610–636.

- Salama F., Bakes E. L. O., Allamandola L. J., Tielens A. G. G. M.* Assessment of the Polycyclic Aromatic Hydrocarbon–Diffuse Interstellar Band Proposal // *ApJ*. II 1996. 458. 621.
- Salama F., Ehrenfreund P.* A Critical Review of PAHs as DIB Carriers - Progress and Open Questions // *The Diffuse Interstellar Bands*. 297. II 2014. 364–369. (IAU Symposium).
- Salama F., Galazutdinov G. A., Krełowski J., Allamandola L. J., Musaev F. A.* Polycyclic Aromatic Hydrocarbons and the Diffuse Interstellar Bands: A Survey // *ApJ*. XI 1999. 526. 265–273.
- Salama F., Galazutdinov G. A., Krełowski J., Biennier L., Beletsky Y., Song I.-O.* Polycyclic Aromatic Hydrocarbons and the Diffuse Interstellar Bands: A Survey // *ApJ*. II 2011. 728. 154.
- Sale S. E., Magorrian J.* Three-dimensional extinction mapping using Gaussian random fields // *MNRAS*. XI 2014. 445. 256–269.
- Santiago B. X., Brauer D. E., Anders F., Chiappini C., Queiroz A. B., Girardi L., Rocha-Pinto H. J., Balbinot E., da Costa L. N., Maia M. A. G., Schultheis M., Steinmetz M., Miglio A., Montalbán J., Schneider D. P., Beers T. C., Frinchaboy P. M., Lee Y. S., Zasowski G.* Spectro-photometric distances to stars: A general purpose Bayesian approach // *A&A*. I 2016. 585. A42.
- Sarre P. J.* Diffuse bands in emission // *Nature*. V 1991. 351. 356.
- Sarre P. J.* The diffuse interstellar bands: A major problem in astronomical spectroscopy // *Journal of Molecular Spectroscopy*. VII 2006. 238. 1–10.
- Sarre P. J., Miles J. R., Kerr T. H., Hibbins R. E., Fossey S. J., Somerville W. B.* Resolution of intrinsic fine structure in spectra of narrow diffuse interstellar bands // *MNRAS*. XI 1995. 277. L41–L43.
- Savage B. D., Mathis J. S.* Observed properties of interstellar dust // *ARA&A*. 1979. 17. 73–111.
- Schlafly E. F., Green G., Finkbeiner D. P., Rix H.-W., Bell E. F., Burgett W. S., Chambers K. C., Draper P. W., Hodapp K. W., Kaiser N., Magnier E. A., Martin N. F., Metcalfe N., Price P. A., Tonry J. L.* A Large Catalog of Accurate Distances to Molecular Clouds from PS1 Photometry // *ApJ*. V 2014. 786. 29.
- Schmidt M. R., Krełowski J., Galazutdinov G. A., Zhao D., Haddad M. A., Ubachs W., Linnartz H.* Detection of vibronic bands of C₃ in a translucent cloud towards HD 169454 // *MNRAS*. VI 2014. 441. 1134–1146.

- Seab C. G., Snow T. P. Jr. A search for diffuse interstellar bands in the ultraviolet // *ApJ*. VIII 1985. 295. 485–489.
- Sellgren K., Werner M. W., Ingalls J. G., Smith J. D. T., Carleton T. M., Joblin C. C₆₀ in Reflection Nebulae // *ApJ*. X 2010. 722. L54–L57.
- Sharples R., Bender R., Agudo Berbel A., Bezawada N., Castillo R., Cirasuolo M., Davidson G., Davies R., Dubbeldam M., Fairley A., Finger G., Förster Schreiber N., Gonte F., Hess A., Jung I., Lewis I., Lizon J.-L., Muschelok B., Pasquini L., Pirard J., Popovic D., Ramsay S., Rees P., Richter J., Riquelme M., Rodrigues M., Saviane I., Schlichter J., Schmidtbreick L., Segovia A., Smette A., Szeifert T., van Kesteren A., Wegner M., Wiezorrek E. First Light for the KMOS Multi-Object Integral-Field Spectrometer // *The Messenger*. III 2013. 151. 21–23.
- Skrutskie M. F., Cutri R. M., Stiening R., Weinberg M. D., Schneider S., Carpenter J. M., Beichman C., Capps R., Chester T., Elias J., Huchra J., Liebert J., Lonsdale C., Monet D. G., Price S., Seitzer P., Jarrett T., Kirkpatrick J. D., Gizis J. E., Howard E., Evans T., Fowler J., Fullmer L., Hurt R., Light R., Kopan E. L., Marsh K. A., McCallon H. L., Tam R., Van Dyk S., Wheelock S. The Two Micron All Sky Survey (2MASS) // *AJ*. II 2006. 131. 1163–1183.
- Slyk K., Galazutdinov G. A., Musaev F. A., Bondar A. V., Schmidt M. R., Krelowski J. A search for fine structure inside high resolution profiles of weak diffuse interstellar bands // *A&A*. III 2006. 448. 221–229.
- Smith K. T., Fossey S. J., Cordiner M. A., Sarre P. J., Smith A. M., Bell T. A., Viti S. Small-scale structure in the interstellar medium: time-varying interstellar absorption towards κ Velorum // *MNRAS*. II 2013. 429. 939–953.
- Smoker J., Haddad N., Iwert O., Deiries S., Modigliani A., Randall S., D’Odorico S., James G., Lo Curto G., Robert P., Pasquini L., Downing M., Ledoux C., Martayan C., Dall T., Vinther J., Melo C., Fox A., Pritchard J., Baade D., Dekker H. A Tenth Birthday Present for UVES: A CCD Upgrade of the Red Arm // *The Messenger*. XII 2009. 138. 8–9.
- Diffuse Interstellar Bands: Past and Present. // . 297. II 2014. 3–12. (IAU Symposium).
- Snow T. P., Destree J. D. The Diffuse Interstellar Bands in History and in the UV // *EAS Publications Series*. 46. III 2011. 341–347. (EAS Publications Series).
- Snow T. P., McCall B. J. Diffuse Atomic and Molecular Clouds // *ARA&A*. IX 2006a. 44. 367–414.
- Snow T. P., McCall B. J. Diffuse Atomic and Molecular Clouds // *ARA&A*. IX 2006b. 44. 367–414.

- Snow T. P., Welty D. E., Thorburn J., Hobbs L. M., McCall B. J., Sonnentrucker P., York D. G.* Unusually Weak Diffuse Interstellar Bands toward HD 62542 // *ApJ*. VII 2002. 573. 670–677.
- Snow T. P. Jr., Cohen J. G.* Diffuse interstellar band formation in dense clouds // *ApJ*. XII 1974. 194. 313–322.
- Sollerman J., Cox N., Mattila S., Ehrenfreund P., Kaper L., Leibundgut B., Lundqvist P.* Diffuse Interstellar Bands in μ ASTROBJ NGC 1448/ μ ASTROBJ // *A&A*. I 2005. 429. 559–567.
- Sonnentrucker P., Cami J., Ehrenfreund P., Foing B. H.* The diffuse interstellar bands at 5797, 6379 and 6613 Angstroms. Ionization properties of the carriers // *A&A*. XI 1997. 327. 1215–1221.
- Sonnentrucker P., Foing B. H., Breitfellner M., Ehrenfreund P.* Distribution of gas, dust and the lambda 6613 Å DIB carrier in the Perseus OB2 association // *A&A*. VI 1999. 346. 936–946.
- Sonnentrucker P., Welty D. E., Thorburn J. A., York D. G.* Abundances and Behavior of ^{12}CO , ^{13}CO , and C_2 in Translucent Sight Lines // *ApJS*. I 2007a. 168. 58–99.
- Sonnentrucker P., Welty D. E., Thorburn J. A., York D. G.* Abundances and Behavior of ^{12}CO , ^{13}CO , and C_2 in Translucent Sight Lines // *ApJS*. I 2007b. 168. 58–99.
- Sonnentrucker P., York B., Hobbs L. M., Welty D. E., Friedman S. D., Dahlstrom J., Snow T. P., York D. G.* A Modern Census of the Broadest Diffuse Interstellar Bands // *ApJS*. VIII 2018. 237. 40.
- Sorokin P., Glowina J. H.* Hydrogen Molecules in PDRs: Carriers of the Diffuse Interstellar Bands (DIBs) // *H2 in Space*. 1999.
- Spieler S., Kuhn M., Postler J., Simpson M., Wester R., Scheier P., Ubachs W., Bacalla X., Bouwman J., Linnartz H.* $\{\{\{\text{C}\}\}\}^{\{60\}\{+\}}$ and the Diffuse Interstellar Bands: An Independent Laboratory Check // *ApJ*. IX 2017. 846. 168.
- Steglich M., Bouwman J., Huisken F., Henning T.* Can Neutral and Ionized Polycyclic Aromatic Hydrocarbons Be Carriers of the Ultraviolet Extinction Bump and the Diffuse Interstellar Bands? // *ApJ*. XI 2011. 742. 2.
- Steinacker J., Bacmann A., Henning T., Heigl S.* Prestellar core modeling in the presence of a filament. The dense heart of L1689B // *A&A*. VIII 2016. 593. A6.

- Steinicke W.* William Herschel's 'Hole in the Sky' and the discovery of dark nebulae // *Journal of Astronomical History and Heritage*. XII 2016. 19. 305–326.
- Strom K. M., Strom S. E., Carrasco L., Vrba F. J.* M78: an active region of star formation in the dark cloud Lynds 1630. // *ApJ*. III 1975. 196. 489–501.
- Swings P.* A note on molecular absorption in interstellar space // *MNRAS*. I 1937. 97. 212.
- Swings P., Rosenfeld L.* Considerations Regarding Interstellar Molecules // *ApJ*. XI 1937. 86. 483–486.
- Taylor M. B.* TOPCAT STIL: Starlink Table/VOTable Processing Software // *Astronomical Data Analysis Software and Systems XIV*. 347. XII 2005. 29. (Astronomical Society of the Pacific Conference Series).
- Thorburn J. A., Hobbs L. M., McCall B. J., Oka T., Welty D. E., Friedman S. D., Snow T. P., Sonnentrucker P., York D. G.* Some Diffuse Interstellar Bands Related to Interstellar C₂ Molecules // *ApJ*. II 2003. 584. 339–356.
- Tielens A. G. G. M.* Interstellar Polycyclic Aromatic Hydrocarbon Molecules // *ARA&A*. IX 2008. 46. 289–337.
- Tielens A. G. G. M.* Diffuse Interstellar Bands: The Way Forward // *The Diffuse Interstellar Bands*. 297. II 2014. 399–411. (IAU Symposium).
- Trumpler R. J.* Absorption of Light in the Galactic System // *PASP*. VIII 1930. 42. 214.
- Tuairisg S. Ó., Cami J., Foing B. H., Sonnentrucker P., Ehrenfreund P.* A deep echelle survey and new analysis of diffuse interstellar bands // *A&AS*. III 2000. 142. 225–238.
- Valencic L. A., Clayton G. C., Gordon K. D.* Ultraviolet Extinction Properties in the Milky Way // *ApJ*. XII 2004. 616. 912–924.
- Van Winckel H.* Why is the Red Rectangle Unique? // *The Diffuse Interstellar Bands*. 297. II 2014. 180–186. (IAU Symposium).
- Vergely J.-L., Valette B., Lallement R., Raimond S.* Spatial distribution of interstellar dust in the Sun's vicinity. Comparison with neutral sodium-bearing gas // *A&A*. VII 2010. 518. A31.
- Vos D. A. I., Cox N. L. J., Kaper L., Spaans M., Ehrenfreund P.* Diffuse interstellar bands in Upper Scorpius: probing variations in the DIB spectrum due to changing environmental conditions // *A&A*. IX 2011. 533. A129.

- Vuong M. H., Foing B. H. Dehydrogenation of polycyclic aromatic hydrocarbons in the diffuse interstellar medium // *A&A*. XI 2000. 363. L5–L8.
- Walker G. A. H., Bohlender D. A., Maier J. P., Campbell E. K. Identification of More Interstellar C₆₀⁺ Bands // *ApJ*. X 2015. 812. L8.
- Walker G. A. H., Campbell E. K., Maier J. P., Bohlender D. The 9577 and 9632 Å Diffuse Interstellar Bands: $\{\{\rm{C}}\}\}_{60}^{+}$ as Carrier // *ApJ*. VII 2017. 843. 56.
- Walker G. A. H., Campbell E. K., Maier J. P., Bohlender D., Malo L. Gas-phase Absorptions of C₆₀⁺: A New Comparison with Astronomical Measurements // *ApJ*. XI 2016. 831. 130.
- Walker G. A. H., Webster A. S., Bohlender D. A., Krelowski J. Profiles of the λ 6196 and λ 6379 Diffuse Interstellar Bands // *ApJ*. XI 2001. 561. 272–281.
- Wallerstein G., Cardelli J. A. The diffuse interstellar features at 5780 and 5797 Å in star-formation regions // *AJ*. VI 1987. 93. 1522–1526.
- Wampler E. J. Scanner Observations of λ 4430 // *ApJ*. VI 1966. 144. 921.
- Wegner W. The total-to-selective extinction ratio determined from near IR photometry of OB stars // *Astronomische Nachrichten*. 2003. 324. 219–237.
- Weinreb S., Barrett A. H., Meeks M. L., Henry J. C. Radio Observations of OH in the Interstellar Medium // *Nature*. XI 1963. 200. 829–831.
- Welty D. E., Federman S. R., Gredel R., Thorburn J. A., Lambert D. L. VLT UVES Observations of Interstellar Molecules and Diffuse Bands in the Magellanic Clouds // *ApJS*. VII 2006. 165. 138–172.
- Welty D. E., Hobbs L. M. A High-Resolution Survey of Interstellar K I Absorption // *ApJS*. IV 2001. 133. 345–393.
- Westerlund B. E., Krelowski J. The division of diffuse interstellar bands into families // *A&A*. VII 1989. 218. 216–220.
- Whittet D. C. B. Dust in the galactic environment. 2003.
- Willner S. P., Puetter R. C., Russell R. W., Soifer B. T. Unidentified infrared spectral features // *Ap&SS*. IX 1979. 65. 95–101.
- Wilson J. C., Hearty E., Skrutskie M. F., Majewski S., Schiavon R., Eisenstein D., Gunn J., Blank B., Henderson C., Smee S., Barkhouser R., Harding A., Fitzgerald G., Stolberg T., Arns J., Nelson M., Brunner S., Burton A., Walker E., Lam C., Maseman P., Barr J., Leger F., Carey L., MacDonald N., Horne T., Young E., Rieke G., Rieke M., O'Brien T., Hope S., Krakula J., Crane J., Zhao B., Carr

- M., Harrison C., Stoll R., Vernieri M. A., Holtzman J., Shetrone M., Allende-Prieto C., Johnson J., Frinchaboy P., Zasowski G., Bizyaev D., Gillespie B., Weinberg D.* The Apache Point Observatory Galactic Evolution Experiment (APOGEE) high-resolution near-infrared multi-object fiber spectrograph // Society of Photo-Optical Instrumentation Engineers (SPIE) Conference Series. 7735. VII 2010. 1. (Society of Photo-Optical Instrumentation Engineers (SPIE) Conference Series).
- Wilson R. W., Jefferts K. B., Penzias A. A.* Carbon Monoxide in the Orion Nebula // *ApJ*. VII 1970. 161. L43.
- Xiang F. Y., Li A., Zhong J. X.* Diffuse Interstellar Bands and the Ultraviolet Extinction Curves: The Missing Link Revisited // *ApJ*. I 2017. 835. 107.
- Young R. K.* The Calcium Lines H and K in Early Type Stars // Publications of the Dominion Astrophysical Observatory Victoria. 1920. 1.
- Zasowski G., Johnson J. A., Frinchaboy P. M., Majewski S. R., Nidever D. L., Rocha Pinto H. J., Girardi L., Andrews B., Chojnowski S. D., Cudworth K. M., Jackson K., Munn J., Skrutskie M. F., Beaton R. L., Blake C. H., Covey K., Deshpande R., Epstein C., Fabbian D., Fleming S. W., Garcia Hernandez D. A., Herrero A., Mahadevan S., Mészáros S., Schultheis M., Sellgren K., Terrien R., van Saders J., Allende Prieto C., Bizyaev D., Burton A., Cunha K., da Costa L. N., Hasselquist S., Hearty F., Holtzman J., García Pérez A. E., Maia M. A. G., O'Connell R. W., O'Donnell C., Pinsonneault M., Santiago B. X., Schiavon R. P., Shetrone M., Smith V., Wilson J. C.* Target Selection for the Apache Point Observatory Galactic Evolution Experiment (APOGEE) // *AJ*. X 2013. 146. 81.
- Zasowski G., Ménard B., Bizyaev D., García-Hernández D. A., García Pérez A. E., Hayden M. R., Holtzman J., Johnson J. A., Kinemuchi K., Majewski S. R., Nidever D. L., Shetrone M., Wilson J. C.* Mapping the Interstellar Medium with Near-infrared Diffuse Interstellar Bands // *ApJ*. I 2015. 798. 35.
- Zhang Y., Kwok S.* Detection of C₆₀ in the Protoplanetary Nebula IRAS 01005+7910 // *ApJ*. IV 2011. 730. 126.
- van Dishoeck E. F., Black J. H.* The excitation of interstellar C₂ // *ApJ*. VII 1982. 258. 533–547.
- van Dishoeck E. F., Black J. H.* Comprehensive models of diffuse interstellar clouds - Physical conditions and molecular abundances // *ApJS*. IX 1986. 62. 109–145.
- van Leeuwen F.* Validation of the new Hipparcos reduction // *A&A*. XI 2007. 474. 653–664.

- van Loon J. T., Bailey M., Tatton B. L., Maíz Apellániz J., Crowther P. A., de Koter A., Evans C. J., Hénault-Brunet V., Howarth I. D., Richter P., Sana H., Simón-Díaz S., Taylor W., Walborn N. R.* The VLT-FLAMES Tarantula Survey. IX. The interstellar medium seen through diffuse interstellar bands and neutral sodium // *A&A.* II 2013. 550. A108.
- van der Zwet G. P., Allamandola L. J.* Polycyclic aromatic hydrocarbons and the diffuse interstellar bands // *A&A.* V 1985. 146. 76–80.

RÉSUMÉ

Les bandes interstellaires diffuses (DIBs) sont une série d'absorptions détectées dans les spectres optiques et infrarouges des objets galactiques et extra-galactiques. Depuis la détection des premières DIBs optiques au début des années 1920, leur nombre a progressivement augmenté suite à l'évolution de l'instrumentation spectroscopique et dépasse maintenant les 500 bandes. Cependant, aucune des centaines de bandes n'a pu être identifiée avec certitude avec un porteur spécifique. Le consensus actuel sur leur nature affirme qu'il s'agit très probablement de macromolécules riches en carbone. Le cycle de la matière interstellaire, de la formation des étoiles à la reconstitution du milieu interstellaire (MIS) par éjection stellaire, ne peut être pleinement compris sans une clarification des sites de formation et de destruction de cette forme de matière organique et son rôle potentiel dans l'émergence de la vie.

En utilisant les spectres proche-infrarouges (NIR) de haute qualité du relevé SDSS/APOGEE, les spectres optiques de haute résolution et haut signal sur bruit du relevé optique EDIBLES au VLT, et les données NIR d'un programme ciblé avec l'instrument KMOS au VLT, les principaux produits de ce travail de thèse sont :

- la production de nouveaux catalogues de DIBs infrarouges et l'identification de nouvelles DIBs,
- la première tomographie en 3D d'une DIB infrarouge dans un nuage dense,
- l'établissement des liens supplémentaires entre les conditions d'ionisation, l'opacité de la poussière, le contenu moléculaire et la force des DIBs,
- la caractérisation de nouveaux profils spectraux d'une trentaine de DIBs, dont l'intéressante série de bandes associées à la molécule C₂.

MOTS CLÉS

milieu interstellaire - profils - nuages - raies - bandes - spectroscopie

ABSTRACT

The diffuse interstellar bands (DIBs) are a series of absorption features that are detected in the optical and infrared spectra of Galactic and extra-Galactic objects. Since the detection of the first DIB in the optical waveband in the early 1920s, their number has progressively increased following evolving spectroscopic instrumentation and is now exceeding 500 bands. Despite decades-long efforts, none of the DIBs have been identified with any known species with absolute certainty. The current consensus on their nature claims that they are most likely large carbon-rich molecules. The life cycle of interstellar matter from star formation to interstellar medium (ISM) replenishment by stellar ejecta cannot be fully understood without a clarification of the formation and destruction sites of this form of organic matter and its potential role in the emergence of life.

Using the high-quality spectra of the SDSS/APOGEE near infrared (NIR) survey, the high-resolution and signal spectra of the EDIBLES optical survey at the VLT, and the NIR data of a specific program recorded with KMOS at the VLT, the main products of this thesis work are:

- new extended catalogs of NIR DIBs and the identification of potential new DIBs,
- the first 3D tomography of a DIB in a single dense cloud,
- additional links between ionizing conditions, opacity of dust, molecular content and DIB strength,
- new spectral profiles of about 30 DIBs, including the interesting series of weak DIBs associated with C₂ molecule.

KEYWORDS

interstellar medium - profiles - clouds - lines - bands - spectroscopy